AUGUST 2022

AJNR

VOLUME 43 • PP 1079–1227

AJNR

AMERICAN JOURNAL OF NEURORADIOLOGY

AUGUST 2022
VOLUME 43
NUMBER 8
WWW.AJNR.ORG

THE JOURNAL OF DIAGNOSTIC AND INTERVENTIONAL NEURORADIOLOGY

Radiomic features of progression-free survival in glioblastoma
Neuroimaging of CHANTER syndrome
Treatment of PICA aneurysms with intrasaccular flow disruption
Imaging of craniofacial giant cell granulomas

Official Journal ASNR • ASFNR • ASHNR • ASPNR • ASSR

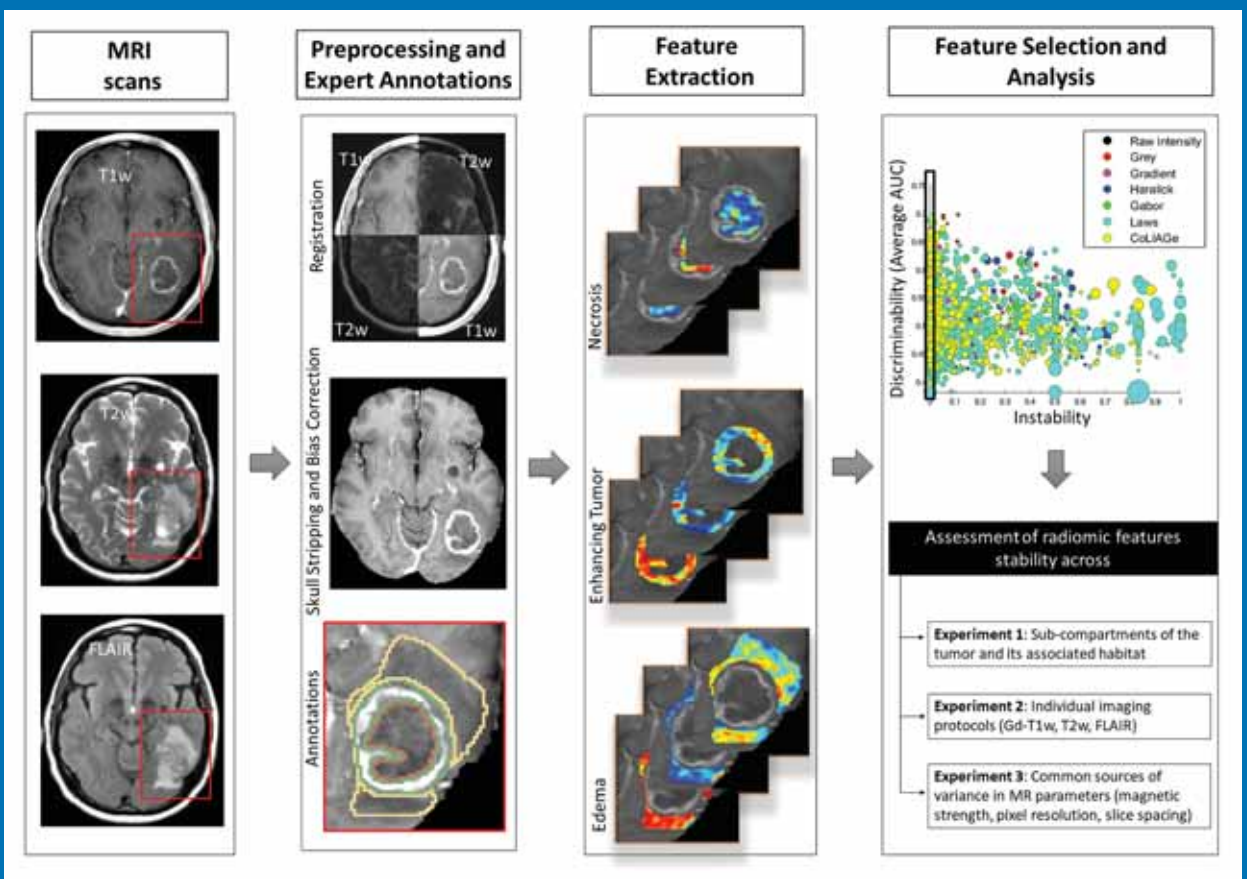

Introducing FRED™ X™

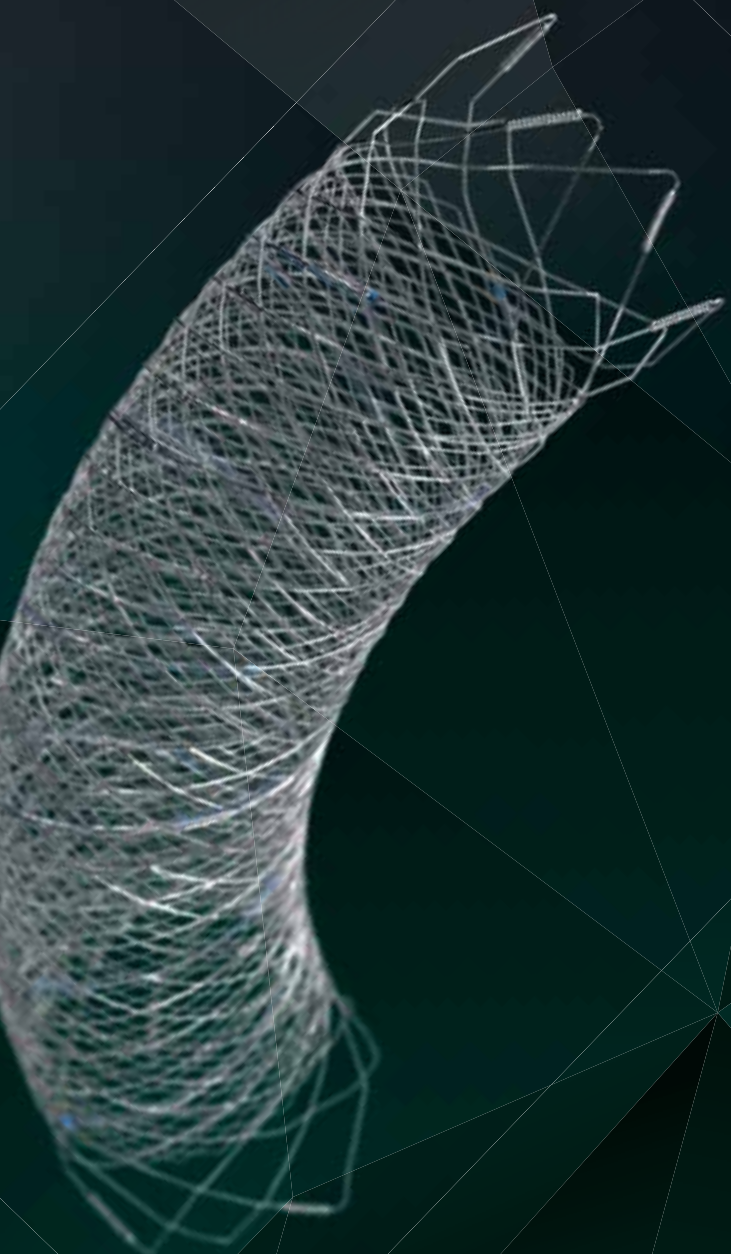

THE NEXT ADVANCEMENT
IN FLOW DIVERSION TECHNOLOGY

The FRED™ X Flow Diverter features the same precise placement and immediate opening of the FRED™ Device, now with X Technology. X Technology is a covalently bonded, nanoscale surface treatment, designed to:

- ***Reduce material thrombogenicity[1]***
- ***Maintain natural vessel healing response[2,3,4]***
- ***Improve device deliverability and resheathing[1]***

The only FDA PMA approved portfolio with a 0.021″ delivery system for smaller device sizes, and no distal lead wire.

MicroVention™ TERUMO

For more information, contact your local MicroVention sales representative or visit our website. ***www.microvention.com***

* Data is derived from in vivo and ex vitro testing and may not be representative of clinical performance.

1. Data on file
2. Tanaka M et al. Design of biocompatible and biodegradable polymers based on intermediate water concept. Polymer Journal. 2015;47:114-121.
3. Tanaka M et al. Blood compatible aspects of poly(2-methoxyethylacrylate) (PMEA) – relationship between protein adsorption and platelet adhesion on PMEA surface. Biomaterials. 2000;21:1471-1481.
4. Schiel L et al. X Coating™: A new biopassive polymer coating. Canadian Perfusion Canadienne. June 2001;11(2):9.

Indications for Use: The FRED X System is indicated for use in the internal carotid artery from the petrous segment to the terminus for the endovascular treatment of adult patients (22 years of age or older) with wide-necked (neck width 4 mm or dome-to-neck ratio < 2) saccular or fusiform intracranial aneurysms arising from a parent vessel with a diameter 2.0 mm and 5.0 mm.

Rx Only: Federal (United States) law restricts this device to sale by or on the order of a physician.

MICROVENTION, FRED and HEADWAY are registered trademarks of MicroVention, Inc. in the United States and other jurisdictions. Stylized X is a trademark of MicroVention, Inc. © 2022 MicroVention, Inc. MM1222 US 02/22

WEB™ 17

Aneurysm Embolization System

LOWER PROFILE

NEW SIZES

MORE ACCESS OPTIONS

INDICATIONS FOR USE:
The WEB Aneurysm Embolization System is intended for the endovascular embolization of ruptured and unruptured intracranial aneurysms and other neurovascular abnormalities such as arteriovenous fistulae (AVF). The WEB Aneurysm Embolization System is also intended for vascular occlusion of blood vessels within the neurovascular system to permanently obstruct blood flow to an aneurysm or other vascular malformation

POTENTIAL COMPLICATIONS:
Potential complications include but are not limited to the following: hematoma at the site of entry, aneurysm rupture, emboli, vessel perforation, parent artery occlusion, hemorrhage, ischemia, vasospasm, clot formation, device migration or misplacement, premature or difficult device detachment, non-detachment, incomplete aneurysm filling, revascularization, post-embolization syndrome, and neurological deficits including stroke and death. For complete indications, potential complications, warnings, precautions, and instructions, see instructions for use (IFU provided with the device).

VIA 21, 27, 33 - The VIA Microcatheter is intended for the introduction of interventional devices (such as the WEB device/stents/flow diverters) and infusion of diagnostic agents (such as contrast media) into the neuro, peripheral, and coronary vasculature.

VIA 17,17 Preshaped - The VIA Microcatheter is intended for the introduction of interventional devices (such as the WEB device/stents/flow diverters) and infusion of diagnostic agents (such as contrast media) into the neuro, peripheral, and coronary vasculature.

The VIA Microcatheter is contraindicated for use with liquid embolic materials, such as n-butyl 2-cyanoacrylate or ethylene vinyl alcohol & DMSO (dimethyl sulfoxide).

The device should only be used by physicians who have undergone training in all aspects of the WEB Aneurysm Embolization System procedure as prescribed by the manufacturer.

RX Only: Federal law restricts this device to sale by or on the order of a physician.

For healthcare professional intended use only.

MicroVention™
TERUMO

MicroVention Worldwide Innovaton Center — PH +1.714.247.8000

35 Enterprise
Aliso Viejo, CA 92656 USA

MicroVention UK Limited — PH +44 (0) 191 258 6777
MicroVention Europe, S.A.R.L. — PH +33 (1) 39 21 77 46
MicroVention Deutschland GmbH — PH +49 211 210 798-0
Website — microvention.com

CE 0297

WEB™ and VIA™ are registered trademarks of Sequent Medical, Inc. in the United States.

©2021 MicroVention, Inc. MM1184 WW 11/2021

multihance®
(gadobenate dimeglumine)
injection, 529 mg/mL

TRUST EARNED

What does seeing better with MultiHance® mean?[1-4*]

MultiHance® demonstrated significantly improved visualization and contrast enhancement of CNS lesions when compared with Gadavist® at 0.1 mmol/kg.[1†]

- The 0.1 mmol/kg dose of MultiHance demonstrated consistently better lesion visualization for all readers compared to all tested MR contrast agents.[1-4]
- 3 blinded independent readers reported superiority for MultiHance in significantly (*P*=.0001) more patients for all evaluated end points. The opinions of the 3 readers were identical for 61.9%–73.5% of the patients, resulting in values of 0.414–0.629 for inter-reader agreement.

The individuals who appear are for illustrative purposes. All persons depicted are models and not real patients.
Please see Brief Summary of Prescribing Information including Boxed Warning on adjacent page.
*MRI imaging of the CNS in adult and pediatric patients to visualize lesions with abnormal BBB or abnormal vascularity of the brain, spine and associated tissues or to evaluate adults with known or suspected renal or aorto-ilio-femoral occlusive vascular disease.

MultiHance® (gadobenate dimeglumine) injection, 529 mg/mL and
MultiHance® Multipack™ (gadobenate dimeglumine) injection, 529 mg/mL

Indications and Usage:
MultiHance® (gadobenate dimeglumine) injection, 529 mg/mL is a gadolinium-based contrast agent indicated for intravenous use in:
- Magnetic resonance imaging (MRI) of the central nervous system (CNS) in adults and pediatric patients (including term neonates) to visualize lesions with abnormal blood-brain barrier or abnormal vascularity of the brain, spine, and associated tissues and
- Magnetic resonance angiography (MRA) to evaluate adults with known or suspected renal or aorto-ilio-femoral occlusive vascular disease

IMPORTANT SAFETY INFORMATION:

WARNING: NEPHROGENIC SYSTEMIC FIBROSIS

Gadolinium-based contrast agents (GBCAs) increase the risk for NSF among patients with impaired elimination of the drugs. Avoid use of GBCAs in these patients unless the diagnostic information is essential and not available with non-contrasted MRI or other modalities. NSF may result in fatal or debilitating systemic fibrosis affecting the skin, muscle and internal organs.
- **The risk for NSF appears highest among patients with:**
  - **chronic, severe kidney disease (GFR < 30 mL/min/1.73m²), or**
  - **acute kidney injury.**
- **Screen patients for acute kidney injury and other conditions that may reduce renal function. For patients at risk for chronically reduced renal function (e.g. age > 60 years, hypertension or diabetes), estimate the glomerular filtration rate (GFR) through laboratory testing.**
- **For patients at highest risk for NSF, do not exceed the recommended MultiHance dose and allow a sufficient period of time for elimination of the drug from the body prior to re-administration.**

CONTRAINDICATIONS
MultiHance is contraindicated in patients with known allergic or hypersensitivity reactions to gadolinium-based contrast agents.

WARNINGS AND PRECAUTIONS
Nephrogenic Systemic Fibrosis: NSF has occurred in patients with impaired elimination of GBCAs. Higher than recommended dosing or repeated dosing appears to increase risk.
Hypersensitivity Reactions: Anaphylactic and anaphylactoid reactions have been reported, involving cardiovascular, respiratory, and/or cutaneous manifestations. Some patients experienced circulatory collapse and died. In most cases, initial symptoms occurred within minutes of MultiHance administration and resolved with prompt emergency treatment. Consider the risk for hypersensitivity reactions, especially in patients with a history of hypersensitivity reactions or a history of asthma or other allergic disorders.
Gadolinium Retention: Gadolinium is retained for months or years in several organs. The highest concentrations have been identified in the bone, followed by brain, skin, kidney, liver, and spleen. At equivalent doses, retention varies among the linear agents. Retention is lowest and similar among the macrocyclic GBCAs. Consequences of gadolinium retention in the brain have not been established, but they have been established in the skin and other organs in patients with impaired renal function. Minimize repetitive GBCA imaging studies, particularly closely spaced studies when possible.
Acute Renal Failure: In patients with renal insufficiency, acute renal failure requiring dialysis or worsening renal function have occurred with the use of GBCAs. The risk of renal failure may increase with increasing dose of the contrast agent. Screen all patients for renal dysfunction by obtaining a history and/or laboratory tests.
Extravasation and Injection Site Reactions: Extravasation of MultiHance may lead to injection site reactions, characterized by local pain or burning sensation, swelling, blistering, and necrosis. Exercise caution to avoid local extravasation during intravenous administration of MultiHance.
Cardiac Arrhythmias: Cardiac arrhythmias have been observed in patients receiving MultiHance in clinical trials. Assess patients for underlying conditions

or medications that predispose to arrhythmias. The effects on QTc by MultiHance dose, other drugs, and medical conditions were not systematically studied.
Interference with Visualization of Certain Lesions: Certain lesions seen on non-contrast images may not be seen on contrast images. Exercise caution when interpreting contrast MR images in the absence of companion non-contrast MR images.

ADVERSE REACTIONS
The most commonly reported adverse reactions are nausea (1.3%) and headache (1.2%).

USE IN SPECIFIC POPULATIONS
Pregnancy: GBCAs cross the human placenta and result in fetal exposure and gadolinium retention. Use only if imaging is essential during pregnancy and cannot be delayed.
Lactation: There is no information on the effects of the drug on the breastfed infant or the effects of the drug on milk production. However, limited literature reports that breastfeeding after MultiHance administration to the mother would result in the infant receiving an oral dose of 0.001%-0.04% of the maternal dose.
Pediatric Use: MultiHance is approved for intravenous use for MRI of the CNS to visualize lesions with abnormal blood brain barrier or abnormal vascularity of the brain, spine, and associated tissues in pediatric patients from birth, including term neonates, to less than 17 years of age. Adverse reactions in pediatric patients were similar to those reported in adults. No dose adjustment according to age is necessary in pediatric patients two years of age and older. For pediatric patients, less than 2 years of age, the recommended dosage range is 0.1 to 0.2 mL/kg. The safety of MultiHance has not been established in preterm neonates.

Please see full Prescribing Information and Patient Medication Guide for additional important safety information for/regarding MultiHance (gadobenate dimeglumine) injection, 529 mg/mL at https://www.braccoimaging.com/us-en/products/magnetic-resonance-imaging/multihance

You are encouraged to report negative side effects of prescription drugs to the FDA. Visit www.fda.gov/medwatch or call 1-800-FDA-1088.

MultiHance is manufactured for Bracco Diagnostics Inc. by BIPSO GmbH – 78224 Singen (Germany) and by Patheon Italia S.p.A., Ferentino, Italy.
MultiHance is a registered trademark of Bracco International B.V.
MultiHance Multipack is a trademark of Bracco International B.V.
All other trademarks and registered trademarks are the property of their respective owners.

References: 1. Seidl Z, Vymazal J, Mechi M, et al. Does higher gadolinium concentration play a role in the morphologic assessment of brain tumors? Results of a multicenter intraindividual crossover comparison of gadobutrol versus gadobenate dimeglumine (the MERIT Study). *AJNR Am J Neuroradiol.* 2012;33(6):1050-1058. **2.** Maravilla KR, Maldjian JA, Schmalfuss IM, et al. Contrast enhancement of central nervous system lesions: multicenter intraindividual crossover comparative study of two MR contrast agents. *Radiology.* 2006;240(2):389-400. **3.** Rowley HA, Scialfa G, Gao PY, et al. Contrast-enhanced MR imaging of brain lesions: a large-scale intraindividual crossover comparison of gadobenate dimeglumine versus gadodiamide. *AJNR Am J Neuroradiol.* 2008;29(9):1684-1691. **4.** Vaneckova M, Herman M, Smith MP, et al. The benefits of high relaxivity for brain tumor imaging: results of a multicenter intraindividual crossover comparison of gadobenate dimeglumine with gadoterate meglumine (The BENEFIT Study). *AJNR Am J Neuroradiol.* 2015 Sep;36(9):1589–1598.

Bracco Diagnostics Inc.
259 Prospect Plains Road, Building H
Monroe Township, NJ 08831 USA
Phone: 609-514-2200
Toll Free: 1-877-272-2269 (U.S. only)
Fax: 609-514-2446
© 2022 Bracco Diagnostics Inc. All Rights Reserved. US-MH-2100019 02/22

BRACCO **Bracco Diagnostics**

multihance® (gadobenate dimeglumine) injection, 529 mg/mL

Rx ONLY

Please see full prescribing information.

A brief summary follows.

WARNING: NEPHROGENIC SYSTEMIC FIBROSIS

Gadolinium-based contrast agents (GBCAs) increase the risk for NSF among patients with impaired elimination of the drugs.

Avoid use of GBCAs in these patients unless the diagnostic information is essential and not available with non-contrasted MRI or other modalities. NSF may result in fatal or debilitating systemic fibrosis affecting the skin, muscle and internal organs.

- The risk for NSF appears highest among patients with:
  - chronic, severe kidney disease (GFR <30 mL/min/1.73m2), or
  - acute kidney injury.
- Screen patients for acute kidney injury and other conditions that may reduce renal function. For patients at risk for chronically reduced renal function (e.g. age > 60 years, hypertension or diabetes), estimate the glomerular filtration rate (GFR) through laboratory testing.
- For patients at highest risk for NSF, do not exceed the recommended MultiHance dose and allow a sufficient period of time for elimination of the drug from the body prior to re-administration. [see ***Warnings and Precautions (5.1)***]

1 INDICATIONS AND USAGE

1.1 MRI of the Central Nervous System (CNS)

MultiHance is indicated for intravenous use in magnetic resonance imaging (MRI) of the central nervous system (CNS) in adults and pediatric patients (including term neonates), to visualize lesions with abnormal blood-brain barrier or abnormal vascularity of the brain, spine, and associated tissues.

1.2 MRA of Renal and Aorto-ilio-femoral Vessels

MultiHance is indicated for use in magnetic resonance angiography (MRA) to evaluate adults with known or suspected renal or aorto-ilio-femoral occlusive vascular disease.

4 CONTRAINDICATIONS MultiHance is contraindicated in patients with known allergic or hypersensitivity reactions to gadolinium-based contrast agents [see ***Warnings and Precautions (5.2)***].

5 WARNINGS AND PRECAUTIONS

5.1 Nephrogenic Systemic Fibrosis (NSF) Gadolinium-based contrast agents (GBCAs) increase the risk for nephrogenic systemic fibrosis (NSF) among patients with impaired elimination of the drugs. Avoid use of GBCAs among these patients unless the diagnostic information is essential and not available with non-contrast enhanced MRI or other modalities. The GBCA-associated NSF risk appears highest for patients with chronic, severe kidney disease (GFR <30 mL/min/1.73m^2) as well as patients with acute kidney injury. The risk appears lower for patients with chronic, moderate kidney disease (GFR 30-59 mL/min/1.73m^2) and little, if any, for patients with chronic, mild kidney disease (GFR 60-89 mL/min/1.73m^2). NSF may result in fatal or debilitating fibrosis affecting the skin, muscle and internal organs. Report any diagnosis of NSF following MultiHance administration to Bracco Diagnostics (1-800-257-5181) or FDA (1-800-FDA-1088 or www.fda.gov/medwatch).

Screen patients for acute kidney injury and other conditions that may reduce renal function.

Features of acute kidney injury consist of rapid (over hours to days) and usually reversible decrease in kidney function, commonly in the setting of surgery, severe infection, injury or drug-induced kidney toxicity. Serum creatinine levels and estimated GFR may not reliably assess renal function in the setting of acute kidney injury. For patients at risk for chronically reduced renal function (e.g., age > 60 years, diabetes mellitus or chronic hypertension), estimate the GFR through laboratory testing.

Among the factors that may increase the risk for NSF are repeated or higher than recommended doses of a GBCA and the degree of renal impairment at the time of exposure. Record the specific GBCA and the dose administered to a patient. For patients at highest risk for NSF, do not exceed the recommended MultiHance dose and allow a sufficient period of time for elimination of the drug prior to re-administration. For patients receiving hemodialysis, physicians may consider the prompt initiation of hemodialysis following the administration of a GBCA in order to enhance the contrast agent's elimination. The usefulness of hemodialysis in the prevention of NSF is unknown [see ***Dosage and Administration (2) and Clinical Pharmacology (12)***].

5.2 Hypersensitivity Reactions Anaphylactic and anaphylactoid reactions have been reported, involving cardiovascular, respiratory, and/or cutaneous manifestations. Some patients experienced circulatory collapse and died. In most cases, initial symptoms occurred within minutes of MultiHance administration and resolved with prompt emergency treatment. Prior to MultiHance administration, ensure the availability of personnel trained and medications to treat hypersensitivity reactions. If such a reaction occurs stop MultiHance and immediately begin appropriate therapy. Additionally, consider the risk for hypersensitivity reactions, especially in patients with a history of hypersensitivity reactions or a history of asthma or other allergic disorders. Observe patients for signs and symptoms of a hypersensitivity reaction during and for up to 2 hours after MultiHance administration.

5.3 Gadolinium Retention Gadolinium is retained for months or years in several organs. The highest concentrations (nanomoles per gram of tissue) have been identified in the bone, followed by other organs (e.g. brain, skin, kidney, liver, and spleen. The duration of retention also varies by tissue and is longest in bone. Linear GBCAs cause more retention than macrocyclic GBCAs. At equivalent doses, gadolinium retention varies among the linear agents with Omniscan (gadodiamide) and Optimark (gadoversetamide) causing greater retention than other linear agents [Eovist (gadoxetate disodium), Magnevist (gadopentetate dimeglumine), MultiHance (gadobenate dimeglumine)]. Retention is lowest and similar among the macrocyclic GBCAs [Dotarem gadoterate meglumine), Gadavist (gadobutrol), ProHance (gadoteridol)].

Consequences of gadolinium retention in the brain have not been established. Pathologic and clinical consequences of GBCA administration and retention in skin and other organs have been established in patients with impaired renal function [see ***Warnings and Precautions (5.1)***]. There are rare reports of pathologic skin changes in patients with normal renal function. Adverse events involving multiple organ systems have been reported in patients with normal renal function without an established causal link to gadolinium retention [see ***Adverse Reactions (6.2)***]. While clinical consequences of gadolinium retention have not been established in patients with normal renal function, certain patients might be at higher risk. These include patients requiring multiple lifetime doses, pregnant and pediatric patients, and patients with inflammatory conditions. Consider the retention characteristics of the agent when choosing a GBCA for these patients. Minimize repetitive GBCA imaging studies, particularly closely spaced studies when possible.

5.4 Acute Renal Failure In patients with renal insufficiency, acute renal failure requiring dialysis or worsening renal function have occurred with the use of gadolinium-based contrast agents. The risk of renal failure may increase with increasing dose of the contrast agent. Screen all patients for renal dysfunction by obtaining a history and/or laboratory tests. Consider follow-up renal function assessments for patients with a history of renal dysfunction.

5.5 Extravasation and Injection Site Reactions Extravasation of MultiHance may lead to injection site reactions, characterized by local pain or burning sensation, swelling, blistering, and necrosis. In animal experiments, local reactions including eschar and necrosis were noted even on Day 8 post perivenous injection of MultiHance. Exercise caution to avoid local extravasation during intravenous administration of MultiHance. If extravasation occurs, evaluate and treat as necessary if local reactions develop.

5.6 Cardiac Arrhythmias Cardiac arrhythmias have been observed in patients receiving MultiHance in clinical trials [see ***Adverse Reactions (6.1)***]. Assess patients for underlying conditions or medications that predispose to arrhythmias.

A double-blind, placebo-controlled, 24-hour post dose continuous monitoring, crossover study in 47 subjects evaluated the effect of 0.2 mmol/kg MultiHance on ECG intervals, including QTc. The average changes in QTc values compared with placebo were minimal (<5 msec). QTc prolongation between 30 and 60 msec were noted in 20 subjects who received MultiHance vs. 11 subjects who received placebo. Prolongations ≥ 61 msec were noted in 6 subjects who received MultiHance and in 3 subjects who received placebo. None of these subjects had associated malignant arrhythmias. The effects on QTc by MultiHance dose, other drugs, and medical conditions were not systematically studied.

5.7 Interference with Visualization of Certain Lesions Certain lesions seen on non-contrast images may not be seen on contrast-images. Exercise caution when interpreting contrast MR images in the absence of companion non-contrast MR images.

6 ADVERSE REACTIONS

The following adverse reactions are discussed in greater detail in other sections of the label:

- Nephrogenic systemic fibrosis [see ***Warnings and Precautions (5.1)***]
- Hypersensitivity reactions [see ***Warnings and Precautions (5.2)***]

6.1 Clinical Trials Experience

Because clinical trials are conducted under widely varying conditions, adverse reaction rates observed in the clinical trials of a drug cannot be directly compared to rates in the clinical trials of another drug and may not reflect the rates observed in practice.

Adult In clinical trials with MultiHance, a total of 4967 adult subjects (137 healthy volunteers and 4830 patients) received MultiHance at doses ranging from 0.005 to 0.4 mmol/kg. There were 2838 (57%) men and 2129 (43%) women with a mean age of 56.5 years (range 18 to 93 years). A total of 4403 (89%) subjects were Caucasian, 134 (3%) Black, 275 (6%) Asian, 40 (1%) Hispanic, 70 (1%) in other racial groups, and for 45 (1%) subjects, race was not reported.

The most commonly reported adverse reactions in adult subjects who received MultiHance were nausea (1.3%) and headache (1.2%). Most adverse reactions were mild to moderate in intensity. One subject experienced a serious anaphylactoid reaction with laryngeal spasm and dyspnea [see ***Warnings and Precautions (5.2)***]. Serious adverse reactions consisting of convulsions, pulmonary edema, acute necrotizing pancreatitis, and anaphylactoid reactions were reported in 0.1% of subjects in clinical trials.

Adverse reactions that occurred in at least 0.5% of 4967 adult subjects who received MultiHance are listed below (Table 2), in decreasing order of occurrence within each system.

TABLE 2: ADVERSE REACTIONS REPORTED IN ≥ 0.5% OF ADULT SUBJECTS WHO RECEIVED MULTIHANCE IN CLINICAL TRIALS

Number of subjects dosed	4967
Number of subjects with any adverse reaction	517 (10.4%)
Gastrointestinal Disorders	
Nausea	67 (1.3%)
General Disorders and Administration Site Disorders	
Injection Site Reaction	54 (1.1%)
Feeling Hot	49 (1.0%)
Nervous System Disorders	
Headache	60 (1.2%)
Dysgeusia	33 (0.7%)
Paresthesia	24 (0.5%)
Dizziness	24 (0.5%)

The following adverse reactions occurred in less than 0.5% of the 4967 adult subjects who received MultiHance. Serious adverse reactions described above are not repeated below.

Blood and Lymphatic System Disorders: Basophilia; **Cardiac Disorders:** Atrioventricular block first degree; **Eye Disorders:** Eye pruritus, eye swelling, ocular hyperemia, visual disturbance; **Gastrointestinal Disorders:** Abdominal pain or discomfort, diarrhea, dry mouth, lip swelling, paraesthesia oral, tongue edema, vomiting; **General Disorders and Administration Site Conditions:** Chest pain or discomfort, chills, malaise; **Immune System Disorders:** Hypersensitivity; **Investigations:** Nonspecific changes in laboratory tests (including hematology, blood chemistry, liver enzymes and urinalysis), blood pressure and electrocardiogram parameters (including PR, QRS and QT intervals and ST-T segment changes). **Musculoskeletal and Connective Tissue Disorders:** Myalgia; **Nervous System Disorders:** Parosmia, tremor; **Respiratory, Thoracic and Mediastinal Disorders:** Dyspnea, laryngospasm, nasal congestion, sneezing, wheezing; **Skin and Subcutaneous Tissue Disorders:** Hyperhidrosis, pruritus, rash, swelling face, urticaria.

Pediatric In clinical trials of MultiHance in MRI of the CNS, 217 pediatric subjects received MultiHance at a dose of 0.1 mmol/kg. A total of 112 (52%) subjects were male and the overall mean age was 8.3 years (range 4 days to 17 years). A total of 168 (77%) subjects were Caucasian, 12 (6%) Black, 12 (6%) Asian, 24 (11%), Hispanic, and 1 (<1%) in other racial groups.

Adverse reactions were reported for 14 (6.5%) of the subjects. The frequency and the nature of the adverse reactions were similar to those seen in the adult patients. The most commonly reported adverse reactions were vomiting (1.4%), pyrexia (0.9%), and hyperhidrosis (0.9%). No subject died during study participation. A serious adverse reaction of worsening of vomiting was reported for one (0.5%) patient with a brain tumor (glioma) for which a causal relationship to MultiHance could not be excluded.

Pediatric Patients In clinical trials of MultiHance in MRI of the CNS, 307 pediatric subjects received MultiHance at a dose of 0.1 mmol/kg. A total of 160 (52%) subjects were male and the overall mean age was 6.0 years (range, 2 days to 17 years). A total of 211 (69%) subjects were Caucasian, 24 (8%) Black, 15 (5%) Asian, 39 (13%), Hispanic, 2 (<1%) in other racial groups, and for 16 (5%), race was not reported. Adverse reactions were reported for 14 (4.6%) of the subjects. The frequency and the nature of the adverse reactions were similar to those seen in the adult patients. The most commonly reported adverse reactions were vomiting (1.0%), pyrexia (0.7%), and hyperhidrosis (0.7%). No subject died during study participation.

6.2 Post-marketing Experience

The following adverse reactions have been identified during post approval use of MultiHance. Because these reactions are reported voluntarily from a population of uncertain size, it is not always possible to reliably estimate their frequency or establish a causal relationship to drug exposure.

Immune System Disorders: Anaphylactic, anaphylactoid and hypersensitivity reactions manifested with various degrees of severity up to anaphylactic shock, loss of consciousness and death. The reactions generally involved signs or symptoms of respiratory, cardiovascular, and/or mucocutaneous abnormalities.

General Disorders and Administration Site Conditions: Extravasation of MultiHance may lead to injection site reactions, characterized by local pain or burning sensation, swelling, blistering, and necrosis [***see Warnings and Precautions (5.4)***]. Adverse events with variable onset and duration have been reported after GBCA administration [***see Warnings and Precautions (5.3)***]. These include fatigue, asthenia, pain syndromes, and heterogeneous clusters of symptoms in the neurological, cutaneous, and musculoskeletal systems.

Skin: Gadolinium associated plaques.

7 DRUG INTERACTIONS

7.1 Transporter-Based Drug-Drug Interactions MultiHance and other drugs may compete for the canalicular multispecific organic anion transporter (MOAT also referred to as MRP2 or ABCC2). Therefore MultiHance may prolong the systemic exposure of drugs such as cisplatin, anthracyclines (e.g. doxorubicin, daunorubicin), vinca alkaloids (e.g. vincristine), methotrexate, etoposide, tamoxifen, and paclitaxel. In particular, consider the potential for prolonged drug exposure in patients with decreased MOAT activity (e.g. Dubin Johnson syndrome).

8 USE IN SPECIFIC POPULATIONS

8.1 Pregnancy Risk Summary GBCAs cross the placenta and result in fetal exposure and gadolinium retention. The human data on the association between GBCAs and adverse fetal outcomes are limited and inconclusive (see Data). In animal reproduction studies, gadobenate dimeglumine has been shown to be teratogenic in rabbits following repeated intravenous administration during organogenesis at doses up to 6 times the recommended human dose. There were no adverse developmental effects observed in rats with intravenous administration of gadobenate dimeglumine during organogenesis at doses up to three times the recommended human dose (see Data). Because of the potential risks of gadolinium to the fetus, use MultiHance only if imaging is essential during pregnancy and cannot be delayed. The estimated background risk of major birth defects and miscarriage for the indicated population is unknown. All pregnancies have a background risk of birth defect, loss, or other adverse outcomes. In the U.S. general population, the estimated background risk of major birth defects and miscarriage in clinically recognized pregnancies is 2 to 4% and is 15 to 20%, respectively.

Data *Human Data* Contrast enhancement is visualized in the human placenta and fetal tissues after maternal GBCA administration. Cohort studies and case reports on exposure to GBCAs during pregnancy have not reported a clear association between GBCAs and adverse effects in the exposed neonates. However, a retrospective cohort study, comparing pregnant women who had a GBCA MRI to pregnant women who did not have an MRI, reported a higher occurrence of stillbirths and neonatal deaths in the group receiving GBCA MRI. Limitations of this study include a lack of comparison with non-contrast MRI and lack of information about the maternal indication for MRI. Overall, these data preclude a reliable evaluation of the potential risk of adverse fetal outcomes with the use of GBCAs in pregnancy. *Animal Data* Gadolinium Retention GBCAs administered to pregnant non-human primates (0.1 mmol/kg on gestational days 85 and 135) result in measurable gadolinium concentration in the offspring in bone, brain, skin, liver, kidney, and spleen for at least 7 months. GBCAs administered to pregnant mice (2 mmol/kg daily on gestational days 16 through 19) result in measurable gadolinium concentrations in the pups in bone, brain, kidney, liver, blood, muscle, and spleen at one month postnatal age.

Reproductive Toxicology Gadobenate dimeglumine has been shown to be teratogenic in rabbits when administered intravenously at 2 mmol/kg/day (6 times the recommended human dose based on bodysurface area) during organogenesis (day 6 to 18) inducing microphthalmia/small eye and/or focal retinal fold in 3 fetuses from 3 separate litters. In addition, MultiHance intravenously administered at 3 mmol/kg/day (10 times the recommended human dose based on body surface area) has been shown to increase intrauterine deaths in rabbits. There was no evidence that MultiHance induced teratogenic effects in rats at doses up to 2 mmol/kg/day (3 times the recommended human dose based on body surface area), however, rat dams exhibited no systemic toxicity at this dose. There were no adverse effects on the birth, survival, growth, development and fertility of the F1 generation at doses up to 2 mmol/kg in a rat peri- and post-natal (Segment III) study.

10 OVERDOSAGE

Clinical consequences of overdosage with MultiHance have not been reported. Treatment of an overdosage should be directed toward support of vital functions and prompt institution of symptomatic therapy. In a Phase 1 clinical study, doses up to 0.4 mmol/kg were administered to patients. MultiHance has been shown to be dialyzable [see ***Clinical Pharmacology (12.3)***].

12 CLINICAL PHARMACOLOGY

12.1 Mechanism of Action Gadobenate dimeglumine is a paramagnetic agent and, as such, develops a magnetic moment when placed in a magnetic field. The large magnetic moment produced by the paramagnetic agent results in a large local magnetic field, which can enhance the relaxation rates of water protons in its vicinity leading to an increase of signal intensity (brightness) of tissue.

In magnetic resonance imaging (MRI), visualization of normal and pathological tissue depends in part on variations in the radiofrequency signal intensity that occur with 1) differences in proton density; 2) differences of the spin-lattice or longitudinal relaxation times (T1); and 3) differences in the spin-spin or transverse relaxation time (T2). When placed in a magnetic field, gadobenate dimeglumine decreases the T1 and T2 relaxation time in target tissues. At recommended doses, the effect is observed with greatest sensitivity in the T1-weighted sequences.

12.2 Pharmacodynamics Unlike other tested paramagnetic contrast agents (See Table 3), MultiHance demonstrates weak and transient interactions with serum proteins that causes slowing in the molecular tumbling dynamics, resulting in strong increases in relaxivity in solutions containing serum proteins. The improved relaxation effect can contribute to increased contrast-to-noise ratio and lesion-to-brain ratio, which may improve visualization.

TABLE 3: RELAXIVITY (mM^{-1}s^{-1}) OF GADOLINUM CHELATES

	Human plasma	
	r_1	r_2
Gadobenate	9.7[1]	12.5[1]
Gadopentetate	4.9[1]	6.3[1]
Gadodiamide	5.4[2]	---
Gadoteridol	5.4[2]	---

r_1 and r_2 relaxivities indicate the efficiency in shortening T1 and T2 relaxation times, respectively.
[1] In heparinized human plasma, at 39°C.
[2] In citrated human plasma, at 37°C.
--- Not available

Disruption of the blood-brain barrier or abnormal vascularity allows enhancement by MultiHance of lesions such as neoplasms, abscesses, and infarcts. Uptake of MultiHance into hepatocytes has been demonstrated.

12.3 Pharmacokinetics Three single-dose intravenous studies were conducted in 32 healthy male subjects to assess the pharmacokinetics of gadobenate dimeglumine. The doses administered in these studies ranged from 0.005 to 0.4 mmol/kg. Upon injection, the meglumine salt is completely dissociated from the gadobenate dimeglumine complex. Thus, the pharmacokinetics is based on the assay of gadobenate ion, the MRI contrast effective ion in gadobenate dimeglumine. Data for plasma concentration and area under the curve demonstrated linear dependence on the administered dose. The pharmacokinetics of gadobenate ion following intravenous administration can be best described using a two-compartment model.

Distribution Gadobenate ion has a rapid distribution half-life (reported as mean ± SD) of 0.084 ± 0.012 to 0.605 ± 0.072 hours. Volume of distribution of the central compartment ranged from 0.074 ± 0.017 to 0.158 ± 0.038 L/kg, and estimates of volume of distribution by area ranged from 0.170 ± 0.016 to 0.282 ± 0.079 L/kg. These latter estimates are approximately equivalent to the average volume of extracellular body water in man. *In vitro* studies showed no appreciable binding of gadobenate ion to human serum proteins.

Elimination Gadobenate ion is eliminated predominately via the kidneys, with 78% to 96% of an administered dose recovered in the urine. Total plasma clearance and renal clearance estimates of gadobenate ion were similar, ranging from 0.093 ± 0.010 to 0.133 ± 0.270 L/hr/kg and 0.082 ± 0.007 to 0.104 ± 0.039 L/hr/kg, respectively. The clearance is similar to that of substances that are subject to glomerular filtration. The mean elimination half-life ranged from 1.17 ± 0.26 to 2.02 ± 0.60 hours. A small percentage of the administered dose (0.6% to 4%) is eliminated via the biliary route and recovered in feces.

Metabolism There was no detectable biotransformation of gadobenate ion. Dissociation of gadobenate ion *in vivo* has been shown to be minimal, with less than 1% of the free chelating agent being recovered alone in feces.

Pharmacokinetics in Special Populations

Renal Impairment: A single intravenous dose of 0.2 mmol/kg of MultiHance was administered to 20 subjects with impaired renal function (6 men and 3 women with moderate renal impairment [urine creatinine clearance >30 to <60 mL/min] and 5 men and 6 women with severe renal impairment [urine creatinine clearance >10 to <30 mL/min]). Mean estimates of the elimination half-life were 6.1 ± 3.0 and 9.5 ± 3.1 hours for the moderate and severe renal impairment groups, respectively as compared with 1.0 to 2.0 hours in healthy volunteers.

Hemodialysis: A single intravenous dose of 0.2 mmol/kg of MultiHance was administered to 11 subjects (5 males and 6 females) with end-stage renal disease requiring hemodialysis to determine the pharmacokinetics and dialyzability of gadobenate. Approximately 72% of the dose was recovered by hemodialysis over a 4-hour period. The mean elimination half-life on dialysis was 1.21 ± 0.29 hours as compared with 42.4 ± 24.4 hours when off dialysis.

Hepatic Impairment: A single intravenous dose of 0.1 mmol/kg of MultiHance was administered to 11 subjects (8 males and 3 females) with impaired liver function (Class B or C modified Child-Pugh Classification). Hepatic impairment had little effect on the pharmacokinetics of MultiHance with the parameters being similar to those calculated for healthy subjects.

Gender, Age, Race: A multiple regression analysis performed using pooled data from several pharmacokinetic studies found no significant effect of sex upon the pharmacokinetics of gadobenate. Clearance appeared to decrease slightly with increasing age. Since variations due to age appeared marginal, dosage adjustment for geriatric population is not recommended. Pharmacokinetic differences due to race have not been systematically studied.

Pediatric: A population pharmacokinetic analysis incorporated data from 25 healthy subjects (14 males and 11 females) and 15 subjects undergoing MR imaging of the central nervous system (7 males and 8 females) betweenages of 2 and 16 years. The subjects received a single intravenous dose of 0.1 mmol/kg of MultiHance. The geometric mean Cmax was 62.3 µg/mL (n=16) in children 2 to 5 years of age, and 64.2 µg/mL (n=24) in children older than 5 years. The geometric mean AUC 0–∞ was 77.9 µg·h/mL in children 2-5 years of age (n=16) and 82.6 µg·h/mL in children older than 5 years (n=24). The geometric mean half-life was 1.2 hours in children 2 to 5 years of age and 0.93 hours in children older than 5 years. There was no significant gender-related difference in the pharmacokinetic parameters in the pediatric patients. Over 80% of the dose was recovered in urine after 24 hours. Pharmacokinetic simulations indicate similar AUC and Cmax values for MultiHance in pediatric subjects less than 2 years when compared to those reported for adults; no age-based dose adjustment is necessary forthis pediatric population.

17 PATIENT COUNSELING INFORMATION

17.1 Nephrogenic Systemic Fibrosis Instruct patients to inform their physician if they:

• have a history of kidney and/or liver disease, or • have recently received a GBCA.

GBCAs increase the risk for NSF among patients with impaired elimination of the drugs. To counsel patients at risk for NSF: • Describe the clinical manifestations of NSF • Describe procedures to screen for the detection of renal impairment.

Instruct the patients to contact their physician if they develop signs or symptoms of NSF following MultiHance administration, such as burning, itching, swelling, scaling, hardening and tightening of the skin; red or dark patches on the skin; stiffness in joints with trouble moving, bending or straightening the arms, hands, legs or feet; pain in the hip bones or ribs; or muscle weakness.

17.2 Common Adverse Reactions

Inform patients that they may experience:

• reactions along the venous injection site, such as mild and transient burning or pain or feeling of warmth or coldness at the injection site • side effects of feeling hot, nausea, and headache.

17.3 General Precautions

Instruct patients scheduled to receive MultiHance to inform their physician if they:

• are pregnant or breast feeding • have a history of renal disease, heart disease, seizure, asthma or allergic respiratory diseases • are taking any medications • have any allergies to any of the ingredients of MultiHance.

Rx only US Patent No. 4,916,246 Manufactured for Bracco Diagnostics Inc. Monroe Township, NJ 08831 By Patheon Italia S.p.A. - 03013 Ferentino (Italy) Revised October 2018 18-061418B

[†]Multicenter double-blind randomized intraindividual crossover study design of 123 patients with known or suspected brain tumors. Each patient received 0.1-mmol/kg doses of MultiHance and Gadavist in 2 identical MR imaging examinations. Contrast agents were administered by IV using manual bolus injection (n=118) or a power injector (n=4). Both agents were administered at 0.1 mmol/kg of body weight, corresponding to 0.2 mL/kg for MultiHance and 0.1 mL/kg for Gadavist. The interval between the 2 MR imaging examinations was >48 hours to avoid carryover effects but <14 days to minimize the chance of measurable disease progression or lesion evolution. All images were evaluated by 3 blinded, independent experienced radiologists who were unaffiliated with the study centers. Each reader evaluated the patient images separately and independently. Images were evaluated qualitatively for diagnostic information and scored for: 1) lesion border delineation, 2) disease extent, 3) visualization of lesion internal morphology, and 4) lesion contrast enhancement compared with surrounding normal tissue. All assessments used a 3-point scales from 1 (examination 1 superior) through 0 (examinations equal) to 1 (examination 2 superior).

Gadavist® (gadobutrol) is a registered trademark of Bayer Healthcare. **Reference:** Seidl Z, Vymazal J, Mechl M, et al. Does higher gadolinium concentration play a role in the morphologic assessment of brain tumors? Results of a multicenter intraindividual crossover comparison of gadobutrol versus gadobenate dimeglumine (the MERIT Study). *AJNR Am J Neuroradiol*. 2012 Jun-Jul;33(6):1050–1058.

AJNR go green

AJNR urges American Society of Neuroradiology members to reduce their environmental footprint by voluntarily suspending their print subscription.

The savings in paper, printing, transportation, and postage directly fund new electronic enhancements and expanded content.

The digital edition of *AJNR* presents the print version in its entirety, along with extra features including:

- **Publication Preview**
- **Case Collection**
- **Podcasts**
- **The *AJNR* News Digest**
- **The *AJNR* Blog**

It also reaches subscribers much faster than print. An electronic table of contents will be sent directly to your mailbox to notify you as soon as it publishes.

Readers can search, reference, and bookmark current and archived content 24 hours a day on www.ajnr.org.

ASNR members who wish to opt out of print can do so by using the AJNR Go Green link on the *AJNR* Website (http://www.ajnr.org/content/subscriber-help-and-services). Just type your name in the email form to stop print and spare our ecosystem.

I am a trained neuroradiologist.
I am a teacher.
I am compassionate.
I am a researcher.
I am a leader.
I am part of a talented community.
I am curious.
I am a collaborative team player.
I am a volunteer.

I am ASNR.

Don’t miss out on the tools, resources and relationships you’ve come to rely on. Log in and renew your ASNR membership today! ***www.asnr.org***

ASNR
American Society of Neuroradiology

Explore the New ASNR Career Center

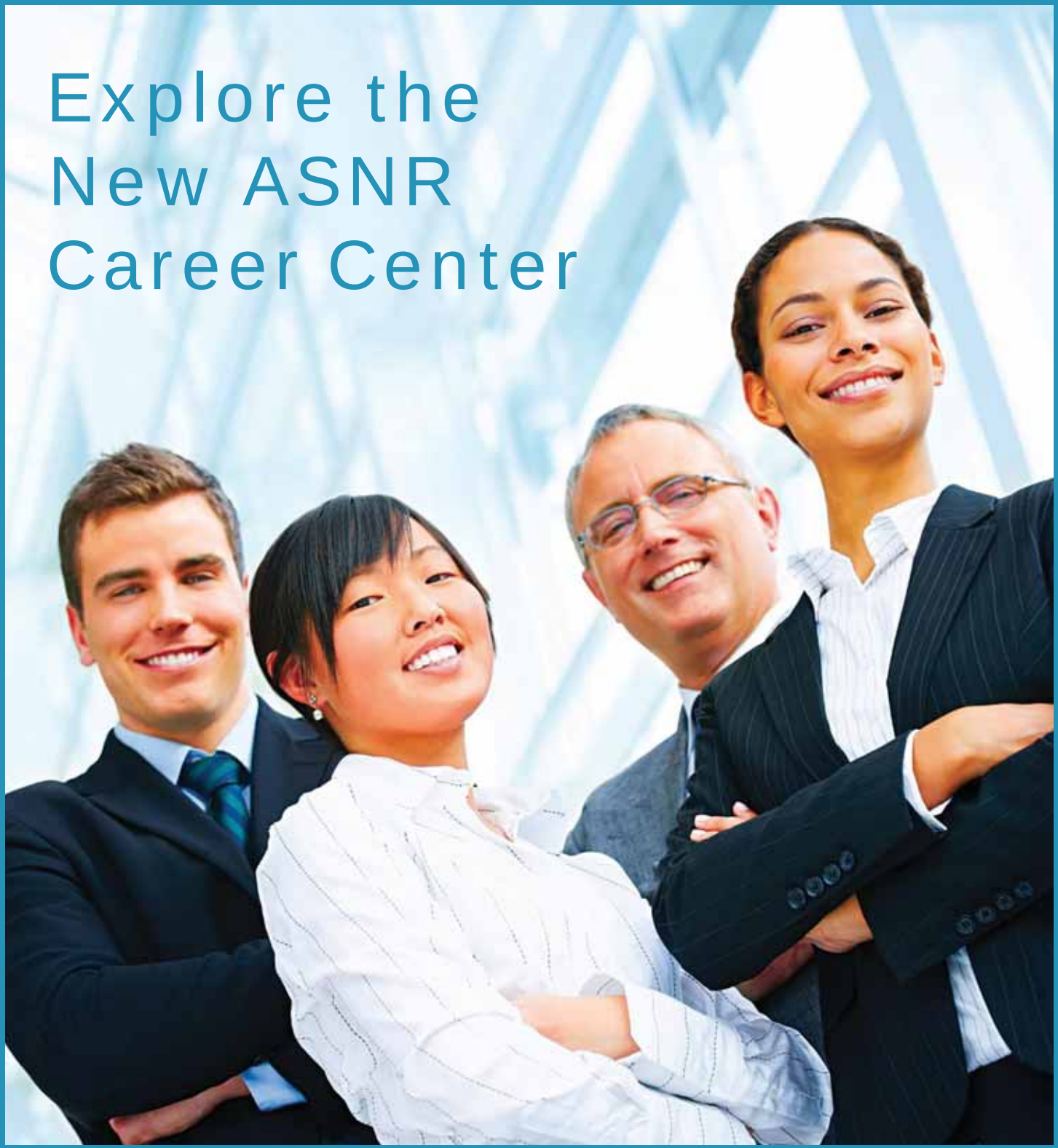

Your Premier Resource for Professional Development

- Access to jobs in the National Healthcare Career Network
- Confidential resume posting
- One-time free resume review
- Professional online profile
- Saved jobs capability

Start here: careers.asnr.org

ASNR
American Society of Neuroradiology

ASNR
American Society of Neuroradiology

Celebrating 60 Years

1962-2022

The American Society of Neuroradiology was formed on April 18, 1962, in New York City. The following purposes of the organization were unanimously adopted by the fourteen founding members:

1. To develop and support standards for the training in the practice of Neuroradiology.
2. To foster independent research in Neuroradiology.
3. To promote a closer fellowship and exchange of ideas among Neuroradiologists.

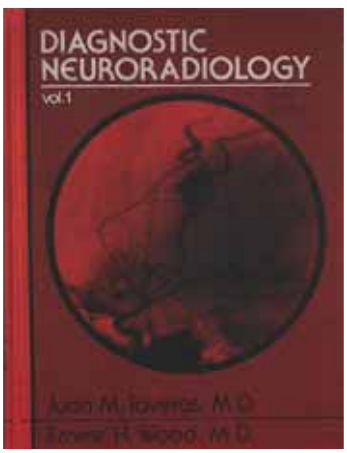

Visit ***www.asnr.org*** for more photos, videos and historical facts and be sure to follow **#ASNR60th** on social media so you don't miss a single thing. We have lots planned for 2022!

ADVERTISEMENT

In Planning for Brain Metastases Treatment, Imaging may be the Missing Link in Cost Containment[1]

When faced with a patient presenting with metastatic brain cancer, determining whether to use up-front stereotactic radiosurgery (SRS) vs. first treating with whole brain radiotherapy (WBRT) is a significant clinical decision.

WBRT: The whole story on cognitive impairment

While whole brain radiotherapy (WBRT) has been the main treatment option for many years, experts agree that it often results in cognitive deterioration and a negative impact on quality of life. This mental decline has a devastating impact on patients and their families and adds ongoing costs for the healthcare systems managing these symptoms.

Using WBRT instead of SRS in some patients is estimated to decrease the total costs of brain metastasis management, though with increased toxicity.

SRS: Fewer side effects but greater risk of missed tumors

The cost of upfront SRS is the greatest contributor to cost of brain metastasis management.[1] SRS is often more expensive than WBRT. What's more, multiple applications of SRS can increase the cost of treatment greatly.

Stereotactic radiosurgery (SRS) has far fewer side effects, but upfront use of SRS is expensive and can carry the risk of missed tumors, requiring repeat procedures such as salvage SRS.[1]

Number of lesions and lesion size are key factors to be considered when determining the treatment plan for these patients. It follows that increased diagnostic information and accuracy could be beneficial in directing the proper therapy and improving overall long-term patient outcomes and containing costs. Getting the diagnosis right the first time is crucial to ensure proper treatment begins quickly, and high cost/high stakes procedures such as SRS need precise surgical planning.

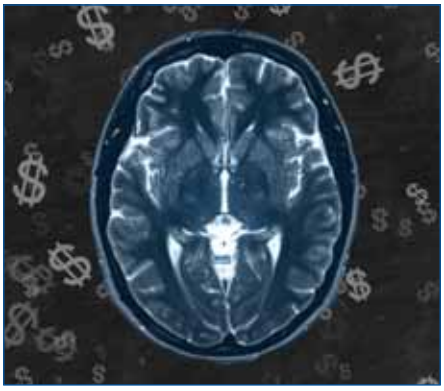

Getting the diagnosis right the first time is crucial to ensure proper treatment begins quickly.

What does optimal visualization mean for outcomes and cost?

For surgical planning with SRS, radiologists need the best visualization achievable to accurately count the number and size of the lesions. These metrics are the key predictors of the need for SRS,[1] WBRT, or a combination of both.

By selecting the ideal contrast agent and equipment protocols, neuroradiologists can identify the proximate numbers of metastases for upfront treatment and reduced salvage treatment occurrences.

The role of radiology

As medical care for oncology patients continues to evolve, it will be increasingly important to assess the cost of various interventions given the often-limited life expectancy of cancer patients, the rising costs of cancer therapy, and the increasing prevalence of cancer in an aging population.

Through seeing all the tumors and tumor borders as clearly as technology allows, radiology can play a part in ensuring that proper treatment can begin quickly, while containing costs through optimized patient care. Efforts to carefully manage treatment approaches require improvements in protocol design, contrast administration in imaging, and utilizing multimodal imaging approaches.

In this era of precision medicine, radiology departments' contribution to this improved standard of care will have significant short and long-term implications by reducing cost of care, providing a more proximate diagnosis, and ensuring optimal patient outcomes. ■

Reference: 1. Shenker, R. F., McTyre, E. R., Taksler, D et al. Analysis of the drivers of cost of management when patients with brain metastases are treated with upfront radiosurgery. *Clin Neurol Neurosurg.* 2019 Jan;176:10-14.

BRACCO
LIFE FROM INSIDE

For more information on MRI contrast agents, precision medicine, and reducing cost of care please visit braccomr.com

© 2022 Bracco Diagnostics Inc.

ASNR COMPREHENSIVE NEURORADIOLOGY COURSE

SEPTEMBER 15-17, 2022
CHICAGO, IL, OR VIRTUAL

ASNR is again hosting its popular **Comprehensive Neuroradiology Course** with attendees able to choose their learning environment: in-person in Chicago OR virtual. This intensive, image-rich review of neuroradiology is taught by award-winning educators and covers the essentials of neuroradiology practice, including:

Adult Brain Imaging
Head and Neck Imaging
Spine Imaging
Pediatric Neuroradiology
Advanced Imaging Techniques in Neuroradiology

Take advantage of Early Bird Rates through August 15! Get all the details and register now: *www.asnr.org/2022cnc*.

Meet the Faculty

Joshua Nickerson, MD
Division Chief of Neuroradiology, Associate Professor, Oregon Health & Science University

Tabassum Kennedy, MD
Division Chief of Neuroradiology, University of Wisconsin, Madison

Judith Gadde, DO, MBA
Pediatric Neuroradiologist and Director of Academic Innovation, Lurie Children's Hospital of Chicago

Mahmud Mossa-Basha, MD
Associate Professor of Radiology, University of Washington; Vice Chair of Clinical Operations, Medical Director of MRI and Radiology Chief of Service

Wende Gibbs, MD, MA
Director of Spine Imaging and Intervention, Barrow Neurological Institute

Ashley Aiken, MD,
Director of Head and Neck Imaging, Fellowship Program Director and Professor of Radiology and Imaging Sciences, Emory University

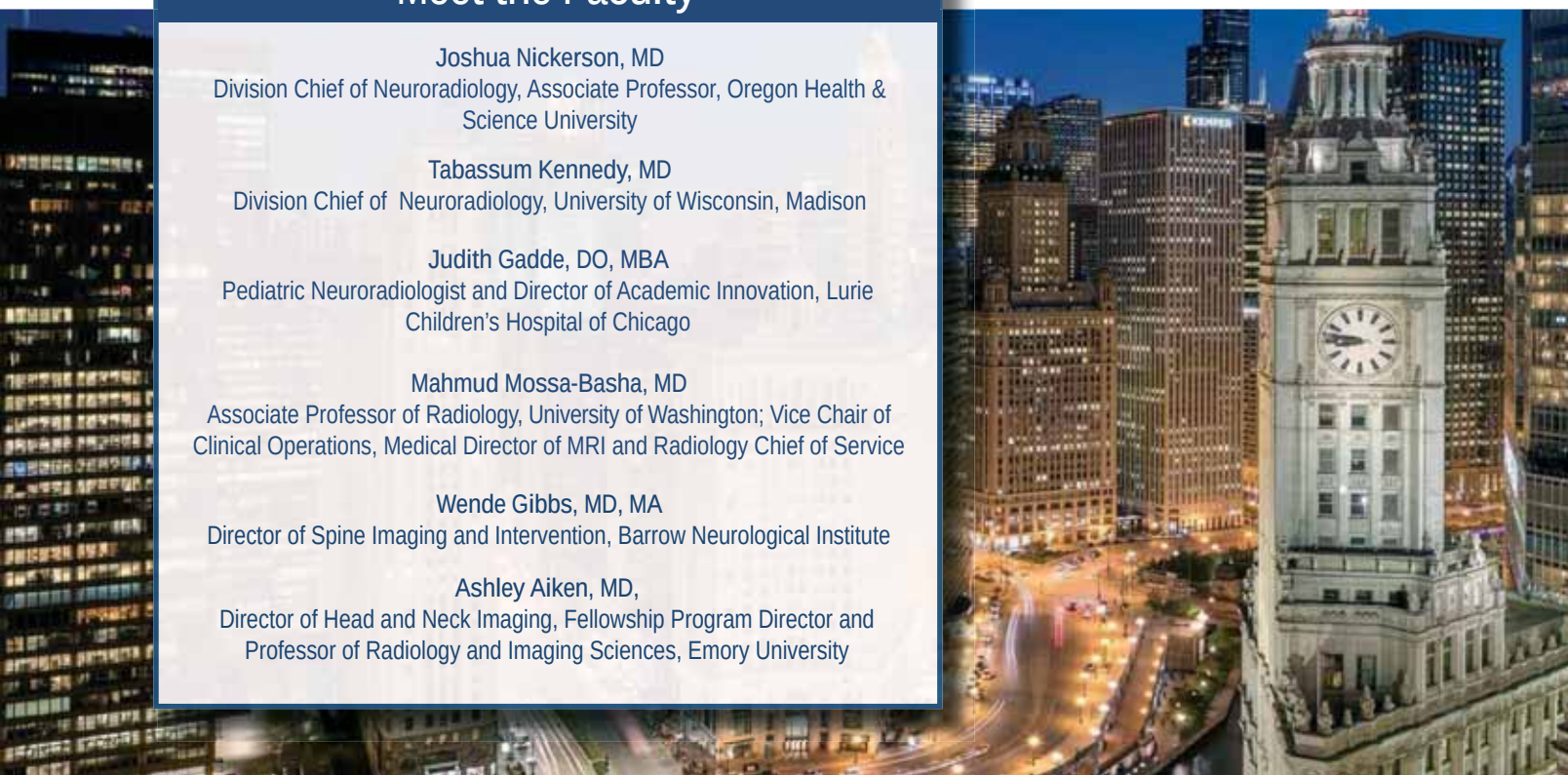

AJNR

AMERICAN JOURNAL OF NEURORADIOLOGY

AUGUST 2022
VOLUME 43
NUMBER 8
WWW.AJNR.ORG

Publication Preview at www.ajnr.org features articles released in advance of print. Visit www.ajnrblog.org to comment on AJNR content and chat with colleagues and AJNR's News Digest at http://ajnrdigest.org to read the stories behind the latest research in neuroimaging.

1079 **PERSPECTIVES** *J.P. Nickerson*

REVIEW ARTICLES

1080 **Uncommon Glioneuronal Tumors: A Radiologic and Pathologic Synopsis** *A. Vaz, et al.* — ADULT BRAIN

1090 **Intraosseous Venous Malformations of the Head and Neck** *S.B. Strauss, et al.* — HEAD & NECK

GENERAL CONTENTS

1099 **Validation of a Denoising Method Using Deep Learning–Based Reconstruction to Quantify Multiple Sclerosis Lesion Load on Fast FLAIR Imaging** *T. Yamamoto, et al.* — ADULT BRAIN FUNCTIONAL

1107 **Unsupervised Deep Learning for Stroke Lesion Segmentation on Follow-up CT Based on Generative Adversarial Networks** *H. van Voorst, et al., on behalf of the CONTRAST Consortium Collaborators* — ADULT BRAIN FUNCTIONAL

1115 **Stable and Discriminatory Radiomic Features from the Tumor and Its Habitat Associated with Progression-Free Survival in Glioblastoma: A Multi-Institutional Study** *R. Verma, et al.* — ADULT BRAIN FUNCTIONAL

1124 **Absence of the Anterior Communicating Artery on Selective MRA is Associated with New Ischemic Lesions on MRI after Carotid Revascularization** *S. Yamashita, et al.* — ADULT BRAIN

1131 **Characteristics of Radiation-Related Intracranial Aneurysms: A Multicenter Retrospective Study** *Z.-Q. Huang, et al.* — ADULT BRAIN

1136 **Neuroimaging Findings in CHANTER Syndrome: A Case Series** *K.S. Mallikarjun, et al.* — ADULT BRAIN

1142 **Tumor Embolization through Meningohypophyseal and Inferolateral Trunks is Safe and Effective** *E. Raz, et al.* — INTERVENTIONAL

1148 **Emergency Department Visits for Chronic Subdural Hematomas within 30 Days after Surgical Evacuation with and without Middle Meningeal Artery Embolization** *J.S. Catapano, et al.* — INTERVENTIONAL

1152 **Effect of the Shelving Technique on the Outcome of Embolization in Intracranial Bifurcation Aneurysms** *F. Çay, et al.* — INTERVENTIONAL

AJNR (Am J Neuroradiol ISSN 0195–6108) is a journal published monthly, owned and published by the American Society of Neuroradiology (ASNR), 820 Jorie Boulevard, Oak Brook, IL 60523. Annual dues for the ASNR include approximately 21% for a journal subscription. The journal is printed by Intellicor Communications, 330 Eden Road, Lancaster, PA 17601; Periodicals postage paid at Oak Brook, IL and additional mailing offices. Printed in the U.S.A. POSTMASTER: Please send address changes to American Journal of Neuroradiology, P.O. Box 3000, Denville, NJ 07834, U.S.A. Subscription rates: nonmember $430 ($505 foreign) print and online, $320 online only; institutions $495 ($565 foreign) print and basic online, $980 ($1050 foreign) print and extended online, $380 online only (basic), $825 online only (extended); single copies are $35 each ($40 foreign). Indexed by PubMed/MEDLINE, BIOSIS Previews, Current Contents (Clinical Medicine and Life Sciences), EMBASE, Google Scholar, HighWire Press, Q-Sensei, RefSeek, Science Citation Index, SCI Expanded, ReadCube, and Semantic Scholar. Copyright © American Society of Neuroradiology.

1158 **Treatment of Proximal Posterior Inferior Cerebellar Artery Aneurysms by Intrasaccular Flow Disruption: A Multicenter Experience** *L. Goertz, et al.* — INTERVENTIONAL

1164 **High-Resolution MRI for Evaluation of the Possibility of Successful Recanalization in Symptomatic Chronic ICA Occlusion: A Retrospective Study** *M. Tang, et al.* — EXTRACRANIAL VASCULAR

1172 **Deep Learning for Synthetic CT from Bone MRI in the Head and Neck** *S. Bambach, et al.* — HEAD & NECK FUNCTIONAL

1180 **DTI of the Olfactory Bulb in COVID-19-Related Anosmia: A Pilot Study** *F. Sherif, et al.* — HEAD & NECK FUNCTIONAL

1184 **Normalized Parameters of Dynamic Contrast-Enhanced Perfusion MRI and DWI-ADC for Differentiation between Posttreatment Changes and Recurrence in Head and Neck Cancer** *A. Baba, et al.* — HEAD & NECK FUNCTIONAL

1190 **Imaging Features of Craniofacial Giant Cell Granulomas: A Large Retrospective Analysis from a Tertiary Care Center** *R. Chanda, et al.* — HEAD & NECK

1196 **MR Imaging of Pediatric Low-Grade Gliomas: Pretherapeutic Differentiation of *BRAF* V600E Mutation, *BRAF* Fusion, and Wild-Type Tumors in Patients without Neurofibromatosis-1** *A. Trasolini, et al.* — PEDIATRICS

1202 **MR Imaging Detection of CNS Lesions in Tuberous Sclerosis Complex: The Usefulness of T1WI with Chemical Shift Selective Images** *H. Fujii, et al.* — PEDIATRICS

1210 **Evaluation of the Prevalence of Punctate White Matter Lesions in a Healthy Volunteer Neonatal Population** *S. Kular, et al.* — PEDIATRICS

1214 **The Construction of a Predictive Composite Index for Decision-Making of CSF Diversion Surgery in Pediatric Patients following Prenatal Myelomeningocele Repair** *F.T. Mangano, et al.* — PEDIATRICS

1222 **Percutaneous Sacroplasty with or without Radiofrequency Ablation for Treatment of Painful Sacral Metastases** *Q.-H. Tian, et al.* — SPINE

ONLINE FEATURES

LETTERS

E15 **2018–2022 Radiology Residency and Neuroradiology Fellowship Match Data: Preferences and Success Rates of Applicants** *F. Rafiee, et al.*

E17 **The Nosologic Term "Conversive" Disorder Should Be Abandoned** *D.A. Lizarazo, et al.*

E18 ***Reply*** *E. Prodi, et al.*

BOOK REVIEWS *R.M. Quencer, Section Editor*

Please visit www.ajnrblog.org to read and comment on Book Reviews.

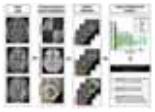

From Verma R, et al, in this issue: Incorporating stable and discriminatory radiomic features extracted from tumors and associated habitats across multisite MR imaging sequences may yield robust prognostic classifiers of patient survival in glioblastoma tumors.

Indicates Editor's Choices selection
Indicates Fellows' Journal Club selection
Indicates open access to non-subscribers at www.ajnr.org
Indicates article with supplemental online data
Indicates article with supplemental online video
Evidence-Based Medicine Level 1
Evidence-Based Medicine Level 2

AJNR

AMERICAN JOURNAL OF NEURORADIOLOGY

Publication Preview at www.ajnr.org features articles released in advance of print. Visit www.ajnrblog.org to comment on AJNR content and chat with colleagues and AJNR's News Digest at http://ajnrdigest.org to read the stories behind the latest research in neuroimaging.

AUGUST 2022 • VOLUME 43 • NUMBER 8 • WWW.AJNR.ORG

EDITOR-IN-CHIEF

Jeffrey S. Ross, MD
Professor of Radiology, Department of Radiology, Mayo Clinic College of Medicine, Phoenix, AZ

SENIOR EDITORS

Harry J. Cloft, MD, PhD
Professor of Radiology and Neurosurgery, Department of Radiology, Mayo Clinic College of Medicine, Rochester, MN

Christopher G. Filippi, MD
Professor and Alice Ettinger-Jack R. Dreyfuss Chair of Radiology, Tufts University School of Medicine, Radiologist-in-Chief Tufts University Medical Center, Boston, MA

Thierry A.G.M. Huisman, MD, PD, FICIS, FACR
Radiologist-in-Chief and Chair of Radiology, Texas Children's Hospital, Professor of Radiology, Pediatrics, Neurosurgery, and OBGYN, Baylor College of Medicine, Houston, TX

Yvonne W. Lui, MD
Associate Professor of Radiology, Chief of Neuroradiology, New York University School of Medicine, New York, NY

C.D. Phillips, MD, FACR
Professor of Radiology, Weill Cornell Medical College, Director of Head and Neck Imaging, New York-Presbyterian Hospital, New York, NY

Lubdha M. Shah, MD, MS
Professor of Radiology and Director of Spine Imaging, University of Utah Department of Radiology and Imaging Sciences, Salt Lake City, UT

STATISTICAL SENIOR EDITOR

Bryan A. Comstock, MS
Senior Biostatistician, Department of Biostatistics, University of Washington, Seattle, WA

ARTIFICIAL INTELLIGENCE DEPUTY EDITOR

Peter D. Chang, MD
Assistant Professor-in-Residence, Departments of Radiological Sciences, Computer Sciences, and Pathology, Director, Center for Artificial Intelligence in Diagnostic Medicine (CAIDM), University of California, Irvine, Irvine, CA

EDITORIAL BOARD

Ashley H. Aiken, *Atlanta, GA*
Matthew D. Alexander, *Salt Lake City, UT*
Lea M. Alhilali, *Phoenix, AZ*
Jason W. Allen, *Atlanta, GA*
Mohammed A. Almekhlafi, *Calgary, Alberta, Canada*
Niranjan Balu, *Seattle, WA*
Matthew J. Barkovich, *San Francisco, CA*
Joachim Berkefeld, *Frankfurt, Germany*
Karen Buch, *Boston, MA*
Judah Burns, *New York, NY*
Danielle Byrne, *Dublin, Ireland*
Federico Cagnazzo, *Montpellier, France*
Gloria C. Chiang, *New York, NY*
Daniel Chow, *Irvine, CA*
Kars CJ. Compagne, *Rotterdam, The Netherlands*
Yonghong Ding, *Rochester, MN*
Birgit Ertl-Wagner, *Toronto, Ontario, Canada*
Aaron Field, *Madison, WI*
Nils D. Forkert, *Calgary, Alberta, Canada*
Frank Gaillard, *Melbourne, Australia*
Joseph J. Gemmete, *Ann Arbor, Michigan*
Brent Griffith, *Detroit, MI*
Michael J. Hoch, *Philadelphia, PA*
Joseph M. Hoxworth, *Phoenix, AZ*
Raymond Y. Huang, *Boston, MA*
Susie Y. Huang, *Boston, MA*
Ferdinand K. Hui, *Honolulu, HI*
Christof Karmonik, *Houston, TX*
Gregor Kasprian, *Vienna, Austria*
Timothy J. Kaufmann, *Rochester, MN*
Hillary R. Kelly, *Boston, MA*
Toshibumi Kinoshita, *Akita, Japan*
Ioannis Koktzoglou, *Evanston, IL*
Stephen F. Kralik, *Houston, TX*
Luke Ledbetter, *Los Angeles, CA*
Franklin A. Marden, *Chicago, IL*
Markus A. Möhlenbruch, *Heidelberg, Germany*
Mahmud Mossa-Basha, *Morrisville, NC*
Renato Hoffmann Nunes, *Sao Paulo, Brazil*
Sam Payabvash, *New Haven, CT*
Johannes A.R. Pfaff, *Salzburg, Austria*
Eike I. Piechowiak, *Bern, Switzerland*
Laurent Pierot, *Reims, France*
Alexander R. Podgorsak, *Chicago, IL*
Eytan Raz, *New York, NY*
Jeff Rudie, *San Diego, CA*
Paul M. Ruggieri, *Cleveland, OH*
Fatih Seker, *Heidelberg, Germany*
Maksim Shapiro, *New York, NY*
Timothy Shepherd, *New York, NY*
Mark S. Shiroishi, *Los Angeles, CA*
Neetu Soni, *Rochester, NY*
Ashok Srinivasan, *Ann Arbor, MI*
Jason F. Talbott, *San Francisco, CA*
Anderanik Tomasian, *Los Angeles, CA*
Fabio Triulzi, *Milan, Italy*
Arastoo Vossough, *Philadelphia, PA*
Richard Watts, *New Haven, CT*
Elysa Widjaja, *Toronto, Ontario, Canada*
Ronald Wolf, *Philadelphia, Pennsylvania*
Shuang Xia, *Tianjin, China*
Leonard Yeo, *Singapore*
Woong Yoon, *Gwangju, South Korea*
David M. Yousem, *Evergreen, CO*
Carlos Zamora, *Chapel Hill, NC*
Chengcheng Zhu, *Seattle, WA*

EDITORIAL FELLOW

Alexandre Boutet, *Toronto, Ontario, Canada*

SPECIAL CONSULTANTS TO THE EDITOR

AJNR Blog Editor
Neil Lall, *Denver, CO*
Case of the Month Editor
Nicholas Stence, *Aurora, CO*
Case of the Week Editors
Matylda Machnowska, *Toronto, Ontario, Canada*
Anvita Pauranik, *Calgary, Alberta, Canada*
Vinil Shah, *San Francisco, CA*
Classic Case Editor
Sandy Cheng-Yu Chen, *Taipei, Taiwan*
Health Care and Socioeconomics Editor
Pina C. Sanelli, *New York, NY*
Physics Editor
Greg Zaharchuk, *Stanford, CA*
Podcast Editor
Courtney Tomblinson, *Nashville, TN*
Deputy Podcast Editor
Kevin Hiatt, *Winston-Salem, NC*
Twitter Editor
Jacob Ormsby, *Albuquerque, NM*

Official Journal:

American Society of Neuroradiology
American Society of Functional Neuroradiology
American Society of Head and Neck Radiology
American Society of Pediatric Neuroradiology
American Society of Spine Radiology

Founding Editor
Juan M. Taveras
Editors Emeriti
Mauricio Castillo, Robert I. Grossman, Michael S. Huckman, Robert M. Quencer

Managing Editor
Karen Halm
Assistant Managing Editor
Laura Wilhelm
Executive Director, ASNR
Mary Beth Hepp

Title: "Bowl of Cthulhu." Inspired by the short story written by HP Lovecraft in 1926, this stoneware piece measures 14" in height by 12" in diameter and combines 2 wheel-thrown elements with hand-built accents to simulate the tentacled monstrous "Old One" referenced frequently in the Lovecraft mythos. The bowl is glazed with Ancient Copper (AMACO, Indianapolis), which develops metallic crystals as it cools from a firing temperature of over 2200° F. The process is somewhat difficult to control, and the uncertainty associated with each opening of the kiln is an enjoyable injection of entropy into the highly structured life of a physician.

Joshua P. Nickerson, MD, Associate Professor of Radiology, Division Chief of Neuroradiology, Oregon Health & Sciences University, Portland, Oregon

Uncommon Glioneuronal Tumors: A Radiologic and Pathologic Synopsis

A. Vaz, M.S. Cavalcanti, E.B. da Silva Junior, R. Ramina, and B.C. de Almeida Teixeira

ABSTRACT

SUMMARY: Glioneuronal tumors are characterized exclusively by neurocytic elements (neuronal tumors) or a combination of neuronal and glial features (mixed neuronal-glial tumors). Most of these tumors occur in young patients and are related to epilepsy. While gangliogliomas, dysembryoplastic neuroepithelial tumor, and desmoplastic infantile tumor are common glioneuronal tumors, anaplastic gangliogliomas, papillary glioneuronal tumor, rosette-forming glioneuronal tumor, gangliocytoma, and central neurocytoma are less frequent. Advances in immunohistochemical and molecular diagnostics have improved the characterization of these tumors and favored the description of variants and new subtypes, some not yet classified by the World Health Organization. Not infrequently, the histologic findings of biopsies of glioneuronal tumors simulate low-grade glial neoplasms; however, some imaging findings favor the correct diagnosis, making neuroimaging essential for proper management. Therefore, the aim of this review was to present key imaging, histopathology, immunohistochemistry, and molecular findings of glioneuronal tumors and their variants.

ABBREVIATIONS: DNET = dysembryoplastic neuroepithelial tumor; GFAP = glial fibrillary acidic protein; MAP = microtubule-associated protein; rCBV = relative CBV; WHO = World Health Organization

Neuronal and mixed neuronal-glial tumors (generically called glioneuronal tumors) are a heterogeneous group of lesions exhibiting different degrees of biologic behavior.[1] Neuronal tumors are composed exclusively of ganglionic elements, and neuronal-glial tumors contain a combination of neuronal and glial features.[1-5] Glioneuronal tumors usually affect children and young adults with a predilection for the temporal lobe and frequently result in epilepsy, and most are cured with surgery.[2,4] Some types present peculiar imaging findings that aid preoperative diagnosis and distinction from more common glial tumors, such as calcification, blood by-products, and absent perilesional edema or mass effect.[2,3]

Low-grade gliomas and glioneuronal tumors may present overlapping histologic findings; however, advances in immunohistochemical and molecular techniques have favored the distinction between these entities and led to the emergence of new subtypes of glioneuronal tumors.[1,4,6] In the latest update of the CNS tumor classification, the World Health Organization (WHO) added multinodular and vacuolating neuronal tumor, myxoid glioneuronal tumor, and diffuse glioneuronal tumor with oligodendroglioma-like features and nuclear clusters to the glioneuronal tumors category (the latter provisionally, for lack of published characterizations; it is, therefore, not addressed in this review).[6,7]

The most common glioneuronal tumors of the brain are ganglioglioma, dysembryoplastic neuroepithelial tumor (DNET), and desmoplastic infantile tumor (they represent up to 2% of the CNS tumors).[3,4,8] Conversely, anaplastic ganglioglioma, papillary glioneuronal tumor, rosette-forming glioneuronal tumor, gangliocytoma, and central neurocytoma are uncommon glioneuronal tumors whose incidence is still unknown.[3,4,8] In general, glioneuronal tumors are low-grade lesions, with rare or absent mitotic figures and a low *MIB1* labeling index (except in anaplastic subtypes).[4] Immunohistochemistry may reveal glial elements by glial fibrillary acidic protein (GFAP) positivity; neuronal elements, by synaptophysin immunoreactivity; and glioneuronal progenitor cells, by CD34 positivity.[4] Although some of these tumors are well-described, others have not been widely demonstrated.

Received October 15, 2021; accepted after revision December 18.

From the Department of Pediatric Radiology (A.V., B.C.d.A.T.), Hospital Pequeno Príncipe, Curitiba, Paraná, Brazil; Department of Internal Medicine (A.V., B.C.d.A.T.), Universidade Federal do Paraná, Curitiba, Paraná, Brazil; Department of Pathology (M.S.C.), Neopath Diagnostics & Research Center, Curitiba, Paraná, Brazil; and Departments of Neurosurgery (E.B.d.S.J., R.R.) and Neuroradiology (B.C.d.A.T.), Instituto de Neurologia de Curitiba, Curitiba, Paraná, Brazil.

Please address correspondence to André Vaz, MD, Hospital Pequeno Príncipe, Centro de Imagem, Rua Desembargador Motta, 1070, 80250-060 Curitiba, Brazil; e-mail: andrevaz7@gmail.com

Indicates open access to non-subscribers at www.ajnr.org

Indicates article with online supplemental data.

http://dx.doi.org/10.3174/ajnr.A7465

FIG 1. Diagnostic approach for glioneuronal and low-grade glial tumors with cystic components (high-grade glial neoplasms were not considered for the creation of this flow chart). Predominantly cystic tumors (*A*), cystic with mural nodule (*B*), and mixed solid and cystic tumors (*C*) are presented. PLNTY indicates polymorphous low-grade neuroepithelial tumor of the young; mI, myo-inositol.

Therefore, this review discusses key MR imaging and pathologic findings of uncommon mixed neuronal-glial and neuronal tumors. Additionally, a table comparing the imaging aspects of different glioneuronal tumors is presented in the Online Supplemental Data. A flow chart presenting a simple diagnostic approach to suspected glioneuronal and low-grade glial tumors is available in Fig 1, and, finally, a brief discussion on imaging findings of the differential diagnosis of uncommon glioneuronal tumors can be found at the end of the article.

Anaplastic Ganglioglioma

Epidemiology. Anaplastic ganglioglioma is a rare neuronal-glial tumor, defined as a grade III by the 2016 WHO Classification of Tumors of the CNS.[1,3,5,8] It accounts for 6%–10% of all gangliogliomas,

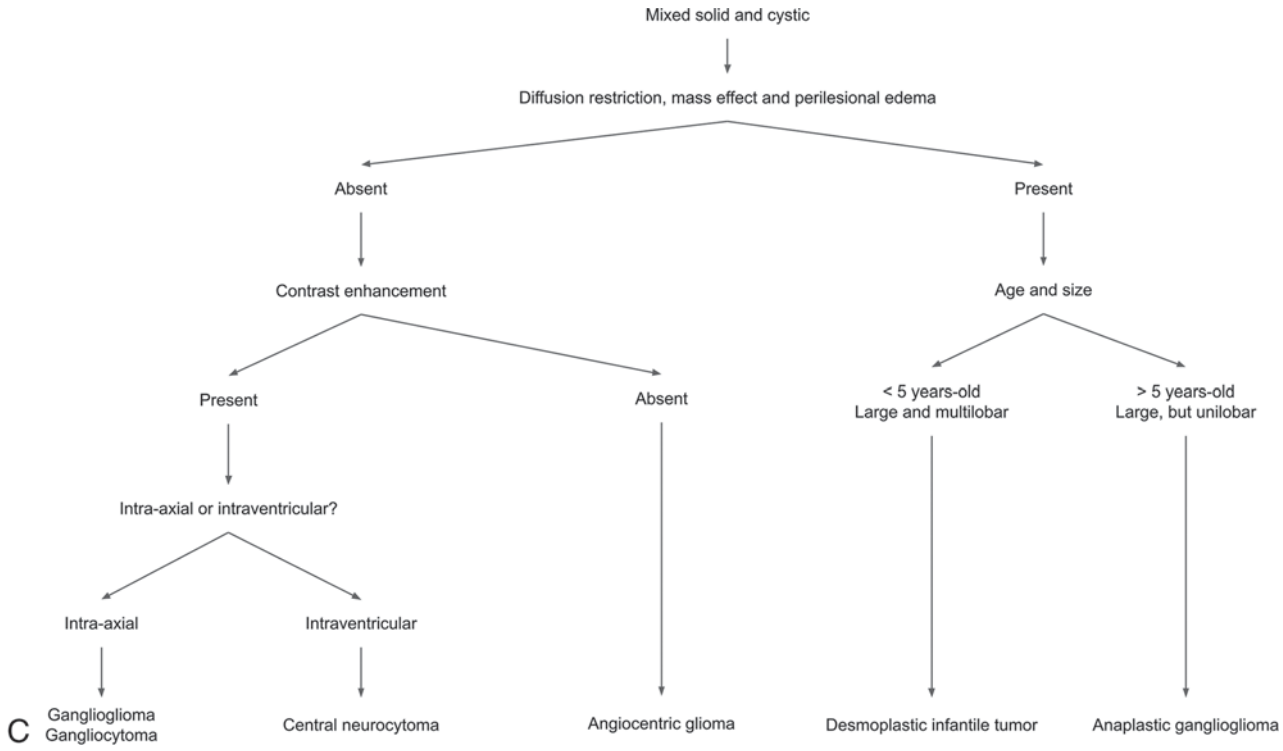

FIG 1. Continued

and it is still unclear whether it occurs through anaplastic transformation or is induced by radiation therapy, which may occur, on average, after 1 year and usually within 10 years of treatment.[1,3,5] It mostly affects children and young adults, with no predilection for sex.[1]

Location. The deep temporal (27% of cases) or frontal (22%) lobe is regularly affected.[1,3]

Clinical Presentation. The presentation is seizures, focal neurologic deficits, and increased intracranial pressure.[3,5]

Imaging Findings. Imaging findings are a mixed solid and cystic lesion, mass effect, and perilesional edema (Fig 2).[5] The solid component presents hypointense signal on T1-weighted images, hyperintense signal on T2-weighted images, calcification, diffusion restriction, high Cho peak, an increased lactate-lipid peak, increased perfusion (relative CBV [rCBV] > 1.75), and heterogeneous enhancement.[1,5,9,10] Comparison of imaging aspects of different glioneuronal tumors is presented in the Online Supplemental Data.

Pathology Findings. The pathology findings are dysplastic neuronal cells with an anaplastic glial component and increased cellularity, cellular pleomorphism, and vascular proliferation.[3-5] Mitoses are frequent, necrotic foci may be present, and the *MIB1* labeling index is generally high.[4] Immunohistochemistry depicts glial cells positive for GFAP, neurons positive for synaptophysin,

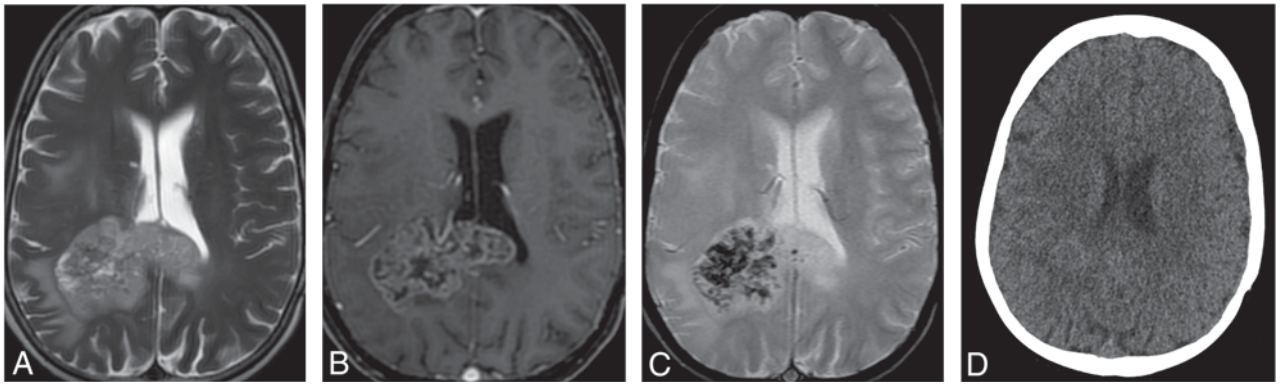

FIG 2. An anaplastic ganglioglioma in a 15-year-old boy with treated cerebellar meduloblastoma 10 years ago. An infiltrative parieto-occipital mass lesion with heterogeneous enhancement and vasogenic edema, both extending to the contralateral hemisphere through the splenium of the corpus callosum. Also note blood by-products (*C* and *D*). Immunohistochemistry was positive for *GFAP*, *p53*, synaptophysin, and an *MIB1* labeling index of 80% (not shown). Axial T2-weighted image (*A*). Axial T1-weighted fat-saturated contrast-enhanced image (*B*). Axial gradient-echo T2*-weighted image (*C*). Axial CT image (*D*).

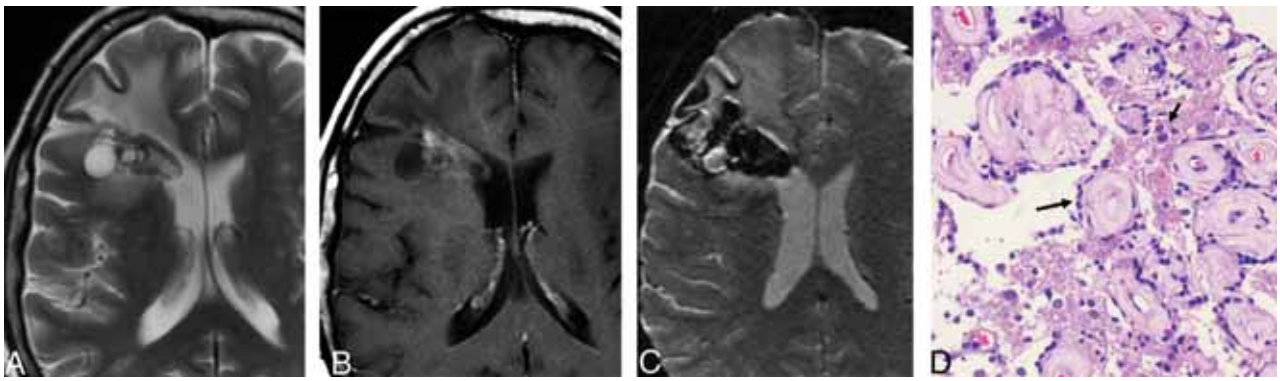

FIG 3. Papillary glioneuronal tumor in a 45-year-old man with migraine. A mixed solid and cystic periventricular tumor associated with vasogenic edema, blood products, and localized superficial siderosis. Microscopic findings are pseudopapillary structures composed of hyalinized vessels (*long arrow*) and surrounded by flattened/cuboidal glial cells. Round cells between pseudopapillae correspond to neurocytic cells (*short arrow*). Axial T2-weighted image (*A*). Axial TI-weighted fat-saturated contrast-enhanced image (*B*). Axial gradient-echo T2*-weighted image (*C*). Hematoxylin and eosin, original magnification ×100 (*D*).

and cells positive for CD34.[4] Molecular study may identify *BRAF* V600E and H3 histone mutation.[1,3]

Treatment. The treatment is an operation, adjuvant chemotherapy, and radiation therapy.[1] Postsurgical recurrence and craniospinal leptomeningeal metastases are common, and long-term survival is poor.[1,3]

Papillary Glioneuronal Tumor

Epidemiology. The papillary glioneuronal tumor is a WHO grade I, rare, neuronal-glial tumor and comprises 0.02% of all CNS tumors.[4,8] It occurs in young adults, typically in the second decade, with no predilection for sex.[3-5]

Location. The location is deep periventricular white matter, adjacent to the lateral ventricles, in the frontal (40% of cases), temporal (30%), or parietal (30%) lobes.[3,5,11,12]

Clinical Presentation. The presentation is headache, seizures, or, occasionally absent.[3,4,11]

Imaging Findings. The most common presentation is a well-circumscribed cyst, with an avid, enhancing wall or mural nodule; however, the morphology may vary from a purely cystic lesion to a completely solid mass (Fig 3).[3-5,11] The cystic component may be suppressed on FLAIR, and the solid component presents with hypo- to isointense signal on T1-weighted imaging, iso- to hyperintense signal on T2-weighted imaging, no diffusion restriction, an increased Cho/creatine ratio, and a low rCBV.[5,13] Superficial siderosis, hemosiderin, and calcification may be present, mass effect is mild, and mild perilesional edema is rare.[4,5,11,14]

Pathology Findings. Pathologic findings are flat or cuboid glial cells (astrocytes and oligodendrocyte-like cells) in a pseudopapillary arrangement with interpapillary collections of neuronal elements (ganglioid, ganglion, or neurocytes).[3-5,11] Immunohistochemistry depicts GFAP; S-100 and nestin-positive glial cells lining hyalinized vascular pseudopapillae; synaptophysin, neuron-specific enolase, and neuronal nuclear protein–positive interpapillary neuronal cells; and *OLIG2*-positive oligodendrocyte-like cells.[3,4,11,15] Molecular assessment may demonstrate t(9;17)(q(31;q24) translocation, resulting in the SLC44A1-PRKCA oncogene.[4,15]

Differential Diagnosis. The differential diagnosis is gangliogliomas, polymorphous low-grade neuroepithelial tumor of the young, pleomorphic xanthoastrocytoma, angiocentric glioma, and oligodendrocytoma.[3]

Treatment. The treatment is an operation, and prognosis is good after complete resection.[4]

Variant. An atypical papillary glioneuronal subtype has been described, with diffusion restriction, mass effect, perilesional edema, higher rCBV, intraventricular dissemination, mitoses, vascular endothelial hyperplasia, an *MIB1* labeling index of 4%–17%, and recurrence.[5,12,16,17]

Rosette-Forming Glioneuronal Tumor

Epidemiology. The rosette-forming glioneuronal tumor is a WHO grade I, rare, neuronal-glial tumor.[3,4,8,18] It occurs in children and in young and middle-aged adults, with no predilection for sex.[3-5,18,19]

Location. The location is medial and infratentorial, often in the fourth ventricle/cerebellar vermis, secondarily in the pineal region, and rarely at the septum pellucidum, hypothalamus, and temporal lobe.[1,3-5,18-20]

Clinical Presentation. The clinical presentation is headache, vomiting, visual disturbances, vertigo, ataxia, intracranial hypertension, and, rarely, epilepsy.[1,3,5,19]

Imaging Findings. The imaging findings are a heterogeneous, circumscribed multicystic intra-axial mass with hypointense signal on T1-weighted imaging, hyperintense signal on T2-weighted imaging, hemorrhage, fluid levels, no diffusion restriction, mild Cho peak elevation, mild NAA peak reduction, an absent or rare lactate doublet, and septal and parietal wall enhancement (may resemble a green bell pepper cross-section) (Fig 4).[3,5,19,21,22]

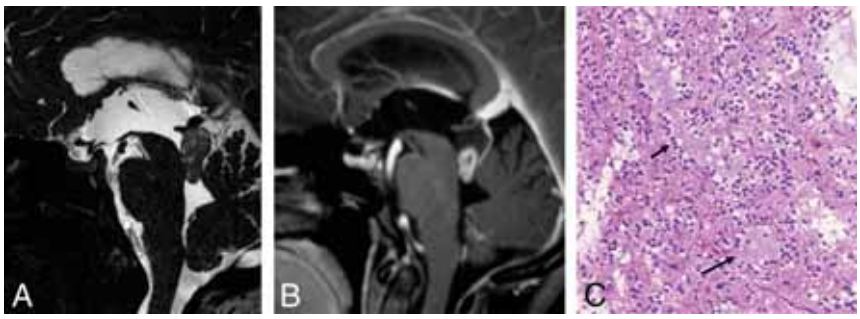

FIG 4. Rosette-forming glioneuronal tumor. A lobulated multicystic tumor in the tectal plate extending to the mesencephalic aqueduct, with nodular contrast enhancement (*short arrow*) and displacement of a supracerebellar vein (*long arrow)* (*A* and *B*). Microscopic findings are small, round cells (neurocytic cells) (*short arrow*) surrounding mucinous extracellular matrix (DNET-like morphology) (*long arrow*). Sagittal T2-weighted CISS image (*A*). Sagittal T1-weighted fat-saturated contrast-enhanced image (*B*). Hematoxylin and eosin, original magnification ×100 (*C*).

Calcification (25% of cases), CSF dissemination, and multiple satellite lesions may occasionally appear.[3,21]

Pathology Findings. Uniform neurocyte-forming rosettes or perivascular pseudorosettes and astrocytic elements (similar to pilocytic astrocytoma or oligodendroglioma).[1,3-5,18] Immunohistochemistry shows synaptophysin, *MAP2,* and neuron-specific enolase positive neuronal cells; and GFAP, *OLIG2* and S-100 positive glial cells.[4,18] Molecular studies may demonstrate *PIK3CA*, *KIAA1549-BRAF*, *FGFR1*, and *NF1* variations.[1,4,18,20]

Differential Diagnosis. The differential diagnosis is pilocytic astrocytoma, medulloblastoma, ependymoma, and fourth ventricle choroid plexus papilloma.[3,19]

Treatment The treatment is an operation.[4] Prognosis is favorable after complete resection.[4]

Myxoid Glioneuronal Tumor

Epidemiology. Myxoid glioneuronal tumor is a low-grade tumor with components resembling rosette-forming glioneuronal tumor and DNET.[7,23-25] As of the 2021 WHO classification, it is considered a different glioneuronal type.[7,23-25] It occurs in children and young adults, with no predilection for sex.[24,25]

Location. The location is the subcallosal area or septum pellucidum.[23-25]

Clinical Presentation. The clinical presentation is asymptomatic, cognitive disturbance, or headache.[23,25]

Imaging Findings. Imaging findings are a solid tumor, with hypointense signal on T1WI, hyperintense signal on T2WI, partial suppression and a peripheral rim of hyperintensity on FLAIR, no gadolinium enhancement, and mucin-filled small pseudocysts and a slight hypointense signal on susceptibility-weighted images (corresponds to hemosiderin-laden macrophages).[23-25]

Pathology Findings. Pathology findings are proliferation of oligodendrocyte-like cells with a columnar arrangement in a mucin-rich stroma, which may be associated with "floating" neurons, neurocytic rosettes, and perivascular neuropil.[7,23-25] Immunohistochemistry shows a pattern similar to that of rosette-forming glioneuronal tumor and DNET; however, the molecular profile lacks the typical variations of these tumors and presents as a PDGFRA p. K385L/I mutation.[7,23-25]

Differential Diagnosis. The differential diagnosis is central neurocytoma, subependymoma, dysembryoplastic neuroepithelial tumor, rosette-forming glioneuronal tumor, and colloid cyst.[24,25]

Treatment. The treatment is an operation, radiation therapy, and/or temozolomide.[23] Prognosis is variable, due to recurrence.[23]

Diffuse Leptomeningeal Glioneuronal Tumor

Epidemiology. Diffuse leptomeningeal glioneuronal tumor is a WHO grade I, rare, neuronal-glial tumor (previously known as disseminated oligodendroglial-like leptomeningeal tumor of childhood).[3,5,8,26] It occurs in children and adolescents, with a predilection for males.[4,5,26]

Location. The location is the basal cisterns, posterior fossa, and spinal cord.[3,26-28]

Clinical Presentation. It presents as headache, nausea, vomiting, cranial nerve dysfunction, papilledema, and CSF abnormalities, including increased protein and lymphocytosis.[3,5,26]

Imaging Findings. The imaging findings are widespread leptomeningeal thickening and intra-axial lesions.[1,3,5,26-29] The leptomeningeal disease involves mostly the posterior fossa, spinal cord, nerve roots, and perivascular spaces and is characterized by leptomeningeal thickening and enhancement and leptomeningeal cystlike lesions (corresponding to mucin-rich nodular leptomeningeal infiltration) with hypointense signal on T1-weighted imaging, hyperintense signal on T2-weighted imaging and FLAIR, and no contrast enhancement (Fig 5).[1,3,5,26-29] Intra-axial lesions are present in up to 80% of patients; they occur mostly in the spinal cord and present with hyperintense signal on T2-weighted imaging, cystic areas (corresponding to fluid and cellular debris), reduced rCBV, and usually no enhancement.[1,5,26,27,29] Hydrocephalus is common, and a large intramedullary mass without leptomeningeal disease may also occur.[3,26,29,30] Despite the description of intra-axial lesions, it is not clear whether they really are primary intraparenchymal lesions or the result of invasion of leptomeningeal lesions along Virchow-Robin spaces.[28]

Pathology Findings. The pathology findings are diffuse and multifocal leptomeningeal lesions with an oligodendroglial-like cytology in a desmoplastic or myxoid background.[1,3,6,27,28] Immunohistochemistry shows *OLIG2*-, S-10-0-, *MAP2*-positive oligodendroglial-like cells; astrocytes positive for GFAP; and neuron cells positive for synaptophysin.[1,3,4,26-28] Molecular profiling may identify *KIAA1549-BRAF*

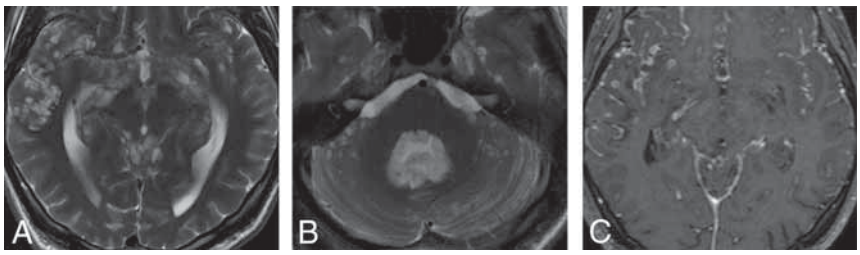

FIG 5. Diffuse leptomeningeal glioneuronal tumor in a 20-year-old man previously diagnosed 10 years earlier. Multiple superficial small cystlike lesions are seen in the brain sulci, basal cisterns, cerebellar folia, and filling the fourth ventricle (*A* and *B*). Also note extensive irregular leptomeningeal enhancement (*C*). Axial T2-weighted images (*A* and *B*). Axial T1-weighted fat-saturated contrast-enhanced image (*C*).

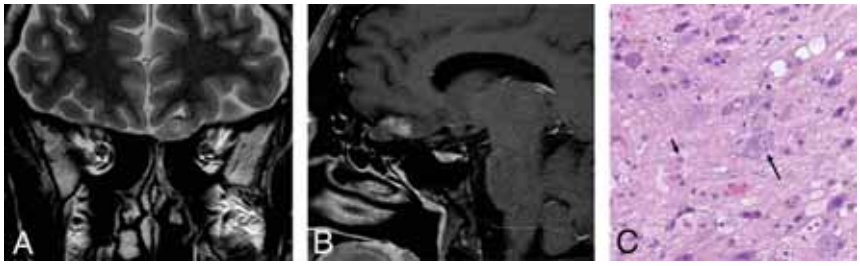

FIG 6. Gangliocytoma in a 40-year-old man with epilepsy. A lobulated tumor extending along the course of the left olfactory bulb and tract with foci of contrast enhancement (*A* and *B*). Microscopic findings are tumor composed of large (*long arrow*) and small (*short arrow*) ganglioneuronal cells, haphazardly distributed. Coronal T2-weighted image (*A*). Sagittal T1-weighted fat-saturated contrast-enhanced image (*B*). Hematoxylin and eosin, original magnification ×100 (*C*).

fusion, *BRAF* duplication, the *BRAF* V600E mutation, 1p/19q codeletion or isolated 1p deletion, and no *IDH* mutation.[1,3,4,6,26-28,30] Diagnosis may be particularly difficult when the biopsy shows only hyperplastic meningothelial cells, inflammation, or low-grade glioma (in these cases, rebiopsy is recommended).[28,31]

Differential Diagnosis. Other causes of leptomeningeal thickening, such as infectious meningitis, neurocysticercosis, primary diffuse leptomeningeal gliomatosis, leptomeningeal carcinomatosis, leukemia, and lymphoma leptomeningeal infiltration.[3,26]

Treatment. There is no standard management. Surgery may be indicated for potentially resectable lesions.[1,26,27] Radiation therapy and/or chemotherapy may also play a role.[1,26,27]

Variant. Most cases progress slowly; however, an anaplastic subtype with increased mitoses, an *MIB1* labeling index higher than 4%, and glomeruloid microvascular proliferation may have a more aggressive course.[1,3,4,28,31]

Gangliocytoma

Epidemiology. Gangliocytoma is a WHO grade I, rare, neuronal tumor.[4,8] It occurs in children and young adults, with no predilection for sex.[3,4] Most articles address gangliocytomas (a purely neuronal tumor) in conjunction with gangliogliomas (a neuronal-glial tumor), and research focused specifically on the former is rare.[32]

Location. These are located in the periphery of the temporal (75% of cases), frontal, or parietal lobes; they are occasionally exophytic and rarely extra-axial.[2-4,33]

Clinical Presentation. These present with medically refractory temporal lobe epilepsy.[3,4]

Imaging Findings. The imaging findings are a mixed, solid, and cystic lesion with iso- to hypointense signal on T1-weighted imaging, hyperintense signal in T2-weighted imaging, a high Cho peak, a low NAA peak, variable contrast enhancement (from none-to-intense), and calcification (33% of cases) of the solid component (Fig 6).[2-4,34] Mass effect and perilesional edema are minimal or absent.[4] A dural tail signal may be seen in superficially located tumors.[2]

Pathology Findings. The pathology findings are clusters of mature and often dysplastic (binucleated) neurons and nonneoplastic glial stroma, unlike gangliogliomas.[2,3] Perivascular lymphocytic infiltration is common, and mitotic figures are rare.[3,4] Immunohistochemistry may demonstrate cells positive for CD3.[3] To date, there are no genetic variations specifically described for gangliocytomas.[3]

Differential Diagnosis. The differential diagnosis is ganglioglioma (imaging may be indistinguishable), DNET, and pleomorphic xanthoastrocytoma.[2-4]

Treatment. The treatment is an operation.[3] Prognosis is favorable after complete resection.[3]

Variant. Lhermitte-Duclos disease or dysplastic cerebellar gangliocytoma may be considered a subtype of gangliocytoma; however, it is still unclear whether it is a true neoplasm, hamartoma, or malformation.[3,5] It is considered a WHO grade I tumor and may be sporadic (60% of cases) or related to Cowden syndrome (multiple hamartoma autosomal-dominant phacomatosis caused by *PTEN* mutations).[3-5,35] Young adults are mainly affected, with no predilection for sex.[2-5,35] It usually is located in the cerebellar hemisphere, vermis, or both (particularly on the left side).[2,3,5] Imaging findings are quite characteristic: nonenhancing grossly thickened cerebellar folia with the "tiger-striped" pattern (alternating layers of signal intensity on T1-weighted and T2-weighted imaging) and prominent venous channels (flow voids on susceptibility imaging with contrast enhancement) (Fig 7).[2-5,35] Histopathology depicts disruption of the normal cortical layers, dysplastic neurons, vacuoles, diffuse hypertrophy and

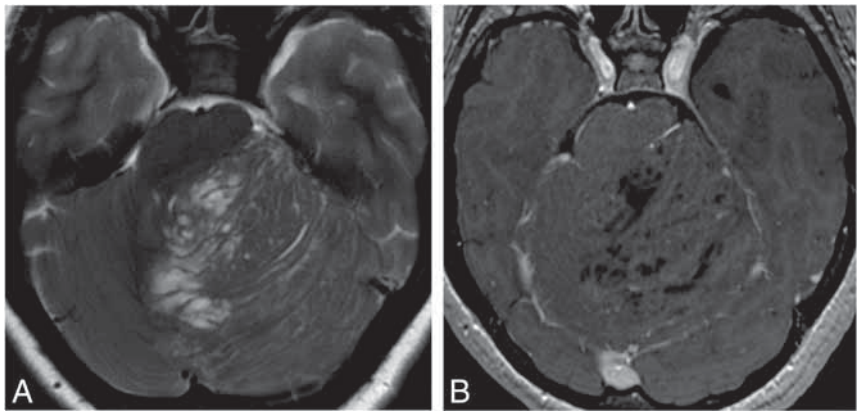

FIG 7. Dysplastic gangliocytoma of the cerebellum in a 19-year-old man with Cowden syndrome. Grossly thickened cerebellar folia with a tiger-striped pattern and rare patchy enhancement in the superior vermis and left cerebellar hemisphere. Axial T2-weighted image (*A*). Axial T1-weighted fat-saturated contrast-enhanced image (*B*).

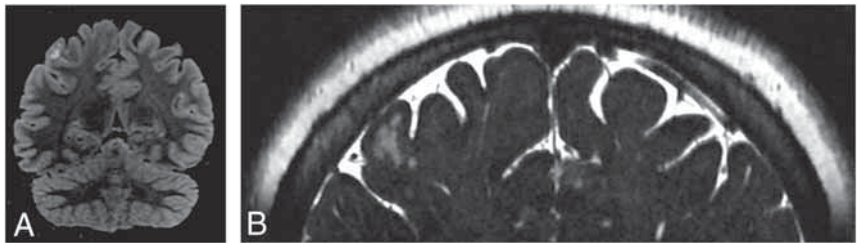

FIG 8. Multinodular and vacuolating neuronal tumor of the cerebrum in a 33-year-old asymptomatic woman. Confluent, small, round lesions in a subcortical location with hypersignal in a T2-weighted FLAIR image (*A*). They clearly show different signal from the adjacent CSF in a T2-weighted FIESTA image, differentiating them from perivascular spaces (*B*).

increased myelination of the granular and molecular layers, and reduction or absence of the Purkinje layer.[2,3,5] Immunohistochemistry demonstrates dysplastic neurons positive for synaptophysin and negative for *PTEN*.[4] Molecular assessment may show a *PTEN* germline mutation when related to Cowden syndrome.[3,4,35]

Multinodular and Vacuolating Neuronal Tumor

Epidemiology. Multinodular and vacuolating neuronal tumor is a rare lesion recently categorized as a glioneuronal tumor in the 6th edition of the WHO Classification (in the previous edition, it was considered a unique architectural pattern, whose nature may be related to neuronal tumors or malformative abnormalities).[3,5,7,8,36] Identification of clonal genetic abnormalities favors a neoplastic rather than a malformative origin, hence, the status update in the WHO classification.[6,7] It occurs in adults older than 30 years of age, with no predilection for sex.[5,36]

Location. The location is the superficial parietal, frontal, or temporal lobe and, rarely, in the posterior fossa.[4-6,36-38]

Clinical Presentation. It presents as asymptomatic and, rarely, seizures or headache.[3-6,36,38]

Imaging Findings. Imaging findings are multiple, small, and coalescent cortical and subcortical nodules, isointense to gray matter on T1-weighted imaging, hyperintense on T2-weighted imaging and FLAIR, with no mass effect, perilesional edema, calcification, diffusion restriction, and contrast enhancement (though faint enhancement may occasionally be present) (Fig 8).[3,5,36,38] Spectroscopy and perfusion are usually normal.[3-5,36,38]

Pathology Findings. Pathology findings are ambiguous neuronal cells or dysplastic glial cells with cytoplasmic and stromal vacuolation.[3-5,36] Immunohistochemistry demonstrates HuC/HuD neuronal antigens, *OLIG2*, and cells positive for internexin-a and cells weakly positive or negative for synaptophysin and neurofilament.[3,36] Molecular studies may identify *MAP2K1*, *FGFR2*, and non-*BRAF* V600E variations.[6,39]

Differential Diagnosis. The differential diagnosis is DNET, polymorphous low-grade neuroepithelial tumor of the young, and angiocentric glioma.[3,4,36]

Treatment. Follow-up imaging and expectant management if the patient is stable is usually recommended, and surgery may be indicated if the patient is clearly symptomatic.[4,36] Total resection is curative.[4]

Central Neurocytoma

Epidemiology. Central neurocytoma is a WHO grade I, rare, neuronal tumor.[1,3,5,8] It occurs in young and middle-aged adults, with no predilection for sex.[1,3,5]

Location. It is adjacent to the septum pellucidum and foramen of Monro.[1-4]

Clinical Presentation. It presents with headache, mental status change, visual disturbance, and intracranial hypertension.[1,3,5]

Imaging Presentation. The presentation is an intraventricular, heterogeneous, and "bubbly" mixed, solid and cystic lesion, with a solid component presenting heterogeneous signal, isointense to gray matter on T1-weighted imaging, hyperintense on FLAIR, with flow voids, calcification (50% of cases) with hemorrhage, diffusion restriction, a decreased NAA peak, a moderately elevated Cho peak, and the presence of glycine and alanine peaks, increased rCBV, and moderate-to-intense enhancement (Fig 9).[1-3,5,19]

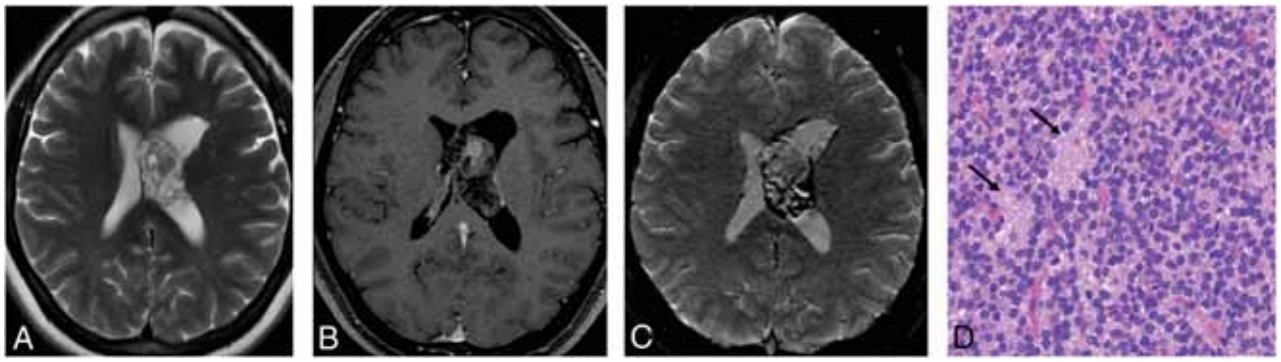

FIG 9. Central neurocytoma. An intraventricular bubbly lesion adjacent to the septum showing honeycombing contrast enhancement and extensive signs of calcification and hemorrhage (*A–C*). Microscopic findings are sheets of round cells with scant cytoplasm. Neurocytic rosettes are present (*arrows*). Axial T2-weighted image (*A*). Axial T1-weighted fat-saturated contrast-enhanced image (*B*). Axial gradient-echo T2*-weighted image (*C*). Hematoxylin and eosin, original magnification ×200 (*D*).

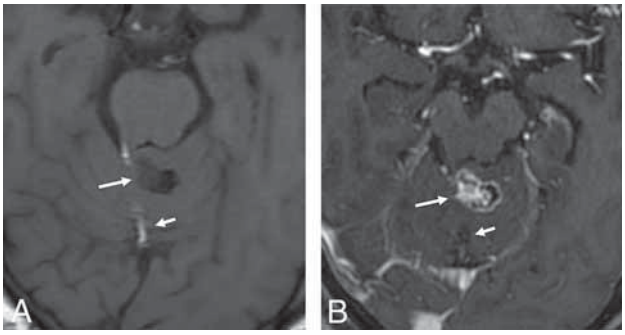

FIG 10. Cerebellar liponeurocytoma in a 71-year-old woman with transient neurologic deficits. A heterogeneously enhancing nodule (*long arrow*) in the superior vermis associated with a linear component compatible with macroscopic fat (*short arrow*). Axial T1-weighted image (*A*). Axial T1-weighted fat-saturated contrast-enhanced image (*B*).

Pathology Findings. It presents with uniform, mature, neurocytic elements arranged in sheets or lobules.[1,3] Immunohistochemistry identifies cells positive for synaptophysin and neuron-specific enolase and cells negative for *OLIG2*.[2,3] Molecular profiling depicts *N-MYC, IGF2*, *PTEN*, *PDGFD*, and NRG2, *WNT*, 1p/19q, and *Tp53* variations.[1,4]

Differential Diagnosis. The differential diagnosis is subependymoma, ependymoma, subependimal giant cell astrocytoma, meningioma, and intraventricular oligodendroglioma.[2,3]

Treatment. The treatment is an operation and adjuvant radiation therapy if there is subtotal resection or a high *MIB1* labeling index.[1,3] The prognosis is usually favorable, though rare recurrence may occur, especially if increased mitoses or *MIB1* labeling index higher than 2% is observed.[1-4]

Variants. Variants are extraventricular and cerebellar liponeurocytoma. Extraventricular neurocytoma is histologically similar to central neurocytoma, except for necrosis, vascular proliferation, and increased mitoses.[1,3-5,40] It is located outside the ventricular system, usually in the cerebral hemispheres, and imaging depicts hemorrhage, perilesional edema, and a low or absent NAA peak.[1,3-5,40] Cerebellar liponeurocytoma is composed of neurocytic elements and lipomalike features, usually with a low *MIB1* labeling index.[1,3-5,40] Imaging may depict fat areas on T1-weighted images, confirmed with fat-suppression, chemical shift imaging, or a prominent lipid peak (Fig 10).[1,3-5,40]

Differential Diagnosis. The imaging findings of glioneuronal tumors are quite varied, and the number of differential diagnoses is high. The identification of a focal lesion with a cystic component in the CNS should signal the possibility of glioneuronal and low-grade glial tumors. The diagnostic approach can be facilitated with a flow chart organized according to the morphology of the lesion, its location, and ancillary findings (Fig 1). Next, imaging features of the main differential diagnosis of uncommon glioneuronal tumors will be summarized.

Gangliogliomа, DNET, and desmoplastic infantile tumors are common WHO grade I neuronal-glial tumors that usually affect the superficial temporal or frontal lobes of children and young adults.[1-5,8] Gangliogliomа presents as a mixed solid and cystic lesion with calcification, increased rCBV, and homogeneous enhancement of the solid portion; however, atypical finding, such as heterogeneous enhancement and superficial siderosis may also occur (Online Supplemental Data).[1-5] DNET is characterized by a cortically based bubbly wedge-shaped lesion with an increased myo-inositol peak, heterogeneously reduced rCBV, usually no contrast enhancement, and a thin halo of hyperintense signal in FLAIR (Online Supplemental Data).[1-5] Calvarial remodeling, adjacent focal cortical dysplasia, and displacement of white matter tracts rather than disruption in tractography may also be present in both, mass effect is minimal if present, and perilesional edema is usually absent.[1-5] Desmoplastic infantile tumor presents as a large multilobar mixed solid and cystic lesion with a deep cystic component and a superficial solid plaquelike or dural-based
portion, with the dural tail sign, diffusion restriction, avid heterogeneous enhancement, mass effect, and mild perilesional edema (Online Supplemental Data).[2,3,5]

Polymorphous low-grade neuroepithelial tumor of the young is a rare and recently described entity, the categorization of which is not well-defined. It is not yet graded by the WHO and may be

considered a low-grade neuroepithelial or a glioneuronal tumor.[6,41,42] The temporal lobe is the most frequent site, and seizures are the major clinical presentation.[41,42] Imaging depicts a superficial, solid tumor with isointense-to-hyperintense signal on T1-weighted imaging, hyperintense signal on T2-weighted and FLAIR imaging, calcification, cystic degeneration, and irregular or nodular contrast enhancement (Online Supplemental Data).[41-43] Small nodular diffusion restriction foci and focal high rCBV may rarely occur; however, mass effect and perilesional edema are absent.[41-43] Pathology and molecular diagnostics are characterized by oligodendroglioma-like cellular features, an infiltrative growth pattern, pseudorosette formation, intense CD34 immunopositivity, *BRAF* p.V600E mutation, or *FGFR2/3* fusion.[6,41,42]

Pleomorphic xanthoastrocytoma and angiocentric glioma are low-grade glial epilepsy-related tumors that usually affect the superficial temporal, frontal, or parietal lobes of children and young adults.[3,4,8,44] Pleomorphic xanthoastrocytoma is characterized by a cyst and a leptomeningeal-based mural nodule with avid contrast enhancement and an adjacent dural tail sign (Online Supplemental Data).[3,4] Angiocentric glioma presents as a diffusely infiltrating and noncircumscribed lesion, with increased ribbonlike signal on T1-weighted imaging, hyperintense signal on T2-weighted and FLAIR imaging, a high Cho peak, a low NAA peak, reduced rCBV, and no contrast enhancement (Online Supplemental Data).[44] Additionally, although pilocytic astrocytoma is not an epilepsy-related tumor, it still is the most common low-grade glioma of young patients and also is a differential diagnosis of glioneuronal tumors, especially papillary.[3] Pilocytic astrocytoma is commonly seen in children and characterized by a posterior fossa solid-cystic tumor with a marked enhancement of the solid portion.[13]

CONCLUSIONS

Glioneuronal tumors are an uncommon group of brain tumors with heterogeneous pathologic, radiologic, and prognostic features. With the growing description of immunohistochemistry and molecular findings of these tumors, new subtypes are being reported. The typical imaging findings of some glioneuronal tumors may facilitate the distinction from low-grade glial tumors and guide the pathologic investigation with targeted immunohistochemistry and molecular research. Therefore, neuroimaging may play a pivotal role in the correct diagnosis and management of glioneuronal tumors.

Disclosure forms provided by the authors are available with the full text and PDF of this article at www.ajnr.org.

REFERENCES

1. Gatto L, Franceschi E, Nunno VD, et al. **Glioneuronal tumors: clinicopathological findings and treatment options.** *Future Neurol* 2020;15:FNL47 CrossRef
2. Shin JH, Lee HK, Khang SK, et al. **Neuronal tumors of the central nervous system: radiologic findings and pathologic correlation.** *Radiographics* 2002;22:1177–89 CrossRef Medline
3. Osborn AG, Hedlund GL, Salzman KL. *Osborn's Brain: Imaging, Pathology, and Anatomy*. 2nd ed. Elsevier; 2017
4. Chougule M. *Neuropathology of Brain Tumors with Radiologic Correlates*. Springer-Verlag; 2020
5. Abdel Razek AA, Elsebaie NA, Zamora C, et al. **Imaging of neuronal and mixed glioneuronal tumors.** *J Comput Assist Tomogr* 2020;44:356–69 CrossRef Medline
6. Louis DN, Wesseling P, Aldape K, et al. **cIMPACT-NOW update 6: new entity and diagnostic principle recommendations of the cIMPACT-Utrecht meeting on future CNS tumor classification and grading.** *Brain Pathol* 2020;30:844–56 CrossRef Medline
7. Louis DN, Perry A, Wesseling P, et al. **The 2021 WHO Classification of Tumors of the Central Nervous System: a summary.** *Neuro Oncol* 2021;23:1231–51 CrossRef Medline
8. Louis DN, Perry A, Reifenberger G, et al. **The 2016 World Health Organization Classification of Tumors of the Central Nervous System: a summary.** *Acta Neuropathol* 2016;131:803–20 CrossRef Medline
9. Lucas JT Jr. Huang AJ, Mott RT, et al. **Anaplastic ganglioglioma: a report of three cases and review of the literature.** *J Neurooncol* 2015;123:171–77 CrossRef Medline
10. Baño AN, Fernández-Hernández CM, García CS, et al. **Parietal anaplastic ganglioglioma in a 3-year-old girl.** https://www.eurorad.org/case/14890. Accessed July 1, 2021
11. Williams SR, Joos BW, Parker JC, et al. **Papillary glioneuronal tumor: a case report and review of the literature.** *Ann Clin Lab Sci* 2008;38:287–92 Medline
12. Myung JK, Byeon SJ, Kim B, et al. **Papillary glioneuronal tumors: a review of clinicopathologic and molecular genetic studies.** *Am J Surg Pathol* 2011;35:1794–1805 CrossRef Medline
13. Yadav N, Rao S, Saini J, et al. **Papillary glioneuronal tumors: a radiopathologic correlation.** *Eur J Radiology* 2017;97:44–52 CrossRef Medline
14. Konya D, Peker S, Ozgen S, et al. **Superficial siderosis due to papillary glioneuronal tumor.** *J Clin Neurosci* 2006;13:950–52 CrossRef Medline
15. Bridge JA, Liu XQ, Sumegi J, et al. **Identification of a novel, recurrent SLC44A1-PRKCA fusion in papillary glioneuronal tumor.** *Brain Pathol* 2013;23:121–28 CrossRef Medline
16. Vaquero J, Coca S. **Atypical papillary glioneuronal tumor.** *J Neurooncol* 2007;83:319–23 CrossRef Medline
17. Javahery RJ, Davidson L, Fangusaro J, et al. **Aggressive variant of a papillary glioneuronal tumor: report of 2 cases.** *J Neurosurg Pediatr Pediatr* 2009;3:46–52 CrossRef Medline
18. Sievers P, Appay R, Schrimpf D, et al. **Rosette-forming glioneuronal tumors share a distinct DNA methylation profile and mutations in FGFR1, with recurrent co-mutation of PIK3CA and NF1.** *Acta Neuropathol* 2019;138:497–504 CrossRef Medline
19. Gao L, Han F, Jin Y, et al. **Imaging features of rosette-forming glioneuronal tumours.** *Clin Radiology* 2018;73:275–82 CrossRef Medline
20. Ellezam B, Theeler BJ, Luthra R, et al. **Recurrent PIK3CA mutations in rosette-forming glioneuronal tumor.** *Acta Neuropathol* 2012;123:285–87 CrossRef Medline
21. Hsu C, Kwan G, Lau Q, et al. **Rosette-forming glioneuronal tumour: imaging features, histopathological correlation and a comprehensive review of literature.** *Br J Neurosurg* 2012;26:668–73 CrossRef Medline
22. Medhi G, Prasad C, Saini J, et al. **Imaging features of rosette-forming glioneuronal tumours (RGNTs): a series of seven cases.** *Eur Radiol* 2016;26:262–70 CrossRef Medline
23. Lucas CG, Villanueva-Meyer JE, Whipple N, et al. **Myxoid glioneuronal tumor, PDGFRA p.K385-mutant: clinical, radiologic, and histopathologic features.** *Brain Pathol* 2020;30:479–94 CrossRef Medline
24. Solomon DA, Korshunov A, Sill M, et al. **Myxoid glioneuronal tumor of the septum pellucidum and lateral ventricle is defined by a recurrent PDGFRA p.K385 mutation and DNT-like methylation profile.** *Acta Neuropathol* 2018;136:339–43 CrossRef Medline
25. Narvaez ED, Inada BS, Almeida P, et al. **Myxoid glioneuronal tumour–report of three cases of a new tumour in a typical location and review of literature.** *BJR Case Rep* 2021;6:20200139 CrossRef Medline

26. Lakhani DA, Mankad K, Chhabda S, et al. **Diffuse leptomeningeal glioneuronal tumor of childhood.** *AJNR Am J Neuroradiol* 2020;41:2155–59 CrossRef Medline
27. Dodgshun AJ, SantaCruz N, Hwang J, et al. **Disseminated glioneuronal tumors occurring in childhood: treatment outcomes and BRAF alterations including V600E mutation.** *J Neurooncol* 2016;128:293–302 CrossRef Medline
28. Rodriguez FJ, Perry A, Rosenblum MK, et al. **Disseminated oligodendroglial-like leptomeningeal tumor of childhood: a distinctive clinicopathologic entity.** *Acta Neuropathol* 2012;124:627–41 CrossRef Medline
29. Xu H, Chen F, Zhu H, et al. **Diffuse leptomeningeal glioneuronal tumor in a Chinese adult: a novel case report and review of literature.** *Acta Neurol Belg* 2020;120:247–56 CrossRef Medline
30. Appay R, Pages M, Colin C, et al. **Diffuse leptomeningeal glioneuronal tumor: a double misnomer? A report of two cases.** *Acta Neuropathol Commun* 2020;8:95 CrossRef Medline
31. Rossi S, Rodriguez FJ, Mota RA, et al. **Primary leptomeningeal oligodendroglioma with documented progression to anaplasia and t(1;19)(q10;p10) in a child.** *Acta Neuropathol* 2009;118:575–77 CrossRef Medline
32. Odia Y. **Gangliocytomas and gangliogliomas: review of clinical, pathologic and genetic features.** *Clin Oncol* 2016;1:1017
33. Kim HS, Lee HK, Jeong AK, et al. **Supratentorial gangliocytoma mimicking extra-axial tumor: a report of two cases.** *Korean J Radiol* 2001;2:108–12 CrossRef Medline
34. Miyake Y, Mishima K, Suzuki T, et al. **A case of suspicious gangliocytoma with heterogeneously distributed lesions in the thalamus and basal ganglia.** *NMC Case Rep J* 2018;5:61–64 CrossRef Medline
35. Shinagare AB, Patil NK, Sorte SZ. **Case 144: dysplastic cerebellar gangliocytoma (Lhermitte-Duclos disease).** *Radiology* 2009;251:298–303 CrossRef Medline
36. Nunes RH, Hsu CC, da Rocha AJ, et al. **Multinodular and vacuolating neuronal tumor of the cerebrum: a new "leave me alone" lesion with a characteristic imaging pattern.** *AJNR Am J Neuroradiol* 2017;38:1899–1904 CrossRef Medline
37. Agarwal A, Lakshmanan R, Devagnanam I, et al. **Multinodular and vacuolating neuronal tumor of the cerebrum: does the name require review?** *AJNR Am J Neuroradiol* 2019;40:E69–70 CrossRef Medline
38. Lecler A, Bailleux J, Carsin B, et al.; ENIGMA Investigation Group (EuropeaN Interdisciplinary Group for MVNT Analysis), **Multinodular and vacuolating posterior fossa lesions of unknown significance.** *AJNR Am J Neuroradiol* 2019;40:1689–94 CrossRef Medline
39. Pekmezci M, Stevers M, Phillips JJ, et al. **Multinodular and vacuolating neuronal tumor of the cerebrum is a clonal neoplasm defined by genetic alterations that activate the MAP kinase signaling pathway.** *Acta Neuropathol* 2018;135:485–88 CrossRef Medline
40. Gembruch O, Junker A, Mönninghoff C, et al. **Liponeurocytoma: systematic review of a rare entity.** *World Neurosurg* 2018;120:214–33 CrossRef Medline
41. Huse JT, Snuderl M, Jones DT, et al. **Polymorphous low-grade neuroepithelial tumor of the young (PLNTY): an epileptogenic neoplasm with oligodendroglioma-like components, aberrant CD34 expression, and genetic alterations involving the MAP kinase pathway.** *Acta Neuropathol* 2017;133:417–29 CrossRef Medline
42. Sumdani H, Shahbuddin Z, Harper G, et al. **Case report of rarely described polymorphous low-grade neuroepithelial tumor of the young and comparison with oligodendroglioma.** *World Neurosurg* 2019;127:47–51 CrossRef Medline
43. Benson JC, Summerfield D, Carr C, et al. **Polymorphous low-grade neuroepithelial tumor of the young as a partially calcified intra-axial mass in an adult.** *AJNR Am J Neuroradiol* 2020;41:573–78 CrossRef Medline
44. da Silva JF, de Souza Machado GH, Pedro MK, et al. **Angiocentric glioma: literature review and first case in Brazil.** *Interdiscip Neurosurg* 2019;18:100508 CrossRef

Intraosseous Venous Malformations of the Head and Neck

S.B. Strauss, J.M. Steinklein, C.D. Phillips, and D.R. Shatzkes

ABSTRACT

SUMMARY: Intraosseous venous malformations represent a subtype of venous vascular malformations that arise primarily in bone. In the head and neck, intraosseous venous malformations are most frequently found in the skull, skull base, and facial skeleton, with location at the geniculate ganglion of the facial nerve perhaps the most widely recognized. These non-neoplastic lesions are characterized by dilated venous channels with characteristic internal bony spicules on CT but may present with a more complex appearance on MR imaging and may share features with more aggressive lesions. Further confounding the imaging-based diagnosis of intraosseous venous malformation is the frequent misrepresentation of these lesions as hemangiomas in the radiology and clinical literature, as well as in daily practice. Because most intraosseous venous malformations can be left alone, their correct diagnosis may spare a patient unnecessary concern and intervention.

ABBREVIATIONS: FN = facial nerve; FS = fat saturated; GLUT1 = glucose transporter 1; IOVM = intraosseous venous malformation; ISSVA = International Society for the Study of Vascular Anomalies

Venous malformations are part of the spectrum of vascular malformations designated by their vessel of origin, based on the widely accepted classification of vascular anomalies endorsed by the International Society for the Study of Vascular Anomalies (ISSVA).[1] They represent congenitally malformed and dilated venous channels with sluggish internal flow that occur commonly in soft tissue; in the head and neck, the muscles of mastication are a particularly frequent site. Intraosseous venous malformations (IOVMs) are less common compared with soft-tissue venous malformations in the head and neck. When found within the facial skeleton, calvaria, and skull base, IOVMs may demonstrate an aggressive appearance, with medullary space expansion, enhancement, and cortical thinning. Identification of coarsened internal trabeculae, best appreciated on CT, is nearly pathognomonic of this entity[2,3] and may obviate the need for biopsy.

Incorrect nomenclature is often applied to soft-tissue vascular malformations within the head and neck. This is particularly true of cavernous venous vascular malformations within the orbit, cavernous sinus, or brain parenchyma, which consist of cavernous venous spaces lined by endothelial cells. Because these lesions have a pseudoencapsulated appearance, they are often inappropriately referred to as "cavernous hemangioma" or "angioma," suggesting neoplasia rather than the more appropriate designation of "cavernous venous malformation."

Similarly, a major factor in the confusion surrounding the correct diagnosis of vascular malformations within bone derives from the inconsistency and inaccuracy in nomenclature used in the small body of literature on the topic. These lesions are frequently incorrectly referred to as "ossifying hemangiomas" or when in the temporal bone, as "facial nerve hemangioma" and qualified as "cavernous" or "capillary." The more apt description of such lesions as venous malformation was first introduced by Mulliken and Glowacki,[4] in 1982, who proposed a classification scheme based on the pathophysiology of vascular lesions and differentiated between vascular tumors and vascular malformations. In this binary classification system, the term "hemangioma" is reserved for the common benign vascular tumor of infancy, a true neoplasm that grows by endothelial hyperplasia and expresses markers of cellular proliferation such as vascular endothelial growth factor and cell nuclear antigen, as well as the immunohistochemical marker glucose transporter protein-1 (glucose transporter 1 [GLUT1]). Hemangiomas additionally manifest a unique triphasic growth pattern, with rapid enlargement during infancy followed by spontaneous involution and, typically, complete

Received February 10, 2022; accepted after revision May 10.

From the Department of Radiology (S.B.S., C.D.P.), NewYork-Presbyterian/Weill Cornell Medical Center, New York, New York; and Department of Radiology (J.M.S., D.R.S.), Zucker School of Medicine at Hofstra/Northwell, New York, New York.

Please address correspondence to Deborah R. Shatzkes, MD, Department of Radiology, Lenox Hill Hospital, Zucker School of Medicine at Hofstra/Northwell, New York, NY 10075; e-mail: dshatzkes@northwell.edu; @DShatzkes; @CDP_Rad

Indicates open access to non-subscribers at www.ajnr.org

http://dx.doi.org/10.3174/ajnr.A7575

Table 1: Commonly used terms and the corresponding correct terminology

Category	Incorrect	Correct
Calvaria	Calvarial hemangioma	Intraosseous vascular malformation (venous)
	Ossifying hemangioma	Low-flow vascular malformation of the bone
	Cavernoma of the skull	
Facial skeleton	Facial bone hemangioma	Intraosseous vascular malformation (venous)
	Intrabony hemangioma	Low-flow vascular malformation of the bone
	Cellular hemangioma	
Skull base/facial nerve	FN capillary hemangioma	Intraosseous vascular malformation (venous)
	FN cavernous hemangioma	Low-flow vascular malformation of the bone

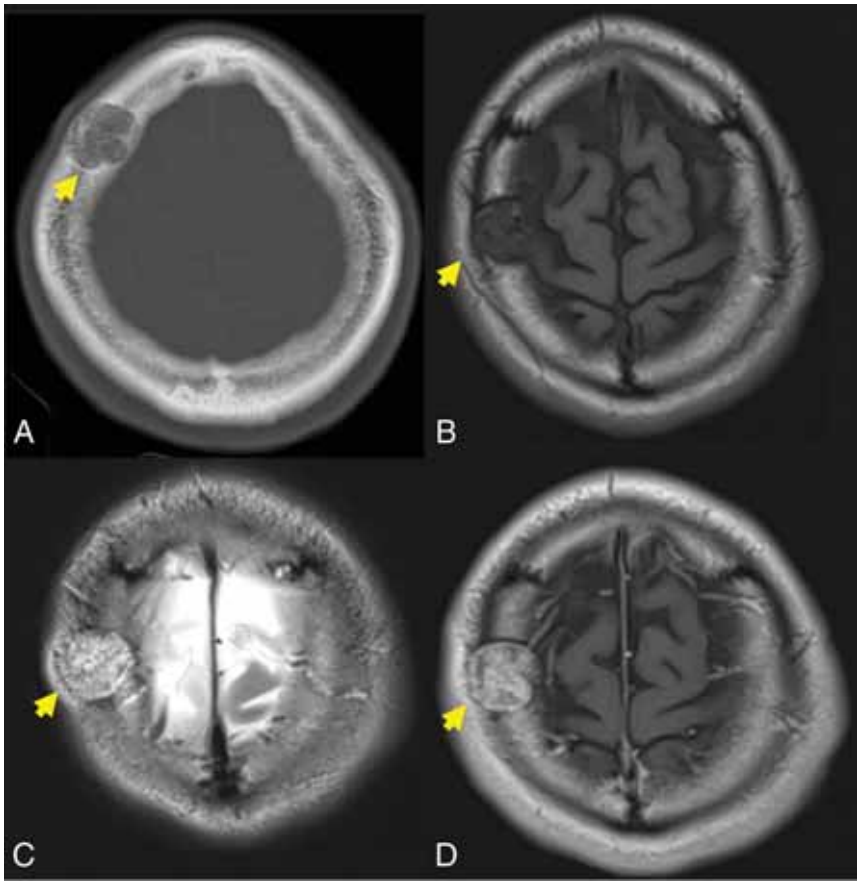

FIG 1. A 39-year-old man with a slowly growing calvarial mass. Axial CT (*A*) demonstrates a lucent right frontal bone lesion centered in the diploic space with a honeycomb pattern of internal calcification (*arrow*). Note a minimal overlying scalp deformity; the patient was able to palpate this slowly growing lesion. The lesion (*arrow* in *B–D*) demonstrates intermediate signal on T1WI (*B*), marked hyperintensity on T2WI (*C*), and prominent contrast enhancement, T1WI C+ (*D*). Note the internal foci of low signal most prominent on the T2-weighted examination (*C*) corresponding to the internal bone spicules evident on the CT. The diagnosis of IOVM was made on the basis of the characteristic imaging appearance. C+ indicates with contrast.

resolution by mid-childhood. Conversely, vascular malformations are non-neoplastic, static errors of vascular morphogenesis that will not regress spontaneously and are composed of dysmorphic forms of the vessels of origin (capillary, venous, lymphatic, arterial) with growth occurring on the basis of progressive vascular ectasia, rather than cellular proliferation. IOVMs are part of the latter category, representing dilated and ectatic venous channels within bone. In fact, it has been argued that true intraosseous hemangiomas do not exist, and one should assume that all such lesions identified within bone represent IOVM.[5] This is true not only for venous malformations of the head and neck but for those found in vertebral bodies as well.[6] In 2014, the ISSVA published an updated classification based on the work of Mulliken and Glowacki,[4] similarly classifying lesions as vascular tumors and vascular malformations.[7]

Although the nomenclature of Mulliken and Glowacki[4] has been in existence for >30 years, incorrect terminology remains prevalent in the literature. Hassanein et al[8] performed a literature review and found the term "hemangioma" incorrectly used in about 70% of all articles published in 2009; most important, 20% of these patients received inappropriate therapy because of this seemingly trivial error in nosology. Whereas infantile hemangioma causing substantial disturbance in form or function may be treated pharmacologically, venous malformations will not respond to antiangiogenic treatment. Sclerotherapy, possibly in combination with surgical excision, may be required.[5] Fábián et al[9] performed a literature search for terminology used for intraosseous vascular lesions, including intraosseous hemangioma and "intraosseous malformation" of the face. Of 272 cases reported between 1950 and 2016, 50.7% were incorrectly described as hemangiomas.[9] Further analysis, however, demonstrated that before the first ISSVA publication in 1996, almost 91% of cases were reported as intraosseous hemangiomas, while in subsequent years, usage of this incorrect terminology dropped to 39%.[9]

Despite increasing familiarity with the ISSVA classification and nomenclature on the part of clinicians and researchers, much work

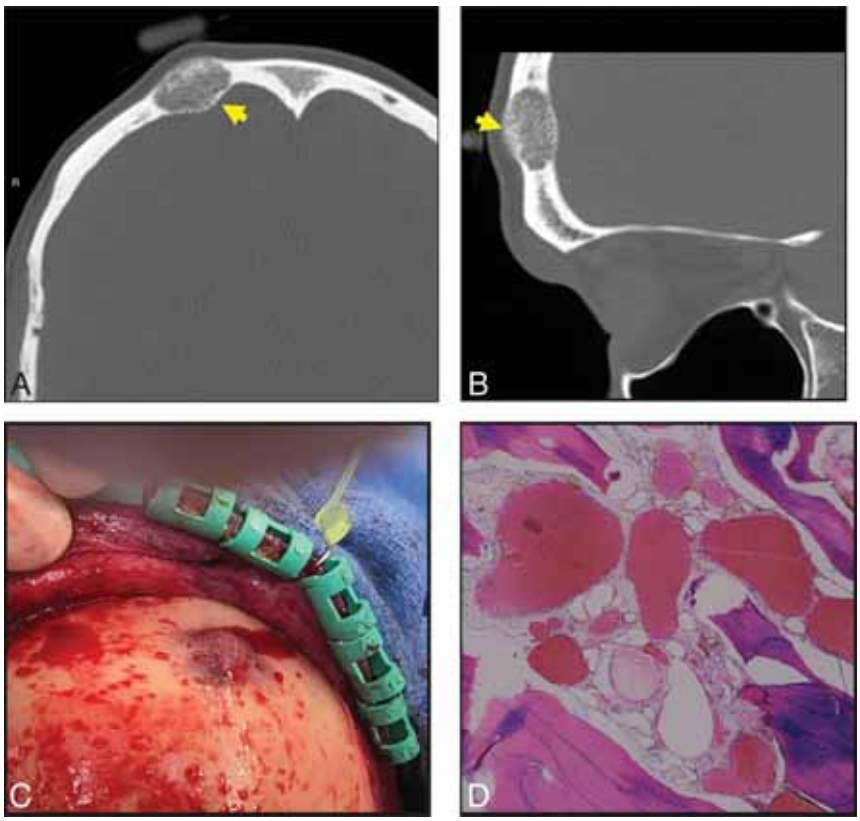

FIG 2. A 40-year-old man with a palpable frontal bump. Axial (*A*) and sagittal (*B*) thin-section CT images demonstrate a typical expansile lucent lesion with internal spiculated calcification (*yellow arrow*, *A* and *B*). Intraoperative photograph (*C*) shows a raised, red, porous-appearing calvarial lesion. H&E-stained photomicograph (*D*) shows dilated cavernous blood-filled spaces lined by flattened epithelium, characteristic of a venous malformation. There is focal hemosiderin staining, which is evidence of prior hemorrhage.

remains regarding the use of correct terminology when dealing with vascular lesions. It is the authors' opinion that the incorrect nomenclature should not be used in reports, even if discrepant from the vernacular used by referring physicians, because inappropriate descriptions of a vascular malformation such as a hemangioma will only further serve to perpetuate confusion surrounding the topic. Instead, the authors suggest using the correct term and then adding "previously known as hemangioma" within the report. Clarification and collegial education regarding the choice of terminology might accompany the report via phone or email communication to the ordering provider. Table 1 shows commonly used terms and the corresponding correct terminology.

Like all vascular malformations, IOVMs are present at birth and will grow in tandem with the somatic growth of the child, occasionally punctuated by periods of more rapid enlargement stimulated by hormonal, inflammatory, or traumatic factors.[10] Politi et al[11] report a female predilection, which suggests possible endothelial growth by hormone stimulation. Similarly, malformations

Table 2: Imaging findings of IOVM and common lesions in the differential diagnosis

Diagnosis	CT Findings	MR Imaging Findings
IOVM	Expansile and well-circumscribed Cortex intact, but thin/scalloped Stippled internal trabeculae, or, Honeycomb/spoke wheel ossification	T2-very hyperintense, with internal stippled or striated signal void T1 signal varies, thrombus may be bright T1 + gadolinium–avid enhancement
Intraosseous meningioma	Dense marrow sclerosis and shaggy cortical hyperostosis Extraosseous soft tissue	T2 intermediate T1 + gadolinium Intraosseous: ± enhancement Extraosseous: avid plaquelike enhancement
Fibrous dysplasia	Ground-glass matrix, ± cystic or more sclerotic elements	T2 low-intermediate signal, though varies depending on cystic change T1 + gadolinium: avid enhancement
Metastasis, myeloma	No matrix Cortical lysis Multiplicity	Variable, depending on primary tumor
Lymphoma	No matrix Hyperdense soft tissue	T2 intermediate, T1 + gadolinium: bland enhancement Diffusion-restriction, hypercellularity
Chondrosarcoma	Rings/whorls of calcified matrix Classic location, petroclival	T2 marked hyperintensity Enhancement, variable but often mild
Epidermoid cyst	Low density No internal matrix	T1-hypointense, T2-hyperintense Diffusion restriction No internal enhancement

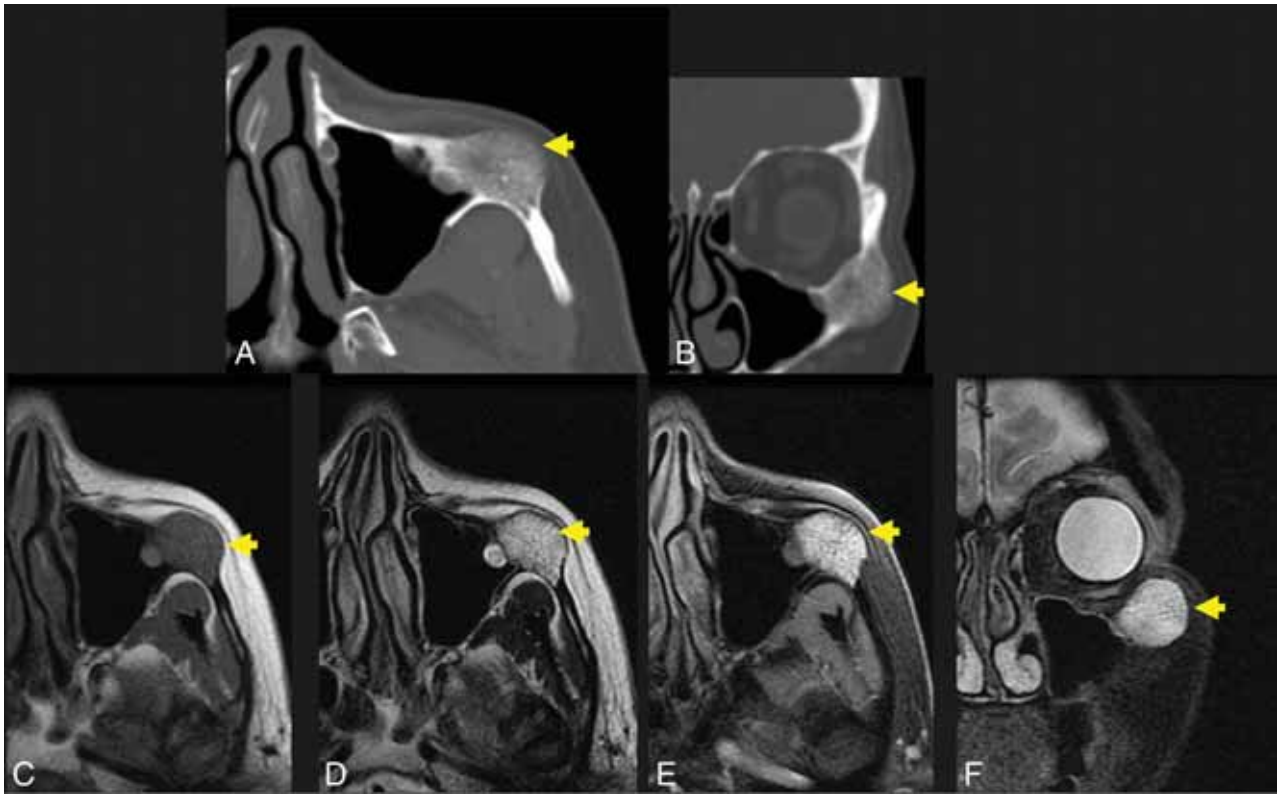

FIG 3. A 56-year-old woman with a palpable facial mass. The *yellow arrow* indicates a lesion in *A–F*. Axial (*A*) and coronal (*B*) thin-section CT in bone windows demonstrates an expansile, low-density lesion with internal coarsened trabeculae. The characteristic internal honeycomb pattern is typical of an IOVM. Axial T1 C– (*C*) and axial T1 C+ FS (*D*) sequences demonstrate a T1-intermediate, avidly enhancing lesion that extends beyond the cortical margin; the cortex is thinned but identifiable. Axial T2 FS (*E*) and coronal T2 FS (*F*) sequences demonstrate that the lesion is markedly T2 hyperintense. The diagnosis of IOVM was made on the basis of the characteristic imaging appearance, and the lesion remained stable on surveillance imaging for 3 years. C+ indicates with contrast; C–, without contrast.

may present in adolescence during growth spurts and presumably also under the influence of endogenous hormones. Within the lesion, repetitive intralesional hemorrhage may contribute to lesion expansion. IOVMs are often discovered incidentally on imaging studies performed for an unrelated indication; though in more superficial locations, such as in the zygoma, they may be visible or palpable. In the temporal bone, IOVMs are most frequently identified adjacent to the geniculate ganglion of the facial nerve. At this site, clinical presentation may be of progressive facial nerve paresis. Given that most lesions are asymptomatic, the overall prevalence of IOVMs in the population is difficult to estimate, though they are thought to represent <1% of osseous neoplastic and tumorlike lesions.[12] Treatment is predicated on symptoms; incidentally discovered, asymptomatic lesions do not require therapy. IOVMs that result in cosmetic or functional issues are treated by surgical excision.[13,14]

On gross pathology, IOVMs are described as spongy or porous, raised hemorrhagic lesions, often with ill-defined margins relative to adjacent normal bone. On histopathologic analysis, mature bony trabeculae are separated by thin-walled dilated cavernous vascular spaces that are lined by flattened endothelial cells.[15-17] Immunohistochemical analysis can definitively distinguish IOVMs and other vascular malformations from infantile hemangiomas by assaying for GLUT1.[10,18]

IOVMs demonstrate low-to-intermediate signal intensity on T1WI; there may be areas of sporadic internal T1-shortening at sites of hemorrhage or thrombosis.[19] On T2WI, IOVMs will demonstrate heterogeneous, high signal intensity.[2] There is heterogenous, avid contrast enhancement, which may be delayed.[20] Internal areas of signal void may be visible, often in a spiculated "sunburst" pattern, representing the characteristic radiating internal bony trabeculae. The sunburst pattern results from bony displacement by a network of vascular spaces, with reactive new bone formation resulting in thickened trabeculae. When these trabeculae are viewed in cross-section, a "honeycomb" or "soap bubble" appearance is described. On CT, this trabecular pattern will be highlighted against a background of an expansile lucent osseous lesion, with intact cortical margins. Phleboliths, appearing as rounded areas of signal void on MR imaging and calcification on CT, are occasionally identified, though they are considerably less frequent in IOVMs compared with their soft-tissue counterparts. Because IOVMs are low-flow lesions, there is no role for either cross-sectional or catheter angiographic studies in their diagnosis or characterization. IOVMs may demonstrate an atypical appearance on MR imaging when relatively lipid-poor and may also exhibit a more aggressive-type behavior, leading to soft-tissue extension, cortical expansion, and potentially pathologic fracture.[21-23] Some authors postulate that aggressive features are more commonly seen in underlying combined capillary-venous

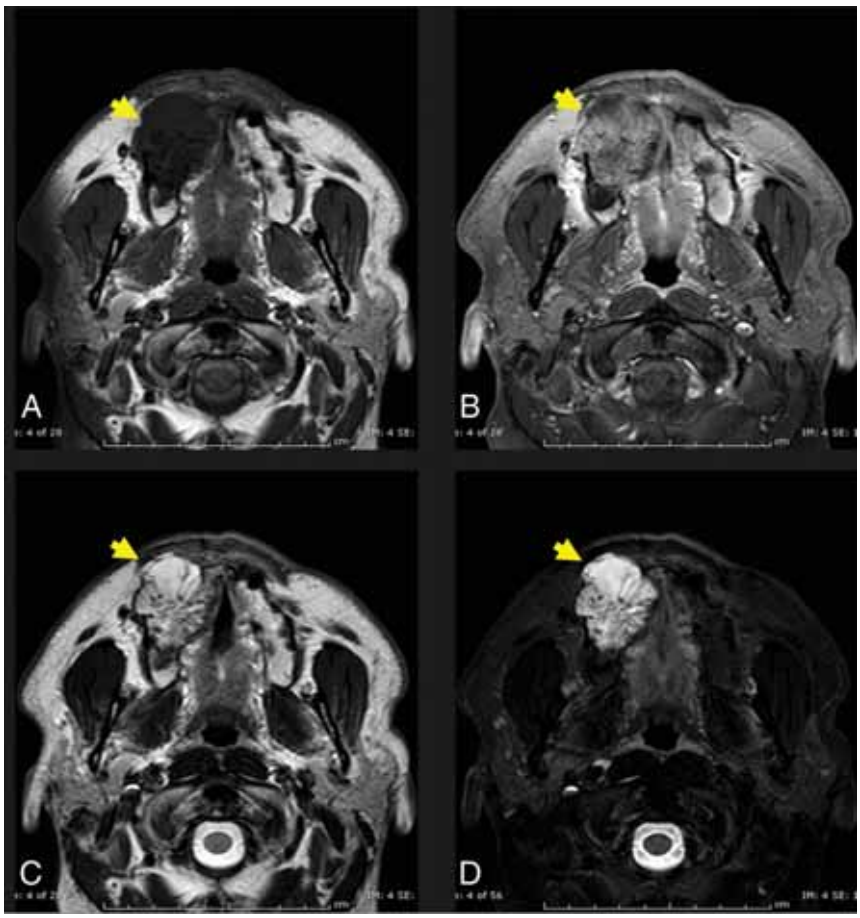

FIG 4. Axial T1 (*A*) and axial T1 C+ FS (*B*) images through the maxilla demonstrate a T1-intermediate, heterogeneously enhancing expansile lesion centered in the right maxillary alveolus (*yellow arrow*, *A* and *B*). The lesion extends beyond the cortical margin, and there is poor identification of the normal cortex. Axial T2 (*C*) and axial T2 FS (*D*) sequences demonstrate that the lesion is T2-hyperintense with internal T2-hypointense trabeculae (*yellow arrows*, *C* and *D*). The diagnosis of IOVM was confirmed on pathology. C+ indicates with contrast.

malformations, particularly in the familial cerebral cavernous malformation population.[22] The presence of other features such as homogeneous soft-tissue enhancement, honeycomb pattern of internal trabeculation, T1 hyperintensity, absence of periosteal reaction and lack of erosive change, help to support the correct diagnosis despite otherwise atypical features.[2,24-27] Such lesions can still be referred to as IOVMs. Differential diagnoses for less characteristic appearances will vary by site but may include intraosseous meningioma, fibrous dysplasia, osteochondroma, osteosarcoma, and ossifying fibroma.[19]

Subsites of IOVM in the Head and Neck: Calvarium

First described in 1845 by Toynbee and perpetually miscategorized as cavernous or osseous hemangiomas, calvarial IOVMs present clinically as slowly growing or indolent firm, nonmobile masses with freely mobile overlying skin.[11,28] They are often encountered on CT or MR imaging of the brain as incidental findings and may prove problematic if misdiagnosed. Because the lesion is composed of malformed venous channels within bone trabeculae, calvarial IOVMs primarily occur within the diploic space with an expansile appearance and thinning of the overlying cortex. This appearance is best delineated with high-resolution CT imaging, which easily depicts the characteristic elements, variously described as stippled, spiculated, honeycomb, spoke wheel, or sunburst in appearance (Figs 1 and 2).[20] The variable ossific density is thought reflective of osteoblastic activity from chronic and repeat hemorrhage.[28]

The imaging appearance of calvarial IOVMs with MR imaging is variable. IOVMs have strikingly hyperintense signal on T2-weighted imaging, reflecting slow-flowing blood or subacute thrombus. On T1-weighted imaging, some lesions have high signal from thrombus or fat, which may be differentiated with a fat-suppressed technique. Residual cortex has thin and hypointense signal on all MR pulse sequences, and the internal ossific spicules may be evident as internal areas of signal void (Fig 1*C*). Extraosseous soft-tissue extension is possible and better discriminated on MR imaging, given its advantage in soft-tissue contrast resolution.

The differential diagnosis includes intraosseous meningioma,[29,30] also showing avid contrast enhancement and T2 hyperintensity,[31] though typically presenting in an older age group and with associated osseous sclerosis. Fibrous dysplasia on CT classically has a ground-glass or heterogeneously cystic appearance and intermediate-to-low T2 signal intensity reflecting its fibrous content.[29] Dermoid and epidermoid cysts typically demonstrate low CT density without an internal matrix, without enhancement on MR imaging and with characteristic diffusion restriction. When a calvarial lesion is large or growing at a worrisome pace, malignant lesions such as metastasis or myeloma or inflammatory lesions such as eosinophilic granuloma may be considered, and prompt lesion excision and/or tissue sampling may be necessary.[32] As with most lesions at the skull or skull base, diagnostic accuracy is improved when both the CT and MR imaging appearance are co-interpreted as complementary examinations. Table 2 summarizes typical CT and MR imaging findings of IOVM and other lesions within the imaging differential diagnosis.

Facial Skeleton

As expected, primary IOVMs of the facial bones are more likely than calvarial lesions to present clinically as a recognizable deformity and firm, palpable masses. The maxilla is most frequently involved, with classic locations for IOVM at the malar eminence, orbital rim, and zygomaticomaxillary junction

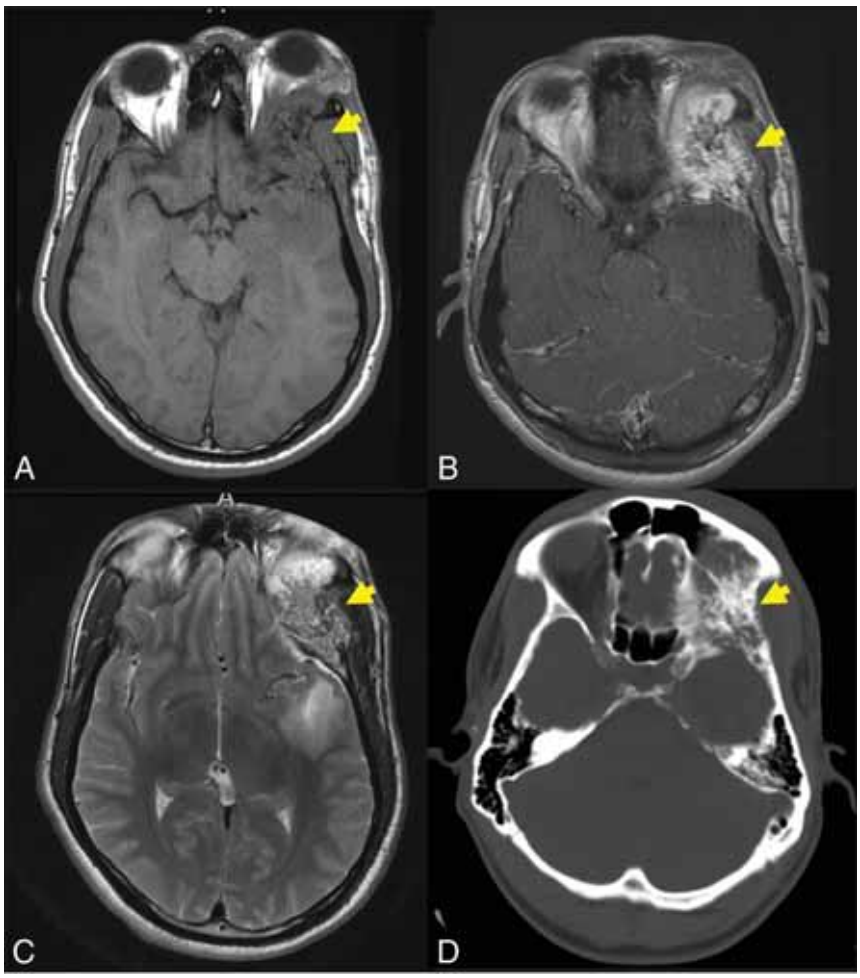

FIG 5. Axial T1-weighted (*C*) and axial T1-weighted C+ (*B*) demonstrate an expansile lesion centered within the left greater wing of the sphenoid, with internal T1-hypointense trabeculae and avid enhancement (*yellow arrows*, *A* and *B*). There is mass effect on the left orbit, with resultant proptosis. Axial T2WI (*C*) demonstrates that the lesion is heterogeneous but predominantly T2 hyperintense (*yellow arrow, C*). There is vasogenic edema in the subjacent left temporal operculum, presumably based on mass effect, a response to hypervascularity, and venous congestion. Axial CT (*D*) is confirmatory for the diagnosis of the IOVM, given the presence of thickened internal trabeculae (*yellow arrow, D*) in a characteristic pattern. The patient was treated with surgical resection. The diagnosis of IOVM was confirmed on pathology, which showed dilated thin-walled blood vessels distending and replacing medullary bone. C+ indicates with contrast. Case courtesy of Phillip Chapman, MD, Professor of Radiology, Duke University School of Medicine.

(Figs 3 and 4). Less common sites include the nasal bones and mandible.[33] On occasion, the facial bones may be secondarily involved with more complex and transspatial venous malformations of the facial soft tissues. Dentition may be altered as result of a maxillary or mandibular IOVM, though jaw deformity is more commonly encountered with arteriovenous malformations.[34] Surgical treatment is often pursued to correct the cosmetic deformity and/or to restore function. Imaging is necessary not only for lesion characterization and anatomic mapping before surgery but also for providing image data for navigational surgical planning. In the setting of large IOVMs, preoperative lesion embolization may be offered.[24]

Differential diagnostic considerations for facial IOVMs are as previously described for calvarial IOVMs and include fibrous dysplasia, primary bone neoplasm, metastasis, and myeloma. Mandibular or maxillary osteosarcoma may result in a sunburst periosteal reaction, though this is typically limited to the periphery of the lesion.[35] Of course, the rapid growth of osteosarcoma represents a substantially different clinical course than IOVM.

Skull Base

Given the deep location of skull base IOVMs, clinical signs and symptoms are rare, and these lesions are almost exclusively discovered incidentally at imaging for other indications. The skull base is a rarely reported site of IOVM, and it is often not considered as a leading differential diagnosis for an expansive bony mass in this location.[19] Instead, it may be mistaken for malignancy or other osteoblastic or sclerotic lesions such as meningioma, Paget disease, or fibrous dysplasia. The greater sphenoid wing is a common location for an intraosseous meningioma, also known as an en plaque or hyperostotic meningioma.[36] Both lesions may expand bone, but intraosseous meningiomas more often result in uniform bony sclerosis rather than lucency and do not typically demonstrate the trabecular matrix characteristic of IOVMs (Fig 5). The internal areas of signal void within a posterior skull base IOVM may simulate the "salt and pepper" MR imaging appearance of a glomus jugulare tumor; however, CT will readily distinguish these entities because paragangliomas lack an internal calcified matrix (Fig 6). Additionally, careful consideration of anatomy will localize these lesions to the bone rather than skull base foramina. Within the central skull base, an additional consideration is a chondrosarcoma, which may show similar T2-hyperintense signal but often less avid contrast enhancement and a more flocculent pattern of internal calcification.[37] As with IOVMs in other locations, the MR imaging appearance may be nonspecific, and CT often provides the most diagnostic utility with a characteristic internal spiculated matrix (Table 2).

Facial Nerve

The facial nerve (FN) IOVM is the most well-recognized vascular malformation within the head and neck (Fig 7). The

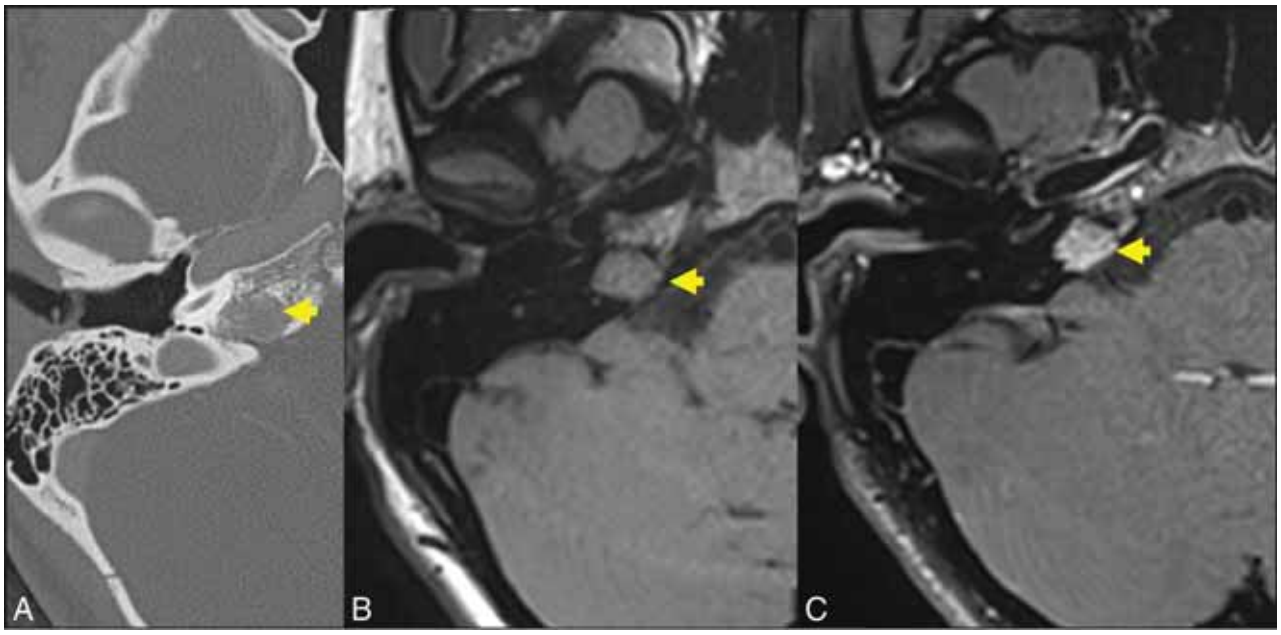

FIG 6. A 17-year-old girl referred for suspicion of paraganglioma identified incidentally on head CT for trauma. Axial thin-section CT (*A*) demonstrates a hypodense lesion centered in the right petrous apex (*yellow arrow*). The presence of internal trabeculae in a honeycomb pattern as well as the lesion location differentiate the correct diagnosis (IOVM of the skull base) and the suspected diagnosis of glomus jugulare paraganglioma. Axial T1 C– (*B*) and axial T1 C+ (*C*) sequences through the skull base demonstrate that the lesion is T1-intermediate (*yellow arrow, B*) and avidly enhancing (*yellow arrow, C*). A diagnosis of IOVM was made on the basis of characteristic imaging appearance. C+ indicates with contrast; C–, without contrast.

literature is confounded by inconsistent terminology across multiple medical disciplines and improper pathologic designation of lesions, though recent reviews have aimed to reconcile this issue.[38] While most craniofacial IOVMs are incidental or cosmetically deforming, FN IOVMs are typically discovered because of related clinical symptomatology. The more common FN schwannoma may compress the nerve and cause dysfunction, whereas a venous malformation may directly infiltrate the nerve and/or cause a vascular steal phenomenon.[39] Therefore, symptoms such as facial paresis or hemifacial spasm or both are much more common with FN IOVMs than the more prevalent schwannoma. When compared with facial neuritis such as Bell palsy, FN dysfunction in IOVMs is more insidious and progressive and will not spontaneously resolve.

The location for an IOVM is characteristically at the geniculate portion of the FN, which is not surprising given its rich venous and capillary plexus. There is a rarer occurrence elsewhere along the FN, namely at the internal auditory canal or second genu.[39] FN IOVMs often infiltrate beyond the margins of the FN canal and geniculate ganglion, aiding in discrimination from facial nerve schwannoma.

CT typically reveals an expansile lesion with irregular margins centered at the geniculate fossa, demonstrating characteristic internal bony spicules or trabeculae, a honeycomb pattern, or small, needle-shaped calcifications as recently described by Yue et al.[40] However, when small, an FN IOVM may fail to show typical bony densities and only widen the FN canal. Discrimination may then prove difficult between an IOVM and neoplasm, most commonly a schwannoma in this location.[41] MR imaging typically reveals a mass of T1-hypointense or -isointense and T2-hyperintense signal that may be heterogeneous depending on degree of bony matrix. Typically, an FN IOVM appears as a patchy or geographic focus of enhancement, whereas a schwannoma may appear ovoid or tubular. Particularly when lesions are small, differentiation may be very difficult, and ultimately both CT and MR imaging are frequently required in this differential diagnosis.

Definitive treatment of an FN IOVM is surgical, especially if there is documented progression in FN dysfunction. Early detection and shorter duration of symptoms lead to a greater chance of FN function following surgery. The surgical approach may be subtemporal or via the middle cranial fossa, with the goal being FN identification and preservation. The lesion is most often encountered as a deep red, sinusoidal, and hemorrhagic mass with a honeycomb or spongy consistency.[40] Depending on lesion location and surgical skill and resources, interposition nerve grafting can be performed to improve clinical outcomes.

CONCLUSIONS

IOVMs are rare-but-underdiagnosed entities that have been miscategorized as hemangiomas in the literature across multiple disciplines. In the head and neck, these are found in the skull, skull base, and facial skeleton, with lesions at the geniculate ganglion

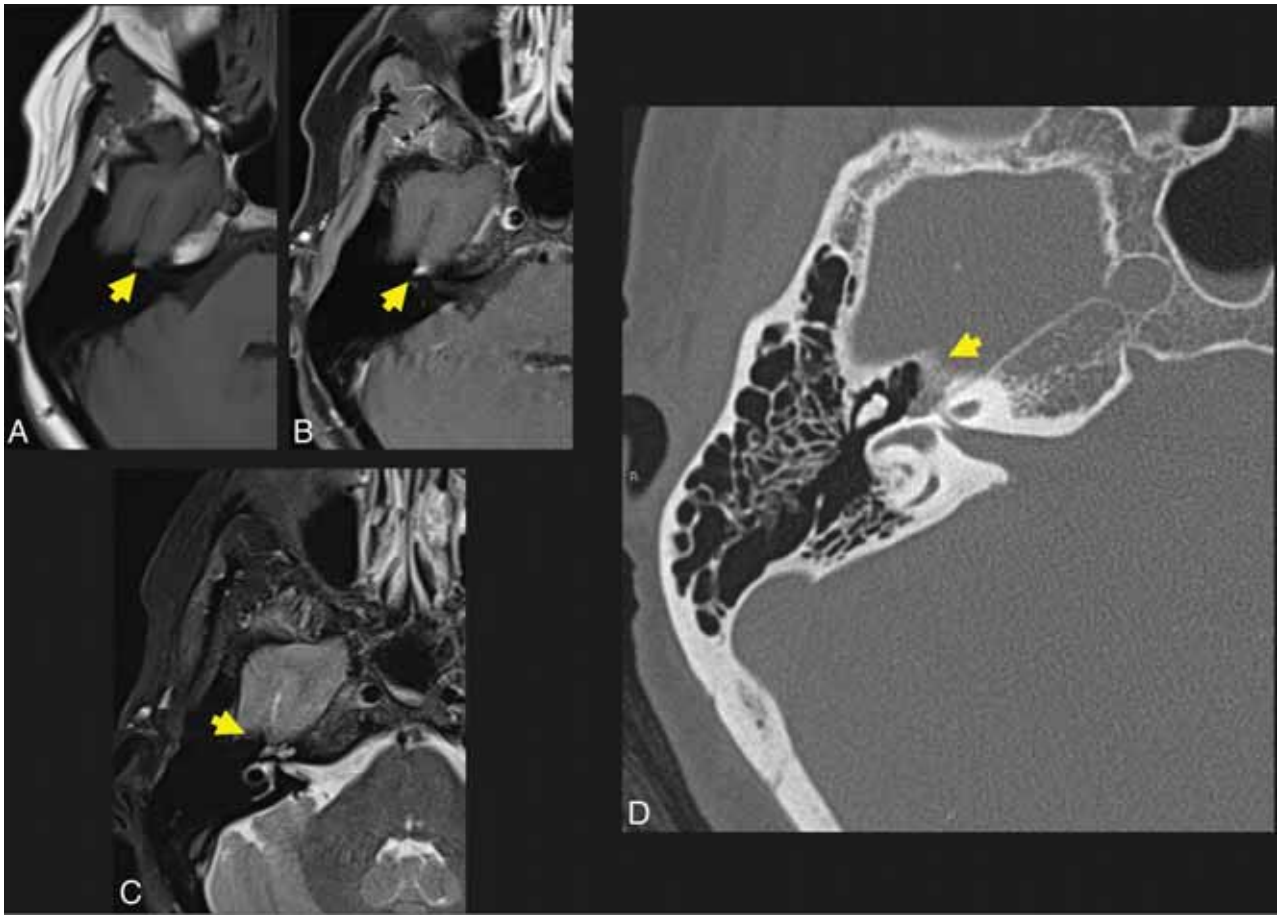

FIG 7. A 57-year-old woman who presented with right facial synkinesis. Noncontrast T1WI (*A*) and contrast-enhanced T1WI (*B*) demonstrate an enhancing lesion centered at the level of the right FN hiatus (*yellow arrow, A* and *B*), with corresponding increased signal on T2WI (*C*, *yellow arrow* indicates lesion). Differential considerations included both schwannoma and IOVM of the FN. Axial (*D*) thin-section CT of the temporal bone demonstrates an expansile, lucent lesion at the level of the anterior genu of the FN and FN hiatus (*yellow arrow, D*). The internal trabeculae help to confirm the diagnosis of IOVM because schwannoma would be less likely to show internal calcification. The diagnosis of IOVM was confirmed on pathology.

(incorrectly termed "facial nerve hemangiomas") perhaps the most widely known. While a seemingly aggressive appearance may be of concern to patients, clinicians, and radiologists, a generally indolent clinical course and the presence of near-pathognomonic internal bony spicules on CT should suggest this diagnosis.

Disclosure forms provided by the authors are available with the full text and PDF of this article at www.ajnr.org.

REFERENCES

1. International Society for the Study of Vascular Anomalies. **Vascular anomalies.** April 2014. Last revision May 2018. https://www.issva.org/UserFiles/file/ISSVA-Classification-2018.pdf. Accessed December 31, 2021
2. Moore SL, Chun JK, Mitre SA, et al. **Intraosseous hemangioma of the zygoma: CT and MR findings.** *AJNR Am J Neuroradiol* 2001;22:1383–85 Medline
3. Liberale C, Rozell-Shannon L, Moneghini L, et al. **Stop calling me cavernous hemangioma! A literature review on misdiagnosed bony vascular anomalies.** *J Invest Surg* 2022;35:141–50 CrossRef Medline
4. Mulliken JB, Glowacki J. **Hemangiomas and vascular malformations in infants and children: a classification based on endothelial characteristics.** *Plast Reconstr Surg* 1982;69:412–22 CrossRef Medline
5. Greene AK, Rogers GF, Mulliken JB. **Intraosseous "hemangiomas" are malformations and not tumors.** *Plast Reconstr Surg* 2007;119:1949–50 CrossRef Medline
6. Kaban LB, Mulliken JB. **Vascular anomalies of the maxillofacial region.** *J Oral Maxillofac Surg* 1986;44:203–13 CrossRef Medline
7. Dasgupta R, Fishman SJ. **ISSVA classification.** *Semin Pediatr Surg* 2014;23:158–61 CrossRef Medline
8. Hassanein AH, Mulliken JB, Fishman SJ, et al. **Evaluation of terminology for vascular anomalies in current literature.** *Plast Reconstr Surg* 2011;127:347–51 CrossRef Medline
9. Fábián Z, Szabó G, Petrovan C, et al. **Intraosseous venous malformation of the zygomatico-orbital complex: case report and literature review with focus on confusions in vascular lesion terms.** *Oral Maxillofac Surg* 2018;22:241–47 CrossRef Medline
10. Cohen MM Jr. **Vasculogenesis, angiogenesis, hemangiomas, and vascular malformations.** *Am J Med Genet* 2002;108:265–74 CrossRef Medline
11. Politi M, Barbera L, Roth C, et al. **Diagnosis and treatment of vascular malformations.** *Hellenic Journal of Radiology* 2018;3:41–53
12. Colletti G, Ierardi AM. **Understanding venous malformations of the head and neck: a comprehensive insight.** *Med Oncol* 2017;34:42 CrossRef Medline
13. Cheng NC, Lai DM, Hsie MH, et al. **Intraosseous hemangiomas of the facial bone.** *Plast Reconstr Surg* 2006;117:2366–72 CrossRef Medline
14. DeFazio MV, Kassira W, Camison L, et al. **Intraosseous venous malformations of the zygoma: clarification of misconceptions regarding**

diagnosis and management. *Ann Plast Surg* 2014;72:323–27 CrossRef Medline
15. Kadlub N, Dainese L, Coulomb-L'Hermine A, et al. **Intraosseous haemangioma: semantic and medical confusion.** *Int J Oral Maxillofac Surg* 2015;44:718–24 CrossRef Medline
16. Bruder E, Perez-Atayde AR, Jundt G, et al. **Vascular lesions of bone in children, adolescents, and young adults: a clinicopathologic reappraisal and application of the ISSVA classification.** *Virchows Arch* 2009;454:161–79 CrossRef Medline
17. Werdich XQ, Jakobiec FA, Curtin HD, et al. **A clinical, radiologic, and immunopathologic study of five periorbital intraosseous cavernous vascular malformations.** *Am J Ophthalmol* 2014;158:816–26. e1 CrossRef Medline
18. North PE, Waner M, Mizeracki A, et al. **GLUT1: a newly discovered immunohistochemical marker for juvenile hemangiomas.** *Hum Pathol* 2000;31:11–22 CrossRef Medline
19. Nagy CZ, Cantrell S, Wu X, et al. **Vascular malformation of the sphenoid and temporal bone: a diagnostic dilemma.** *Am J Otolaryngol* 2019;40:334–36 CrossRef Medline
20. Bastug D, Ortiz O, Schochet SS. **Hemangiomas in the calvaria: imaging findings.** *AJR Am J Roentgenol* 1995;164:683–87 CrossRef Medline
21. Laredo J, Assouline E, Gelbert F, et al. **Vertebral hemangiomas: fat content as a sign of aggressiveness.** *Radiology* 1990;177:467–72 CrossRef Medline
22. Tandberg SR, Bocklage T, Bartlett MR, et al. **Vertebral intraosseous vascular malformations in a familial cerebral cavernous malformation population: prevalence, histologic features, and associations with CNS disease.** *AJR Am J Roentgenol* 2020;214:428–36 CrossRef Medline
23. Gaudino S, Martucci M, Colantonio R, et al. **A systematic approach to vertebral hemangioma.** *Skeletal Radiol* 2015;44:25–36 CrossRef Medline
24. Srinivasan B, Ethunandan M, Van der Horst C, et al. **Intraosseous 'haemangioma' of the zygoma: more appropriately termed a venous malformation.** *Int J Oral Maxillofac Surg* 2009;38:1066–70 CrossRef Medline
25. Hoyle J, Layfield L, Crim J. **The lipid-poor hemangioma: an investigation into the behavior of the "atypical" hemangioma.** *Skeletal Radiol* 2020;49:93–100 CrossRef Medline
26. Cloran FJ, Pukenas BA, Loevner LA, et al. **Aggressive spinal haemangiomas: imaging correlates to clinical presentation with analysis of treatment algorithm and clinical outcomes.** *Br J Radiol* 2015;88:20140771 CrossRef Medline
27. Sahajwalla D, Vorona G, Tye G, et al. **Aggressive vertebral hemangioma masquerading as neurological disease in a pediatric patient.** *Radiol Case Rep* 2021;16:1107–12 CrossRef Medline
28. Heckl S, Aschoff A, Kunze S. **Cavernomas of the skull: review of the literature 1975–2000.** *Neurosurg Rev* 2002;25:56–62 CrossRef Medline
29. Gomez CK, Schiffman SR, Bhatt AA. **Radiological review of skull lesions.** *Insights Imaging* 2018;9:857–82 CrossRef Medline
30. Politi M, Romeike BF, Papanagiotou P, et al. **Intraosseous hemangioma of the skull with dural tail sign: radiologic features with pathologic correlation.** *AJNR Am J Neuroradiol* 2005;26:2049–52 Medline
31. Tokgoz N, Oner YA, Kaymaz M, et al. **Primary intraosseous meningioma: CT and MRI appearance.** *AJNR Am J Neuroradiol* 2005;26:2053–56 Medline
32. Kirmani AR, Sarmast AH, Bhat AR. **A unique case of calvarial hemangioma.** *Surg Neurol Int* 2016;7:S398–401 CrossRef Medline
33. Aldridge E, Cunningham LL, Gal T, et al. **Intraosseous venous malformation of the mandible: a review on interdisciplinary differences in diagnostic nomenclature for vascular anomalies in bone and report of a case.** *J Oral Maxillofac Surg* 2012;70:331–39 CrossRef Medline
34. Colletti G, Frigerio A, Giovanditto F, et al. **Surgical treatment of vascular malformations of the facial bones.** *J Oral Maxillofac Surg* 2014;72:1326.e1–18 CrossRef Medline
35. ElKordy MA, ElBaradie TS, ElSebai HI, et al. **Osteosarcoma of the jaw: challenges in the diagnosis and treatment.** *J Egypt Natl Canc Inst* 2018;30:7–11 CrossRef Medline
36. Gokce E, Beyhan M, Acu L. **Cranial intraosseous meningiomas: CT and MRI findings.** *Turk Neurosurg* 2020;30:542–49 CrossRef Medline
37. Kunimatsu A, Kunimatsu N. **Skull base tumors and tumor-like lesions: a pictorial review.** *Pol J Radiol* 2017;82:398–409 CrossRef Medline
38. Benoit MM, North PE, McKenna MJ, et al. **Facial nerve hemangiomas: vascular tumors or malformations?** *Otolaryngol Head Neck Surg* 2010;142:108–14 CrossRef Medline
39. Guerin JB, Takahashi EA, Lane JI, et al. **Facial nerve venous malformation: a radiologic and histopathologic review of 11 cases.** *Laryngoscope Investig Otolaryngol* 2019;4:347–52 CrossRef Medline
40. Yue Y, Jin Y, Yang B, et al. **Retrospective case series of the imaging findings of facial nerve hemangioma.** *Eur Arch Otorhinolaryngol* 2015;272:2497–2503 CrossRef Medline
41. Mundada P, Purohit BS, Kumar TS, et al. **Imaging of facial nerve schwannomas: diagnostic pearls and potential pitfalls.** *Diagn Interv Radiol* 2016;22:40–46 CrossRef Medline

Validation of a Denoising Method Using Deep Learning–Based Reconstruction to Quantify Multiple Sclerosis Lesion Load on Fast FLAIR Imaging

T. Yamamoto, C. Lacheret, H. Fukutomi, R.A. Kamraoui, L. Denat, B. Zhang, V. Prevost, L. Zhang, A. Ruet, B. Triaire, V. Dousset, P. Coupé, and T. Tourdias

ABSTRACT

BACKGROUND AND PURPOSE: Accurate quantification of WM lesion load is essential for the care of patients with multiple sclerosis. We tested whether the combination of accelerated 3D-FLAIR and denoising using deep learning–based reconstruction could provide a relevant strategy while shortening the imaging examination.

MATERIALS AND METHODS: Twenty-eight patients with multiple sclerosis were prospectively examined using 4 implementations of 3D-FLAIR with decreasing scan times (4 minutes 54 seconds, 2 minutes 35 seconds, 1 minute 40 seconds, and 1 minute 15 seconds). Each FLAIR sequence was reconstructed without and with denoising using deep learning–based reconstruction, resulting in 8 FLAIR sequences per patient. Image quality was assessed with the Likert scale, apparent SNR, and contrast-to-noise ratio. Manual and automatic lesion segmentations, performed randomly and blindly, were quantitatively evaluated against ground truth using the absolute volume difference, true-positive rate, positive predictive value, Dice similarity coefficient, Hausdorff distance, and F1 score based on the lesion count. The Wilcoxon signed-rank test and 2-way ANOVA were performed.

RESULTS: Both image-quality evaluation and the various metrics showed deterioration when the FLAIR scan time was accelerated. However, denoising using deep learning–based reconstruction significantly improved subjective image quality and quantitative performance metrics, particularly for manual segmentation. Overall, denoising using deep learning–based reconstruction helped to recover contours closer to those from the criterion standard and to capture individual lesions otherwise overlooked. The Dice similarity coefficient was equivalent between the 2-minutes-35-seconds-long FLAIR with denoising using deep learning–based reconstruction and the 4-minutes-54-seconds-long reference FLAIR sequence.

CONCLUSIONS: Denoising using deep learning–based reconstruction helps to recognize multiple sclerosis lesions buried in the noise of accelerated FLAIR acquisitions, a possibly useful strategy to efficiently shorten the scan time in clinical practice.

ABBREVIATIONS: AVD = absolute volume difference; dDLR = denoising using deep learning–based reconstruction; DSC = Dice similarity coefficient; HD = Hausdorff distance; MS = multiple sclerosis; PPV = positive predictive value; TPR = true-positive rate

Multiple sclerosis (MS) is the most common inflammatory disease of the central nervous system affecting young patients,[1] in which demyelination mediated by autoimmune mechanisms is spatially and temporally disseminated. MR imaging plays an essential role not only in the initial diagnosis of MS[2] but also in regular monitoring as a sensitive marker of disease activity for promptly switching therapy if progression is observed.[3] Life-long imaging follow-up is, therefore, required for most patients with MS. A short examination time is necessary to improve the patient's comfort and to cope with the high number of demands in imaging centers.

Received December 20, 2021; accepted after revision June 13, 2022.

From the Institut de Bio-imagerie (T.Y., H.F., L.D., V.D., T.T.), University Bordeaux, Bordeaux, France; Neuroimagerie Diagnostique et Thérapeutique (C.L., V.D., T.T.) and Service de Neurologie (A.R.), Centre Hospitalier Universitaire de Bordeaux, Bordeaux, France; Laboratoire Bordelais de Recherche en Informatique (R.A.K., P.C.), University Bordeaux, Le Centre National de la Recherche Scientifique, Bordeaux Institut National Polytechnique, Talence, France; Canon Medical Systems Europe (B.Z.), Zoetermeer, the Netherlands; Canon Medical Systems (V.P., B.T.), Tochigi, Japan; Canon Medical Systems China (L.Z.), Beijing, China; and Neurocentre Magendie (V.D., T.T.), University of Bordeaux, L'Institut National de la Santé et de la Recherche Médicale, Bordeaux, France.

T. Yamamoto and C. Lacheret are co-first authors and have contributed equally to this study.

This study was supported by Roche Laboratory and the public grant from the French Agence Nationale de la Recherche within the context of the investments for the future program referenced ANR-10-LABX-57 and named TRAIL. The work was also supported by the fondation pour l'aide à la recherche sur la sclérose en plaques foundation.

The sponsors did not participate in any aspect of the design or performance of the study, including data collection, management, analysis and the interpretation or preparation, review, and approval of the manuscript.

Please address correspondence to Thomas Tourdias MD, PhD, Centre Hospitalier Universitaire de Bordeaux, Neuroimagerie Diagnostique et Thérapeutique, Place Amélie Raba Léon, 33300 Bordeaux, France; e-mail: thomas.tourdias@chu-bordeaux.fr

Indicates open access to non-subscribers at www.ajnr.org

Indicates article with online supplemental data.

http://dx.doi.org/10.3174/ajnr.A7589

Parameters of MR imaging acquisitions

	3D FLAIR				
	Standard	Fast	Ultrafast	Shortest	MPRAGE
TR (ms)	7000	5000	4000	3000	6.3
TE (ms)/effective TE (ms)	445.5/145.0	445.5/145.0	445.5/145.0	445.5/145.0	2.8
TI (ms)	2070	1580	1270	910	950
BW (Hz)	558	558	558	558	279
Echo space (ms)	4.5	4.5	4.5	4.5	
FOV (mm)	230 × 230	230 × 230	230 × 230	230 × 230	230 × 230
Matrix	224 × 224	224 × 224	224 × 224	224 × 224	224 × 224
Thickness (mm)	1	1	1	1	1
Parallel imaging	2.0 × 3.0	2.0 × 3.0	2.0 × 3.0	2.0 × 3.0	1.8 × 1.5
Frequency oversampling	1.4	1.2	1.2	1.2	1.2
Half Fourier		85%	70%	70%	
Flip angle	90°	90°	90°	90°	9°
Refocus angle	VFA	VFA	VFA	VFA	
Shot interval (ms)					2500
Recovery time (ms)					744
Scan time (minute : second)	4:54	2:35	1:40	1:15	6:18

Note:—VFA indicates variable flip angle; BW, Bandwidth.

3D-FLAIR imaging is considered the core sequence for diagnosis and monitoring of MS and has been shown to provide better diagnostic performance than 2D sequences,[4] explaining why 3D acquisitions are now recommended by international guidelines.[5,6] In return for its high sensitivity, 3D acquisition comes at the expense of a longer scan time, which can be mitigated by acceleration techniques, such as the partial Fourier technique,[7] parallel imaging,[8] simultaneous multislice imaging,[9] or, more recently, compressed sensing.[10] These techniques are still being improved; however, the image quality inevitably decreases due to reduced *k*-space sampling. As the images become noisy, the accuracy of lesion detection could be affected. Therefore, one of the central objectives was to remove noise associated with image-acquisition acceleration to maintain high image quality for accurate lesion identification. Although several denoising methods take the complexity of MR imaging artifacts into account, 1 critical drawback of these sophisticated denoising methods is the processing time, which makes them not easily applicable in routine clinical practice.

Artificial intelligence is now providing new solutions with denoising algorithms based on deep learning, enabling instant execution.[11] New generations of MR imaging with the denoising using deep learning–based reconstruction (dDLR) are now becoming available on commercial magnets,[12-15] with the goal of accurately removing the noise associated with higher-resolution acquisitions or with significantly shorter scan times. Such dDLR is rapidly growing, but at the same time, its validity in clinical settings has not yet been well-investigated, and how these methods could impact the detectability of lesions for radiologists is unknown. Before adoption, it is mandatory to validate such effects on pathologic lesion detection and to quantify possible false-positives or negatives. Therefore, in this research study, we tested whether the combination of accelerated 3D-FLAIR and dDLR could provide a relevant strategy to monitor the WM lesion load of patients with MS with shorter examinations.

MATERIALS AND METHODS

Study Population

The study prospectively recruited 31 participants with MS who were followed at Centre Hospitalier Universitaire de Bordeaux in 2020 and 2021. The inclusion criterion was to have a confirmed relapsing-remitting form of MS according to the 2017 McDonald criteria.[2] The exclusion criteria were MR imaging examination contraindications and other concomitant neurologic disorders. One patient with a low lesion load had no more visible brain lesions under treatment, and 2 patients did not properly complete the MR imaging; thus, we evaluated 28 participants in this analysis. The institutional ethics committee approved the protocol, and all participants provided written informed consent.

Image Acquisition

Imaging examinations were performed on a 3T scanner (Vantage Galan 3T/ZGO; Canon Medical Systems) with a 32-channel phased array head coil. The acquired sequences included a 3D T1WI and 4 implementations of 3D variable flip angle FLAIR sequences with decreasing scan times that we will call "standard FLAIR" (4 minutes 54 seconds), "fast FLAIR" (2 minutes 35 seconds), "ultrafast FLAIR" (1 minute 40 seconds), and "shortest FLAIR" (1 minute 15 seconds). Acceleration was obtained with parallel imaging and with a progressive decrease in the TR along the 4 different implementations. The corresponding TI values were adjusted accordingly to maintain CSF nulling based on simulations of the magnetization of 3D-FLAIR that we conducted in Matlab (MathWorks) using T1/T2 values of CSF from the literature.[16,17] Spatial resolution was identical for the 4 FLAIR sequences (see the Table for details of scan parameters).

dDLR was directly available in the scanner as a product called advanced intelligent clear-IQ engine (AiCE) and developed by Canon. The dDLR method has been described in detail by Kidoh et al[14] and is based on a "plain" convolutional neural network (CNN) that performs denoising by learning noise thresholds in the high-frequency components extracted from images by a discrete cosine transform. The algorithm has been originally trained

on pairs of high SNR ground truth images collected on healthy subjects (10 average repetitions) and noisy input images (generated by adding various amounts of noise on the ground truth). After data augmentation, 32,400 image pairs were used for the training of the dDLR. In our study, each FLAIR sequence was processed once with dDLR (<1 minute of reconstruction time) and another time with conventional reconstruction, which will be referred to as "with or without dDLR." Therefore, 8 FLAIR sequences were available per patient, corresponding to a total of 224 FLAIR sequences for the 28 patients.

Image Analyses

To create the ground truth segmentation of MS lesions, 2 senior neuroradiologists (with 14 and 12 years of experience) manually delineated MS lesions in collaboration on the standard FLAIR sequence using 3D Slicer software (www.slicer.org).[18] Each segmentation was first performed by 1 of these 2 experienced readers and carefully and independently checked by the second, who could correct any missing lesions. We considered this segmentation the criterion standard against which the other segmentations were evaluated.

To evaluate the impact of combining "image acceleration + dDLR" on the radiologist, the 2 neuroradiologists and another reader (a radiology resident with 5 years of experience and expertise in neuroimaging) blindly evaluated the overall image quality of the 224 FLAIR sequences. The sequences were presented in random order to limit possible bias, especially between images processed with or without dDLR. Qualitative aspects of the sequences were assessed using a 5-point Likert-type scale: ++, +, 0, −, −−, where 0 stands for the image quality that can be used for diagnostic purpose in clinical settings, while + and − stand for higher and lower quality, respectively.

Then, MS lesions of the 224 FLAIR sequences were manually and section-by-section delineated by the third reader during random presentation under 3D Slicer. Automatic segmentation was also conducted independently using the lesionBrain module,[19] which is freely available on the volBrain platform[20] (https://www.volbrain.upv.es).

Performance Metrics for Evaluation

Several metrics are usually evaluated to assess the performances of segmentation methods, such as the index of similarity, voxel-wise metrics, and lesion-wise metrics.[21]

Therefore, we first computed the relative absolute volume difference (AVD):

$$AVD = \frac{abs(|A| - |GS|)}{|GS|},$$

where $|A|$ represents the volume of MS lesions from the sequence under evaluation, *GS* is the volume of MS lesions from the criterion standard, and *abs* means the absolute value.

Second, we computed the following overlap metrics (voxel-wise metrics) to quantify the contour similarity between 1 segmentation and the criterion standard: positive predictive value (PPV), true-positive rate (TPR), Dice similarity coefficient (DSC), and the 95th percentile of Hausdorff distance (HD). These metrics are defined as follows:

$$PPV = \frac{|TP|}{|TP| + |FP|}$$
$$TPR = \frac{|TP|}{|TP| + |FN|}$$

$$DSC = \frac{2 \times |TP|}{|GS| + |A|}$$

$$HD = \max_{a \in A} \left\{ \min_{gs \in GS} \{dist\ (a, gs)\} \right\},$$

where TP, FP, FN represent the numbers of voxels that are true-positive, false-positive, and false-negative, respectively. *Dist* refers to Euclidean distance.

Finally, to understand whether all the MS lesions were detected, independent of the delineating precision, we computed the connected components of GS and A (lesion-wise metrics). We adopted the F1 score (F1) as follows:

$$Se_L = \frac{count(TP_{GS})}{count(GS)}$$

$$P_L = \frac{count(TP_A)}{count(A)}$$

$$F_1 = 2 \times \frac{Se_L \times P_L}{Se_L + P_L},$$

where TP_{GS} is lesions of A among the lesions in GS that are correctly detected by A, TP_A is—vice versa—overlapped lesions of GS among the lesions of A, Se_L is lesion sensitivity, and P_L is the lesion positive predictive value for individual lesions. Lesion counting and labeling were performed using the multidimensional image processing (ndimage) submodule in the sciPy library (Version 1.7.0, www.scipy.org). Then, the overlapping labels between GS and A were counted to compute TP_{GS} and TP_A.

Before computing these metrics, all FLAIR images were coregistered to the individual 3D-T1WI sequences using the FMRIB Linear Image Registration Tool (FLIRT; http://www.fmrib.ox.ac.uk/fsl/fslwiki/FLIRT) program to minimize the positional displacement during the scan.

Statistical Analyses

All statistical analyses were performed with R software (Version 4.1.0; www.r-project.org). First, the interreader agreement among the 3 readers for image quality was analyzed by the Kendall Concordance Coefficient W. Then, we considered 2 factors: the type of FLAIR sequence (standard, fast, ultrafast, shortest) and the type of reconstruction (without or with dDLR). For the Likert scale, which is a categoric metric, the effects of the type of reconstruction were tested with the Wilcoxon signed-rank test. For AVD, TPR, PPV, DSC, HD, and F1 scores, we used nonparametric repeat 2-way ANOVA with the aligned rank transform procedure from the package ARTool (Version 2.1.0; https://depts.washington.edu/acelab/proj/art/).[22] Post hoc tests were conducted with a Wilcoxon signed-rank test, especially to evaluate the impact of

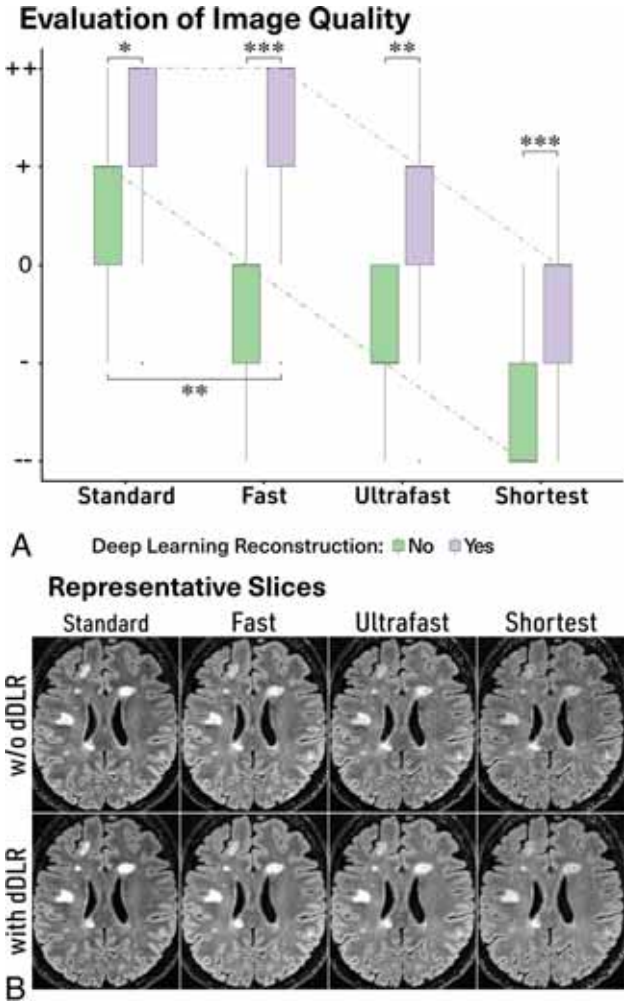

FIG 1. *A*, Boxplots of image-quality evaluation. The median values are connected with *dotted lines*. dDLR generally improved the image quality. Even images of inferior quality were retrieved to moderate quality. *B*, Representative reconstructed axial slices of the different FLAIR acquisitions without (*upper row*) and with dDLR (*lower row*). The amount of noise and the progressive shadowing of lesions when the scan time decreased can be appreciated. One, 2, and 3 *asterisks* indicate $P < .05$, $P < .01$, and $P < .001$, respectively.

dDLR. Finally, to confirm the similarity of metrics between the standard FLAIR and accelerated FLAIR with dDLR, we used a nonparametric version of the equivalence test implemented in the package "EQUIVNONINF" (Version 1.0; https://cran.r-project.org/package=EQUIVNONINF). *P* value corrections were always performed with the Holm method.

RESULTS

Demographics of Participants

The participants ranged from young to middle-aged (mean, 41 years of age; range, 24–56 years) and had a median disease duration of >10 years. Most patients (96.4%) underwent second-line natalizumab disease-modifying treatment and were recruited during one of the monthly perfusions. None of them had experienced any recent relapse, and the median Expanded Disability Status Scale score was 2.0. The characteristics are summarized in the Online Supplemental Data.

Visual Assessment of Image Quality

The agreement among the 3 readers for image quality with the 5-point Likert scale was substantial (Kendall W = .82). We observed a deterioration in image quality by reducing the scan time ($P < .001$, $P < .001$, and $P < .001$ for standard versus fast, fast versus ultrafast, ultrafast versus shortest FLAIR, respectively) (Fig 1*A*). Notably, rapid sequences (fast, ultrafast, and shortest FLAIR) scored lower than the acceptable quality without dDLR but significantly improved their appearance with dDLR ($P < .001$, $P < .001$, $P < .001$, $P < .001$ for standard, fast, ultrafast, and shortest FLAIR, respectively). The visual quality of fast and ultrafast FLAIR with dDLR even recovered up to more than the acceptable quality. The shortest FLAIR with dDLR was still inferior to the acceptable quality, but some ultrafast images improved to a score of 0 or +1. Compared with standard FLAIR without dDLR, fast FLAIR with dDLR was better ($P < .01$).

Quantitative Results

Regarding manual delineation of the MS lesions, the 2-way ANOVA showed that both the type of FLAIR sequence and the type of reconstruction significantly affected the segmentations ($P < .001$ in all the cases) but without any significant interaction (Fig 2 and Online Supplemental Data). PPV was the only metric not significantly affected by the type of FLAIR sequence.

The differences in terms of segmentation volumes compared with the criterion standard progressively increased with the shorter FLAIR sequences. Nevertheless, dDLR significantly reduced such differences in all cases ($P = .038$, $P = .022$, $P < .01$, $P < .001$ for standard, fast, ultrafast, and shortest FLAIR, respectively; Fig 2*A*). Such lower volume differences compared with the criterion standard were mainly driven by a reduction in false-negative voxels, as indicated by a significant improvement in TPR in all cases ($P < .001$, $P < .001$, $P < .001$, $P < .001$ for standard, fast, ultrafast, and shortest FLAIR, respectively; Fig 2*B*). There were also more voxels considered false-positives with dDLR for the standard and fast FLAIR as indicated by a significant reduction in the PPV ($P < .001$ and $P = .047$ for standard and fast FLAIR, respectively; Fig 2*C*), but this effect was less pronounced than that on TPR. The DSC was essential to analyze because it is a composite metric attempting to summarize all such influences onto a single scalar measure. The DSC progressively decreased with shorter FLAIR sequences, but dDLR significantly improved the DSCs in all cases ($P < .001$, $P < .001$, $P < .001$ for fast, ultrafast, and shortest FLAIR, respectively; Fig 2*D*), also in line with shorter HD (Fig 2*E*). The dark arrows in Fig 3 and the Online Supplemental Data show a few examples of manual segmentations (blue) becoming indeed closer to the criterion standard (red) after applying dDLR on an ultrafast FLAIR sequence (which would translate into lower AVD, higher TPR, higher DSC, and lower HD).

To understand whether dDLR could also help to correctly capture more individual MS lesions, even more clinically relevant than the accuracy of the segmentation contours, we also computed Se_L, P_L, and F1 score. The details of Se_L and P_L are shown in the Online Supplemental Data. The resulting F1 score progressively decreased with shorter FLAIR sequences, but most interesting, dDLR improved this metric, especially when used on the

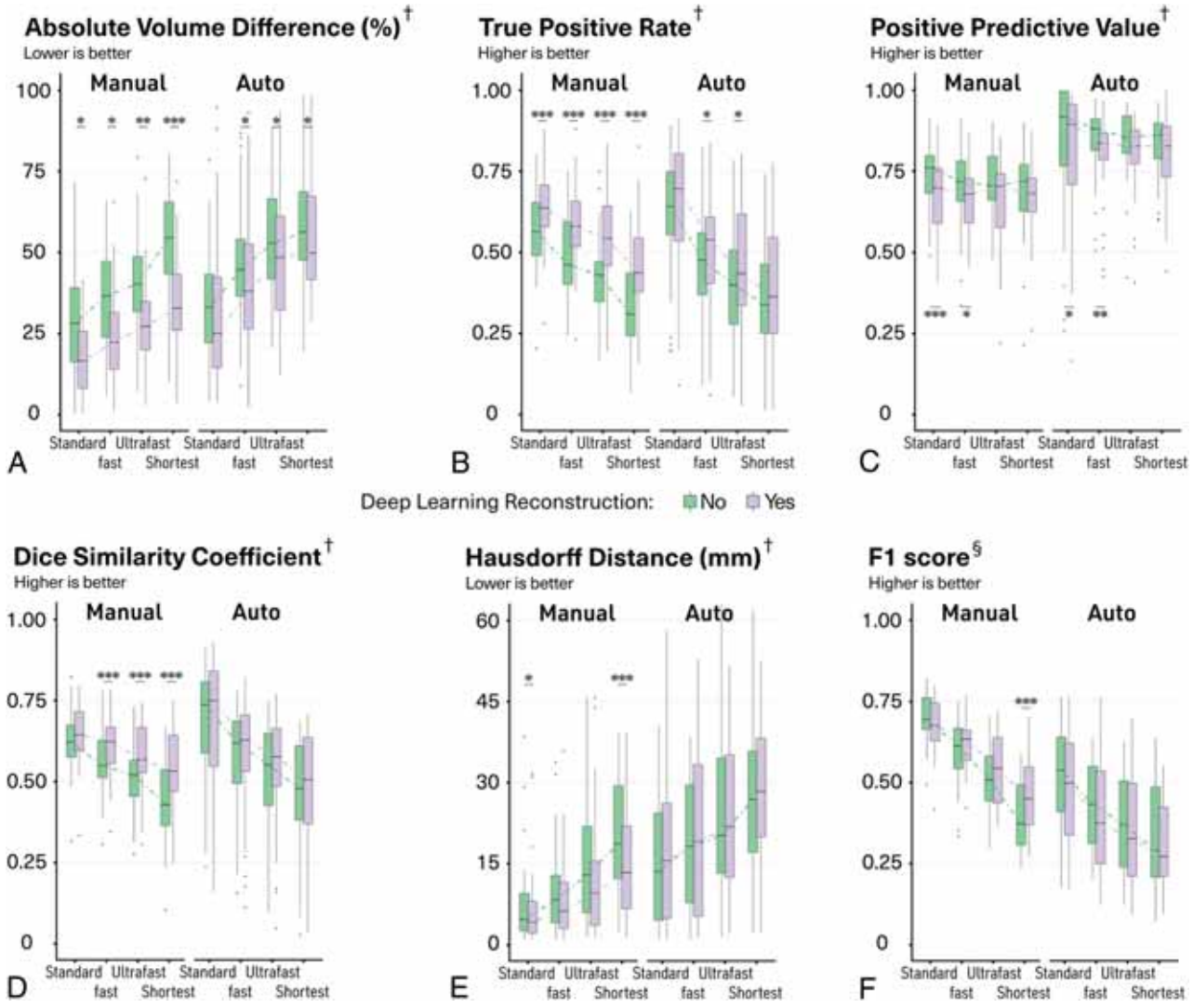

FIG 2. Boxplots of quantitative metrics to evaluate the manual and automatic segmentation. The median values are connected with *dotted lines*. One, 2, and 3 *asterisks* indicate $P < .05$, $P < .01$, and $P < .001$, respectively, for post hoc paired comparisons with Wilcoxon signed-rank test after 2-way ANOVA with the aligned rank transform procedure. † indicates voxelwise metric; §, lesion-wise metric.

shortest sequences ($P < .001$ for shortest FLAIR; Fig 2*F* and the Online Supplemental Data). The white arrows in Fig 3 and the Online Supplemental Data illustrate a few lesions that were missed on an ultrafast FLAIR sequence without dDLR but were correctly captured after denoising (blue) according to the criterion standard (red).

We used equivalence tests to understand whether 1 accelerated strategy could replace the current standard FLAIR. Fast FLAIR with dDLR showed equivalency to standard FLAIR without dDLR in regard to DSC and AVD, and ultrafast FLAIR with dDLR also showed equivalency to standard FLAIR without dDLR in regard to DSC and TPR.

To evaluate whether dDLR would still be beneficial for automatic detection of MS lesions by software, we computed the same metrics after running the lesionBrain module. We observed the same profiles as those for the effects on the manual delineations even though the impact of dDLR was less pronounced (Figs 2 and 3 and Online Supplemental Data).

DISCUSSION

In this article, we provided qualitative and quantitative evidence for combining accelerated FLAIR sequences with a denoising approach using deep learning–based reconstruction to maintain accurate lesion-load quantification in patients with MS while reducing the scan time. We expect that this strategy promoting short MR imaging examinations could improve comfort and help scan more patients.[23]

The SNR, spatial resolution, and scan time are closely related; if one of them is prioritized, the others will inevitably degrade. Denoising is one of the strategies that can break this close link. Several denoising methods have been reported for many years and are traditionally classified into 3 categories:[24] filtering, transform domain, and statistical approaches. All of them can have problems achieving a high accuracy of denoising, which has stimulated the development of adaptive approaches and their combinations.[25] In this context, recent studies have shown the flexibility of machine learning approaches, especially deep

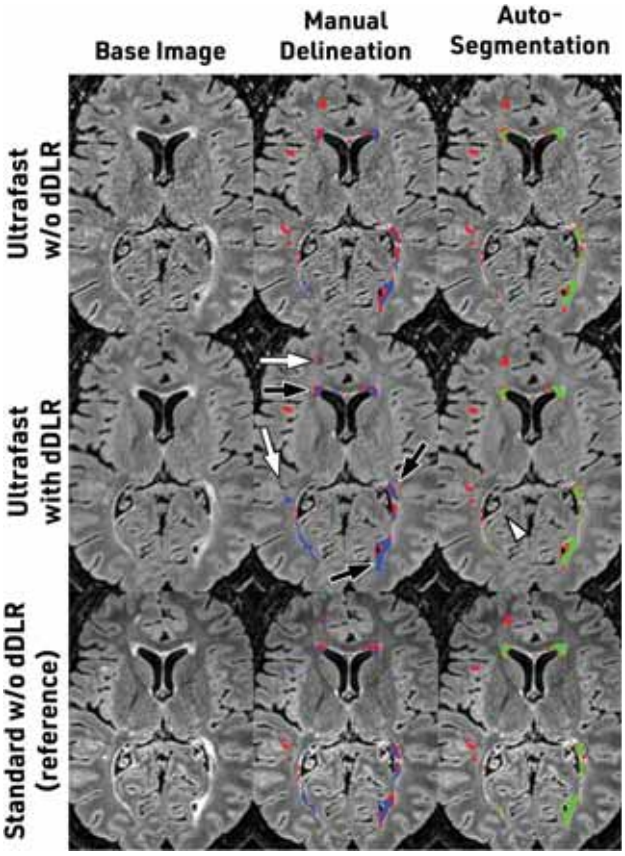

FIG 3. Illustrative axial slices of ultrafast FLAIR without and with dDLR. Standard FLAIR without dDLR is also shown for reference. The *red mask* represents the criterion standard that comes from the delineation of standard FLAIR by 2 expert readers; the *blue mask* is the manual delineation from a third reader; and the *green mask* is the automatic segmentation from volBrain software. After we applied dDLR, some lesions showed contours closer to the criterion standard (*black arrows*). dDLR also retrieved lesions that were missed on the original image (*white arrows and arrowhead*).

learning techniques and their robustness for any type of noise.[26,27] Most important, the reconstruction speed of the deep learning–based approach outperforms conventional methods.[28] The objective of this study was not to compare denoising performances of different approaches but rather to take advantage of 1 solution that is clinically viable, due to almost instantaneous results, and to investigate its clinical validation. Indeed, new deep learning–based denoising algorithms have become accessible in clinical practice recently, but only the first few articles have demonstrated their benefits in some clinical situations.[29-31] However, possible interest in the context of MS, for which lesion detectability is crucial, has never been explored before. Validation inevitably requires tedious manual delineation or lesion counting by expert readers, which we report here.

We found a clear benefit of dDLR in improving image quality due to a higher apparent SNR as measured in vivo and in a phantom (Online Supplemental Data). Our results showed that the major impact of dDLR is on the lesion edge with improved identification of the voxels at the transition between the lesion "core" and the normal-appearing parenchyma. This finding was expected, considering the concentric model of MS plaques[32] with an inflammatory attack that starts around a central vein and progresses centrifugally. In this model, histologic modifications are less pronounced at the periphery, and we can expect that this feature translates into voxels with intermediate gray levels on FLAIR, which can be missed if confounded with noise. The improvement of lesion-contour detection can be particularly relevant in the clinic to facilitate the monitoring of a subtype known as a slowly expanding lesion.[33,34] Furthermore, the detection of additional lesions is also very important because it will impact whether the objectives of no evidence of disease activity are reached.[35] The effect of dDLR on lesion detectability was more challenging to demonstrate, but we identified several examples of "difficult-to-recognize lesions" that were small, with low signal, and in locations where the noise was higher (central location around the deep nuclei or posterior fossa) that were overlooked without dDLR. This finding translated into an improvement of the F1 score that reached statistical significance for the shortest FLAIR sequences. It is likely that 2 individual-but-close lesions could finally be considered as 1 confluent lesion after dDLR by the lesion-counting algorithm, possibly obscuring part of the positive effect on lesion counting.

The results of automatic segmentation followed the same trend as for manual segmentation but with a lower effect. A denoising process was already implemented inside volBrain;[36] in other words, the denoising effect was duplicated. Nonetheless, dDLR still showed beneficial consequences because the dDLR algorithm is fundamentally different from the conventional denoising technique and works complementarily. T1WI is used for such automatic segmentation, and we always used the same nonaccelerated and nondenoised sequence in this study, which could also contribute to these results.

The progressive loss of lesion detectability from standard-to-ultrafast FLAIR sequences likely resulted from the combined effects of lower apparent SNR and a lower contrast-to-noise ratio. The denoising procedure positively influenced both the apparent SNR and the contrast-to-noise ratio (Online Supplemental Data). However, dDLR could not compensate for all the effects of this acceleration strategy. The dDLR applied to the ultrafast or shortest FLAIR sequences did not allow to recover the same performances as standard FLAIR. Clinical use of such extreme accelerations may pose a concern. However, the fast FLAIR combined with dDLR, which already cuts scan time by a factor of close to 2, caught up to the standard FLAIR in image quality and provided equivalent DSC performances for manual segmentation. In the future, we could test the benefit of dDLR with other acceleration strategies.

This study has limitations. First, the number of participants was small. However, we conducted sequence-wise and lesion-wise analyses, which already provided a reasonable amount of data (total of 224 FLAIR sequences). Second, our results came from a specific population of patients with MS monitored under second-line therapy. How this would translate at an earlier stage (clinically isolated syndrome) and for MS diagnosis performances is unknown. Similarly, generalization to other sequences and other magnets has not been tested in this single-center and single-scanner study. Third, only 1 reader manually segmented lesions, and a few segmentation errors cannot be excluded even though they should not have favored 1 type of sequence. Fourth,

we cannot exclude the fact that the reader, while blinded, could recognize the type of FLAIR sequence because of relatively strong noise in ultrafast and the shortest implementations. However, the time spent drawing was within the same range for all types of sequences (Online Supplemental Data), ensuring that all the images were considered equally. It was possible as well that the reader could remember the delineation of lesions from ≥1 FLAIR sequence from the same patient segmented before. However, this recognition bias was likely minor because of the random presentation of 224 sequences segmented intermittently during several months. Fifth, we conducted only 1 automatic segmentation, while new segmentations using deep learning technologies have become mainstream.[37] Finally, the criterion standard was created on the basis of the standard FLAIR without dDLR. Additional FLAIR hyperintense areas detected on standard FLAIR with dDLR explained the decrease in PPV, but the underlying histologic substrate (authentic lesions or real false-positives) cannot be known without conducting a postmortem study.

CONCLUSIONS

In this study, dDLR allows a reduced FLAIR scan time while preserving the image quality in the context of MS. dDLR is adaptable to different noise levels with significant positive effects at different acceleration levels and awaits further clinical validation in several applications.

Disclosure forms provided by the authors are available with the full text and PDF of this article at www.ajnr.org.

REFERENCES

1. Compston A, Coles A. **Multiple sclerosis.** *Lancet* 2008;372:1502–17 CrossRef Medline
2. Thompson AJ, Banwell BL, Barkhof F, et al. **Diagnosis of multiple sclerosis: 2017 revisions of the McDonald criteria.** *Lancet Neurol* 2018;17:162–73 CrossRef Medline
3. Ziemssen T, Derfuss T, de Stefano N, et al. **Optimizing treatment success in multiple sclerosis.** *J Neurol* 2016;263:1053–65 CrossRef Medline
4. Tan IL, Pouwels PJ, van Schijndel RA, et al. **Isotropic 3D fast FLAIR imaging of the brain in multiple sclerosis patients: initial experience.** *Eur Radiol* 2002;12:559–67 CrossRef Medline
5. Traboulsee A, Simon JH, Stone L, et al. **Revised Recommendations of the Consortium of MS Centers Task Force for a Standardized MRI Protocol and Clinical Guidelines for the Diagnosis and Follow-Up of Multiple Sclerosis.** *AJNR Am J Neuroradiol* 2016;37:394–401 CrossRef Medline
6. Wattjes MP, Ciccarelli O, Reich DS, et al; Magnetic Resonance Imaging in Multiple Sclerosis study group; Consortium of Multiple Sclerosis Centres; North American Imaging in Multiple Sclerosis Cooperative MRI guidelines working group. **MAGNIMS–CMSC–NAIMS consensus recommendations on the use of MRI in patients with multiple sclerosis.** *Lancet Neurol* 2021;20:653–70 CrossRef Medline
7. Feinberg DA, Hale JD, Watts JC, et al. **Halving MR imaging time by conjugation: demonstration at 3.5 kG.** *Radiology* 1986;161:527–31 CrossRef Medline
8. Deshmane A, Gulani V, Griswold MA, et al. **Parallel MR imaging.** *J Magn Reson Imaging* 2012;36:55–72 CrossRef Medline
9. Barth M, Breuer F, Koopmans PJ, et al. **Simultaneous multislice (SMS) imaging techniques.** *Magn Reson Med* 2016;75:63–81 CrossRef Medline
10. Toledano-Massiah S, Sayadi A, de Boer R, et al. **Accuracy of the compressed sensing accelerated 3D-FLAIR sequence for the detection of MS plaques at 3T.** *AJNR Am J Neuroradiol* 2018;39:454–58 CrossRef Medline
11. Tian C, Fei L, Zheng W, et al. **Deep learning on image denoising: an overview.** *Neural Netw* 2020;131:251–75 CrossRef Medline
12. Manjón JV, Coupe P. MRI denoising using deep learning. In: Bai W, Sanrona G, Wu G, eds. *Patch-Based Techniques in Medical Imaging.* Springer-Verlag International Publishing 2018:12–19
13. Chaudhari AS, Fang Z, Kogan F, et al. **Super-resolution musculoskeletal MRI using deep learning.** *Magn Reson Med* 2018;80:2139–54 CrossRef Medline
14. Kidoh M, Shinoda K, Kitajima M, et al. **Deep learning based noise reduction for brain MR imaging: tests on phantoms and healthy volunteers.** *MRMS* 2020;19:195–206 CrossRef Medline
15. Marc Lebel R. **Performance characterization of a novel deep learning-based MR image reconstruction pipeline.** *arXiv* [eessIV] 2020 Aug 14. https://arxiv.org/abs/2008.06559. Accessed May 31, 2022
16. Drake-Pérez M, Delattre BM, Boto J, et al. **Normal values of magnetic relaxation parameters of spine components with the synthetic MRI sequence.** *AJNR Am J Neuroradiol* 2018;39:788–95 CrossRef Medline
17. Saranathan M, Worters PW, Rettmann DW, et al. **Physics for clinicians: fluid-attenuated inversion recovery (FLAIR) and double inversion recovery (DIR) imaging.** *J Magn Reson Imaging* 2017;46:1590–600 CrossRef Medline
18. Fedorov A, Beichel R, Kalpathy-Cramer J, et al. **3D Slicer as an image computing platform for the Quantitative Imaging Network.** *Magn Reson Imaging* 2012;30:1323–41 CrossRef Medline
19. Coupé P, Tourdias T, Linck P, et al. **LesionBrain: an online tool for white matter lesion segmentation.** In: Coupé P, Tourdias T, Linck P. *Patch-Based Techniques in Medical Imaging.* September 15, 2018. https://doi.org/10.1007/978-3-030-00500-9_11. Accessed May 31, 2022
20. Manjón JV, Coupé P. **volBrain: an online MRI brain volumetry system.** *Front Neuroinform* 2016;10:30 CrossRef Medline
21. Commowick O, Istace A, Kain M, et al. **Objective evaluation of multiple sclerosis lesion segmentation using a data management and processing infrastructure.** *Sci Rep* 2018;8:13650 CrossRef Medline
22. Wobbrock JO, Findlater L, Gergle D, et al. **The aligned rank transform for nonparametric factorial analyses using only ANOVA procedures.** In: *Proceedings of the ACM Conference on Human Factors in Computing Systems (CHI '11).* Vancourver, British Columbia, Canada. May 7–12, 2011 CrossRef
23. Brisset JC, Kremer S, Hannoun S, et al. **New OFSEP recommendations for MRI assessment of multiple sclerosis patients: special consideration for gadolinium deposition and frequent acquisitions.** *J Neuroradiol* 2020;47:250–58 CrossRef Medline
24. Mohan J, Krishnaveni V, Guo Y. **A survey on the magnetic resonance image denoising methods.** *Biomed Signal Processing and Control* 2014;9:56–69 CrossRef
25. Annavarapu A, Borra S. **Development of magnetic resonance image de-noising methodologies: a comprehensive overview of the state-of-the-art.** *Smart Health* 2020;18:100138 CrossRef
26. Moreno López M, Frederick JM, Ventura J. **Evaluation of MRI denoising methods using unsupervised learning.** *Front Artif Intell* 2021;4:642731 CrossRef Medline
27. Ilesanmi AE, Ilesanmi TO. **Methods for image denoising using convolutional neural network: a review.** *Complex & Intelligent Systems* 2020;7:2179–98 CrossRef
28. Lundervold AS, Lundervold A. **An overview of deep learning in medical imaging focusing on MRI.** *Z Med Phys* 2019;29:102–27 CrossRef Medline
29. Benou A, Veksler R, Friedman A, et al. **Ensemble of expert deep neural networks for spatio-temporal denoising of contrast-enhanced MRI sequences.** *Med Image Anal* 2017;42:145–59 CrossRef Medline
30. Yokota Y, Takeda C, Kidoh M, et al. **Effects of deep learning reconstruction technique in high-resolution non-contrast magnetic resonance coronary angiography at a 3-Tesla machine.** *Can Assoc Radiol J* 2021;72:120–27 CrossRef Medline

31. Bash S, Wang L, Airriess C, et al. **Deep learning enables 60% accelerated volumetric brain MRI while preserving quantitative performance: a prospective, multicenter, multireader trial.** *AJNR Am J Neuroradiol* 2021;42:2130–37 CrossRef Medline
32. Gaitán MI, Shea CD, Evangelou IE, et al. **Evolution of the blood-brain barrier in newly forming multiple sclerosis lesions.** *Ann Neurol* 2011;70:22–29 CrossRef Medline
33. Jäckle K, Zeis T, Schaeren-Wiemers N, et al. **Molecular signature of slowly expanding lesions in progressive multiple sclerosis.** *Brain* 2020;143:2073–88 CrossRef Medline
34. Elliott C, Wolinsky JS, Hauser SL, et al. **Slowly expanding/evolving lesions as a magnetic resonance imaging marker of chronic active multiple sclerosis lesions.** *Mult Scler* 2019;25:1915–25 CrossRef Medline
35. Lu G, Beadnall HN, Barton J, et al. **The evolution of "no evidence of disease activity" in multiple sclerosis.** *Mult Scler Relat Disord* 2018;20:231–38 CrossRef Medline
36. Coupe P, Yger P, Prima S, et al. **An optimized blockwise nonlocal means denoising filter for 3-D magnetic resonance images.** *IEEE Trans Med Imaging* 2008;27:425–41 CrossRef Medline
37. Danelakis A, Theoharis T, Verganelakis DA. **Survey of automated multiple sclerosis lesion segmentation techniques on magnetic resonance imaging.** *Comput Med Imaging Graph* 2018;70:83–100 CrossRef Medline

Unsupervised Deep Learning for Stroke Lesion Segmentation on Follow-up CT Based on Generative Adversarial Networks

H. van Voorst, P.R. Konduri, L.M. van Poppel, W. van der Steen, P.M. van der Sluijs, E.M.H. Slot, B.J. Emmer, W.H. van Zwam, Y.B.W.E.M. Roos, C.B.L.M. Majoie, G. Zaharchuk, M.W.A. Caan, and H.A. Marquering, on behalf of the CONTRAST Consortium Collaborators

ABSTRACT

BACKGROUND AND PURPOSE: Supervised deep learning is the state-of-the-art method for stroke lesion segmentation on NCCT. Supervised methods require manual lesion annotations for model development, while unsupervised deep learning methods such as generative adversarial networks do not. The aim of this study was to develop and evaluate a generative adversarial network to segment infarct and hemorrhagic stroke lesions on follow-up NCCT scans.

MATERIALS AND METHODS: Training data consisted of 820 patients with baseline and follow-up NCCT from 3 Dutch acute ischemic stroke trials. A generative adversarial network was optimized to transform a follow-up scan with a lesion to a generated baseline scan without a lesion by generating a difference map that was subtracted from the follow-up scan. The generated difference map was used to automatically extract lesion segmentations. Segmentation of primary hemorrhagic lesions, hemorrhagic transformation of ischemic stroke, and 24-hour and 1-week follow-up infarct lesions were evaluated relative to expert annotations with the Dice similarity coefficient, Bland-Altman analysis, and intraclass correlation coefficient.

RESULTS: The median Dice similarity coefficient was 0.31 (interquartile range, 0.08–0.59) and 0.59 (interquartile range, 0.29–0.74) for the 24-hour and 1-week infarct lesions, respectively. A much lower Dice similarity coefficient was measured for hemorrhagic transformation (median, 0.02; interquartile range, 0–0.14) and primary hemorrhage lesions (median, 0.08; interquartile range, 0.01–0.35). Predicted lesion volume and the intraclass correlation coefficient were good for the 24-hour (bias, 3 mL; limits of agreement, −64–59 mL; intraclass correlation coefficient, 0.83; 95% CI, 0.78–0.88) and excellent for the 1-week (bias, −4 m; limits of agreement,−66–58 mL; intraclass correlation coefficient, 0.90; 95% CI, 0.83–0.93) follow-up infarct lesions.

CONCLUSIONS: An unsupervised generative adversarial network can be used to obtain automated infarct lesion segmentations with a moderate Dice similarity coefficient and good volumetric correspondence.

ABBREVIATIONS: AIS = acute ischemic stroke; BL = baseline; DSC = Dice similarity coefficient; FU = follow-up; FU2BL-GAN = follow-up to baseline generative adversarial network; GAN = generative adversarial network; 24H = 24 hours; HT = hemorrhagic transformation; ICC = intraclass correlation coefficient; IQR = interquartile range; L1-loss = voxelwise absolute difference between generated baseline and real baseline NCCTs; L1+adv = L1 and adversarial loss; LoA = limits of agreement; nnUnet = no new Unet; PrH = primary hemorrhagic lesions; 1W = 1 week

Hemorrhagic transformation (HT) and malignant cerebral edema are severe complications after acute ischemic stroke (AIS), which frequently result in functional deterioration and death.[1-3] Computer-guided visualization and segmentation of these hemorrhagic and infarct lesions can assist radiologists in detecting small lesions.[4,5] Furthermore, lesion volume computed from a segmentation predicts

Received January 27, 2022; accepted after revision June 2.

From the Departments of Radiology and Nuclear Medicine (H.v.V., P.R.K., L.M.v.P., B.J.E., C.B.L.M.M., H.A.M.), Biomedical Engineering and Physics (H.v.V., P.R.K., L.M.v.P., M.W.A.C., H.A.M.), and Neurology (Y.B.W.E.M.R.), Faculty of Medicine, Amsterdam University Medical Centers, University of Amsterdam, Amsterdam, the Netherlands; Departments of Neurology (W.v.d.S., P.M.v.d.S.) and Radiology and Nuclear Medicine (W.v.d.S., P.M.v.d.S.), Erasmus University Medical Center, Rotterdam, the Netherlands; Department of Neurology and Neurosurgery (E.M.H.S.), University Medical Center Utrecht, Utrecht, the Netherlands; Department of Radiology and Nuclear Medicine (W.H.v.Z.), Maastricht University Medical Center, Maastricht, the Netherlands; and Department of Radiology (G.Z.), Stanford University, Stanford, California.

The funding sources were not involved in study design, monitoring, data collection, statistical analyses, interpretation of results, or manuscript writing.

This study was funded by the CONTRAST consortium. The CONTRAST consortium acknowledges the support from the Netherlands Cardiovascular Research Initiative, an initiative of the Dutch Heart Foundation (CVON2015-01: CONTRAST) and from the Brain Foundation of the Netherlands (HA2015.01.06). The collaboration project is additionally financed by the Ministry of Economic Affairs by means of the Public-private partnerships Allowance made available by the Top Sector Life Sciences & Health to stimulate public-private partnerships (LSHM17016). This work was funded, in part, through unrestricted funding by Stryker, Medtronic, and Cerenovus.

Please address correspondence to Henk van Voorst, MD, Amsterdam UMC locatie AMC, Meibergdreef 9, 1105 AZ Amsterdam, Noord-Holland, the Netherlands, Department of Biomedical Engineering and Physics, Department of Radiology and Nuclear Medicine, Room L0147, 020 566 9111; e-mail: h.vanvoorst@amsterdamumc.nl

Indicates open access to non-subscribers at www.ajnr.org

Indicates article with online supplemental data.

http://dx.doi.org/10.3174/ajnr.A7582

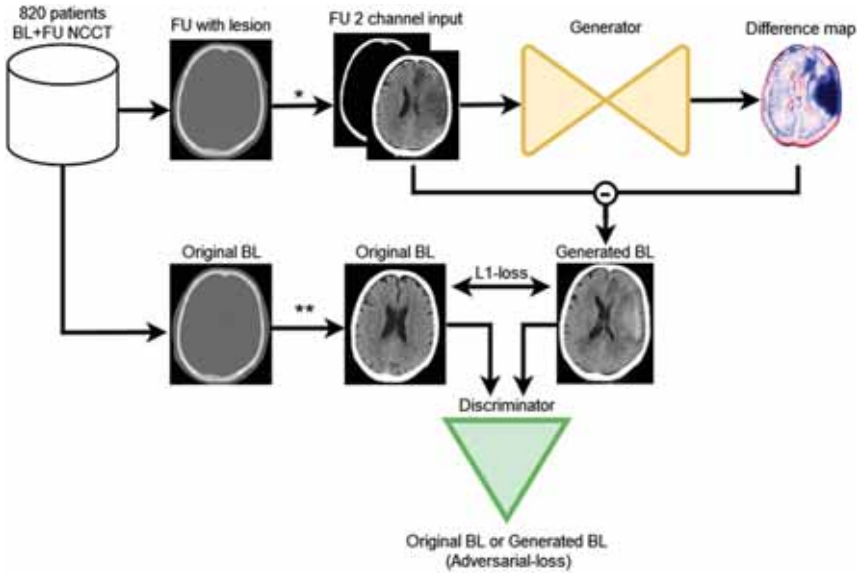

FIG 1. The FU2BL-GAN global architecture (*asterisk*). The follow-up (FU) NCCT with lesion is clipped between Hounsfield unit ranges of 0–100 and 100–1000 and normalized to (−1) (*double asterisks*). The original BL NCCT is only clipped between 0 and 100 HU and normalized to (−1). The FU NCCT with a lesion is passed through the generator network to compute a difference map. This difference map is subtracted from the input FU NCCT to construct a generated BL NCCT. Original BL and generated BL are optimized on the basis of the absolute voxelwise difference (L1-loss) and the binary cross-entropy loss (adversarial-loss) of the discriminator networks classification (original or generated BL).

long-term functional outcome[3,6] and can be used to guide additional treatment such as decompressive craniectomy.[7] Compared with an AIS baseline (BL) NCCT, follow-up (FU) NCCT imaging of a hemorrhagic lesion is characterized by an attenuation increase, while infarct lesions are characterized by an attenuation decrease.[8,9] This attenuation change between NCCT scans can be exploited by specific deep learning algorithms to identify tissue changes and, in turn, can be used to obtain lesion segmentations.

Supervised deep learning with convolutional neural networks is the state-of-the-art computer-guided method for volumetric segmentation of hemorrhagic and infarct lesions in NCCT.[4,5,8-10] The supervised part in the case of segmentation refers to the use of human-, often an expert radiologist, guided annotations per voxel that represent the ground truth of the lesion on NCCT. These annotations are subsequently used to optimize a convolutional neural network for automated segmentation.[11] However, acquiring manual annotations is time-consuming and is subject to intra- and interrater variability. As a result, it is difficult to create large data sets with comprehensive ground truth annotations. This issue is a challenge for the training of supervised deep learning models, affecting the performance and generalizability of these models.

Generative adversarial networks (GANs) are a type of deep learning model that can be used to generate new images or transform existing images.[12,13] Because a GAN is optimized without an explicitly defined ground truth, such as manual lesion annotations, it is considered an unsupervised deep learning method. Recently, Baumgartner et al[14] introduced the use of a GAN to transform an MR image of a patient with symptoms to a scan before symptom onset of Alzheimer disease. From this transformation, structural maps were extracted to visually represent pathologic changes relative to a generated BL MR imaging scan without Alzheimer disease.[14] Such structural pathology maps could subsequently be used to segment and quantify the pathologic changes.

The aim of this study was to accurately segment stroke lesions on follow-up NCCT scans with a GAN trained in an unsupervised manner. In line with Baumgartner et al,[14] we developed a GAN to remove hemorrhagic and ischemic stroke lesions from follow-up NCCT scans by generating difference maps with a lesion and BL NCCT scans without a lesion.

MATERIALS AND METHODS

GANs for BL NCCT Generation

The GAN structure as adopted in this study consists of 2 competing deep learning models, referred to as generator and discriminator models. The generator model generates artificial images, while the discriminator model tries to distinguish the generated artificial image from the original images.[12,13] In this study, the generator receives as input a follow-up NCCT scan with the lesion and generates a difference map. This difference map is subtracted from the input follow-up NCCT scan with the lesion to generate an artificial BL NCCT scan without the lesion. Because an infarct lesion is visually subtle in AIS BL NCCTs acquired in the acute stage (0–6 hours after symptom onset), the transformation from a follow-up scan at 24 hours (24H) or 1 week (1W) with a well-defined lesion to a BL scan entails essentially the removal of the lesion. Subsequently, the discriminator model classifies the presented images as being either an original BL or a generated BL NCCT. This classification is used to provide feedback to the generator model and to optimize the difference map.[12,13] The generated difference map is expected to have high positive values at the location of a hemorrhagic lesion and negative values at the location of an infarct lesion on a follow-up NCCT. Similarly, the attenuation change between BL and follow-up NCCT is positive in the case of a HT and negative if edema or brain tissue necrosis occurs in the infarct lesion. Thresholding of the generated difference map values can then be used to obtain a lesion segmentation.

The proposed GAN method is optimized with 2 types of loss functions: the voxelwise absolute difference between generated BL and real BL NCCTs (L1-loss) and the binary cross-entropy of the discriminator (adversarial-loss) for classifying generated and real BL NCCTs.[12,13] Figure 1 presents the GAN model architecture we refer to as the follow-up to BL GAN (FU2BL-GAN).

Patient Populations

In this study, 820 patients were included between January 2018 and July 2021 in the training data set from the MR CLEAN-NO-IV ($n = 297$), MR CLEAN-MED ($n = 377$), and MR CLEAN-

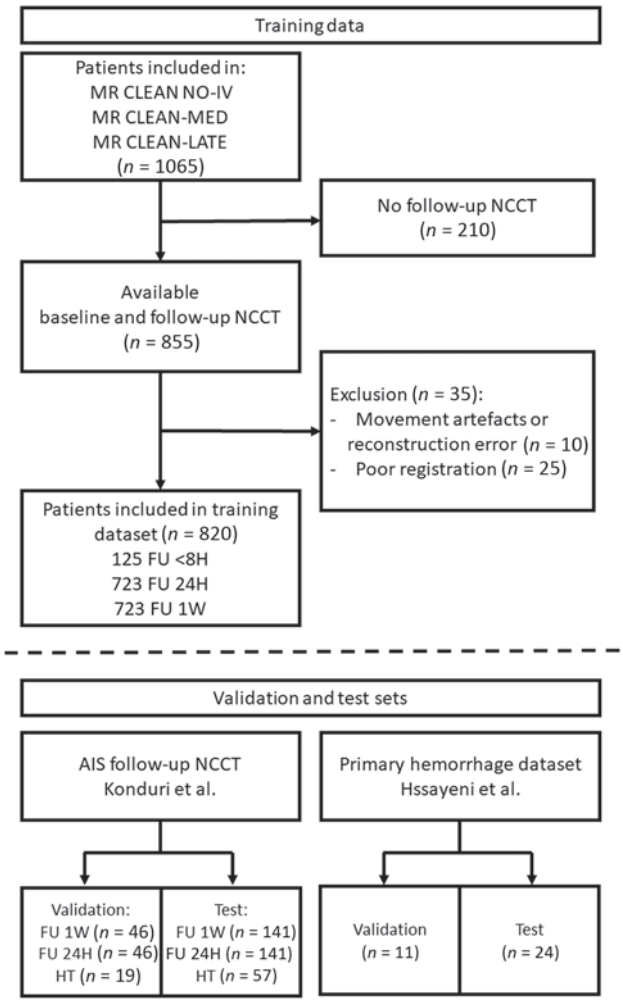

FIG 2. Patients included in the training, validation, and test sets. The training data consisted of a BL and at least 1 follow-up (FU) NCCT. FU of <8 hours: FU NCCT acquired within 8 hours; FU 24H: FU NCCT acquired 8–72 hours; FU 1W: FU NCCT acquired 72 hours to 2 weeks after endovascular treatment or randomization. Validation and test sets were constructed with data from the studies by Konduri et al[18] and Hssayeni et al.[19] 8H indicates 8 hours.

LATE ($n = 146$) randomized controlled trials if BL and follow-up NCCTs were available. Specific imaging protocols, inclusion, and exclusion criteria of each of these randomized controlled trials have been published previously.[15-17] Scans of these 820 patients were used to train the FU2BL-GAN. NCCT scans with lesion annotation from previously published studies by Konduri et al[18] and Hssayeni et al[19] were used to construct 4 randomly split dedicated validation and test sets (depicted in Fig 2): ischemic stroke lesions between 8- and 72-hour (24H infarct; N validation: 46; N test: 141) and 72-hour and 2-week (1W infarct; N validation: 46; N test: 141) follow-up after endovascular treatment or randomization; hemorrhagic transformation lesions after AIS (HT; N validation: 19; N test: 57);[20] and primary hemorrhagic lesions (PrH; N validation: 11; N test: 24). The data from Konduri et al was originally included in the MR CLEAN trial between December 2010 and March 2014.[21] In compliance with the declaration of Helsinki, informed consent has been received for the use of data for substudies from patients included in the training data randomized controlled trials and the validation and test data of ischemic and HT lesions.[15-18,20] The PrH data from Hssayeni et al[19] was accessed through physionet.org and obtained with a "Restricted Health Data License 1.5.0," because the authors stated that collection and sharing of the retrospectively collected anonymized and defaced CTs were authorized by the Iraq Ministry of Health Ethics board.

Training Data and Training Protocol

All NCCT volumes were converted from DICOM to NIfTI format with dcm2niix available in MRIcroGL, Version 1.2.20211006.[22] Elastix, Version 5.0.0 (https://elastix.lumc.nl/) was used to coregister the follow-up and BL NCCTs of the training data;[23] the scan with the thinnest slices was used as a moving image. Poor coregistration was detected by inspecting the overlay of the 2 images at the 30th, 50th, and 80th percentile sections. Up to 3 follow-up NCCTs were used per patient if clinical deterioration occurred within 8 hours after endovascular treatment or randomization (8 hours) and as part of the imaging protocols of 8–72 hours (24H) and 72 hours to 2 weeks (1W) after AIS.[15-17] To ensure stable optimization and prevent overfitting, per training iteration, we used 1 follow-up NCCT and 1 corresponding BL NCCT section (512×512). Slices were sampled at random on the 10th and the 95th percentile sections. Furthermore, to emphasize the variation in attenuation between different tissues, the generator model received 2D slices from follow-up NCCTs with 2 channels on the basis of different Hounsfield unit ranges as input: The attenuation was clipped between both 0 and 100 HU for brain and infarct differentiation and 100 and 1000 HU for hemorrhage and skull differentiation. The images were subsequently normalized to a -1 to 1 range. BL NCCTs were only clipped between 0 and 100 HU and normalized to a -1 to 1 range. The discriminator network receives 2D slices of either generated BL or real BL NCCT scans. To make the FU2BL-GAN robust to differences in contrast and noise between the BL and follow-up NCCTs, we applied multiple intensity and noise-altering image augmentations (details available in the Online Supplemental Data). A batch size of 2 with a learning rate of 0.00002 for 500 epochs was used, subsequently linearly reduced to zero over the following 500 epochs (Nvidia TITAN V [https://www.nvidia.com/en-us/titan/titan-v/] with 12-gb RAM). The Online Supplemental Data contains a detailed description of the FU2BL-GAN architecture.

Lesion Segmentation

To obtain lesion segmentations, we passed validation and test set NCCTs through the generator model to generate difference maps. Due to computational constraints, the validation set difference maps were computed every 10th training epoch. Subsequently, segmentations were obtained by applying a threshold to the difference maps. The resulting Dice similarity coefficient (DSC) of the segmentations relative to the ground truth was used to determine the optimal threshold for the difference map -0.2 to $+0.3$ with steps of 0.01 (equivalent to 0.5 HU). An automatically computed brain mask based on intensity thresholds and region growing was used to remove false-positive segmentations that were not allocated inside the skull.[9] In the Online Supplemental Data, validation set results are depicted. Finally, the optimal epoch and threshold were used to obtain segmentations for the test sets.

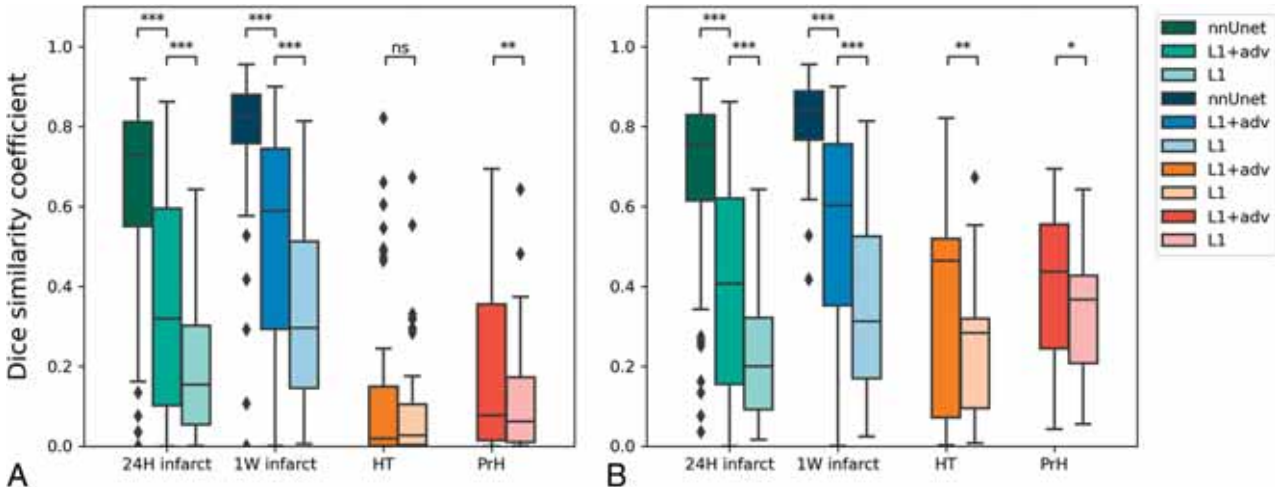

FIG 3. Dice similarity coefficients of test sets: 24-hour follow-up after AIS (24H infarct), 1-week follow-up after AIS (1W infarct), HT, and PrH. *A*, The results of all the test set data. *B*, Only results from lesions that are >10 mL. Each shade of color represents the results based on the supervised nnUnet approach, the FU2BL-GAN approach trained with L1+adv, and the generator trained with L1-loss only (L1) respectively. The *Asterisk* indicates $P < .05$; *double asterisks*, $P < .001$; *triple asterisks*, $P <$ 1e-10; NS, nonsignificant difference.

Evaluation and Outcome Metrics

Reported results were based on test set segmentations and were reported relative to expert-based ground truth segmentations. The DSC and Hausdorff distance in millimeters were used to compute spatial correspondence. Results from the FU2BL-GAN approach trained with L1 and adversarial loss (L1+adv) were compared statistically with the Wilcoxon rank-sum test with a simpler approach trained with L1-loss (L1) only. Furthermore, the results of the FU2BL-GAN were compared with two 2D Unets trained on segmentations from the 24H and 1W infarct validation sets using the no new Unet (nnUnet) framework as a conventional supervised learning BL.[24] Volumetric correspondence between the ground truth and predicted segmentations were analyzed with Bland-Altman plots with bias (mean between methods) and limits of agreement (LoA, ±1.96 SDs from the bias) and the intraclass correlation coefficient (ICC) with 95% CIs. The 2-way mixed-effects approach for consistency of a single fixed rate was used to describe differences between the FU2BL-GAN-based segmentations and the expert-based ground truth lesion segmentations. A subgroup analysis was performed for lesions of >10 mL to address the effect of lesion size on our outcome metrics. Results were reported as median with interquartile range (IQR) or mean with 95% CIs.

RESULTS

Ischemic and hemorrhagic lesions in our test sets were relatively small; the distribution of volumes was skewed toward smaller lesions. Ground truth lesion volume of test sets had a median of 35 mL (IQR, 16–78 mL) in the 24H and 66 mL (IQR, 29–125mL) and in the 1W infarct NCCTs, respectively. For the HT and PrH test sets respectively, the mean lesion size was 6 mL (IQR, 2—12 mL) and 6 mL (IQR, 1–12 mL). Characteristics of the training data can be found in the Online Supplemental Data. Training characteristics and the optimal difference map thresholds are available in the Online Supplemental Data.

Quantitative Results

As depicted in Figs 3 and the Online Supplemental Data, DSC and lesion volume were positively related. The median DSC of the FU2BL-GAN was 0.31 (IQR, 0.08–0.59) in the 24H infarct test set, 0.59 (IQR, 0.29–0.74) for the 1W infarct test set, 0.02 (IQR, 0–0.14) for the HT test set, and 0.08 (IQR, 0.01–0.35) for the PrH test set. The FU2BL-GAN (L1+adv) had a statistically significant higher DSC than the model trained with only L1-loss (L1) for all test sets but a significantly lower DSC compared with the nnUnet approach (Fig 3). The subgroup of lesions of >10 mL (Fig 3*B*) had a higher DSC than the overall population (Fig 3*A*), especially for the HT (median, 0.46; IQR, 0.07–0.51) and PrH (median, 0.44; IQR, 0.24–0.55) test sets but also for the follow-up infarct (24H infarct: median, 0.41; IQR, 0.15–0.62; 1W infarct: median, 0.60; IQR, 0.35–0.75) test sets. For all the infarct and hemorrhage test sets, the Hausdorff distances of both the FU2BL-GAN and L1 approach were poor with a median varying between 83 and 87 mm (Online Supplemental Data). Bland-Altman plots of the 4 test sets are depicted in Fig 4. Bias and LoA for the FUB2BL-GAN of the 24H (bias, −3 mL; LoA, −64–59 mL) and 1W (bias, –4 mL; LoA, –66–58 mL) test sets were low, representing good correspondence of the segmentations with ground truth annotations. However, both the HT (bias, 22 mL; LoA, –49–92 mL) and PrH (bias, 23 mL; LoA, –10–57 mL) segmentations overestimated lesion volume and had several outliers that affected volumetric correspondence. The ICC for the FUB2BL-GAN was excellent in the 1W infarct test set (ICC, 0.90; 95% CI, 0.83–0.93), good in the 24H infarct (ICC, 0.83; 95% CI, 0.78–0.88) and PrH (ICC, 0.84; 95% CI, 0.66–0.93) test sets, and poor in the HT (ICC, 0.11; 95% CI, –0.15–0.36) test sets. However, the nnUnet approach resulted in a lower bias and LoA, a higher ICC, and a lower Hausdorff distance than the FU2BL-GAN for both the 24H (bias, –14 mL; LoA, −57–29 mL; ICC, 0.91; 95% CI, 0.88–0.92; Hausdorff distance, 28 mm; IQR, 18–42 mm) and 1W (bias, –6 mL; LoA, –36–23 mL;

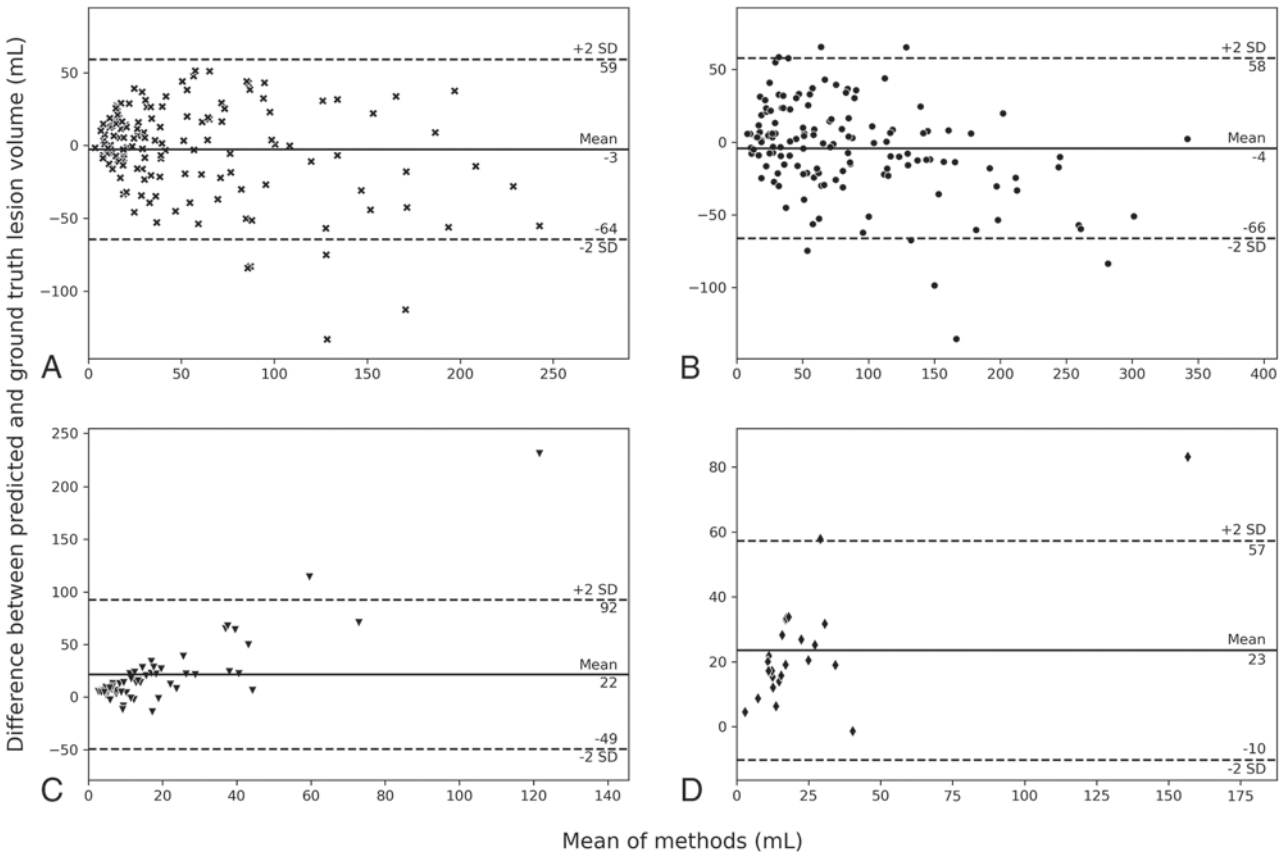

FIG 4. Bland-Altman plots of predicted lesion size for the FU2BL-GAN. *A*, 24H infarct follow-up. *B*, 1W infarct follow-up. *C*, HT. *D*, PrH.

ICC, 0.98; 95% CI, 0.97–0.99; Hausdorff distance, 21 mm; IQR, 14–37 mm) infarct lesions test sets (Online Supplemental Data).

Qualitative Visual Results

Figure 5 depicts visual examples of each test set in the first 4 rows, while the last 2 rows depict examples with poor segmentation performance. In contrast to the examples shown in the first 3 rows, the input NCCT of the PrH test set is the acute-phase NCCT with hemorrhagic lesions. For this case, the generated scan can be regarded as a prehemorrhagic stroke NCCT scan. Although lesions visually appear to be removed accurately, the generator model was not able to completely reconstruct 24H infarcted brain tissue similar to the BL NCCTs (columns 1 versus 3). False-positive hemorrhage segmentations were present when the input NCCT scan had beam-hardening artifacts in the brain close to the skull or when the overall scan attenuation was higher (arrows in PrH and HT column 2). False-negative hemorrhage segmentations were present if the hemorrhage was small and the attenuation increase was low (row 6, poor HT). False-positive infarct segmentations occurred close to the ventricles and other locations, where CSF results in a hypoattenuated region (row 5). False-negative infarct segmentation errors mainly occurred in the 24H infarct data set because the infarct lesion was not yet significantly hypoattenuated (row 5).

DISCUSSION

Our study shows that when one uses a GAN deep learning structure, it is possible to obtain follow-up ischemic and large hemorrhagic lesion segmentations without using manually annotated training data. Although the visual quality of generated BL scans was not always optimal, lesion segmentation quality was often not affected. External validation in 4 test sets revealed reasonable segmentation quality in terms of DSC and good-to-excellent volumetric correspondence with the ground truth for follow-up infarct lesions in NCCT at 24H and 1W follow-up after AIS. In terms of DSC and volumetric correspondence, our work performs on a par with previous work on supervised deep-for-follow-up infarct lesion segmentation (DSC median, 0.57 [SD:0.26]; ICC, 0.88).[9] However, the presented unsupervised FU2BL-GAN did not outperform the supervised nnUnet benchmark model with respect to all outcome measures. Kuang et al[25] also used a GAN to segment infarct lesions but achieved much higher segmentation quality (DSC mean, 0.70 [SD, 0.12]). However, the approach by Kuang et al required a training set with manual lesion annotations because the adversarial (GAN) loss was used in addition to the supervised loss functions. DSC and volumetric correspondence for segmenting the HT and PrH lesions were worse than those of existing supervised methods.[4,5,8,10] Poor detection and segmentation of hemorrhagic lesions are likely due to the small lesion size in our test sets and an under-representation of hemorrhages in the training data.

The unsupervised approach to training is a major advantage compared with conventional supervised deep learning methods. With the growing availability of unlabeled and weakly labeled imaging data bases, unsupervised GAN-based approaches can be

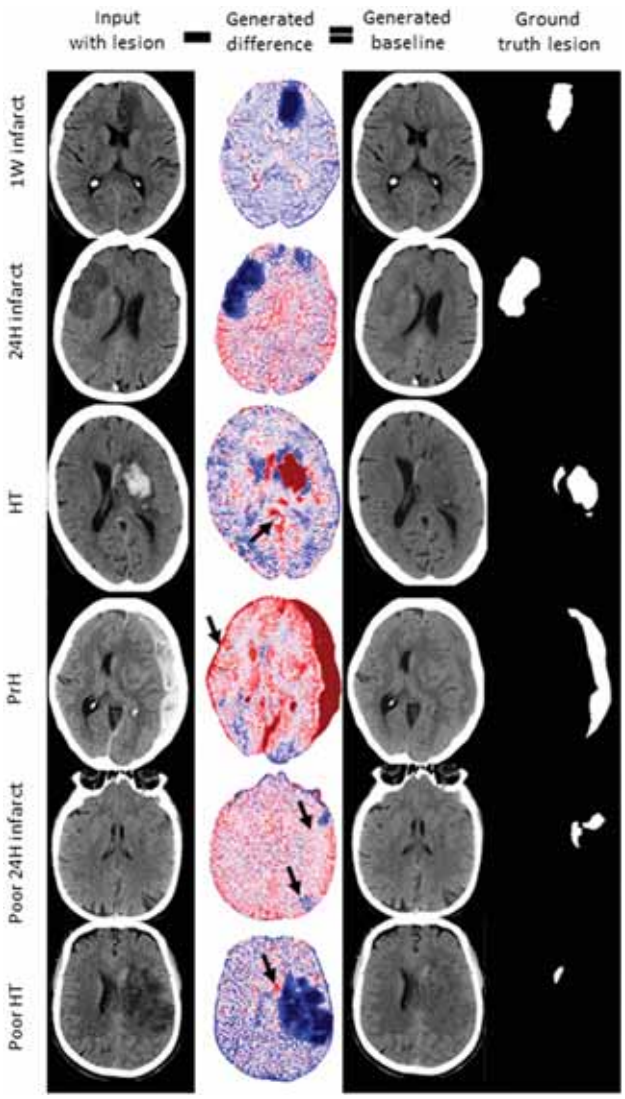

FIG 5. Visual results of the FU2BL-GAN. The first column contains the input NCCT with lesion used as input for the generator model to generate a difference map (column 2). The difference map is subtracted from the input NCCT (column 1) to obtain a generated BL scan (column 3). The negative (blue) and positive (red) values of the difference map correspond to the deviation of the difference map from zero. A higher deviation from zero implies a higher attenuation adjustment of the follow-up NCCT to generate the BL NCCT without a lesion. Column 4 contains the ground truth lesion annotations. *Arrows* show false-positive hemorrhage (rows 3 and 4), false-negative infarct (row 5, *upper arrow*), false-positive infarct (row 5, *lower arrow*), and false-negative hemorrhage segmentation (*arrow*, row 6).

used without the manual annotation effort for automated lesion segmentation. However, the downside of the presented approach is the requirement of paired training images, coregistered images with and without lesions from the same patient. Such high-quality registration is often difficult to achieve when considering medical imaging because most organs, tissues, and body parts deform or move between acquisition moments. Because the brain only slightly deforms and moves between acquisition moments, the use of a GAN-based lesion segmentation method similar to the presented FU2BL-GAN seems promising for other brain pathologies.

One of the main shortcomings of the presented FU2BL-GAN is that it can only be trained on CT slices sampled at random. Because not every section in an NCCT volume of a patient contains an initial AIS lesion and only a minority of the volumes contain a hemorrhagic lesion, the FU2BL-GAN likely experienced an under-representation of brain lesions. This under-representation during the training of NCCT slices with a lesion, especially with a hemorrhagic lesion, compared with slices without lesions, is known to result in poorer segmentation performance; in technical literature, this is often referred to as the "class imbalance problem."[26] In contrast, supervised deep learning methods often use adjusted sampling techniques that require ground truth annotations;[8] most class (nonlesion tissue) is undersampled relative to the minority class (the lesion) to balance class representation. A valuable improvement in our FU2BL-GAN would be to manually classify slices for lesion presence and volumes for the presence of a hemorrhage. Although these section- or volume-level annotations would take some time to acquire, such sparse annotation methods are still less time-consuming than manually segmenting lesions required for supervised deep learning. Alternatively, automated NCCT-section classification algorithms for infarct or hemorrhage presence can be used to classify NCCT slices on the basis of lesion presence.[27] Subsequently, this information can be used to select training data for further improvement of the FU2BL-GAN.

Although the test sets used in this study are from multiple centers, it remains largely unclear what scanners, settings, and postprocessing methods were used. Furthermore, Konduri et al[18] reported extensive exclusion criteria related to the image quality and noise level, excluding 93 of 280 patients in their data set. These factors influence the ability to generalize results from this study and require additional external validation on subgroups and other data sets.

CONCLUSIONS

The presented FU2BL-GAN is an unsupervised deep learning approach trained without manual lesion annotations to segment stroke lesions. With the FU2BL-GAN, it is feasible to obtain automated infarct lesion segmentations with moderate DSC and good volumetric correspondence.

ACKNOWLEDGMENTS

CONTRAST Clinical Trial Collaborators

Research Leaders

Diederik Dippel (MD, PhD),[1] Charles Majoie (MD, PhD)[3]

Consortium Coordinator

Rick van Nuland, (PhD)[24]

Imaging Assessment Committee

Charles Majoie (MD, PhD)–Chair,[3] Aad van der Lugt (MD, PhD)–Chair,[1] Adriaan van Es, (MD, PhD),[1,2] Pieter-Jan van Doormaal (MD),[1] René van den Berg, (MD, PhD),[3] Ludo Beenen (MD),[3] Bart Emmer (MD, PhD),[3] Stefan Roosendaal (MD, PhD),[3] Wim van Zwam (MD, PhD),[4] Alida Annechien Postma (MD, PhD),[25] Lonneke Yo (MD, PhD),[6] Menno Krietemeijer (MD),[6]

Geert Lycklama (MD, PhD),[7] Jasper Martens (MD),[8] Sebastiaan Hammer (MD, PhD),[10] Anton Meijer (MD, PhD),[10] Reinoud Bokkers (MD, PhD),[15] Anouk van der Hoorn (MD, PhD),[15] Ido van den Wijngaard (MD, PhD),[2,7] Albert Yoo (MD, PhD),[26] Dick Gerrits (MD)[27]

Adverse Events Committee

Robert van Oostenbrugge (MD, PhD)–Chair,[4] Bart Emmer (MD, PhD),[3] Jonathan M. Coutinho (MD, PhD),[3] Martine Truijman (MD, PhD),[4] Julie Staals (MD, PHD),[4] Bart van der Worp (MD, PhD),[5] J. Boogaarts (MD, PhD),[10] Ben Jansen (MD, PhD),[16] Sanne Zinkstok (MD, PhD)[28]

Outcome Assessment Committee

Yvo Roos (MD, PhD)–Chair,[3] Peter Koudstaal (MD, PhD),[1] Diederik Dippel (MD, PhD),[1] Jonathan M. Coutinho (MD, PhD),[3] Koos Keizer (MD, PhD),[5] Sanne Manschot (MD, PhD),[7] Jelis Boiten (MD, PhD),[7] Henk Kerkhoff (MD, PhD),[14] Ido van den Wijngaard (MD, PhD)[2,7]

Data Management Group

Hester Lingsma (PhD),[1] Diederik Dippel (MD, PhD),[1] Vicky Chalos (MD),[1] Olvert Berkhemer (MD, PhD)[1,3]

Imaging Data Management

Aad van der Lugt (MD, PhD),[1] Charles Majoie (MD, PhD),[3] Adriaan Versteeg,[1] Lennard Wolff (MD),[1] Matthijs van der Sluijs (MD),[1] Henk van Voorst (MD),[3] Manon Tolhuisen (MSc),[3]

Biomaterials and Translational Group

Hugo ten Cate (MD, PhD),[4] Moniek de Maat (PhD),[1] Samantha Donse-Donkel (MD),[1] Heleen van Beusekom (PhD),[1] Aladdin Taha (MD),[1] Aarazo Barakzie (MD)[1]

Local Collaborators

Vicky Chalos (MD, PhD),[1] Rob van de Graaf (MD, PhD),[1] Wouter van der Steen (MD),[1] Aladdin Taha (MD),[1] Samantha Donse-Donkel (MD),[1] Lennard Wolff (MD),[1] Kilian Treurniet (MD),[3] Sophie van den Berg (MD),[3] Natalie LeCouffe (MD),[3] Manon Kappelhof (MD),[3] Rik Reinink (MD),[3] Manon Tolhuisen (MD),[3] Leon Rinkel (MD),[3] Josje Brouwer (MD),[3] Agnetha Bruggeman (MD),[3] Henk van Voorst (MD),[3] Robert-Jan Goldhoorn (MD),[4] Wouter Hinsenveld (MD),[4] Anne Pirson (MD),[4] Susan Olthuis (MD),[4] Simone Uniken Venema (MD),[4] Sjan Teeselink (MD),[10] Lotte Sondag (MD),[10] Sabine Collette (MD)[15]

Research Nurses

Martin Sterrenberg,[1] Naziha El Ghannouti,[1] Laurine van der Steen,[3] Sabrina Verheesen,[4] Jeannique Vranken,[4] Ayla van Ahee,[5] Hester Bongenaar,[6] Maylee Smallegange,[6] Lida Tilet,[6] Joke de Meris,[7] Michelle Simons,[8] Wilma Pellikaan,[9] Wilma van Wijngaarden,[9] Kitty Blauwendraat,[9] Yvonne Drabbe,[11] Michelle Sandiman-Lefeber,[11] Anke Katthöfer,[11] Eva Ponjee,[12] Rieke Eilander,[12] Anja van Loon,[13] Karin Kraus,[13] Suze Kooij,[14] Annemarie Slotboom,[14] Marieke de Jong,[15] Friedus van der Minne,[15] Esther Santegoets[16]

Study Monitors

Leontien Heiligers,[1] Yvonne Martens,[1] Naziha El Ghannouti[1]

On behalf of the CONTRAST consortium collaborators.

Affiliations

[1]Erasmus MC University Medical Center, Rotterdam, the Netherlands; [2]Leiden University Medical Center, Leiden, the Netherlands; [3]Amsterdam University Medical Centers, location AMC, Amsterdam, the Netherlands; [4]Cardiovascular Research Institute Maastricht (CARIM), Maastricht University Medical Centre, Maastricht, The Netherlands; [5]University Medical Center Utrecht, Brain Center Rudolf Magnus, Utrecht, the Netherlands; [6]Catharina Hospital, Eindhoven, the Netherlands; [7]Haaglanden Medical Centre, the Hague, the Netherlands; [8]Rijnstate Hospital, Arnhem, the Netherlands; [9]St. Antonius Hospital, Nieuwegein, the Netherlands; [10]Radboud University Medical Center, Nijmegen, the Netherlands; [11]HagaZiekenhuis, the Hague, the Netherlands; [12]Isala, Zwolle, the Netherlands; [13]Amphia Hospital, Breda, the Netherlands; [14]Albert Schweitzer Hospital, Dordrecht, the Netherlands; [15]University Medical Center Groningen, Groningen, the Netherlands; [16]Elisabeth-TweeSteden Hospital, Tilburg, the Netherlands; [17]University Hospital of Nancy, Nancy, France; [18]Foch Hospital, Suresnes, France; [19]Fondation Rothschild Hospital, Paris, France; [20]University Hospital of Bordeaux, Bordeaux, France; [21]Pitié-Salpêtrière University hospital, Paris, France; [22]John Radcliffe Hospital, Oxford, United Kingdom; [23]University of Washington, Seattle, Washington, United States; [24]Lygature, Utrecht, the Netherlands; [25]School for Mental Health and Sciences (Mhens), Maastricht University Medical Center, Maastricht, The Netherlands; [26]Texas Stroke Institute, Dallas-Fort Worth, Texas, United States of America; [27]Medisch Spectrum Twente, Enschede, The Netherlands; [28]TerGooi, Hilversum, The Netherlands.

We would also like to thank Nvidia Corporation, Santa Clara, California, for the providing of a graphics processing unit.

Disclosure forms provided by the authors are available with the full text and PDF of this article at www.ajnr.org.

REFERENCES

1. Katramados AM, Hacein-Bey L, Varelas PN. **What to look for on post-stroke neuroimaging.** *Neuroimaging Clin N Am* 2018;28:649–62 CrossRef Medline
2. Park TH, Lee JK, Park MS, et al. **Neurologic deterioration in patients with acute ischemic stroke or transient ischemic attack.** *Neurology* 2020;95:e2178–91 CrossRef Medline
3. Seners P, Turc G, Oppenheim C, et al. **Incidence, causes and predictors of neurological deterioration occurring within 24 h following acute ischaemic stroke: a systematic review with pathophysiological implications.** *J Neurol Neurosurg Psychiatry* 2015;86:87–94 CrossRef Medline
4. Karthik R, Menaka R, Johnson A, et al. **Neuroimaging and deep learning for brain stroke detection: a review of recent advancements and future prospects.** *Comput Methods Programs Biomed* 2020;197:105728 CrossRef Medline
5. Yeo M, Tahayori B, Kok HK, et al. **Review of deep learning algorithms for the automatic detection of intracranial hemorrhages on computed tomography head imaging.** *J Neurointerv Surg* 2020;13:369–78 CrossRef Medline

6. Boers AM, Jansen IG, Beenen LF, et al. **Association of follow-up infarct volume with functional outcome in acute ischemic stroke: a pooled analysis of seven randomized trials.** *J Neurointerv Surg* 2018;10:1137–42 CrossRef Medline
7. Hemphill JC, Greenberg SM, Anderson CS, et al; Council on Clinical Cardiology. **Guidelines for the Management of Spontaneous Intracerebral Hemorrhage: a Guideline for Healthcare Professionals from the American Heart Association/American Stroke Association.** *Stroke* 2015;46:2032–60 CrossRef Medline
8. Barros RS, van der Steen WE, Boers AMM, et al. **Automated segmentation of subarachnoid hemorrhages with convolutional neural networks.** *Informatics Med Unlocked* 2020;19:100321 CrossRef
9. Barros RS, Tolhuisen ML, Boers AM, et al. **Automatic segmentation of cerebral infarcts in follow-up computed tomography images with convolutional neural networks.** *J Neurointerv Surg* 2020;12:848–52 CrossRef Medline
10. Zhao X, Chen K, Wu G, et al. **Deep learning shows good reliability for automatic segmentation and volume measurement of brain hemorrhage, intraventricular extension, and peripheral edema.** *Eur Radiol* 2021;31:5012–20 CrossRef Medline
11. Goodfellow I, Bengio Y, Courville A. **Deep learning.** MIT Press 2016. deeplearningbook.org. Accessed July 11, 2022
12. Yi X, Walia E, Babyn P. **Generative adversarial network in medical imaging: a review.** *Med Image Anal* 2019;58:101552 CrossRef Medline
13. Goodfellow IJ, Pouget-Abadie J, Mirza M, et al. **Generative adversarial nets.** *Adv Neural Inf Process Syst* 2014;3:2672–80
14. Baumgartner CF, Koch LM, Tezcan KM, et al. **Visual Feature Attribution using Wasserstein GANs.** In: *Proceedings of the IEEE Conference on Computer Vision and Pattern Recognition*, Salt Lake City, Utah. June 18–23, 2018:8309–19
15. Treurniet KM, LeCouffe NE, Kappelhof M, et al; MR CLEAN-NO IV Investigators. **MR CLEAN-NO IV: intravenous treatment followed by endovascular treatment versus direct endovascular treatment for acute ischemic stroke caused by a proximal intracranial occlusion—study protocol for a randomized clinical trial.** *Trials* 2021;22:1–15 CrossRef Medline
16. Chalos V, Van De Graaf RA, Roozenbeek B, et al; MR CLEAN-MED investigators. **Multicenter randomized clinical trial of endovascular treatment for acute ischemic stroke: the effect of periprocedural medication—acetylsalicylic acid, unfractionated heparin, both, or neither (MR CLEAN-MED). Rationale and study design.** *Trials* 2020;21:1–17 CrossRef Medline
17. Pirson FA, Hinsenveld WH, Goldhoorn R-JB, et al; MR CLEAN-LATE investigators. **MR CLEAN-LATE study protocol.** *Trials* 2021;22:160 CrossRef Medline
18. Konduri P, van Kranendonk K, Boers A, et al; MR CLEAN Trial Investigators (Multicenter Randomized Clinical Trial of Endovascular Treatment for Acute Ischemic Stroke in the Netherlands). **The role of edema in subacute lesion progression after treatment of acute ischemic stroke.** *Front Neurol* 2021;12:705221 CrossRef Medline
19. Hssayeni MD, Croock MS, Salman AD, et al. **Intracranial hemorrhage segmentation using a deep convolutional model.** *Data* 2020;5:14–18 CrossRef
20. Van Kranendonk KR, Treurniet KM, Boers AM, et al; MR CLEAN investigators. **Hemorrhagic transformation is associated with poor functional outcome in patients with acute ischemic stroke due to a large vessel occlusion.** *J Neurointerv Surg* 2019;11:464–68 CrossRef Medline
21. Berkhemer OA, Fransen PS, Beumer D, et al. MR CLEAN Investigators, **A randomized trial of intraarterial treatment for acute ischemic stroke.** *N Engl J Med* 2015;372:11–20 CrossRef Medline
22. dcm2niix. 2021. https://github.com/rordenlab/dcm2niix. Accessed November 3, 2021
23. Klein S, Staring M, Murphy K, et al. **Elastix: a toolbox for intensity-based medical image registration.** *IEEE Trans Med Imaging* 2010;29:196–205 CrossRef Medline
24. Isensee F, Jaeger PF, Kohl SA, et al. **nnU-Net: a self-configuring method for deep learning-based biomedical image segmentation.** *Nat Methods* 2021;18:203–11 CrossRef Medline
25. Kuang H, Menon BK, Qiu W. **Automated stroke lesion segmentation in non-contrast CT scans using dense multi-path contextual generative adversarial network.** *Phys Med Biol* 2020;65:215013 CrossRef Medline
26. Lin TY, Goyal P, Girshick R, et al. **Focal loss for dense object detection.** *IEEE Trans Pattern Anal Mach Intel* 2020;42:318–27 CrossRef Medline
27. Flanders AE, Prevedello LM, Shih G, et al; RSNA-ASNR 2019 Brain Hemorrhage CT Annotators. **Construction of a Machine Learning Dataset through Collaboration: The RSNA 2019 Brain CT Hemorrhage Challenge.** *Radiology Artif Intell* 2020;2:e209002 CrossRef Medline

Stable and Discriminatory Radiomic Features from the Tumor and Its Habitat Associated with Progression-Free Survival in Glioblastoma: A Multi-Institutional Study

R. Verma, V.B. Hill, V. Statsevych, K. Bera, R. Correa, P. Leo, M. Ahluwalia, A. Madabhushi, and P. Tiwari

ABSTRACT

BACKGROUND AND PURPOSE: Glioblastoma is an aggressive brain tumor, with no validated prognostic biomarkers for survival before surgical resection. Although recent approaches have demonstrated the prognostic ability of tumor habitat (constituting necrotic core, enhancing lesion, T2/FLAIR hyperintensity subcompartments) derived radiomic features for glioblastoma survival on treatment-naive MR imaging scans, radiomic features are known to be sensitive to MR imaging acquisitions across sites and scanners. In this study, we sought to identify the radiomic features that are both stable across sites and discriminatory of poor and improved progression-free survival in glioblastoma tumors.

MATERIALS AND METHODS: We used 150 treatment-naive glioblastoma MR imaging scans (Gadolinium-T1w, T2w, FLAIR) obtained from 5 sites. For every tumor subcompartment (enhancing tumor, peritumoral FLAIR-hyperintensities, necrosis), a total of 316 three-dimensional radiomic features were extracted. The training cohort constituted studies from 4 sites ($n = 93$) to select the most stable and discriminatory radiomic features for every tumor subcompartment. These features were used on a hold-out cohort ($n = 57$) to evaluate their ability to discriminate patients with poor survival from those with improved survival.

RESULTS: Incorporating the most stable and discriminatory features within a linear discriminant analysis classifier yielded areas under the curve of 0.71, 0.73, and 0.76 on the test set for distinguishing poor and improved survival compared with discriminatory features alone (areas under the curve of 0.65, 0.54, 0.62) from the necrotic core, enhancing tumor, and peritumoral T2/FLAIR hyperintensity, respectively.

CONCLUSIONS: Incorporating stable and discriminatory radiomic features extracted from tumors and associated habitats across multisite MR imaging sequences may yield robust prognostic classifiers of patient survival in glioblastoma tumors.

ABBREVIATIONS: AUC = area under the curve; CoLlAGe = Co-occurrence of Local Anisotropic Gradient Orientations; GBM = Glioblastoma; Gd = Gadolinium; LOSO = leave-one-site-out; PI = preparation-induced instability; PFS = progression-free survival; $\hat{T}$ = training set; TCIA = The Cancer Imaging Archive; VS = validation set; TS = test set

Glioblastoma (GBM) is an aggressive brain tumor in which survival without treatment is typically 3 months. A conventional first-line treatment regimen involves maximally safe surgical resection followed by concomitant chemotherapy and radiation therapy. Despite this aggressive treatment, patient outcomes are highly variable with >40% of patients with GBM inevitably developing recurrence within 6 months following treatment initiation. While GBM heterogeneity may be reflected in the MR

Received April 29, 2021; accepted after revision June 13, 2022.

From the Department of Biomedical Engineering (R.V., K.B., R.C., P.L.), Case Western Reserve University, Cleveland, Ohio; Department of Neuroradiology (V.B.H.), Feinberg School of Medicine, Northwestern University, Chicago, Illinois; Brain Tumor and Neuro-Oncology Center (V.S.), Cleveland Clinic, Cleveland, Ohio; Alberta Machine Intelligence Institute (R.V.), Edmonton, Alberta; Miami Cancer Institute (M.A.), Miami, FL and Herbert Wertheim College of Medicine, Florida International University, Florida; Department of Biomedical Engineering (A.M.), Emory University, Atlanta Veterans Administration Medical Center; Departments of Radiology and Biomedical Engineering (P.T.), University of Wisconsin Madison, Wisconsin.

Research reported in this publication was supported by the National Cancer Institute of the National Institutes of Health under award Nos. 1U24CA199374-01, R01CA202752-01A1, R01CA208236-01A1, R01 CA216579-01A1, R01 CA220581-01A1, R01CA264017, 1U01 CA239055-01, 1U01CA248226-01; the National Institute for Biomedical Imaging and Bioengineering (1R43EB028736-01); the National Center for Research Resources under award No. 1 C06 RR12463-01; the VA Merit Review Award (IBX004121A) from the US Department of Veterans Affairs Biomedical Laboratory Research and Development Service; the Department of Defense Breast Cancer Research Program Breakthrough Level 1 Award No. W81XWH-19-1-0668; the Department of Defense Prostate Cancer Idea Development Award (W81XWH-15-1-0558); the Department of Defense Lung Cancer Investigator-Initiated Translational Research Award (W81XWH-18-1-0440); the Department of Defense Peer Reviewed Cancer Research Program (W81XWH-16-1-0329); the Kidney Precision Medicine Project Glue Grant (5T32DK747033); the Case Western Reserve University Nephrology Training Grant; the Neptune Career Development Award; the Ohio Third Frontier Technology Validation Start-up Fund; the Wallace H. Coulter Foundation Program in the Department of Biomedical Engineering and the Clinical and Translational Science Award Program at Case Western Reserve University (NCI 1U01CA248226-01); the Department of Defense Peer Reviewed Cancer Research Program (W81XWH-18-1-0404); the Dana Foundation David Mahoney Neuroimaging Program; and the V Foundation Translational Research Award.

The content is solely the responsibility of the authors and does not necessarily represent the official views of the National Institutes of Health, the US Department of Veterans Affairs, the Department of Defense, or the US Government.

Please address correspondence to Ruchika Verma, PhD, Alberta Machine Intelligence Institute, 10065 Jasper Ave, Edmonton, AB, T5J3B1; e-mail: ruchika@amii.ca; @Ruchika__Verma

Indicates open access to non-subscribers at www.ajnr.org

Indicates article with online supplemental data.

http://dx.doi.org/10.3174/ajnr.A7591

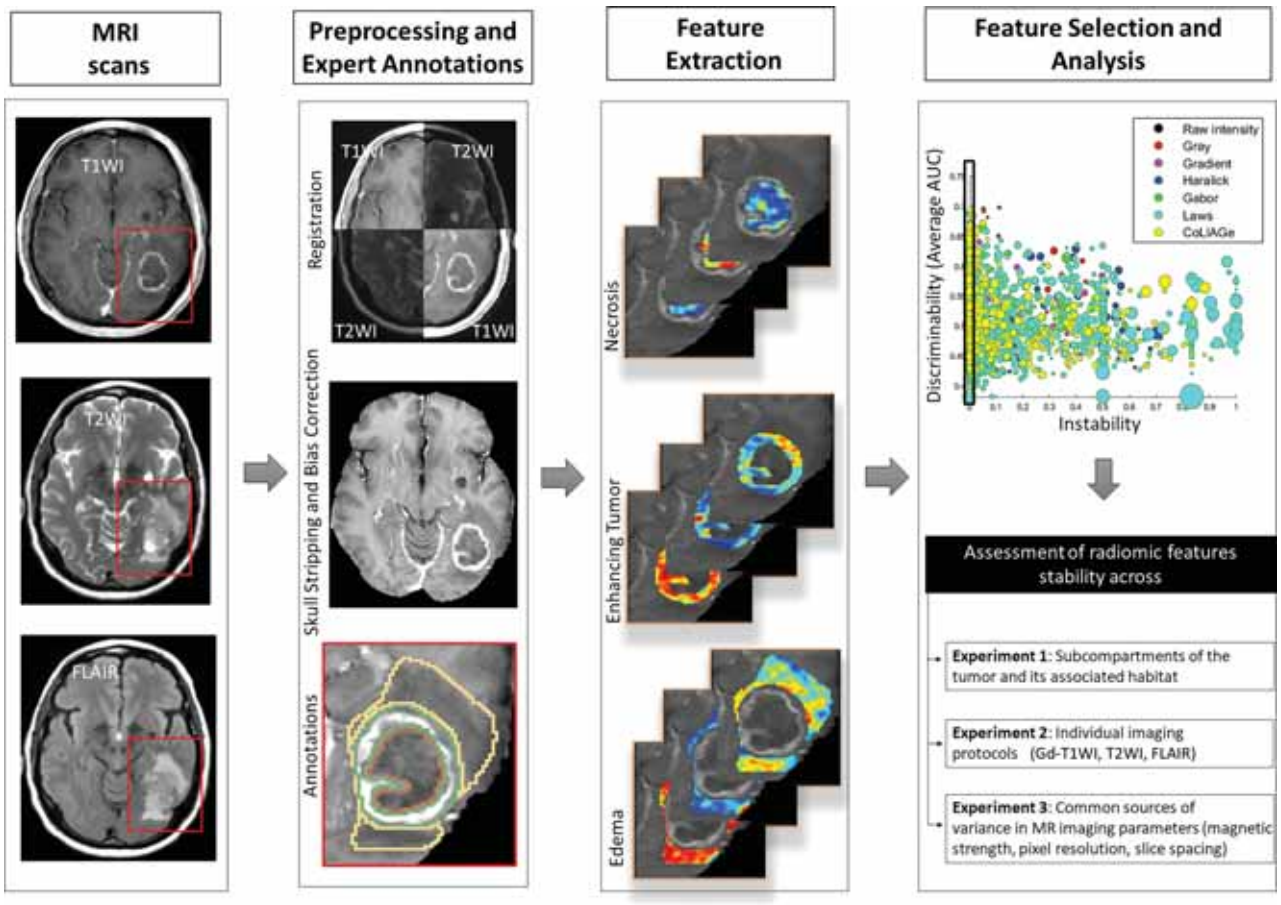

FIG 1. Overview of the methodology and overall workflow. MR imaging scans (Gd-T1w, T2w, and FLAIR) were preprocessed and segmented into 3 tumor subcompartments (necrosis, enhancing tumor, and peritumoral edema). Next, a set of radiomic features was obtained for each of the MR imaging scans across the 3 tumor subcompartments. The most stable and discriminatory features were identified using the PI score and AUC measures across every subcompartment and every MR imaging protocol. The identified stable and discriminatory features were used for stability assessment across tumor subcompartments (with the associated habitat), individual imaging protocols (Gd-T1w, T2w, FLAIR), and MR imaging acquisition parameters (magnetic field strength, pixel resolution, and slice spacing).

imaging phenotypes with different intensity profiles across the enhancing tumor and its associated habitat (comprising necrotic core, peritumoral T2/FLAIR hyperintensity), these image-based differences may not be visually appreciable to build prognostic models of survival in patients with GBM using routine MR imaging scans (Gadolinium-enhanced T1w [Gd-T1w], T2w, FLAIR).

Radiomic approaches (ie, high-throughput extraction of quantitative features) have provided a surrogate mechanism for capturing image-based phenotypes of disease heterogeneity on routine MR imaging (ie, Gd-T1w, T2w, FLAIR) toward outcome prediction in GBM and other tumors. Specifically, in GBM tumors, the availability of large, multi-institutional imaging cohorts such as The Cancer Imaging Archive-GBM (TCIA-GBM) has enabled development of prognostic models using a variety of radiomic feature families (ie, Gray, Haralick,[1] Gradient,[2] Laws,[3] Gabor,[4] Co-occurrence of Local Anisotropic Gradient Orientations [CoLlAGe][5]). These prognostic models have leveraged radiomic features extracted from the tumor habitat (necrotic core, enhancing tumor, peritumoral T2/FLAIR hyperintensity) using routine MR imaging toward outcome prediction in GBM tumors.[6,7]

However, a key challenge in enabling the clinical utility of these radiomic approaches is to demonstrate their generalizability to variations in image-acquisition protocols across scanners and sites. Sources of variations in MR imaging acquisition can include differing slice thicknesses, image contrast, voxel resolutions, magnetic field strengths, echo times, and repetition times.[8-10] This issue is of particular concern when including data from publicly available repositories such as TCGA-GBM, where imaging scans are pooled-in from across different institutions (Fig 1*A*).

While preprocessing steps including bias field correction and intensity standardization, to some extent, have allowed correction of site- and scanner-specific variations in MR imaging, multiple studies have demonstrated[9,11,12] that these steps may not be sufficient to ensure stability of radiomic features during downstream analysis. More recently, studies have used stability measures such as the preparation-induced instability (PI) score[13] to identify radiomic features that are stable (across sites) in the context of lung[14] and prostate cancer.[13,15,16] However, in the context of GBM, most studies have focused on "controlled" test-retest studies[12] or identifying stable features across lesion segmentations obtained from different expert readers.[9,17,18] No work, to our knowledge, has explicitly

Table 1: Summary of patient demographics and the most commonly varying MR parameters across our cohort curated from 5 different sites (S1–S5)

Imaging Source Site	S1, MD Anderson Cancer Center, Houston, Texas	S2, Ivy Glioblastoma Atlas Project	S3, Henry Ford Hospital, Detroit, Michigan	S4, University of California, San Francisco, California	S5, Cleveland Clinic, Ohio
No. of cases	17	33	28	15	57
Magnetic field strength					
1.5T	11	9	16	14	48
3T	6	24	12	1	9
Sex					
Female	7	17	5	6	23
Male	10	16	23	9	34
Scanner					
GE Healthcare	17	30	28	15	57
Siemens	0	3	0	0	0
Slice thickness (range) (mm)	6.5	0.9–6.5	1–6	1.5–6	0.9–7.5
Pixel spacing (range) (mm)	0.47–0.86	0.43–1.05	0.43–0.94	0.45–1.02	0.23–1

interrogated the stability of radiomic features across inherent site-specific acquisition variations within a multisite retrospective cohort in GBM tumors. Additionally, existing approaches have not explicitly interrogated the stability of radiomic features from across different subcompartments of the GBM tumor habitat. In this study, we sought to address 2 specific questions in the context of building robust prognostic image-based markers for GBM tumors–Can we identify the following: 1) a subset of radiomic features from across imaging protocols such as Gd-T1w, T2w, and FLAIR scans that are most stable across sites; and 2) a set of cross-site stable radiomic features from each tumor subcompartment that are also discriminatory of progression-free-survival (PFS) in GBM tumors?

MATERIALS AND METHODS

Data Description

A total of 150 retrospectively analyzed treatment-naive multiparametric GBM MR imaging scans (Gd-T1w, T2w, FLAIR) along with their PFS information were obtained from 5 different institutions, including studies from TCGA-GBM ($n = 60$)[19] and the Ivy Glioblastoma Atlas Project ($n = 33$)[20] cohorts, as illustrated in Table 1. We used median PFS obtained from our training cohort to segregate the studies into improved (PFS $>$ 6.5 months) and poor (PFS $\leq$ 6.5 months) GBM survivors. Additional details regarding the data curation and preprocessing are provided in the Online Supplemental Data.

Segmentation of the Tumor Habitat. Following preprocessing, each 2D MR imaging slice with visible tumor was annotated by expert readers (V.B.H. with >15 years of experience, V.S. with 12 years of experience, and K.B. with >3 years of experience in neuroradiology) into 3 subcompartments: 1) enhancing tumor, 2) FLAIR hyperintensities (edema and nonenhancing tumor), and 3) necrosis. Tumor lesion annotations were also used to select the nontumor ROI for every patient volume. The nontumor region was defined as the region obtained by mirroring the tumor lesion (all 3 subcompartments in conjunction) onto the contralateral hemisphere. The nontumor region for each study was manually inspected by expert readers to verify that it did not contain any proportion of the tumor region or skull. An overview of the entire radiomics analysis workflow (including preprocessing and segmentation) is provided in Fig 1.

Radiomic Feature Extraction. For every tumor subcompartment (enhancing tumor, peritumoral FLAIR hyperintensities, and necrosis), a set of 1264 radiomic features were extracted across all 3 multiparametric MR imaging (Gd-T1w, T2w, and FLAIR) scans. These radiomic features included Laws energy,[3] Haralick,[1] Gabor,[4] CoLlAGe,[5] Gradient,[2] and first-order gray level co-occurrence matrices (additional details provided in the Supplemental Online Data, A.3). A total of 316 three-dimensional radiomic textural features were extracted on a per-voxel basis with window sizes of 3 and 5 from each tumor subcompartment per the MR imaging scan. Four first-order statistics (median, variance, skewness, kurtosis) per feature descriptor were computed within each tumor subcompartment, yielding 1264 statistical features per region (enhancing tumor, peritumoral FLAIR hyperintensity, and necrosis) per the MR imaging protocol. When statistical features were concatenated across all 3 MR imaging sequences (Gd-T1w, T2w, and FLAIR), a total of 3792 texture features were obtained for analysis from each tumor subcompartment. Additionally, to identify stable features across multiple sites, we extracted 3792 statistical features from the nontumor brain parenchyma (mirroring the tumor mask on the opposite brain hemisphere). Following feature extraction, z score feature normalization[21] was applied to ensure that radiomic features extracted from different sites lie within a comparable range of values for leave-one-site-out (LOSO) analysis. The mean and standard deviation (SD) feature values obtained from the training data were further used to apply z score normalization on the independent holdout validation set.

Computation of Feature Instability across Sites. As described in Leo et al,[13] the PI uses a statistical t test to compare the number of feature distributions that are significantly different across data sets from different sites. The PI score ranges between 0 and 1 with a high PI score for a feature representing low stability across site-specific variations, while a low PI score (closer to 0) indicates that the feature may not be affected by acquisition variations and is likely stable across sites.[13]

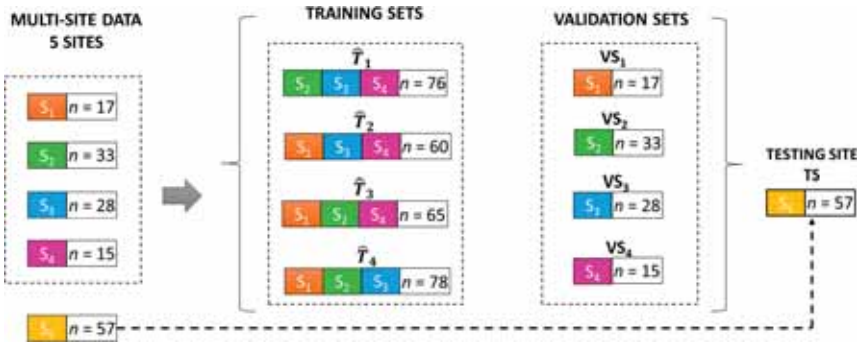

FIG 2. The strategy used for segregating our cohort into training ($\hat{T}_1$–$\hat{T}_4$), validation (VS_1–VS_4), and TSs. The training and the validation sets were created using the LOSO scheme.

Statistical Analysis

To perform a rigorous evaluation of feature stability across sites, our multi-institutional GBM cohort was segregated into 3 groups: training set ($\hat{T}$), validation set (VS), and test set (TS) (Fig 2). Using these 3 groups, we assessed radiomic feature stability across subcompartments of the tumor and its associated habitat, individual imaging protocols (Gd-T1w, T2w, and FLAIR), and common sources of variance in MR imaging parameters (magnetic strength, pixel spacing, slice thickness). Specifically, we used sites S1–S4 in a LOSO fashion so that studies from 3 sites at a time consisted of $\hat{T}$ where $i \in (1,...,4)$, while studies from the remaining fourth site were used as VS_i. Finally, the TS consisted of studies obtained from our hold-out site (Cleveland Clinic Foundation), which was used for independent evaluation. For every training set $\hat{T}$, $i \in (1,...,4)$, we computed the PI score to measure the variability in radiomic feature values engendered due to acquisition variations across the 3 sites within the $\hat{T}$. The features with PI $>$ 0 indicated that they were significantly different in the nontumor regions across different sites in the TS and hence were excluded from further analysis. After this triage, the remaining stable feature set was used to identify the most discriminatory features using minimum redundancy maximum relevance (mRMR) feature selection within a linear discriminant analysis classifier across 100 iterations of bootstrapping.

This LOSO analysis was performed separately for each of the 3 tumor subcompartments (enhancing tumor, peritumoral hyperintensity, necrotic core) to identify the most stable and discriminatory features from the training set for every MR imaging protocol (Gd-T1w, T2w, and FLAIR). The average area under the curve (AUC) across different iterations of LOSO was used to obtain discriminability values in identifying poor and improved survival across each of the tumor subcompartments. Furthermore, for each tumor subcompartment, we concatenated and rank-ordered stable and discriminatory features in terms of their frequency of occurrence across 400 trials (100 bootstrapped iterations across 4 runs of LOSO evaluation as shown in Fig 2) of cross-validation run on our training set. The 5 most-frequently selected features using $\hat{T}$ and VS were obtained and evaluated on the TS for their efficacy in distinguishing poor from improved survival in GBMs using the AUC and accuracy measures. Additionally, for comparison, we selected radiomic features using only minimum Redundancy–Maximum Relevance (discriminatory features) without inclusion of the PI metric for feature pruning. We performed the LOSO runs on discriminatory features using a linear discriminant analysis classifier to evaluate their performance (for distinguishing poor and improved survival) in terms of the AUC and accuracy on our hold-out validation set.

Lastly, we interrogated the feature distributions of stable and discriminatory radiomic features and compared them with discriminatory features using box-and-whisker plots. Specifically, the comparisons were made using the Wilcoxon rank-sum test in the context of evaluating variability in feature distributions across 3 commonly varying MR imaging parameters: 1) slice thickness ($\leq$2 mm, 2–5 mm, $\geq$5 mm), 2) pixel spacing ($<$0.5 mm, $\geq$0.5 mm), and 3) magnetic field strength (1.5T versus 3T), across our multi-institutional cohort.

RESULTS

Experiment 1: Assessing the Stability of Radiomic Features across Different Subcompartments of the Tumor and Its Associated Habitat

Figure 3*A*–*C* shows 2D scatterplots of discriminability (average AUC on the y-axis) versus instability (PI on the x-axis), where each data point in the 2D space corresponds to 1 of the 3792 radiomic features across every tumor subcompartment (necrosis, enhancing tumor, and FLAIR hyperintensity, respectively). The size of the data point on the scatterplot was used to represent the SD in AUC values for a specific feature across different LOSO runs. Our results suggested that the features with PI closer to zero also had a consistent diagnostic performance (in terms of AUC values) across sites as evident from the small size of the data points (reflecting a small deviation in the AUC) in Fig 3. The top 5 most frequent stable and discriminatory radiomic features per subcompartment selected using LOSO subexperiments are listed in Table 2.

Figure 4 illustrates the AUC values for training ($\hat{T}_1$–$\hat{T}_4$) and validation (VS_1–VS_4) cohorts using the top 5 stable and discriminatory radiomic features versus discriminatory features alone (without inclusion of the stability metric) from each of the 3 tumor subcompartments using LOSO analysis. Confidence intervals derived from across the bootstrapped experiments for the AUC values in the training set are available in the Online Supplemental Data. The AUC values on the training set did not show much improvement between stable and discriminatory and discriminatory classifiers.

However, on the validation set (VS_1–VS_4), the compartment-specific linear discriminant analysis classifiers trained using the top 5 stable and discriminatory radiomic features yielded at least 5%–10% improvement in AUC values (0.78, 0.64, 0.66, 0.71 for VS_1–VS_4 respectively), compared with the linear discriminant analysis classifiers trained using discriminatory features alone (0.57, 0.51, 0.52, 0.32 for VS_1–VS_4, respectively) in the enhancing tumor and T2/FLAIR hyperintensity subcompartments (0.76,

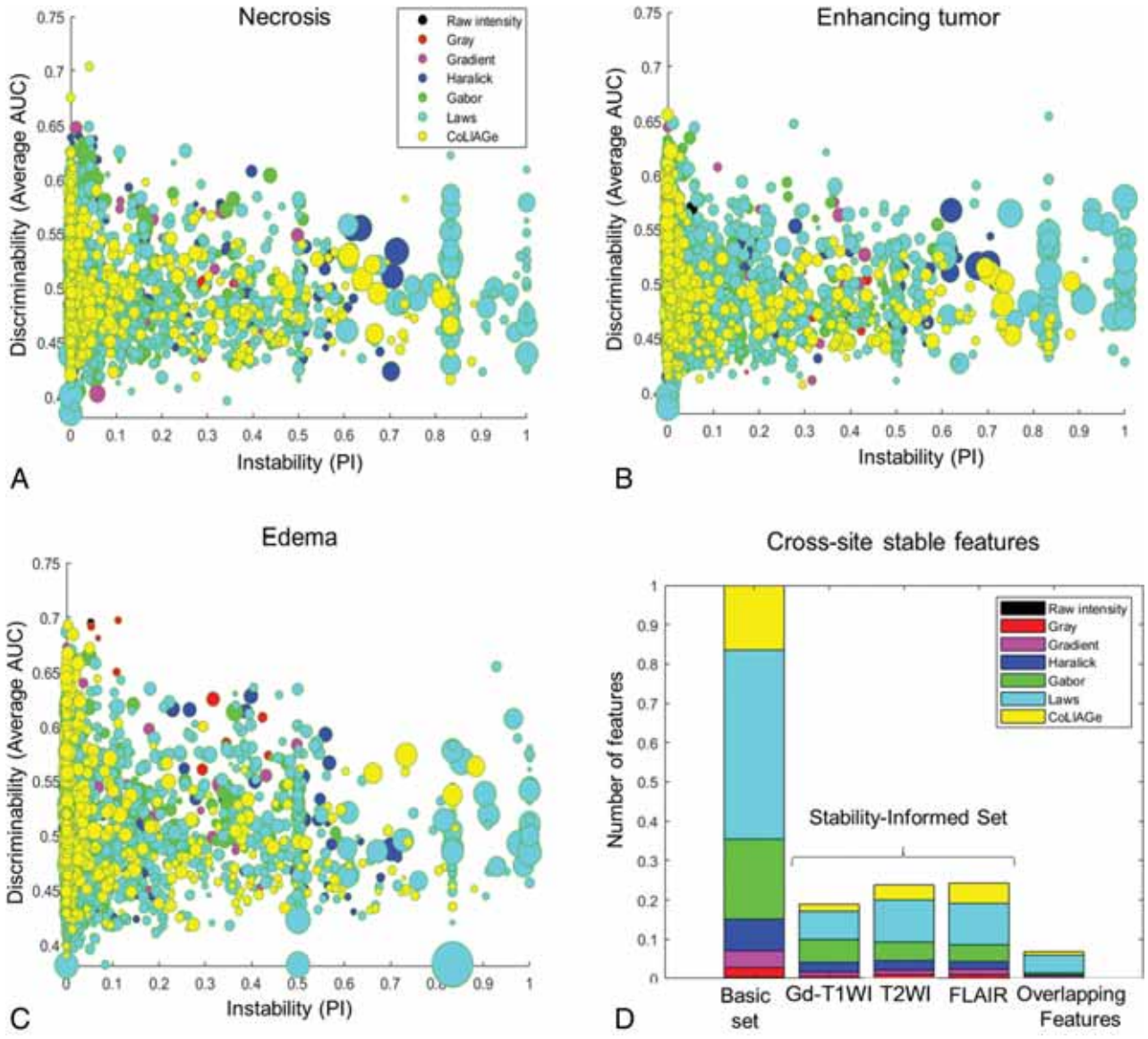

FIG 3. 2D plots of discriminability (average AUC, y-axis) versus instability (PI score, x-axis) for each tumor subcompartment (*A*, Necrosis. *B*, Enhancing tumor. *C*, T2/FLAIR hyperintensity). Each radiomic feature is shown as a bubble where its size represents the SD between the AUC values across different LOSO runs. *D*, The stacked barplot of the total number of extracted features, the features that were identified as stable (PI = 0) from across different feature families per MR imaging sequence (Gd-T1w, T2w, and FLAIR), and the overlapping stable features across multiparametric MR imaging sequences. Different colors represent different feature families.

0.69, 0.73, 0.77 using stable and discriminatory features compared with 0.51, 0.59, 0.53, 0.70 from discriminatory features alone across VS_1–VS_4). For the necrosis subcompartment, the AUC values for VS were identified as 0.68, 0.52, 0.58, and 0.75 using discriminatory-alone across VS_1–VS_4 and 0.69, 0.68, 0.73, and 0.70 for stable and discriminatory features, respectively.

Our compartment-specific classifiers trained using the top 5 stable and discriminatory radiomic features yielded AUCs of 0.71, 0.73, and 0.76, while discriminatory-alone features yielded AUCs of 0.65, 0.54, and 0.62 for necrotic core, enhancing tumor, and FLAIR hyperintensities, respectively, on the hold-out testing cohort. Additionally, combining stable and discriminatory features from across the tumor habitat yielded an AUC of 0.78 compared with using discriminatory features alone, which yielded an AUC of 0.69 on the hold-out test set.

Experiment 2: Assessing the Stability of Radiomic Features across Individual Imaging Protocols (Gd-T1w, T2w, and FLAIR)

Figure 3*D* shows stacked barplots corresponding to the total number of features (basic set) along with the proportion of features that were identified as cross-site stable with a PI = 0 (stability-informed set) from each feature family across Gd-T1w, T2w, and FLAIR sequences. Of a total of 3792 features for every protocol (1264 features per subcompartment), a total of 240 features from Gd-T1w, 302 features from T2w and 306 features from

Table 2: A list of the top 5 features identified to reliably differentiate poor from improved survival in patients with GBM from the training set for every tumor subcompartment (necrosis, enhancing tumor, peritumoral T2/FLAIR hyperintensity, and nonenhancing tumor)

No.	Feature Family	Descriptor	Window Size	MRI Sequence	Statistic
Top 5 features selected from necrosis					
1	Laws	Edge-edge-level	5	T1	Skewness
2	Laws	Level-level-level	3	T1	Skewness
3	Laws	Wave-wave-level	5	FLAIR	Median
4	CoLIAGe	Sum variance	3	FLAIR	Skewness
5	CoLIAGe	Sum variance	3	FLAIR	Kurtosis
Top 5 features selected from enhancing tumor					
1	CoLIAGe	Sum average	3	T2	Median
2	CoLIAGe	Sum average	5	T2	Median
3	CoLIAGe	Energy	3	FLAIR	Median
4	CoLIAGe	Sum average	3	FLAIR	Median
5	Laws	Spot-level-ripple	5	T1	Skewness
Top 5 features selected from edema and nonenhancing tumor					
1	Laws	Level-edge-level	5	T1	Median
2	CoLIAGe	Sum variance	5	T2	Variance
3	CoLIAGe	Sum variance	5	T2	Skewness
4	Haralick	Sum entropy	5	FLAIR	Skewness
5	Gabor	$-\theta = 1.178$, XZ $-\theta = 0$, $\lambda = 1.482$, BW = 1	5	T2	Kurtosis

Note:—BW indicates bandwidth.

FLAIR were found to be stable (using PI = 0) across the studies from the training set ($\widehat{T}$) sets. While ~20% of features from every feature family were identified as stable across all the 3 MR imaging protocols, the greatest number of stable features was found to belong to Laws, CoLlAGe, and Gabor feature families (Online Supplemental Data).

Experiment 3: Assessing the Radiomic Stability across Common Sources of Variance in MR Imaging Parameters (Magnetic Strength, Pixel Resolution, Slice Spacing)

Figure 2 demonstrates the boxplots representing feature distributions for a stable and discriminatory radiomic feature (CoLIAGe sum average feature) along with a corresponding discriminatory feature (Haralick info2), both extracted from enhancing tumor of FLAIR MR imaging across test sets, dichotomized across different slice thicknesses (millimeter): ≤2, (n = 34), and >2 (n = 23). Similarly, Fig 3*A*, -*B* and Fig 4 represent feature distributions of the corresponding features acquired at different pixel spacing categorized such as < 0.5 (n = 16) and ≥0.5 mm (n = 41), as well as across different magnetic strengths (1.5T [n = 48] versus 3T [n = 9]), respectively. We observed the range and median values of stable and discriminatory radiomic features at different slice thicknesses, pixel spacing, and magnetic strengths to be more consistent (Online Supplemental Data) than the feature distributions obtained for discriminatory features (Online Supplemental Data). Similarly, we observed statistically significant separations (demonstrated with *asterisks* in the boxplots of Online Supplemental Data) in feature distributions between poor and improved survivors for stable and discriminatory radiomic features, compared with the discriminatory features, across slice thicknesses, pixel spacing, and magnetic strength variations in our training and testing cohorts.

DISCUSSION

Estimation of PFS often serves as a surrogate marker for predicting therapeutic efficacy in GBM tumors. Previous approaches have investigated radiomic features extracted from different subcompartments of the tumor habitat (constituting necrotic core, enhancing tumor, and T2/FLAIR hyperintensity subcompartments) on routine MR imaging in prognosticating PFS in patients with GBM. However, most of these studies do not explicitly take into account the sensitivity of radiomic features to site- and scanner-specific variations in MR imaging parameters, including variations in slice thicknesses, image contrast, voxel resolutions, and magnetic field strengths, which ultimately impact the generalizability and clinical applicability of these approaches.

More recently, a few approaches have focused on identifying stable and discriminatory features (using preparation-induced instability score[13]) across multi-institutional studies in the context of other tumor sites (lung,[14] prostate[13,15,16]). Our work leveraged a similar approach to identify radiomic features that are stable as well as discriminatory of poor- and improved-survival groups in the context of brain tumors. To rigorously evaluate the reproducibility of our selected radiomic features, we performed a comparison of stable and discriminatory features with discriminatory-alone features in a LOSO fashion (across 4 training sites) for distinguishing poor and improved GBM survivors on the basis of their PFS. This analysis was performed across each of the tumor subcompartments of the tumor habitat on routine multiparametric pretreatment MR imaging scans (Gd-T1w, T2w, FLAIR). Lastly, for each tumor subcompartment, the most frequent stable and discriminatory radiomic features in the training set were used to risk-stratify patients with GBM into poor and good survivors on an independent cohort obtained from a collaborating institute (Cleveland Clinic). Our findings on training and test

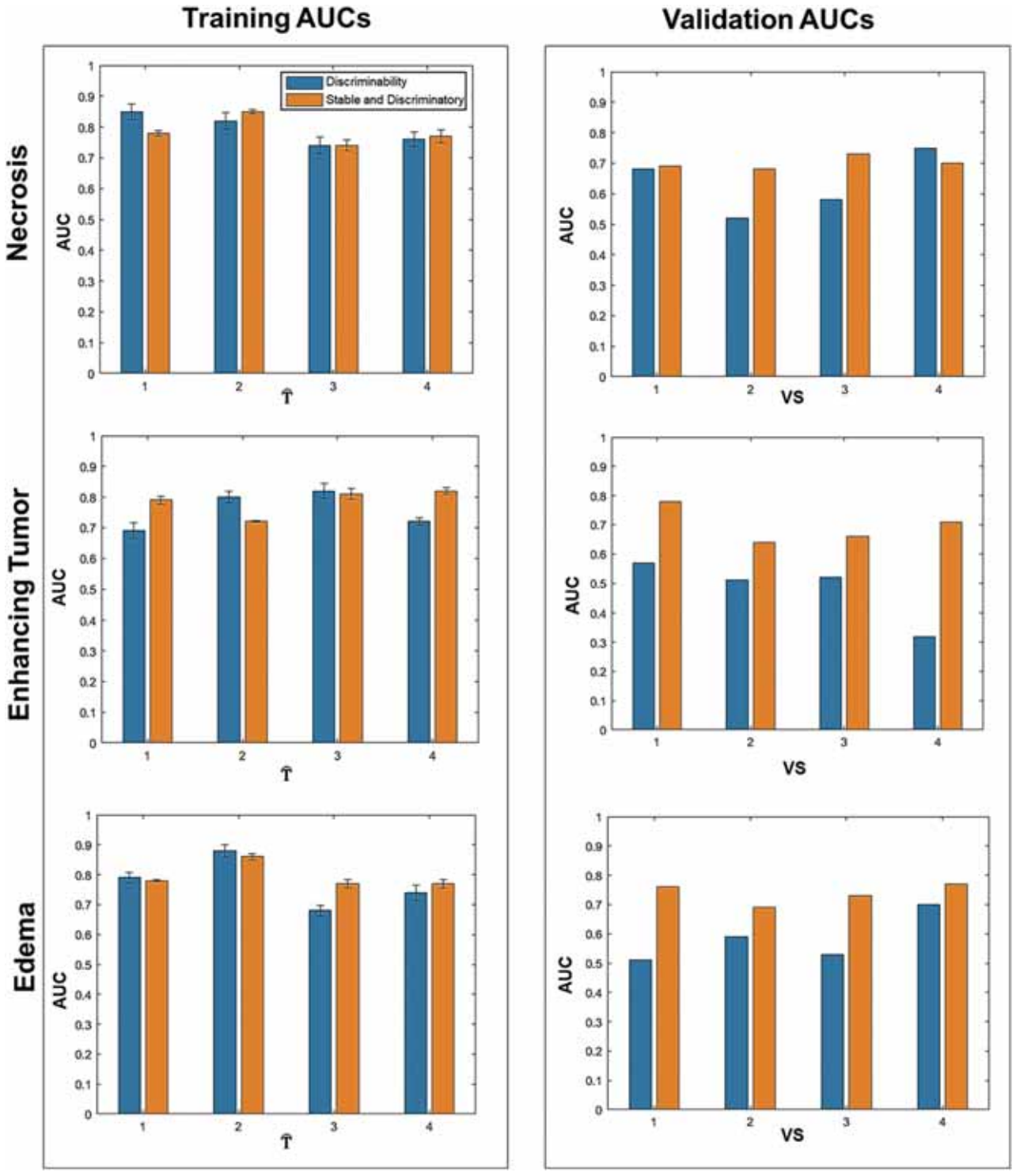

FIG 4. Barplots showing training and validation AUCs to distinguish patients with improved and poor outcomes using the top 5 stable and discriminatory radiomic versus discriminatory-only features. *Blue barplots* depict the AUC values using discriminatory features, while *orange bars* represent AUC values using stable and discriminatory radiomic features from the respective training and validation cohorts.

sets are in line with those in previous work,[13,14] in which the use of PI score within feature selection allowed building improved diagnostic and prognostic classifiers using stable and discriminatory features.

In the context of GBM prognosis, a few studies that have interrogated variations in radiomic features have focused on the reproducibility across segmentations of the tumor obtained from across different experts/institutions[9,12,17,18] or, in terms of repeatability, using test-retest studies.[12] For instance, Tixier et al[17] explored the robustness of radiomic features extracted from the TCGA-GBM data set of 90 studies across segmentations obtained from different experts. They reported that the features computed

from the histogram and co-occurrence matrices were the most robust with an intraclass correlation coefficient value of ≥0.8. Similarly, Lee et al[22] compared radiomic features (textural, morphometric, and first-order) across segmentations of the tumor habitat obtained from 2 semiautomated segmentation software programs on 45 studies and identified the first-order statistic-feature family (across all 3 tumor subcompartments) to be the most stable across the automated segmentations. In a recent study, Shiri et al[12] evaluated the repeatability of radiomic features across 17 patients with GBM using T1- and T2-weighted MR imaging scans obtained within the same imaging unit on 2 consecutive days. By means of the intraclass correlation coefficient, the study demonstrated that the textural features from the gray-level run length matrix and gray-level dependence matrix were highly repeatable (intraclass correlation coefficient, >95%) with respect to image preprocessing, different image-registration algorithms, and test-retest analysis. Similar features, including difference variance, inverse different moment, fraction, and long- and short-run emphasis were found to be highly reproducible among different field sizes and phantom positions in Rastegar et al.[23] In Suter et al,[24] the authors applied multiple perturbations, including variability in the imaging protocols (voxel size and axial slice spacing), artificial deformation in the segmentation labels, *k*-space subsampling on MR imaging, and selected robust features based on the intraclass correlation coefficient from a single site. Selected robust features along with machine learning classifiers evaluated on multicenter data demonstrated an improvement in the prognostic power of the models compared with the machine learning classifiers trained with nonrobust features.

Our work is different from previous related studies[25-29] in a few ways. First, our work presented the first approach in the context of GBM tumors to jointly explore the stability and discriminability of radiomic features. Our results suggest that the radiomic features from T2/FLAIR hyperintensity are the most stable and discriminatory across different tumor subcompartments. Second, we carefully interrogated a set of stable features from across different MR imaging sequences (Gd-T1w, T2w, FLAIR). Finally, we leveraged retrospective MR imaging scans acquired from 5 different institutions to build a robust prognostic classifier that incorporated both stable and discriminatory features. Uniquely, we demonstrated that feature distributions across different slice thicknesses, pixel spacing, and magnetic field strengths were more consistent across stable and discriminatory radiomic features than the feature distributions obtained for the discriminatory features.

While the performance accuracy across stable and discriminatory features was similar to that of discriminatory features alone on the training set, there are 2 key points worth noting: 1) The model trained on stable and discriminatory was robust to the variability in training data because the SD of the AUC values was much higher for discriminatory-alone compared with stable and discriminatory features (Online Supplemental Data). 2) We observed an improvement in AUC values on the independent hold-out test set, suggesting that the model trained on stable and discriminatory features may be more generalizable and hence more amenable to providing reliable AUC assessments on the hold-out set, compared with the model trained on discriminatory features alone.

Our work did have some limitations. While our analysis included 150 patients from 5 different institutions, it was limited to a small cohort of studies per site. The retrospective nature of our cohort led to an unequal number of patients per site, which may have further impacted our analysis of radiomic variations in slice thickness, pixel spacing, and magnetic strengths across sites. Notably, our model yielded the lowest AUCs when validated on VS_2 (the Ivy Glioblastoma Atlas Project cohort). A possible reason may be the high variability in acquisition parameters across scanners (GE Healthcare and Siemens), variations in the magnetic field strength, and a high range of slice thicknesses (0.9–6.5 mm) and pixel spacing (0.43–1.05 mm), compared with data sets from the other cohorts. Additional work is warranted to rigorously validate the reproducibility of the identified features across multiple different imaging parameters on a much larger multisite cohort. We will additionally also investigate the repeatability of the radiomic features from across the tumor habitat via a prospectively collected test-retest study for the GBM cohort.

CONCLUSIONS

Our approach demonstrated that the radiomic features from the T2/FLAIR hyperintentensity subcompartment were the most stable and discriminatory of PFS in GBM tumors compared with the features from enhancing tumor and necrotic core. Identification of stable and discriminatory radiomic features across multisite multiparametric MR imaging (Gd-T1w, T2w, FLAIR) sequences from within the tumor and its associated habitat may yield robust prognostic classifiers for patient survival in GBM tumors.

Disclosures: Virginia Hill—*UNRELATED: Other:* Google,* *Comments:* I am our departmental liaison with Google. They hire some of our radiologists to consult. Kaustav Bera—*UNRELATED: Employment:* Case Western Reserve University. Patrick Leo—*RELATED: Grant:* National Science Foundation,* *Comments:* Graduate Research Fellowship Program (CON501692). Manmeet Ahluwalia—*RELATED: Consulting Fee or Honorarium, Comments: None, UNRELATED: Consultancy:* Bayer, Novocure, Kiyatec, Insightec, GSK, Xoft, Nuvation, Cellularity, SDP Oncology, Apollomics, Prelude, Janssen, Tocagen, Voyager Therapeutics, Viewray, Caris Lifesciences, Pyramid Biosciences, Varian Medical Systems, Cairn Therapeutics, Anheart Therapeutics; *Grants/Grants Pending:* Astrazeneca, Abbvie, BMS, Bayer, Incyte, Pharmacyclics, Novocure, Merck, Mimivax, Novartis, Roswell Park Cancer Foundation, Velosano; *Royalties: Comments:* Wiley; *Stock/Stock Options:* Cytodyn, Doctible, Mimivax, Medinnovate Advisors LLC; *Other:* MedInnovate Advisors LLC. Anant Madabhushi—*UNRELATED: Board Membership:* Aiforia; *Consultancy: Aiforia; Grants/Grants Pending:* Bristol Myers Squibb, Astrazeneca, Boehringer-Ingelheim;* *Stock/Stock Options:* Elucid Bioimaging. Pallavi Tiwari—*RELATED: Grant:* National Institute of Health/National Cancer Institute U01 (1U01CA248226-01), Department of Defense Peer Reviewed Cancer Research Program (W81XWH-18-1-0404), Dana Foundation David Mahoney Neuroimaging Grant, the CCCC Brain Tumor Pilot Award, the CWRU Technology Validation Start-Up Fund (CTP), Johnson and Johnson WiSTEM2D Research Scholar Award, and The V Foundation Translational Research Award* —*UNRELATED: Employment:* Case Western Reserve University. *Money paid to the institution.

REFERENCES

1. Haralick RM, Shanmugam K, Dinstein I. **Textural features for image classification.** *IEEE Transactions on Systems, Man, and Cybernetics* 1973;SMC-3:610–21 CrossRef
2. Huang LL, Shimizu A, Hagihara Y, et al. **Gradient feature extraction for classification-based face detection.** *Pattern Recognition* 2003;36:2501–11 CrossRef
3. Laws KI. **Rapid texture identification.** *Image Processing for Missile Guidance* 1980;0238:376–81 CrossRef
4. Manjunath BS, Ma WY. **Texture features for browsing and retrieval of image data.** *IEEE Trans Pattern Anal Mach Intell* 996;18:837–42 CrossRef

5. Prasanna P, Tiwari P, Madabhushi A. **Co-occurrence of Local Anisotropic Gradient Orientations (CoLlAGe): a new radiomics descriptor.** *Sci Rep* 2016;6:37241 CrossRef Medline
6. Coroller TP, Grossmann P, Hou YC, et al. **CT-based radiomic signature predicts distant metastasis in lung adenocarcinoma.** *Radiother Oncol* 2015;114:345–50 CrossRef Medline
7. Lao J, Chen Y, Li Z-C, et al. **A deep learning-based radiomics model for prediction of survival in glioblastoma multiforme.** *Sci Rep* 2017;7:10353 CrossRef Medline
8. Styner MA, Charles HC, Park J, et al. **Multisite validation of image analysis methods: assessing intra- and intersite variability.** *Proc SPIE Int Soc Opt Eng* 2002;46841:278–86 CrossRef
9. Um H, Tixier F, Bermudez D, et al. **Impact of image preprocessing on the scanner dependence of multi-parametric MRI radiomic features and covariate shift in multi-institutional glioblastoma datasets.** *Phys Med Biol* 2019;64:165011 CrossRef Medline
10. Zhao B, Tan Y, Tsai WY, et al. **Reproducibility of radiomics for deciphering tumor phenotype with imaging.** *Sci Rep* 2016;6:23428 CrossRef Medline
11. Bakas S, Akbari H, Sotiras A, et al. **Advancing The Cancer Genome Atlas glioma MRI collections with expert segmentation labels and radiomic features.** *Sci Data* 2017;4:170117 CrossRef Medline
12. Shiri I, Hajianfar G, Sohrabi A, et al. **Repeatability of radiomic features in magnetic resonance imaging of glioblastoma: test-retest and image registration analyses.** *Med Phys* 2020;47:4265–80 CrossRef Medline
13. Leo P, Lee G, Shih NC, et al. **Evaluating stability of histomorphometric features across scanner and staining variations: prostate cancer diagnosis from whole slide images.** *J Med Imaging (Bellingham)* 2016;3:047502 CrossRef Medline
14. Khorrami M, Bera K, Leo P, et al. **Stable and discriminating radiomic predictor of recurrence in early stage non-small cell lung cancer: multi-site study.** *Lung Cancer* 2020;142:90–97 CrossRef Medline
15. Hiremath A, Shiradkar R, Merisaari H, et al. **Test-retest repeatability of a deep learning architecture in detecting and segmenting clinically significant prostate cancer on apparent diffusion coefficient (ADC) maps.** *Eur Radiol* 2021;31:379–91 CrossRef Medline
16. Merisaari H, Taimen P, Shiradkar R, et al. **Repeatability of radiomics and machine learning for DWI: short-term repeatability study of 112 patients with prostate cancer.** *Magn Reson Med* 2020;83:2293–309 CrossRef Medline
17. Tixier F, Um H, Young RJ, et al. **Reliability of tumor segmentation in glioblastoma: impact on the robustness of MRI-radiomic features.** *Med Phys* 2019;46:3582–91 CrossRef
18. Pati S, Verma R, Akbari H, et al. **Reproducibility analysis of multi-institutional paired expert annotations and radiomic features of the Ivy Glioblastoma Atlas Project (Ivy GAP) dataset.** *Med Phys* 2020;47:6039–52 CrossRef Medline
19. Clark K, Vendt B, Smith K, et al. **The Cancer Imaging Archive (TCIA): maintaining and operating a public information repository.** *J Digit Imaging* 2013;26:1045–57 CrossRef Medline
20. Shah N, Feng X, Lankerovich M, et al. **Data from Ivy GAP.** *The Cancer Imaging Archive* 2016 CrossRef
21. Jain A, Nandakumar K, Ross A. **Score normalization in multimodal biometric systems.** *Pattern Recognition* 2005;38:2270–85 CrossRef
22. Lee M, Woo B, Kuo MD, et al. **Quality of radiomic features in glioblastoma multiforme: impact of semi-automated tumor segmentation software.** *Korean J Radiol* 2017;18:498–509 CrossRef Medline
23. Rastegar S, Beigi J, Saeedi E, et al. **Radiographic image radiomics feature reproducibility: a preliminary study on the impact of field size.** *J Med Imaging Radiat Sci* 2020;51:128–36 CrossRef Medline
24. Suter Y, Knecht U, Alão M, et al. **Radiomics for glioblastoma survival analysis in pre-operative MRI: exploring feature robustness, class boundaries, and machine learning techniques.** *Cancer Imaging* 2020;20:55 CrossRef Medline
25. Moradmand H, Aghamir SMR, Ghaderi R. **Impact of image preprocessing methods on reproducibility of radiomic features in multimodal magnetic resonance imaging in glioblastoma.** *J Appl Clin Med Phys* 2020;21:179–90 CrossRef Medline
26. Aerts HJ, Velazquez ER, Leijenaar RTH, et al. **Decoding tumour phenotype by noninvasive imaging using a quantitative radiomics approach.** *Nat Commun* 2014;5:4006 CrossRef Medline
27. Verma R, Correa R, Hill VB, et al. **Tumor habitat-derived radiomic features at pretreatment MRI that are prognostic for progression-free survival in glioblastoma are associated with key morphologic attributes at histopathologic examination: a feasibility study.** *Radiol Artif Intell* 2020;2:190168 CrossRef Medline
28. Balagurunathan Y, Gu Y, Wang H, et al. **Reproducibility and prognosis of quantitative features extracted from CT images.** *Transl Oncol* 2014;7:72–87 CrossRef Medline
29. Peng H, Long F, Ding C. **Feature selection based on mutual information criteria of max-dependency, max-relevance, and min-redundancy.** *IEEE Trans Pattern Anal Mach Intell* 2005;27:1226–38 CrossRef Medline

Absence of the Anterior Communicating Artery on Selective MRA is Associated with New Ischemic Lesions on MRI after Carotid Revascularization

S. Yamashita, M. Kohta, K. Hosoda, J. Tanaka, K. Matsuo, H. Kimura, K. Tanaka, A. Fujita, and T. Sasayama

ABSTRACT

BACKGROUND AND PURPOSE: ICA-selective MRA using a pencil beam presaturation pulse can accurately visualize anterior communicating artery flow. We evaluated the impact of anterior communicating artery flow on the perioperative hemodynamic status and new ischemic lesions after carotid revascularization.

MATERIALS AND METHODS: Eighty-three patients with carotid artery stenosis were included. We assessed anterior communicating artery flow using ICA-selective MRA. The preoperative hemodynamic status was measured using SPECT. We also measured the change in regional cerebral oxygen saturation after temporary ICA occlusion. New ischemic lesions were evaluated by DWI on the day after treatment.

RESULTS: Anterior communicating artery flow was detected in 61 patients, but it was not detected in 22 patients. Preoperative cerebrovascular reactivity was significantly higher in patients with (versus without) anterior communicating artery flow with a mean peak systolic velocity of ≥200 cm/s (39.6% [SD, 23.8%] versus 25.2% [SD, 16.4%]; $P = .030$). The decrease in mean regional cerebral oxygen saturation was significantly greater in patients without (versus with) anterior communicating artery flow (8.5% [SD, 5.6%] versus 3.7% [SD, 3.8%]; $P = .002$). New ischemic lesions after the procedure were observed in 23 patients. The multivariate logistic regression analysis revealed that anterior communicating artery flow (OR, 0.07; 95% CI, 0.012–0.45; $P = .005$) was associated with new ischemic lesions.

CONCLUSIONS: The absence of anterior communicating artery flow influenced the perioperative hemodynamic status in patients with carotid stenosis and was associated with an increased incidence of new ischemic lesions after carotid revascularization.

ABBREVIATIONS: AcomA = anterior communicating artery; BeamSAT = pencil beam presaturation; CAS = carotid artery stenting; CEA = carotid endarterectomy; CVR = cerebrovascular reactivity; PSV = peak systolic velocity; rSO_2 = regional cerebral oxygen saturation

Collateral flow via the circle of Willis plays an important role in hemodynamic status in patients with steno-occlusive ICA disease, and its presence is associated with favorable outcomes.[1-4] In addition, the development of collateral flow via the circle of Willis is important for maintaining blood flow during temporary ICA occlusion in carotid endarterectomy (CEA) and carotid artery stenting (CAS).[5] Previous studies have demonstrated that reduced cerebrovascular reactivity (CVR) and reduced cerebral perfusion during temporary ICA occlusion predict new ischemic lesions on MR imaging after CEA and CAS.[6-8]

Conversely, the development of collateral flow via the circle of Willis is related to arterial morphologic features in the circle of Willis, such as the presence of anterior communicating artery (AcomA) flow or posterior communicating artery flow.[9,10] The collateral route via the AcomA is considered particularly important.[11] However, the relationship between the configuration of the circle of Willis and new ischemic lesions on MR imaging after carotid revascularization has been poorly investigated.[12] In particular, no reports have focused on the relationship between the presence of AcomA flow and new ischemic lesions on MR imaging after carotid revascularization.

Pencil beam presaturation (BeamSAT) pulse, which is a new MR imaging method, enables suppression of the flow signal of a target vessel using 3D TOF-MRA and allows ICA-selective MRA to be performed.[13,14] Previously, we reported that ICA-selective MRA using a BeamSAT pulse can accurately detect AcomA flow and predict ischemic intolerance to temporary ICA occlusion during CEA or CAS.[14]

As the degree of ICA stenosis progresses, cerebral perfusion pressure decreases. CBV increases in response to reduced cerebral perfusion pressure by dilation of intracranial cerebral vessels,

Received February 20, 2022; accepted after revision May 17.

From the Department of Neurosurgery (S.Y., M.K., J.T., K.M., H.K., K.T., A.F., T.S.), Kobe University Graduate School of Medicine, Kobe, Japan; and Department of Neurosurgery (K.H.), Kobe City Nishi-Kobe Medical Center, Kobe, Japan.

Please address correspondence to Masaaki Kohta, MD, PhD, Department of Neurosurgery, Kobe University Graduate School of Medicine, 7-5-1, Kusunoki-cho, Chuo-ku, Kobe, 650-0017, Japan; e-mail: kohta@med.kobe-u.ac.jp
http://dx.doi.org/10.3174/ajnr.A7570

leading to CBF preservation and a reduction in CVR.[15] In contrast, collateral flow development is thought to preserve CBF and might contribute to the preservation of CVR.[2] Accordingly, we hypothesized the following: In patients with cervical ICA stenosis, inadequate collateral flow via the circle of Willis due to the absence of AcomA flow leads to development of new ischemic lesions after carotid revascularization because of impaired CVR and reduced cerebral perfusion during temporary ICA occlusion.

The objective of this study was to validate this hypothesis and to evaluate the impact of AcomA flow on perioperative hemodynamic status in patients with carotid stenosis and new ischemic lesions on MR imaging after carotid revascularization. First, we investigated the association between the presence of AcomA flow on ICA-selective MRA and preoperative CBF and CVR on SPECT. Second, we examined the association between the presence of AcomA flow on ICA-selective MRA and regional oxygen saturation (rSO_2) changes during temporary ICA occlusion. Third, we determined whether the absence of AcomA flow on ICA-selective MRA predicted development of new ischemic lesions on MR imaging after carotid revascularization.

MATERIALS AND METHODS

Patients

We prospectively recruited patients who were under consideration for either CEA or CAS and retrospectively reviewed the BeamSAT results of these patients. Between March 2015 and December 2020, eighty-three patients who underwent preoperative examinations before carotid revascularization were included. The inclusion criteria were carotid stenosis of ≥50% for symptomatic patients and stenosis of ≥60% for asymptomatic patients according to the criteria outlined in previous studies.[16,17] Symptomatic patients were defined as patients who experienced amaurosis fugax, TIA, or stroke in the territory of the ipsilateral carotid artery within 6 months before entry. The institutional review board of Kobe University approved this study, and written informed consent was obtained from all patients.

MR Imaging Study

We performed MR imaging, including DWI, before and the day after the CEA or CAS, as well as MR imaging with the BeamSAT pulse before the procedure. No clinical signs or symptoms of a new ischemic event developed between the last DWI examination and the procedure.

DWI was performed using a 3T MR imaging scanner (Achieva; Philips Healthcare). The images were obtained using a spin-echo EPI sequence: TR, 3000 ms; TE, 48 ms; flip angle, 90°; sensitivity encoding, 3; FOV, 350 mm (rectangular FOV, 65%); matrix, 142 × 176 (reconstruction, 256 × 256); section thickness, 4 mm; gap, 1 mm; sections, 24–26; fat suppression, spectral presaturation with inversion recovery; b-value, 1000 s/mm^2; number of excitations, 2; scan time, 1 minute 3 seconds.

ICA-selective MRA was performed using a 1.5T MR imaging scanner (Echelon Vega; Hitachi) and an 8-channel head coil, as previously reported.[14] The 3D TOF-MRA parameters were as follows: TR, 23.0 ms; TE, 6.9 ms; flip angle, 20°; FOV, 230 mm; matrix, 512 × 200; section interval, 0.55 mm (after zero-fill interpolation); number of slices, 152; scan time, 4 minutes 50 seconds. For selective 3D TOF-MRA, BeamSAT pulse positioning was performed on a TOF source image from conventional MRA, and suppression of the flow signal in the region of the arteries covered by the BeamSAT pulse on 3D TOF-MRA was achieved. To depict the target artery, we suppressed other arteries with a 30-mm-diameter BeamSAT pulse.

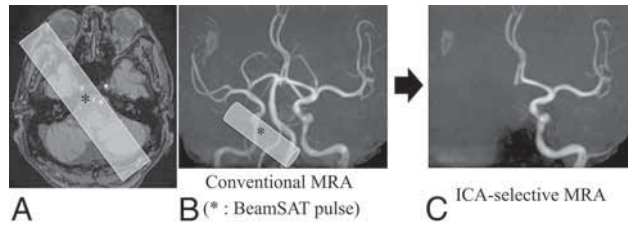

FIG 1. *A*, The BeamSAT pulse is positioned to cover the unilateral petrous portion of the ICA and bilateral vertebral arteries in an axial TOF source image obtained with conventional MRA (*A*). By adding the BeamSAT pulse to the unilateral ICA and bilateral vertebral arteries on 3D TOF-MRA (*B*), we performed ICA-selective MRA (*C*). The *asterisk* indicates BeamSAT.

ICA-selective MRA was performed as follows: When we adjusted the insertion direction of the BeamSAT pulse to penetrate and suppress the flow signals of the 3 major vessels (contralateral ICA and bilateral vertebral arteries) (Figs 1*A*, -*B*), only the target ICA flow signal remained, and ICA-selective MRA was performed (Fig 1*C*).

AcomA Flow Evaluation

We performed bilateral ICA-selective MRA for AcomA flow evaluation for all subjects. The method used to evaluate AcomA flow using ICA-selective MRA has been reported previously.[14] When the bilateral anterior cerebral arteries (distal to A2) were perfused from the unilateral ICA, they were classified into the AcomA (+) group (Fig 2*A*). When the anterior cerebral artery (distal to A2) on each side was perfused only from the ipsilateral ICA, they were classified into the AcomA (−) group (Fig 2*B*). The presence of AcomA flow was assessed by 2 observers blinded to the clinical information, both of whom are Japan Neurosurgical Society board–certified neurosurgeons.

SPECT

All patients were scanned with a rotating dual-headed γ-camera with dynamic SPECT for 50 minutes (ECAM GMS7700; Toshiba Medical) before and the day after the operation. A dual-table autoradiographic method was used, which was developed for use with diffusible tracers to quantify CBF at rest and after pharmacologic stress from a single session of dynamic scanning with dual-bolus administration of N-isopropyl-[^{123}I]-p-iodoamphetamine.[18] The subjects were administered 2 doses of N-isopropyl[^{123}I]-p-iodoamphetamine (111 MBq each) with a constant infusion for 1 minute at the beginning and at 30 minutes of dynamic SPECT imaging, and acetazolamide was injected 10 minutes before the second injection of N-isopropyl[^{123}I]-p-iodoamphetamine. The SPECT scans (both resting and acetazolamide-challenged scans) started immediately after administration of N-isopropyl[^{123}I]-p-iodoamphetamine. Arterial blood sampling was performed 10 minutes after the first N-isopropyl[^{123}I]-p-iodoamphetamine administration.

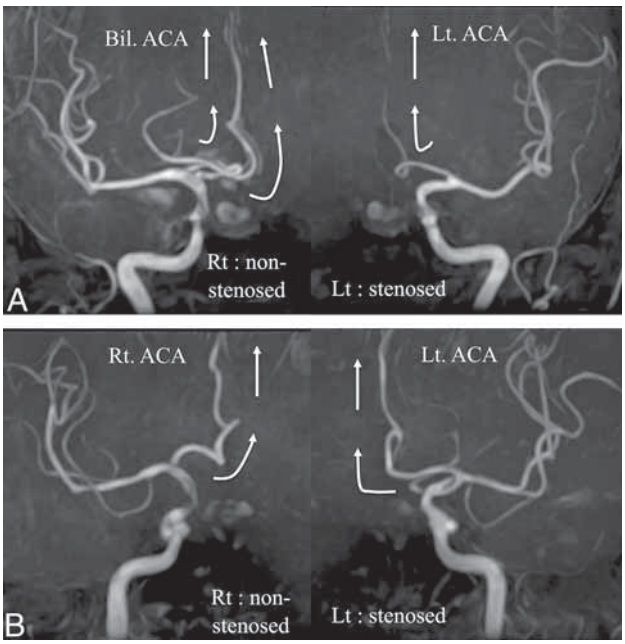

FIG 2. *A*, A case with an AcomA. The bilateral anterior cerebral arteries are perfused from the ICA of the nonstenotic side. Only the ipsilateral anterior cerebral artery is perfused by the ICA of the stenotic side. *B*, A case without an AcomA. Each ICA perfuses only the ipsilateral anterior cerebral artery. *White arrows* show the direction of blood flow. Bil. indicates bilateral; Rt., right; Lt., left.

CBF quantification was performed using the quantitative SPECT/dual-table autoradiography method, which automatically and accurately corrects attenuated absorption and scattered radiation.[19] We used the NEUROSTAT software library (http://128.95.65.28/~Download/) for anatomic standardization of SPECT images. This software generates standardized 3D stereotactic surface projection data sets for individual patients. ROIs were automatically placed in both the cerebral and cerebellar hemispheres with a NEURO FLEXER (https://neuro-flexer.software.informer.com/) template.[20] The mean CBF in the resting state and with the acetazolamide challenge was measured in the MCA territory ipsilateral to the carotid stenosis. Then, the CVR to the acetazolamide challenge was calculated as follows: CVR (%) = [(Acetazolamide-Challenged CBF – Resting CBF)/resting CBF] × 100.

Carotid Artery Sonography

All patients underwent carotid Doppler ultrasonography to observe the carotid artery and atherosclerotic plaque characteristics before the procedure. The peak systolic velocity (PSV) of the ICA and plaque characteristics, such as ulceration and calcification, was evaluated.

Surgical Procedures

Surgical procedures for CEA and CAS have been previously reported.[14,21,22] In cases of CEA, patients were administered at least 1 antiplatelet agent for a minimum of 7 days before the procedure. CEA was performed with the patient under general anesthesia and somatosensory-evoked potential monitoring for selective shunt placement. In cases of CAS, patients were administered 2 antiplatelet agents for a minimum of 7 days before the procedure. CAS was performed with the patient under local anesthesia and general heparinization with embolic-protection devices.

rSO_2 Monitoring

We monitored the rSO_2 using a near-infrared spectroscopy oximeter (INVOS 5100C Cerebral Oximeter; Medtronic), as previously reported.[14] Adhesive optode pad sensors were placed at the bilateral frontotemporal area. Monitoring of the rSO_2 was started before anesthetic induction, and the rSO_2 value was checked every 1 minute during the procedure. We measured the change in rSO_2 before and after ICA clamping during external carotid artery occlusion for CEA and the change before and after distal ICA balloon inflation for CAS.

Statistical Analysis

Statistical analyses were performed using open-source software (R4.0.3; http://www.r-project.org). Descriptive statistics are presented as mean (SD) and were compared using the Welch 2-sample *t* test. The proportion of patients with each parameter was compared using the Fisher exact test. The relationships between patients' baseline characteristics and new ischemic lesions on MR imaging were evaluated using the multivariate logistic regression model. The covariates included in the model were age, procedure (CEA or CAS), the presence of AcomA flow, the presence of ulcerated plaques, and preoperative CVR. These covariates were selected on the basis of previous literature and expert opinion.[7,8,23-27] The ORs of age and CVR are presented as estimated odds of outcome for a 1 year increase in age and a 1% increase in percentage. *P* values $< .05$ were considered statistically significant.

RESULTS

Association between AcomA Flow and Hemodynamic Status on SPECT

Of the 83 patients, 61 patients were classified into the AcomA (+) group, while 22 patients were classified into the AcomA (−) group. Patients' baseline characteristics are summarized in Table 1. There were no statistically significant differences in the baseline characteristics between the 2 groups, except in the case of new ischemic lesions on postoperative DWI. Figure 3 shows preoperative ipsilateral CBF and preoperative ipsilateral CVR in response to acetazolamide according to the presence of AcomA flow. Preoperative ipsilateral CBF was not significantly different between the 2 groups (Fig 3*A*). Although preoperative ipsilateral CVR was higher in the AcomA (+) group than in the AcomA (−) group, the mean difference was not statistically significant (43.4% [SD, 25.3%] versus 31.6% [SD, 22.2%]; $P = .056$; Fig 3*B*). In addition, we extracted patients with a PSV ≥200 cm/s, which indicates 70% stenosis,[28] from both groups. The patients were subdivided into the AcomA (+)/PSV ≥200 cm/s group ($n = 40$) and the AcomA (−) / PSV ≥200 cm/s group ($n = 12$). Preoperative ipsilateral CBF was not significantly different between the 2 groups (Fig 4*A*). The mean preoperative ipsilateral CVR was significantly lower in the AcomA (−) / PSV ≥200 cm/s group than in the AcomA (+) / PSV ≥200 cm/s group (25.2% [SD, 16.4%] versus 39.6% [SD, 23.8%], respectively; $P = .030$) (Fig 4*B*).

Table 1: Patients' baseline characteristics[a]

	AcomA (+) (n = 61)	AcomA (–) (n = 22)	P Value
Age (yr)	75.1 (SD, 7.4)	76.9 (SD, 5.9)	.24
Male	53 (87%)	19 (86%)	1
Rt. ICS	30 (49%)	8 (36%)	.33
CAS	26 (43%)	6 (27%)	.31
Symptomatic	24 (39%)	12 (55%)	.32
Degree of stenosis (%)	74.7 (SD, 12.7)	76.0 (SD, 10.4)	.77
PSV (cm/s)	281.1 (SD, 120.5)	250.8 (SD, 138.5)	.37
Hypertension	45 (74%)	19 (86%)	.37
Hyperlipidemia	33 (54%)	16 (73%)	.14
Diabetes mellitus	21 (34%)	7 (32%)	1
Ischemic heart disease	11 (18%)	2 (9%)	.50
Smoking	31 (51%)	13 (59%)	.62
COPD	6 (10%)	2 (9%)	1
Postoperative DWI high	12 (20%)	11 (50%)	.011

Note:—Rt indicates right; ICS, ICA stenosis; COPD, chronic obstructive pulmonary disease.
[a] Values are presented as mean (SD) or number (%).

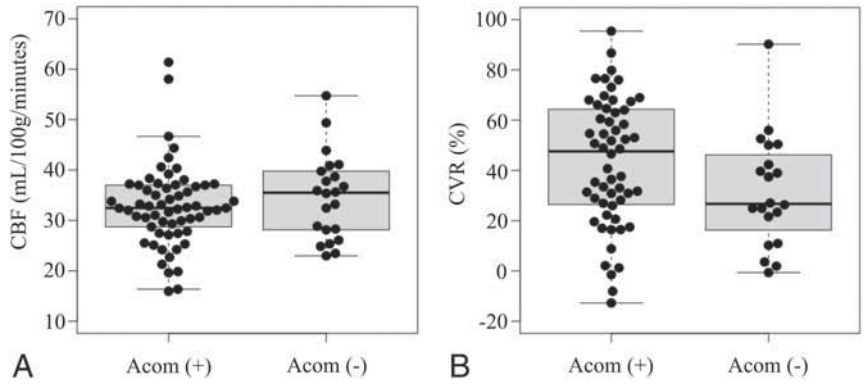

FIG 3. *A*, Box-and-whisker plots of preoperative CBF on the stenotic side in the AcomA (+) group and the AcomA (−) group. Preoperative CBF is not significantly different between the 2 groups. *B*, Box-and-whisker plots of preoperative CVR on the stenotic side in the AcomA (+) group and the AcomA (−) group. The CVR to the acetazolamide challenge is not significantly different between the 2 groups. The *thick horizontal lines* divide the boxes at the median values. The *bottom and top* of the boxes indicate the first and third quartiles. The *whiskers* extend to the most extreme data points, which are no more than 1.5 times the interquartile range from the box.

Association between AcomA Flow and the Change in rSO_2 before-versus-after Temporary ICA Occlusion

Of 83 patients, 80 patients underwent carotid revascularization. Although CAS was attempted in 2 patients, the guiding catheter failed to navigate into the common carotid artery and the procedure was abandoned. One patient refused CEA immediately before the procedure. CEA was performed in 48 patients, and CAS was performed in 32 patients. The mean decrease in rSO_2 after ICA occlusion during CEA or CAS was significantly greater in the AcomA (−) group than in the AcomA (+) group (8.5% [SD, 5.6%] versus 3.7% [SD, 3.8%], respectively; $P = .002$) (Fig 5).

Association between AcomA Flow and New Ischemic Lesions on MR Imaging

New ischemic lesions in the ICA territory ipsilateral to the surgery site on postoperative DWI were recognized in 23 patients (DWI-positive group), while there were no new lesions in 57 patients (DWI-negative group). In the 23 patients with new ischemic lesions, 2 were symptomatic, while 21 were asymptomatic. Among 48 patients who underwent CEA, 7 patients had CEA with carotid shunting, while 41 had CEA without carotid shunting. There were no statistically significant differences in the incidence of new ischemic lesions on postoperative DWI between the patients who underwent CEA with carotid shunting (3/7 [43%]) or without carotid shunting (5/41 [12%]) ($P = .080$).

In the univariate analysis of factors related to postoperative ischemic lesions on MR imaging, there were significant differences between the DWI-positive group and the DWI-negative group in relation to age, the percentage of subjects undergoing CAS, and the percentage of subjects with AcomA flow (Table 2). The mean age of patients was 78.0 (SD, 5.7) years in the DWI-positive group and 74.4 (SD, 7.3) years in the DWI-negative group ($P = .023$). The percentage of subjects undergoing CAS was higher in the DWI-positive group than in the DWI-negative group (65% versus 30%, $P = .005$). The presence of AcomA was more common in the DWI-negative group than in the DWI-positive group (81% versus 52%, $P = .014$). There were no statistically significant differences between the 2 groups in the preoperative CVR and the rate of ulcerated plaques.

In the multivariate analysis, the presence of AcomA (OR, 0.07; 95% CI, 0.012–0.45; $P = .005$) was significantly associated with a decreased odds of new ischemic lesions on postoperative DWI. CAS (OR, 12.99; 95% CI, 2.09–80.86; $P = .006$) and age (OR, 1.14; 95% CI, 1.01–1.29; $P = .039$, estimated odds of outcome for a 1 increase in age) were significantly associated with an increased odds of new ischemic lesions on postoperative DWI (Table 2).

The results of univariate analysis of factors related to postoperative ischemic lesions on MR imaging in patients with a PSV ≥200 cm/s are summarized in Table 3. The mean age of patients was 78.7 (SD, 4.3) years in the DWI-positive group and 75.0 (SD, 7.4) years in the DWI-negative group ($P = .032$). The presence of the AcomA was more common in the DWI-negative group than in the DWI-positive group (87% versus 46%, $P = .005$). Multivariate analysis in patients with a PSV ≥200 cm/s revealed that only the presence of the AcomA (OR, 0.08; 95% CI, 0.014–0.64; $P = .017$) was significantly associated with a decreased odds of new ischemic lesions on postoperative DWI.

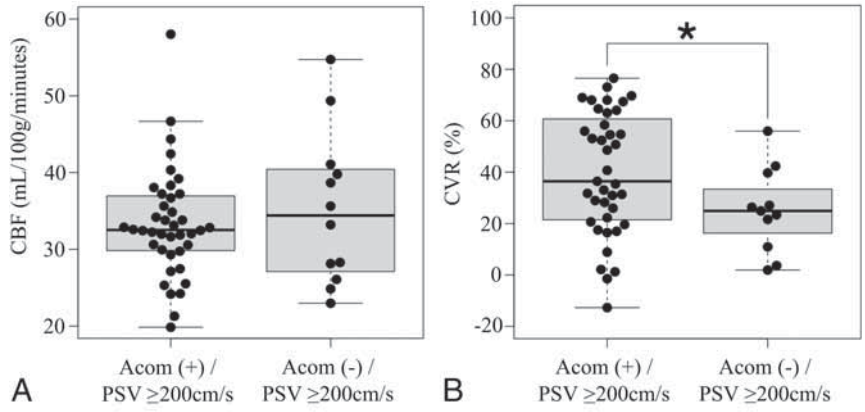

FIG 4. *A*, Box-and-whisker plots of preoperative CBF on the stenotic side in the AcomA (+)/PSV ≥200 cm/s group and the AcomA (−) / PSV ≥200 cm/s group. Preoperative CBF is not significantly different between the 2 groups. *B*, Box-and-whisker plots of preoperative CVR on the stenotic side in the AcomA (+) / PSV ≥200 cm/s group and the AcomA (−) / PSV ≥200 cm/s group. The CVR to the acetazolamide challenge is significantly lower in the AcomA (−) / PSV ≥200 cm/s group than in the AcomA (+) / PSV ≥200 cm/s group. The *thick horizontal lines* divide the boxes at the median values. The *bottom and top* of the boxes indicate the first and third quartiles. The whiskers extend to the most extreme data points, which are no more than 1.5 times the interquartile range from the box. The *asterisk* indicates $P < .05$.

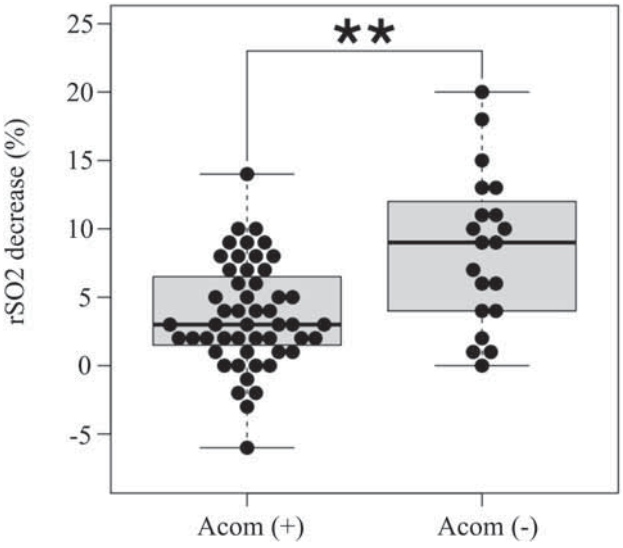

FIG 5. Box-and-whisker plots of the decrease in rSO_2 after temporary ICA occlusion on the stenotic side during CEA or CAS. The decrease in rSO_2 is significantly greater in the AcomA (−) group than in the AcomA (+) group. The *thick horizontal lines* divide the boxes at the median values. The *bottom and top* of the boxes indicate the first and third quartiles. The *whiskers* extend to the most extreme data points, which are no more than 1.5 times the interquartile range from the box. *Double asterisks* indicate $P < .01$.

DISCUSSION

In this study, we analyzed the impact of AcomA flow on perioperative hemodynamic status and new ischemic lesions on MR imaging after carotid revascularization in patients with carotid stenosis. We showed that preoperative ipsilateral CVR was significantly lower in the AcomA (−) group than in the AcomA (+) group when the PSV was ≥200 cm/s. The decrease in rSO_2 after temporary ICA occlusion was significantly greater in the AcomA (−) group than in the AcomA (+) group. Furthermore, the multivariate logistic regression analysis demonstrated that CAS, age, and the absence of AcomA flow were significantly associated with new ischemic lesions on MR imaging after carotid revascularization.

The results showed that preoperative ipsilateral CVR was significantly lower in the AcomA (−) group than in the AcomA (+) group in patients with severe cervical ICA stenosis. This result suggested the importance of collateral flow via the AcomA for preservation of CVR in patients with severe cervical ICA stenosis, which is consistent with a previous study.[11] In contrast, it might not be necessary for collateral flow via the circle of Willis to develop for preservation of CVR in mild cervical ICA stenosis; the possibility is supported by no significant difference in CVR between the AcomA (−) group and AcomA (+) group in all patients in the current study.

The decrease in rSO_2 after temporary occlusion of the ICA was significantly greater in the AcomA (−) group than in the AcomA (+) group. These results are consistent with those in a previous study[14] and suggest that inadequate collateral flow via the circle of Willis due to the absence of AcomA flow might lead to hypoperfusion during clamping of the ICA.

The absence of AcomA flow was significantly associated with new ischemic lesions on MR imaging after carotid revascularization. Dislodgement of thrombotic material or atherosclerotic debris can lead to new ischemic lesions on MR imaging.[23] In addition, decreased blood flow during temporary ICA occlusion impedes the clearance of emboli and can lead to new ischemic lesions on MR imaging.[29] During temporary ICA occlusion, collateral flow via the circle of Willis develops to maintain CBF.[30] Therefore, inadequate collateral flow in patients without AcomA flow might contribute to new ischemic lesions on MR imaging due to impaired emboli clearance. Our decrease in rSO_2 after temporary ICA occlusion supports this hypothesis.

Previous studies have reported that reduced CVR is associated with new ischemic lesions on MR imaging after CEA and CAS.[7,8] In these studies, it has been hypothesized that the CVR measured with acetazolamide challenge can identify low MCA blood flow during ICA clamping, which might impair clearance of microemboli, leading to ischemic lesions on MR imaging. However, the CVR measured with the acetazolamide challenge was not associated with ischemic lesions on MR imaging in the present study. Although the reason for the inconsistency between our results and previous studies was unclear, CVR was considered to be affected by not only collateral flows via the AcomA but also the degree of ICA stenosis and collateral flows via the posterior communicating and cortical leptomeningeal arteries. In contrast, our result suggested that collateral flow via the AcomA substantially contributed to

Table 2: Univariate and multivariate logistic regression analyses of factors for new ischemic lesions on MR imaging[a]

Predictor	Univariate Analysis			Multivariate Analysis	
	DWI-Positive (n = 23)	DWI-Negative (n = 57)	P Value	OR (95% CI)	P Value
Presence of AcomA	12 (52%)	46 (81%)	.014	0.07 (0.012–0.45)	.005
Age (mean)	78.0 (SD, 5.7)	74.4 (SD, 7.3)	.023	1.14 (1.01–1.29)	.039
CAS	15 (65%)	17 (30%)	.005	12.99 (2.01–80.86)	.006
Preoperative CVR (mean) (%)	43.4 (SD, 25.9)	37.8 (SD, 24.1)	.40	1.02 (0.99–1.05)	.20
Ulcerated plaque	7 (30%)	15 (26%)	.78	3.07 (0.60–15.76)	.18

[a] ORs of age and CVR are presented as estimated odds of outcome for a 1 year increase in age and a 1% increase in percentage.

Table 3: Univariate and multivariate logistic regression analyses of factors for new ischemic lesions on MR imaging in patients with a PSV of ≥200 cm/s[a]

Predictor	Univariate Analysis			Multivariate Analysis	
	DWI-Positive (n = 13)	DWI-Negative (n = 39)	P Value	OR (95% CI)	P Value
Presence of AcomA	6 (46%)	34 (87%)	.005	0.08 (0.011–0.64)	.017
Age (mean)	78.7 (SD, 4.3)	75.0 (SD, 7.4)	.032	1.13 (0.96–1.32)	.13
CAS	7 (54%)	14 (36%)	.33	4.23 (0.62–28.89)	.14
Preoperative CVR (mean) (%)	35.7 (SD, 18.7)	36.7 (SD, 24.5)	.88	1.02 (0.98–1.06)	.34
Ulcerated plaque	5 (38%)	8 (21%)	.27	4.71(0.77–28.83)	.094

[a] ORs of age and CVR are presented as estimated odds of outcome for a 1 year increase in age and a 1% increase in percentage.

MCA blood flow during ICA clamping, which was an important factor for new ischemic lesions on MR imaging. Among patients with reduced CVR, it might be important to recognize the pattern of collateral flow development for predicting new ischemic lesions on postoperative MR imaging.

The occurrence of new ischemic lesions on MR imaging after carotid revascularization has been recently considered to lead to clinical consequences in the long term. New ischemic lesions on DWI are associated with a higher risk of cerebrovascular events.[31,32] In addition, the presence of silent ischemic lesions may lead to early-onset cognitive decline and dementia.[33] Therefore, it is important to predict the risk of new ischemic lesions on MR imaging after the procedure. The current results suggest that evaluating the presence of AcomA flow using ICA-selective MRA constructed by applying a BeamSAT pulse is helpful for predicting the risk of new ischemic lesions and for deciding the treatment and perioperative management strategies.

There were some limitations to the current study. First, the assessment of AcomA flow by ICA-selective MRA was not quantitative but subjective. However, a previous study demonstrated that interobserver agreement in these measurements was excellent.[14] Second, collateral flow via anatomic variants in the posterior circulation might also be important, and such variants were not evaluated in this study. However, previous studies have reported that the collateral route via the AcomA is most important.[11,14] Therefore, we focused on the presence of AcomA to establish a simple method for predicting new ischemic lesions on MR imaging after carotid revascularization. Third, collateral flow via the ophthalmic artery and via the cortical leptomeningeal artery could not be assessed using this MR imaging technique. Finally, the small sample size was the main limitation of this study. We did not include other important risk factors, such as plaque vulnerability on MR imaging, as predictors of new ischemic lesions after the procedure to avoid further overfitting. Thus, a large-scale study is needed to clarify our results.

CONCLUSIONS

In this study, the absence of AcomA flow was associated with a reduced CVR in the ipsilateral MCA territory in patients with severe cervical ICA stenosis and with hypoperfusion during temporary ICA occlusion. In addition, the absence of AcomA flow was associated with the occurrence of new ischemic lesions after CEA and CAS. Evaluating AcomA flow on ICA-selective MRA might be helpful for predicting the risk of ischemic lesions after the procedure and determining the treatment and perioperative management strategies for ICA stenosis.

ACKNOWLEDGMENTS

The authors would like to thank Katsusuke Kyotani and Youta Takemoto for their technical assistance with the MR imaging study and Kazuhiro Kubo for his technical assistance with the SPECT study.

Disclosure forms provided by the authors are available with the full text and PDF of this article at www.ajnr.org.

REFERENCES

1. Kluytmans M, van der Grond J, van Everdingen KJ, et al. **Cerebral hemodynamics in relation to patterns of collateral flow.** *Stroke* 1999;30:1432–39 CrossRef Medline
2. Boorder MJ, Grond J, Dongen AJ, et al. **SPECT measurements of regional cerebral perfusion and carbon dioxide reactivity: correlation with cerebral collaterals in internal carotid artery occlusive disease.** *J Neurol* 2006;253:1285–91 CrossRef Medline
3. Henderson RD, Eliasziw M, Fox AJ, et al. **Angiographically defined collateral circulation and risk of stroke in patients with severe carotid artery stenosis.** *Stroke* 2000;31:128–32 CrossRef Medline
4. Lau AY, Wong EH, Wong A, et al. **Significance of good collateral compensation in symptomatic intracranial atherosclerosis.** *Cerebrovasc Dis* 2012;33:517–24 CrossRef Medline
5. Banga PV, Varga A, Csobay-Novak C, et al. **Incomplete circle of Willis is associated with a higher incidence of neurologic events during carotid**

eversion endarterectomy without shunting. *J Vasc Surg* 2018;68:1764–71 CrossRef Medline
6. Mille T, Tachimiri ME, Klersy C, et al. **Near infrared spectroscopy monitoring during carotid endarterectomy: which threshold value is critical?** *Eur J Vasc Endovasc Surg* 2004;27:646–50 CrossRef Medline
7. Koyanagi M, Yoshida K, Kurosaki Y, et al. **Reduced cerebrovascular reserve is associated with an increased risk of postoperative ischemic lesions during carotid artery stunting.** *J Neurointerv Surg* 2016;8:576–80 CrossRef Medline
8. Aso K, Ogasawara K, Sasaki M, et al. **Preoperative cerebrovascular reactivity to acetazolamide measured by brain perfusion SPECT predicts development of cerebral ischemic lesions caused by microemboli during carotid endarterectomy.** *Eur J Nucl Med Mol Imaging* 2009;36:294–301 CrossRef Medline
9. Hartkamp MJ, van Der Grond J, van Everdingen KJ, et al. **Circle of Willis collateral flow investigated by magnetic resonance angiography.** *Stroke* 1999;30:2671–78 CrossRef Medline
10. Hendrikse J, Rutgers DR, Klijn CJ, et al. **Effect of carotid endarterectomy on primary collateral blood flow in patients with severe carotid artery lesions.** *Stroke* 2003;34:1650–54 CrossRef Medline
11. Lopez-Bresnahan MV, Kearse LA, Yanez P, et al. **Anterior communicating artery collateral flow protection against ischemic change during carotid endarterectomy.** *J Neurosurg* 1993;79:379–82 CrossRef Medline
12. Pascot R, Parat B, Teurnier YL, et al. **Predictive factors of silent brain infarcts after asymptomatic carotid endarterectomy.** *Ann Vasc Surg* 2018;51:225–33 CrossRef Medline
13. Ito K, Sasaki M, Kobayashi M, et al. **Noninvasive evaluation of collateral blood flow through circle of Willis in cervical carotid stenosis using selective magnetic resonance angiography.** *J Stroke Cerebrovasc Dis* 2014;23:1019–23 CrossRef Medline
14. Tanaka J, Hosoda K, Matsuo K, et al. **Pencil beam presaturation magnetic resonance imaging helps to identify patients at risk for intolerance to temporary internal carotid artery occlusion during carotid endarterectomy and carotid artery stenting.** *World Neurosurg* 2019;130: E899–907 CrossRef Medline
15. Powers WJ, Grubb RI Jr, Raichle ME. **Physiological responses to focal cerebral ischemia in humans.** *Ann Neurol* 1984;16:546–52 CrossRef Medline
16. **Endarterectomy for asymptomatic carotid artery stenosis: Executive Committee for the Asymptomatic Carotid Atherosclerosis Study.** *JAMA* 1995;273:1421–48 Medline
17. Barnett HJ, Taylor DW, Eliasziw M, et al. **Benefit of carotid endarterectomy in patients with symptomatic moderate or severe stenosis: North American Symptomatic Carotid Endarterectomy Trial Collaborators.** *N Engl J Med* 1998;339:1415–25 CrossRef Medline
18. Iida H, Itoh H, Nakazawa M, et al. **Quantitative mapping of regional cerebral blood flow using iodine-123-IMP and SPECT.** *J Nucl Med* 1994;35:2019–30 Medline
19. Iida H, Nakagawara J, Hayashida K, et al. **Multicenter evaluation of a standardized protocol for rest and acetazolamide cerebral blood flow assessment using a quantitative SPECT reconstruction program and split-dose ^{123}I-iodoamphetamine.** *J Nucl Med* 2010;51:1624–31 CrossRef Medline
20. Ogura T, Hida K, Masuzuka T, et al. **An automated ROI setting method using NEUROSTAT on cerebral blood flow SPECT images.** *Ann Nucl Med* 2009;23:33–41 CrossRef Medline
21. Akutsu N, Hosoda K, Fujita A, et al. **A preliminary prediction model with MR plaque imaging to estimate risk for new ischemic brain lesions on diffusion-weighted imaging after endarterectomy or stenting in patients with carotid stenosis.** *AJNR Am J Neuroradiol* 2012;33:1557–64 CrossRef Medline
22. Imahori T, Hosoda K, Fujita A, et al. **Long-term outcomes of carotid endarterectomy and carotid artery stenting for carotid artery stenosis: real-world status in Japan.** *J Stroke Cerebrovasc Dis* 2016;25:360–67 CrossRef Medline
23. Bonati LH, Jongen LM, Haller S, et al. **New ischemic brain lesions on MRI after stenting or endarterectomy for symptomatic carotid stenosis: a substudy of the International Carotid Stenting Study (ICSS).** *Lancet Neurol* 2010;9:353–62 CrossRef Medline
24. Rots ML, Meershoek AJ, Bonati LH, et al. **Predictors of new ischaemic brain lesions on diffusion weighted imaging after carotid stenting and endarterectomy: a systematic review.** *Eur J Vasc Endovasc Surg* 2019;58:163–74 CrossRef Medline
25. Schnaudigel S, GröSchel K, Pilgram SM, et al. **New brain lesions after carotid stenting versus carotid endarterectomy: a systematic review of the literature.** *Stroke* 2008;39:1911–19 CrossRef Medline
26. Gargiulo G, Sannino A, Stabile E, et al. **New cerebral lesions at magnetic resonance imaging after carotid artery stenting versus endarterectomy: an updated meta-analysis.** *PLoS One* 2015;10:e0129209 CrossRef Medline
27. Xu X, Feng Y, Bai X, et al. **Risk factors for silent new ischemic cerebral lesions following carotid artery stenting.** *Neuroradiology* 2020;62:1177–84 CrossRef Medline
28. Koga M, Kimura K, Minematsu K, et al. **Diagnosis of internal carotid artery stenosis greater than 70% with power Doppler duplex sonography.** *AJNR Am J Neurodradiol* 2001;22:413–17 Medline
29. Caplan LR, Hennerici M. **Impaired clearance of emboli (washout) is an important link between hypoperfusion, embolism, and ischemic stroke.** *Arch Neurol* 1998;55:1475–82 CrossRef Medline
30. Doblar DD, Plyushcheva NV, Jordan W, et al. **Predicting the effect of carotid artery occlusion during carotid endarterectomy: comparing transcranial Doppler measurements and cerebral angiography.** *Stroke* 1998;29:2038–42 CrossRef Medline
31. Gensicke H, van der Worp HB, Nederkoorn PJ, et al; ICSS-MRI Substudy Investigators. **Ischemic brain lesions after carotid artery stenting increase future cerebrovascular risk.** *J Am Coll Cardiol* 2015;65:521–29 CrossRef Medline
32. Wolf O, Heider P, Heinz M, et al. **Frequency, clinical significance and course of cerebral ischemic events after carotid endarterectomy evaluated by serial diffusion weighted imaging.** *Eur J Vasc Endovasc Surg* 2004;27:167–71 CrossRef Medline
33. Pendlebury ST, Rothwell PM. **Prevalence, incidence, and factors associated with pre-stroke and post-stroke dementia: a systematic review and meta-analysis.** *Lancet Neurol* 2009;8:1006–18 CrossRef Medline

Characteristics of Radiation-Related Intracranial Aneurysms: A Multicenter Retrospective Study

Z.-Q. Huang, W.-J. Yang, G. Xiao, Z. Yang, H. Yu, J.-W. Wu, S.-S. Li, J.-W. Zhang, and X.-W. Zhou

ABSTRACT

BACKGROUND AND PURPOSE: Intracranial aneurysms, a rare complication of radiation therapy, have been reported mainly in case reports or case series. We performed a multicenter, retrospective cohort study to investigate the characteristics of radiation-induced intracranial aneurysms.

MATERIALS AND METHODS: Data on 2641 patients with intracranial aneurysms were retrospectively collected from 3 hospitals between January 2005 and June 2014. An additional 1519 patients were recruited from a single center between July 2014 and March 2020. Aneurysms in patients with a history of radiation therapy for at least 6 months were defined as radiation-related aneurysms. Patients' demographic profiles, clinical characteristics, and aneurysm parameters detected on CTA were compared between radiation-related and control groups.

RESULTS: Of the 4160 patients, the average age was 57.9 (SD, 13.5) years, 2406 (57.8%) were women, 477 (11.5%) had multiple aneurysms, 3009 (72.3%) had SAH, and 34 (0.8%) had radiation-related aneurysms. The male-to-female ratio in the radiation-related group was significantly higher than that in the control group (2.4:1 versus 0.72:1, $P = .001$). The mean age of the radiation-related group was significantly younger than in the control group (51.4 [SD, 15.0] years versus 58.2 [SD, 13.5] years, $P = .003$). More patients in the radiation-related group presented with SAH than in the control group (without age and sex matching, 88.2% versus 72.2%, $P = .037$; with age and sex matching, 88.2% versus 58.8%, $P = .006$). Of the 4813 intracranial aneurysms, only 43 (0.9%) aneurysms were categorized as in the radiation-related group, whereas 4770 (99.1%) aneurysms constituted the control group. Compared with the control group, there was a significantly higher proportion of sidewall aneurysms (46.5% versus 32.3%, $P = .048$) and a predilection for aneurysms involving the ICA and posterior circulation arteries (72.1% versus 52.2%, $P = .046$) in the radiation-related group.

CONCLUSIONS: Compared with the control group, radiation-related aneurysms are more prone to occur in men and young patients, with a higher percentage of sidewall aneurysms located in the ICA and posterior circulation arteries. Furthermore, SAH is highly prevalent in patients with radiation-induced aneurysms, indicating that dedicated screening for aneurysms after radiation therapy is necessary, but further studies are needed to determine when and how to screen.

Radiation therapy is one of the mainstay treatment modalities for head and neck tumors, including nasopharyngeal carcinoma and medulloblastoma.[1,2] Nasopharyngeal carcinoma is characterized by a distinct geographic distribution and is particularly prevalent in East and Southeast Asia.[1,3] Medulloblastoma is an ordinary childhood CNS tumor.[4] Clinicians can precisely deliver effective therapeutic doses to the target zone for patients with head and neck tumors while preserving adjacent functionally important tissues using modern devices. Nevertheless, radiation therapy fields often encompass the skull base neurovascular structures,[1,4,5] and attendant radiation-related vasculopathies may be unavoidable due to the destructive effects on arteries of irradiation.[6-8]

The short-term sequelae of radiation have been extensively described during the past century, but long-term complications of radiation therapy were not well-understood.[6,7,9,10] With the improvement of radiation therapy technology and comprehensive treatment, there has been a remarkable increase in the survival rates of patients with head and neck cancer. With this increase in life span, clinicians have had the opportunity to study potential delayed effects of radiation therapy, such as cognitive decline, hearing impairment, secondary cancers, stroke, and vascular diseases,[2,4,6,7] which may require specific monitoring and screening.

Received December 14, 2021; accepted after revision June 2, 2022.

From the Department of Diagnostic Radiology and Nuclear Medicine (Z.-Q.H., W.-J.Y.), University of Maryland, Baltimore, Maryland; Departments of Neurosurgery (G.X.), and Neurology (Z.Y.), and Medical Image Center (J.-W.Z., X.-W.Z.), Yuebei People's Hospital, Shantou University Medical College, Shantou, Guangdong Province, China; Department of Radiology (H.Y.), The Affiliated Hospital of Jining Medical University, Jining, Shandong Province, China; Department of Radiology (J.-W.W.), Fujian Provincial Hospital, Provincial Clinic Medical College of Fujian Medical University, Fuzhou, Fujian Province, China; and Department of Radiology (S.-S.L.), The First Affiliated Hospital of Guangxi Traditional Chinese Medical University, Nanning, Guangxi Province, China.

Please address correspondence to Xin-Wei Zhou, MD, Yuebei People's Hospital, 133 Huiming Rd, Shaoguan, 512025, China; e-mail: xinwe.2019@gmail.com

http://dx.doi.org/10.3174/ajnr.A7592

The delayed vascular diseases include atherosclerosis, cavernous malformation, and intracranial aneurysm, but previous studies mainly focused on the risk of intracranial atherosclerosis.[4,10] Intracranial aneurysm is one of the most common vascular diseases,[7] but an aneurysm following radiation therapy is a rare complication and less commonly recognized, sometimes leading to a catastrophic event of spontaneous SAH.[5,6] Despite the scarcity of reported cases, previous reports concluded that various radiation therapy methods can cause aneurysms, including external beam radiation therapy, gamma knife surgery, and brachytherapy,[5,7] as well as the histopathologic features of radiation-related aneurysms, including irregular fibrous thickening of the media and intima with smooth-muscle loss, necrosis of the media with lipid-laden macrophages, and mononuclear cell infiltration within the intima and media wall of the aneurysm.[9,11] However, there is limited information available in the literature about the clinical characteristics of patients with radiation-related aneurysms, and previous studies on such aneurysms mostly consisted of case reports that lack statistical analysis with a comparison group. We, therefore, conducted this retrospective cohort study to explore the unique characteristics of the radiation-related aneurysm by comparing it with a cohort.

MATERIALS AND METHODS

Patient Selection and Data Collection

This retrospective study was approved by the institutional review board (Yuebei People's Hospital), and patient informed consent was waived due to the study design that entailed no diagnostic tests or treatment. Patients who were diagnosed with intracranial aneurysms by CTA with at least 64 sections were recruited. Patient exclusion criteria for the study were the following: 1) an insufficient clinical data set and image data set on record; 2) fusiform, traumatic, or mycotic aneurysms; and 3) an intracranial aneurysm related to arteriovenous malformation or comorbidity with Moyamoya disease. Patients were dichotomized into the radiation-related aneurysm group and control group. The inclusion criteria for the radiation-related aneurysm group were the following: 1) a previous diagnosis of head and neck tumor with a history of radiation therapy, and 2) at least a 6-month time interval between radiation therapy and a diagnosis of an intracranial aneurysm. Patients with aneurysms without a history of radiation therapy constituted the control group.

Among all patients with intracranial aneurysms, 2641 consecutive patients were retrospectively included from 3 hospitals (Yuebei People's Hospital, The Second Affiliated Hospital of Guangzhou Medical University, and Zhujiang Hospital) from January 2005 to June 2014, as previously described,[12] and the following 1519 patients were recruited consecutively from a single center (Yuebei People's Hospital) between July 2014 and March 2020. The demographic profiles and cerebrovascular risk factors (including diabetes, hypertension, and hyperlipidemia) were collected for this study through chart reviews on each site. Diabetes was defined as a random serum glucose level of ≥11.1 mmol/L, glycosylated hemoglobin level of ≥5.8%, or the use of antidiabetic medication. Hypertension was defined as systolic blood pressure of ≥140 mm Hg and/or diastolic blood pressure of ≥90 mm Hg. Hyperlipidemia was described as a total cholesterol of >240 mg/dL, high-density lipoprotein cholesterol of <40 mg/dL, or the use of cholesterol-lowering medication.

Table 1: Characteristics of the patients (n = 4160)

Characteristics	Radiation-Related Group (No.) (%)	Control Group (No.) (%)	*P* Value
Male	24 (70.6)	1730 (41.9)	.001
Age (mean) (yr)	51.4 (SD, 15.0)	58.2 (SD, 13.5)	.003
Hyperlipidemia	3 (8.8)	348 (8.4)	NS
Hypertension	15 (44.1)	2187 (53.0)	NS
Diabetes	2 (5.9)	281 (6.8)	NS
Multiple aneurysms	7 (20.6)	470 (11.4)	NS
Presented with SAH	30 (88.2)	2979 (72.2)	.037

Note:—NS indicates not significant.

CTA Analysis

All patients underwent CTA with an FOV of 160 mm and a section thickness of 0.5 or 0.625 mm reconstructed at 0.5 or 0.625 mm. As previously described, the sites of the aneurysms were categorized by 4 locations: 1) the anterior cerebral artery (including the anterior communicating artery and anterior cerebral artery); 2) the MCA; 3) the ICA, including the ICA terminus, posterior communicating artery, cavernous ICA; and 4) the posterior circulation arteries (including the posterior cerebral artery and the vertebrobasilar system).[12,13] The aneurysm type was dichotomized into bifurcation aneurysms if they were located at the parent artery bifurcations in the cerebral vasculature based on CTA and sidewall aneurysms if they originated from only 1 parent vessel without an artery emerging from the top of the dome.[13] The aneurysm wall was defined as an irregular wall if the blebs, lobes, or protrusions were present on the wall. The size of the aneurysm was measured as in our previous report.[14] Two neuroradiologists reviewed CTA images and recorded the imaging characteristics independently. In case of disagreement, a consensus reading was performed with a third neuroradiologist on the classification parameters (including aneurysm location, type, and irregular wall); then, the values were used for statistical analyses afterward. Regarding the quantitative parameter (aneurysm size), the values were averaged for subsequent statistical analyses.

Statistical Analysis

SPSS 19.0 (IBM) was used for all statistical analyses. Quantitative data are presented as mean (SD) and were compared between the radiation-related group and the control group using an independent-samples t test. Categoric variables are presented in percentages and analyzed between groups using the χ^2 or Fisher exact test.

RESULTS

Of the 4160 patients, the average age was 57.9 (SD, 13.5) years (Table 1), 2406 (57.8%) were women, 477 (11.5%) had multiple aneurysms, 3009 (72.3%) had SAH, and 34 (0.8%) had radiation-related aneurysms. Of the 34 patients with radiation-induced aneurysms, 23 were diagnosed with nasopharyngeal carcinoma before radiation therapy; 2, with medulloblastomas; 2, with lymphomas; and 7, with other head and neck tumors. The average time interval of the 34 patients between radiation therapy and a diagnosis of an intracranial aneurysm was 6.8 (SD, 5.1) years. As Table 1 shows, the male-to-female ratio in the radiation-related group was significantly higher than in the control group (2.4:1 versus 0.72:1, P = .001). The mean age of the radiation-related group was

Table 2: Characteristics of the aneurysms (n = 4813)

Characteristics	Radiation-Related Group	Control Group	*P* Value
Aneurysm size (mean) (mm)	4.9 (SD, 2.3)	5.2 (SD, 2.2)	NS
Location of aneurysm (No.) (%)			.046
ICA	23 (53.5)	2015 (42.2)	
Anterior cerebral artery	6 (14.0)	1213 (25.4)	
MCA	6 (14.0)	1066 (22.3)	
Posterior circulation artery	8 (18.6)	476 (10.0)	
Type of aneurysm (No.) (%)			.048
Sidewall	20 (46.5)	1543 (32.3)	
Bifurcation	23 (53.5)	3227 (67.7)	
Irregular wall	12 (27.9)	1438 (30.1)	NS

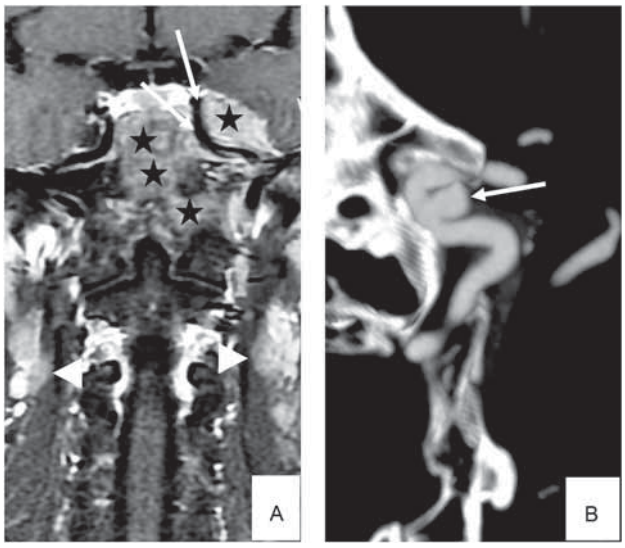

FIG 1. A 52-year-old man with nasopharyngeal cancer (T4N2M0, stage IVA). T1-weighted image (1.5T) with contrast shows that the tumor (*A*, *black stars*) has grown into the skull base and embraces the left ICA (*A*, *white arrows*) with swollen lymph nodes bilaterally (*A*, *white arrowhead*). Five years after irradiation, the patient presented with headache, and a sidewall aneurysm (5.1 mm) was detected at the left ICA using CTA (*B*, *white arrow*).

significantly younger than the control group (51.4 [SD, 15.0] years versus 58.2 [SD, 13.5] years, $P = .003$). The number of patients who presented with SAH in the radiation-related group was significantly higher than in the control group (88.2% versus 72.2%, $P = .037$), implying that radiation-related aneurysms may be more fragile and prone to rupture. For a subanalysis, we confirmed a 1:1 match in the age and sex of the radiation-related group and the controls. If >1 patient from the control group matched, to avoid possible selection bias, the patient used for comparison was randomly chosen by 1 neuroradiologist without knowledge of the participant's characteristics. The prevalence of SAH (88.2% versus 58.8%, $P = .006$) in the radiation-related group was significantly higher than in the age- and sex-matched controls.

Of the 4813 intracranial aneurysms (Table 2), only 43 (0.9%) aneurysms were categorized as in the radiation-related group, and the remaining 4770 (99.1%) aneurysms constituted the control group. The most frequent location for radiation-related aneurysms was the ICA (53.5%, Fig 1), followed by the posterior circulation arteries (18.6%, Fig 2), whereas aneurysms in the control group predominantly involved the ICA (42.2%) and anterior cerebral artery (25.4%) ($P < .05$). Compared with the control group, more sidewall aneurysms were found in the radiation-related group (46.5% versus 32.3%, $P < .05$). There was no difference in aneurysm size and wall irregularity between the 2 groups.

DISCUSSION

With improvement in comprehensive therapies, patients with head and neck cancer may have a reasonably long life expectancy, but they may have an increased risk of delayed complications resulting from radiation therapy. Most previous studies were case reports that lacked a comparison group due to the extremely low incidence of radiation-related aneurysms and the need for long-term follow-up after radiation therapy. The present study provided substantial insight into the demographic and clinical characteristics of patients with radiation-related aneurysms by comparing them with a cohort.

Unlike classic intracranial aneurysms, which are more common in women,[12] our study showed that radiation-related aneurysms were more common in men (the male-to-female ratio was 2.4:1). Previous literature reviews have documented that most patients with radiation-related aneurysms were men,[5,7,11] consistent with findings in our study. The percentage of men was even as high as 80%.[8] The average age of patients at the time of intracranial aneurysm diagnosis was 51.4 years, much younger than in the control group. This average age trend was similarly noted in the literature,[8,11] but our results are distinct from those in other literature.[5-7]

One possible explanation for the higher prevalence of radiation-induced aneurysms in men and younger patients could be because nasopharyngeal carcinoma and medulloblastoma, which are the main indications for radiation in our study, occur more often in men (male/female ratios were 2.5:1[1] and 1.8:1[15] for nasopharyngeal carcinoma and medulloblastoma, respectively) and are diagnosed at a relatively young age (incidence peaks in the fourth to sixth decades[1,16] and at 5–7 years[4,15] for nasopharyngeal carcinoma and medulloblastoma, respectively). One would postulate that younger patients and those with a favorable prognosis after treatment are most at risk of developing an aneurysm and potential rupture.[6,17]

Compared with the control group, radiation-related aneurysms had a significantly higher proportion of sidewall locations and a predilection for location in the ICA and posterior circulation arteries. A previous study revealed a similar result, with 53% of radiation-related aneurysms located at the ICA and 40% located at the posterior circulation arteries.[5] The exact mechanism is unknown, but vessel sensitivity to irradiation and hemodynamic factors may be responsible for the phenomenon. First, the CBF in each branch is different (ie, CBF in the ICA is significantly higher than in the basilar artery),[18] and the ICA is tortuous and transitions from elastic-to-muscular intracranial arteries.[19] The adverse effects of radiation on tissues are complex, including the possibility of inducing an inflammatory cascade and subsequently weakened blood vessels.[11,17,20] The combination of

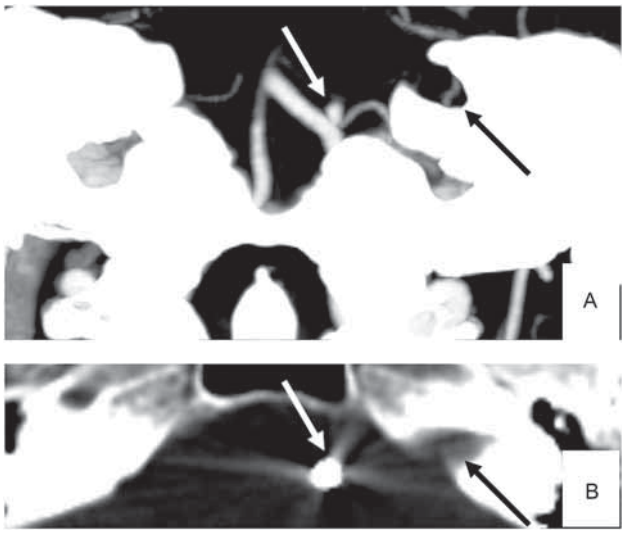

FIG 2. A 43-year-old woman with vestibular schwannoma. Eight years after irradiation, SAH and a ruptured bifurcation aneurysm (2.7 mm) were diagnosed by noncontrast CT and CTA (*A*, *white arrow*), which was treated with endovascular coiling (*B*, *white arrow*). Note a funnel-shaped enlargement of the left internal auditory canal (*A* and *B*, *black arrow*).

hemodynamic wall characteristics and a weakened vessel wall may affect hemodynamic force formation, which, in turn, affects aneurysm development.[14,21] Second, compared with the anterior cerebral artery and MCA, the posterior circulation has a relatively sparse sympathetic innervation.[22,23] However, cerebral autoregulation that depends on sympathetic nerve innervation may decrease and cause fibrosis after radiation,[24,25] leading to a passive overdistention of the vessel.[26] Recently, Pesce et al[7] reported that the posterior circulation is vulnerable even at low irradiation.

SAH was present in 88.2% of radiation-induced aneurysms, much higher than in the control group, implying that radiation-related aneurysms are more fragile and prone to rupture. Previous studies have shown that most patients with radiation-related aneurysms presented with SAH[5,11,17] and consequently had higher mortality and morbidity than patients with classic aneurysms.[5,6] Therefore, early detection of radiation-related aneurysms is crucial to allow monitoring or therapeutic intervention while the aneurysm is still unruptured. We think that it is reasonable to recommend dedicated screening for aneurysms after radiation therapy, but further studies are needed to determine the ideal timing to screen because the latency period remains highly variable (as early as 3 months[27] or as late as 37 years[28] after radiation therapy) and how to screen in terms of avoiding additional radiation exposure. The reasons for the high percentage of SAH in patients with radiation-related aneurysms should be cautiously interpreted. We postulate that the following reasons may contribute to this phenomenon: 1) the weakened and inflammatory vessel wall in the radiation-related aneurysm, as aforementioned, is vulnerable to rupture;[11,14,17,20,21] 2) as the longevity of treated patients increases (especially for young patients), the damaged blood vessels are correspondingly exposed to wall shear stress for an extended period, allowing a longer time for aneurysmal formation and rupture; and 3) radiation-related aneurysms are more likely to develop necrosis,[17] which is uncommon in classic intracranial aneurysms, and radiation-related aneurysms are associated more often with an inflammatory aneurysmal wall,[17] which is known to be a critical element of aneurysm rupture.[29]

Limitations

There are some limitations to our study: 1) The shape of an aneurysm may be affected by radiation therapy,[17] but we lost a chance to report this feature because the fusiform aneurysms were excluded in the first data collection, which was completed before January 2016, and the criteria of the second data collection followed the first one. 2) Because an intracranial aneurysm is a rare complication of radiation therapy, we included a small number of radiation-induced aneurysms. The gigantic difference in the sample size between groups, regardless of data types, might provide insufficient statistical power for analysis. 3) Clinically, we performed CT or/and MR imaging with contrast to evaluate the head and neck mass before radiation but did not regularly acquire CTA or TOF-MR angiography for those patients. Therefore, some radiation-related aneurysms could be coincidental because no vascular examination acquired before radiation therapy was available to prove the absence of the aneurysm. 4) CTA has a high sensitivity and specificity for the detection of intracranial aneurysms,[13,14] but we did not compare the results with the current criterion standard, DSA. Hence, we may have missed and/or misdiagnosed a fraction of smaller intracranial aneurysms. 5) Although the shortest time interval between delivery of radiation and the diagnosis of an aneurysm, to our knowledge, is 3 months,[27] the risk of a coincidental aneurysm may increase because the inclusion criterion of the latency interval (≥6 months) may not be long enough for aneurysm formation and development.

CONCLUSIONS

Compared with control group, patients with radiation-related aneurysms showed different characteristics related to their sex and age and the location and type of aneurysm. Furthermore, a higher percentage of these patients presented with SAH. Therefore, it is reasonable to recommend dedicated screening for aneurysms after radiation therapy, but further studies are needed to determine when to screen because the latency period remains highly variable and how to screen in terms of avoiding additional radiation exposure.

ACKNOWLEDGMENTS

The authors thank Xing Zhou, Wanlin Peng, Shufeng Cai, Jingni Chen, Jinpei Luo, Lvjin feng, Feifei Sun, Kai Pang, Jingyu Zhou, and Man Zhang for spending so much time and effort collecting patient clinical data. Without them, the present study could not be completed.

Disclosure forms provided by the authors are available with the full text and PDF of this article at www.ajnr.org.

REFERENCES

1. Chen YP, Chan AT, Le QT, et al. **Nasopharyngeal carcinoma.** *Lancet* 2019;394:64–80 CrossRef Medline

2. Xu J, Cao Y. **Radiation-induced carotid artery stenosis: a comprehensive review of the literature.** *Interv Neurol* 2014;2:183–92 CrossRef Medline
3. Li K, Lin GZ, Shen JC, et al. **Time trends of nasopharyngeal carcinoma in urban Guangzhou over a 12-year period (2000-2011): declines in both incidence and mortality.** *Asian Pac J Cancer Prev* 2014;15:9899–9903 CrossRef Medline
4. Tanyildizi Y, Keweloh S, Neu MA, et al. **Radiation-induced vascular changes in the intracranial irradiation field in medulloblastoma survivors: an MRI study.** *Radiother Oncol* 2019;136:50–55 CrossRef Medline
5. Chan SH, Woo YM, Wong KS, et al. **The angiographic and clinical outcomes of intracranial aneurysms following irradiation in patients with nasopharyngeal carcinoma: a 13-year experience and literature review.** *J Neuroradiol* 2018;45:224–29 CrossRef Medline
6. Wu YH, Lin SS, Chen HH, et al. **Radiotherapy-related intracranial aneurysm: case presentation of a 17-year male and a meta-analysis based on individual patient data.** *Childs Nerv Syst* 2016;32:1641–52 CrossRef Medline
7. Pesce A, Palmieri M, Zancana G, et al. **Radiation-induced brain aneurysms: institutional experience and state of the art in the contemporary literature.** *World Neurosurg* 2020;135:339–51 CrossRef Medline
8. Yang WH, Yang YH, Chen PC, et al. **Intracranial aneurysms formation after radiotherapy for head and neck cancer: a 10-year nationwide follow-up study.** *BMC Cancer* 2019;19:537 CrossRef Medline
9. Yucesoy K, Feiz-Erfan I, Spetzler RF, et al. **Anterior communicating artery aneurysm following radiation therapy for optic glioma: report of a case and review of the literature.** *Skull Base* 2004;14:169–73 CrossRef Medline
10. O'Connor MM, Mayberg MR. **Effects of radiation on cerebral vasculature: a review.** *Neurosurgery* 2000;46:138–49; discussion 150–51 CrossRef Medline
11. Nanney AD 3rd, El Tecle NE, El Ahmadieh TY, et al. **Intracranial aneurysms in previously irradiated fields: literature review and case report.** *World Neurosurg* 2014;81:511–19 CrossRef Medline
12. Huang ZQ, Zhou XW, Hou ZJ, et al. **Risk factors analysis of mirror aneurysms: a multi-center retrospective study based on clinical and demographic profile of patients.** *Eur J Radiol* 2017;96:80–84 CrossRef Medline
13. Backes D, Vergouwen MD, Velthuis BK, et al. **Difference in aneurysm characteristics between ruptured and unruptured aneurysms in patients with multiple intracranial aneurysms.** *Stroke* 2014;45:1299–1303 CrossRef Medline
14. Huang ZQ, Meng ZH, Hou ZJ, et al. **Geometric parameter analysis of ruptured and unruptured aneurysms in patients with symmetric bilateral intracranial aneurysms: a multicenter CT angiography study.** *AJNR Am J Neuroradiol* 2016;37:1413–17 CrossRef Medline
15. Northcott PA, Robinson GW, Kratz CP, et al. **Medulloblastoma.** *Nat Rev Dis Primers* 2019;5:11 CrossRef Medline
16. Petersson F. **Nasopharyngeal carcinoma: a review.** *Semin Diagn Pathol* 2015;32:54–73 CrossRef Medline
17. Sheehan JP, Starke RM. **Aneurysm formation associated with ionizing radiation.** *World Neurosurg* 2014;81:487–89 CrossRef Medline
18. Buijs PC, Krabbe-Hartkamp MJ, Bakker CJ, et al. **Effect of age on cerebral blood flow: measurement with ungated two-dimensional phase-contrast MR angiography in 250 adults.** *Radiology* 1998;209:667–74 CrossRef Medline
19. Masuoka T, Hayashi N, Hori E, et al. **Distribution of internal elastic lamina and external elastic lamina in the internal carotid artery: possible relationship with atherosclerosis.** *Neurol Med Chir (Tokyo)* 2010;50:179–82 CrossRef Medline
20. Stone HB, Coleman CN, Anscher MS, et al. **Effects of radiation on normal tissue: consequences and mechanisms.** *Lancet Oncol* 2003;4:529–36 CrossRef Medline
21. Takao H, Murayama Y, Otsuka S, et al. **Hemodynamic differences between unruptured and ruptured intracranial aneurysms during observation.** *Stroke* 2012;43:1436–39 CrossRef Medline
22. Beausang-Linder M, Bill A. **Cerebral circulation in acute arterial hypertension–protective effects of sympathetic nervous activity.** *Acta Physiol Scand* 1981;111:193–99 CrossRef Medline
23. Peerless SJ, Yasargil MG. **Adrenergic innervation of the cerebral blood vessels in the rabbit.** *J Neurosurg* 1971;35:148–54 CrossRef Medline
24. Mahfoud F, Tunev S, Ruwart J, et al. **Efficacy and safety of catheter-based radiofrequency renal denervation in stented renal arteries.** *Circ Cardiovasc Interv* 2014;7:813–20 CrossRef Medline
25. Waksman R, Barbash IM, Chan R, et al. **Beta radiation for renal nerve denervation: initial feasibility and safety.** *EuroIntervention* 2013;9:738–44 CrossRef Medline
26. Schwartz RB, Mulkern RV, Gudbjartsson H, et al. **Diffusion-weighted MR imaging in hypertensive encephalopathy: clues to pathogenesis.** *AJNR Am J Neuroradiol* 1998;19:859–62 Medline
27. Yoon WS, Lee KS, Jeun SS, et al. **De novo aneurysm after treatment of glioblastoma.** *J Korean Neurosurg Soc* 2011;50:457–59 CrossRef Medline
28. Ghoshhajra BB, McLean GK; SIR Foundation. **SIR 2006 annual meeting film panel case: radiation-induced cerebral aneurysms.** *J Vasc Interv Radiol* 2006;17:1891–96 CrossRef Medline
29. Chalouhi N, Ali MS, Starke RM, et al. **Cigarette smoke and inflammation: role in cerebral aneurysm formation and rupture.** *Mediators Inflamm* 2012;2012:271582 CrossRef Medline

Neuroimaging Findings in CHANTER Syndrome: A Case Series

K.S. Mallikarjun, M.S. Parsons, Z. Nigogosyan, M.S. Goyal, and R.W. Eldaya

ABSTRACT

SUMMARY: Recently, a distinct clinicoradiologic entity involving cerebellar, hippocampal, and basal nuclei transient edema with restricted diffusion (CHANTER) on MR imaging was identified. Patients present in an unresponsive state following exposure to drugs of abuse. Very little information exists regarding this entity, particularly in the radiology literature. We identify and describe 3 patients at our institution with similar clinical and radiographic findings. Multifocal restricted diffusion in the brain is typically associated with poor outcomes. By contrast, CHANTER involves intraventricular obstructive hydrocephalus that, when treated, can lead to substantial recovery. This novel syndrome should be on the differential in patients who present in an unresponsive state after recent opioid use in the context of the above imaging findings. Additional diagnoses on the differential can include ischemic stroke, hypoxic-ischemic encephalopathy, "chasing the dragon," leukoencephalopathy, opioid-associated amnestic syndrome, and pediatric opioid-use-associated neurotoxicity with cerebellar edema.

ABBREVIATIONS: CHANTER = cerebellar, hippocampal, and basal nuclei transient edema with restricted diffusion; EVD = external ventricular drain; HIE = hypoxic-ischemic encephalopathy; OAA = opioid-associated amnestic syndrome; POUNCE = pediatric opioid use-associated neurotoxicity with cerebellar edema

Cerebellar, hippocampal, and basal nuclei transient edema with restricted diffusion (CHANTER) syndrome is a recently described novel disease entity involving distinct radiologic and clinical findings. The initial case series that identified this constellation consisted of 6 patients who presented with stupor or coma in the setting of intoxication with drugs of abuse.[1] The initial CT in these patients showed a consistent pattern of progressively worsening acute cerebellar edema, which eventually progressed to intraventricular obstructive hydrocephalus. MR imaging showed diffusion restriction in the bilateral hippocampi, cerebellar cortices, and basal ganglia, without substantial cortical involvement.

This combination of distinct radiologic findings and clinical course is distinct from that of other similar etiologies, such as acute ischemic stroke, hypoxic-ischemic encephalopathy (HIE), and heroin-associated spongiform leukoencephalopathy. Despite its suggestive and unique imaging features, there is a scarcity of data regarding CHANTER syndrome in the radiology literature, and clinical services often drive its diagnosis. However, prompt recognition or suggestion of CHANTER by the radiologist on MR imaging is essential. It may allow aggressive early treatment, which might not be offered in cases of HIE or multifocal diffusion restriction with obstructive hydrocephalus, given a presumed poor neurologic outcome.[1,2]

Preliminary data suggest an association between the use of drugs of abuse, particularly opioids, and the eventual diagnosis of CHANTER syndrome. Fentanyl overdoses are now the leading cause of death among those 18–45 years of age in the United States.[3] The coronavirus disease 2019 (COVID-19) pandemic and response have caused a spike in opioid overdoses, predicted to worsen further.[4] The increasing scope of the opioid epidemic elucidates the necessity for radiologists and clinicians to recognize the findings of CHANTER because the disease prevalence is expected to increase.

Since the initial series of patients with CHANTER syndrome, only 1 case report in the literature of suspected CHANTER syndrome has been published.[5] Additionally, further classification has occurred for 2 syndromes that bear a resemblance to CHANTER: pediatric opioid use-associated neurotoxicity with cerebellar edema (POUNCE)[6] and opioid-associated amnestic syndrome (OAA).[7] Thus, the relationship of these patterns to CHANTER has yet to be discussed. We believe that our case series supports CHANTER as an essential entity that radiology can suggest on the basis of imaging.

Received February 26, 2022; accepted after revision May 13.

From the Mallinckrodt Institute of Radiology (K.S.M., M.S.P., Z.N., M.S.G., R.W.E.), Washington University School of Medicine, Ringgold Standard Institution, St. Louis, Missouri; and MD Anderson Cancer Center, Diagnostic Imaging Division (R.W.E.), Houston, Texas.

Please address correspondence to Kushanth S. Mallikarjun, MD, Mallinckrodt Institute of Radiology, Washington University School of Medicine, 510 S Kingshighway Blvd, St. Louis, MO 63110; e-mail: kushi.mallikarjun@wustl.edu; @MIRimaging

Indicates article with online supplemental data.

http://dx.doi.org/10.3174/ajnr.A7569

Case Series

Patient 1. A 54-year-old woman with a history of HIV and IV drug use presented in an unresponsive state after a fentanyl overdose. Naloxone was administered, but the patient remained encephalopathic and was intubated for airway protection.

The initial CT showed subtle edema and hypoattenuation in the cerebellar hemispheres, with a developing mass effect on the fourth ventricle. There was no hydrocephalus at the time nor any hypoattenuation within the basal ganglia. The patient continued to deteriorate clinically. CT performed the day after admission showed progressive hypoattenuation and edema within the cerebellar hemispheres; new edema within the posterior hippocampi, basal ganglia, and cortex; and developing hydrocephalus (Fig 1). The patient was given IV mannitol, admitted to the neurocritical care unit, and had an external ventricular drain (EVD) placed for CSF flow diversion. CTA showed no large-vessel occlusions, and CTP data showed no evidence of core or penumbra to suggest a stroke or hypoperfusion. Continued deterioration led to the patient requiring a suboccipital decompressive craniectomy.

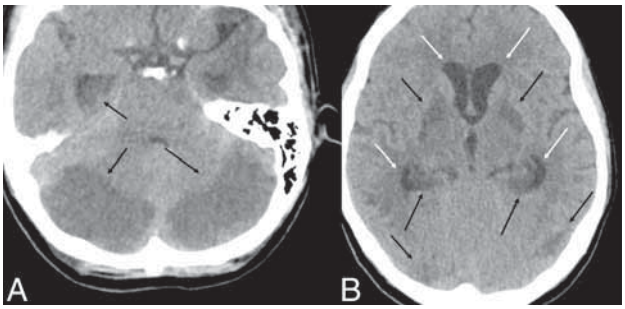

FIG 1. Representative findings on initial head CT. Axial NCCT demonstrates hypoattenuation within the cerebellar hemispheres and hypoattenuation within the posterior hippocampi (*black arrows, A*) and hypoattenuation within the basal ganglia, hippocampi, and cortex (*black arrows, B*). Developing hydrocephalus is present (*white arrows, B*).

MR imaging showed areas of diffusion restriction in the bilateral cerebellar hemispheres, bilateral hippocampi, bilateral basal ganglia, and deep WM, and scattered cortical involvement (Fig 2). Blood products were seen in the right cerebellum. TOF-MRA confirmed the lack of large-vessel occlusion.

In 1 week, the patient was extubated, and her EVD was weaned and removed. The patient's mental status was slowly improving. A repeat MR imaging 2 weeks postadmission (Online Supplemental Data) showed the evolution of known injury involving the cerebellum, temporo-occipital lobes, hippocampi, and basal ganglia with decreased T2/FLAIR hyperintensity and increased areas of enhancement, as well as increased abnormal T2/FLAIR signal within the subcortical WM of the pre- and postcentral gyri bilaterally, without enhancement, restricted diffusion, or susceptibility artifacts.

Although the patient required tracheostomy and gastrostomy, she improved enough for transfer to the floor and subsequently to a long-term acute care facility. At follow-up 5 weeks after admission, the patient had a substantially improved mental status with mild memory, speech, and gait deficits. The estimated mRS score was a 3. CT showed encephalomalacia in the bilateral cerebellar hemispheres, occipital lobes, and left parietal lobe and scattered hypodensities in the deep WM.

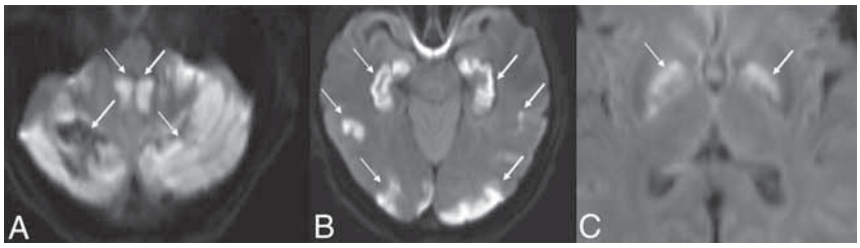

FIG 2. MR DWI from patient 1, thirty hours after presentation, shows diffusion restriction in the cerebellum (*white arrows, A*), hippocampi and cortex (*white arrows, B*), and basal ganglia (*white arrows, C*). The ADC map is not shown.

Patient 2. A 33-year-old man with a medical history of treated HIV and IV drug use presented after being found unresponsive. A urine drug screen was positive for amphetamines, cocaine, fentanyl, and benzodiazepines. He was given naloxone with minimal arousal. He was subsequently intubated for airway protection, given IV hypertonic saline, and admitted to the neurocritical care unit.

The initial CT demonstrated bilateral cerebellar hypoattenuation and hypoattenuation involving the basal ganglia, posterior hippocampi, and parieto-occipital cortex. It also showed developing obstructive hydrocephalus with partial effacement of the fourth ventricle and cerebral aqueduct as well as dilation of the lateral and third ventricles. MR imaging showed diffusion restriction in the cerebellar hemispheres, hippocampi, temporo-occipital cortex, and basal ganglia (Fig 3). TOF-MRA showed no evidence of large-vessel occlusion.

The patient had a posterior fossa craniectomy with resection of the cerebellar tissue and EVD placement for intraventricular obstructive hydrocephalus. His EVD was weaned and removed. An MR

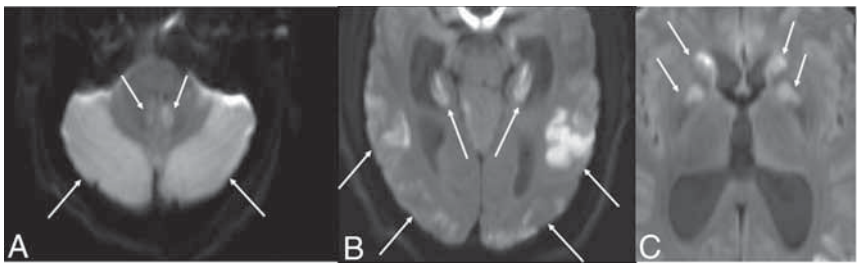

FIG 3. MR DWI from patient 2, six hours after presentation, shows diffusion restriction in the cerebellar hemispheres (*white arrows, A*), hippocampi and temporo-occipital cortex (*white arrows, B*), and basal ganglia (*white arrows, C*). The ADC map is not shown.

imaging performed 2 weeks postadmission demonstrated the expected evolution with normalization of the abnormal findings on DWI involving the cerebellum, hippocampi, and basal ganglia (Online Supplemental Data).

The patient could not be extubated secondary to mental status and ultimately had a tracheostomy. The patient improved enough for transfer to the floor and subsequently to a long-term acute care facility. CT at discharge showed resolution of hypoattenuation and mass effect in the posterior fossa. At follow-up 14 weeks after admission, the patient could follow simple commands and communicate with eye contact, and the estimated mRS score was 5.

Patient 3. A 42-year-old woman with a medical history of polysubstance abuse presented in an unresponsive state after being found down after a fentanyl overdose. Her urine drug screen was positive for fentanyl, amphetamines, and cannabinoids. She was given naloxone and had minimal responsiveness. She was intubated for airway protection due to a somnolent mental status.

The initial CT demonstrated areas of decreased attenuation and edema involving the bilateral cerebellar hemispheres, the right basal ganglia, and hippocampi. The patient continued to deteriorate. A repeat CT the following day revealed increased prominence of the hypoattenuation and edema in the previously mentioned areas, dilation of the lateral ventricles consistent with developing hydrocephalus, and a new area of marked hypoattenuation in the left caudate. Initial MR imaging showed diffusion restriction in the bilateral cerebellum, bilateral hippocampi, cortex, and basal ganglia with blood products in the right cerebellum (Fig 4). TOF-MRA showed no large-vessel occlusions.

The patient had EVD placement for obstructive hydrocephalus. Her EVD was weaned and eventually removed. An MR imaging at 2 weeks postadmission showed resolving areas of the initially noted diffusion restriction, along with FLAIR hyperintensity and postcontrast enhancement within the cerebellum, hippocampi, cortex, and basal ganglia consistent with evolving injury (Online Supplemental Data).

The patient was extubated successfully but had a gastrostomy tube placed due to dysphagia. The patient's condition improved enough for transfer to a skilled nursing facility. At discharge, the patient regarded the examiner briefly but was mute and did not reliably track or follow commands. The estimated mRS score was 5.

DISCUSSION

All 3 patients in our series had presentations, imaging findings, clinical courses, and outcomes similar to those in patients first identified and categorized as having CHANTER by Jasne et al.[1] No other documented syndrome fit these findings as well as CHANTER. Thus, we concur with the classification of this unique constellation of symptoms as a distinct clinicoradiographic syndrome of CHANTER.

Radiographic Features

The 3 patients in our series had consistent NCCT findings. The initial CT findings showed cerebellar edema with eventual mass effect on the fourth ventricle and intraventricular obstructive hydrocephalus requiring shunting and decompression. A varying degree of involvement of the basal ganglia and cortex was noted on the initial CT, with subsequent development of these findings on CT the following day. All patients had vessel imaging showing no large-vessel occlusion to suggest arterially mediated infarctions. No evidence of hemorrhage was seen on NCCT in any of these cases. CTP and regional CBF images in 1 patient showed no evidence of a stroke or decreased blood flow to the basal ganglia and cerebellum. This finding suggests that the injury in CHANTER is not related to vascular flow restriction but rather likely internal cellular injury.

While patients who present in an unconscious state are likely to have NCCT as their first imaging study, MR imaging findings, especially diffusion restriction, are the distinct radiologic hallmark of CHANTER and necessary for diagnosis. The initial MR imaging findings among our 3 patients were also consistent. On initial MR imaging, all patients showed diffusion restriction in the cerebellum, hippocampi, basal ganglia, and cortex. Only 1 of the patients had subcortical WM involvement of the centrum semiovale. Initial MR imaging was performed within several hours for 2 patients but was delayed in patient 3. A follow-up MR imaging generally obtained 2–3 weeks later in all cases showed expected injury evolution with normalization of signal on DWI, FLAIR hyperintensity, and postcontrast enhancement in these areas, consistent with evolving injury. All patients had TOF-MRA demonstrating the absence of occlusion in large vessels.

The radiologic findings among the 3 patients in our series are largely consistent with those of the 6 patients in the Jasne et al[1] series, including the initial CT findings, development of obstructive hydrocephalus following cerebellar edema, and diffusion restriction in the cerebellar cortex, hippocampi, and basal ganglia, typical of CHANTER. The only substantial discrepancy was the presence or absence of cerebral cortical involvement. Jasne et al reported that all 6 of their patients had the typical diffusion restriction findings but sparing of the cerebral cortex. However, all 3 patients in our series had some extent of cerebral cortical involvement, though this was not a dominant feature. The involvement of subcortical WM was rare in both case series. Only 1 patient in the series of Jasne et al showed areas of restricted diffusion in the subcortical WM. In contrast, no patients in this series exhibited such findings.

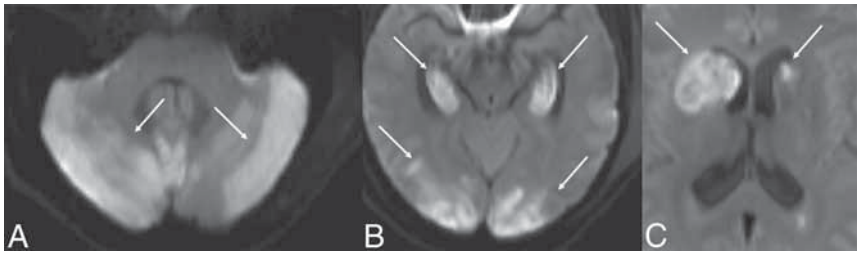

FIG 4. DWI of patient 3, fifty-eight hours after presentation, shows diffusion restriction in the cerebellum (*white arrows, A*), hippocampi and cortex (*white arrows, B*), and basal ganglia (*white arrows, C*). There is mass effect from the diffusion restriction in the right caudate nucleus on the frontal horn of the right lateral ventricle (*C*). The ADC map is not shown.

Clinical Course. Clinicians often approach a pattern of large symmetric areas of restricted diffusion in the brain as representing severe, irreversible injury and a poor neurologic outcome

with a small chance of improvement. This belief could stem from the poor prognosis in patients with multifocal diffusion restriction caused by HIE, with only one-quarter of patients with HIE surviving to hospital discharge and those surviving having severe neurologic deficits.[2] While the initial presentation of patients with CHANTER syndrome is severe, the outcomes in these patients illustrate the potential for substantial clinical improvement with prompt detection and treatment of the edema.

Regarding the 6 patients classified as having CHANTER by Jasne et al,[1] 4 patients had EVD placement for CSF flow diversion and 3 had suboccipital decompression. Although 1 patient died during hospitalization due to brain herniation, 5 had notable levels of functional improvement. The patients in our series are all different individuals from those reported by Jasne et al.

After medical and surgical intervention, our patients had similar outcomes compared with those in the initial CHANTER series. All 3 had EVD placement, and 2 had further neurosurgical decompression. Obstructive hydrocephalus resolved in all patients. All survived and showed substantial-but-variable neurologic improvement compared with their presenting status. Similarly, Kobayashi et al,[5] in 2021, described a case of CHANTER syndrome in which the patient had a dramatic clinical improvement with the only deficit being mild leg weakness. In contrast, the presence of large areas of symmetric restricted diffusion following anoxic brain injury typically predicts very poor neurologic outcome.

Differential Diagnoses and Classification

Acute ischemic stroke is unlikely to be confused with CHANTER because patients with CHANTER do not have any vessel occlusion on imaging. Additionally, patients with CHANTER typically have injuries in multiple vascular territories. A related pathology that is closer with respect to radiologic features to CHANTER is HIE. Patients with HIE can present in an unresponsive state, similar to that in patients with CHANTER. However, they do not necessarily have acute exposure to drugs of abuse. The outcomes are typically extremely poor compared with patients with CHANTER syndrome.[2] This pattern of injury tends to affect areas of high metabolic demand. Notably, cerebellar and hippocampal edema can be seen in HIE. However, when this occurs, other areas, such as the cerebral cortex, are often diffusely involved.[8,9] In HIE, NCCT will typically show a diffuse loss of gray-white matter differentiation and effacement of the sulci with cytotoxic edema.[10,11] These findings were not seen in any patients classified as having CHANTER.

Additionally, in HIE, the cerebellum is more likely to be spared, giving rise to the white cerebellum sign, contrary to the cerebellar hypoattenuation seen on CT in all patients with CHANTER syndrome. Last, while obstructive hydrocephalus developed in all patients with CHANTER syndrome, it is not common in patients with HIE.[12] However, it is possible that some patients described here and previously with CHANTER syndrome might also have some degree of superimposed HIE, which might partially account for the variability in outcomes.

Heroin-associated spongiform leukoencephalopathy is a toxic leukoencephalopathy with distinct imaging features. Because it is exclusively associated with heroin vapor inhalation, it is also known as "chasing the dragon" leukoencephalopathy. Although it can present with cerebellar restricted diffusion, it almost always presents with changes in the WM, including symmetric confluent deep WM hyperintensity on T2 and FLAIR sequences, with sparing of the gray matter, which is not typical of CHANTER.[11,13] Contrary to CHANTER, it also presents during a more extended period.

Another recent case remarkably similar to CHANTER consisted of cerebellar edema in a young child following accidental opioid ingestion and fentanyl administration.[14,15] It appears that this case, as well as several others in the pediatric population, may fit under the recently described constellation of POUNCE.[6,16-21] Children with POUNCE are generally accidentally exposed to opioids and present with a decreased level of consciousness. Similar to CHANTER, the prominent feature of POUNCE is malignant cerebellar edema, with diffusion restriction occasionally reported.[14,18,22] This cerebellar edema can lead to obstructive hydrocephalus.[14] However, contrary to CHANTER, these cases rarely have hippocampal and basal ganglia involvement, instead involving WM areas with lesions that are hyperintense on T2 and hypoattenuated on CT.[14,15,18,20,22] Some of these differences in injury patterns have been speculated to be due to the differences in opioid receptor expression between childhood and adulthood.[23,24]

Another syndrome that has some overlapping features with CHANTER is OAA. Patients with OAA present with new-onset amnesia after exposure to opioids, most notably fentanyl.[7,25-29] Radiologically, the prominent finding is symmetric diffusion restriction and FLAIR hyperintensity of the hippocampi. Edema in the cerebellum and basal ganglia occurs only rarely, and patients do not present with obstructive hydrocephalus. Presentation and outcomes are milder than in CHANTER, with amnesia as the defining deficit.

The similarities between patients with CHANTER, POUNCE, and OAA perhaps indicate that these syndromes exist along a spectrum with several overlapping clinical and imaging features and a common underlying etiology (Table). It has been thought

Proposed spectrum of opioid syndromes

	Clinical Data	Imaging Findings
CHANTER	Decreased level of consciousness in adults, cerebellar edema leading to obstructive hydrocephalus, mixed prognosis	Cerebellar edema with hippocampal and basal ganglia involvement on DWI
POUNCE	Decreased level of consciousness in children, cerebellar edema leading to obstructive hydrocephalus, poor prognosis	Cerebellar edema without hippocampal and basal ganglia involvement on DWI, more WM involvement with T2 hyperintensity
OAA	New-onset amnesia, mild prognosis	Symmetric diffusion restriction and FLAIR hyperintensity of the hippocampi

that CHANTER represents the more severe end of this spectrum, while OAA represents a milder form.[1]

Febrile infections, including acute cerebellitis, would also be on the differential. However, apart from a different clinical history, cerebellitis is more likely to have leptomeningeal and cortical enhancement in the acute setting and less likely to have extensive supratentorial involvement, for example, in the basal nuclei, cortex, and hippocampi as in CHANTER.[29,30]

Etiology and Mechanism

There is a clear association of the presentation of CHANTER syndrome and acute intoxication with drugs of abuse, particularly opioids. Four of the 6 patients identified by Jasne et al[1] had acute exposure to opiates. In our series, all 3 patients had a fentanyl overdose. Thus, although the pathogenesis of CHANTER is still uncertain, it appears that direct opioid toxicity plays a key role. The injury pattern is thought to be due to a combination of neurotoxicity and hypoxic effects, resulting in mitochondrial failure with anoxic injury.[1] Other proposed mechanisms for the effect of opioids on the cerebellum have been proposed in POUNCE syndrome, including direct oligodendrocyte toxicity, demyelination, and apoptotic upregulation.[6,31,32] An underlying susceptibility to CHANTER syndrome due to genetic or environmental factors might also be present. The expression of the *OPRM1* gene, which encodes the μ-opioid receptor, which is the primary target of morphine-derivative opioids, is higher in key regions affected in CHANTER, particularly the cerebellum.[33-35]

In the adult literature, heroin-associated spongiform leukoencephalopathy has preferential cerebellar involvement. It has been postulated that this is due to the high concentration of opioid receptors in the cerebellum,[22,36] which are also highly expressed in affected regions of the WM.[33-35] The injury in OAA is thought to be due to fentanyl-induced hippocampal excitotoxicity in the context of hypoventilatory hypoxemia.[37] Accordingly, we propose that the regional topography of CHANTER might be due to an overlap of brain regions most vulnerable to both opioid toxicity and hypoxic-ischemic injury, with similar conditions falling on either side of this spectrum. However, although the patients in our case series all had acute exposure to fentanyl specifically, the exposures reported by Jasne et al[1] appear more heterogeneous, including 2 not having any acute opioid exposures.

CONCLUSIONS

Because of the distinct imaging features of CHANTER syndrome, radiologists can often be the first to consider this syndrome as a possible diagnosis. We believe that CHANTER syndrome is under-recognized, to the detriment of these patients who can often experience strong neurologic improvement from baseline if identified early and provided with an urgent medical and surgical intervention. While the opioid epidemic continues to worsen and synthetic opioids like fentanyl cause an even larger portion of overdoses, this syndrome will likely only increase in prevalence. Further research can better clarify the inciting factors for CHANTER, determine a more consistent radiologic presentation, elucidate its underlying mechanisms, and implicate the possibility of CHANTER being part of a spectrum of overlapping injury patterns.

Disclosure forms provided by the authors are available with the full text and PDF of this article at www.ajnr.org.

REFERENCES

1. Jasne AS, Alsherbini KH, Smith MS, et al. **Cerebellar hippocampal and basal nuclei transient edema with restricted diffusion (CHANTER) syndrome.** *Neurocrit Care* 2019;31:288–96 CrossRef Medline
2. Howard RS, Holmes PA, Koutroumanidis MA. **Hypoxic-ischaemic brain injury.** *Pract Neurol* 2011;11:4–18 CrossRef Medline
3. Centers for Disease Control and Prevention. National Center for Health Statistics. **Drug Overdose Deaths in the US Top 100,000 Annually.** November 17, 2021. https://www.cdc.gov/nchs/pressroom/nchs_press_releases/2021/20211117.htm. Accessed December 8, 2021
4. Niles JK, Gudin J, Radcliff J, et al. **The opioid epidemic within the COVID-19 pandemic: drug testing in 2020.** *Popul Health Manag* 2021;24:S43–51 CrossRef Medline
5. Kobayashi N, Antimisiaris M, Lakhani S. **CHANTER syndrome: a case report with near complete recovery.** *Neurology* 2021;96(15 Suppl): Apr 17. https://n.neurology.org/content/96/15_Supplement/2050. Accessed December 20, 2021
6. Kim DD, Prasad AN. **Clinical and radiologic features of pediatric opioid use-associated neurotoxicity with cerebellar edema (POUNCE) syndrome.** *Neurology* 2020;94:710–12 CrossRef Medline
7. Barash JA, Whitledge J, Watson CJ, et al. **Opioid-associated amnestic syndrome: description of the syndrome and validation of a proposed definition.** *J Neurol Sci* 2020;417:117048 CrossRef Medline
8. Arbelaez A, Castillo M, Mukherji SK. **Diffusion-weighted MR imaging of global cerebral anoxia.** *AJNR Am J Neuroradiol* 1999;20:999–1007 Medline
9. Gutierrez LG, Rovira À, Portela LAP, et al. **CT and MR in non-neonatal hypoxic-ischemic encephalopathy: radiological findings with pathophysiological correlations.** *Neuroradiology* 2010;52:949–76 CrossRef Medline
10. Huang BY, Castillo M. **Hypoxic-ischemic brain injury: imaging findings from birth to adulthood.** *Radiographics* 2008;28:417–39 CrossRef Medline
11. Bates DD, Gallagher K, Yu H, et al. **Acute radiologic manifestations of America's opioid epidemic.** *Radiographics* 2018;38:109–23 CrossRef Medline
12. Inamasu J, Miyatake S, Suzuki M, et al. **Early CT signs in out-of-hospital cardiac arrest survivors: temporal profile and prognostic significance.** *Resuscitation* 2010;81:534–38 CrossRef Medline
13. Keogh CF, Andrews GT, Spacey SD, et al. **Neuroimaging features of heroin inhalation toxicity: "chasing the dragon."** *AJR Am J Roentgenol* 2003;180:847–50 CrossRef Medline
14. Chen CH, Mullen AJ, Hofstede D, et al. **Malignant cerebellar edema in three-year-old girl following accidental opioid ingestion and fentanyl administration.** *Neuroradiol J* 2019;32:386–91 CrossRef Medline
15. Jasne AS, Alsherbini KA, Smith MS, et al. **Response to "malignant cerebellar edema in three-year-old girl following accidental opioid ingestion and fentanyl administration."** *Neuroradiol J* 2020;33:158 CrossRef Medline
16. Nanan R, von Stockhausen HB, Petersen B, et al. **Unusual pattern of leukoencephalopathy after morphine sulphate intoxication.** *Neuroradiology* 2000;42:845–48 CrossRef Medline
17. Riascos R, Kumfa P, Rojas R, et al. **Fatal methadone intoxication in a child.** *Emerg Radiol* 2008;15:67–70 CrossRef Medline
18. Duran D, Messina RD, Beslow LA, et al. **Malignant cerebellar edema subsequent to accidental prescription opioid intoxication in children.** *Front Neurol* 2017;8:362 CrossRef Medline
19. Villelli N, Hauser N, Gianaris T, et al. **Severe bilateral cerebellar edema from ingestion of ketamine: case report.** *J Neurosurg Pediatr* 2017;20:393–96 CrossRef Medline

20. Wheaton T, Toll BJ, Breznak K, et al. **Opioid-induced toxic leukoencephalopathy: a case report and review of the literature.** *Heliyon* 2019;5: e03005 CrossRef Medline
21. Tiong SC, Chieng JSL, Khoo HW, et al. **Methadone-induced toxic encephalopathy in pediatric patients: two case reports.** *J Radiol Case Rep* 2019;13:1–9 CrossRef Medline
22. Shrot S, Poretti A, Tucker EW, et al. **Acute brain injury following illicit drug abuse in adolescent and young adult patients: spectrum of neuroimaging findings.** *Neuroradiol J* 2017;30:144–50 CrossRef Medline
23. Ahmed U, Wilson R, Hung SC. **Bilateral cerebellar hemorrhagic infarcts as an early presentation following opioid-induced toxic encephalopathy in an adult patient.** *Radiol Case Rep* 2021;16:1207–10 CrossRef Medline
24. Zagon IS, Gibo DM, McLaughlin PJ. **Adult and developing human cerebella exhibit different profiles of opioid binding sites.** *Brain Res* 1990;523:62–68 CrossRef Medline
25. Small JE, Butler PM, Zabar Y, et al. **Complete, bilateral hippocampal ischemia: a case series.** *Neurocase* 2016;22:411–15 CrossRef Medline
26. Bhattacharyya S, Gholipour T, Colorado RA, et al. **Bilateral hippocampal restricted diffusion: same picture many causes.** *J Neuroimaging* 2017;27:300–305 CrossRef Medline
27. Barash JA, Somerville N, DeMaria A. Jr., **Cluster of an unusual amnestic syndrome: Massachusetts, 2012-2016.** *MMWR Morb Mortal Wkly Rep* 2017;66:76–79 CrossRef Medline
28. Barash JA, Ganetsky M, Boyle KL, et al. **Acute amnestic syndrome associated with fentanyl overdose.** *N Engl J Med* 2018;378:1157–58 CrossRef Medline
29. Taylor RG, Budhram A, Lee DH, et al. **Opioid-associated amnestic syndrome observed with fentanyl patch use.** *CMAJ* 2019;191:E337–39 CrossRef Medline
30. Yildirim M, Gocmen R, Konuskan B, et al. **Acute cerebellitis or post-infectious cerebellar ataxia? Clinical and imaging features in acute cerebellitis.** *J Child Neurol* 2020;35:380–88 CrossRef Medline
31. Cunha-Oliveira T, Rego AC, Garrido J, et al. **Street heroin induces mitochondrial dysfunction and apoptosis in rat cortical neurons.** *J Neurochem* 2007;101:543–54 CrossRef Medline
32. Alambyan V, Pace J, Miller B, et al. **The emerging role of inhaled heroin in the opioid epidemic: a review.** *JAMA Neurol* 2018;75:1423–34 CrossRef Medline
33. Markello RD, Arnatkeviciute A, Poline JB, et al. **Standardizing workflows in imaging transcriptomics with the abagen toolbox.** *Elife* 2021;10:e72129 CrossRef Medline
34. Arnatkeviciute A, Fulcher BD, Fornito A. **A practical guide to linking brain-wide gene expression and neuroimaging data.** *Neuroimage* 2019;189:353–67 CrossRef Medline
35. Hawrylycz MJ, Lein ES, Guillozet-Bongaarts AL, et al. **An anatomically comprehensive atlas of the adult human brain transcriptome.** *Nature* 2012;489:391–99 CrossRef Medline
36. Schadrack J, Willoch F, Platzer S, et al. **Opioid receptors in the human cerebellum: evidence from [11C] diprenorphine PET, mRNA expression and autoradiography.** *Neuroreport* 1999;10:619–24 CrossRef Medline
37. Barash JA, Kofke WA. **Connecting the dots: an association between opioids and acute hippocampal injury.** *Neurocase* 2018;24:124–31 CrossRef Medline

Tumor Embolization through Meningohypophyseal and Inferolateral Trunks is Safe and Effective

E. Raz, D.D. Cavalcanti, C. Sen, E. Nossek, M. Potts, S. Peschillo, E. Lotan, V. Narayan, A. Ali, V. Sharashidze, P.K. Nelson, and M. Shapiro

ABSTRACT

BACKGROUND AND PURPOSE: Skull base tumors are commonly supplied by dural branches of the meningohypophyseal and inferolateral trunks. Embolization through these arteries is often avoided due to technical challenges and inherent risks; however, successful embolization can be a valuable surgical adjunct. We aimed to review the success and complications in our series of tumor embolizations through the meningohypophyseal and inferolateral trunks.

MATERIALS AND METHODS: We performed a retrospective review of patients with tumor treated with preoperative embolization at our institution between 2010 and 2020. We reviewed the following data: patients' demographics, tumor characteristics, endovascular embolization variables, and surgical results including estimated blood loss, the need for transfusion, and operative time.

RESULTS: Among 155 tumor embolization cases, we identified 14 patients in whom tumor embolization was performed using the meningohypophyseal ($n = 13$) or inferolateral ($n = 4$) trunk. In this group of patients, on average, 79% of tumors were embolized. No mortality or morbidity from the embolization procedure was observed in this subgroup of patients. The average estimated blood loss in the operation was 395 mL (range, 200–750 mL). None of the patients required a transfusion, and the average operative time was 7.3 hours.

CONCLUSIONS: Some skull base tumors necessitate embolization through ICA branches such as the meningohypophyseal and inferolateral trunks. Our series demonstrates that an effective and safe embolization may be performed through these routes.

ABBREVIATION: PVA = polyvinyl alcohol

Preoperative embolization of extra-axial brain tumors is often performed to devascularize a tumor and facilitate a safe surgical resection.[1-6] Such embolization has been associated with improved outcomes, including reduced surgical blood loss,[7-11] shorter operative times,[9] more complete resections,[3] increased progression-free survival,[12] and decreased surgical complications.[13] Preoperative embolization for skull base tumors, however, remains controversial, particularly for tumors supplied by the meningohypophyseal and inferolateral trunks. Embolization through these ICA branches poses several challenges. The meningohypophyseal and inferolateral trunks can be small and, therefore, difficult to catheterize. They supply the vasa nervorum of cranial nerves, placing those nerves at risk of ischemia during embolization. Finally, the short course of these branches risks reflux of embolic material into the ICA itself. Thus, tumor embolization through the meningohypophyseal and inferolateral trunks has been considered a "precarious undertaking."[13]

Despite these concerns, there is mounting evidence that preoperative embolization of skull base tumors through the meningohypophyseal and inferolateral trunks can be both safe and effective if done properly.[14-16]

In this study, we aimed to review our series of skull base tumors treated with preoperative embolization through the meningohypophyseal and/or inferolateral trunk to better characterize the safety and efficacy of embolization in this subgroup.

MATERIALS AND METHODS

Study Design

This study was approved by NYU institutional review board and conducted in accordance with the Health Portability and Accountability Act. We performed a retrospective review of all

Received January 18, 2022; accepted after revision June 2.

From the Departments of Radiology (E.R., D.D.C., E.L., V.N., A.A., V.S., P.K.N., M.S.), Neurointerventional Section, and Neurosurgery (C.S., E.N. P.K.N.), NYU Langone Health, New York, New York; Department of Neurological Surgery (M.P.), Northwestern Memorial Hospital, Northwestern University Feinberg School of Medicine, Chicago, Illinois; and Department of Neurosurgery (S.P.), University of Catania, Catania, Italy.

Please address correspondence to Eytan Raz, MD, PhD, Department of Radiology, NYU Langone Health, 660 First Ave, New York, NY 10016; e-mail: eytan.raz@gmail.com; @eytanraz; @neuroangio1; @Enossek; @SharashidzeVera; @S_Pesch

Indicates article with online supplemental data.

http://dx.doi.org/10.3174/ajnr.A7579

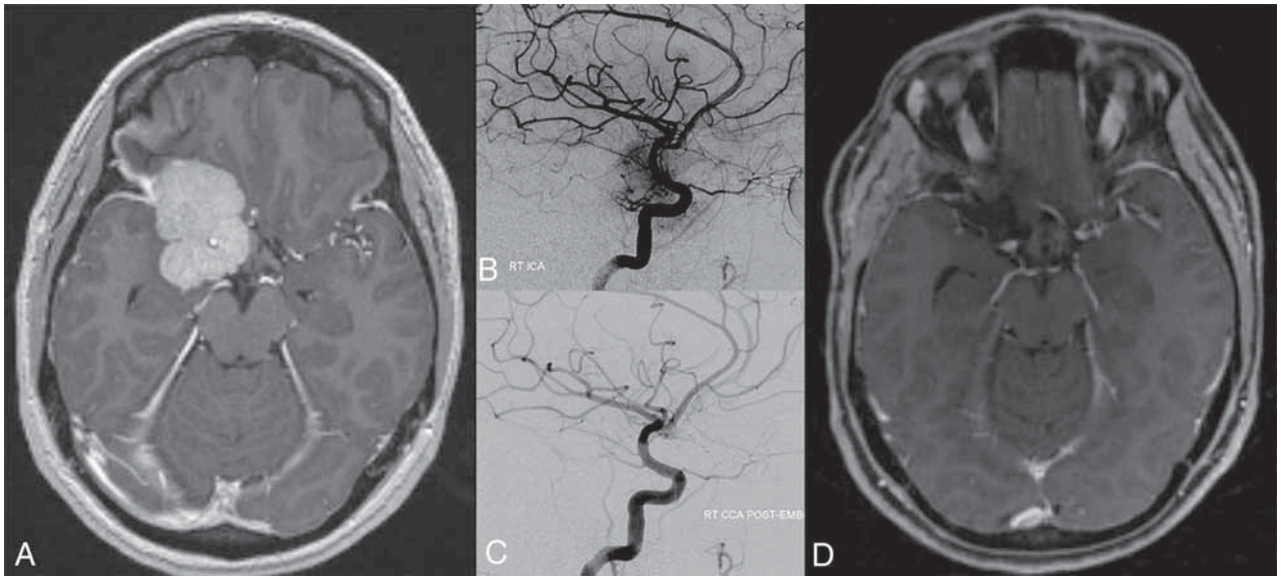

FIG 1. A patient with a large right sphenoid wing meningioma with encasement of the ICA visible on a T1-weighted, axial, postcontrast image (*A*). Right ICA DSA injection in a lateral view (*B*) demonstrates the supply to the tumor from an enlarged meningohypophyseal trunk. After selective embolization through both the meningohypophyseal trunk and indirectly from the middle meningeal artery, a final right common carotid artery injection in a lateral view (*C*) demonstrates interval 90% tumor embolization. Complete gross resection of the meningioma is visible on the T1-weighted, axial, postcontrast image (*D*). RT indicates right; CCA, common carotid artery; EMB, embolization.

patients who underwent preoperative brain tumor embolization from 2010 to 2020. Patient and tumor data were collected, including patient age and sex, tumor size and location, and the final pathologic diagnosis. In addition, details of the embolization procedure were collected, including the vessels embolized, percentage of tumor devascularization, and any intra- or postprocedural complications. Finally, surgical variables were collected, including estimated blood loss, the need for transfusion, and operative time. Two neurointerventionalists (E.R., and M.S.) independently evaluated the angiographic images before and after embolization to evaluate the percentage of tumor embolization and arrived at a final value by consensus.

Embolization Procedure

The decision to perform preoperative embolization and its goals were discussed in a multidisciplinary fashion among the treating neurosurgeons and neurointerventionalists. Patients were typically scheduled for embolization 1 to 2 days before the planned surgical resection. All embolization procedures were performed with the patient under general anesthesia, and intravenous steroids were administered at the start of each procedure. The procedure was performed using a sheathless 5F catheter to minimize the size of the arteriotomy. A comprehensive angiographic evaluation was first performed to completely characterize the supply to each artery. Once the target arteries for embolization were identified, there was an additional discussion in the control room with the neurosurgeon to reassess the goals and safety. For embolization, either an Excelsior SL-10 (Stryker) or a Headway Duo (MicroVention) microcatheter was navigated over a Synchro-14 or -10 soft microwire (Stryker). After appropriate superselective microangiography to verify the catheter position and the collateral anastomoses, embolization was performed using Contour Polyvinyl Alcohol (PVA) particles (Boston Scientific) diluted in 100% contrast. Embolization began with 45- to 150-μm PVA particles until remarkable stagnation was noted in the tumor bed. Subsequent embolization was then performed with 150- to 250-μm PVA particles, which were sometimes followed with deployment of detachable coils in the main trunk. At the end of the embolization, a full angiographic evaluation was obtained to demonstrate the possible presence of collateral flow and an accurate estimation of devascularization. The patient was then extubated and kept in the neurointensive care unit overnight for neurologic observation.

RESULTS

Among 155 tumor embolization cases performed from 2010 and 2020, we identified 14 patients in whom embolization was performed through the meningohypophyseal ($n = 13$) or inferolateral ($n = 4$) trunk. Three patients had embolization through both trunks (Online Supplemental Data).

In the included patients, on average, 79% (range, 50%–95%) of the tumor was embolized. No morbidity or mortality postembolization was observed in this subgroup of patients. The mean estimated blood loss during surgical resection was 395 mL (range, 200–750 mL). None of the patients required a transfusion, and the average operative time was 7.3 hours.

Case Examples

In a patient with a large, right sphenoid wing meningioma with encasement of the ICA (Fig 1), a right ICA injection demonstrated the supply to the tumor from an enlarged meningohypophyseal trunk. After selective embolization through the meningohypophyseal trunks and indirectly from the middle meningeal artery, the final right common carotid artery injection demonstrated interval 90% tumor embolization. The patient woke up from the procedure

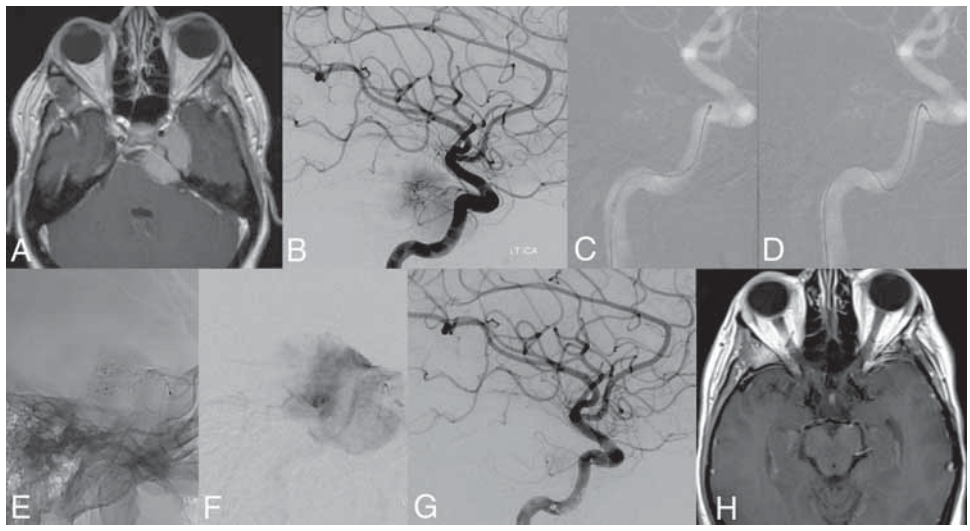

FIG 2. A patient with a Meckel cave meningioma also with involvement of the cavernous sinus visible on a T1-weighted, axial, postcontrast image (*A*). Right ICA DSA injection in lateral view (*B*) demonstrates the supply to the tumor from an enlarged inferolateral trunk from the left ICA. Inferolateral trunk catheterization is performed with a Headway Duo over a Synchro-14 microguidewire (*C* and *D*). MICRO DSA performed through a microcatheter on a lateral view (unsubtracted, *E*, and subtracted, *F*) better demonstrates the selective supply to the meningioma. Final lateral view ICA injection (*G*) demonstrates marked interval reduction of blush in the region of the tumor. Complete gross resection of the meningioma is visible on a T1-weighted, axial, postcontrast image (*H*). LT indicates left.

at baseline and underwent an operation the following day with estimated blood loss of 200 mL without the need for a transfusion with complete gross resection of the meningioma.

In a patient with a Meckel cave meningioma with involvement of the cavernous sinus, an angiogram showed most of the supply arising from the inferolateral trunk from the left ICA, (Fig 2) and the inferolateral trunk arising from the lateral inferior aspect of the horizontal cavernous ICA. Catheterization was performed with a Headway Duo over a Synchro-14 microguidewire. MICRO DSA performed through a microcatheter better demonstrated the selective supply to the meningioma. It is important to have runoff in the vessel and not aim for a wedged position if embolization with particles is planned. At the end of the embolization, coils are placed at the proximal inferolateral trunk with the final angiography demonstrating marked interval reduction of blush in the region of the tumor. The patient woke up from the procedure at baseline and underwent an operation the following day with an estimated blood loss of 250 mL without the need for a transfusion, with complete gross resection of the meningioma.

Additional cases are illustrated in detail in Figs 3 and 4 and the Online Supplemental Data.

DISCUSSION

Preoperative tumor embolization is typically performed to facilitate surgical resection. Significant devascularization not only reduces surgical blood loss but also induces necrosis within the tumor, which makes the tumor more amenable to aspiration. Meningiomas and other extra-axial brain tumors that arise from the dura receive most of their blood supply from the dural feeders. Surgical control of the dural supply is straightforward for a convexity meningioma, in which the dural base is encountered and circumferentially disconnected before tumor resection. The dural base of skull base tumors, however, is typically deep within the surgical view; therefore, tumor resection must be performed before the dural arterial supply can be surgically controlled. In these cases, preoperative embolization can provide that dural arterial control. Skull base tumors such as medial sphenoid wing and clival or clinoidal meningiomas often receive dural supply from the meningohypophyseal and/or inferolateral trunk and may benefit most from embolization.[9] We present a series of 14 patients with skull base tumors who underwent preoperative embolization through the meningohypophyseal and/or inferolateral trunks. We demonstrate that this procedure can be both safe and highly effective in terms of tumor devascularization. To our knowledge, this is the largest such series published to date.

The meningohypophyseal trunk is classically described as arising from the posterior vertical cavernous segment of the ICA and, as the name indicates, it gives off supply to the pituitary gland and the meninges. The inferolateral trunk instead is usually a pure meningeal vessel, arising from the lateral horizontal cavernous ICA. The supply to the meninges of the medial middle cranial fossa has been described in detail elsewhere.[17-19] Briefly, feeders may come off the meningohypophyseal trunk, inferolateral trunk, and middle meningeal artery and the accessory meningeal, recurrent ophthalmic, and ascending pharyngeal arteries. The amount of territory supplied by each of these branches is extremely variable from human to human, confirming the extreme importance of thorough angiographic detailed evaluation before performing skull base tumor embolization.

Several prior series of tumor embolization through the meningohypophyseal and/or inferolateral trunk have also reported excellent outcomes: Robinson et al[14] with 5 patients and no complications; Hirohata et al[15] with 7 patients and no complications; and Waldron et al[16] with 10 patients and no complications.

The reluctance of performing embolization through the meningohypophyseal and inferolateral trunks arises from 2 concerns: First, there is a risk of reflux of embolic material into the parent

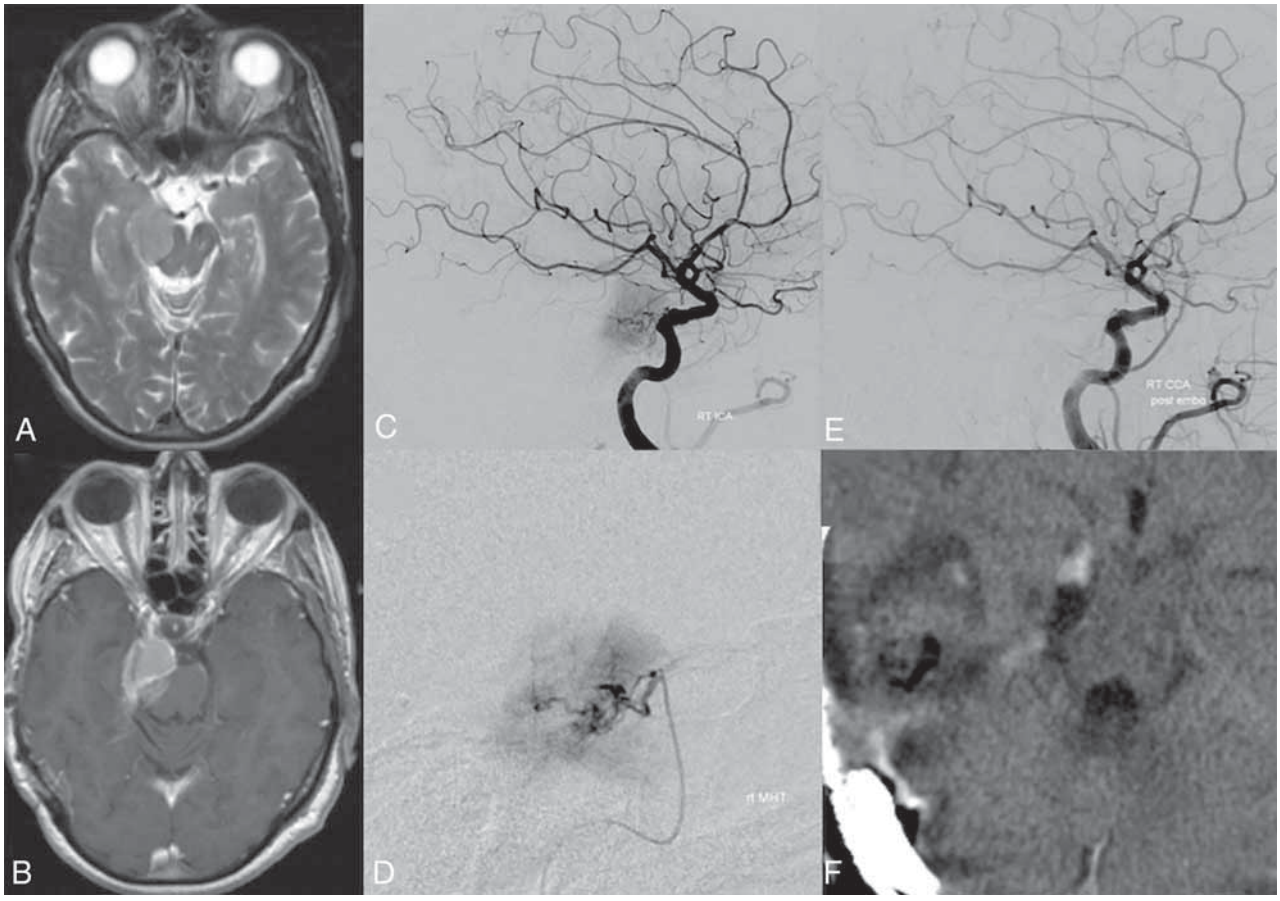

FIG 3. A patient with a right petroclival meningioma as shown on MR imaging T2 (*A*) and postcontrast T1 (*B*). A right ICA injection lateral view DSA (*C*) demonstrates a large blush supplied by the meningohypophyseal trunk. Selective catheterization and DSA (*D*) with a Marathon microcatheter (Medtronic), followed by embolization with 45- to 150- and 150- to 250-μm particles. Final right ICA injection, lateral view DSA (*E*) demonstrates resolution of the previously seen blush. Final CT (*F*) postsurgical resection demonstrates complete excision with a small amount of retraction injury in the right temporal lobe.

ICA, which can lead to embolic infarcts within the ICA territory. Second, there is a risk of causing ischemia to the cranial nerves commonly supplied by these vessels.[13] On the basis of this experience and others, however, it seems that reluctance to embolize through the meningohypophyseal and inferolateral trunks is dogmatic and unjustified, and safe embolization can be achieved if the following principles are followed.

Thorough Anatomic Evaluation

The main risk of tumor embolization is inadvertent embolization into the cerebral circulation. The dural arteries that supply most skull base tumors form a rich anastomotic network, creating potential, dangerous collaterals to the ICA, ophthalmic artery, and vertebrobasilar circulation. It is, therefore, important to perform a thorough investigation of the arterial supply to a tumor, which typically includes injections of the bilateral ICAs, external carotid arteries, and at least 1 vertebral artery. Most important, skull base tumors may also receive significant pial supply that should be well-characterized. It is also important after the embolization to evaluate possible residuals related to reorganization of the tumor vascular supply induced by embolization and to properly assess the extent of the embolization achieved.[4,6,20-22]

Catheter Positioning

Catheterization of the meningohypophyseal trunk is typically easier than of the inferolateral trunk. The meningohypophyseal trunk arises from the posterior genu of the cavernous ICA and courses posteriorly. Conversely, the inferolateral trunk arises from the lateral aspect of the horizontal segment of the cavernous ICA and curves posteriorly, forming a double curve. With the use of particles, we believe it is safest to obtain a nonwedged position with the catheter. While wedging provides flow arrest that can promote penetration of liquid embolics, a nonwedged position allows persistent flow through the target vessel. This can help carry particles distally as close as possible to the capillary bed.

Choice of Embolic Material

Several different options exist for embolic materials in tumor embolization. Particles include PVA (Contour) microspheres (Embosphere Microspheres; Merit Medical) and absorbable gelatin powder (Gelfoam; Pfizer). Liquid embolics include *n*-butyl cyanoacrylate (Trufill; Cerenovus) and ethylene-vinyl alcohol copolymer (Onyx; Medtronic). Finally, coils can also be used for proximal embolization. In our experience, particles provide the safest and most effective means of tumor embolization for skull

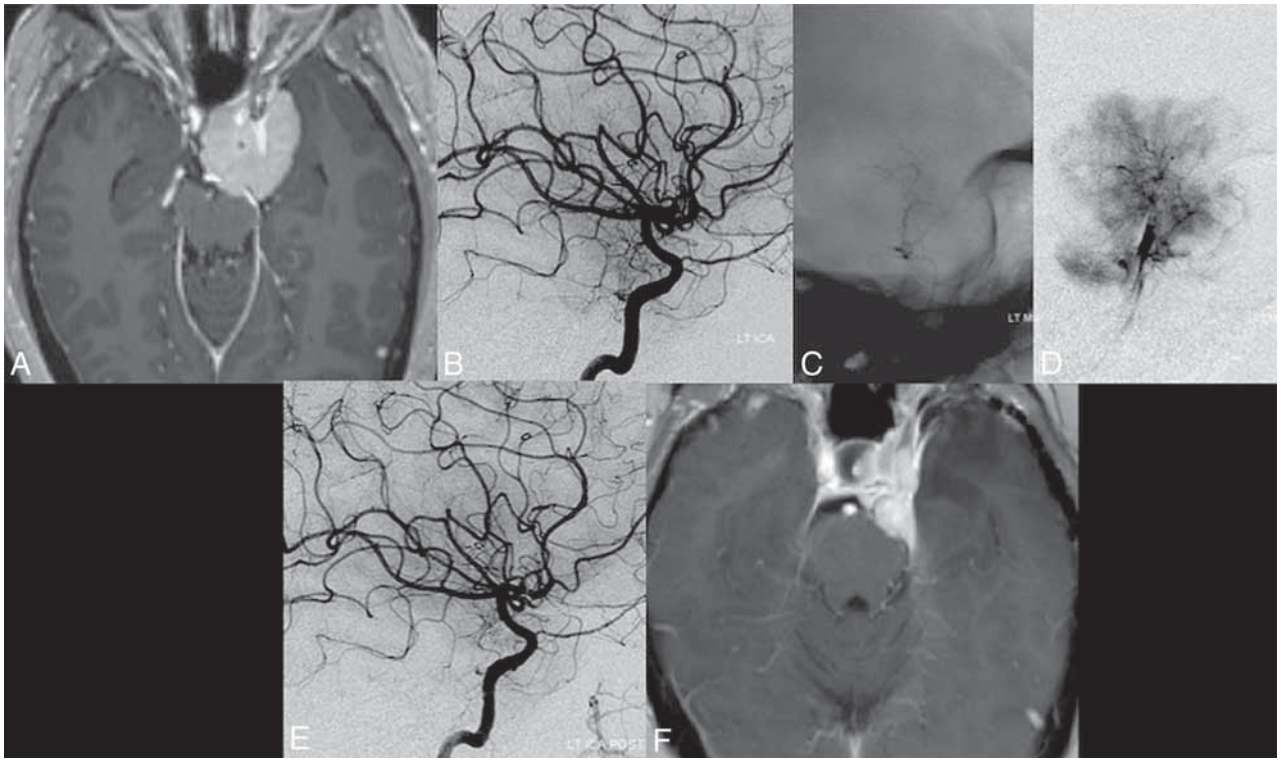

FIG 4. A patient with a left anterior clinoid meningioma as shown on postcontrast T1 MR imaging (*A*). A left ICA injection, lateral view DSA (*B*), demonstrates a large blush supplied by the meningohypophyseal trunk. Selective catheterization with unsubtracted (*C*) and subtracted (*D*) views with a Marathon microcatheter, followed by embolization with 45- to 150-μm particles. A final left ICA injection, lateral view DSA (*E*) demonstrates 60% embolization of the tumor. A final MR imaging T1 postcontrast (*F*) postsurgical resection demonstrates partial excision of the mass.

base tumors. Small particles (ie, PVA, 45–150 μm; Embosphere Microspheres, 40–120 μm) can penetrate the vascular bed of a tumor up to the distal arterioles. Progressively larger particles then fill the more proximal arterioles. By this method, the tumor is devascularized from the distal bed outward. While liquid embolics can similarly penetrate deep into a tumor, they can also permeate the vasa nervorum of cranial nerves and can more quickly reflux into unwanted territories.

As Low as Reasonably Achievable Principles

Embolization of large skull base tumors can be a time-consuming process with long fluoroscopy times. This can, therefore, risk radiation injury such as hair loss or skin burns. It is, therefore, important to follow as low as reasonably achievable principles. Collimation, reduced roadmap fluoroscopic rates (ie, 4 pulses per second), use of only a single plane at a time, and frequent changes of the fluoroscopic angles can help minimize the risk of radiation injury.[21]

Embolization

Paramount to safe embolization is preventing reflux into the ICA or any other potentially dangerous collaterals. The operator should define acceptable limits for reflux. This can be aided by reference images demonstrating the relevant anatomy or marking limits on the roadmap screen with a washable marker. We recommend significantly diluting particles to prevent clumping, which can inadvertently occlude the arterioles before effective tumor devascularization.[21,22] Repeat dilution is often required to maintain sufficient dilution. The injections should be brief, gentle, and pulsatile, giving time between injections for the particles to flow distally.

Postembolization Anatomic Evaluation

Embolization can lead to reorganization of the tumor vascular supply. We, therefore, recommend thoroughly evaluating the relevant feeders after embolization for additional embolic targets and to properly assess the extent of embolization.

Balancing Risks of Embolization versus Surgical Resection

Surgery and embolization must be coordinated toward a shared goal. The ultimate purpose is not just to control blood flow but to minimize the overall morbidity and maximize the efficiency of surgical resection. A conservative or inefficient embolization is a low risk–but-unhelpful procedure. Conversely, a thoroughly aggressive embolization may be more hazardous but ultimately more helpful to the surgeon. The embolization and resection should be viewed by the patient and treating physicians as a single combined treatment with shared risks and benefits. Also, a tumor that benefits the most from embolization is one in which the supplying vessels come from its deep part away from the surgical view, in the "dark side" of the tumor; thus, a convexity meningioma is the least challenging with respect to devascularizing its blood supply because the dural blood supply is encountered as soon as the cranial flap is elevated and the dura overlying the tumor is exposed; medially located skull base tumors instead, such as tuberculum sellae, medial

sphenoid wing, or clinoid meningioma, often supplied by ICA branches of the meningohypophyseal and inferolateral trunks, are ones that may benefit the most from embolization,[9] unless they have significant pial blood supply as well.

We did not encounter complications such as neuropathy or intratumoral hemorrhage in our series; however, the association between the use of a small amount of PVA and hemorrhage has been previously reported.[23] We agree with other authors[24] who believe that the finalization of the tumor embolization with larger particles and possibly with coils, as was routinely done in the current series, may mitigate this risk.

We acknowledge several limitations to this study. First, it is retrospective in nature, which limits the available treatment and outcome details. Second, it is difficult to identify a metric that directly proves the utility of preoperative embolization. On an institutional basis, the best measure of utility is often the surgeon's subjective opinion of the tumor resection after embolization. Blood loss can be a good surrogate for effective tumor devascularization, though estimated blood loss during an operation is a notoriously inaccurate measure.

CONCLUSIONS

Preoperative embolization of skull base tumors through the meningohypophyseal and inferolateral trunks can be performed safely and with high efficacy if certain procedural principles are followed.

Disclosure forms provided by the authors are available with the full text and PDF of this article at www.ajnr.org.

REFERENCES

1. Manelfe C, Guiraud B, David J, et al. **Embolization by catheterization of intracranial meningiomas [in French].** *Rev Neurol (Paris)* 1973;128:339–51 Medline
2. Richter HP, Schachenmayr W. **Preoperative embolization of intracranial meningiomas.** *Neurosurgery* 1983;13:261–68 CrossRef Medline
3. Teasdale E, Patterson J, McLellan D, et al. **Subselective preoperative embolization for meningiomas: a radiological and pathological assessment.** *J Neurosurg* 1984;60:506–11 CrossRef Medline
4. Manelfe C, Lasjaunias P, Ruscalleda J. **Preoperative embolization of intracranial meningiomas.** *AJNR Am J Neuroradiol* 1986;7:963–72 Medline
5. Dean BL, Flom RA, Wallace RC, et al. **Efficacy of endovascular treatment of meningiomas: evaluation with matched samples.** *AJNR Am J Neuroradiol* 1994;15:1675–80 Medline
6. Nelson PK, Setton A, Choi IS, et al. **Current status of interventional neuroradiology in the management of meningiomas.** *Neurosurg Clin N Am* 1994;5:235–59 CrossRef Medline
7. Manaka H, Sakata K, Tatezuki J, et al. **Safety and efficacy of preoperative embolization in patients with meningioma.** *J Neurol Surg B Skull Base* 2018;79:S328–33 CrossRef Medline
8. Gruber A, Killer M, Mazal P, et al. **Preoperative embolization of intracranial meningiomas: a 17-years single center experience.** *Minim Invasive Neurosurg* 2000;43:18–29 CrossRef Medline
9. Chen L, Li DH, Lu YH, et al. **Preoperative embolization versus direct surgery of meningiomas: a meta-analysis.** *World Neurosurg* 2019;128:62–68 CrossRef Medline
10. Raper DM, Starke RM, Henderson F Jr, et al. **Preoperative embolization of intracranial meningiomas: efficacy, technical considerations, and complications.** *AJNR Am J Neuroradiol* 2014;35:1798–804 CrossRef Medline
11. Suzuki K, Nagaishi M, Matsumoto Y, et al. **Preoperative embolization for skull base meningiomas.** *J Neurol Surg B Skull Base* 2017;78:308–14 CrossRef Medline
12. Macpherson P. **The value of pre-operative embolisation of meningioma estimated subjectively and objectively.** *Neuroradiology* 1991;33:334–37 CrossRef Medline
13. Ilyas A, Przybylowski C, Chen CJ, et al. **Preoperative embolization of skull base meningiomas: a systematic review.** *J Clin Neurosci* 2019;59:259–64 CrossRef Medline
14. Robinson DH, Song JK, Eskridge JM. **Embolization of meningohypophyseal and inferolateral branches of the cavernous internal carotid artery.** *AJNR Am J Neuroradiol* 1999;20:1061–67 Medline
15. Hirohata M, Abe T, Morimitsu H, et al. **Preoperative selective internal carotid artery dural branch embolisation for petroclival meningiomas.** *Neuroradiology* 2003;45:656–60 CrossRef Medline
16. Waldron JS, Sughrue ME, Hetts SW, et al. **Embolization of skull base meningiomas and feeding vessels arising from the internal carotid circulation.** *Neurosurgery* 2011;68:162–66; discussion 69 CrossRef Medline
17. Geibprasert S, Pongpech S, Armstrong D, et al. **Dangerous extracranial-intracranial anastomoses and supply to the cranial nerves: vessels the neurointerventionalist needs to know.** *AJNR Am J Neuroradiol* 2009;30:1459–68 CrossRef Medline
18. Shapiro M. **Middle Meningeal Artery.** *Neuroangio.org* 2022. http://neuroangio.org/anatomy-and-variants/middle-meningeal-artery. Accessed July 12, 2022
19. Shapiro M. **Ascending Pharyngeal Artery.** *Neuroangio.org* 2022; http://neuroangio.org/anatomy-and-variants/ascending-pharyngeal-artery/2020. Accessed July 12, 2022
20. Jo KI, Kim B, Cha MJ, et al. **Safety and efficacy of medium-sized particle embolisation for skull-base meningioma.** *Clin Radiol* 2016;71:335–40 CrossRef Medline
21. Thierry-Chef I, Simon SL, Miller DL. **Radiation dose and cancer risk among pediatric patients undergoing interventional neuroradiology procedures.** *Pediatr Radiol* 2006;36(Suppl 2):159–62 CrossRef Medline
22. Wakhloo AK, Juengling FD, Van Velthoven V, et al. **Extended preoperative polyvinyl alcohol microembolization of intracranial meningiomas: assessment of two embolization techniques.** *AJNR Am J Neuroradiol* 1993;14:571–82 Medline
23. Carli DF, Sluzewski M, Beute GN, et al. **Complications of particle embolization of meningiomas: frequency, risk factors, and outcome.** *AJNR Am J Neuroradiol* 2010;31:152–54 CrossRef Medline
24. Kallmes DF, Evans AJ, Kaptain GJ, et al. **Hemorrhagic complications in embolization of a meningioma: case report and review of the literature.** *Neuroradiolog* 1997;39:877–80 CrossRef Medline

Emergency Department Visits for Chronic Subdural Hematomas within 30 Days after Surgical Evacuation with and without Middle Meningeal Artery Embolization

J.S. Catapano, L. Scherschinski, K. Rumalla, V.M. Srinivasan, T.S. Cole, J.F. Baranoski, M.T. Lawton, A.P. Jadhav, A.F. Ducruet, and F.C. Albuquerque

ABSTRACT

BACKGROUND AND PURPOSE: Middle meningeal artery embolization after surgical evacuation of a chronic subdural hematomas is associated with fewer treatment failures than surgical evacuation. We compared emergency department visits within 30 days for patients with chronic subdural hematomas with and without adjunctive middle meningeal artery embolization.

MATERIALS AND METHODS: All cases of chronic subdural hematoma treated from January 1, 2018, through December 31, 2020, were retrospectively reviewed. Treatment was classified as surgery only or surgery combined with middle meningeal artery embolization. The primary outcome was 30-day emergency department presentation and readmission.

RESULTS: Of 137 patients who met the study criteria, 28 (20%) underwent surgery combined with middle meningeal artery embolization. Of these 28 patients, 15 (54%) underwent planned middle meningeal artery embolization and 13 (46%) underwent embolization after surgical failure. The mean chronic subdural hematoma size at presentation in the group with surgery only ($n = 109$, 20.5 [SD, 6.9] mm) was comparable with that in the combined group ($n = 28$, 18.7 [SD, 4.5] mm; $P = .16$). A significantly higher percentage of the surgery-only group presented to the emergency department within 30 days compared with the combined group (32 of 109 [29%] versus 2 of 28 [7%] patients; $P = .02$). No significant difference was found with respect to readmission (16 [15%] versus 1 [4%] patient; $P = .11$). Nine patients (8%) in the surgery-only group were readmitted for significant reaccumulation or residual subdural hematoma compared with only 1 patient (4%) in the combined group ($P = .40$).

CONCLUSIONS: Surgical evacuation combined with middle meningeal artery embolization in patients with chronic subdural hematoma is associated with fewer 30-day emergency department visits compared with surgery alone.

ABBREVIATIONS: cSDH = chronic subdural hematoma; ED = emergency department; GCS = Glasgow Coma Scale; MMA = middle meningeal artery; SDH = subdural hematoma

Chronic subdural hematoma (cSDH) is a common neurosurgical condition that is most prevalent among elderly patients and can be challenging to treat.[1-6] Surgical evacuation using burr- hole irrigation or craniotomy is the preferred treatment option for patients with primary or recurrent subdural hematoma (SDH) who present with symptomatic brain compression.[1-3,7] However, these procedures are associated with recurrence rates as high as 28%, with nearly one-tenth of patients requiring re-operation within 30–60 days.[3,7,8] Conservative management may be indicated in patients with small or asymptomatic SDHs, but many cSDHs may eventually require surgical evacuation.[9-11] Middle meningeal artery (MMA) embolization has recently been proposed as an alternative or adjunct to surgery for primary or recurrent cSDHs, and it has been associated with a decreased risk of treatment failure.[3,9,12]

Although several case series have outlined the potential benefits of MMA embolization during the past few years, no studies have used standard outcome measures to examine these findings. In this single-center study conducted during a 3-year study period, we compared the rates of emergency department (ED) use and readmission within 30 days for patients with cSDHs who underwent surgical evacuation with and without adjunctive MMA embolization.

MATERIALS AND METHODS

The medical records of all patients who presented with a cSDH to a single quaternary center from January 1, 2018, through December 31, 2020, were retrospectively reviewed. The study was approved by the institutional review board at St. Joseph's Hospital and Medical Center in Phoenix, Arizona, and informed consent was waived because of the low risk to patients. The endovascular treatment

Received February 10, 2022; accepted after revision May 16.

From the Department of Neurosurgery, Barrow Neurological Institute, St. Joseph's Hospital and Medical Center, Phoenix, Arizona.

Please address correspondence to Felipe C. Albuquerque, MD, c/o Neuroscience Publications, Barrow Neurological Institute, St. Joseph's Hospital and Medical Center, 350 W Thomas Rd, Phoenix, AZ 85013; e-mail: Neuropub@barrowneuro.org
http://dx.doi.org/10.3174/ajnr.A7572

Table 1: Characteristics of 137 patients with cSDH who underwent surgery only versus surgery combined with MMA embolization[a]

Characteristic	Surgery-Only Group (n = 109)	Combined Group (n = 28)	P Value
Age (mean) (SD) (yr)	70 (12.8)	71 (10.2)	.86
Sex			.94
Male	81 (74)	21 (75)	
Female	28 (26)	7 (25)	
GCS score (mean) (SD)			
At presentation	14 (2.2)	14 (2.6)	.77
At discharge	14 (2.1)	14 (2.3)	.70
Comorbid condition			
Hypertension	54 (50)	16 (57)	.47
Diabetes mellitus	27 (25)	8 (29)	.68
CAD	36 (33)	12 (43)	.33
Liver disease	3 (3)	1 (4)	.82
Alcohol abuse	14 (13)	1 (4)	.16
CVA	10 (9)	2 (7)	.73
Coagulopathy	4 (4)	3 (11)	.13
Previous trauma	78 (72)	17 (61)	.27
Length of hospital stay (mean) (SD) (day)	9.9 (6.3)	8.6 (5.5)	.51
Disposition home	60 (55)	18 (64)	.38

Note:—CAD indicates coronary artery disease; CVA, cerebrovascular accident.
[a] Data are presented as No. (%) unless otherwise indicated.

Table 2: ED visits and readmissions within 30 days for patients with cSDH who underwent surgery only versus surgery combined with MMA embolization

Characteristic	Surgery-Only Group, No. (%) (n = 109)	Combined Group, No. (%) (n = 28)	P Value
ED visits	32 (29)	2 (7)	.02
Readmissions	16 (15)	1 (4)	.11

database was reviewed to abstract data on age, sex, Glasgow Coma Scale (GCS) scores at admission and discharge, comorbid conditions, and previous trauma. Patients in this cohort were assigned to 2 groups: surgical evacuation only or surgery combined with MMA embolization. The group with surgery only included patients who presented during the first 2 years of the study, whereas the surgery and MMA embolization group (the combined group) included patients who received the combined treatment during the entire 3-year study period. The medical records of patients in the surgery-only and combined groups were analyzed for ED visits and readmission within 30 days as primary outcomes.

Statistical analysis was performed using SPSS Statistics for Windows, Version 26.0 (IBM). Comparisons of ED visits and readmissions within 30 days were performed using an independent samples t test. The level of significance was set at $P < .05$. Patient data and outcomes are expressed as mean (SD) or as frequency (percentage) or both.

RESULTS

The total study cohort consisted of 137 patients, of whom 109 (80%) underwent surgery only and 28 (20%) underwent combined surgery and MMA embolization. Of the 28 patients in the combined group, 15 (54%) underwent planned elective MMA embolization and 13 (46%) underwent unplanned MMA embolization after surgical failure. No significant differences were found in age or sex between the 2 groups (Table 1). The mean age was 70 (SD, 12.8) years in the surgery-only group and 71 (SD, 10.2) years in the combined group. Most patients in both groups were men (81 of 109 [74%] in the surgery-only group and 21 of 28 [75%] in the combined group). Both groups of patients had a mean GCS score of 14 at both admission and discharge. No significant differences were found in comorbid conditions between the 2 groups. Comorbid conditions for the 2 groups are presented in Table 1.

The mean size of the cSDHs at presentation was not significantly different in the surgery-only group (20.5 [SD, 6.9] mm) compared with the combined group (18.7 [SD, 4.5] mm; $P = .16$). The overall rate of ED visits within 30 days for the entire cohort was 24% (33 of 137 patients). This rate was significantly higher in patients who underwent surgery only (29%, 32 of 109) compared with those who underwent MMA embolization with surgery (7%, 2 of 28; $P = .02$) (Table 2).

The overall rate of readmission within 30 days was 12% (17/137 patients). The readmission rate was higher in the surgery only group (15%, 16/109) compared with the combined group (4%, 1/28), but this difference could not be compared statistically because of the small number of ED presentations in each group and because of the small sample size of the combined group. Most readmissions (59%, 10/17) were due to reaccumulation or residual cSDH. Only 1 patient who underwent both surgery and MMA embolization was readmitted for reaccumulation or residual cSDH compared with 9 in the surgery-only group. In the 10 patients with reaccumulated/residual SDH, the mean cSDH diameter was 12.3 (SD, 2.2) mm.

DISCUSSION

MMA embolization has emerged as a promising minimally invasive procedure to treat primary and refractory cSDH.[3,8,9,12-15] Compared with surgery alone, it has been associated with fewer treatment failures and a reduced rate of hematoma reaccumulation in patients with cSDH.[9,12] To examine this association, we compared the 30-day ED use and readmission rates among patients with surgery only with those among patients with surgery combined with MMA embolization during a 3-year study period at a single institution. We found significantly less ED use in the combined treatment group than in the surgery-only group ($P = .02$).

In this era of continually increasing health care costs, institutions are under pressure to identify ways to reduce expenditures while maintaining and improving the quality of care. Returns to the hospital within 30 days can be devastating for both patients and the health care system. Federal policies and insurance payors

even penalize hospitals for unplanned readmissions. To our knowledge, this study is the first to demonstrate that MMA embolization for SDHs decreases the likelihood of ED visits and hospital readmissions. Our results indicate that the recurrence of cSDH is the most common reason for readmission. However, only 1 patient who underwent MMA embolization was readmitted for recurrence. These findings suggest that MMA embolization may reduce hospital readmissions and their associated cost to both the patient and the health care system. A previous analysis of the National Surgical Quality Improvement Program database similarly found that recurrent SDH was the most common reason for hospital readmission within 30 days for patients who had undergone cSDH evacuation.[16]

Previous estimates of readmission rates after treatment of cSDH are limited. The lack of a specific billing code for cSDH has hindered analyses of nationwide administrative databases. Lakomkin et al[16] reported a 30-day readmission rate of 7.7% (45 of 585) in patients who underwent surgery for SDH. However, several limitations minimize the generalizability of this and other reported readmission rates. Their study was conducted using an administrative billing database, and cSDH was defined by International Classification of Disease, Ninth Revision (https://www.cdc.gov/nchs/icd/icd9cm.htm) billing code 432.1 for "nontraumatic" SDH. This code has not been validated against institutional records to accurately detect cSDH. Furthermore, the National Surgical Quality Improvement Program does not have a specific code for burr- hole evacuation, which is the criterion standard surgical approach for evacuating cSDHs. In addition, their readmission rates were calculated without consideration of how many patients died before discharge, possibly leading to further underestimates.

Previous studies have demonstrated the safety and efficacy of MMA embolization for cSDH. A recent meta-analysis and systematic review by Srivatsan et al[2] identified 3 two-arm studies (embolization versus conventional surgery) and 6 single-arm case series. The authors' pooled analysis showed that hematoma recurrence was significantly less common among patients who underwent embolization (2.1%) than among those who underwent conventional surgical treatment (27.7%; $P < .001$). In our study, only 1 of 28 patients who underwent MMA embolization was readmitted for cSDH recurrence, a finding consistent with that of Srivatsan et al. In addition to the outstanding efficacy of MMA embolization for cSDHs, the procedure has been found to be relatively safe, largely because of the recent advent of newer endovascular techniques (eg, transradial access).[17-25]

Limitations to the study include those inherent in all retrospective analyses. Additionally, the study included only 28 patients in the combined group, limiting its power, and the patients were treated at a single institution by multiple neurosurgeons who ultimately decided which patients underwent surgery with no standardized guidelines.

CONCLUSIONS

Our results show that surgical evacuation combined with MMA embolization in patients with cSDH is associated with decreased ED visits within 30 days compared with surgery alone. Most readmissions after cSDH treatment were due to hematoma recurrences, which were markedly decreased in patients who underwent MMA embolization. These findings warrant the design of future prospective, large-cohort studies to substantiate our data and expand on this preliminary research.

ACKNOWLEDGMENTS

The authors thank the Neuroscience Publications staff at Barrow Neurological Institute for assistance with manuscript preparation. The authors acknowledge Candice L. Nguyen, BS, and Caleb Rutledge, MD, for their assistance.

Disclosure forms provided by the authors are available with the full text and PDF of this article at www.ajnr.org.

REFERENCES

1. Catapano JS, Nguyen CL, Wakim AA, et al. **Middle meningeal artery embolization for chronic subdural hematoma.** *Front Neurol* 2020;11:557233 CrossRef Medline
2. Srivatsan A, Mohanty A, Nascimento FA, et al. **Middle meningeal artery embolization for chronic subdural hematoma: meta-analysis and systematic review.** *World Neurosurg* 2019;122:613–19 CrossRef Medline
3. Link TW, Boddu S, Paine SM, et al. **Middle meningeal artery embolization for chronic subdural hematoma: a series of 60 cases.** *Neurosurgery* 2019;85:801–07 CrossRef Medline
4. Balser D, Farooq S, Mehmood T, et al. **Actual and projected incidence rates for chronic subdural hematomas in United States Veterans Administration and civilian populations.** *J Neurosurg* 2015;123:1209–15 CrossRef Medline
5. Foreman P, Goren O, Griessenauer CJ, et al. **Middle meningeal artery embolization for chronic subdural hematomas: cautious optimism for a challenging pathology.** *World Neurosurg* 2019;126:528–29 CrossRef Medline
6. Miranda LB, Braxton E, Hobbs J, et al. **Chronic subdural hematoma in the elderly: not a benign disease.** *J Neurosurg* 2011;114:72–76 CrossRef Medline
7. Mehta V, Harward SC, Sankey EW, et al. **Evidence based diagnosis and management of chronic subdural hematoma: a review of the literature.** *J Clin Neurosci* 2018;50:7–15 CrossRef Medline
8. Catapano JS, Ducruet AF, Nguyen CL, et al. **Middle meningeal artery embolization for chronic subdural hematoma: an institutional technical analysis.** *J Neurointerv Surg* 2021;13:657–60 CrossRef Medline
9. Catapano JS, Ducruet AF, Nguyen CL, et al. **A propensity-adjusted comparison of middle meningeal artery embolization versus conventional therapy for chronic subdural hematomas.** *J Neurosurg* 2021 Feb 26. [Epub ahead of print] CrossRef Medline
10. Chan DY, Chan DT, Sun TF, et al. **The use of atorvastatin for chronic subdural haematoma: a retrospective cohort comparison study.** *Br J Neurosurg* 2017;31:72–77 CrossRef Medline
11. Jiang R, Zhao S, Wang R, et al. **Safety and efficacy of atorvastatin for chronic subdural hematoma in Chinese patients: a randomized clinical trial.** *JAMA Neurol* 2018;75:1338–46 CrossRef Medline
12. Ban SP, Hwang G, Byoun HS, et al. **Middle meningeal artery embolization for chronic subdural hematoma.** *Radiology* 2018;286:992–99 CrossRef Medline
13. Shapiro M, Walker M, Carroll KT, et al. **Neuroanatomy of cranial dural vessels: implications for subdural hematoma embolization.** *J Neurointerv Surg* 2021;13:471–77 CrossRef Medline
14. Rajah GB, Tso MK, Dossani R, et al. **Transradial embolization of the left middle meningeal artery and accessory middle meningeal artery for treatment of subacute-chronic subdural hematoma.** *J Neurointerv Surg* 2020;12:436 CrossRef Medline
15. Fiorella D, Hirsch JA, Arthur AS. **Embolization of the middle meningeal artery for the treatment of chronic subdural hematoma: considerations for pragmatic trial design.** *J Neurointerv Surg* 2021;13:295–97 CrossRef Medline

16. Lakomkin N, Graffeo CS, Hadjipanayis CG. **Specific causes and predictors of readmissions following acute and chronic subdural hematoma evacuation.** *J Clin Neurosci* 2020;75:35–39 CrossRef Medline
17. Majmundar N, Wilkinson DA, Catapano JS, et al. **Reaccessing an occluded radial artery for neuroendovascular procedures: techniques and complication avoidance.** *J Neurointerv Surg* 2021;13:942–45 CrossRef Medline
18. Luther E, Chen SH, McCarthy DJ, et al. **Implementation of a radial long sheath protocol for radial artery spasm reduces access site conversions in neurointerventions.** *J Neurointerv Surg* 2021;13:547–51 CrossRef Medline
19. Luther E, Burks J, Abecassis IJ, et al. **Navigating radial artery loops in neurointerventions.** *J Neurointerv Surg* 2020;13:1027–31 CrossRef Medline
20. Kuhn AL, de Macedo Rodrigues K, Singh J, et al. **Distal radial access in the anatomical snuffbox for neurointerventions: a feasibility, safety, and proof-of-concept study.** *J Neurointerv Surg* 2020;12:798–801 CrossRef Medline
21. Khan NR, Peterson J, Dornbos Iii D, et al. **Predicting the degree of difficulty of the trans-radial approach in cerebral angiography.** *J Neuronterv Surg* 2021;13:552–58 CrossRef Medline
22. Dossani R, Waqas M, Tso MK, et al. **Navigating a proximal loop in the radial artery and avoiding the recurrent radial artery.** *J Neurointerv Surg* 2020;12:724 CrossRef Medline
23. Catapano JS, Fredrickson VL, Fujii T, et al. **Complications of femoral versus radial access in neuroendovascular procedures with propensity adjustment.** *J Neurointerv Surg* 2020;12:611–15 CrossRef Medline
24. Catapano JS, Ducruet AF, Nguyen CL, et al. **Propensity-adjusted comparative analysis of radial versus femoral access for neurointerventional treatments.** *Neurosurgery* 2021;88:E505–09 CrossRef Medline
25. Catapano JS, Ducruet AF, Koester SW, et al. **Propensity-adjusted cost analysis of radial versus femoral access for neuroendovascular procedures.** *J Neurointerv Surg* 2021;13:752–54 CrossRef Medline

Effect of the Shelving Technique on the Outcome of Embolization in Intracranial Bifurcation Aneurysms

F. Çay and A. Arat

ABSTRACT

BACKGROUND AND PURPOSE: Stent bulging technique has been introduced as a technique that improves the outcome of aneurysm coiling. Our aim was to evaluate the utility of this technique, which involves the intentional herniation of stents into the bifurcation aneurysms during coiling.

MATERIALS AND METHODS: Unruptured bifurcation aneurysms treated by stent-assisted coiling using a single type of low-profile braided (LEO Baby) stent between November 2012 and October 2018 were retrospectively evaluated. The clinical (age and sex) and morphologic characteristics (aneurysm size, neck size, proximal/distal diameters of the stented artery, incorporation of the origins of the side branches to the aneurysm neck, and bifurcation angle) and response to antiplatelet therapy were evaluated.

RESULTS: Sixty-one patients (29 men, 47.5%; mean age, 55.95 [SD, 12.33] years) with 66 aneurysms were included. There were 36 aneurysms in group A (treated with the stent bulging technique) and 30 aneurysms in group B (treated by classic stent-assisted coiling). There was no significant difference in the patient and aneurysm characteristics in the groups except for the larger size and wider neck of the aneurysms in group A ($P = .02$ and $P = .04$, respectively). At the mean follow-up of 27.30 (SD, 17.45) months, there was no significant difference in the complication rate, the occlusion status, and the early and long-term occlusion rates between the groups. The stent bulging technique did not predict total occlusion (Raymond-Roy I) at the final imaging follow-up.

CONCLUSIONS: The stent bulging technique enables the coiling of larger, wide-neck aneurysms; however, we did not observe an added flow-diversion effect with the stent bulging technique compared with conventional stent-assisted coiling. We, therefore, suggest that bifurcation aneurysms should be coiled as densely and as safely as possible using this technique.

ABBREVIATIONS: ACA = anterior cerebral artery; RDPD = regional diameter percentage difference; RR = Raymond-Roy score; SAC = stent-assisted coiling; SBT = stent bulging technique; SCA = superior cerebellar artery

Stent-assisted coiling (SAC) is a safe and effective option in the treatment of wide-neck intracranial aneurysms. The stent provides a scaffold for the neointima formation and prevents coil protrusion into the parent artery. In addition, intracranial stents may result in the development of hemodynamic changes inside the aneurysm, which may lead to further aneurysm occlusion. These hemodynamic changes relate to the type (braided versus laser-cut stents), the number of stents, and the technique of stent deployment.[1,2] In some patients, SAC with a single stent may not provide sufficient neck coverage, and in these cases, dual stent placement in an X or Y configuration may be necessary. Dual stent placement is technically more challenging than basic SAC and is known to be associated with an increased rate of thromboembolic complications.[3-6] The stent bulging technique (SBT, also known as the shelf technique) has been proposed as an alternative to dual stent placement to overcome its drawbacks.[7,8] The compression technique is based on the compaction of a stent at the neck of an aneurysm, which creates a bulge and allegedly results in a higher "flow diversion effect" compared with a "uniform stent" due to the higher metallic ratio at the aneurysm neck in sidewall aneurysms.[1] Some authors have further suggested that the added flow diversion secondary to compaction is also observed in bifurcation aneurysms.[9-12] The aim of this study was to evaluate the utility of the SBT in bifurcation aneurysms by comparing the clinical and imaging outcomes of bifurcation aneurysms that are treated using a single type of stent, the classic SAC versus the SAC with SBT.

Received March 7, 2022; accepted after revision June 4.

From the Department of Radiology (F.Ç., A.A.), Hacettepe University School of Medicine, Ankara, Turkey; and TOBB ETU Medical School Hospital (A.A.), Ankara, Turkey.

This study was supported, in part, by the Scientific Research Projects Coordination Unit of the authors' institution (Hacettepe University, Project No.: 19386).

Please address correspondence to Anıl Arat, MD, Hacettepe University Hospital, Department of Radiology, Sıhhiye 06100 Ankara, Turkey; e-mail: anilarat@hotmail.com

Indicates article with online supplemental data.

http://dx.doi.org/10.3174/ajnr.A7583

MATERIALS AND METHODS

After ethics approval was obtained from the institutional review board, of Hacettepe University, we retrospectively evaluated patients with unruptured intracranial bifurcation aneurysms who underwent SAC that used a single type of low-profile braided stent (LEO Baby stent; Balt Extrusion) between November 2012 and October 2018. Patients with dual stent placement, T-stent placement, half T-stent placement, temporary stent placement, stent placement after balloon remodeling, and telescoping stent placement were excluded from the study. Additionally, patients without follow-up imaging studies were excluded from the angiographic analysis; however, their clinical findings were included in the clinical follow-up data. If the patients had multiple eligible aneurysms that were treated by the same type of stent, all their eligible aneurysms were included in the study. Patients with recurrent or residual aneurysms after a previous SAC or a flow diversion were also excluded from the study. The patient characteristics, including age and sex, and the aneurysm characteristics (aneurysm size, neck size, proximal and distal diameters of the stented artery, incorporation of the origins of the side branches into the aneurysm neck, and bifurcation angle) and the level of on-treatment platelet reactivity (measured by VerifyNow; Accumetrics) were noted. The bifurcation angle was calculated as described in the literature.[13] The aneurysm occlusion status that was based on the Raymond-Roy score (RR) immediately after the procedure and during follow-up, and clinical complications were analyzed. The mRS was used to determine the neurologic status of the patients before the procedure and during the postoperative and follow-up period.

"Recanalization" was defined as the deterioration of the RR during follow-up, whereas "progressive occlusion" was defined as an improvement of the RR during the follow-up. Incorporation of the origins of the side branches into the aneurysm neck and stent compaction were independently assessed by each of the authors, and a consensus was required if discrepancies existed regarding the arterial branch involvement or compaction. For the quantification of the compaction, the regional diameter percentage difference (RDPD) was calculated—that is, the stent diameter was measured at the parent artery (dPA) on the working projection. Then the largest diameter of the deployed stent (dMax) was measured at the aneurysm neck on the same projection. RDPD was calculated as dMax/dPA $\times$100. A receiver operating characteristic curve was calculated, and we noted that when the cutoff value of the RDPD was set at 110% (in other words, if the dMax was, at most, 10% over the diameter of the parent artery we classified the procedure as a "basic SAC" technique), we achieved the best sensitivity and specificity values (97.2% and 96.7%, respectively) for the prediction of compaction as assessed by the operators. Hence stent bulging (compaction) was defined as compression of the braided stent beyond 110% of the diameter of the parent artery. The ranges of the RDPD were from 111.06% to 154.81% for the SBT group and from 87.21% to 109.68% for the basic SAC group.

The aneurysms were divided into groups A and B on the basis of the type of SAC procedure. Group A consisted of aneurysms that were treated with SBT. Group B consisted of aneurysms that were treated with the basic SAC technique. For each group, the imaging data at $\leq$4 months, between 5 and 12 months, and during the long term were evaluated.

General Description of the Interventional Procedure

A written informed consent form was signed by all patients before the procedure. The patients were administered antiplatelet medications (300 mg of aspirin and a thienopyridine, that is, 75 mg of clopidogrel or 10 mg of prasugrel) starting at least 5 days before the procedure. Patients were only treated if they had an adequate response to antiplatelet therapy (P2Y12 reaction units of $\geq$60 and/or percentage inhibition of $>$40%). All procedures were performed by a single surgeon. With the patient under general anesthesia, femoral access was achieved and a 6F guiding sheath was navigated to the target, which was the carotid or vertebral artery. After we inserted the guiding sheath, anticoagulation was started with a bolus injection of 70–100 IU/kg of heparin, followed by a heparin infusion to keep the activated clotting time 2–3 times higher than its baseline value. Then, using a triaxial system, we catheterized the aneurysm sac with a microcatheter for the coil embolization, and a second microcatheter was advanced across the neck of the aneurysm for the stent deployment. Before the detachment of the first coil, a LEO Baby stent was released at approximately 50%–80% of its length across the neck of the aneurysm. The coiling procedure was continued with bare platinum coils. If a coil protrusion into the parent artery was noted, stent bulging was performed by pushing the microcatheter gently forward, while an antegrade push was maintained on the stent delivery wire. The force on the microcatheter was gently withdrawn as the stent was deployed in a bulging fashion during further deployment of the stent (Online Supplemental Data). After we achieved a stable coil mass by placing more coils, the stent was detached from its deployment wire. Following the procedure, the patient's anticoagulation therapy was reversed, and dual antiplatelet therapy was continued for at least 6 months. Thienopyridines were generally discontinued after 6 months, and the patients were asked to stay on 300 mg of aspirin indefinitely.

Follow-up

Immediate postprocedural angiograms were obtained on anterior-posterior, lateral, and working projections to evaluate the occlusion status. Early follow-up MRAs were performed at 1–4 months postoperatively. At 5–12 months postoperatively, the second follow-up with a DSA was performed. After that, long-term follow-up imaging examinations were performed. These follow-up angiograms were reviewed for stent patency, in-stent stenosis, and aneurysm occlusion status.

Data Analysis

The SPSS 20.0 (IBM) program was used for the statistical analysis. Continuous data are presented as the mean (SD), and categoric data are presented as percentages. Between the groups, categoric variables were compared using the χ^2 test or Fisher exact test on the basis of the number of variables, and continuous variables were compared using the independent samples t test or Mann-Whitney U test on the basis of the distribution of variables. Statistical significance was set at $P < .05$.

RESULTS

Sixty-one patients with 66 aneurysms were included in our analysis. Two patients did not have imaging follow-up. Both of these patients had uneventful endovascular treatments without clinical

Table 1: Aneurysm locations

Location	Group A (%)	Group B (%)	Total No. (%)
AcomA	9 (25)	11 (36.7)	20 (30.3)
Basilar tip	1 (2.8)		1 (1.5)
Distal ACA	1 (2.8)	1 (3.3)	2 (3)
MCA bifurcation	25 (69.4)	14 (46.7)	39 (59.1)
SCA		2 (6.7)	2 (3)
Terminal ICA		2 (6.7)	2 (3)
	36 (100)	30 (100)	66 (100)

Note:—AcomA indicates anterior communicating artery.

complications and were excluded from the analysis. Twenty-nine (47.5%) patients were men, and 32 (52.5%) were women. The mean age of the patients was 55.95 (SD, 12.33) years. The locations of the aneurysms are listed in Table 1. There were 36 and 30 aneurysms in groups A and B, respectively. The results of the univariate analysis of the patient and aneurysm characteristics between the groups are listed in Table 2. The aneurysms in group A were larger. The mean aneurysm sizes were 7.95 (SD, 2.88) cm and 6.29 (SD, 2.90) cm ($P = .02$) for groups A and B, respectively. The aneurysm necks in group A were also wider, with a mean neck size of 4.68 (SD, 1.67) cm compared with 3.91 (SD, 1.39) cm ($P = .04$) in Group B. The mean age of the patients was older in group A than group B, 58.89 (SD, 10.95) years and 52.43 (SD, 13.14) years, respectively ($P = .03$). There was no statistically significant difference between the groups in terms of sex, proximal and distal diameters of the stented artery, bifurcation angle, response to antiplatelet therapy, follow-up duration, rate of complications, or rate of incorporation of the origins of the side branches to the aneurysm neck (Table 2). The overall mean follow-up duration was 27.30 (SD, 17.45) months. There was only 1 case (1,5%) with recanalization in this cohort, and this patient was in group A. In this patient, the postoperative RR score was I, and it increased to II at the 6-month follow-up and then remained stable until the final follow-up at 36 months.

There were 13 (19.7%) patients with progressive occlusions. Progressive occlusion was noted in 8 (22.2%) of the patients in group A and in 5 (16.7%) in group B. There was no difference between the groups regarding the progressive occlusion rate ($P = .57$). The overall angiographic occlusion rates at the final follow-up (mean follow-up, 27.30 [SD, 17.45] months) included an RR of I in 59 (89.4%) patients, an RR of II in 6 (9.1%) patients, and an RR of III in 1 (1.5%) patient. The patient with an RR score of III in group B was re-treated 3 months after the initial treatment without any complications. The occlusion statuses of the aneurysms immediately after the procedure and during the follow-up based on the patient's group are listed in Table 3. There was no statistically significant difference between the groups regarding the occlusion status. Additionally, there was no statistically significant difference between the groups in the imaging technique used for the follow-up, including in the early- (≤4 months), medium-term (5–12 months), and longer-term (>12 months) evaluations (P values = 1, .24, and .71, respectively). The type of follow-up modalities that were used for each of these time periods is listed in the Online Supplemental Data.

There were 3 (8.3%, based on the aneurysm count) adverse events in group A. One patient had a minor stroke after we changed the patient's antiplatelet regimen from prasugrel and acetylsalicylic acid to only acetylsalicylic acid at 6 months. There was a decline in that patient's baseline mRS from 0 to 2. The final status of the patient is an mRS score of 1. Two patients had stent stenosis without clinical sequelae. Both of these patients had a peculiar stenosis of the parent artery, which was at the transition zone immediately proximal to the bulged segment (Online Supplemental Data). There were 4 (13.3%, based on the aneurysm count) adverse events in group B. Of these 4 complications, 2 patients had minor strokes during the follow-up without deterioration in their final mRS score. One patient had stent stenosis without clinical sequelae. One patient with an MCA bifurcation aneurysm had stenosis of the origin of

Table 2: Univariate analysis of the patient and aneurysm characteristics between the 2 groups

	Group A	Group B	*P* Value
Total No. (%)	36 (100)	30 (100)	
Female sex (No.) (%)	20 (55.6)	15 (50)	.65
Age (mean) (years)	58.89 (SD, 10.95)	52.43 (SD, 13.14)	.03
Aneurysm size (mean) (mm)	7.95 (SD, 2.88)	6.29 (SD, 2.90)	.02
Neck width (mean) (mm)	4.68 (SD, 1.67)	3.91 (SD, 1.39)	.04
Proximal diameter of the stented artery (mean) (mm)	2.64 (SD, 0.37)	2.50 (SD, 0.37)	.13
Distal diameter of the stented artery (mean) (mm)	2.04 (SD, 0.50)	1.89 (SD, 0.40)	.18
Follow-up duration (mean) (mo)	28.28 (SD, 17.47)	26.13 (SD, 17.65)	.62
Bifurcation angle (mean) (IQR)	92.50° (SD, 25.23°) (43.38°)	92.75° (SD, 34.84°) (65.40°)	.97
Platelet inhibition (%) (mean)[a]	79.03 (SD, 17.65)	81.39 (SD, 16.27)	.58
Complications (in-stent restenosis or stroke) (No.) (%)	3 (8.3)	4 (13.3)	.69
Incorporation of the origins of at least 1 of the side branches to the aneurysm neck (No.) (%)	23 (63.9)	19 (63.3)	.96
Incorporation of the origins of both side branches to the aneurysm neck (No.) (%)	12 (33.3)	5 (16.7)	.12
Progressive occlusion (No.) (%)	8 (22.2)	5 (16.7)	.57

Note:—IQR indicates interquartile range.
[a] As measured by the VerifyNow assay.

the upper branch. Additionally, in this patient, a follow-up MR imaging showed enhancing brain lesions that are consistent with a foreign body reaction, as it is described in the literature,[14] and the patient is currently asymptomatic.

The rate of incorporation of at least 1 side branch into the aneurysm neck was similar ($P = .96$, Table 2). However, when both of the side branch origins were incorporated into the aneurysm neck, 12 (group A, 12 of 36, 33.3%) aneurysms were treated with SBT, and although not statistically significant, this rate was higher than that of the 5 (5 of 30, 16.7%) aneurysms in group B that were treated with basic SAC ($P = .12$)—that is, of the 17 aneurysms in which both of the side branches were incorporated into the aneurysm neck, 12 (70.6%) aneurysms were treated with SBT. The results of the univariate analysis of the predictors for total occlusion (RR I) on the final imaging follow-up are shown in Table 4. No significant differences were found between the groups in any of the analyzed variables, including the bulging of the stent.

Table 3: The aneurysm occlusion status during the follow-up[a]

		Group A (%)	Group B (%)	*P* Value
Initial	RR I	24 (66.7)	23 (76.7)	.69
	RR II	11 (30.6)	6 (20)	
	RR III	1 (2.8)	1 (3.3)[b]	
≤4 mo	RR I	18 (72)	17 (89.5)	.08
	RR II	7 (28)	1 (5.3)	
	RR III		1 (5.3)	
5–12 mo	RR I	28 (84.8)	26 (92.9)	.43
	RR II	5 (15.2)	2 (7.1)	
	RR III			
≥12 mo	RR I	26 (83.9)	23 (95.8)	.21
	RR II	5 (16.1)	1 (4.2)	
	RR III			
Final follow-up	RR I	31 (86.1)	28 (93.3)	.14
	RR II	5 (13.9)	1 (3.3)	
	RR III		1 (3.3)	

[a] Aneurysm occlusion is classified according to the Raymond Roy (RR) scale.
[b] The patient was re-treated after 3 months with complete obliteration, so the patient was not included in further angiographic analyses but was included in the final follow-up as a having a residual aneurysm case.

DISCUSSION

The SBT has been described using various terms in the literature, such as the "shelf technique," "barrel technique," "stent bulging," "compressed stent," "intentional stent herniation," "intentional shortening," "compaction," or "wrapped-candy" techniques.[8,11,12,15-19] Although some authors prefer to use the term "compression/compaction" for all types of aneurysms, on the basis of our review of the relevant literature, we think that the terms "compression," "compaction," "shortening," and "wrapped-candy" should be reserved for sidewall aneurysms, whereas "shelf," "herniation," or "bulging" should be used for bifurcation aneurysms. Technically, the maneuvers performed to achieve a compacted stent are similar in both scenarios; however, the intent (the ability to preserve a side branch versus the desire to achieve a better flow diversion) and the immediate angiographic results (bulged stent versus shortened stent) are different.

Supposedly, the SBT may obviate the need for Y-stent placement,[8] and it results in an increased flow diversion compared with a uniformly deployed stent.[9-11] The proponents of this technique suggest that the rate of aneurysm occlusion increases, without a risk of increased complications, due to the enhancement of the flow diversion by the increased metallic coverage (compaction) at the aneurysm neck.[12,19] To date, the studies on SBT have been limited to retrospective, small-scale, single-arm case series that have evaluated the safety and efficacy of the technique.[11] In addition, most publications about SBT relate to a single type of braided stent (LVIS family of stents; MicroVention).[8,11,15,20,21] There is only 1 study[7] and a case report[10] about stent compaction with the LEO Baby stent. With no prior comparative studies

Table 4: Univariate analysis of the predictors for total occlusion on the final imaging follow-up

	Total Occlusion (RR I)	Non-Total Occlusion (RR II and RR III)	*P* Value
Total (No.) (%)	59 (100)	7 (100)	
Female sex (No.) (%)	30 (50.8)	5 (71.4)	.43
Age (mean) (yr)	56.76 (SD, 12.06)	49.14 (SD, 13.42)	.20
Aneurysm size (mean) (mm)	7.07 (SD, 3.02)	8.21 (SD, 2.64)	.26
Neck width (mean) (mm)	4.22 (SD, 1.56)	5.28 (SD, 1.54)	.08
Proximal diameter of the stented artery (mean) (mm)	2.55 (SD, 0.37)	2.77 (SD, 0.39)	.23
Distal diameter of the stented artery (mean) (mm)	1.94 (SD, 0.46)	2.21 (SD, 0.39)	.11
Follow-up duration (mean) (mo)	27.42 (SD, 18.14)	26.29 (SD, 10.79)	.89
Complications (in-stent restenosis or stroke) (No.) (%)	7 (11.9)	0	1
Incorporation of the origins of at least 1 of the side branches to the aneurysm neck (No.) (%)	36 (61)	6 (85.7)	.40
Incorporation of the origins of both side branches to the aneurysm neck (No.) (%)	16 (27.1)	1 (14.3)	.66
Stent bulging (No.) (%)	31 (52.5)	5 (71.4)	.44
Bifurcation angle (mean)	92.38° (SD, 30.06°)	94.54° (SD, 29.08°)	.85
Platelet inhibition (%) (mean)[a]	80.66 (SD, 17.66)	75.43 (SD, 9.14)	.36

[a] As measured by the VerifyNow assay.

between the conventional SAC and the SAC with the SBT, the increased flow diversion and comparable complication rates have remained hypothetic to date.

Our study showed that challenging bifurcation aneurysms, in which the aneurysm neck incorporates both of the origins of the side branches, may also be treatable with conventional SAC (29.4% of such aneurysms in this cohort), yet as a technical option, SBT may provide further benefit to the surgeon but without a significant increase in the procedure-related complications. However, we did not observe a higher aneurysm obliteration rate when the stents were bulged/compacted. This is an unexpected finding given the abundance of clinical and simulation studies that have suggested that there is a possible relationship between the aneurysm obliteration rate and a decreased porosity/increased pore density at the aneurysm neck.[12,17,22-24] One reason for the lack of such an association in our study may be that bifurcation aneurysms do not respond to flow diversion as well as sidewall aneurysms. All of the aneurysms in our study were bifurcation aneurysms. In addition, bulging invariably creates transition zones at the edges of the aneurysm neck that reduce the flow diversion.[25,26] Another reason for the lack of association may be the diminished effect of the flow diversion in coiled bifurcation aneurysms—that is, the strong effect of coiling on the final angiographic result may override the moderate flow diversion that is induced by the woven stent. After all, in approximately 80% of the aneurysms that are coiled without stents, an adequate occlusion is achieved in the long term.[27] Although the flow diversion properties of braided stents have not been definitively proved clinically, the data in the literature have suggested that the recurrence or persistence of aneurysms are further lowered if braided stents are used, which diminishes the rate of an inadequate obliteration (RR III) to approximately 5%–10% of the aneurysms on follow-up.[17,28-31]

Very large cohorts of patients may be required to demonstrate an additional flow diversion by compaction/bulging beyond the diversion that is provided by the coils[32] and the braided stents themselves. In addition, the clinical implications of a significant-yet-small difference in the residual or recurrent aneurysm filling, if it exists, may not be profound. Given the risk of the inability to regain access into the aneurysms once a microcatheter is kicked out of the aneurysm, the higher risk of loss of endovascular access to the aneurysm through the compacted stent (and secondary "undercoiling") needs to be weighed against the potential advantages of flow diversion. We, thus, suggest that aneurysms should be coiled as densely and yet as safely as possible when the SBT is used, and the surgeon should not undercoil the aneurysm expecting an extra flow diversion to complete the aneurysm occlusion.

Our study adds to the literature because it is the only study that has compared the classic SAC with the SBT, and this study defined the exact role of SBT for the first time. Additionally, among similar studies, our study has the longest follow-up duration that has been reported for the SBT. On the other hand, this study has limitations. The limitations of the study are related to the retrospective methodology, the generalizability of the results to other centers, and the use of a single type of braided stent. Because the data collection was retrospective, we categorized the follow-up intervals as $\leq$4 months, 5–12 months, and $>$12 months. Furthermore, compaction was selectively used for aneurysms in which a propensity of coil encroachment onto the parent artery was suggested during the deployment of the first coil—that is, a selection bias inherently occurred by performing SBT in aneurysm cases in which regular SAC was likely to be unsuccessful.

CONCLUSIONS

The final occlusion rates in bifurcation aneurysms that were treated with classic SAC compared with those that were treated with SAC with the SBT were similar. Because SBT was used as a bailout technique for the classic SAC in this study, we infer that in comparison with the classic method, SBT had a favorable effect on the initial success of embolization but without an added influence on the long-term occlusion rate in complex bifurcation aneurysms. The lack of a clear-cut supplementary flow-diversion effect during the follow-up implies a need for dense coiling of aneurysms when the SBT is used because re-entry into a recanalized aneurysm for retreatment may be too cumbersome or impossible.

Disclosure forms provided by the authors are available with the full text and PDF of this article at www.ajnr.org.

REFERENCES

1. Tian Z, Zhang M, Li G, et al. **Hemodynamic differences by increasing Low Profile Visualized Intraluminal Support (LVIS) stent local compaction across intracranial aneurysm orifice.** *Interv Neuroradiol* 2020;26:557–65 CrossRef Medline
2. Wang C, Tian Z, Liu J, et al. **Flow diverter effect of LVIS stent on cerebral aneurysm hemodynamics: a comparison with Enterprise stents and the Pipeline device.** *J Transl Med* 2016;14:1–10 CrossRef Medline
3. Bartolini B, Blanc R, Pistocchi S, et al. **"Y" and "X" stent-assisted coiling of complex and wide-neck intracranial bifurcation aneurysms.** *AJNR Am J Neuroradiol* 2014;35:2153–58 CrossRef Medline
4. Fargen KM, Mocco J, Neal D, et al. **A multicenter study of stent-assisted coiling of cerebral aneurysms with a Y configuration.** *Neurosurgery* 2013;73:466–72 CrossRef Medline
5. Spiotta AM, Lena J, Chaudry MI, et al. **Y-stenting for bifurcation aneurysm coil embolization: what is the risk?** *Stroke Res Treat* 2014;2014:762389 CrossRef Medline
6. Sayin B, Karaman A, Balci S, et al. **Dual stenting with new-generation stents for aneurysm embolization in acute subarachnoid hemorrhage.** *World Neurosurg* 2021;154:e102–08 CrossRef Medline
7. Onay M, Binboga AB, Altay CM. **Analysis of branch artery orifice angulation: feasibility of the shelf technique for the treatment of wide-neck bifurcation aneurysms.** *Interv Neuroradiol* 2021;27:362–71 CrossRef Medline
8. Du EH, Shankar JS. **LVIS Jr 'shelf' technique: an alternative to Y stent-assisted aneurysm coiling.** *J Neurointerv Surg* 2016;8:1256–59 CrossRef Medline
9. Raymond J, Darsaut T, Bing F, et al. **Stent-assisted coiling of bifurcation aneurysms may improve endovascular treatment: a critical evaluation in an experimental model.** *AJNR Am J Neuroradiol* 2013;34:570–76 CrossRef Medline
10. Londhe S, Gupta V, Parthasarathy R, et al. **Blister aneurysm of middle cerebral artery division: stent-assisted coiling using shelfing technique.** *J Clin Interv Radiol ISVIR* 2019;03:126–29 CrossRef
11. Inoue A, Tagawa M, Matsumoto S, et al. **Utility of bulging technique for endovascular treatment of small and wide-necked aneurysms with a low-profile visualized intraluminal support (LVIS Jr.) device: a case report and review of the literature.** *Interv Neuroradiol* 2018;24:125–29 CrossRef Medline

12. Zhou Y, Peng Q, Wu X, et al. **Endovascular treatment of tiny aneurysms with Low-Profile Visualized Intraluminal Support devices using a "compressed" stent technique.** *Front Neurol* 2020;11:610126 CrossRef Medline
13. Gao B, Baharoglu M, Cohen A, et al. **Stent-assisted coiling of intracranial bifurcation aneurysms leads to immediate and delayed intracranial vascular angle remodeling.** *AJNR Am J Neuroradiol* 2012;33:649–54 CrossRef Medline
14. Cruz JP, Marotta T, O'Kelly C, et al. **Enhancing brain lesions after endovascular treatment of aneurysms.** *AJNR Am J Neuroradiol* 2014;35:1954–88 CrossRef Medline
15. Darflinger RJ, Chao K. **Using the barrel technique with the LVIS Jr (Low-profile Visualized Intraluminal Support) stent to treat a wide neck MCA bifurcation aneurysm.** *J Vasc\Interv Neurol* 2015;8:25
16. Sakata H, Ezura M, Abe T, et al. **Intentional stent herniation technique using Neuroform Atlas Stent System for embolization of a wide-necked basilar tip aneurysm.** *Journal of Neuroendovascular Therapy* 2021;15:823–0155 CrossRef
17. Yatomi K, Mitome-Mishima Y, Fujii T, et al. **Outcomes following aneurysmal coil embolization with intentionally shortened low-profile visible intraluminal support stent deployment.** *Neuroradiol J* 2022;35:77–85 CrossRef Medline
18. Imahori T, Mizobe T, Fujinaka T, et al. **An aneurysm at the origin of a duplicated middle cerebral artery treated by stent-assisted coiling using the "wrapped-candy" Low-Profile Visualized Intraluminal Support (LVIS) technique: a technical case report and review of the literature.** *World Neurosurg* 2020;143:353–59 CrossRef Medline
19. Maus V, Weber W, Fischer S. **"Shelf" technique using a novel braided self-expandable stent for the treatment of wide-necked bifurcation aneurysms.** *Clin Neuroradiol* 2021;31:1187–93 CrossRef Medline
20. Yan Y, Zeng Z, Wu Y, et al. **The use of single low-profile visualized intraluminal support stent-assisted coiling in the treatment of middle cerebral artery bifurcation unruptured wide-necked aneurysm.** *Interv Neuroradiol* 2020;26:461–67 CrossRef Medline
21. Yamashita T, Ikeda H, Otsuka R, et al. **A patient with a large basilar artery aneurysm in whom coil embolization was performed by protruding an LVIS into the aneurysmal neck in a barrel-like shape and preserving a branch vessel.** *Journal of Neuroendovascular Therapy* 2020;14:447–53 CrossRef
22. Ge H, Lv X, Yang X, et al. **LVIS stent versus Enterprise stent for the treatment of unruptured intracranial aneurysms.** *World Neurosurg* 2016;91:365–70 CrossRef Medline
23. Dholakia RJ, Kappel AD, Pagano A, et al. **In vitro angiographic comparison of the flow-diversion performance of five neurovascular stents.** *Interv Neuroradiol* 2018;24:150–61 CrossRef Medline
24. Gentric JC, Salazkin I, Gevry G, et al. **Compaction of flow diverters improves occlusion of experimental wide-necked aneurysms.** *J Neurointerv Surg* 2016;8:1072–77 CrossRef Medline
25. Raymond J, Darsaut TE, Makoyeva A, et al. **Endovascular treatment with flow diverters may fail to occlude experimental bifurcation aneurysms.** *Neuroradiology* 2013;55:1355–63 CrossRef Medline
26. Peker A, Akgul E, Daglioglu E, et al. **Tapered flow diverters in the treatment of intracranial aneurysms.** *Turk Neurosurg* 2017;27:863–66 CrossRef Medline
27. Naggara ON, White PM, Guilbert F, et al. **Endovascular treatment of intracranial unruptured aneurysms: systematic review and meta-analysis of the literature on safety and efficacy.** *Radiology* 2010;256:887–97 CrossRef Medline
28. Gupta M, Cheung VJ, Abraham P, et al. **Low-profile Visualized Intraluminal Support Junior device for the treatment of intracranial aneurysms.** *Cureus* 2017;9:e1037 CrossRef Medline
29. Park SY, Oh JS, Oh HJ, et al. **Safety and efficacy of low-profile, self-expandable stents for treatment of intracranial aneurysms: initial and midterm results-a systematic review and meta-analysis.** *Interv Neurol* 2017;6:170–82 CrossRef Medline
30. Aydin K, Arat A, Sencer S, et al. **Stent-assisted coiling of wide-neck intracranial aneurysms using low-profile LEO baby stents: initial and midterm results.** *AJNR Am J Neuroradiol* 2015;36:1934–41 CrossRef Medline
31. Poncyljusz W, Biliński P, Safranow K, et al. **The LVIS/LVIS Jr. stents in the treatment of wide-neck intracranial aneurysms: multicentre registry.** *J Neurointerv Surg* 2015;7:524–29 CrossRef Medline
32. Goubergrits L, Schaller J, Kertzscher U, et al. **Hemodynamic impact of cerebral aneurysm endovascular treatment devices: coils and flow diverters.** *Expert Rev Med Devices* 2014;11:361–73 CrossRef Medline

Treatment of Proximal Posterior Inferior Cerebellar Artery Aneurysms by Intrasaccular Flow Disruption: A Multicenter Experience

L. Goertz, T. Liebig, E. Siebert, Y. Özpeynirci, L. Pennig, E. Celik, M. Schlamann, F. Dorn, and C. Kabbasch

ABSTRACT

BACKGROUND AND PURPOSE: Treatment of PICA aneurysms can be technically challenging by either surgical or endovascular means. Our aim was to report our preliminary experience with intrasaccular flow disruption using the Woven EndoBridge (WEB) for the treatment of proximal PICA aneurysms.

MATERIALS AND METHODS: Sixteen PICA aneurysms treated with the WEB at 3 institutions were retrospectively reviewed. Baseline patient and aneurysm characteristics, procedural specifics, clinical outcomes, and angiographic results were evaluated.

RESULTS: All aneurysms were located at the proximal, anteromedullary segment of the PICA. Seven aneurysms were ruptured. The median aneurysm size was 3.9 mm (range, 2–12 mm), and all aneurysms were wide-neck. WEB deployment failed in 1 case due to WEB protrusion in a small PICA aneurysm. Additional stent implantation was required for 2 aneurysms to improve intra-aneurysmal WEB positioning. One patient developed a partial posterior cerebral artery territory infarction with transient hemianopsia. Intraoperative rerupture of a ruptured aneurysm could be immediately stopped by WEB deployment due to intrasaccular stasis; however, it might have contributed to a slight disability of the patient. At last angiographic follow-up, 12/15 aneurysms (80%) were completely occluded and 3/15 (20%) had a neck remnant.

CONCLUSIONS: The preliminary results indicate that WEB treatment of proximal PICA aneurysms is feasible with a reasonable safety and efficacy profile. The advantages of intrasaccular flow disruption include preservation of the PICA, durable aneurysm occlusion, and omission of antiplatelet therapy. The low-profile WEB 17 delivery system might enable navigation to distal PICA aneurysms, which needs to be addressed further.

ABBREVIATIONS: RROC = Raymond-Roy occlusion classification; SL = single-layer

Aneurysms located at the PICA are rare and account for approximately 0.5%–3.0% of intracranial aneurysms. Most PICA aneurysms arise from the proximal (anteromedullary) PICA segment near the PICA–vertebral artery junction.[1] PICA aneurysms can be treated by both surgical and endovascular means; however, their location and geometry pose individual challenges for either treatment option. Microsurgical clipping is hampered by a narrow surgical corridor and the proximity to the brainstem and cranial nerves IX–XI, allowing only minimal manipulation.[2] Established endovascular treatment options for PICA aneurysms include conventional coiling, stent-assisted coiling, balloon-assisted coiling, flow diversion, and, last, parent artery occlusion as the final option. Challenges of the endovascular technique include a broad-based neck anatomy and a small PICA caliber, especially at peripheral aneurysm locations. Moreover, particularly in the proximal location, parent vessel sacrifice should be prevented due to the risk of brainstem and cerebellar infarction.

The concept of intrasaccular flow disruption has not yet been evaluated systematically for PICA aneurysms. The Woven EndoBridge (WEB; Sequent Medical) represents the most studied flow disrupter to date. It consists of a spherical mesh of nitinol wires, which is placed within the aneurysm sac, leaving the parent artery unaffected. It causes an immediate flow-disrupting effect at the aneurysm ostium, leading to subsequent thrombosis of the aneurysm sac with time. The safety and efficacy of the WEB have been demonstrated by numerous studies, predominantly for wide-neck bifurcation aneurysms located at the anterior communicating artery, the middle cerebral artery bifurcation, and the basilar apex.[3-6] Further refinements of the WEB include a

Received January 24, 2022; accepted after revision May 12.

From the Department of Radiology and Neuroradiology (L.G., L.P., E.C., M.S., C.K.), University of Cologne, Faculty of Medicine, University Hospital Cologne, Cologne, Germany; Department of Neuroradiology (T.L., Y.Ö.), University Hospital Munich, Munich, Germany; Department of Neuroradiology (E.S.), University Hospital of Berlin (Charité), Berlin, Germany; and Department of Neuroradiology (F.D.), University Hospital Bonn, Bonn, Germany.

Please address correspondence to Lukas Goertz, MD, University Hospital Cologne, Kerperner Str 62, Cologne, 50931, Germany; e-mail: lukas.goertz@uk-koeln.de

http://dx.doi.org/10.3174/ajnr.A7566

low-profile, 0.017-inch delivery system for navigation into small-vessel diameters.[7]

The present case series reports our preliminary multicenter experience in treating PICA aneurysms with the WEB.

MATERIALS AND METHODS

All patients treated with the WEB for a PICA aneurysm at 3 neurovascular institutions between 2011 and 2021 were retrospectively reviewed and included on an intention-to-treat basis. There were no exclusion criteria. In accordance with the institutional guidelines, an ethics committee approval was waived due to the retrospective study design.

Procedure

Treatment options for each individual PICA aneurysm were discussed between interventional neuroradiologists and vascular neurosurgeons. The WEB was predominantly selected for wide-neck bifurcation aneurysms, which were inappropriate for conventional coiling as an alternative endovascular treatment option for stent-assisted procedures and parent artery occlusion.

All procedures were performed via a transfemoral approach with the patient under general anesthesia in a biplane angiosuite (Philips AlluraClarity FD 20/15, Philips Healthcare and Siemens Artis Q, Siemens). The standard setup consisted of a triaxial system. A 6F guide catheter was navigated via a 6F sheath to the vertebral artery/PICA junction. The Sofia 5F catheter (MicroVention) was used as an intermediate catheter. Finally, a dedicated VIA microcatheter (Sequent Medical) was inserted coaxially to deploy the WEB.

As measured on 2D DSA, the WEB device was chosen to be slightly larger than the aneurysm width and slightly smaller than the aneurysm height (+1/–1 rule) for optimal aneurysm occlusion.

Antiaggregation Therapy

Patients with unruptured aneurysms were loaded with acetylsalicylic acid, 100 mg/day, 5–7 days before the procedure. After groin puncture, 5000 IU of heparin was administered, followed by aliquots of 1000 IU/h until the end of the procedure. After WEB implantation, acetylsalicylic acid, 100 mg/day, was given for 4–6 weeks. Patients with ruptured aneurysms received neither antiplatelet therapy nor IV administration of heparin. After additional stent implantation, a dual-antiplatelet regimen of clopidogrel, 75 mg/day, for 4 months and acetylsalicylic acid, 100 mg/day, life-long was administered.

Data Collection

Patient charts were retrospectively reviewed to collect patient age, sex, ruptured/unruptured aneurysm status, World Federation of Neurosurgical Societies grade, endovascular technique, complications, and clinical outcome. Baseline angiograms were reviewed to determine PICA location, aneurysm size, neck width, dome-to-neck ratio, and shape. Proximal PICA location refers to the PICA–vertebral artery junction and the anteromedullary segment of the PICA. Aneurysms arising beyond the anteromedullary segment were classified as distal. All complications are reported regardless of their clinical significance. The single-layer (SL) and single-layer sphere WEB types were used. Since September 2018, the WEB 17 was used for aneurysms of <7 mm. Clinical outcome was evaluated with the mRS score. Aneurysm occlusion was evaluated immediately after the procedure and on follow-up angiograms using the Raymond-Roy occlusion classification (RROC): complete occlusion (RROC I), neck remnant (RROC II), and aneurysm occlusion (RROC III).

Table 1: Baseline patient and aneurysm characteristics

Case	Age/Sex	Unruptured/ Ruptured (WFNS)	Size (mm)	Neck Width (mm)	D/N Ratio
1	65/F	UR	3.4	2.7	1.3
2	57/F	R (I)	3.2	3.0	1.1
3	48/F	UR	2.9	2.6	1.1
4	51/F	R (IV)	2.2	2.0	1.1
5	64/F	R (II)	4.4	4.4	1.1
6	78/F	R (V)	5.4	3.8	1.4
7	71/F	UR	8.6	4.6	1.9
8	63/F	UR	3.4	3.8	0.9
9	56/F	R (V)	12.0	4.8	2.6
10	51/F	UR	3.0	2.4	1.3
11	70/F	UR	9.2	7.4	1.2
12	58/F	R (V)	2.0	1.7	1.2
13	52/F	R (V)	11.0	6.0	1.8
14	53/F	UR	3.4	2.3	1.5
15	63/F	UR	9.0	4.6	2.0
16	64/F	UR	4.6	2.7	1.7

Note:—F indicates female; UR, unruptured; R, ruptured; WFNS, World Federation of Neurosurgical Societies grading scale; D/N, dome-to-neck ratio.

Statistical Analysis

Descriptive statistics were used.

RESULTS

Patient and Aneurysm Characteristics

Among 105 patients with PICA aneurysms treated at the 3 institutions during the study period, 16 patients underwent WEB embolization (15.2%). The median patient age was 60.5 years (range, 48–78 years), and all patients were women. Seven aneurysms (43.8%) were ruptured. The median aneurysm size was 3.9 mm (range, 2.2–12.0 mm), the median neck width was 3.4 mm (range, 1.7–7.4 mm), and the median dome-to-neck ratio was 1.3 (range, 0.9–2.6). All aneurysms were saccular. Individual patient and aneurysm characteristics are given in Table 1.

Aneurysm Treatment

Procedural specifics and patient outcome are detailed in Table 2. WEB deployment was feasible in all cases except one. In case 12, treatment of a small PICA aneurysm (2 mm) with the smallest available WEB in stock (SL, 3.5 × 2 mm) failed because the WEB was too large and it protruded into the parent artery (Fig 1). Due to WEB-induced vessel stenosis, additional stent implantation seemed inappropriate. Hence, the WEB was carefully removed before detachment, and the aneurysm was subsequently coiled in the same procedure. In case 2, the patient with a ruptured PICA aneurysm was treated with an additional stent in a staged procedure to improve intrasaccular WEB positioning and, subsequently, aneurysm occlusion. This case is presented in Fig 2. In case 11, the WEB tended to protrude into the parent artery as well; this protrusion could be counteracted by additional implantation of a low-profile stent. Complications occurred in 3 procedures (18.8%). In the first patient (case 1), an apposition

Table 2: Procedural specifics

Case	Treatment	Complications	Immediate RROC	RROC at FU (months)	mRS at FU (months)
1	WEB SLS 4 mm	Apposition thrombus, tirofiban, no neurologic deficit	I	I (6)	0 (6)
2	WEB SL 4 × 2 mm + Acclino stent 3.5 × 20 mm (staged)		II	I (3)	0 (20)
3	WEB SL 3.5 × 2 mm		I	I (6)	0 (6)
4	WEB SL 3 × 2 mm	Aneurysm rerupture during WEB deployment, intrasaccular stasis, no deficit	I	I (1)	1 (1)
5	WEB SL 5 × 3 mm	Transient hemianopsia partial posterior infarction, probably due to thromboembolism	II	I (7)	1 (7)
6	WEB SL 6 × 4 mm		III	II (1)	5 (1)
7	WEB DL 7 × 6 mm, 5 coils		II	I (17)	1 (17)
8	WEB SL 3 × 2 mm		III	I (8)	0 (8)
9	WEB SL 6 × 4 mm, 11 coils		III	I (10)	2 (10)
10	WEB SL 3 × 2 mm		III	I (5)	0 (5)
11	WEB SL 9 × 4 mm, LEO Baby[a] stent 4.5 × 25 mm	WEB protrusion into the parent artery, adjunctive stent implantation, no ischemic complications	III	II (6)	0 (6)
12	WEB SL 3.5 × 2 mm, coiling	WEB implantation failed due to WEB protrusion, subsequent coil embolization	II	I (21)	0 (21)
13	WEB SL 11 × 6 mm		III	I (1)	6 (1)
14	WEB SL 4 × 3 mm		III	I (1)	0 (1)
15	WEB SL 9 × 4 mm		III	II (1)	1 (1)
16	WEB SL 3.5 × 2 mm		III		0 (6)

Note:—SLS indicates single-layer sphere; SL, single-layer; FU, follow-up; DL, dual-layer; RROC, Raymond-Roy occlusion classification.
[a] Balt Extrusion.

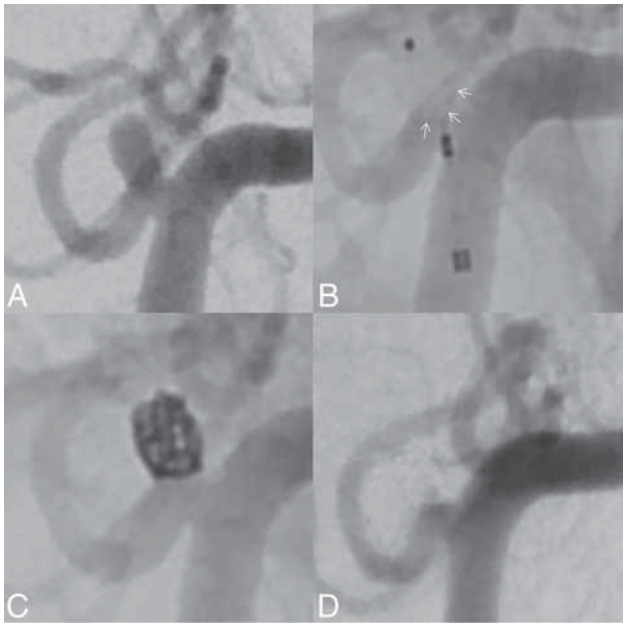

FIG 1. DSA shows a small, proximal PICA aneurysm (2 mm) in a patient with an SAH (*A*). Due to the broad neck of the aneurysm, the smallest available WEB in stock (SL, 3.5 × 2 mm) was deployed (*B*). However, the lower base of the WEB protruded markedly into the parent vessel (WEB contour highlighted by *arrows*). Implantation of an additional microstent seemed contraindicated because it might occlude the parent vessel (diameter, 1.3 mm) and would require permanent antiplatelet therapy. Hence, the WEB was removed before deployment, and the aneurysm was treated by implantation of a single coil (*C*). At final angiographic follow-up (21 months), the aneurysm was fully occluded and the PICA remained patent (*D*).

thrombus occurred at the WEB, which could be dissolved with tirofiban. The patient had no infarction and no neurologic deficits. In the second patient (case 4), a ruptured PICA aneurysm reruptured immediately after intrasaccular WEB deployment; however, the bleeding stopped shortly thereafter due to intrasaccular stasis. Although cerebral infarction was not seen on follow-up imaging, the rebleeding might have contributed to the slight-but-permanent disability of the patient after SAH (mRS 1). This case is illustrated in Fig 3. In the third case (case 5), the patient had a partial posterior infarction, which was associated with transient hemianopsia, probably due to a procedural thromboembolism. Figure 4 depicts a further case of successful WEB embolization.

Angiographic Outcome

Immediate complete aneurysm occlusion was achieved in 3 patients (18.8%), 4 had a neck remnant (25.0%), and 9 (56.3%) had an aneurysm remnant. The coiled PICA aneurysm after failed WEB implantation had a small neck remnant, which progressed to complete occlusion at follow-up (Fig 1). Among 15 patients available for angiographic follow-up in the intention-to-treat cohort (median, 6 months; range, 1–21 months), 12 aneurysms (80.0%) were completely occluded and 3 (20.0%) had a neck remnant. There were no aneurysm remnants. Among 14 patients eventually treated with the WEB, 11 showed complete occlusion (78.6%) and 3 had neck remnants (21.4%). All followed aneurysms with an initial RROC III improved to RROC I or II, respectively. There was no aneurysm recurrence. At clinical follow-up, of 16 patients, 13 (85%) had a favorable outcome (mRS ≤1) and 3

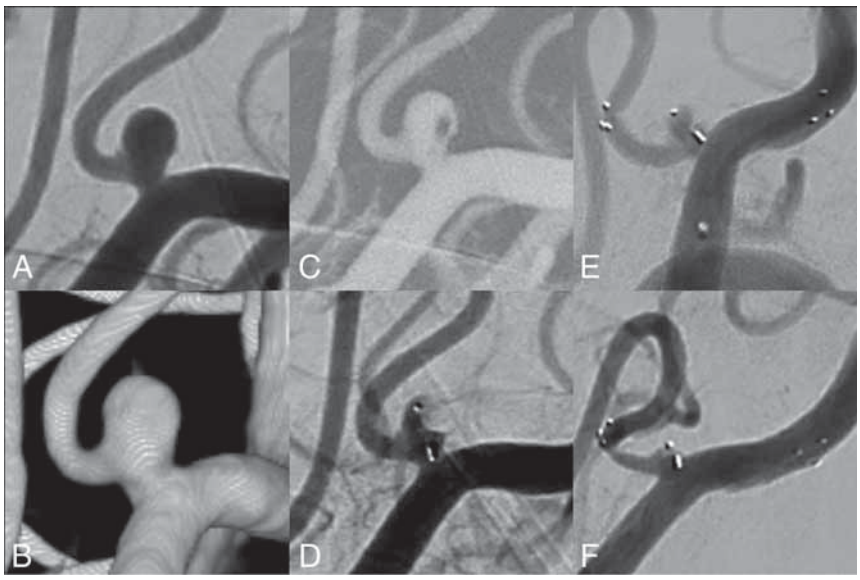

FIG 2. DSA shows a ruptured proximal PICA aneurysm (3.2 mm; neck width, 3.0 mm; dome-to-neck ratio, 1.1 mm) (*A* and *B*). Due to the broad-based geometry and the ruptured aneurysm status, intrasaccular flow disruption was envisaged. After probing the aneurysm with a low-profile VIA 17 microcatheter (*C*), a WEB 17 SL (4 × 2 mm) was placed within the aneurysm sac, achieving immediate contrast stasis to prevent aneurysm rerupture (*D*). After neurointensive care treatment of the patient, the aneurysm showed persistent residual filling. Hence, an Acclino microstent was placed across the aneurysm neck from the PICA into the distal vertebral artery to optimize WEB positioning (*E*). At 3-month angiographic follow-up, the aneurysm was completely occluded. There was a moderate in-stent stenosis, which was asymptomatic (*F*).

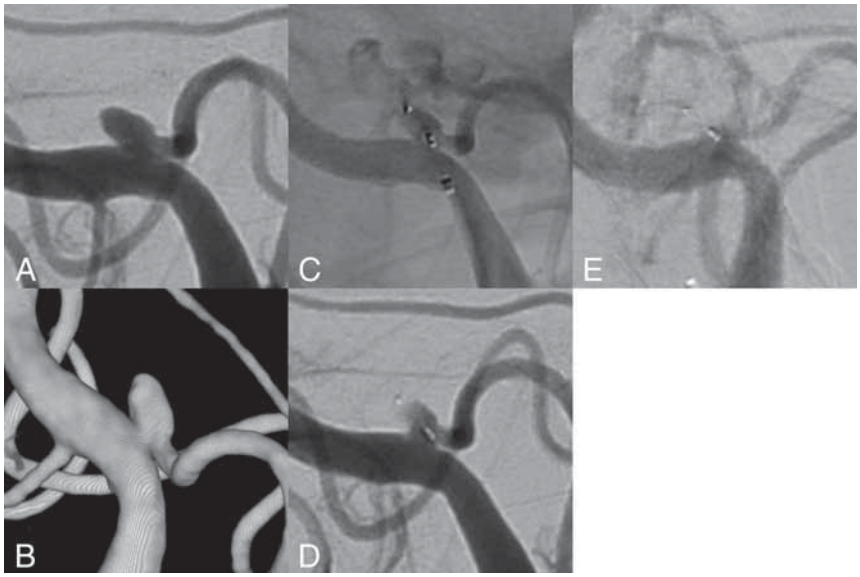

FIG 3. A 51-year-old female patient presented with a ruptured aneurysm at the proximal PICA (*A* and *B*). The aneurysm reruptured while the aneurysm sac was probed with the microcatheter. Extravasating contrast can be seen on the angiogram (*C*). However, directly after WEB deployment, the bleeding stopped due to intrasaccular stasis (*D*). Cerebellar infarction and herniation were excluded by a control CT (not shown). Although experiencing severe vasospasm, the patient survived and was transferred to a rehabilitation center with mild neurologic deficits (mRS 1). At 2 months, the WEB seemed to be fully thrombosed (*E*); however, the origin of the PICA, in particular the V4/PICA junction, appears to be dysplastic, warranting further angiographic control.

patients had an mRS > 1, mainly due to the sequelae of SAH (cases 6, 9, and 13).

DISCUSSION

In the present study, we presented our multicenter experience in the treatment of wide-neck proximal PICA aneurysms with the WEB. WEB deployment was technically successful in all cases except one, and required additional stent implantation in 2 cases. In 1 case, procedural aneurysm rerupture might have contributed to a slight permanent SAH-related disability. At angiographic follow-up, the complete occlusion rates were 80% in the intention-to-treat cohort and 78.6% in the per-protocol group. There was no aneurysm recurrence, and no aneurysms were retreated.

Endovascular embolization has become the treatment of choice for PICA aneurysms because surgical therapy is associated with a high neurologic complication rate due to the proximity to the brainstem and the lower cranial nerves. For instance, Horowitz et al[8] reported an overall complication rate of 68% after surgical PICA repair. In the surgical study by Al-Khayat et al,[2] postoperative temporary and permanent lower cranial nerve palsies were observed in around 50%. Although lower cranial nerve palsies can resolve with time, surgery is generally reserved for complex aneurysms and distal locations that are difficult to treat by endovascular means.

The largest study on endovascular PICA aneurysm treatment to date has been published by Chalouhi et al[9] and comprised 76 patients treated by conventional coiling, stent-assisted coiling, balloon-assisted coiling, and parent artery occlusion. The technical success rate was 96%. Complications were reported in 12.7%, and permanent morbidity, in 2.8%. In 90% of proximal PICA aneurysms, the parent artery could be preserved.

Proximal PICA aneurysms located at the anterior medullary, lateral medullary, and tonsillomedullary segments pose a particular challenge because parent artery sacrifice should be avoided due to brainstem perforators.[10] Among 6 proximal PICA aneurysms treated by parent artery occlusion in the study by Peluso et al,[11] 1 patient developed hemiparesis due

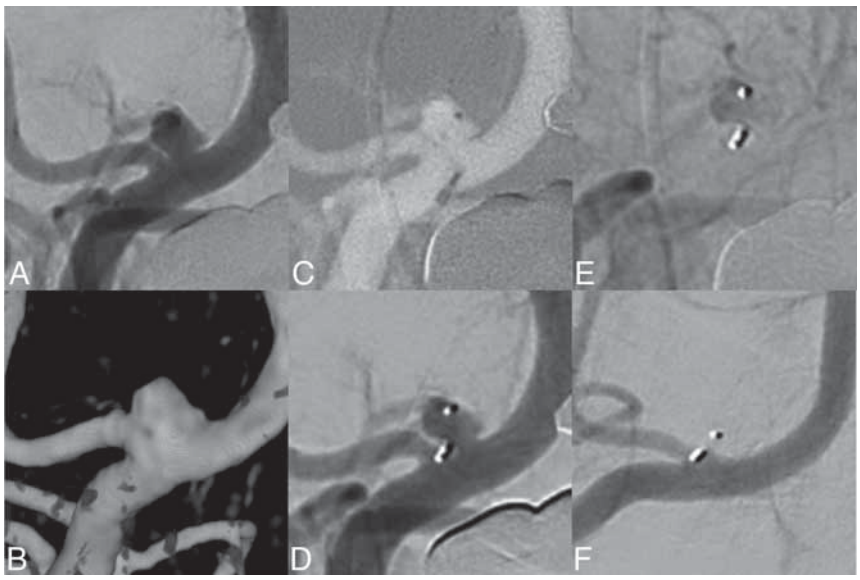

FIG 4. DSA (*A*) and 3D reconstructions of rotational data sets (*B*) show an unruptured wide-neck aneurysm at the branching of the PICA from the vertebral artery. Due to its very broad-based geometry, treatment by conventional coiling is not feasible. To avoid crossing-over stent-assisted coiling, WEB embolization was envisaged. After we probed the aneurysm sac with a low-profile VIA 17 microcatheter (*C*), a WEB SL 3.5 × 2 cm was implanted (*D*), which sealed the aneurysm at its neck level and maintained full patency of the PICA. Immediate angiographic control after WEB implantation shows contrast stasis within the WEB (*E*). Six-month DSA shows complete aneurysm occlusion (RROC I) and patency of the PICA (*F*).

to lateral medullary and cerebellar infarction and 3 had small asymptomatic infarctions. For small-neck aneurysms, conventional coiling is often feasible, but recurrence rates were reported to be >20%.[9] Furthermore, PICA aneurysms often present with a wide neck, which would require stent- or balloon-assisted coiling or flow diversion. However, navigation of conventional 0.021- and 0.027-inch stent delivery systems into the PICA is hampered by a sharp angle at the vertebral artery/PICA junction and the small-vessel caliber.[11] In this context, low-profile stents and delivery systems seem to bring benefit for stent implantation in the PICA. In a small series by Samaniego et al,[12] treatment with the Low-profile Visualized Intraluminal Support (LVIS Jr; MicroVention) device was successful in all 7 cases, and there was no treatment-related morbidity. However, even if stent implantation is possible, there is an enhanced risk of acute thrombotic stent occlusion due to the small-vessel diameter of the PICA.

Intrasaccular flow disruption with the WEB has become a proved treatment concept for wide-neck bifurcation aneurysms. In 2019, the WEB received US FDA approval for anterior communicating artery, MCA bifurcation, terminal ICA, and basilar apex aneurysms.[13] As a purely intrasaccular device, the WEB causes immediate flow disruption through the aneurysm ostium, leading to subsequent aneurysm thrombosis, and it does not require antiaggregant therapy urgently, making the device suitable for treatment of ruptured aneurysms.[14] Due to its spherical shape, the WEB can be generally securely anchored in wide-neck aneurysms without a supporting stent.

The efficiency of the WEB is well-documented. In the cumulative population of the WEB Clinical Assessment of IntraSaccular Aneurysm Therapy (WEBCAST) trial, WEBCAST-2, and the French Observatory studies, complete and adequate occlusion was reported in 52.9% and 79% at 1 year, respectively.[15] Between the 1- and 3-year follow-ups, aneurysm occlusion was stable or improved in 87%, and the overall retreatment rate was 11.4%.[4]

Owing to these promising results, the indication for WEB embolization has been subsequently extended to further aneurysm locations such as the paraophthalmic ICA[16] and narrow-neck aneurysms.[17]

In our experience, PICA aneurysms often have a spherical, saccular shape, which is suitable for the WEB. Moreover, the novel WEB 17 can be delivered via a 0.017-inch low-profile microcatheter, which might facilitate navigation into the PICA.

Recently, Khattar et al[18] reported a case of WEB embolization of a ruptured, dissection-related distal PICA aneurysm (5 mm) with a WEB SL 4 × 3 mm, which is compatible with a low-profile 0.017-inch microcatheter. Navigation toward the aneurysm and WEB deployment were not problematic despite the small-vessel caliber. The authors reported immediate intrasaccular stasis and complete aneurysm occlusion at follow-up.

In the current series, we presented 16 broad-based aneurysms at the PICA–vertebral artery junction, which were treated with the WEB. However, treatment with WEB implantation only was feasible in 13 cases (81%). In 1 case, WEB embolization failed due to WEB protrusion, and in 2 further cases, additional stent implantation was necessary to improve the WEB positioning. In the 2 latter cases, the advantages of the WEB, namely preservation of the parent artery and omission of antiplatelet therapy, were counteracted. However, additional stent implantation can serve as salvage therapy if treatment by the WEB is technically impossible. All aneurysms showed complete occlusion or neck remnants at angiographic follow-up, comparing favorably with the 21% recurrence rate reported by Chalouhi et al[9] for coiling. The PICA remained patent in all cases, both during the intervention and at follow-up. One patient developed transient anopsia, which was probably caused by a detached apposition thrombus.

In 1 case, the aneurysm reruptured during WEB deployment caused by the microcatheter. PICA aneurysms have been reported to be susceptible to intraoperative rupture, as demonstrated by a 19% rupture rate in the study by Peluso et al.[11] The authors suggested that a small aneurysm size and the upward projection of most PICA aneurysms could lead to a slack in the microcatheter caused by the V3 loop of the vertebral artery, which could be transferred in an upward jump of the catheter during pushing, resulting in rupture of the aneurysm dome.[11] Noteworthy, the bleeding stopped directly after subsequent WEB

deployment due to intra-aneurysmal stasis. Most important, there was no treatment-related permanent morbidity in our series.

In conclusion, the results imply that the WEB is suitable for proximal PICA aneurysms, offering good angiographic results and sufficient safety. Hence, the WEB may become a further treatment option for PICA aneurysms, in particular for wide-neck aneurysms that are difficult to treat by coiling only. However, further studies will be required to establish the WEB as a primary tool for PICA aneurysms, especially at more distant locations.

Limitations

The limitations of the current study include a moderate number of included patients and the retrospective study design. All aneurysms were located at the proximal PICA; hence, the feasibility of the WEB for distal PICA aneurysms remains uncertain. Finally, long-term angiographic outcome was not reported and needs to be addressed further.

CONCLUSIONS

Due to the typically broad-based anatomy of PICA aneurysms, bare coiling can be challenging and might require implantation of a supporting stent. Due to the saccular, broad-based shape, WEB implantation would often be suitable for PICA aneurysms, as was the case in the present study. Additional stent implantation could be avoided in most cases, there was no major treatment-related morbidity, and retreatment was not required in any case. Further studies are warranted to confirm our preliminary results and establish the WEB for this specific aneurysm location.

Disclosure forms provided by the authors are available with the full text and PDF of this article at www.ajnr.org.

REFERENCES

1. Hudgins RJ, Day AL, Quisling RG, et al. **Aneurysms of the posterior inferior cerebellar artery: a clinical and anatomical analysis.** *J Neurosurg* 1983;58:381–87 CrossRef Medline
2. Al-Khayat H, Al-Khayat H, Beshay J, et al. **Vertebral artery-posteroinferior cerebellar artery aneurysms: clinical and lower cranial nerve outcomes in 52 patients.** *Neurosurgery* 2005;56:2–11 Medline
3. Kabbasch C, Goertz L, Siebert E, et al. **WEB embolization versus stent-assisted coiling: comparison of complication rates and angiographic outcomes.** *J Neurointerv Surg* 2019;11:812–16 CrossRef Medline
4. Pierot L, Szikora I, Barreau X, et al. **Aneurysm treatment with WEB in the cumulative population of two prospective, multicenter series: 3-year follow-up.** *J Neurointerv Surg* 2021;13:363–68 CrossRef Medline
5. Al Saiegh F, Hasan D, Mouchtouris N, et al. **Treatment of acutely ruptured cerebral aneurysms with the Woven EndoBridge device: experience post-FDA approval.** *Neurosurgery* 2020;87:E16–22 CrossRef Medline
6. Kabbasch C, Goertz L, Siebert E, et al. **Comparison of WEB embolization and coiling in unruptured intracranial aneurysms: safety and efficacy based on a propensity score analysis.** *World Neurosurg* 2019;126:e937–43 CrossRef Medline
7. Goertz L, Liebig T, Siebert E, et al. **Low-profile intra-aneurysmal flow disruptor WEB 17 versus WEB predecessor systems for treatment of small intracranial aneurysms: comparative analysis of procedural safety and feasibility.** *AJNR Am J Neuroradiol* 2019;40:1766–72 CrossRef Medline
8. Horowitz M, Kopitnik T, Landreneau F, et al. **Posteroinferior cerebellar artery aneurysms: surgical results for 38 patients.** *Neurosurgery* 1998;43:1026–31 CrossRef Medline
9. Chalouhi N, Jabbour P, Starke RM, et al. **Endovascular treatment of proximal and distal posterior inferior cerebellar artery aneurysms.** *J Neurosurg* 2013;118:991–99 CrossRef Medline
10. Lewis SB, Chang DJ, Peace DA, et al. **Distal posterior inferior cerebellar artery aneurysms: clinical features and management.** *J Neurosurg* 2002;97:756–66 CrossRef Medline
11. Peluso J, Van Rooij W, Sluzewski M, et al. **Posterior inferior cerebellar artery aneurysms: incidence, clinical presentation, and outcome of endovascular treatment.** *AJNR Am J Neuroradiol* 2008;29:86–90 CrossRef Medline
12. Samaniego EA, Abdo G, Hanel RA, et al. **Endovascular treatment of PICA aneurysms with a Low-profile Visualized Intraluminal Support (LVIS Jr) device.** *J Neurointerv Surg* 2016;8:1030–33 CrossRef Medline
13. Goertz L, Liebig T, Siebert E, et al. **Woven EndoBridge embolization versus microsurgical clipping for unruptured anterior circulation aneurysms: a propensity score analysis.** *Neurosurgery* 2021;88:779–84 CrossRef Medline
14. Pennig L, Goertz L, Hoyer UCI, et al. **The Woven EndoBridge (WEB) versus conventional coiling for treatment of patients with aneurysmal subarachnoid haemorrhage: propensity score-matched analysis of clinical and angiographic outcome data.** *World Neurosurg* 2021;146:e1326–34 CrossRef Medline
15. Pierot L, Moret J, Barreau X, et al. **Safety and efficacy of aneurysm treatment with WEB in the cumulative population of three prospective, multicenter series.** *J Neurointerv Surg* 2018;10:553–59 CrossRef Medline
16. Goertz L, Liebig T, Siebert E, et al. **Extending the indication of Woven EndoBridge (WEB) embolization to internal carotid artery aneurysms: a multicenter safety and feasibility study.** *World Neurosurg* 2019;126:e965–74 CrossRef Medline
17. Goertz L, Liebig T, Siebert E, et al. **Intrasaccular flow disruption with the Woven EndoBridge for narrow-necked aneurysms: a safety and feasibility study.** *World Neurosurg* 2021;151:e278–85 CrossRef Medline
18. Khattar NK, White AC, Cruz AS, et al. **Woven EndoBridge device for treatment of dissection-related PICA aneurysm.** *Interv Neuroradiol* 2021;27:388–90 CrossRef Medline

High-Resolution MRI for Evaluation of the Possibility of Successful Recanalization in Symptomatic Chronic ICA Occlusion: A Retrospective Study

M. Tang, X. Yan, J. Gao, L. Li, X. Zhe, Xin Zhang, F. Jiang, J. Hu, N. Ma, K. Ai, and Xiaoling Zhang

ABSTRACT

BACKGROUND AND PURPOSE: Accurate radiologic evaluation of the possibility of successful recanalization in symptomatic chronic ICA occlusion remains challenging. This study aimed to investigate the high-resolution MR imaging characteristics of symptomatic chronic ICA occlusion and their association with successful recanalization.

MATERIALS AND METHODS: Consecutive patients with symptomatic chronic ICA occlusion who underwent balloon dilation plus stent implantation were identified retrospectively and divided into 2 groups: a successful recanalization group and an unsuccessful recanalization group. Clinical and high-resolution MR imaging characteristics were compared between the groups. Univariate and multivariate analyses were used to identify the characteristics associated with successful recanalization.

RESULTS: A total of 114 patients were included in the study. High-resolution MR imaging characteristics independently associated with unsuccessful recanalization were longer lesion length (OR, 0.41; 95% CI, 0.36–0.55; $P = .009$) and larger calcification volume (OR, 0.56; 95% CI, 0.37–0.68; $P = .002$) for proximal occlusion and reversed distal ICA flow at the level of ophthalmic segment or above (OR, 0.14; 95% CI, 0.08–0.48; $P = .001$). Reversed distal ICA flow at the level of the petrous segment or below (OR, 4.07; 95% CI, 1.65–8.38; $P = .001$) and lumen area (OR, 1.13; 95% CI, 1.04–1.61; $P = .002$) for distal occlusion were risk factors of successful recanalization.

CONCLUSIONS: In symptomatic chronic ICA occlusion, lesion length and calcification volume (for proximal occlusion), the level of reversed distal ICA flow, and the lumen area (for distal occlusion) appear to be predictors of successful recanalization. High-resolution MR imaging can evaluate chronic ICA occlusion and help in clinical decision-making.

ABBREVIATIONS: CE = contrast-enhanced; CICAO = chronic ICA occlusion; HR = high-resolution; IPH = intraplaque hemorrhage; NSA = number of signals averaged

ICA occlusion occurs in 6 per 100,000 persons per year and is one of the main causes of ischemic stroke.[1,2] While recurrence is uncommon in asymptomatic patients, 10%–18% of symptomatic patients will experience another cerebral ischemic event within 1 year. In chronic ICA occlusion (CICAO), morbidity and mortality are 40%–69%, and 16%–55%, respectively.[3,4] Studies have demonstrated decreased psychomotor speed, executive function, and working memory in patients with CICAO,[5,6] and a possible relationship between CICAO and cognitive impairment has been suggested.

Recanalization of CICAO can restore blood supply to ischemic brain tissue, reduce mortality and disability rates, and improve neurocognitive function[7-9] and quality of life. Successful recanalization is achieved in 23%–93% of patients.[10-13] The possibility of success depends on factors such as the duration of the occlusion,[14] the length of the occlusion, the composition of the thrombus or plaque,[15-17] the stump condition[18,19] of occluded vessels, and the adequacy of collateral circulation.[20]

In CICAO, the real duration of occlusion is not known, so indirect estimations are made on the basis of the time of onset of symptoms and the imaging features. DSA, CTA, ultrasound, and MR imaging are complementary modalities for the evaluation of CICAO. DSA can dynamically display the stump condition, occlusion length, distal reflux, and collateral circulation, but it cannot analyze the course or the wall and lumen of occluded vessels.[21-23] CTA can reliably demonstrate occlusion length, collateral circulation, and the course of occluded vessels, but it cannot accurately analyze the

Received January 13, 2022; accepted after revision May 31.

From the Departments of MRI (M.T., X.Y., J.G., L.L., X. Zhe., X. Zhang., N.M., X. Zhang) and Neurology (F.J., J.H.), Shaanxi Provincial People's Hospital, Beilin District, Xi'an City, Shaanxi Province, China; and Department of Clinical Science (K.A.), Philips Healthcare, Xian, China.

This research was supported by the Shanxi Provincial Key Research and Development Project of Shaanxi Province of China (2021SF-064).

Please address correspondence to Xiaoling Zhang, MD, Department of MRI, Shaanxi Provincial People's Hospital, Beilin District, Xi'an City 710068, Shaanxi Province, China; e-mail: zxl.822@163.com

Indicates open access to non-subscribers at www.ajnr.org

http://dx.doi.org/10.3174/ajnr.A7576

age of the thrombus, the components of plaque, or the intracranial ICA (because of intervening skull bone).[19,24] Ultrasound is a noninvasive, economical, and highly operator-dependent tool for the evaluation of carotid artery occlusion; it can show the plaque composition but is useful only for analysis of the extracranial ICA.[25] High-resolution MR imaging (HR-MR imaging), which is being increasingly used in the evaluation of intracranial and extracranial vascular diseases, can provide direct visualization of the vessel wall and lumen, composition of the thrombus or plaque, occlusion length, collateral circulation, and the course of the occluded vessels[26-28] and can compensate for the weaknesses of other imaging modalities.

We hypothesized that accurate evaluation of symptomatic CICAO using HR-MR imaging may help in the choice of treatment strategy, improve the success rate of interventional treatment, and reduce perioperative complications. The purpose of this retrospective study was to identify the HR-MR imaging characteristics of symptomatic patients with CICAO who were successfully recanalized. This information will be of use to clinicians during treatment selection and help avoid complications.

MATERIALS AND METHODS

Patients

We retrospectively analyzed consecutive CICAO recanalizations attempted at Shaanxi Provincial People's Hospital between October 2014 and December 2021. All patients underwent HR-MR imaging before the procedure. Patients were eligible for inclusion if they had the following:[29] 1) ipsilateral transient cerebral ischemia, ischemic stroke, or amaurosis for >1 month; 2) unilateral ICA occlusion diagnosed by CTA, ultrasound, or contrast-enhanced (CE)-MRA; 3) the diagnosis of CICAO confirmed by DSA; and 4) failure of medical treatment. Exclusion criteria included dissection, cardiogenic embolism, allergy to contrast medium, bleeding tendency, and poor-quality imaging. Clinical data, which included the patient's age, smoking, hypertension, diabetes mellitus, hyperlipidemia, history of stroke and stroke, and imaging data, were collected from the hospital records for analysis.

This study was approved by the Ethics Committee of Shaanxi Provincial People's Hospital (Xian, Shaanxi Province, China). Informed consent form was signed by all participants.

HR-MR Imaging

HR-MR imaging was performed with the patient in a supine position. A 16-channel head-neck coil was used with an Ingenia 3T MR imaging scanner (Philips Healthcare). The HR-MR imaging protocol included TOF-MRA, 3D-T1WI, T1WI-TSE and T2WI-TSE, CE-MRA, and CE 3D-T1WI. The axial views were perpendicular to the arterial course. Scan parameters for the different sequences were as follows: 3D-T1WI and CE 3D-T1WI: FOV = 200 × 200 mm^2, TR/TE = 1000/16 ms, acquisition matrix = 400 × 400, image resolution = 0.5 × 0.5 × 0.5 mm^3, number of signals averaged (NSA) = 1, acceleration factor = 2; CE-MRA: FOV = 320 × 320 mm^2, TR/TE = 175/4.8 ms, acquisition matrix = 456 × 456, image resolution = 0.7 × 0.7 mm^3, dynamic scans = 3, NSA = 1; T1WI-TSE: FOV = 140 × 101 mm^2, TR/TE = 477/13 ms, acquisition matrix = 312 × 216, image resolution = 0.45 × 0.45 mm^3, NSA = 2; T2WI-TSE: FOV = 140 × 101 mm^2, TR/TE = 3000/90 ms, acquisition matrix = 312 × 216, image resolution = 0.45 × 0.45 mm^3, NSA = 2. CE T1WI was performed following intravenous administration of gadoterate meglumine at a dose of 0.1 mmol/kg. The total acquisition time was approximately 30 minutes.

Image Analysis

The image quality was divided into 4 levels:[30] Poor indicated that the outline of vessel wall and lumen was unclear accompanied by obvious artifacts; medium, the parts of the wall and lumen were clear with a few artifacts; good, the wall and lumen were clear with a few artifacts; excellent, the wall and lumen were clear without artifacts. Image quality below medium could not be analyzed. Raw data were imported into Plaque View postprocessing software (VPDiagnostics) to generate axial, coronal, and sagittal reconstructions of the CICAO. The senior neuroradiologists (X. Zhe and X. Yan, each with 5 years' experience in interpreting HR-MR imaging of the arterial wall), who were blinded to the patients' clinical information, independently analyzed the images for plaque composition, shape of the stump, and signal characteristics of the wall and lumen in proximal and distal ICA occlusions, location of contrast agent reflux, and the collateral circulation. Differences in interpretation were settled by discussion. Imaging characteristics at the proximal and distal occlusive segments (ie, collateral circulation, location of contrast agent reflux, morphologic characteristics of the stump, and the lumen and wall of the occluded segment) were noted.

We first used CE-MRA to assist in localization and then find collateral circulation vessels and to evaluate collateral vessel diameter on HR-MRI. Collateral circulation was divided into primary (anterior or posterior communicating artery) and secondary (ophthalmic artery and meningeal artery) collaterals.[31] Primary collateral vessels were graded as follows: 1, absent; 2, probably present; 3, definitely present or greater than the normal side. Adequate primary collateral vessels were defined as grade 3. Secondary collateral vessels were graded in the comparison of the symptomatic and normal side as follows: 1, absent; 2, less than the normal side; 3, equal to the normal side; 4, greater than the normal side. "Diminished" was defined as grades 1–2, and "adequate" was defined as grades 3–4.[32] "Distal reflux" was defined as the presence of contrast agent in the ICA distal to the occlusion on CE-MRA and the lumen showing no signal on HR-MRI during the ipsilateral injection; the location of reflux was categorized as the petrous segment or below, cavernous segment, clinoid segment, ophthalmic segment, or communicating segment.[18] The stump, if present, was categorized as tapered and nontapered if there was contrast filling within the segment of the cervical ICA after it bifurcates from the common carotid artery proximal to the occluded segment. Hyperintensity, isointensity, and hypointensity were defined as higher, equal, and lower intensity, respectively, relative to the sternocleidomastoid muscle at the same level.[33]

Lipid-rich necrotic core, calcification, hemorrhage, loose matrix, and dense fibrous tissue were identified using MR imaging criteria.[34] The proximal occlusion segment—extending from the occlusion site to the site of disappearance of signal or the appearance of significantly different signal in the lumen—was the primary lesion. Its length and plaque composition were measured (Fig 1*A–C* and Fig 2*B*). Distal occlusion was defined as the secondary lesion, with no enhancement in the lumen. Three measurement

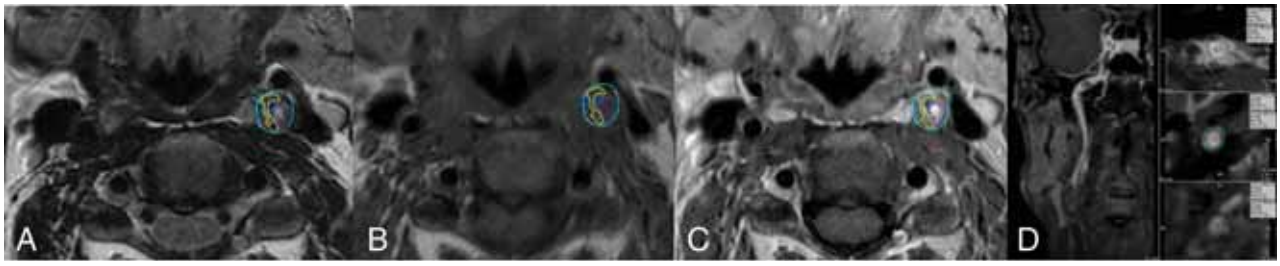

FIG 1. *A–C*, T2WI, T1WI, and CE-T1WI show the measurement of the proximal segment; the loose matrix (purple) shows hyperintensity on T2WI, iso- or hypointensity on T1WI, and enhancement on CE-T1WI. Calcification (blue) appears as hypointensity on all sequences; hemorrhage (orange) appears as hyperintensity on T1WI, iso- or hypointensity on T2WI, and no enhancement on CE-T1WI. The lipid-rich necrotic core (yellow) shows iso- or hyperintensity on T1WI, iso- or hyperintensity on T2WI, and enhancement on CE-T1WI. *D*, The lumen and wall area were measured in the distal occlusion.

points were selected in the distal occlusion segment (proximal, middle, and distal; Fig 1*D*). Then, the average lumen and wall values of the 3 points were obtained. An independent interventionist reviewed the procedural angiograms off-line and recorded the morphologic characteristics of the stump and occlusion segment.

Interventional Therapy

Antiplatelet therapy (aspirin, 100 mg, and clopidogrel, 75 mg daily) was started before the operation. Heparin was administered to maintain an activated clotting time within the range of 200–250 seconds. An 8F femoral sheath was inserted into the common carotid artery, and a guidewire and a multifunctional angiography catheter were inserted through it using the Seldinger technique. Angiography was performed to define the position of the ICA occlusion and observe the stump, distal ICA, reflux position, and collateral circulation. A microwire was passed through the occluded ICA segment. When the wire had entered the distal true lumen, it was exchanged for a 1.5-mm-diameter coronary balloon for predilation. A distal embolic protection device (SpiderFX, 4 mm; Medtronic) was deployed if an adequate landing zone was identified. The occluded segment of the ICA was dilated by the balloon, and a self-expandable stent of the appropriate size was placed.

Outcome of Events

Success was defined as[18] successful stent placement of the occlusion segment, with a final residual stenosis of ≤20% and establishment of grade III TICI antegrade flow, without the patient experiencing any complications. The procedure was deemed unsuccessful under the following circumstances: 1) The patient experienced complications after stent placement, or 2) no retrograde blood flow was observed after recanalization. Complications included ICA dissection, appearance of cerebral infarction in >1 lobe, cerebral hemorrhage, ipsilateral retinal infarction, reocclusion in the perioperational stage, and death. Finally, the patients were divided into 2 groups: a successful group, comprising patients who underwent successful recanalization without experiencing any complication, and an unsuccessful group, comprising patients who had recanalization failure and/or experienced complications.

Statistical Analysis

The normality test of continuous variable distribution was performed first. Then the variables were presented as mean (SD) or median (interquartile range) accordingly. The Student *t* test or the Mann-Whitney *U* test was used to compare differences in means or interquartile ranges between groups, and the χ^2 test or the Fisher exact test was used to compare differences in proportions, respectively. The intraclass correlation coefficient was used to assess interobserver consistency in the interpretation of HR-MR imaging. κ analysis was used to assess agreement between HR-MR imaging and DSA and was graded as good ($\kappa \geq 0.75$), moderate ($0.75 > \kappa \geq 0.4$), or poor ($\kappa < 0.4$). Multivariable logistic regression was applied to identify the independent predictors of recanalization failure, and a forward likelihood ratio method with a significance level for entry of .05 was performed to select variables included in the model. Statistical analysis was performed using SPSS 22.0 (IBM.). $P \leq .05$ indicated a statistically significant difference.

RESULTS

Clinical Data

From among the 129 patients who met the inclusion criteria, we excluded 15 patients; these included patients with CICAO related to trauma ($n = 2$), arteritis ($n = 4$), and Moyamoya disease ($n = 3$), as well as those with poor-quality imaging ($n = 6$). The 114 patients included in this study had a median age of 57 years (interquartile range, 32–73 years). Presentations were with transient cerebral ischemia, retinal ischemia, or stroke. Recanalization was successful in 76/114 (66.7%) patients (the successful group), but it was unsuccessful in 38/114 (33.3%) patients (the unsuccessful group). While recanalization failed in 34/114 (29.8%) patients, 4/114 (3.5%) patients had complications after recanalization; the complications included ICA dissection ($n = 1$), intracranial hemorrhage ($n = 2$), and cerebral infarction progression ($n = 1$). Table 1 summarizes the characteristics of the patients.

HR-MR Imaging Features

A tapered stump was observed in 64/114 (56.1%) patients and in 48/76 (63.2%) patients in the successful group (Fig 2*C*, -*D*). Secondary collateral circulation was more often seen in the unsuccessful group (Fig 3*C*, -*E*) than in the successful group ($P = .025$). Among the 114 patients, the level of reversed distal ICA flow was visualized at the communicating segment, ophthalmic segment, clinoid segment, cavernous segment, and petrous segment or below in 7%, 10.5%, 20.2%, 28.1%, and 34.2% patients, respectively. The reversed distal ICA flow tended to be at lower levels in the successful group than in the unsuccessful group ($P < .001$; Fig 2*A–C*; Fig 3*A*,

Table 1: Characteristics of patients with CICAO

	Successful ($n = 76$)	Unsuccessful ($n = 38$)	*P*
Age (mean) (yr)	53.9 (SD, 15.9)	58.5 (SD, 11.0)	.115
Male (No.) (%)	49 (64.5)	23 (60.5)	.680
Smoking (No.) (%)	44 (57.9)	26 (68.4)	.276
Hypertension (No.) (%)	29 (38.1)	14 (36.8)	.891
Diabetes mellitus (No.) (%)	22 (28.9)	5 (13.2)	.062
Hyperlipidemia (No.) (%)	39 (51.3)	15 (39.5)	.233
History of stroke (No.) (%)	12 (15.8)	8 (21.1)	.500
Stroke (No.) (%)	55 (72.4)	32 (84.2)	.161

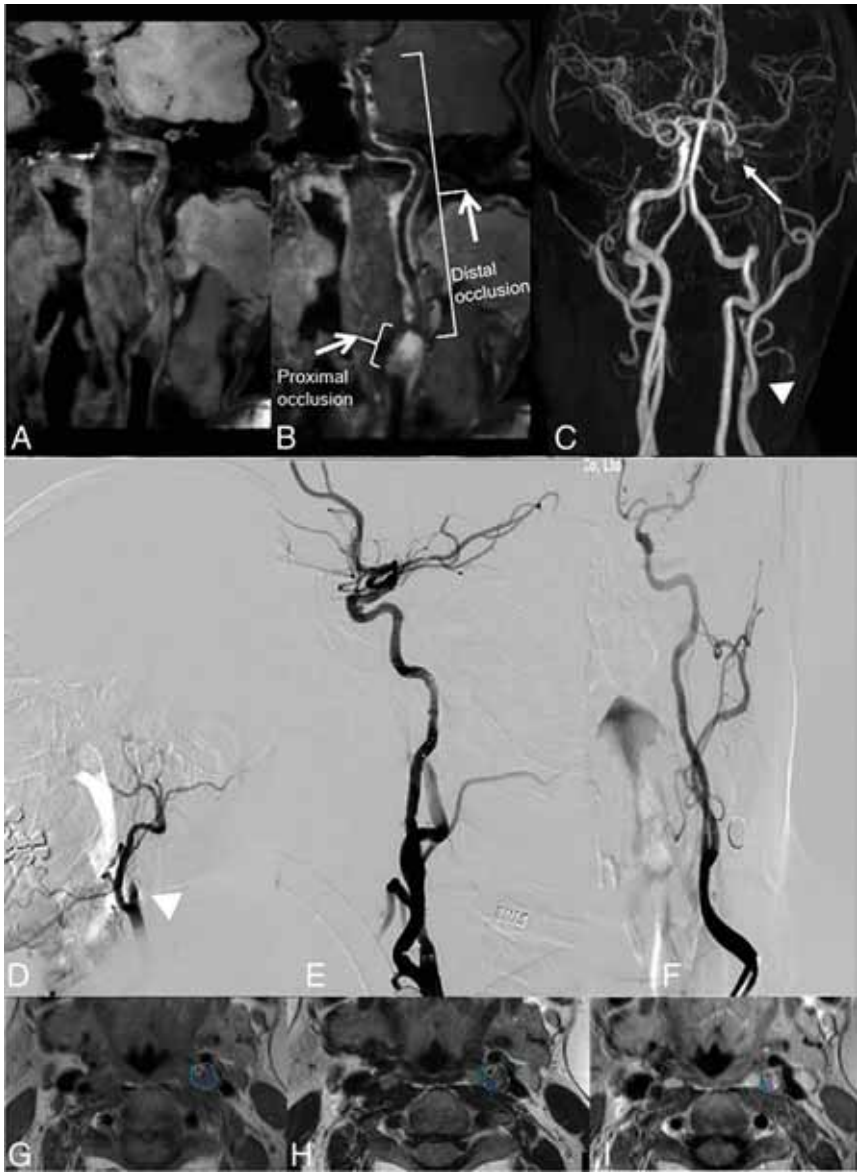

FIG 2. Successful recanalization cases. *A*, Curved planar reformation (CPR) on T1WI-volume isotropic turbo spin-echo acquisition (VISTA) shows moderate hypointensity in the proximal occlusion and iso- or hypointensity in the lumen of the distal occlusion. *B*, CPR on T1WI-VISTA-CE shows inhomogeneous enhancement in the origin of the left ICA and hypointensity in the distal occlusion. *C* and *D*, CE-MRA and preoperative DSA show a tapered stump (*triangle*) and reversal of flow above the clinoid segment of left ICA (*arrow*). *E* and *F*, Postoperative DSA shows successful recanalization. *G–I*, Plaque composition is shown in the proximal occlusion on T1WI and T2WI and enhancement on T1WI (blue, calcification; orange, hemorrhage; yellow, lipid-rich/necrotic core; purple, loose matrix).

B, *C*, *E*). The mean volume of lipid-rich necrotic core (for proximal occlusion, Fig 2*G–I*; Fig 3*F–H*) and lumen iso- or hypointensity and lumen area (for distal occlusion, Figs 2 and 3 *A*, *-B*) were significantly larger in the successful group than in the unsuccessful group (167.2 [SD, 74.2] mm^3 versus 139.8 [SD, 54.5] mm^3, $P < .050$; 59.2% versus 39.5%, $P = .047$; 7.4 [SD, 3.4] mm^2 versus 3.9 [SD, 2.3] mm^2, $P < .001$, respectively). The mean lesion length and calcification volume (for proximal occlusion, Fig 2*A*, *B*, *G–I*; Fig 3*A*, *B*, *F–H*) were significantly lower in the successful group than in the unsuccessful group (20.7 [SD, 5.4] mm versus 23.9 [SD, 4.8] mm, $P < .005$, and 41.3 [SD, 39.5] mm^3 versus 141.9 [SD, 107.8] mm^3, $P < .001$, respectively). Lesion volume, hemorrhage, dense fibrous tissue, loose matrix (for proximal occlusion); wall area (for distal occlusion); and primary collateral circulation were not significantly different between the 2 groups ($P > .05$). Table 2 summarizes the lesion characteristics.

Relationship between HR-MR Imaging Features and Success of Recanalization

In univariate analysis, the presence of a tapered stump, reversed distal ICA flow at the petrous segment or below, larger volume of the lipid-rich necrotic core (for proximal occlusion), and lumen iso- or hypointensity and larger lumen area (for distal occlusion) were significantly associated with successful recanalization (all, $P < .05$). Conversely, reversed distal ICA flow at the ophthalmic segment or above, longer lesion length, and more calcification volume (for proximal occlusion) were significantly associated with failure of recanalization (all, $P < .05$). In multivariate analysis, the following variables were protective factors of successful recanalization: lesion length: OR, 0.41; 95% CI, 0.36–0.55; $P = .009$; larger calcification volume for proximal occlusion: OR, 0.56; 95% CI, 0.37–0.68; $P = .002$; and reversed distal ICA flow at the ophthalmic segment or above: OR, 0.14; 95% CI, 0.08–0.48; $P = .001$; Table 3. The following variables were risk factors for successful recanalization: reversed distal ICA flow at petrous segment or below: OR, 4.07; 95% CI, 1.65–8.38; $P = .001$;

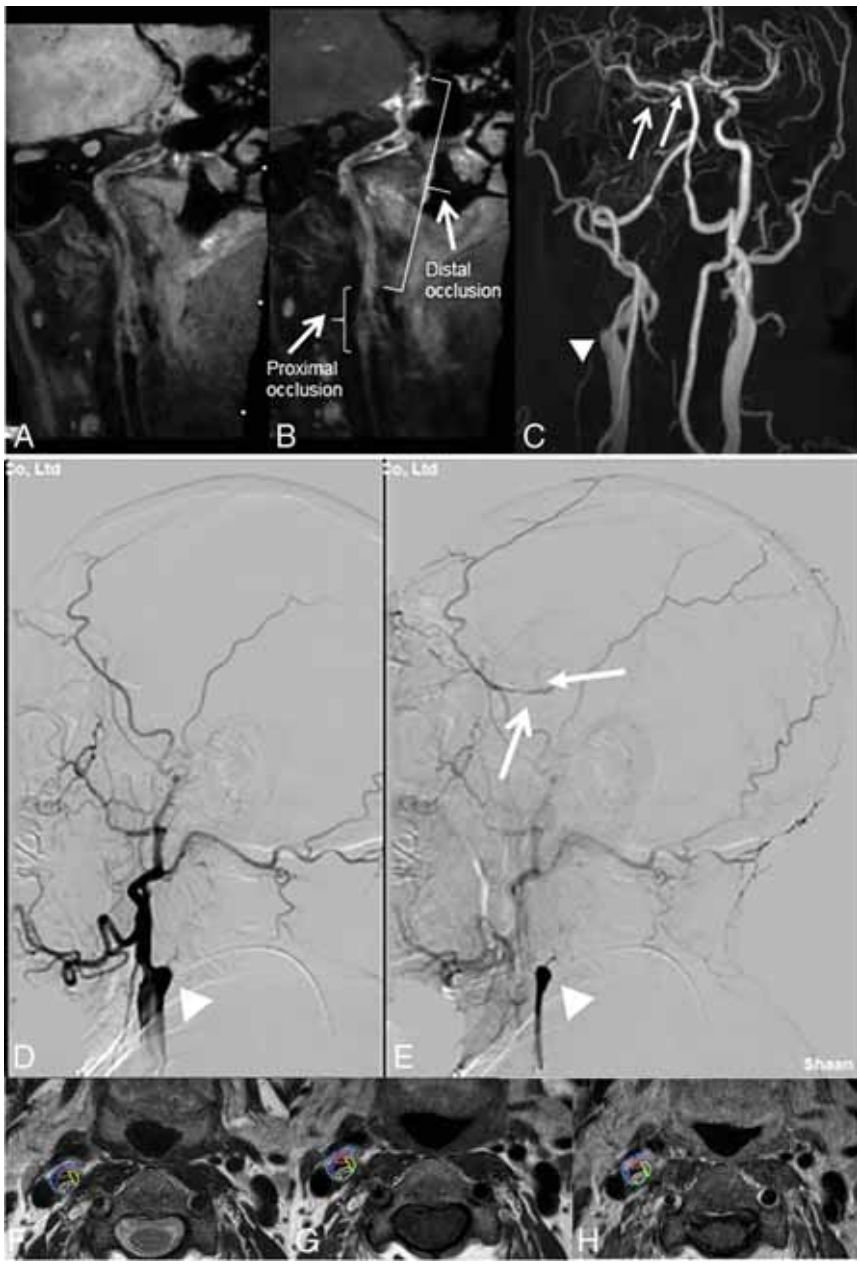

FIG 3. Unsuccessful recanalization cases. *A*, Curved planar reformation (CPR) on T1WI-volume isotropic turbo spin-echo acquisition (VISTA) shows mixed signal and wall collapse in the lumen distal to the occlusion. *B*, CPR on T1WI-VISTA-CE shows inhomogeneous enhancement in the proximal occlusion and distal segment of the right ICA (*arrowhead*). *C–E*, CE-MRA and DSA show a blunt stump (*triangle*), secondary collateral circulation (*arrowhead*), and reversal flow above the communicating segment of right ICA (*arrows*). *F–H*, Plaque composition is shown in the proximal occlusion (blue, calcification; orange, hemorrhage; yellow, lipid-rich/necrotic core; purple, loose matrix).

and larger lumen area for distal occlusion: OR, 1.13; 95% CI, 1.04–1.61; $P = .002$; Table 3.

Reproducibility Assessment between DSA and MR Imaging

There was good agreement between DSA and HR-MRI for the evaluation of stump status, the level of reversed distal ICA flow, and major and minor collateral circulations ($\kappa = 0.92$, $\kappa = 0.88$, $\kappa = 0.89$, and $\kappa = 0.84$, respectively). The intraclass correlation coefficients for lesion length, lesion volume, lipid-rich necrotic core, hemorrhage, calcification, dense fibrous tissue, loose matrix (for proximal occlusion), and lumen area and wall area (for distal occlusion) were 0.94, 0.87, 0.78, 0.76, 0.81, 0.84, 0.88, 0.91, and 0.90, respectively.

DISCUSSION

HR-MR imaging has a crucial role in the imaging evaluation of symptomatic patients with CICAO. HR-MR imaging can accurately evaluate the vessel lumen, wall, and course; it can provide information on the degree of inflammation of the wall and the collateral circulation and distinguish lumen blood stasis and thrombus distal to the occlusion.[35,36] In this study, the HR-MR imaging characteristics of patients with successful recanalization included a tapered stump, less secondary collateral circulation, reversed distal ICA flow at the level of petrous segment or below, more lipid-rich necrotic core, less calcification volume, shorter lesion length (for proximal occlusion), and lumen iso- or hypointensity and larger lumen area (for distal occlusion). Multivariate analysis showed that shorter lesion length and less calcification volume (for proximal occlusion) and reversed distal ICA flow at the petrous segment or below and larger lumen area (for distal occlusion) were independent predictors of successful recanalization.

Atherosclerosis is responsible for 70% of cases of CICAO. Because patients are asymptomatic in the early stages, the real duration of occlusion cannot be accurately defined.[37] With prolongation of the occlusion time, the stump morphology changes from tapered to blunt or no stump, the proximal plaque and distal lumen thrombus hardens due to fibrosis and calcification, and the occlusive length gradually increases due to the thrombotic process and a collapsed lumen in the distal occlusion.[38] These changes increase the difficulty of recanalization in CICAO, as has also been observed in chronic coronary occlusion.[14]

Our study showed that reversed distal ICA flow at the petrous segment or below was a risk factor for successful recanalization in CICAO, while reversed distal flow at the ophthalmic segment or above was a protective factor of success. This finding is consistent with those in previous studies.[11,18] In addition, we found that successful recanalization was also related to lesion length and calcification volume (for proximal occlusion) and lumen area (for distal occlusion). A previous study showed that HR-MR imaging can

Table 2: HR-MR imaging characteristics of lesions in symptomatic patients with CICAO

	Total (n = 114)	Successful (n = 76)	Unsuccessful (n = 38)	P
Right (No.) (%)	67 (58.8)	42 (55.2)	25 (65.8)	.282
Tapered stump (No.) (%)	64 (56.1)	48 (63.2)	16 (42.1)	.033
Level of reversed distal ICA flow				<.001
Communicating segment (No.) (%)	8 (7.0)	2 (2.6)	6 (15.8)	
Ophthalmic segment (No.) (%)	12 (10.5)	2 (2.6)	10 (26.3)	
Clinoid segment (No.) (%)	23 (20.2)	14 (18.4)	9 (23.7)	
Cavernous segment (No.) (%)	32 (28.1)	24 (31.6)	8 (21.1)	
Petrous segment or below (No.) (%)	39 (34.2)	34 (44.7)	5 (13.2)	
Collateral circulation				
Primary (No.) (%)	64 (56.1)	39 (51.3)	25 (65.8)	.142
Secondary (No.) (%)	25 (21.9)	12 (15.7)	13 (34.2)	.025
Proximal occlusion				
Lesion length (mean) (mm)	21.9 (SD, 4.2)	20.7 (SD, 5.4)	23.9 (SD, 4.8)	<.005
Lesion volume (mean) (mm^3)	1084.8 (SD, 472.5)	1007.3 (SD, 453.4)	1159.1 (SD, 486.1)	.110
Lipid-rich necrotic core (mean) (mm^3)	143.3 (SD, 76.6)	167.2 (SD, 74.2)	139.8 (SD, 54.5)	<.050
Hemorrhage (mean) (mm^3	54.5 (SD, 43.1)	58.4 (SD, 46.7)	53.6 (SD, 40.4)	.510
Calcification (mean) (mm^3)	112.9 (SD, 96.4)	41.3 (SD, 39.5)	141.9 (SD, 107.8)	<.001
Dense fibrous tissue (mean) (mm^3)	708.2 (SD, 391.1)	689.6 (SD, 372.3)	738.8 (SD, 437.6)	.611
Loose matrix (mean) (mm^3)	250.3 (SD, 130.5)	219.7 (SD, 103.8)	257.9 (SD, 141.6)	.120
Distal occlusion				
Lumen iso -to hypointensity (No.) (%)	60 (52.6)	45 (59.2)	15 (39.5)	.047
Lumen area (mean) (mm^2)	6.28 (SD, 3.5)	7.4 (SD, 3.4)	3.9 (SD, 2.3)	<.001
Wall area (mean) (mm^2)	32.7 (SD, 6.9)	32.0 (SD, 6.8)	33.4 (SD, 8.7)	.340

Table 3: Factors associated with recanalization success in univariable and multivariable analysis

	Univariable Analysis		Multivariable Analysis	
Characteristic	OR (95% CI)	P	OR (95% CI)	P
Right	0.64 (0.51–1.33)	.282		
Tapered stump	2.36 (1.02–3.11)	.035	2.23 (0.87–3.36)	.091
Level of reversed distal ICA flow				
Communicating segment	0.14 (0.07–0.21)	.001	0.13 (0.07–0.24)	.010
Ophthalmic segment	0.08 (0.03–0.44)	<.001	0.14 (0.08–0.48)	.001
Clinoid segment	0.73 (0.63–1.21)	.214	0.62 (0.36–1.22)	.160
Cavernous segment	1.73 (0.96–3.89)	.07	1.66 (0.87–3.54)	.550
Petrous segment or below	5.34 (1.41–11.37)	<.001	4.07 (1.65–8.38)	.001
Collateral circulation				
Primary	0.55 (0.35–1.59)	.143		
Secondary	0.36 (0.14–0.71)	.027	1.32 (0.98–1.47)	.210
Proximal occlusion				
Lesion length	0.51 (0.13–0.74)	.005	0.41 (0.36–0.55)	.009
Lesion volume	2.11 (0.71–4.49)	.110		
Lipid-rich necrotic core	3.26 (1.45–6.36)	.024	2.36 (0.94–5.33)	.060
Hemorrhage	1.35 (0.65–2.38)	.510		
Calcification	0.71 (0.44–0.90)	<.001	0.56 (0.37–0.68)	.002
Dense fibrous tissue	3.31 (0.93–10.36)	.615		
Loose matrix	1.66 (0.87–3.88)	.120		
Distal occlusion				
Lumen iso- to hypointensity	2.23 (1.06–5.29)	.047	1.87 (0.91–4.66)	.091
Lumen area	1.32 (1.02–2.17)	<.001	1.13 (1.04–1.61)	.002
Wall area	1.76 (0.71–3.38)	.230		

accurately indicate the hardness of plaque by identifying its composition.[39] Chronic atherosclerotic plaque is hard (fibrotic-calcified plaque) due to the presence of relatively more calcification and dense fibrous tissue and less lipid-necrotic core.[39,40] Hard plaque and longer occlusion length at the proximal occlusion can make wiring across the occlusion difficult and result in vessel injury and arterial dissection. With prolongation of the occlusion time, the lumen distal to the occlusion wall collapses. In this study, we found that the lumen area for distal occlusion was a risk factor of successful recanalization. The lumen area was higher in the successful recanalization group than in the failed group, in which the lumen area for distal occlusion reflected the degree of collapsed vessel wall and affected the successful recanalization. HR-MR imaging can display these features, which are important reasons for failure of recanalization of CICAO. Archie,[41] therefore, suggested that when the distal ICA occlusion is small or poorly visualized, carotid endarterectomy should be performed.

In this study, tapered stump, lipid-rich necrotic core (for proximal occlusion), and lumen iso- or hypointensity (for distal occlusion) were more prevalent in the successful group. However, in

multivariable analysis, these factors were not independently associated with successful recanalization and may not be the main factors related to it. For distal occlusion, the size and composition of the thrombus may affect the success of recanalization.[42] The histologic characteristics of the thrombus might reflect the pathologic process of CICAO.[43,44] MR imaging can accurately define the duration of thrombosis in vivo through signal changes.[45] However, in some of our patients, lumen iso- or hypointensity for the distal occlusions was recanalized after stent implantation and no thrombi were found in the distal embolic protection device. We speculate that, for distal occlusion, lumen iso- or hypointensity might indicate blood stagnation.

DSA remains the criterion standard for the diagnosis of CICAO because it can accurately evaluate the stump, the position of reflux, and the collateral blood supply beyond the occlusion that flows retrograde into the distal ICA. We found good consistency between HR-MR imaging and DSA in the evaluation of stump status, the level of reversed distal ICA flow, and primary and secondary collateral circulation. The limitation of HR-MR imaging is that it cannot evaluate direction of flow. Meanwhile, DSA cannot analyze the course or wall and lumen of the occluded segment of the vessel;[22,23] moreover, it is an expensive, invasive procedure involving exposure to radiation. Although the key predictors of successful recanalization can be obtained using CTA, it cannot be used to accurately assess the intracranial ICA for intervening skull bone, the age of thrombus, intraplaque hemorrhage (IPH), and lipid-rich necrotic core. Currently, the IPH and lipid-rich necrotic core are possible to detect using CT and MR imaging, but the limitation of CT is that the IPH cannot be distinguished from lipid-rich necrotic core for overlapping density values.[46,47] Some authors have suggested that HR-MRI is the best imaging technique for the detection of IPH.[48] Otherwise, the view that HR-MRI can sensitively detect IPH has been strengthened by the Vessel Wall Imaging Study Group.[49] HR-MR imaging—which is a noninvasive, higher soft-tissue contrast, and radiationless evaluation of the vessel wall and lumen, plaque composition, the vessel distal to the occlusion, and the collateral blood supply beyond the occlusion—can, therefore, be expected to become a first-line technique for preoperative evaluation of CICAO.

This study has several limitations. First, this was a retrospective study, so a selection bias cannot be ruled out. Second, we did not analyze other imaging indices such as the structure and perfusion of brain parenchyma; this analysis might have affected the outcome. Third, when HR-MR imaging is used to observe collateral circulation, only the thickness of collateral vessels can be judged, not the direction of blood flow and leptomeningeal collateral circulation, possibly affecting the results.

CONCLUSIONS

HR-MR imaging is a noninvasive tool that can evaluate CICAO and guide decision-making in symptomatic patients with CICAO. Lesion length and calcification volume (for proximal occlusion), the level of reversed distal ICA flow, and lumen area (for distal occlusion) appear to be associated with the success of recanalization performed using balloon dilation and stent implantation. Further studies are needed to clarify how HR-MR imaging characteristics can be applied for selection of the treatment method.

Disclosure forms provided by the authors are available with the full text and PDF of this article at www.ajnr.org.

REFERENCES

1. Flaherty ML, Flemming KD, McClelland R, et al. **Population-based study of symptomatic internal carotid artery occlusion: incidence and long-term follow-up.** *Stroke* 2004;35:e349–52 CrossRef Medline
2. Iwata T, Mori T, Tajiri H, et al. **Long-term angiographic and clinical outcome following stenting by flow reversal technique for chronic occlusions older than 3 months of the cervical carotid or vertebral artery.** *Neurosurgery* 2012;70:82–90 CrossRef Medline
3. Powers WJ, Derdeyn CP, Fritsch SM, et al. **Benign prognosis of never-symptomatic carotid occlusion.** *Neurology* 2000;54:878–82 CrossRef Medline
4. Buslovich S, Hines GL. **Spontaneous recanalization of chronic internal carotid artery occlusions: report of 3 cases.** *Vasc Endovascular Surg* 2011;45:93–97 CrossRef Medline
5. Chmayssani M, Festa JR, Marshall RS. **Chronic ischemia and neurocognition.** *Neuroimaging Clin N Am* 2007;17:313–24 CrossRef Medline
6. Kao HL, Hung CS, Li HY, et al. **Long-term outcomes after endovascular recanalization in patients with chronic carotid artery occlusion.** *Am J Cardiol* 2018;122:1779–83 CrossRef Medline
7. Lin MS, Chiu MJ, Wu YW, et al. **Neurocognitive improvement after carotid artery stenting in patients with chronic internal carotid artery occlusion and cerebral ischemia.** *Stroke* 2011;42:2850–54 CrossRef Medline
8. Chen YH, Lin MS, Lee JK, et al. **Carotid stenting improves cognitive function in asymptomatic cerebral ischemia.** *Int J Cardiol* 2012;157:104–07 CrossRef Medline
9. Huang CC, Chen YH, Lin MS, et al. **Association of the recovery of objective abnormal cerebral perfusion with neurocognitive improvement after carotid revascularization.** *J Am Coll Cardiol* 2013;61:2503–09 CrossRef Medline
10. Rubiera M, Ribo M, Delgado-Mederos R, et al. **Tandem internal carotid artery/middle cerebral artery occlusion: an independent predictor of poor outcome after systemic thrombolysis.** *Stroke* 2006;37:2301–05 CrossRef Medline
11. Lee CW, Lin YH, Liu HM, et al. **Predicting procedure successful rate and 1-year patency after endovascular recanalization for chronic carotid artery occlusion by CT angiography.** *Int J Cardiol* 2016;221:772–76 CrossRef Medline
12. Kappelhof M, Marquering HA, Berkhemer OA, et al. **Intra-arterial treatment of patients with acute ischemic stroke and internal carotid artery occlusion: a literature review.** *J Neurointerv Surg* 2015;7:8–15 CrossRef Medline
13. Duijsens HM, Spaander F, van Dijk LC, et al. **Endovascular treatment in patients with acute ischemic stroke and apparent occlusion of the extracranial internal carotid artery on CTA.** *J Neurointerv Surg* 2015;7:709–14 CrossRef Medline
14. Morino Y, Abe M, Morimoto T, et al; J-CTO Registry Investigators. **Predicting successful guidewire crossing through chronic total occlusion of native coronary lesions within 30 minutes: the J-CTO (Multicenter CTO Registry in Japan) score as a difficulty grading and time assessment tool.** *JACC Cardiovasc Interv* 2011;4:213–21 CrossRef Medline
15. Liebeskind DS, Sanossian N, Yong WH, et al. **CT and MRI early vessel signs reflect clot composition in acute stroke.** *Stroke* 2011;42:1237–43 CrossRef Medline
16. Puig J, Pedraza S, Demchuk A, et al. **Quantification of thrombus Hounsfield units on noncontrast CT predicts stroke subtype and early recanalization after intravenous recombinant tissue plasminogen activator.** *AJNR Am J Neuroradiol* 2012;33:90–96 CrossRef Medline
17. Mo L, Ma G, Dai C, et al. **Endovascular recanalization for symptomatic subacute and chronically occluded internal carotid artery:**

feasibility, safety, a modified radiographic classification system, and clinical outcomes. *Neuroradiology* 2020;62:1323–34 CrossRef Medline
18. Chen YH, Leong WS, Lin MS, et al. **Predictors for successful endovascular intervention in chronic carotid artery total occlusion.** *JACC Cardiovasc Interv* 2016;9:1825–32 CrossRef Medline
19. Michel P, Ntaios G, Delgado MG, et al. **CT angiography helps to differentiate acute from chronic carotid occlusion: the "carotid ring sign."** *Neuroradiology* 2012;54:139–46 CrossRef Medline
20. Hugenholtz H, Elgie RG. **Carotid thromboendarterectomy: a reappraisal: criteria for patient selection.** *J Neurosurg* 1980;53:776–83 CrossRef Medline
21. Zanaty M, Howard S, Roa JA, et al. **Cognitive and cerebral hemodynamic effects of endovascular recanalization of chronically occluded cervical internal carotid artery: single-center study and review of the literature.** *J Neurosurg* 2019;132:1158–66 CrossRef Medline
22. Wang X, Wang Z, Ji Y, et al. **Enterprise stent in recanalizing non-acute atherosclerotic intracranial internal carotid artery occlusion.** *Clin Neurol Neurosurg* 2017;162:47–52 CrossRef Medline
23. Namba K, Shojima M, Nemoto S. **Wire-probing technique to revascularize subacute or chronic internal carotid artery occlusion.** *Interv Neuroradiol* 2012;18:288–96 CrossRef Medline
24. Hong JM, Lee SE, Lee SJ, et al. **Distinctive patterns on CT angiography characterize acute internal carotid artery occlusion subtypes.** *Medicine (Baltimore)* 2017;96:e5722 CrossRef Medline
25. Liu Y, Jia L, Liu B, et al. **Evaluation of endarterectomy recanalization under ultrasound guidance in symptomatic patients with carotid artery occlusion.** *PloS One* 2015;10:e0144381 CrossRef Medline
26. Jiang Y, Zhu C, Peng W, et al. **Ex-vivo imaging and plaque type classification of intracranial atherosclerotic plaque using high resolution MRI.** *Atherosclerosis* 2016;249:10–16 CrossRef Medline
27. Bodle JD, Feldmann E, Swartz RH, et al. **High-resolution magnetic resonance imaging: an emerging tool for evaluating intracranial arterial disease.** *Stroke* 2013;44:287–92 CrossRef Medline
28. Cai JM, Hatsukami TS, Ferguson MS, et al. **Classification of human carotid atherosclerotic lesions with in vivo multicontrast magnetic resonance imaging.** *Circulation* 2002;106:1368–73 CrossRef Medline
29. Iwata T, Mori T, Tajiri H, et al. **Successful stenting by combination technique of reverse flow and downstream filtering for long chronic total occlusion of the cervical vertebral artery: technical case report.** *Neurosurgery* 2009;65:E378–79 CrossRef Medline
30. Zhou Z, Li R, Zhao X, et al. **Evaluation of 3D multi-contrast joint intra-and extracranial vessel wall cardiovascular magnetic resonance.** *J Cardiovasc Magn Reson* 2015;17:41 CrossRef Medline
31. Liebeskind DS. **Collateral circulation.** *Stroke* 2003;34:2279–84 CrossRef Medline
32. Maas MB, Lev MH, Ay H, et al. **Collateral vessels on CT angiography predict outcome in acute ischemic stroke.** *Stroke* 2009;40:3001–05 CrossRef Medline
33. Truong M, Håkansson C, HaileMichael M, et al. **The potential role of T2*-weighted multi-echo data image combination as an imaging marker for intraplaque hemorrhage in carotid plaque imaging.** *BMC Med Imaging* 2021;21:121 CrossRef Medline
34. Saam T, Ferguson MS, Yarnykh VL, et al. **Quantitative evaluation of carotid plaque composition by in vivo MRI.** *Arterioscler Thromb Vasc Biol* 2005;25:234–39 CrossRef Medline
35. Sui B, Gao P. **High-resolution vessel wall magnetic resonance imaging of carotid and intracranial vessels.** *Acta Radiol* 2019;60:1329–40 CrossRef Medline
36. Joseph P, Ishai A, Mani V, et al. **Short-term changes in arterial inflammation predict long-term changes in atherosclerosis progression.** *Eur J Nucl Med Mol Imaging* 2017;44:141–50 CrossRef Medline
37. Paraskevas KI, Mikhailidis DP, Liapis CD. **Internal carotid artery occlusion: association with atherosclerotic disease in other arterial beds and vascular risk factors.** *Angiology* 2007;58:329–35 CrossRef Medline
38. Stone GW, Kandzari DE, Mehran R, et al. **Percutaneous recanalization of chronically occluded coronary arteries: a consensus document: Part I.** *Circulation* 2005;112:2364–72 CrossRef Medline
39. Tartari S, Rizzati R, Righi R, et al. **High-resolution MRI of carotid plaque with a neurovascular coil and contrast-enhanced MR angiography: one-stop shopping for the comprehensive assessment of carotid atherosclerosis.** *AJR Am J Roentgenol* 2011;196:1164–71 CrossRef Medline
40. Naghavi M, Libby P, Falk E, et al. **From vulnerable plaque to vulnerable patient: a call for new definitions and risk assessment strategies: Part I.** *Circulation* 2003;108:1664–72 CrossRef Medline
41. Archie JP Jr. **Carotid endarterectomy when the distal internal carotid artery is small or poorly visualized.** *J Vasc Surg* 1994;19:23–30 CrossRef Medline
42. Morais LT, Leslie-Mazwi TM, Lev MH, et al. **Imaging-based selection for intra-arterial stroke therapies.** *J Neurointerv Surg* 2013;5 (Suppl 1):i13–20 CrossRef Medline
43. Furie B, Furie BC. **Mechanisms of thrombus formation.** *N Engl J Med* 2008;359:938–49 CrossRef Medline
44. Marder VJ, Chute DJ, Starkman S, et al. **Analysis of thrombi retrieved from cerebral arteries of patients with acute ischemic stroke.** *Stroke* 2006;37:2086–93 CrossRef Medline
45. Saha P, Andia ME, Modarai B, et al. **Magnetic resonance T-1 relaxation time of venous thrombus is determined by iron processing and predicts susceptibility to lysis.** *Circulation* 2013;128:729–36 CrossRef Medline
46. U-King-Im JM, Fox AJ, Aviv RI, et al. **Characterization of carotid plaque hemorrhage: a CT angiography and MR intraplaque hemorrhage study.** *Stroke* 2010;41:1623–29 CrossRef Medline
47. Trelles M, Eberhardt KM, Buchholz M, et al. **CTA for screening of complicated atherosclerotic carotid plaque: American Heart Association type VI lesions as defined by MRI.** *AJNR Am J Neuroradiol* 2013;34:2331–37 CrossRef Medline
48. Bitar R, Moody AR, Leung G, et al. **In vivo 3D high-spatial-resolution MR imaging of intraplaque hemorrhage.** *Radiology* 2008;249:259–67 CrossRef Medline
49. Saba L, Yuan C, Hatsukami TS, et al; Vessel Wall Imaging Study Group of the American Society of Neuroradiology. **Carotid artery wall imaging: perspective and guidelines from the ASNR Vessel Wall Imaging Study Group and Expert Consensus Recommendations of the American Society of Neuroradiology.** *AJNR Am J Neuroradiol* 2018;39:E9–31 CrossRef Medline

Deep Learning for Synthetic CT from Bone MRI in the Head and Neck

S. Bambach and M.-L. Ho

ABSTRACT

BACKGROUND AND PURPOSE: Bone MR imaging techniques enable visualization of cortical bone without the need for ionizing radiation. Automated conversion of bone MR imaging to synthetic CT is highly desirable for downstream image processing and eventual clinical adoption. Given the complex anatomy and pathology of the head and neck, deep learning models are ideally suited for learning such mapping.

MATERIALS AND METHODS: This was a retrospective study of 39 pediatric and adult patients with bone MR imaging and CT examinations of the head and neck. For each patient, MR imaging and CT data sets were spatially coregistered using multiple-point affine transformation. Paired MR imaging and CT slices were generated for model training, using 4-fold cross-validation. We trained 3 different encoder-decoder models: Light_U-Net (2 million parameters) and VGG-16 U-Net (29 million parameters) without and with transfer learning. Loss functions included mean absolute error, mean squared error, and a weighted average. Performance metrics included Pearson *R*, mean absolute error, mean squared error, bone precision, and bone recall. We investigated model generalizability by training and validating across different conditions.

RESULTS: The Light_U-Net architecture quantitatively outperformed VGG-16 models. Mean absolute error loss resulted in higher bone precision, while mean squared error yielded higher bone recall. Performance metrics decreased when using training data captured only in a different environment but increased when local training data were augmented with those from different hospitals, vendors, or MR imaging techniques.

CONCLUSIONS: We have optimized a robust deep learning model for conversion of bone MR imaging to synthetic CT, which shows good performance and generalizability when trained on different hospitals, vendors, and MR imaging techniques. This approach shows promise for facilitating downstream image processing and adoption into clinical practice.

ABBREVIATIONS: DL = deep learning; GRE = gradient recalled-echo; MAE = mean absolute error; MSE = mean squared error; TE = echo time

MR imaging is the workhorse of clinical neuroradiology, providing high tissue contrast for the evaluation of CNS structures. However, CT remains the first-line technique for rapid neurologic screening and cortical bone assessment. A novel class of MR imaging techniques uses very short TE to capture weak and short-lived proton signals from dry tissues such as cortical bone. As MR imaging hardware and software have advanced, "black-bone" MR imaging techniques have progressively improved from gradient recalled-echo (GRE) to ultrashort-TE and zero-TE approaches.[1-3] TE values are on the order of 1–2 ms for GRE, 50–200 ms for ultrashort-TE, and 0–25 ms for zero-TE (Online Supplemental Data). With shorter TEs, the detectable signal from cortical bone increases, scan times become faster, acoustic noise from gradient switching decreases, and resistance to motion and susceptibility artifacts increases.[4-5]

Bone MR imaging offers the potential for both rapid initial screening and comprehensive "one-stop-shop" imaging, without the need for ionizing radiation exposure. Thus, bone MR imaging is a promising alternative to CT for bone imaging. However, current barriers to implementation involve direct comparison of bone MR imaging and CT with regard to multiple factors, including accessibility, cost, convenience, patient awareness, clinician understanding, diagnostic

Received March 30, 2021; accepted after revision June 13, 2022.

From the Abigail Wexner Research Institute at Nationwide Children's Hospital (S.B.), Columbus, Ohio, and Department of Radiology (M.-L.H.), Nationwide Children's Hospital, Columbus, Ohio.

This work was supported by the American Society of Head & Neck Radiology Core Curriculum Fund William N. Hanafee Research Grant, Siemens/Radiological Society of North America Research Scholar Grant, RSCH1804, and the Society for Pediatric Radiology Pilot Award.

Please address correspondence to Mai-Lan Ho, MD, Nationwide Children's Hospital, 700 Children's Dr, ED4106, Columbus, OH, 43205-2664; e-mail: lan.ho@nationwidechildrens.org

Indicates article with online supplemental data.

http://dx.doi.org/10.3174/ajnr.A7588

accuracy, and interventional utility.[6-8] A key step in facilitating clinical understanding and adoption is the automated conversion of bone MR imaging to synthetic CT-like contrast, which is highly desirable for image interpretation, 3D printing, and surgical planning applications. Conventional image-processing approaches, such as intensity thresholding, logarithmic inversion, histogram subtraction, atlas- and voxel-based techniques, have all been investigated.[9-12] In clinical practice, these point operation–based techniques are hampered by false-negatives in the setting of undermineralization (young children or osteopenia), very thin bone (pathologic remodeling), and multiple bone-air interfaces (facial bones, skull base), as well as false-positives including other short-T2 tissues (fascia, dura, ligaments, cartilage, hardware, hemorrhage, mucoid secretions, air) and complex tissue interfaces (tumor, trauma, inflammation).

Deep learning (DL) offers a promising approach for synthetic CT generation, being already routinely used for tissue classification and image-mapping purposes. DL algorithms use multiple layers of neighborhood-based operations to derive complex information from diverse input data sets, including MR imaging signal properties, normal anatomic structures, and pathologic changes. In neuroradiology, DL for synthetic CT has been explored in adult volunteers and a few patient case series, the most frequent application being radiation therapy planning or PET attenuation correction. Despite these early studies suggesting feasibility, synthetic CT approaches have only been successful when applied to anatomically simpler regions such as the torso and extremities or normal adult skull anatomy at low spatial resolution.[13-17] For most cases of head and neck clinical applications, existing synthetic CT algorithms fail due to the wide variety of normal anatomic variants and pathologic conditions. Without sufficient clinical training data and human supervision, DL-powered bone MR imaging conversion approaches show limitations similar to those of conventional processing, yielding a variety of false-negatives and false-positives.

Robust synthetic CT algorithms still have not been developed for head and neck applications, are not routinely used in clinical decision-making, and do not carry added value over source MR images interpreted by experienced radiologists. Therefore, at this time, bone MR imaging is a useful alternative to CT for diagnostic imaging but requires a radiologist's understanding of imaging physics, head and neck anatomy, and pathologic disease processes to optimally analyze the source images. Improvement of automated synthetic CT algorithms could help address existing barriers to technology implementation by providing greater understanding for untrained radiologists and clinicians as well as facilitating downstream processing such as 3D printing and surgical navigation. Therefore, the objective of our study was to optimize a convolutional neural network algorithm for bone MR imaging conversion to synthetic CT based on our diverse data set of patients using different institutions, platforms, and bone MR imaging techniques. In particular, we sought to develop a robust DL model that would show good performance and generalizability, thus facilitating downstream image processing and adoption into clinical practice.

MATERIALS AND METHODS

Data Acquisition

This was an institutional review board–approved retrospective study with de-identified data sequentially collected from 2 institutions. The patient flowchart for study selection is described in the Online Supplemental Data. Originally, 53 patients were included with bone MR imaging and CT of the head and neck performed within a 6-month time period for bone evaluation. Following image review by a neuroradiologist with expertise in bone MR imaging, 14 patients were excluded on the basis of nondiagnostic image quality (MR imaging and/or CT) due to motion, hardware, or other artifacts. This exclusion resulted in a final data set of 39 patients: 16 patients from institution 1 and 23 patients from institution 2. Subjects spanned a broad age range (neonate to 35 years; median age, 4.5 years) with 23 (59%) male and 16 (41%) female patients. Clinical indications for imaging were suspected craniosynostosis ($n = 10$), genetic syndrome ($n = 5$), tumor ($n = 4$), trauma ($n = 4$), preoperative planning ($n = 10$), and postoperative follow-up ($n = 6$). Anatomic imaging coverage included the head, face, neck, and/or cervical spine, based on the indication. For bone MR imaging, an additional bone sequence was added to the examination on the basis of a clinical request and/or the indication for bone imaging. A variety of platforms, techniques, and field strengths were used, depending on the institution and scanner availability.

For MR, thirteen patients were scanned on Siemens Healthineers (Erlangen, Germany) platforms (3 Tesla: Magnetom Prisma, 1.5 Tesla: Magnetom Aera), and 26, on GE Healthcare (Chicago, IL) platforms (3 Tesla: Discovery MR750, MR750w). Bone MR imaging sequences were adapted from commercially available options and included 3D zero-TE, ultrashort-TE, and GRE sequences with a 20- to 30-cm FOV and 0.7- to 1-mm isotropic resolution. Sample parameters are provided in the Online Supplemental Data. Most scans were performed at 3T, with 2 scans performed at 1.5T field strength due to device-compatibility considerations. For CT, 23 examinations were performed on Siemens Healthineers platforms (Somatom Definition Flash, Somatom Definition Edge, Somatom Definition AS, Somatom Force, Somatom Sensation 64); 9, on GE Healthcare platforms (Discovery CT750 HD, Optima CT660, LightSpeed VCT); and 7 on Canon Medical Systems (Tustin, California) platforms (Aquilion ONE) using a standard multidetector technique (age-adjusted radiation dose, 0.5- to 1-mm section thickness, bone reconstruction kernel).

Image Coregistration and Preprocessing

The goal of the image-processing pipeline (Online Supplemental Data) was to generate a diverse set of spatially aligned bone MR imaging and CT pairs for neural network training. A neuroradiologist with experience in bone MR imaging coregistered all MR imaging and CT images on the basis of key anatomic landmarks and inspected the final matched image sets for quality assurance. First, multiple-point affine transformation of MR imaging to CT data was performed in OsiriX MD (http://www.osirix-viewer.com) to yield coregistered 3D volumes. All remaining image-preprocessing steps were implemented in Matlab (MathWorks). The image volumes were resampled to achieve isotropic resolution in all dimensions and then were divided into paired 2D MR imaging and CT slices in axial, coronal, and sagittal planes. While synthesizing only axial CT views may be sufficient for many applications, we were interested in deriving the largest and most diverse training set possible. Each image pair was masked and cropped to disregard irrelevant background artifacts during training. Masks

were created by binarizing the CT image (using Otsu's method to find the ideal threshold[18]) and finding the largest convex area in the binary image. The same convex mask was also applied to the paired MR images. Images were cropped to the smallest possible square containing and centering the masked content.

Finally, each section was resized to the resolution required for neural network input. The resulting images were saved with an 8-bit gray-scale depth based on the entire dynamic range for MR imaging slices and bone window/level for CT slices. On average, this pipeline generated 550 MR imaging/CT pairs per patient (approximately 22,000 image slices total). Additionally, we artificially augmented our training data by randomly flipping (horizontally or vertically), rotating (by $<10°$), or cropping (by $<10\%$) image pairs during training.

We note here that masking the MR image based on a registered CT image would not be possible in a real-world scenario (because CT would not be available). However, we found this approach to work much more robustly, which was necessary to automate the masking pipeline, given the large amount of training slices. Our goal was to have clean training data. Inference based on a nonmasked MR imaging is still possible.

Neural Network Architectures

We tested 3 encoder-decoder networks based on U-Net models.[19] For the first model, we built a lightweight baseline model (Light_U-Net) based on the original U-Net architecture but decreasing the number of filters (channels) for each block, for total of ~2 million trainable parameters. We further changed the filter size of the transposed convolutions from 2×2 to 3×3 so that the decoder path exactly mirrored the encoder path, avoiding the need to crop the filter responses in the skip connections. The output layer was reduced to a single channel with sigmoid activation function, allowing the model to produce a gray-scale image rather than a binary segmentation mask. For the second model, we used the well-established VGG-16 convolutional neural network architecture[20] for the encoder path and mirrored it for the decoder path. The resulting model had a larger number of filters and filter blocks, resulting in ~29 million total trainable parameters. This enabled us to use transfer-learning as a third model variation, VGG-16 U-Net transfer-learning, in which filter weights in the encoder path were initialized with values learned from the public ImageNet (https://image-net.org/index) data set, in which a large variety of annotated objects were classified from >14 million conventional color photographs[21] (Online Supplemental Data).

Model Implementation

All DL models were implemented in Python (Python Software Foundation) using the TensorFlow library (www.tensorflow.org) with the Keras interface (Massachusetts Institute of Technology). All experiments were run on a high-performance computing cluster using either a NVIDIA Tesla V100 or NVIDIA Tesla P100 GPU (Nvidia, Santa Clara, California). The input to the model was a single-channel gray-scale bone MR image with a resolution of 224×224 pixels to match the fixed resolution of the VGG-16 architecture. Each 3×3 convolutional layer was followed by a batch-normalization layer and a ReLU activation layer. The VGG-16 U-Net architecture, which was originally designed for color images, required a 3-channel image input, so the gray-scale image was repeated across all 3 channels. Because the encoder path was an exact copy of the original VGG-16 architecture, its 3×3 convolutional layers were not followed by a batch-normalization layer but only had an ReLU activation. For the decoder path, batch normalization was still added after every 3×3 convolutional layer. For both networks, the synthetic CT image was produced via a 1×1 convolutional layer with a sigmoid activation, creating a continuous gray-scale image on the interval of 0–1 and a resolution of 224×224 pixels. All models were optimized with stochastic gradient descent using the Adam method[22] with default parameters and a batch size of 128 images. Network weights were initialized randomly, except for the VGG-16 U-Net transfer learning variant, in which weights in the encoder path were pretrained on ImageNet. No weights were frozen during optimization.

Loss Functions

We experimented with optimizing 3 different loss functions: mean absolute error (MAE, also called L_1 loss), mean squared error (MSE, also called L_2 loss), and a weighted sum of both:

$$L_1 = \frac{1}{N}\sum_{i=1}^{N} |CT_i - sCT_i|, L_2 = \frac{1}{N}\sum_{i=1}^{N} (CT_i - sCT_i)^2,$$

$$L_w = L_1 + \alpha L_2,$$

where N is the total number of image pairs in the training set and α is a coefficient that was selected empirically as 4.4, resulting in approximately equal contribution of L_1 and L_2 to the total loss.

Model Training and Validation

Because intrapatient image slices are visibly correlated with each other compared with interpatient slices, we trained and evaluated our models on data from separate patients. For every experiment, we performed a patient-level 4-fold cross-validation, with each model trained on three-quarters of the patients and then tested on the remaining quarter. Reported results were aggregated across all 4 models.

Because neural network optimization is stochastic in nature (random initialization and random batching), training on the same data set multiple times may result in a different model convergence. We, therefore, repeated each 4-fold cross-validation experiment 10 times and reported average performance and 95% confidence intervals across the 10 independent runs.

Neural network models additionally require an internal validation set to prevent overfitting. For this purpose, a random 15% of slices from the training data were held out during training. After each training epoch, we computed the internal validation loss and stopped training the model once that validation loss had not decreased for at least 5 epochs. We selected the model weights with the smallest internal validation loss up to that point.

Performance Metrics

Global performance metrics were calculated pixel-wise across the image data sets and included MAE, MSE, and the Pearson correlation coefficient R. To express MAE and MSE in terms of Hounsfield units, we rescaled the neural network output on the basis of a window width of 2000 HU. In addition, we quantified the degree of bone overlap between ground truth CT and synthetic CT by thresholding

Four-fold cross-validation results for different model and loss combinations[a]

Model	Loss	MAE (HU)	MSE (×10³ HU)	*R*	Avg. Bone Precision	Avg. Bone Recall	Avg. Bone Dice
Light_U-Net	MAE	95.6 (94.4–96.9)	54.3 (53.1–55.5)	0.872 (0.869–0.875)	0.665 (0.661–0.669)	0.519 (0.505–0.533)	0.567 (0.558–0.576)
Light_U-Net	MSE	106.0 (103.5–108.4)	51.5 (50.0–53.0)	0.878 (0.875–0.881)	0.621 (0.614–0.629)	0.548 (0.526–0.570)[b]	0.558 (0.544–0.573)
Light_U-Net	Mix	97.6 (96.6–98.7)	51.3 (50.4–52.2)	0.878 (0.876–0.880)[b]	0.641 (0.636–0.646)	0.538 (0.529–0.546)	0.568 (0.562–0.573)[b]
VGG U-Net	MAE	101.5 (99.8–103.3)	60.1 (58.3–61.9)	0.859 (0.856–0.863)	0.667 (0.662–0.672)	0.454 (0.431–0.476)	0.516 (0.497–0.534)
VGG U-Net	MSE	111.5 (106.2–116.7)	55.1 (52.2–58.0)	0.869 (0.864–0.875)	0.614 (0.606–0.622)	0.521 (0.498–0.543)	0.538 (0.517–0.558)
VGG U-Net	Mix	103.4 (100.9–105.9)	55.7 (53.6–57.9)	0.869 (0.865–0.873)	0.643 (0.637–0.648)	0.492 (0.471–0.513)	0.532 (0.514–0.55)
VGG U-Net TL	MAE	99.2 (97.8–100.6)	58.0 (56.6–59.4)	0.864 (0.861–0.867)	0.668 (0.663–0.674)[b]	0.470 (0.450–0.490)	0.530 (0.514–0.546)
VGG U-Net TL	MSE	111.7 (108.7–114.6)	55.0 (54.0–56.1)	0.869 (0.867–0.872)	0.619 (0.611–0.627)	0.503 (0.491–0.514)	0.527 (0.517–0.536)
VGG U-Net TL	Mix	103.8 (101.9–105.7)	55.9 (54.4–57.5)	0.867 (0.864–0.870)	0.630 (0.620–0.640)	0.506 (0.489–0.523)	0.540 (0.528–0.552)

Note:—TL indicates transfer learning; Avg., average.

[a] Ninety-five percent confidence intervals across 10 separate training iterations are shown in parentheses. Loss is computed in Hounsfield units, with lower values better for MAE and MSE and higher values better for Pearson *R*, bone precision, bone recall, and bone Dice scores.

[b] The best score within a column.

both into binary bone maps. Given a threshold *t*, we defined bone precision, bone recall (sensitivity), and bone Dice score as

$$Pre(t) = \frac{\Sigma[CT(t) \cap sCT(t)]}{\Sigma sCT(t)}, Rec(t) = \frac{\Sigma[CT(t) \cap sCT(t)]}{\Sigma CT(t)},$$

$$Dice(t) = \frac{2\Sigma[CT(t) \cap sCT(t)]}{\Sigma CT(t) + \Sigma sCT(t)}.$$

Thresholding was done on a grid of thresholds ranging from 40% gray level to 70% gray level (Online Supplemental Data). We report the average precision, recall (sensitivity), and Dice score across all thresholds.

Model Generalizability

Because our full data set contained images acquired at different hospitals, as well as using difference imaging vendors and bone MR imaging techniques, we conducted a series of experiments to evaluate how well model performance generalizes across all these different dimensions. All models were based on Light_U-Net with MAE loss. For each test set, baseline model performance was computed using patient-based 4-fold cross-validation with a training set from the same data subset (vendor, hospital, or MR imaging technique). These baseline results were compared with a model trained only on data from a separate subset, as well as a model trained on augmented data including both the current and separate subsets (again with 4-fold cross-validation).

RESULTS

Model Architectures and Loss Functions

Performance comparison of the various neural network models and 3 loss functions is summarized in the Table, with visual comparison of model results in Fig 1 and loss functions in Fig 2. Results are based on 10 repetitions of a patient-based 4-fold cross-validation among the 16 patients from institution 1, which contained the best quality and most curated data. Among all model architectures, Light_U-Net achieved the lowest test MAE and MSE when trained with MAE and MSE loss, respectively. Light_U-Net models also achieved the highest correlation coefficients across the board. When trained on the mixture loss, Light_U-Net also achieved a lower test MAE and MSE than both VGG U-Net and VGG U-Net transfer learning. Adding transfer learning to VGG U-Net tended to increase the test performance, though differences between VGG U-Net and VGG U-Net transfer learning were not always significant.

When we compared loss functions, models trained on MAE loss naturally achieved a lower validation MAE than those trained on MSE loss and vice versa, with the mixture loss falling in-between. MAE loss achieved a significantly higher mean bone precision across all network architectures. Visually, the synthetic CT images showed sharper edge contrast with crisper bone detail. In addition, relatively fewer pixels were assigned bone density (white signal) on CT, indicating higher specificity, a lower false-positive rate, and higher false-negative rate for bone. MSE tended to achieve a higher mean bone recall (sensitivity) with various network architectures, though the differences were not statistically significant. Visually, the synthetic CT images showed margins that were more blurry and more homogenized bone detail. In addition, relatively more pixels were assigned bone density (white signal) on CT, indicating a higher sensitivity, higher false-positive rate, and lower false-negative rate for bone. In general, MAE loss tended to undercall bone, and MSE loss tended to overcall bone, with the mixture loss producing intermediate image effects.

Overall, the Light_U-Net architecture models outperform or tie other models in all metrics, with difference loss functions allowing adjustment among higher bone precision, recall, or overlap (Dice score). Additional examples of synthetic CT images in axial, coronal, and sagittal views are provided in the Online Supplemental Data. When reviewed by expert neuroradiologists, the computationally optimized model (Light_U-Net, MAE) yielded visibly superior results compared with previously reported synthetic CT algorithms (eg, conventional logarithmic inversion and vendor-provided processing tools). For example, our algorithm enabled delineation of bone microstructure in typically false-negative areas of thin bone (facial bones, skull base, remodeled bone). In addition, our algorithm better excluded false-positive areas such as the fascia and mucoid secretions. Finally, the synthetic CT images showed distinction of nonbone tissues, including soft tissue, fat, and air, that was comparable with the true CT.

Model Generalizability

Results of generalizability experiments across different hospitals, vendors, and bone MR imaging techniques are summarized in

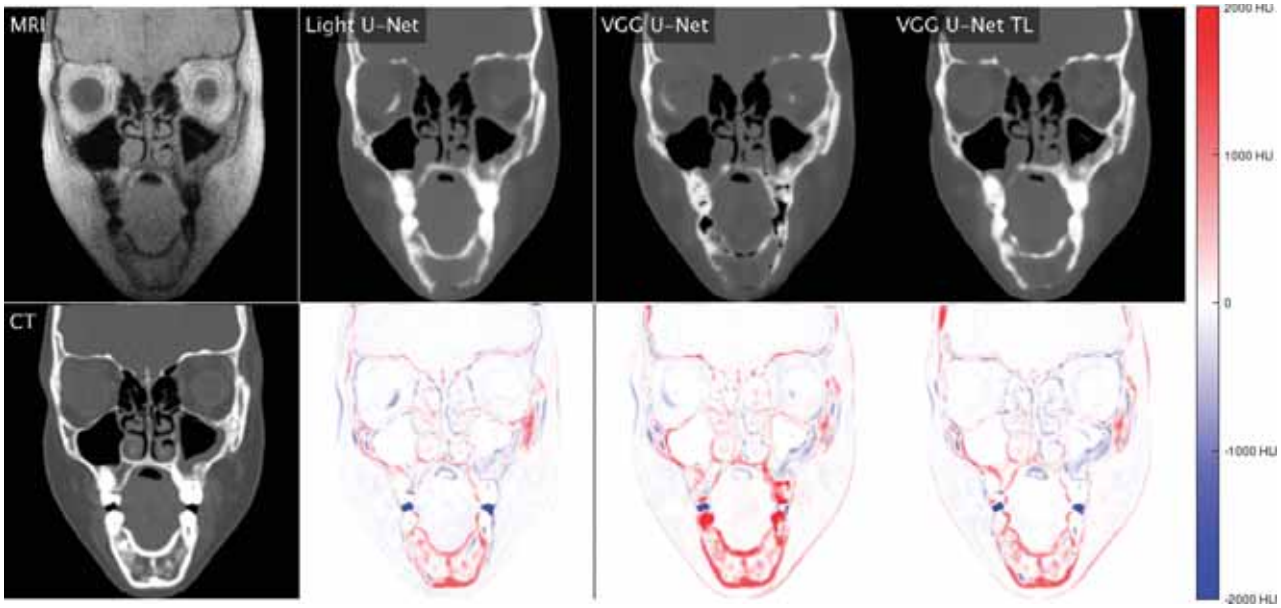

FIG 1. Comparison of different encoder-decoder models. The first column shows real MR imaging and real CT. Subsequent columns show synthetic CTs generated by Light_U-Net, VGG U-Net, and VGG U-Net transfer learning, as well as pixel-wise difference maps between synthetic CT and real CT. Red indicates that synthetic CT is darker than real CT; blue, synthetic CT is brighter than real CT (Refer online version for colors).

the Online Supplemental Data. Training on additional data from a different hospital, vendor, or technique significantly improves performance in terms of MAE, MSE, and the correlation coefficient for all conditions, even when the added patients are few in number compared with the reference data set. Conversely, when one trains models on purely separate hospitals, vendors, or MR imaging techniques, performance significantly decreases across the board.

DISCUSSION

Model Architectures and Loss Functions

With regard to DL architecture, there are 2 classes of models that are suitable for image-to-image translation: encoder-decoder networks and conditional generative adversarial networks. Generative adversarial networks have the distinct advantage of learning to synthesize realistic-looking images when paired images from the source and target domain (eg, coregistered MR imaging and CT slices) are unavailable during training.[23-26] In the presence of paired CT/MR imaging training data, recent experiments suggest that encoder-decoder networks tend to outperform generative adversarial networks in the CT/MR imaging domain in terms of MAE, MSE, and other metrics.[27] We selected the U-Net architecture in particular because its skip connections between each encoder and decoder layer allow precise spatial information from the MR imaging to be propagated to the synthetic CT.

While transfer learning has been traditionally considered helpful when training large models for tasks with relatively small data sets (as is often the case for medical imaging), our study suggests that for MR imaging-to-CT image synthesis, smaller models with fewer training parameters may be more suitable. This result is supported by recent systematic studies that found that the transfer accuracy (specifically with models pretrained on ImageNet) is very sensitive to how exactly the pretraining was done.[28-30] For example, many common forms of regularization may increase ImageNet accuracy but are less suited for transfer learning. An alternative transfer learning approach for future experiments could include finding a related image-translation task for which paired training data are available on a large scale. In general, if more training data are available, larger models may still be able to perform better for this task.

In terms of error minimization, low loss based on pixel-level statistics does not ensure a visually convincing and spatially accurate image rendering. We attempted to numerically quantify synthetic CT image quality by measuring bone precision, recall, and Dice scores on the basis of multiple gray-level thresholds. In addition, clinical assessment of synthetic CT images was performed by a neuroradiologist with expertise in bone MR imaging. Both numerically and visually, there were competing trade-offs in MAE-versus-MSE loss, and these trends persisted across all network architectures. This persistence can be because MAE error is computationally more tolerant of abrupt intensity changes between neighboring pixels, allowing small local errors and less bulk density assignment of bone. Therefore, MAE loss achieves higher precision, higher specificity, a lower false-positive rate, and higher a false-negative rate for bone. Visually, this results in a high-contrast image with sharply defined edges and a tendency to undercall bone. On the other hand, MSE loss penalizes individual outliers more heavily and so enforces a more universally balanced error. Therefore, MSE loss achieves higher recall (sensitivity), a higher false-positive rate, and a lower false-negative rate for bone. Visually, these findings result in a smoother and more regularized image with bulk density assignment to larger areas and a tendency to overcall bone. Using a mixture loss allows a balance among these competing factors, suggesting that the weighting coefficient α could be titrated depending on the clinical use case.

As previously mentioned, prior synthetic CT articles have used conventional or DL-based approaches in anatomically

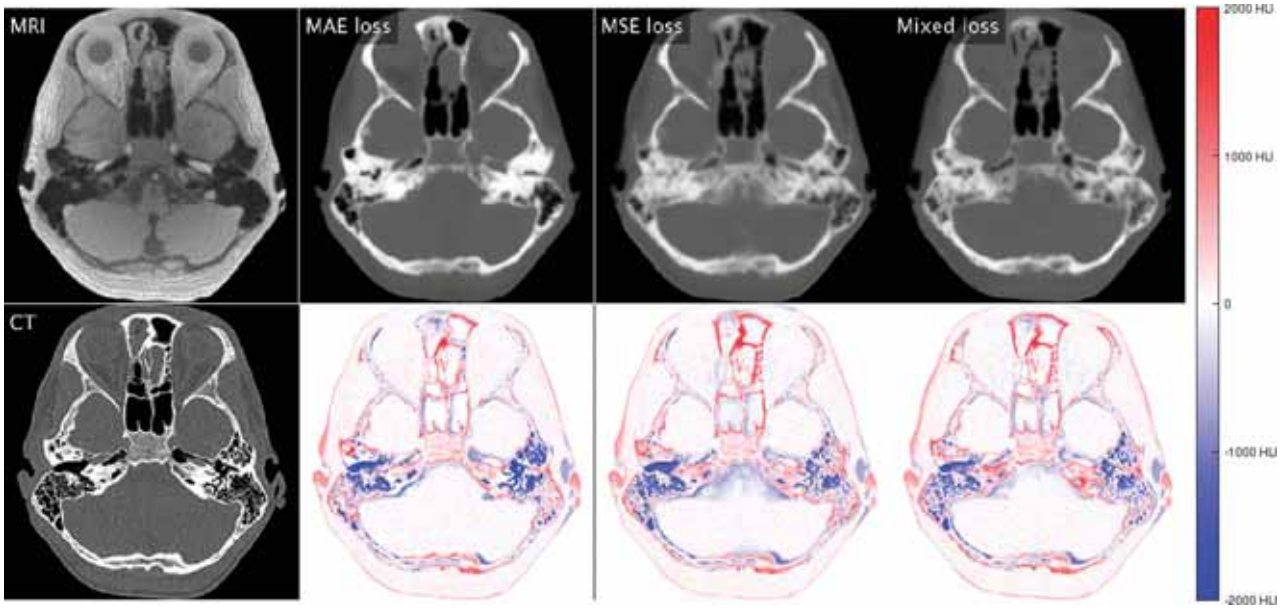

FIG 2. Comparison of different loss functions using a Light_U-Net model. The first column shows real MR imaging and real CT. Subsequent columns show synthetic CTs generated when using a loss function based on MAE, MSE, and a mixed combination, as well as pixel-wise difference maps between synthetic CT and real CT. Red indicates that synthetic CT is darker than real CT; blue, synthetic CT is brighter than real CT (Refer online version for colors).

simpler regions, including the normal adult head, torso, and extremities, for nondiagnostic applications, including radiation therapy planning and PET attenuation and correction.[13-17] More recent work has also described conventional or DL-powered approaches to synthetic CT using other MR imaging sequences such as GRE, T1, and T2.[31,32] The physics of these sequences is inherently less sensitive to cortical bone so that postprocessing approaches are destined to be less accurate. Indeed, the sample synthetic CT output from these articles is low-resolution and insufficient for diagnostic radiology use.

Review of the computationally optimized model (Light_U-Net, MAE) by expert neuroradiologists showed clear potential clinical value over existing conventional and DL algorithms. Our synthetic CT algorithm visibly recaptured bone microstructure in areas pushing the limits of the MR imaging technique, generated fewer false-negative and false-positive bone assignments, and enabled distinction among nonbone tissues. Given that the network architectures and loss functions we used are similar to those described in prior DL studies, our improved results are best attributed to the use of real-world clinical data.

Advancement of clinical implementation will need to include large-scale systematic human reviews of DL algorithms to quantify the usefulness for diagnostic evaluation and interventional planning. At our institution, we are conducting a noninferiority trial of bone MR imaging versus CT, with CT representing the criterion standard technique or ground truth. Expert radiologists are independently evaluating CT, bone MR imaging, and synthetic CT images (Light_U-Net, MAE) to provide numeric scores (0–10) for visibility of key anatomic landmarks (calvaria, sutures, fontanelles, orbits, nose, jaw, teeth, paranasal sinuses, skull base, temporal bone, and cervical spine). For the patients analyzed in this study, CT landmark mean ratings ranged from 9.4 (SD , 0.52) for the calvaria to 9.1 (SD , 0.91) for temporal bone. For MR imaging, the highest rated landmark was also the calvaria (mean, 9.0 [SD , 0.86]) and the lowest was the temporal bone (mean , 7.2 [SD 1.39]). For synthetic CT, the highest rated landmark was the calvaria (mean , 8.1 [SD , 0.92]) and the lowest was the paranasal sinus (mean, 6.8 [SD , 2.31]). These preliminary data suggest that landmark visibility on bone MR imaging and synthetic CT are slightly less than on real CT but sufficient to make most clinical diagnoses.

Furthermore, we are comparing the suitability of CT, bone MR imaging, and synthetic CT data sets for 3D anatomic modeling and virtual surgical planning. Biomedical engineers are processing imaging volumes via bone segmentation, mesh triangulation, and surface generation. Conventional anatomic modeling pipelines use CT with density thresholding to identify bone. Therefore, source bone MR imaging with multiple dark structures is difficult and time-consuming to manually segment. In our experience, synthetic CT algorithms greatly facilitate 3D processing workflow, though as noted by radiologists, anatomic accuracy is less in challenging areas such as facial bones and skull base. For each patient, we coregister image data to calculate a matrix of the reference CT surface and spatial deviation Δ of the nearest point on the test surface (synthetic CT), displayed as a color heat map. We can then calculate statistical metrics over the entire point cloud (mean, range, SD, interquartile range). Based on the surgical accuracy criteria, we can also compute the percentage of data falling within the clinically acceptable tolerance interval $\Delta = (-2\,\text{mm}, +2\,\text{mm})$. For the patients analyzed in this study, 86% (SD, 0.18) of all MR imaging surface data falls within ± 2 mm of coregistered CT surface data. The largest areas of deviation are attributed to missing MR imaging data around regions of hardware and difficult-to-segment anatomic areas, which will guide further investigation.[33-36]

Future comparative effectiveness studies will need to account for the relative risks and benefits of clinical workflow, ionizing radiation exposure, examination duration, anesthesia requirements, diagnostic quality, and treatment outcomes. For example, bone MR imaging represents a key alternative for at-risk patients in whom radiation exposure must be minimized or eliminated, ie, children, pregnant women, and patients with cancer-predisposition syndromes. In such patients, CT dose reduction can yield poor image quality below a certain dose threshold. Therefore, ultra-low-dose CT versus no-dose bone MR imaging may yield a more realistic and equitable image comparison.[7,33-36]

Model Generalizability

In general, DL approaches benefit from larger and more broadly representative training data. This study is limited by the relatively small sample size of 39 patients, which, nevertheless, represents the largest documented database of paired bone MR imaging and CT examinations in clinical patients. Because referring patterns can vary across clinicians and institutions, we chose to include all available head and neck imaging cases to maximize the volume and diversity of the data set. Our study cohort includes varied patient ages, backgrounds, and disease processes with generalizable real-world imaging data, including motion and artifacts. We standardized the preprocessing and conversion of these volumetric data sets into a unique image repository of approximately 22,000 2D paired MR imaging and CT image slices. It would be advisable for multiple institutions interested in bone MR imaging and CT to create a multicenter consortium that can establish best practices with regard to clinical referrals, bone MR imaging techniques, image preprocessing, data sharing, and model development to further increase the available volume and scope of training data. As enrollment numbers increase, it may be possible to develop algorithms tailored to specific clinical indications. This collaborative effort will help elevate collaborations and democratize access among radiologists, clinicians, and patients worldwide.

Our cross-validation experiments evaluated the impact of different hospitals, vendors, and bone MR imaging techniques on model generalizability. These generalizability experiments showed that training on an augmented data set that includes a different hospital, vendor, or technique significantly improves model performance. Conversely, when one trains models only on disparate data sets, performance significantly decreases across the board. Taken together, these results suggest that blindly applying a model trained only on an outside data set can be dangerous due to inherent data variations, but augmenting a local model with additional data sets can boost overall performance. These are key considerations for any institution looking to practically implement bone MR imaging and synthetic CT. Future computational work will involve further model optimization and customization of problem-specific loss functions. We are also considering processing input data in patches, which would permit assembly of higher-resolution output images than our current model.[37-41]

Having established a robust DL pipeline with good performance and generalizability, we hope to facilitate adoption into clinical practice. At our institution, we are already seeing early promise for diagnostic and interventional applications. With larger clinical training sets, continued enhancement of synthetic CT algorithms will improve understanding among untrained radiologists and clinicians and streamline downstream processing for 3D printing and surgical navigation. Further technical advancements could even augment diagnostic value over source MR images, as suggested by the ability to reconstruct bone microstructure approaching MR imaging super-resolution. As synthetic CT algorithms become more robust and accessible, they may be increasingly accepted for clinical decision-making in head and neck imaging. True clinical validation will require comparative effectiveness research across different clinical use cases and multiple iterations of human expert input to guide selection and implementation of optimal algorithms.

CONCLUSIONS

We have optimized a DL model for conversion of bone MR imaging to synthetic CT in the head and neck on the basis of a patient data set inclusive of diverse demographics and clinical use cases. Our unique database consists of 39 paired bone MR imaging and CT examinations, scanned at 2 different institutions with varying MR imaging vendors and techniques. The Light_U-Net model outperformed more complex VGG U-Net models, even after the use of transfer learning. Selection of loss function on the basis of MAE resulted in better bone precision, while MSE tended to provide better bone recall. Performance metrics for a given model decreased when using training data captured only in a different environment and increased when local training data were augmented with those from different hospitals, vendors, and techniques. By establishing a robust DL-powered synthetic CT algorithm with good performance and generalizability, we hope to elevate the applicability of bone MR imaging with downstream image-processing and adoption into clinical practice.

ACKNOWLEDGMENTS

We would like to thank Houchun Harry Hu, PhD, Mark Smith, MS, Aiming Lu, PhD, and Bhavani Selvaraj, MS, for their scientific expertise and collaboration. We would also like to thank Lisa Martin, MD, Diana Rodriguez, MD, Jeremy Jones, MD, Charles Elmaraghy, MD, Eric Sribnick, MD, Ibrahim Khansa, MD, and Gregory Pearson, MD, for their clinical expertise.

Disclosures: Mai-Lan Ho—*RELATED: Grant:* RSNA, SPR, ASHNR *Comments:* RSNA Research Scholar Grant, SPR Pilot Award, ASHNR William N. Hanafee Grant.* *Support for Travel to Meetings for the Study or Other Purposes:* RSNA, SPR, ASHNR *Comments:* RSNA Research Scholar Grant, SPR Pilot Award, ASHNR William N. Hanafee Grant.* *UNRELATED—Royalties:* McGraw-Hill *Comments:* Author, Neuroradiology Signs. *Money paid to the institution.

REFERENCES

1. Du J, Hermida JC, Diaz E, et al. **Assessment of cortical bone with clinical and ultrashort echo time sequences.** *Magn Reson Med* 2013;70:697–704 CrossRef Medline
2. Schieban K, Weiger M, Hennel F, et al. **ZTE imaging with enhanced flip angle using modulated excitation.** *Magn Reson Med* 2015;74:684–93 CrossRef Medline
3. Eley KA, McIntyre AG, Watt-Smith SR, et al. **"Black bone" MRI: a partial flip angle technique for radiation reduction in craniofacial imaging.** *Br J Radiol* 2012;85:272–78 CrossRef Medline

4. Tiberi G, Costagli M, Biagi L, et al. **SAR prediction in adults and children by combining measured B1+ maps and simulations at 7.0 Tesla**. *J Magn Reson Imaging* 2016;44:1048–55 CrossRef Medline
5. Alibek S, Vogel M, Sun W, et al. **Acoustic noise reduction in MRI using Silent Scan: an initial experience.** *Diagn Interv Radiol* 2014;20:360–63 CrossRef Medline
6. Eley KA, Watt-Smith SR, Golding SJ. **"Black bone" MRI: a potential alternative to CT when imaging the head and neck: report of eight clinical cases and review of the Oxford experience.** *Br J Radiol* 2012;85:1457–64 CrossRef Medline
7. Lu A, Gorny KC, Ho ML. **Zero TE MRI for craniofacial bone imaging.** *AJNR Am J Neuroradiol* 2019;40:1562–66 CrossRef Medline
8. Cho SB, Baek HJ, Ryu KH, et al. **Clinical feasibility of zero TE skull MRI in patients with head trauma in comparison with CT: a single-center study.** *AJNR Am J Neuroradiol* 2019;40:109–15 CrossRef Medline
9. Hsu SH, Cao Y, Lawrence TS, et al. **Quantitative characterizations of ultrashort echo (UTE) images for supporting air-bone separation in the head.** *Phys Med Biol* 2015;60:2869–80 CrossRef Medline
10. Ghose S, Dowling JA, Rai R, et al. **Substitute CT generation from a single ultra short time echo MRI sequence: preliminary study.** *Phys Med Biol* 2017;62:2950–60 CrossRef Medline
11. Kraus KM, Jäkel O, Niebuhr NI, et al. **Generation of synthetic CT data using patient specific daily MR image data and image registration.** *Phys Med Biol* 2017;62:1358–77 CrossRef Medline
12. Wiesinger F, Bylund M, Yang J, et al. **Zero TE-based pseudo-CT image conversion in the head and its application in PET/MR attenuation correction and MR-guided radiation therapy planning.** *Magn Reson Med* 2018;80:1440–51 CrossRef Medline
13. Leynes AP, Yang J, Wiesinger F, et al. **Zero-echo-time and Dixon deep pseudo-CT (ZeDD CT): direct generation of pseudo-CT images for pelvic PET/MRI attenuation correction using deep convolutional neural networks with multiparametric MRI.** *J Nucl Med* 2018;59:852–58 CrossRef Medline
14. Gong K, Yang J, Kim K, et al. **Attenuation correction for brain PET imaging using deep neural network based on Dixon and ZTE MR images.** *Phys Med Biol* 2018;63:125011 CrossRef Medline
15. Nie D, Cao X, Gao Y, et al. **Estimating CT image from MRI data using 3D fully convolutional networks.** *Deep Learn Data Label Med Appl (2016)* 2016;2016:170–78 CrossRef Medline
16. Andreasen D, Van Leemput K, Hansen RH, et al. **Patch-based generation of a pseudo CT from conventional MRI sequences for MRI-only radiotherapy of the brain.** *Med Phys* 2015;42:1596–605 CrossRef Medline
17. Boukellouz W, Moussaoui A. **Magnetic resonance-driven pseudo CT image using patch-based multi-modal feature extraction and ensemble learning with stacked generalization.** *Journal of King Saud University: Computer and Information Sciences* 2021;33:999–1007
18. Otsu N. **A threshold selection method from gray-level histograms.** *IEEE Transactions on Systems, Man, and Cybernetics* 1979;9:62–66 CrossRef
19. Ronneberger O, Fischer P, Brox T. **U-net: convolutional networks for biomedical image segmentation: Medical Image Computing and Computer-Assisted Intervention (MICCAI).** *arXiv* 1505.04597 [cs.CV] 2015 https://arxiv.org/abs/1505.04597. Accessed March 30, 2021
20. Simonyan K, Zisserman A. **Very deep convolutional networks for large-scale image recognition.** *arXiv* 1409.1556 2015. https://arxiv.org/abs/1409.1556v4. Accessed March 30, 2021
21. Deng J, Dong W, Socher R, et al. **ImageNet: a large-scale hierarchical image database.** In: *Proceedings of the 2009 IEEE Conference on Computer Vision and Pattern Recognition*, Miami Beach, Florida. June 20–25, 2009
22. Kingma DP, Ba J. **Adam: a method for stochastic optimization.** *arXiv* 1412.6980 2017. https://arxiv.org/abs/1412.6980. Accessed March 30, 2021
23. Goodfellow I, et al. **Generative adversarial nets.** In: *Proceedings of the 27th International Conference on Neural Information Processing Systems*, Montreal, Quebec, Canada. December 8–13, 2014; 2672–80
24. Wolterink JM, Dinkla Am Savenije MH, et al. **Deep MR to CT synthesis using unpaired data. Simulation and Synthesis in Medical Imaging. Lecture Notes in Computer Science.** *arXiv* 1708.01155 [cs.CV] 2017. https://arxiv.org/abs/1708.01155. Accessed March 30, 2021
25. Zhu JY, Park T, Isola P, et al. **Unpaired image-to-image translation using cycle-consistent adversarial networks.** In: *Proceedings of the IEEE International Conference on Computer Vision (ICCV)*, Venice, Italy. October 22–29, 2017 CrossRef
26. Isola P, Zhu JY, Zhou T, et al. **Image-to-image translation with conditional adversarial networks.** In: *Proceedings of the IEEE Conference on Computer Vision and Pattern Recognition (CVPR)*, Honolulu, Hawaii. July 21–26, 2017 CrossRef
27. Li W, Li Y, Qin W, et al. **Magnetic resonance image (MRI) synthesis from brain computed tomography (CT) images based on deep learning methods for magnetic resonance (MR)-guided radiotherapy.** *Quan Imaging Med Surg* 2020;10:1223–36 CrossRef Medline
28. Kornblith S, Shlens J, Le QV. **Do better imagenet models transfer better?** In: *Proceedings of the IEEE/CVF Conference on Computer Vision and Pattern Recognition (CVPR)*, Long Beach, California. June 15–20, 2019 CrossRef
29. Raghu M, Zhang C, Kleinberg J, et al. **Transfusion: understanding transfer learning for medical imaging.** *arXiv* 2019. https://arxiv.org/abs/1902.07208. Accessed March 30, 2021
30. Anwar SM, Majid M, Qayyum A, et al. **Medical image analysis using convolutional neural networks: a review.** *J Med Sys* 2018;42: 226 CrossRef Medline
31. Boulanger M, Nunes JC, Chourak H, et al. **Deep learning methods to generate synthetic CT from MRI in radiotherapy: a literature review.** *Phys Med* 2021;89:265–81 CrossRef Medline
32. Spadea MF, Maspero M, Zaffino P, et al. **Deep learning based synthetic-CT generation in radiotherapy and PET: a review.** *Med Phys* 2021;48:6537–66 CrossRef Medline
33. Bambach S, Ho ML. **Bone MRI: can it replace CT: 2nd AI Award.** In: *Proceedings of the American Society of Functional Neuroradiology, Artificial Intelligence Workshop*, February 5, 2021
34. Smith M, Bambach S, Selvaraj B, et al. **Zero-TE MRI: potential applications in the oral cavity and oropharynx.** *Top Magn Reson Imaging* 2021;30: 105–15 CrossRef Medline
35. Kobayashi N, Bambach S, Ho ML. **Ultrashort echo-time MR imaging of the pediatric head and neck.** *Magn Reson Imaging Clin N Am* 2021;29:583–93 CrossRef Medline
36. Wiesinger F, Ho ML. **Zero-TE MRI: principles and applications in the head and neck.** *Br J Radiol* 2022 June 10. [Epub ahead of print]
37. Aouadi S, Vasic A, Paloor S, et al. **Generation of synthetic CT using multi-scale and dual-contrast patches for brain MRI-only external beam radiotherapy.** *Phys Med* 2017;42:174–84 CrossRef Medline
38. Dinkla AM, Florkow MC, Maspero M, et al. **Dosimetric evaluation of synthetic CT for head and neck radiotherapy generated by a patch-based three-dimensional convolutional neural network.** *Med Phys* 2019;46:4095–104 CrossRef Medline
39. Roy S, Carass A, Jog A, et al. **MR to CT registration of brains using image synthesis.** *Proc SPIE Int Soc Opt Eng* 2014;9034 CrossRef Medline
40. Lee J, Carass A, Jog A, et al. **Multi-atlas-based CT synthesis from conventional MRI with patch-based refinement for MRI-based radiotherapy planning.** *Proc SPIE Int Soc Opt Eng* 2017;10133:1013311 CrossRef Medline
41. Klages P, Benslimane I, Riyahi S, et al. **Patch-based generative adversarial neural network models for head and neck MR-only planning.** *Med Phys* 2020;47:626–42 CrossRef Medline

DTI of the Olfactory Bulb in COVID-19-Related Anosmia: A Pilot Study

F. Sherif, A.H. Elmokadem, A. Abdel Razek, E. Kamal, E.H.E. Abdou, M.A. Salem, and M.M. Ghoneim

ABSTRACT

SUMMARY: This study aimed to assess the utility of DTI in the detection of olfactory bulb dysfunction in COVID-19-related anosmia. It was performed in 62 patients with COVID-19-related anosmia and 23 controls. The mean diffusivity and fractional anisotropy were calculated by 2 readers. The difference between the fractional anisotropy and mean diffusivity values of anosmic and control olfactory bulbs was statistically significant ($P = .001$). The threshold of fractional anisotropy and mean diffusivity to differentiate a diseased from normal olfactory bulb were 0.22 and 1.5, with sensitivities of 84.4% and 96.8%, respectively, and a specificity of 100%.

ABBREVIATIONS: COVID-19 = coronavirus disease 2019; FA = fractional anisotropy; MD = mean diffusivity; OB = olfactory bulb; SARS-COV-2 = Severe Acute Respiratory Syndrome coronavirus 2

In coronavirus disease 2019 (COVID-19), morbidity and mortality are primarily attributed to pulmonary causes. However, there is a substantial body of literature reporting a broad range of neurologic manifestations, including stroke, dural sinus thrombosis, cerebral microhemorrhage, acute necrotizing encephalopathy, and olfactory and gustatory dysfunction.[1-3]

Olfactory dysfunction was underestimated early in the COVID-19 pandemic. Nevertheless, in a study including 1480 patients, anosmia was demonstrated in 68% of patients. Anosmia persisted in 26% of them even after testing negative for Severe Acute Respiratory Syndrome coronavirus 2 (SARS-COV-2).[4] The reported incidence of anosmia varied internationally: as low as 30% in South Korea, and as high as 88% in Europe. The olfactory bulb (OB) is considered an immunologic organ that shields the CNS from viral infection, so its involvement could risk the CNS being subjected to infection. Consequently, the early detection of OB involvement in case of COVID-19 infection is very important.[5,6]

MR imaging can provide anatomic data about the olfactory pathway. One of the primary parameters to evaluate the olfactory pathway is the measurement of OB volume. However, the volume measurements are not routinely used to assess the olfactory pathway because they are more difficult and time-consuming than visual analysis. Moreover, it is not easy to measure these thin structures with great variations, even among healthy individuals, making its efficiency as a diagnostic tool limited.[7-9]

DTI is a noninvasive technique that is increasingly implemented. The 2 main parameters extracted from DTI are mean diffusivity (MD) and fractional anisotropy (FA). MD demonstrates the degree of diffusion restriction of water molecules, while FA reflects the degree of the tissue anisotropy.[10] DTI of the OB has been performed in some diseases, such as OB gliomas and paranasal sinus diseases.[11-13] However, to our knowledge, the validity of DTI in the evaluation of OB neuropathy has been scarcely studied in COVID-19-related anosmia. The aim of the current study was to assess the validity of DTI in the diagnosis of OB dysfunction in COVID-19-related anosmia.

MATERIALS AND METHODS

Subjects

This prospective case-control observational study was approved by the institutional review board. Informed consent was acquired from all patients and controls. The study was conducted on 62 consecutive patients with COVID-19-related anosmia and 23 age- and sex-matched healthy controls. The olfaction in both groups was assessed by the Smell Diskettes olfaction test.[14] All patients were anosmic with a score of zero on the Smell Diskettes olfaction test with the polymerase chain reaction test positivity confirming COVID-19 infection. Control group consisted of individuals who had negative polymerase chain reaction test results for COVID-19, showed no signs of anosmia (scores of 6–9 on the Smell Diskettes olfaction test), no history or prior imaging

Received January 10, 2022; accepted after revision May 22.

From the Departments of Radiology (F.S., A.H.E., A.A.R., M.M.G.) and Otorhinolaryngology (E.K., E.H.E.A., M.A.S.), Mansoura University, Mansoura City, Egypt.

Please address correspondence to Ali H. Elmokadem, MD, Department of Radiology, Mansoura University, Elgomhoria St, Mansoura City, Egypt 35516; e-mail: mokadem83@yahoo.com

Indicates open access to non-subscribers at www.ajnr.org
Indicates article with online supplemental data.

http://dx.doi.org/10.3174/ajnr.A7590

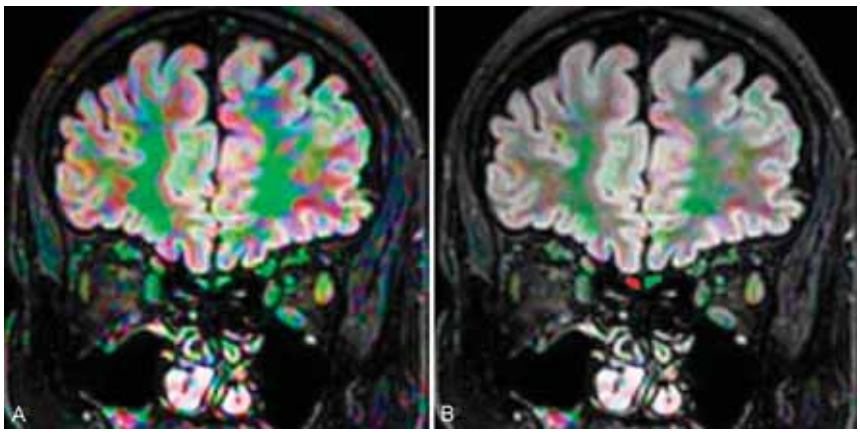

FIG 1. The OB in a patient with COVID-19-related anosmia. DTI of the OB with displays on the 3D-FLAIR image. The mean MD and FA of the OB values were 1.97 mm^2/s and 0.18, respectively.

studies of sinus disease, and no prior neurologic insult nor previous operations.

MR Imaging Protocol

All scans were performed using a 1.5T MR imaging unit (Ingenia; Philips Healthcare). All patients with symptoms of anosmia were scanned using a coronal 3D-FLAIR sequence with the following parameters: TR/TE = 8000/133 ms; bandwidth = 120 Hz/pixel; TSE factor = 80; section thickness = 2mm; interslice gap = 0.5mm; FOV = 230 × 230 × 20 mm^2 (from the nose tip anteriorly to the posterior sphenoidal sinus wall, from the skull vault to the hard palate); voxel size = 0.95 × 0.95 × 2 mm; matrix = 240 × 240; echo-train length = 220 with variable flip angles; time of acquisition = 270 seconds. DTI was performed using a single-shot echo-planar sequence with TR/TE = 3200/90 ms. Diffusion gradients were obtained along 32 axes using b-values of 0 and 1000 s/mm^2. We used the following scanning parameters: FOV = 184 × 184 mm^2; voxel dimensions = 1.8 × 1.8 × 1.8 mm^3; number of averages = 14; data matrix = 92 × 88, obtaining 48 slices with no interslice gap. The total examination time was 7–8 minutes. We used parallel imaging and chose not to cover the whole brain, limiting the acquisition to the olfactory tracts to reduce the acquisition time.

Image Analysis

Image analysis was performed by 2 experienced neuroradiologists (F.S., M.M.G.) with 17 and 14 years of experience, respectively, who were blinded to the clinical history of the studied individuals. Images were transmitted to a workstation (Extended MR WorkSpace 2.6.3.5, Philips Medical Systems) for DTI analysis followed by precise positioning of the ROI. The FA maps were coregistered with the 3D-FLAIR images and positioned at the OB (Fig 1). MD and the FA were measured on the right and the left OBs by each reader separately. Then the mean values of the FA and MD for readings on both sides were calculated independently.

The OB volume was assessed by the box frame method.[15] First, the number of images with clear visibility of the OB was counted. Second, the imaging having the most visibly distinct voxels for both OBs was chosen as the standard image, and the OBs were framed by a box. Furthermore, annotations were drawn between 2 extreme points of the OB box to calculate the width (w) and height (h). The length (l) was calculated by multiplying the total number of images that showed visibly distinct OBs by the section thickness. The final OB volume was calculated as w × h × l in cubic millimeters.

Statistical Analysis

The data were analyzed using SPSS 22 (IBM). Using descriptive statistics, we calculated the mean (SD) of the MD and FA. The significant differences between DTI metrics in anosmic and healthy control group were analyzed. A P value ≤ .05 was considered significant. We implemented κ statistics to calculate the interreader agreement for the estimated DTI parameters. The receiver operating characteristic curve was established, and the area under the curve was calculated to determine the cutoff point of DTI parameters used for diagnosing OB neuropathy. The cutoff point with highest sensitivity and specificity of DTI parameters was determined by the Youden index. Sensitivity, specificity, and accuracy were also registered.

RESULTS

The COVID-19 anosmic group (n = 66) consisted of 48 females and 14 males with an age range of 16−83 years (median, 37 years), while the control group (n = 23) consisted of 17 females and 6 males with an age range of 17–61 years (median, 36 years). The severity of COVID-19 ranged from mild to moderate. All patients in the anosmic group presented with a loss of smell and taste (100%); other presenting symptoms were headache (80.3%), low-grade fever (65.1%), dry cough (27.3%), dyspnea (16.6%), sore throat (46.9%), gastrointestinal symptoms (22.7%), and rhinorrhea (60.6%). The presentation of anosmia ranged from as early as the first day (24 patients) to a slightly delayed presentation within 2–5 days in the remainder of the patients. The median duration of anosmia was 60 days (range, 15–135 days). This study analyzed 124 OBs in 62 patients in comparison with 23 control individuals with 46 OBs. The Online Supplementary Data demonstrate the MD and FA of diseased and control OBs. The Online Supplementary Data show the receiver operating characteristic curve and diagnostic performance of MD and FA for diseased and control OBs.

The mean OB volume calculated by the box frame method was significantly higher (P < .0001) in the anosmic group (83.6 [SD, 29.6] mm^3) compared with control group (30.5 [SD, 8] mm^3). The mean FA values of the 2 included groups in our study were 0.18 (range, 0.12–0.3) for diseased OBs and 0.27 (range, 0.23–0.42) for control OBs. The FA values showed significant variation between diseased and control OBs with P < .0005. The area under the curve of the mean FA to differentiate both entities was 0.949. The resulting threshold of FA to differentiate diseased from normal OBs was 0.22, with a diagnostic accuracy of 88.4%, sensitivity of 84.4%, and specificity of 100% (Fig 2*A*). The mean

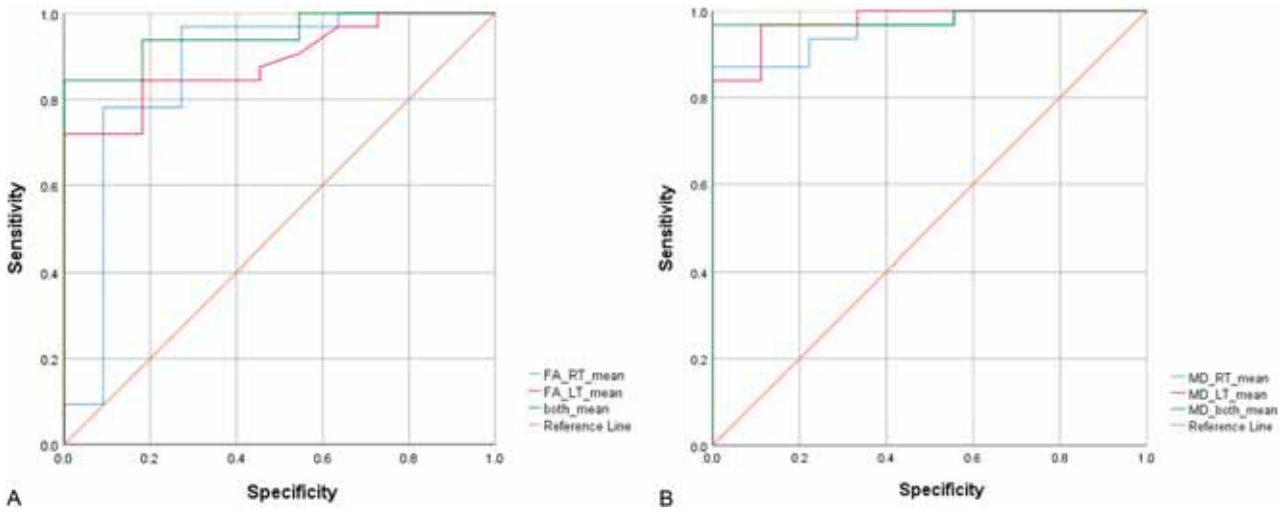

FIG 2. Receiver operating characteristic curves of FA (*A*) and MD (*B*) used for differentiation of a diseased and normal OB by both readers. RT indicates right; LT, left.

MD value of the diseased OBs was 2.3 (range, 1.3–3) and of control OBs, 1.4 (range, 1–1.5) $\times 10^{-3}$mm^2/s. A significant difference between MD values of diseased and control OBs was demonstrated with $P < .0005$. The under the curve of the mean MD to differentiate both entities was 0.982. The resulting threshold of MD to differentiate diseased from normal OBs was 1.51, with a diagnostic accuracy of 97.5%, sensitivity of 96.8%, and specificity of 100% (Fig 2*B*). The diagnostic performance of these cut off values was excellent when tested on 30% of the sample which was chosen at random.

In a secondary analysis, we compared the DTI parameter between patients with COVID-19 and anosmia having sinus disease (26/62) with other patients negative for sinus disease (36/62). There was no significant difference ($P = .6$) in mean FA between positive and negative groups (0.17 [SD, 0.02] and 0.18 [SD, 0.05], respectively). Similarly, there was no significant difference ($P = .6$) in mean MD between both groups (2.3 [SD, 0.7] and 2.2 [SD, 0.4] $\times 10^{-3}$mm^2/s, respectively). The results demonstrated excellent interobserver agreement between both readers using FA and MD in sorting the OBs of diseased and control individuals ($\kappa = 0.915$ and 0.892, respectively).

DISCUSSION

In the current study, DTI with its unique parameters (MD and FA) revealed a noteworthy significance in differentiating patients with COVID-19 and anosmia from control individuals. Moreover, an excellent interobserver agreement of the MD and FA readings was obtained denoting the consistency of their significance. The impact of the MD values of the OB in patients with anosmia must be highlighted because it varied greatly from values of the control group, being much higher in subjects with anosmia. This finding is a mere reflection of the inflammatory edema in the virally infected OBs. This could be a long-lasting sequala, even after the subsidence of the COVID-19 viral infection. It also concurs with studies reporting improvement of the smell sensation after topical and systemic corticosteroid therapy.[16] On the other hand, the FAs of the OBs were significantly less than those in the control group. On the basis of our results, MD was introduced as a more powerful differentiating parameter than FA, as the difference in MD values between the 2 groups was more evident than the difference between the 2 groups regarding the FA values. This finding could be attributed to the relative preservation of the intercellular anisotropy. Similar results were reported by Taha et al,[13] who reported a significantly lower FA in 11 patients with anosmia and 3 with hyposmia secondary to chronic sinonasal polyposis compared with the control group. Another study reported changes in the DTI parameters in Parkinson disease and showed significant FA reduction ($P < .05$) for the hyposmic Parkinson disease group compared with controls.[12] Moreover, Güllmar et al[11] reported improvement in the results of olfaction tests and the DTI parameters measured in the olfactory pathway, including the OBs after functional endoscopic sinus surgery.

The persistent prolonged rise of MD after recovery from SARS-COV-2 infection is suggestive of an extended inflammatory process, even after the subsidence of other COVID-19 symptoms. This inference could be supported by the results of the study of Lu et al,[17] in which MR imaging was performed 3–4 months after SARS-COV-2 infection. Their MR volumetric analyses reported significantly increased gray and white matter volumes compared with those of control noninfected individuals. Lee et al[18] performed MR microscopy, histopathologic evaluation, and immunohistochemical analysis of postmortem brain and olfactory bulbs for patients who died from COVID-19 and found multifocal microvascular injury without evidence of viral infection. These data may explain the changes observed on DTI parameters of the OBs in patients with anosmia and COVID-19.

The current study had some drawbacks. The relatively limited number of patients included in both groups is a shortcoming. Future studies comprising a greater number of patients might yield more applicable results. Moreover, this study was conducted using DTI metrics solely, without correlation between the volume calculation and signal intensity alteration. A more thorough investigation highlighting multiparametric MR imaging parameters including quantitative volumetry, signal intensity analysis, and other clinical tests for olfaction is recommended.

CONCLUSIONS

DTI parameters are valuable noninvasive quantitative tools that could help in diagnosis of the OB dysfunction in COVID-19-related anosmia.

Disclosure forms provided by the authors are available with the full text and PDF of this article at www.ajnr.org.

REFERENCES

1. El Beltagi AH, Vattoth S, Abdelhady M, et al. **Spectrum of neuroimaging findings in COVID-19.** *Br J Radiol* 2021;94:20200812 CrossRef Medline
2. Moonis G, Filippi CG, Kirsch CF, et al. **The spectrum of neuroimaging findings on CT and MRI in adults with coronavirus disease (COVID-19).** *AJR Am J Roentgenol* 2021;217:959–74 CrossRef Medline
3. Elmokadem AH, Bayoumi D, El-Morsy A, et al. **Relationship of the pulmonary disease severity scoring with thromboembolic complications in COVID-19.** *Emerg Radiol* 2021;20:9–21 CrossRef Medline
4. Wölfel R, Corman VM, Guggemos W, et al. **Virological assessment of hospitalized patients with COVID-2019.** *Nature* 2020;581:465–69 CrossRef Medline
5. Chung TW, Sridhar S, Zhang AJ, et al. **Olfactory dysfunction in coronavirus disease 2019 patients: observational cohort study and systematic review.** *Open Forum Infect Dis* 2020;7:ofaa199 CrossRef Medline
6. Lee JC, Nallani R, Cass L, et al. **A systematic review of the neuropathologic findings of post-viral olfactory dysfunction: implications and novel insight for the COVID-19 pandemic.** *Am J Rhinol Allergy* 2021;35:323–33 CrossRef Medline
7. Chung MS, Choi WR, Jeong HY, et al. **MR imaging-based evaluations of olfactory bulb atrophy in patients with olfactory dysfunction.** *AJNR Am J Neuroradiol* 2018;39:532–37 CrossRef Medline
8. Liang YC, Tsai YS, Syue LS, et al. **Olfactory bulb atrophy in a case of COVID-19 with hyposmia.** *Acad Radiol* 2020;27:1649–50 CrossRef Medline
9. Chiu A, Fischbein N, Wintermark M, et al. **COVID-19-induced anosmia associated with olfactory bulb atrophy.** *Neuroradiology* 2021;63:147–48 CrossRef Medline
10. El-Serougy L, Abdel Razek AA, Ezzat A, et al. **Assessment of diffusion tensor imaging metrics in differentiating low-grade from high-grade gliomas.** *Neuroradiol J* 2016;29:400–07 CrossRef Medline
11. Güllmar D, Seeliger T, Gudziol H, et al. **Improvement of olfactory function after sinus surgery correlates with white matter properties measured by diffusion tensor imaging.** *Neuroscience* 2017;360:190–96 CrossRef Medline
12. Nigro P, Chiappiniello A, Simoni S, et al. **Changes of olfactory tract in Parkinson's disease: a DTI tractography study.** *Neuroradiology* 2021;63:235–42 CrossRef Medline
13. Taha T, Megahed A, Taha M, et al. **Diffusion tensor imaging: a smart move to olfactory pathway imaging; comparative study of sinonasal polyposis patients and normal control.** *Egyptian Journal of Radiology and Nuclear Medicine* 2020;51:34–42 CrossRef
14. Briner HR, Simmen D. **Smell Diskettes as screening test of olfaction.** *Rhinology* 1999;37:145–48 Medline
15. Joshi A, Thaploo D, Yan X, et al. **A novel technique for olfactory bulb measurements.** *PLoS One* 2020;15:e0243941 CrossRef Medline
16. Vaira L, Hopkins C, Sandison A, et al. **Olfactory epithelium histopathological findings in long-term coronavirus disease 2019 related anosmia.** *J Laryngol Otol* 2020;134:1123–27 CrossRef Medline
17. Lu Y, Li X, Geng D, et al. **Cerebral microstructural changes in COVID-19 patients: an MR-based 3- month follow-up study.** *EClinicalMedicine* 2020;25:100484 CrossRef
18. Lee MH, Perl DP, Nair G, et al. **Microvascular injury in the brains of patients with Covid-19.** *N Engl J Med* 2021;384:481–83 CrossRef Medline

Normalized Parameters of Dynamic Contrast-Enhanced Perfusion MRI and DWI-ADC for Differentiation between Posttreatment Changes and Recurrence in Head and Neck Cancer

A. Baba, R. Kurokawa, E. Rawie, M. Kurokawa, Y. Ota, and A. Srinivasan

ABSTRACT

BACKGROUND AND PURPOSE: Differentiating recurrence from benign posttreatment changes has clinical importance in the imaging follow-up of head and neck cancer. This study aimed to investigate the utility of normalized dynamic contrast-enhanced MR imaging and ADC for their differentiation.

MATERIALS AND METHODS: This study included 51 patients with a history of head and neck cancer who underwent follow-up dynamic contrast-enhanced MR imaging with DWI-ADC, of whom 25 had recurrences and 26 had benign posttreatment changes. Quantitative and semiquantitative dynamic contrast-enhanced MR imaging parameters and ADC of the ROI and reference region were analyzed. Normalized dynamic contrast-enhanced MR imaging parameters and normalized DWI-ADC parameters were calculated by dividing the ROI by the reference region.

RESULTS: Normalized plasma volume, volume transfer constant between extravascular extracellular space and blood plasma per minute (K^{trans}), area under the curve, and wash-in were significantly higher in patients with recurrence than in those with benign posttreatment change ($P = .003$ to $<.001$). The normalized mean ADC was significantly lower in patients with recurrence than in those with benign posttreatment change ($P < .001$). The area under the receiver operating characteristic curve of the combination of normalized dynamic contrast-enhanced MR imaging parameters with significance (normalized plasma volume, normalized extravascular extracellular space volume per unit tissue volume, normalized K^{trans}, normalized area under the curve, and normalized wash-in) and normalized mean ADC was 0.97 (95% CI, 0.93–1).

CONCLUSIONS: Normalized dynamic contrast-enhanced MR imaging parameters, normalized mean ADC, and their combination were effective in differentiating recurrence and benign posttreatment changes in head and neck cancer.

ABBREVIATIONS: AUC = area under the curve; AUROCC = area under the receiver operating characteristic curve; DCE = dynamic contrast-enhanced; EES = extravascular extracellular space; Kep = rate transfer constant between EES and blood plasma per minute; K^{trans} = volume transfer constant between extravascular extracellular space and blood plasma per minute; n- = normalized; Ve = extravascular extracellular space volume per unit tissue volume; Vp = plasma volume; WI = wash-in; WO = washout

The main aims of imaging evaluation in the follow-up of head and neck cancer after treatment are to determine the effect of treatment, evaluate disease control, and detect local recurrence. Local recurrence is one of the most clinically important forms of recurrence in head and neck cancer,[1] and its early detection is important because it leads to subsequent salvage therapy. Posttreatment changes such as edema, inflammation, and fibrosis may cause difficulty in differentiating recurrences from benign posttreatment changes during follow-up imaging evaluation,[2-4] and tissue biopsy may be required for pathologic confirmation in some patients. Contrast-enhanced CT and PET/CT are the principal imaging modalities for posttreatment evaluation of head and neck cancer;[5] however, patients may undergo MR imaging when it is difficult to distinguish between recurrence and posttreatment changes.

Dynamic contrast-enhanced MR imaging (DCE-MR imaging) is a perfusion imaging technique that uses contrast media and has many important utilities in the pre- and posttreatment evaluation of head and neck cancer.[6-15] Although several studies using DCE-MR imaging have reported the utility of semiquantitative[13,14,16,17] or quantitative parameters such as permeability surface area and

Received January 17, 2022; accepted after revision May 22.

From the Division of Neuroradiology (A.B., R.K., M.K., Y.O., A.S.), Department of Radiology, University of Michigan, Ann Arbor, Michigan; and Department of Radiology (E.R.), Brooke Army Medical Center, San Antonio, Texas.

Please address correspondence to Akira Baba, MD, PhD, Division of Neuroradiology, Department of Radiology, University of Michigan, 1500 E Medical Center Dr, Ann Arbor, MI 48109; e-mail: akirababa0120@gmail.com

Indicates article with online supplemental data.

http://dx.doi.org/10.3174/ajnr.A7567

blood volume[12] for differentiating head and neck cancer recurrence from benign posttreatment changes, there have been no studies that used the relatively new vascular permeability parameters, such as fractional plasma volume (Vp), extravascular extracellular space (EES) volume per unit tissue volume (Ve), volume transfer constant between EES and blood plasma per minute (K^{trans}), and rate transfer constant between EES and blood plasma per minute (Kep), or normalized DCE-MR imaging parameters that consider intervendor and interinstitutional reproducibility.

DWI is a unique sequence of noninvasive MR imaging used to visualize changes in the molecular motion of water and is a surrogate marker for cell density. DWI parameters, especially ADC, were lower in the recurrence of head and neck cancers than in benign changes after treatment.[18-20] To date, there have been no studies that have investigated the differentiation between head and neck cancer recurrences and posttreatment changes using normalized DWI-ADC that also consider intervendor and interinstitutional reproducibility as in the previously described normalized DCE-MR imaging parameters.

This study aimed to evaluate the difference in normalized quantitative and semiquantitative parameters and the normalized DWI-ADC between recurrences and benign posttreatment changes in head and neck cancer and to investigate the combined diagnostic performance of normalized DCE-MR imaging parameters and normalized DWI-ADC.

MATERIALS AND METHODS

We obtained the institutional review board exemption of University of Michigan for this retrospective study, and patient consent was waived. Data were acquired in compliance with all applicable Health Insurance Portability and Accountability Act regulations. All procedures followed were in accordance with Helsinki Declaration of 1975, as revised in 2008. Data were de-identified before any analysis.

Patients

Consecutive patients with a history of head and neck cancers from January 2014 to September 2020 who underwent follow-up DCE-MR imaging were searched by the electronic database of our institution. Seventy-seven patients whose primary malignancies were previously treated were included in this study. In our institution, all postoperative MR imaging protocols for patients with a history of head and neck malignancy include DCE-MR imaging except for patients with limitations such as intolerance to the test, contrast allergy, and narrow veins preventing bolus injection. One patient in whom postoperative changes could not be identified on MR imaging was excluded. Seven patients in whom DWI-ADC was difficult to evaluate due to artifacts and 3 patients in whom DWI-ADC of the neck region was not performed were excluded. Fifteen patients for whom an MR imaging vendor was used other than the one included in this study were excluded. Fifty-one patients matched the selection criteria (Online Supplemental Data). All patients were classified into 2 groups: the recurrence group and the benign posttreatment change group. Patients were included in the recurrence group if they had pathologic or unequivocal radiologic evidence, including follow-up examination or [^{18}F] FDG-PET/CT, of recurrent malignancy. Patients were included in the benign posttreatment change group if they had no pathologic evidence of recurrent malignancy or showed stable or improved imaging findings for >1 year.

MR Imaging Acquisition

MR imaging examinations were performed using 1.5T ($n = 33$) and 3T ($n = 18$) MR imaging systems (Ingenia, Achieva; Philips Healthcare). DWI was performed with b-values of 0 and 1000 s/mm^2 and the following parameters: TR range, 10,000–4000 ms; TE range, 98–55 ms; number of excitations, 1–2; section thickness/gap, 3.5–6/–1–1 mm; FOV, 225–255 × 225–255 mm; matrix, 120–200 × 120–200; and 3 diffusion directions. DCE-MR imaging scans were obtained via 3D T1-weighted fast-field echo. Parameters for 3D T1-weighted fast-field echo were as follows: TR, 4.8 ms; TE, 2 ms; flip angle, 30°; section thickness/gap, 5/–2.5 mm; FOV, 240 × 240 mm; matrix, 240 × 240; number of excitations, 1; number of slices per dynamic scan, 48; temporal resolution, 8.8 seconds; total acquisition time, 4 minutes 24 seconds. An intravenous bolus of 20 mL of gadobenate dimeglumine contrast (MultiHance; Bracco Diagnostics) was administered through a peripheral arm vein using a power injector with a flow rate of 5.0 mL/s, followed by a 20-mL saline flush.

Patients Demographics

The patient demographics, including age, sex, subsite, and histologic diagnosis of primary cancer, treatment method, and the reference method of recurrences or posttreatment changes, were reviewed from the electronic medical records.

ADC Analysis

ADC maps were constructed by a monoexponential fitting model using available software (Olea Sphere, Version 3.0; Olea Medical). Two head and neck radiologists with 11 and 20 years of experience outlined 3 separate ROIs on the ADC maps, predominantly including the low-signal-intensity region while excluding cystic or necrotic regions from ROIs with consensus. Another ROI was placed as a reference in the spinal cord, which was included in the FOV of every study.[21] For each ROI, normalized (n-) mean ADC ($nADC_{mean}$) was calculated by dividing the mean ADC by the reference mean ADC of the spinal cord. The values of mean ADC and $nADC_{mean}$ of 3 ROIs were averaged.

Quantitative and Semiquantitative DCE Analysis

Quantitative DCE-MR imaging analyses were performed using Olea Sphere, Version 3.0, based on the extended Tofts model, by which pixel-based parameter maps are calculated from time-intensity curves. An arterial input function was calculated automatically using cluster analysis techniques, and deconvolution of the arterial input function was performed with a time-insensitive block-circulant singular-value decomposition.[22] The 2 head and neck radiologists outlined 3 separate ROIs in the lesions on permeability maps, predominantly including the enhancing components while excluding cystic or necrotic regions from the ROIs with consensus. The calculated quantitative parameters were Vp, Ve, K^{trans}, and Kep. Semiquantitative analysis was also performed using the same ROIs described above using the Olea Sphere 3.0 software. The average signal intensity within the ROIs was plotted

DCE-MR imaging and ADC parameters

	Recurrence (n = 25) (Median [Range])	Benign Posttreatment Change (n = 26) (Median [Range])	P Value
DCE parameters			
Vp	0.09 (0.02–0.22)	0.05 (0.01–0.14)	
Reference Vp	0.01 (0.01–0.04)	0.02 (0.01–0.05)	
nVp	7.00 (0.50–17.33)	2.02 (0.33–14.33)	.003[a]
Ve	0.39 (0.07–0.98)	0.28 (0.01–1.08)	
Reference Ve	0.14 (0.01–0.26)	0.19 (0.07–0.67)	
nVe	2.55 (0.32–97.66)	1.56 (0.01–6.35)	.014
K^{trans}	0.25 (0.06–1.02)	0.13 (0.01–0.39)	
Reference K^{trans}	0.08 (0.01–0.15)	0.11 (0.04–0.33)	
nK^{trans}	3.87 (0.66–101.00)	1.27 (0.03–8.00)	<.001[a]
Kep	0.61 (0.39–2.03)	0.50 (0.16–2.12)	
Reference Kep	0.48 (0.02–1.36)	0.55 (0.32–1.06)	
nKep	1.45 (0.47–26.17)	0.96 (0.28–2.69)	.009
AUC	28,265 (3523–427,571)	11,887 (537–335,025)	
Reference AUC	7119 (615–188,345)	7890 (3530–185,938)	
nAUC	3.34 (1.31–20.81)	1.39 (0.01–9.96)	<.001[a]
WI	1.03 (0.29–2102.33)	0.70 (0.06–38.00)	
Reference WI	0.38 (0.02–696.00)	0.33 (0.07–21.24)	
nWI	4.13 (0.99–20.17)	1.70 (0.07–32.48)	<.001[a]
WO	0.68 (0.01–472.33)	0.57 (0.01–18.99)	
Reference WO	0.08 (0.01–117.00)	0.43 (0.02–27.28)	
nWO	3.78 (0.31–292.88)	1.35 (0–109.00)	.016
ADC value	1.01 (0.55–1.30)	1.61 (1.02–2.53)	
Reference ADC	0.79 (0.56–0.94)	0.78 (0.67–0.99)	
$nADC_{mean}$	1.31 (0.77–1.65)	2.07 (1.39–3.04)	<.001[a]

[a] Statistically significant.

against time, and time-intensity curves were constructed. The following parameters were calculated on a pixel-by-pixel basis from the time-intensity curves: area under the curve (AUC; the relative quantity of contrast agent across time), wash-in (WI; velocity of enhancement), and washout (WO; velocity of enhancement loss). For each ROI, normalized DCE-MR imaging parameters were calculated by dividing the mean value within the ROI placed in the lesion by the mean value within the reference ROI placed in the muscle tissue. The values of normalized DCE-MR imaging quantitative and semiquantitative parameters of the 3 ROIs were averaged.

Statistics

Shapiro-Wilk tests were performed to confirm the normality of distribution in each parameter. The Mann-Whitney U test was used to compare normalized DCE-MR imaging quantitative and semiquantitative parameters (nVp, nVe, nK^{trans}, nKep, nAUC, nWI, and nWO), age, and $nADC_{mean}$ between the recurrences and benign treatment changes. Sex was compared between the recurrences and benign treatment changes using the Fisher exact test. For parameters that showed a statistically significant difference, the optimal cutoff values in receiver operating characteristic analysis were determined as a value to maximize the Youden index (sensitivity + specificity −1). Diagnostic performances were calculated on the basis of the cutoff values. Several parameters that were significantly different in the univariate analysis described above were combined by logistic regression analysis to calculate the area under the receiver operating characteristic curve (AUROCC) as a combined parameter. Family-wise error–corrected 2-sided P values < .05 were considered statistically significant. Family-wise error correction was performed by the Bonferroni method. All statistical analyses were performed using R, Version 3.6.1 (http://www.r-project.org/).

RESULTS

Fifty-one patients were included in the study, of whom 25 had recurrence and 26 had benign posttreatment changes. The results of demographic and clinical data are summarized in the Online Supplemental Data. The most common sites of primary cancer were major salivary glands (14/51, 27.5%), sinonasal cavity (11/51, 21.6%), oral cavity (10/51, 19.6%), nasopharynx (8/51, 15.7%), and oropharynx (6/51, 11.8%). The histology of primary cancer mainly consisted of squamous cell carcinoma (26/51, 51%), adenoid cystic carcinoma (13/51, 25.5%), and mucoepidermoid carcinoma (7/51, 13.7%). The most common treatment methods were surgery and radiation therapy (15/51, 29.4%), followed by chemoradiotherapy (14/51, 27.5%) and surgery (14/51, 27.5%). The reference method of recurrence was mostly performed by pathology correlation (20/26, 76.9%), and the reference method of benign posttreatment changes was mainly by imaging follow-up (21/25, 84%). No significant differences in median patient age were found between the recurrence and benign posttreatment change groups (65 years; range, 21–89 years) versus 57.5 years (range, 22–77 years), respectively (P = .25). No significant differences in sex were found between the recurrence and benign posttreatment groups (male/female, 14:11 versus 17:9, respectively; P = .57).

DCE-MR Imaging and ADC Parameters

Results of DCE-MR imaging and ADC analyses are summarized in the Table. A pulsed input pattern was observed in the arterial input function curves in all patients. nVp, nK^{trans}, nAUC, and nWI were significantly higher in patients with recurrence than in those with benign posttreatment change (nVp: median, 7.00 [range, 0.50–17.33] versus 2.02 [range, 0.33–14.33]; P = .003; nK^{trans}: median, 3.87 [range, 0.66–101.00] versus 1.27 [range, 0.03–8.00]; P < .001; nAUC: median, 3.34 [range, 1.31–20.81] versus 1.39 [range, 0.01–9.96]; P < .001; nWI: median, 4.13 [range, 0.99–20.17] versus 1.70 [range, 0.07–32.48], respectively; P < .001). The cutoff value of nVp was 3.68 (sensitivity, 0.69; specificity, 0.76; AUROCC, 0.74 [95% CI, 0.76–0.92]); that of nK^{trans} was 3.02 (sensitivity, 0.85; specificity, 0.64; AUROCC, 0.79 [95% CI, 0.67–0.91]); that of nAUC was 2.04 (sensitivity, 0.69; specificity, 0.88; AUROCC, 0.80 [95% CI, 0.68–0.92]); and that of nWI was 2.69 (sensitivity, 0.69; specificity, 0.84; AUROCC, 0.79 [95% CI, 0.66–0.92]) (Fig 3*A*, -*B*). No significant difference was found in nVe, nKep, and nWO between the recurrence and benign

posttreatment change groups. $nADC_{mean}$ was significantly lower in patients with recurrence than in those with benign posttreatment change (recurrence: median, 1.31 [range, 0.77–1.65] versus benign posttreatment change, 2.07 [range, 1.39–3.04]; $P < .001$). The cutoff value of $nADC_{mean}$ was 1.65 (sensitivity, 0.92; specificity, 1.00; AUROCC, 0.97 [95% CI, 0.93–1]). Representative MR images of recurrence and benign posttreatment changes are demonstrated in Figs 1 and 2 and the Online Supplemental Data.

Diagnostic Performance

The AUROCC of the combination of normalized quantitative and semiquantitative DCE-MR imaging parameters with significance (nVp, nK^{trans}, nAUC, and nWI) was 0.81 (95% CI, 0.69–0.93) (Fig 3*C*). Furthermore, the AUROCC of the combination of normalized DCE-MR imaging parameters with significance (nVp, nVe, nK^{trans}, nAUC, and nWI) and $nADC_{mean}$ was 0.97 (95% CI, 0.93–1) (Fig 3*C*).

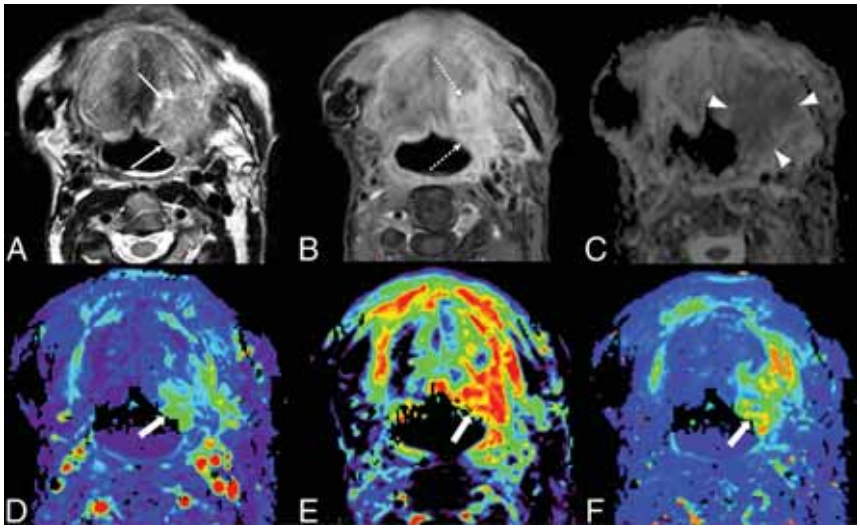

FIG 1. A case of head and neck cancer recurrence. A 72-year-old man after an operation and radiation therapy for squamous cell carcinoma of the floor of the mouth. The left side of the floor of the mouth shows some high signal intensity (*arrows*) on T2WI (*A*) and mild enhancement (*dotted arrows*) on postcontrast fat-suppressed T1WI (*B*). The ADC map (*C*) shows low signal (*arrowheads*), with an $nADC_{mean}$ of 1.38. DCE-MR imaging (*D*, Vp; *E*, Ve; *F*, K^{trans}) shows increased parameters (*thick arrows*), with an nVp of 7.33, nVe of 3.93, and nK^{trans} of 5.44.

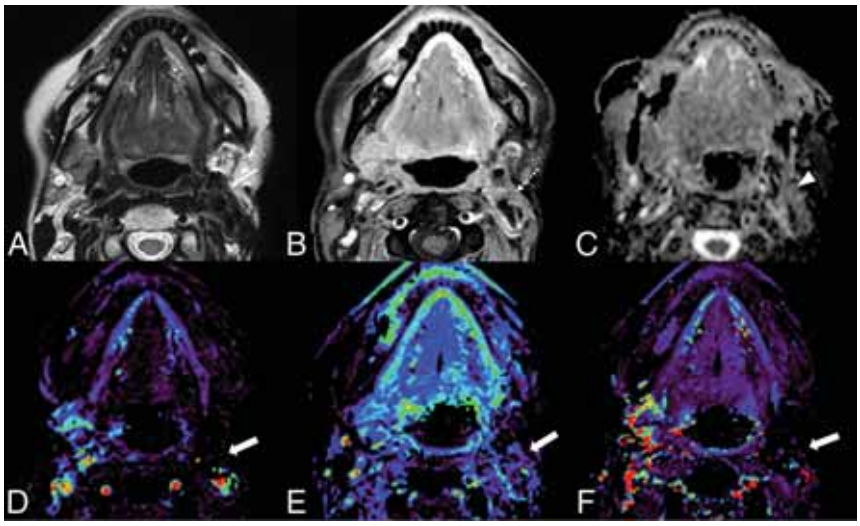

FIG 2. Benign posttreatment change of head and neck cancer in a 64-year-old woman after surgery and radiation therapy for mucoepidermoid carcinoma of the left parotid gland. The left parotid surgical bed shows low signal intensity (*arrow*) on T2WI (*A*) and mild enhancement (*dotted arrow*) on postcontrast fat-suppressed T1WI (*B*). The ADC map (*C*) shows no prominent low signal (*arrowhead*), with an $nADC_{mean}$ of 1.75. DCE-MR imaging (*D*, Vp; *E*, Ve; *F*, K^{trans}) shows no increased parameters (*thick arrows*) with an nVp of 0.33, nVe of 0.33, and nK^{trans} of 0.03.

DISCUSSION

This study evaluated the characteristics and differences of normalized parameters of dynamic contrast-enhanced perfusion MR imaging and DWI-ADC between recurrence and posttreatment changes in head and neck cancer. Normalized quantitative DCE-MR imaging parameters (nVp and nK^{trans}), normalized semiquantitative DCE-MR imaging parameters (nAUC and nWI), and $nADC_{mean}$ were significantly different between the recurrence and benign posttreatment change groups. The combined AUROCC was as high as 0.97 when using these parameters to differentiate recurrence and benign posttreatment changes.

DCE-MR imaging is a type of perfusion imaging technique that uses contrast media, and studies using quantitative parameters in head and neck cancer play important roles in the prediction of tumor hypoxia[6,7] and treatment response,[8,9] determination of treatment response,[10,11] and differentiation between recurrence and posttreatment changes.[12] The utility of semiquantitative parameters on DCE-MR imaging in differentiating head and neck cancer recurrence from posttreatment changes[13,14] and that of quantitative parameters, such as permeability surface area and blood volume,[12] are in agreement with the results of this study. Although these studies and the present study have both used semiquantitative and quantitative parameters, the reliability of semiquantitative parameters cannot be guaranteed, especially when the protocols are different.[23] To compensate for this disadvantage, statistical processing using normalized DCE-MR imaging parameters was performed in this study, and significant differences were confirmed for many of the normalized DCE-MR imaging parameters. If we used normalized data, our results are expected to be reproducible in many other institutions that use DCE-MR imaging if the imaging is

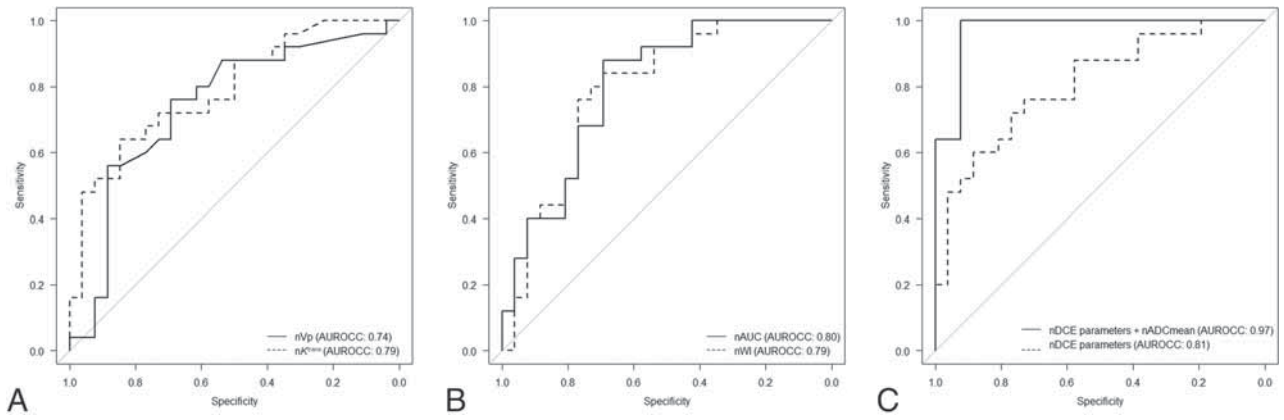

FIG 3. Receiver operating characteristic curves. AUROCCs for nVp (*solid line*) and nK^{trans} (*dashed line*) are 0.74 and 0.79, respectively (*A*). AUROCCs for nAUC (*solid line*) and nWI (*dashed line*) are 0.80 and 0.79, respectively (*B*). AUROCCs for the combination of normalized DCE-MR imaging parameters (nVp, nK^{trans}, nAUC, and nWI) (*dashed line*) and the combination of normalized DCE-MR imaging parameters and $nADC_{mean}$ (*solid line*) are 0.81 and 0.97, respectively (*C*).

performed with the same protocol. In addition, this study used relatively new vascular permeability parameters, such as Vp, Ve, K^{trans}, and Kep, and their usefulness in differentiating recurrence from benign posttreatment changes has not been previously reported.

Previous studies have shown that ADC values in recurrent head and neck cancer lesions are lower than those after benign posttreatment changes,[18-20] consistent with the results in the present study. The use of normalized ADCs in the present study and the aforementioned normalized DCE-MR imaging parameters is expected to be reproducible in other institutions by minimizing the effects of several factors that may affect the ADC values such as differences in MR imaging scanners, magnetic field strength, and patient variability.[24]

In the present study, the AUROCC of the combined normalized DCE-MR imaging parameters was high (0.81). The normalized DCE-MR imaging parameters (nVp, nK^{trans}, nAUC, and nWI), which showed significant differences in the present study, should be evaluated comprehensively rather than separately to be more effective in differentiating head and neck cancer recurrence from benign posttreatment changes. Furthermore, the combined normalized DCE-MR imaging parameters and $nADC_{mean}$ that showed a significant difference in the present study showed a high AUROCC value of 0.97. Notably, [^{18}F] FDG-PET/CT has very high specificity and sensitivity for differentiating head and neck cancer recurrences from posttreatment changes,[25] with a high AUROCC of 0.975,[26] which is comparable with an AUROCC of 0.97 for the combined evaluation of normalized DCE parameters and $nADC_{mean}$ in the present study. Although this study demonstrated the usefulness of normalized DCE parameters and $nADC_{mean}$, further study is needed to determine whether they can be used as a substitute for PET/CT. PET/CT has advantages over MR imaging such as the ability to detect systemic metastases. On the contrary, MR imaging has advantages such as superior spatial and tissue resolution and better medical cost.

There are several limitations in the present study. First, this was a single-center retrospective study. Second, the pathology of the included cases was heterogeneous, with only 51% of squamous cell carcinoma (typical of head and neck cancer) and salivary gland tumor cases included. Future studies with homogeneous cases of pathology are warranted. Third, MR imaging scanners were used with different field strengths for image acquisition. However, using normalized DCE-MR imaging and ADC parameters, we might minimize the risk of parameter heterogeneity. In addition, the analyses of the diagnostic performance in this study were optimistic because out-of-sample testing was not performed.

CONCLUSIONS

Normalized quantitative and semiquantitative DCE-MR imaging parameters and ADC values effectively assessed the difference between recurrence and benign posttreatment changes in head and neck cancer. The diagnostic performance of the combination of normalized DCE-MR imaging parameters and ADC values was very high and expected to be reproducible and effective in clinical practice.

Disclosure forms provided by the authors are available with the full text and PDF of this article at www.ajnr.org.

REFERENCES

1. Wong LY, Wei WI, Lam LK, et al. **Salvage of recurrent head and neck squamous cell carcinoma after primary curative surgery.** *Head Neck* 2003;25:953–59 CrossRef Medline
2. Hermans R. **Posttreatment imaging in head and neck cancer.** *Eur J Radiol* 2008;66:501–11 CrossRef Medline
3. Saito N, Nadgir RN, Nakahira M, et al. **Posttreatment CT and MR imaging in head and neck cancer: what the radiologist needs to know.** *Radiographics* 2012;32:1261–82 CrossRef Medline
4. Baba A, Ojiri H, Ikeda K, et al. **Essentials on oncological imaging: postoperative computed tomography and magnetic resonance imaging of oral tongue cancer.** *Can Assoc Radiol J* 2018;69:458–67 CrossRef Medline
5. Aiken AH, Rath TJ, Anzai Y, et al. **ACR Neck Imaging Reporting and Data Systems (NI-RADS): a White Paper of the ACR NI-RADS Committee.** *J Am Coll Radiology* 2018;15:1097–108 CrossRef Medline
6. Newbold K, Castellano I, Charles-Edwards E, et al. **An exploratory study into the role of dynamic contrast-enhanced magnetic resonance imaging or perfusion computed tomography for detection of intratumoral hypoxia in head-and-neck cancer.** *Int J Radiat Oncol Biol Phys* 2009;74:29–37 CrossRef Medline

7. Jansen JF, Carlson DL, Lu Y, et al. **Correlation of a priori DCE-MRI and 1H-MRS data with molecular markers in neck nodal metastases: initial analysis.** *Oral Oncol* 2012;48:717–22 CrossRef Medline
8. Bernstein JM, Kershaw LE, Withey SB, et al. **Tumor plasma flow determined by dynamic contrast-enhanced MRI predicts response to induction chemotherapy in head and neck cancer.** *Oral Oncol* 2015;51:508–13 CrossRef Medline
9. Ng S, Lin C, Chan S, et al. **Dynamic contrast-enhanced MR imaging predicts local control in oropharyngeal or hypopharyngeal squamous cell carcinoma treated with chemoradiotherapy.** *PLoS One* 2013;8:e72230 CrossRef Medline
10. Chikui T, Kitamoto E, Kawano S, et al. **Pharmacokinetic analysis based on dynamic contrast-enhanced MRI for evaluating tumor response to preoperative therapy for oral cancer.** *J Magn Reson Imaging* 2012;36:589–97 CrossRef Medline
11. Tomura N, Omachi K, Sakuma I, et al. **Dynamic contrast-enhanced magnetic resonance imaging in radiotherapeutic efficacy in the head and neck tumors.** *Am J Otolaryngol* 2005;26:163–67 CrossRef Medline
12. Ishiyama M, Richards T, Parvathaneni U, et al. **Dynamic contrast-enhanced magnetic resonance imaging in head and neck cancer: differentiation of new H&N cancer, recurrent disease, and benign post-treatment changes.** *Clin Imaging* 2015;39:566–70 CrossRef Medline
13. Furukawa M, Parvathaneni U, Maravilla K, et al. **Dynamic contrast-enhanced MR perfusion imaging of head and neck tumors at 3 Tesla.** *Head Neck* 2013;35:923–29 CrossRef Medline
14. Semiz Oysu A, Ayanoglu E, Kodalli N, et al. **Dynamic contrast-enhanced MRI in the differentiation of posttreatment fibrosis from recurrent carcinoma of the head and neck.** *Clin Imaging* 2005;29:307–12 CrossRef Medline
15. Ota Y, Liao E, Kurokawa R, et al. **Diffusion-weighted and dynamic contrast-enhanced MRI to assess radiation therapy response for head and neck paragangliomas.** *J Neuroimaging* 2021;31:1035–43 CrossRef Medline
16. Ailianou A, Mundada P, De Perrot T, et al. **MRI with DWI for the detection of posttreatment head and neck squamous cell carcinoma: why morphologic MRI criteria matter.** *AJNR Am J Neuroradiol* 2018;39:748–55 CrossRef Medline
17. Jajodia A, Aggarwal D, Chaturvedi AK, et al. **Value of diffusion MR imaging in differentiation of recurrent head and neck malignancies from post treatment changes.** *Oral Oncol* 2019;96:89–96 CrossRef Medline
18. Tshering Vogel DW, Zbaeren P, Geretschlaeger A, et al. **Diffusion-weighted MR imaging including bi-exponential fitting for the detection of recurrent or residual tumour after (chemo)radiotherapy for laryngeal and hypopharyngeal cancers.** *Eur Radiol* 2013;23:562–69 CrossRef Medline
19. Hwang I, Choi SH, Kim YJ, et al. **Differentiation of recurrent tumor and posttreatment changes in head and neck squamous cell carcinoma: application of high b-value diffusion-weighted imaging.** *AJNR Am J Neuroradiol* 2013;34:2343–48 CrossRef Medline
20. Baba A, Kurokawa R, Kurokawa M, et al. **ADC for differentiation between benign post-treatment changes and recurrence in head and neck cancer: a systematic review and meta-analysis.** *AJNR Am J Neuroradiol* 2022;43:442–47 CrossRef
21. Koontz NA, Wiggins RH. **Differentiation of benign and malignant head and neck lesions with diffusion tensor imaging and DWI.** *AJR Am J Roentgenol* 2017;208:1110–15 CrossRef Medline
22. Mouridsen K, Christensen S, Gyldensted L, et al. **Automatic selection of arterial input function using cluster analysis.** *Magn Reson Med* 2006;55:524–31 CrossRef Medline
23. Donato H, França M, Candelária I, et al. **Liver MRI: from basic protocol to advanced techniques.** *Eur J Radiol* 2017;93:30–39 CrossRef Medline
24. Ding X, Xu H, Zhou J, et al. **Reproducibility of normalized apparent diffusion coefficient measurements on 3.0-T diffusion-weighted imaging of normal pancreas in a healthy population.** *Medicine (Baltimore* 2019;98:e15104 CrossRef Medline
25. Isles MG, McConkey C, Mehanna HM. **A systematic review and meta-analysis of the role of positron emission tomography in the follow up of head and neck squamous cell carcinoma following radiotherapy or chemoradiotherapy.** *Clin Otolaryngol* 2008;33:210–22 CrossRef Medline
26. Kim S, Roh J, Seung J, et al. **18F-FDG PET/CT surveillance for the detection of recurrence in patients with head and neck cancer.** *Eur J Cancer* 2017;72:62–70 CrossRef Medline

Imaging Features of Craniofacial Giant Cell Granulomas: A Large Retrospective Analysis from a Tertiary Care Center

R. Chanda, S.S. Regi, M. Kandagaddala, A. Irodi, M. Thomas, and M. John

ABSTRACT

BACKGROUND AND PURPOSE: Craniofacial giant cell granulomas are rare lesions with varied appearances on imaging. We aimed to describe the imaging features of giant cell granulomas of the craniofacial bones.

MATERIALS AND METHODS: A retrospective analysis of the clinical features and imaging findings of 20 histopathology-proved cases of craniofacial giant cell granulomas, dating from 2006 to 2022, was performed.

RESULTS: Of the 20 cases, 10 each were seen in men and women. The epicenter of the lesions varied in location: in the maxilla in 8 patients, in the mandible in 5, in the temporal bone in 3, in the sphenoid/clivus in 3, and in the orbit in 1 patient. On the radiographs, the lesions appeared well-circumscribed, expansile, and lytic. On CT, the lesions were predominantly multiloculated, with thin septa, a soft-tissue component, and with expansion and remodeling of the underlying bone. On MR imaging, the solid component of the lesions was isointense on T1WI and hypointense on T2WI, with heterogeneous enhancement of the solid component and rim enhancement of the locules. Fluid-fluid levels were present in 3 patients.

CONCLUSIONS: Giant cell granulomas commonly present as locally aggressive, expansile, multiloculated lytic lesions, with solid as well as cystic areas. The solid component is typically hypointense on T2WI. Certain key imaging features of giant cell granulomas can aid the radiologist in narrowing the differential diagnosis.

ABBREVIATIONS: ABC = aneurysmal bone cyst; GCG = giant cell granuloma; GCRG = giant cell reparative granuloma; GCT = giant cell tumor

The term central giant cell reparative granuloma (GCRC) was first used by Jaffe,[1] in 1953, to describe a lesion that developed in response to intraosseous hemorrhage. There has been much debate about the presence of the reparative component in the pathogenesis of these granulomas;[2] hence, the term giant cell granuloma (GCG) is preferred compared with GCRG. Endosteal GCGs are classified as central, while those arising in the soft tissue are peripheral GCGs. The World Health Organization 2017 classification (updated version) of head and neck tumors classifies GCGs under giant cell lesions along with cherubism, aneurysmal bone cyst (ABC), and simple bone cyst.[3,4]

The craniofacial bones are the usual sites of involvement, followed by small bones of the hands and feet.[5] GCGs of the head and neck region are known to show a female predilection, with some lesions showing accelerated growth during pregnancy, suggesting a possible hormone-dependent nature of these lesions.[6]

Varied imaging appearances of GCGs pose a diagnostic challenge in differentiating them from other bone lesions such as ABCs, brown tumors, fibrous dysplasia, various odontogenic and nonodontogenic cysts, maxillofacial malignancies, and giant cell tumors (GCTs).

On histopathology, GCGs consist of spindled fibroblasts, collagenous stroma, areas of hemorrhage, and numerous multinucleated, osteoclast-type giant cells arranged in small clusters around areas of hemorrhage, usually containing ≤12 nuclei. Secondary changes with hemosiderin deposits, aggregates of foamy macrophages, cystic changes, and reactive bone formation may be seen in GCGs, simulating an ABC.

Solid ABCs have slender and spindle-shaped mononuclear cells and clustering of giant cells resembling GCGs. However, woven bone trabeculae are prominent in ABCs, while hemorrhagic foci are less conspicuous.[7,8] A *USP6* gene rearrangement is seen in ABCs.[9]

GCGs are indistinguishable from brown tumors of hyperparathyroidism on imaging as well as histopathology, with brown tumors usually containing more fibrous septa that

Received March 27, 2022; accepted after revision May 24.

From the Departments of Radiodiagnosis (R.C., S.S.R., M.K., A.I.), Pathology (M.T.), and Otorhinolaryngology (M.J.), Christian Medical College, Vellore, India.

Dr. R. Chanda is first author.

Please address correspondence to Madhavi Kandagaddala, DNB, Department of Radiodiagnosis, Christian Medical College, Vellore, Tamil Nadu, India 632004; e-mail: madhoo116@gmail.com

http://dx.doi.org/10.3174/ajnr.A7568

Table 1: Key histopathologic features of common differentials of GCGs

	GCG	GCT	ABC	Brown Tumor
Epithelioid stroma	Spindled stroma, oval-to-elongated nuclei	Plump epithelioid with oval nuclei	Spindled stroma, oval-to-elongated nuclei	Spindled stroma, oval-to-elongated nuclei with fibrous stroma dividing it into lobules
Giant cells	12 Nuclei in clusters around hemorrhagic foci	>12 Uniformly distributed nuclei	Smaller giant cells, in clusters, woven bone present, less hemorrhage	Few giant cells
Immunohistochemistry (p63 positivity)	Yes	Yes	No	No
Gene mutation				
H3f3a mutation	No	Yes	No	No
USP6 rearrangement	No	No	Yes	No

subcompartmentalize these lesions into multiple lobules.[3,5] On histology, GCGs are also indistinguishable from cherubism.

The mononuclear cells in GCGs are spindle-shaped and not oval or round as in GCT of the bones, with fewer mitotic figures.[7,8] GCTs histologically have numerous large, osteoclast-type giant cells, evenly distributed throughout the tumor with >12 nuclei. The mononuclear cells are arranged in a syncytial pattern in GCTs. On immunohistochemistry, both GCTs and GCGs can show an expression of p63 in mononuclear cells. Mutations in the *H3f3a* gene are seen in GCTs, but not in GCGs.[10-12]

A summary of the key histopathologic features of GCGs, GCTs, ABCs, and brown tumors is provided in Table 1.

It is important to differentiate GCTs and GCGs because the former is associated with a higher recurrence rate, malignant transformation, and metastatic potential compared with the latter.[13]

In this study, we report our experiences and observations from a large case series to highlight the key imaging features of GCGs that could aid in narrowing the differential diagnosis.

MATERIALS AND METHODS

In this institutional review board–approved study, all cases of craniofacial GCGs diagnosed on imaging at our tertiary care center and confirmed by histopathology during 15 years, between 2006 to 2022, were included in this study. A retrospective analysis of their imaging findings was conducted.

The study began with a PACS search using the keywords "GCRG," "GCG," and "giant" in CT and MR imaging modalities. This yielded a list of 33 craniofacial lesions in which GCG was provided as the radiologic/differential diagnosis. Of these cases, 24 patients underwent biopsy and 20 cases were confirmed as GCGs, which were then included in this study. Of the remaining 9 cases, 8 patients did not undergo biopsy and 1 lesion was diagnosed as pyogenic granuloma on histopathology. Thus, these cases were excluded from the study.

Of the 20 patients included in the study, local radiographs were available for 9 patients, of which 8 were orthopantomograms and 1 was a paranasal sinus radiograph. Both CT and MR imaging were performed in 8 patients, and only CT was performed in 12 patients. CT scans were performed using Somatom Emotion 16-section (Siemens) or Discovery 750 HD 128-section (GE Healthcare) scanners with a section thickness of 2 mm, FOV of 230 × 230, and a bolus injection of iohexol in soft-tissue and bone algorithms.

The MR imaging studies were performed on either 1.5T (Avanto; Siemens) or 3T (Achieva; Philips Healthcare) scanners with similar imaging protocols and acquisition parameters: Achieva, 3T T1-weighted spin-echo sequence (TE/TR = 20/630 ms; echo-train length = 6; flip angle = 90°; section thickness = 5 mm; section gap = 0.5); T2-weighted spin-echo sequence (TE/TR = 90/3500 ms; echo-train length = 13; flip angle = 90°; section thickness = 5 mm; section gap = 0.5); and STIR T2-weighted spin-echo sequence (TE/TR = 60/4000 ms; echo-train length = 11; flip angle = 160°); Avanto, 1.5T T1-weighted spin-echo sequence (TE/TR = 17/460 ms; echo-train length = 3; flip angle = 90°; number of averages = 2; section gap = 0.5); T2-weighted spin-echo sequence (TE/TR = 80/3000 ms; echo-train length = 13; flip angle = 90°; section gap = 0.5); and STIR T2-weighted spin-echo sequence (TE/TR = 70/3000 ms; echo-train length = 11; flip angle = 160°). Postcontrast T1-weighted sequences were obtained after a bolus injection of 0.1 mmol/kg of gadoteric acid. SWI and DWI (b-value = 800) with ADC mapping were available for 4 patients.

The 20 confirmed lesions were assessed for location, size, number, extension, margins, matrix, septations, and loculations on all imaging modalities. Additionally, on CT, bony remodeling, tooth resorption, matrix mineralization, enhancement, and extraosseous extension were assessed. On MR imaging, intralesional signal characteristics were assessed on T1WI, T2WI, STIR, SWI, DWI, and postcontrast sequences. Intracranial extension was also assessed on both CT and MRI. Lesions with radiologic features, such as tooth resorption, the presence of extraosseous soft-tissue components, and loss of plane with surrounding structures were classified as aggressive. On the other hand, lesions that were confined to the bone and showed scalloping, rather than erosion of the bone, displacing rather than infiltrating the surrounding structures, were classified as nonaggressive types.

The imaging findings were reviewed by 2 radiologists (R.C. and S.S.R.) with 5 and 6 years of experience, respectively.

RESULTS

Patient Demographics

The 20 patients comprised 10 male and 10 female cases. The mean age of the patients was 28 years (range, 7–65 years); there were 8 pediatric and 12 adult patients. A sex-based distribution of the location of GCGs is provided in Table 2.

Table 2: Sex-wise distribution of craniofacial GCGs

	Male	Female	Total
Orbit	1	0	1
Mandible	3	2	5
Maxilla	3	5	8
Temporal	1	2	3
Sphenoid/clivus	2	1	3

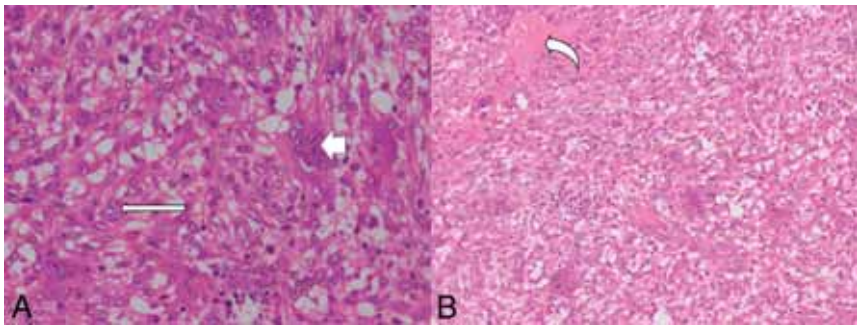

FIG 1. *A*, H&E, original magnification ×200. Cellular lesion composed of sheets of oval- to spindle-shaped cells admixed with many multinucleated giant cells (*short arrow*), the nuclei of which resemble stromal cells (*long arrow*). Mitotic activity is inconspicuous. *B*, H&E original magnification ×100. Hemorrhagic foci (*curved arrow*) and mild lymphocytic infiltrates in the surrounding stroma.

Clinical Presentation

The most common presenting symptom was painless, progressive swelling ($n = 13$). Four patients presented with recurrent episodes of bleeding ($n = 2$ with oral bleed, $n = 1$ with epistaxis, $n = 1$ ear bleed).

Region-specific symptoms, such as otorrhea, ear pain for temporal lesions, diplopia and visual disturbance in lesions involving the orbit, nasal obstruction, and discharge in lesions with nasal extension were also seen. GCG was incidentally identified in 1 patient who underwent a CT of the neck for a soft-tissue lesion in the right parapharyngeal space. Most patients ($n = 16$) presented within 1 year of onset of symptoms. There was no reported history of malignancy, hyperparathyroidism, radiation therapy, or regional trauma in any patient. Among the female patients, there was no reported history of occurrence of a new lesion or change in the size of an existing lesion during pregnancy.

Histopathology Features

Histopathologic diagnosis of GCG was confirmed by the presence of an ill-circumscribed cellular lesion, composed of sheets of oval- to spindle-shaped cells with vesicular nuclei, visible nucleoli, and moderate amounts of eosinophilic cytoplasm, with adjacent areas of stromal fibrosis, hemorrhage, and congested blood vessels (Fig 1). Interspersed with this stroma were many multinucleated giant cells, the nuclei of which resembled the stromal cells. Mitotic activity was inconspicuous. Three lesions with multiple fluid-fluid levels on MR imaging showed features of GCG with secondary ABC on histopathological examination.

Tumor Location and Extension

All 20 lesions in this study were central GCGs, originating in the craniofacial and/or skull base bones; we did not encounter any soft-tissue/peripheral GCGs. The epicenter of 8 lesions was in the maxilla, 5 involved the mandible, 3 were in the temporal bone, another 3 were in the sphenoid sinus with clival involvement, and 1 lesion was in the orbit (Table 2). The most common location of lesions in females was in the maxilla ($n = 5$). In males, the highest number of lesions was in the maxilla and mandible ($n = 3$ each). Of the 5 mandibular lesions, a multifocal mandibular involvement was seen in 1 patient, while the remaining 4 were solitary lesions, 2 of which were in the midline and 2 were peripherally located.

Nine of the 20 lesions had infiltrated into the surrounding bone and/or soft tissue. The orbital lesion extended into the fronto-ethmoid sinuses and into the nasal cavity. Parotid gland infiltration was present in 1 patient with GCG in the temporal bone. Intracranial extension was seen with 1 orbital, 2 sphenoidal, and 2 temporal bone GCGs, with extradural ($n = 1$), dural ($n = 4$), and cavernous sinus ($n = 2$) infiltration; brain parenchymal infiltration was not observed in any of these.

Imaging Features

Plain Radiography. Among the 9 patients who had plain radiographs obtained, the lesions were expansile, lytic, and well-circumscribed. There was no matrix mineralization in 8 of these 9 lesions; 1 patient had a sclerotic lesion with a ground-glass matrix.

CT Features of GCGs. On CT, 6 lesions had predominantly soft-tissue attenuation, 8 had fluid attenuation, 5 had mixed solid-cystic components, and 1 was sclerotic. Expansion and bony remodeling of the involved bone was observed in 15 lesions. Multiple loculations with thin septa were present in 10 lesions. Septal thickening with calcification was seen in 3 lesions. Tooth resorption was seen in 6 lesions involving the maxilla/mandible. There was heterogeneous enhancement of the soft-tissue component. None of the lesions had discrete foci of calcification. There was no encasement or hypertrophy of the adjacent blood vessels.

MR Imaging Features of GCGs. On MR imaging, the solid component was of intermediate-to-low signal intensity on T1WI and predominantly hypointense on T2WI, with interspersed heterogeneous areas of intermediate-to-high signal intensity. There was heterogeneous postcontrast enhancement of the solid areas. On visual assessment, there was an absence of diffusion restriction in the T2-hypointense areas. The ADC values in the areas of iso- to high signal intensity on the T2WI ranged between 8.45 and 1.06×10^{-3} mm^2/s. The fluid component in the GCGs was hypointense on T1WI and hyperintense on T2W1. Multiple fluid-fluid levels of differential signal intensity on T1WI and T2WI were present in 3 cases, indicative of hemorrhage.

Management and Follow-up

Preoperative embolization was performed in 1 patient. Six patients underwent complete surgical resection, and another 6 patients underwent partial or subtotal resection. Two patients underwent

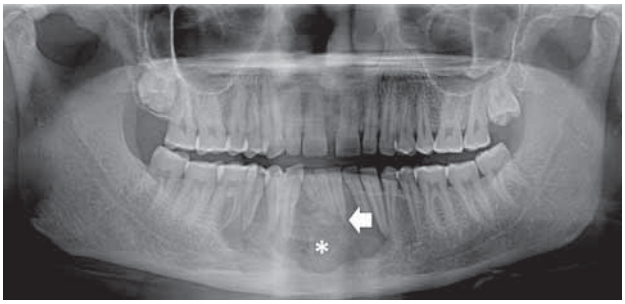

FIG 2. GCG of the mandible. Orthopantomogram shows an expansile, lytic central mandibular lesion with lobulated margins (*asterisk*). Note the resorption of the roots of the central incisors (*arrow*).

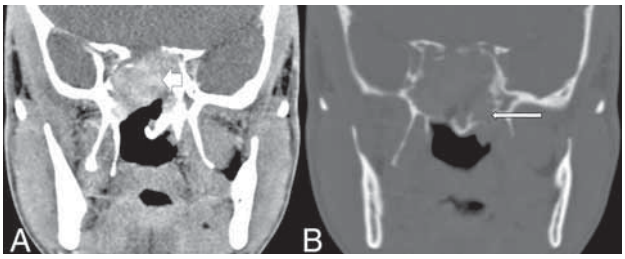

FIG 3. GCG of the sphenoid bone. *A*, Contrast-enhanced CT of the skull base shows a lobulated, enhancing mass in the sphenoid sinus (*short arrow*). *B*, On the bone window, the mass expands the sphenoid bone and there are multiple foci of a cortical breach (*long arrow*) Note the absence of matrix mineralization in the lesion.

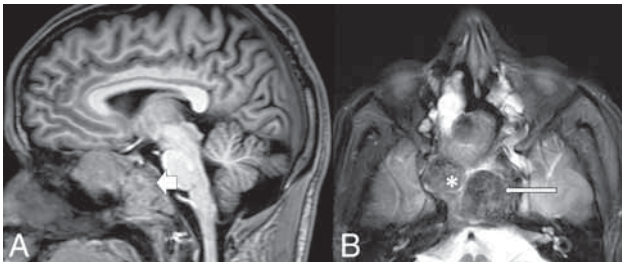

FIG 4. MR imaging features of GCG. *A*, Heterogeneous intermediate-to-high signal intensity (*short arrow*) on the T1-weighted sagittal image. *B*, Mixed intermediate-to-hyperintense (*white asterisk*) and hypointense (*long arrow*) solid components on T2-weighted axial image in the sphenoid bone and clival GCG.

postoperative radiation therapy. Postoperative follow-up imaging was available in 9 patients, with the follow-up period ranging from 4 months to 5 years. No intervention was performed in 7 patients who were lost to follow-up after diagnosis.

Of the 6 patients who underwent complete surgical resection of the lesions, postoperative follow-up imaging, which was available in 3 maxillary GCGs, showed disease recurrence in all 3 at an average interval of 39 months postsurgery. Clinicoradiologic progression occurred in 3 of the 5 patients who underwent subtotal or near-complete resection.

No features of malignant transformation were found in any of the lesions, either at primary imaging or in any of the follow-up imaging.

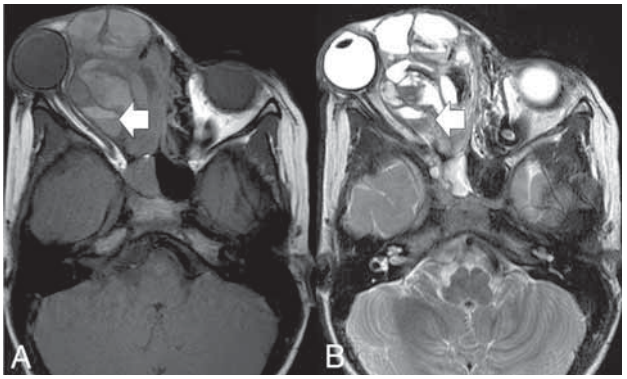

FIG 5. GCG of the orbit with secondary ABC changes appearing as a multiloculated lesion with multiple fluid-fluid levels (*arrow*) of differential signal intensity on T1-weighted (*A*) and T2-weighted (*B*) axial images.

DISCUSSION

GCGs are rare tumors of the head and neck, with a high propensity for recurrence. The rarity of the lesions, along with overlapping imaging features with certain benign as well as malignant lesions, make the preoperative diagnosis of GCGs challenging.

This study presents the observations of craniofacial GCGs in the single largest case series of imaging findings reported in the literature thus far. No age- or sex-specific predilection was observed in any site of involvement. We did not find any association of the lesions with trauma, pregnancy, or a previous malignancy.

On imaging, craniofacial GCGs have a variable appearance. On radiographs, the lesions are commonly solitary, expansile, and lytic (Fig 2). On CT, the lesions are commonly heterogeneous and multiloculated, with remodeling of the involved bone. Interrupted segments of focal cortical breach occur frequently, and this is a reliable indicator of these lesions being locally aggressive (Fig 3*B*). A soft-tissue component, when present, shows heterogeneous postcontrast enhancement (Fig 3*A*). Tooth resorption is a notable feature in GCGs of the mandible.

In the study by Nackos et al[5] in 7 patients, matrix mineralization was reported in all except 1 case, whereas this was an uncommon feature in our study.

On MR imaging in our study, the intralesional soft-tissue component was iso- to hypointense on T1WI sequences (Fig 4*A*). The lesions were heterogeneous on T2WI, with hypointense signal being the predominant finding (Fig 4*B*). This feature of hypointensity on T2WI is in keeping with the limited existing literature available on MR imaging features of GCGs and can be attributed to the presence of fibrous tissue and repetitive hemorrhage seen on histopathology.[5,14,15] Hemorrhage within the lesions appears as multiple fluid-fluid levels of differential signal intensity on T1WI and T2WI sequences (Fig 5). Layered SWI hypointensity can also be observed in multiloculated GCGs, indicating the hemorrhagic nature of the content (Fig 6). Three lesions with multiple fluid-fluid levels on MR imaging (1 in the orbit and 2 in the temporal bone) were reported as GCGs with secondary ABC changes on HPE.

The solid component of GCGs shows heterogeneous enhancement postcontrast (Fig 7*A*). Enhancement of the walls of the locules and septa is also a common feature (Fig 7*B*).

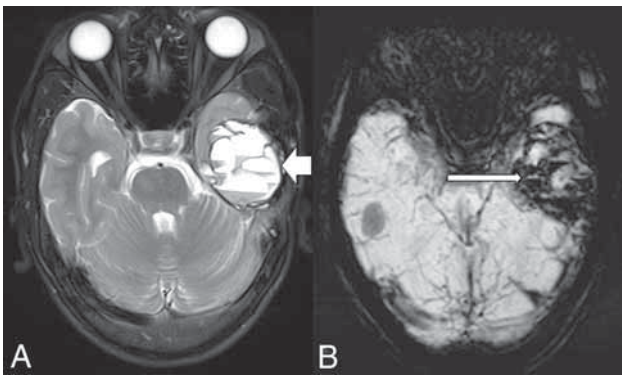

FIG 6. Multiloculated GCG of the left temporal bone with fluid-fluid levels (*short arrow*, *A*) on axial T2-weighted and layers of hypointense signal (*long arrow*, *B*) on a susceptibility-weighted imaging.

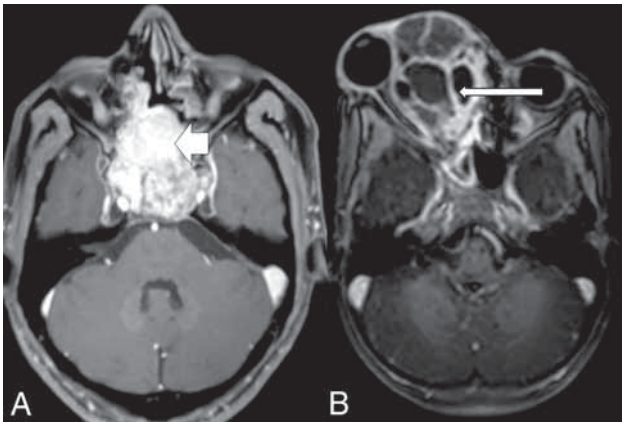

FIG 7. Patterns of enhancement in GCG (on postgadolinium TIWI). *A*, Solid, sphenoidal GCG shows heterogeneous enhancement (*short arrow*). *B*, Multiloculated right-orbital GCG with enhancing walls (*long arrow*).

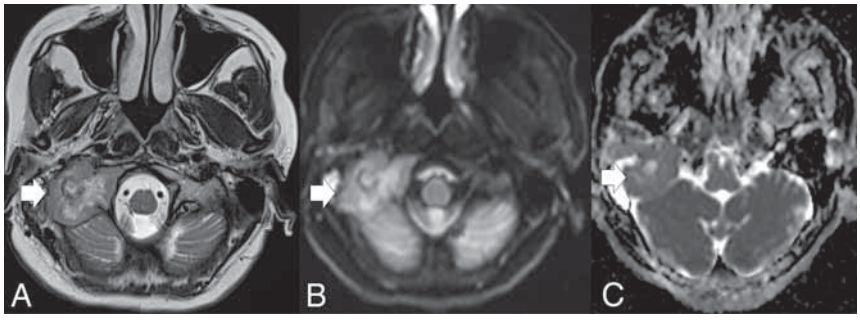

FIG 8. GCG of the right petrous bone. The lesion (*arrow*) is heterogeneous with peripheral, intermediate-signal-intensity soft tissue and central cystic area on (*A*) T2-weighted. DWI (*B*) and ADC map (*C*) of the lesion.

Features of GCG on DWI and ADC maps and on SWI have not been described in literature so far. Rao et al[16] found that an ADC value of 1.3 had the highest sensitivity and specificity in differentiating benign (high ADC) from malignant (low ADC) bone tumors. In the study by Nouh et al,[17] the mean ADC value of $\leq 1.1 \times 10^{-3}$ mm^2/s had a sensitivity of 86.1% for malignant bone lesions. DWI and ADC sequences available for 4 patients in our study did not show any diffusion restriction in the T2WI hypointense solid areas. Furthermore, the ADC values in the intermediate-to-high signal intensity areas were $>1.0 \times 10^{-3}$ mm^2/s (Fig 8). However, Ashikyan et al[18] found that GCTs also have a mean ADC of 1.1×10^{-3} mm$^{2.}$. A larger sample size is required to arrive at a reliable conclusion on the ADC values of GCGs.

In our study, we observed that 12 patients had a combination of >1 aggressive feature. Additionally, 4 lesions demonstrated focal loss of a fat plane as a solitary aggressive feature. Thus, 80% ($n = 16/20$) were locally aggressive.

Recurrence or progression of residual tumor or both were observed in 6 of the 8 patients in whom postoperative follow-up imaging was available. Although the data available are scant, they imply that these lesions are locally aggressive and have an extremely high rate of recurrence, irrespective of the type of operation performed (total-versus-partial excision).

Differential Diagnosis of Craniofacial GCGs

Differentials for lytic, expansile lesions in the craniofacial and skull base bones include aneurysmal bone cyst, brown tumor of hyperparathyroidism, fibrous dysplasia, giant-cell tumors, giant-cell granulomas, and the whole gamut of odontogenic and nonodontogenic jaw lesions.[5,14,19-21]

ABCs are expansile, lytic lesions that are uncommon in the craniofacial bones. They are multiloculated with multiple fluid-fluid levels. Primary ABCs do not have a soft-tissue component. Secondary ABCs can occur with GCGs.[15] Failure to obtain adequate representative biopsy samples from different areas in a GCG can lead to sampling error and under-reporting of secondary ABC changes within the lesions.

A ground-glass matrix and bony remodeling are classic features of fibrous dysplasias; however, a hypointense soft-tissue component on T2WI is not.

Unilocular, cystic central GCGs could be indistinguishable from other cystic jaw and maxillary lesions on imaging, such as dentigerous cysts, odontogenic keratocysts, radicular cysts, and so forth. Cortical breach, however, is not seen in these lesions and they can also be readily differentiated from GCGs on histopathology.

Brown tumors of hyperparathyroidism and GCGs have a similar imaging and pathologic appearance.[3-5,14] While we conducted the present study, 1 patient with a lytic mandibular lesion on imaging and histopathologic features showing osteoclastic granulomas was found to have an elevated serum parathyroid hormone and a functioning parathyroid adenoma. This case was diagnosed as a brown tumor and excluded from the study.

The soft-tissue component in ameloblastoma is usually hyperintense on T2WI. Also in maxillary and mandibular carcinomas, the soft tissue is T2 hyperintense, along with extensive bony destruction and peritumoral fat stranding.

The soft-tissue component in both GCGs and GCTs is of intermediate-to-low signal intensity on T2WI. However, GCTs in the head and neck are extremely uncommon.[5,15,22] GCTs also have a potential to metastasize to other organs such as the lungs, a finding we did not observe with GCGs in our study. Given the considerable overlap in the imaging findings of GCGs and GCTs, it is imperative for the radiologist to be aware of these 2 entities and include both in the differential diagnosis of craniofacial lesions with a hypointense solid component on T2WI.

Limitations

Due to the rarity of craniofacial GCGs, only a limited sample size could be obtained for analysis. Because our study was retrospective in nature, imaging modalities, protocols, and MR imaging sequences were not uniform across all patients.

CONCLUSIONS

GCGs are rare, slow-growing, often painless tumor mimics of osseous lesions of the head and neck. As opposed to findings in the existing literature, no sex predilection or any association with trauma or pregnancy was noted in our study. Key imaging features of GCGs include solitary, expansile, lytic lesions with focal areas of cortical breach, and associated bony remodeling, often with mixed cystic and solid components. The solid component, when present, is hypointense on T2WI and enhances on postcontrast imaging but does not show diffusion restriction. Multiple fluid-fluid levels, when present, are indicative of secondary ABC changes within GCGs. Owing to a high rate of postoperative recurrence, it is imperative to assess, on imaging, all GCGs for aggressive features like tooth resorption, the presence of an extraosseous soft-tissue component, and the loss of plane with the surrounding structures.

ACKNOWLEDGMENT

We are grateful to Dr Pippa Deodhar, Scientist (grade IV), Principal's Office, Christian Medical College, Vellore, for helping us in revising this manuscript.

Disclosure forms provided by the authors are available with the full text and PDF of this article at www.ajnr.org.

REFERENCES

1. Jaffe HL. **Giant-cell reparative granuloma, traumatic bone cyst, and fibrous (fibro-osseous) dysplasia of the jawbones.** *Oral Surg Oral Med Oral Pathol* 1953;6:159–75 CrossRef Medline
2. Ackerman LV, Spjut HJ. **Giant cell reaction**. In: Firminger H, ed. *Atlas of Tumor Pathology: Tumors of Bone and Cartilage, fascicle 5, series 2.* Washington, DC: American Registry of Pathology 1962;293–314
3. Barnes L, Eveson JW, Reichart P, et al eds. *Pathology and Genetics of Head and Neck Tumours.* World Health Organization/International Agency for Research on Cancer; 2005
4. El-Naggar AK, Chan JK, Grandis JR, et al eds. *WHO Classification of Head and Neck Tumours.* Vol 9. 4th ed. World Health Organization/International Agency for Research on Cancer; 2017
5. Nackos JS, Wiggins RH, Harnsberger HR. **CT and MR imaging of giant cell granuloma of the craniofacial bones.** *AJNR Am J Neuroradiol* 2006;27:1651–53 Medline
6. Fechner RE, Fitz-Hugh GS, Pope TL. **Extraordinary growth of giant cell reparative granuloma during pregnancy.** *Arch Otolaryngol Chic Otolaryngol* 1984;110:116–19 CrossRef Medline
7. Nielsen GP, Rosenberg AE. *Diagnostic pathology: Bone.* Elsevier Health Sciences; 2021
8. Fletcher C. *Diagnostic Histopathology of Tumors.* 2 Volume Set. 5th ed. Elsevier; 2019
9. Oliveira AM, Perez-Atayde AR, Inwards CY, et al. **USP6 and CDH11 oncogenes identify the neoplastic cell in primary aneurysmal bone cysts and are absent in so-called secondary aneurysmal bone cysts.** *Am J Pathol* 2004;165:1773–80 CrossRef Medline
10. Presneau N, Baumhoer D, Behjati S, et al. **Diagnostic value of H3F3A mutations in giant cell tumour of bone compared to osteoclast-rich mimics.** *J Pathol Clin Res* 2015;1:113–23 CrossRef Medline
11. Scotto di Carlo F, Divisato G, Iacoangeli M, et al. **The identification of H3F3A mutation in giant cell tumour of the clivus and the histological diagnostic algorithm of other clival lesions permit the differential diagnosis in this location.** *BMC Cancer* 2018;18:358 CrossRef Medline
12. Nagar SR, Bansal S, Jashnani K, et al. **A comparative analysis of p63 expression in giant cell tumour (GCT), central giant cell granuloma (CGCG) and peripheral giant cell granuloma (PGCG).** *Head and Neck Pathol* 2020;14:733–41 CrossRef Medline
13. Ung F, Li KK, Keith DA, et al **Giant cell reparative granuloma of the temporal bone: case report and review of the literature.** *Otolaryngol Head Neck Surg* 1998;118:525–29 CrossRef Medline
14. Regezi JA. **Odontogenic cysts, odontogenic tumors, fibro-osseous, and giant cell lesions of the jaws.** *Mod Pathol* 2002;15:331–41 CrossRef Medline
15. Murphey MD, Nomikos GC, Flemming DJ, et al. **From the archives of AFIP: imaging of giant cell tumor and giant cell reparative granuloma of bone—radiologic-pathologic correlation.** *Radiographics* 2001;21:1283–309 CrossRef Medline
16. Rao A, Sharma C, Parampalli R. **Role of diffusion-weighted MRI in differentiating benign from malignant bone tumors.** *BJR Open* 2019;1:20180048 CrossRef Medline
17. Nouh MR, Doweidar A, Khalil AM. **Apparent diffusion coefficient (ADC): a potential in vivo biological surrogate of the incidentally discovered bone lesions at 3T MRI.** *Eur J Radiol Open* 2021;8:100386 CrossRef Medline
18. Ashikyan O, Chalian M, Moore D, et al. **Evaluation of giant cell tumors by diffusion weighted imaging-fractional ADC analysis.** *Skeletal Radiol* 2019;48:1765–73 CrossRef Medline
19. Shrestha S, Zhang J, Yan J, et al. **Radiological features of central giant cell granuloma: comparative study of 7 cases and literature review.** *Dentomaxillofac Radiol* 2021;50:20200429 CrossRef Medline
20. Jamil OA, Lechpammer M, Prasad S, et al. **Giant cell reparative granuloma of the sphenoid: case report and review of the literature.** *Surg Neurol Int* 2012;3:140 CrossRef Medline
21. Aralasmak A, Aygun N, Westra WH, et al. **Giant cell reparative granuloma of the sphenoid bone.** *AJNR Am J Neuroradiol* 2006;27:1675–77 Medline
22. Borges BB, Fornazieri MA, Correia de Araújo Bezerra AP, et al. **Giant cell bone lesions in the craniofacial region: a diagnostic and therapeutic challenge.** *Int Forum Allergy Rhinol* 2012;2:501–06 CrossRef Medline

MR Imaging of Pediatric Low-Grade Gliomas: Pretherapeutic Differentiation of *BRAF* V600E Mutation, *BRAF* Fusion, and Wild-Type Tumors in Patients without Neurofibromatosis-1

A. Trasolini, C. Erker, S. Cheng, C. Crowell, K. McFadden, R. Moineddin, M.A. Sargent, and D. Mata-Mbemba

ABSTRACT

BACKGROUND AND PURPOSE: The prognosis and treatment of pediatric low-grade gliomas is influenced by their molecular subtype. MR imaging remains the mainstay for initial work-up and surgical planning. We aimed to determine the relationship between imaging patterns and molecular subtypes of pediatric low-grade gliomas.

MATERIALS AND METHODS: This was a retrospective bi-institutional study for patients diagnosed from 2004 to 2021 with pathologically confirmed pediatric low-grade gliomas molecularly defined as *BRAF* fusion, *BRAF* V600E mutant, or wild-type (which is neither *BRAF* V600E mutant nor *BRAF* fusion). Two neuroradiologists, blinded, independently reviewed imaging parameters from diagnostic MRIs, and discrepancies were resolved by consensus. Bivariate analysis was used followed by pair-wise comparison of the Dwass-Steel-Critchlow-Fligner method to compare the 3 molecular subtypes. Interreader agreement was assessed using κ.

RESULTS: We included 70 patients: 30 *BRAF* fusion, 19 *BRAF* V600E mutant, and 21 wild-type. There was substantial agreement between the readers for overall imaging variables ($\kappa = 0.75$). *BRAF* fusion tumors compared with *BRAF* V600E and wild-type tumors were larger ($P = .0022$), and had a greater mass effect ($P = .0053$), increased frequency of hydrocephalus ($P = .0002$), and diffuse enhancement ($p < .0001$). *BRAF* V600E mutant tumors were more often hemispheric ($P < .0001$), appeared more infiltrative ($P = .0002$), and, though infrequent, were the only group demonstrating diffusion restriction (qualitatively; $P = .0042$) with a lower ADC ratio (quantitatively) ($P = .003$).

CONCLUSIONS: *BRAF* fusion and *BRAF* V600E mutant pediatric low-grade gliomas have unique imaging features that can be used to differentiate them from each other and wild-type pediatric low-grade glioma using a standard radiology review with high interreader agreement. In the era of targeted therapy, these features can be useful for therapeutic planning before surgery.

ABBREVIATIONS: IQR = interquartile range; pLGG = pediatric low-grade glioma; WHO = World Health Organization

Pediatric low-grade gliomas (pLGGs) make up the largest proportion, about 30%, of all pediatric CNS tumors.[1] pLGGs have a favorable 10- to 20-year overall survival of approximately 90%–95%.[2] However, pLGGs can lead to severe morbidity.[3] Upfront surgical resection can result in a cure;[4] however, more than half of the pLGGs are not completely resected, and subsequent treatment with chemotherapy is commonly required.[5,6] Five-year progression-free survival for those requiring chemotherapy is 39%–53%.[7,8]

Mutations that cause up-regulation of the RAS/mitogen-activated protein kinase pathway have been implicated in most pLGGs, the most common being *KIAA1549-BRAF* fusion (*BRAF* fusion), followed by neurofibromatosis-1 (*NF1*) alterations and the *BRAF* V600E mutation.[9] Recently there has been a shift to determine the prognosis of pLGGs on a molecular basis,[6] and therapeutics are moving toward targeting the specific pLGG driver mutation.[10-12]

Neuroimaging with MR imaging is the mainstay for the initial diagnostic work-up and surgical planning for a definitive pathologic diagnosis.[13] There is an increasing desire to determine imaging surrogates for molecular subtypes for various pediatric CNS

Received February 9, 2022; accepted after revision May 24.

From the IWK Health Centre (A.T., C.E., C.C., K.M., D.M.-M.), Halifax, Nova Scotia, Canada; Dalhousie University Medical School (A.T.), Halifax, Nova Scotia, Canada; Departments of Pediatrics (C.E.), Pathology (K.M.), Diagnostic Radiology (D.M.-M.), and Faculty of Science (C.C.), Dalhousie University, Halifax, Nova Scotia, Canada; Division of Hematology, Oncology, and Bone Marrow Transplant (S.C.), Department of Pediatrics, University of British Columbia, Vancouver, British Columbia, Canada; University of Toronto Dalla Lana School of Public Health (R.M.), Toronto, Ontario, Canada; Department of Radiology (M.A.S.), British Columbia Children's Hospital and University of British Columbia, Vancouver, British Columbia, Canada; and Department of Diagnostic Imaging (D.M.-M.), IWK Health Centre, Halifax, Nova Scotia, Canada.

This work was funded through a foundation grant from the IWK Health Center.

Please address correspondence to Daddy Mata-Mbemba, MD, PhD, Department of Diagnostic Imaging, IWK Health Centre & Department of Diagnostic Radiology, Dalhousie University. 5850/5980 University Ave, PO Box 9700, Halifax, NS B3K 6R8; e-mail: Daddy.Mata-Mbemba@iwk.nshealth.ca; @matadaddy

Indicates article with online supplemental data.

http://dx.doi.org/10.3174/ajnr.A7574

tumors.[14-16] Currently, determination of the pLGG molecular subtype requires tissue acquisition and subsequent molecular testing, which might not be readily accessible in all centers. A molecular determination using imaging surrogates would be beneficial to guide appropriate therapy, including the aggressiveness of upfront surgical resection, selection of chemotherapy agents, the timeframe to initiating therapy, and to direct the sequence of multimodality therapy application.

To date, few studies have evaluated the correlation between MR imaging features and pLGG molecular subtypes. Ishi et al,[17] in 2021, investigated this correlation in individuals with optic pathway/hypothalamic pilocytic astrocytoma with a small sample size. Wagner et al,[18] in 2021, evaluated the same relationship using machine learning techniques, a promising radiologic tool that still needs full incorporation into the clinical routine. Our study aimed to assess MR imaging features of pLGGs associated with *BRAF* fusions, *BRAF* V600E mutations, and those negative for *BRAF* V600E and *BRAF* fusions (wild-type) in patients without *NF-1*, using an approach that simulates the routine clinical practice, including a radiologist's imaging review.

MATERIALS AND METHODS

This retrospective bi-institutional study was a collaboration between the British Columbia Children's Hospital (Vancouver, British Columbia, Canada) and the IWK Health Center (Halifax, Nova Scotia, Canada) tertiary care hospitals in Canada. There was institutional review board approval and a waiver of consent from both institutions. An interinstitutional data-transfer agreement was obtained for data-sharing.

Patients

Data were retrieved from the 2 tertiary pediatric hospitals from 2004 to 2021. Patients who had a pathologically confirmed diagnosis of *BRAF* fusion, *BRAF* V600E, or wild-type, were younger than 19 years of age at diagnosis, and who had a diagnostic MR imaging at presentation were eligible. *BRAF* fusion tumors in this study refer only to *KIAA1549-BRAF* fusions. Patients with pLGGs in the setting of *NF-1* were excluded, because these patients generally have distinguishing imaging features, a positive family history, and frequently do not undergo confirmatory tissue diagnosis.

Demographics and Clinical Details

Information collected included sex, age at diagnosis, disease progression, molecular subtype, World Health Organization (WHO) grade, tumor location, spine imaging at diagnosis, metastasis within the spine, and metastasis within the brain. Disease progression was determined through retrospective chart review of patients' MR imaging reports and clinical documentation.

Histopathology and Molecular Grouping

BRAF fusion status was determined using NanoString Technologies (https://nanostring.com/) or fluorescence in situ hybridization, while the *BRAF* V600E mutation was determined using immunohistochemistry and/or droplet digital polymerase chain reaction as previously described.[6,19] Molecular analysis was performed with formalin-fixed paraffin-embedded tissue obtained at the time of the operation.

MR Imaging

All patients from the IWK Health Center underwent brain MR imaging, some with spine MR imaging, at 1.5T from a single vendor (Signa HDxt; GE Healthcare). Patients from British Columbia Children's Hospital underwent brain MR imaging, some with spine MR imaging, at 1.5T or 3T (Magnetom Avanto, Magnetom Prisma; Siemens). As expected, MR imaging protocols for brain tumors have changed with time during the 17-year study period. However, the MR imaging protocols used in the 2 institutions include, at minimum, the following: 2D axial and/or coronal T2WI, 2D axial or coronal T2 FLAIR, 2D axial DWI, ADC, 2D axial or sagittal precontrast T1WI, and 2D axial gadolinium-based contrast agent–enhanced T1WI.

MR Imaging Review

Two neuroradiologists (D.M.-M. and M.A.S.), who were blinded to demographic, clinical, pathologic, and molecular data, independently reviewed imaging parameters on the initial diagnostic MR imaging. Before commencement, the 2 readers determined the definition of each imaging parameter through a consensus reading of 10 randomly selected cases that were not included in the study cohort, to refine and standardize the definition of parameters. These included the following: 1) tumor location, which was grouped as cerebral hemisphere, brainstem, optic pathway/hypothalamic glioma, posterior fossa (other than brainstem), or spinal cord; 2) tumor size, which was obtained as a product of perpendicular diameters of the tumor on axial T2 FLAIR; 3) the presence and extent of peritumoral vasogenic edema judged as none, mild, moderate, or massive; 4) the presence and magnitude of mass effect, judged as none, mild, moderate, or massive; 5) diffusion restriction subjectively judged as yes or no relative to normal brain while comparing the ADC with the $b = 1000$ s/mm^2 images; 6) the presence and degree of enhancement based on the tumor solid component, judged as none/minimal if less than one-third of the solid component enhances; moderate if the enhancement involves one-third to two-thirds of the solid component; or diffuse if more than two-thirds of the tumor enhances; 7) tumor signals on T1WI, T2WI, and FLAIR judged as hyper-, iso-, or hypointense; 8) cyst/cavitation change judged as present or not; 9) hemorrhage/calcification judged as present or not; 10) metastatic status judged as present or not; 11) hydrocephalus judged as present or not; and 12) tumor margins judged as infiltrative or well-defined. For MR spectroscopy, the following ratios were obtained from MR imaging–generated data: Cho/Cr, Cho/NAA, and lactate/Cr, which were judged as high, normal, or low. For any discordant readings between the 2 readers, an agreement was reached in a separate meeting through consensus.

MR Imaging Quantitative ADC Ratio Calculation

Quantitative ADC analysis was performed using a US Food and Drug Administration–approved commercial software package (AW Server 3.2; GE Healthcare). Blinded to clinical, pathologic, and molecular data, another author (C.C.) independently created nonoverlapping oval or circular ROIs within the solid portions of the tumor on all consecutive sections. The calcification/hemorrhagic foci or cystic/necrosis foci were excluded. In patients with supratentorial tumors, the ADCs of the normal-appearing

Table 1: Cohort information

Characteristic	Total, No. (%)
Sex	
Male	31 (44)
Female	39 (56)
Age at diagnosis (yr)	
Median (IQR)	6.3 (2.3–11.7)[a]
WHO grade	
Grade I	58 (85)
Grade II	10 (15)
Molecular subtype	
KIAA1549:BRAF fusion	30 (43)
V600E	19 (27)
Wild-type/other	21 (30)
Disease progression	
Yes	30 (43)
No	40 (57)
Tumor location	
Brainstem	4 (6)
Cerebral hemisphere	29 (41)
OPHG	14 (20)
Posterior fossa	21 (30)
Spinal cord	2 (3)
Brain imaging completed	
Yes	100
No	0
Spine imaging completed	
Yes	44 (63)
No	26 (37)
Metastasis present	
Yes, only brain	0 (0)
Yes, only spine	0 (0)
Yes, brain and spine	4 (6)
No	66 (94)

Note:—OPHG indicates optic pathway/hypothalamic glioma.
[a] Median/IQR.

contralateral brain were recorded, and in patients with tumors located in the posterior fossa, the ADC of the normal cerebellum was recorded. The ROI placement on the normal cerebellum was performed as remotely as possible from the tumor and with exclusion of vasogenic edema, when present, and adjacent CSF signal, if any. The mean tumor ADCs were calculated by averaging the ADCs obtained from all the ROIs. Tumor-to-normal brain ADC ratios (hereafter, ADC ratios) were calculated using the mean tumor ADCs.

Statistics and Analysis

All statistical analyses were performed using the software SPSS, Version 26 (IBM), and P values $< .05$ were considered statistically significant. Continuous variables were summarized using descriptive statistics, including number, median, interquartile range (IQR), SD, and range, while categoric variables were summarized using number and percentage. A κ statistic was generated from the 2 readers' data, and values <0.20 were interpreted as poor, 0.21–0.40 as fair, 0.41–0.60 as moderate, 0.61–0.80 as substantial, and 0.81–1.00 as excellent agreements. First, we used bivariate analyses, including the Fisher exact test for categoric variables or ANOVA for continuous variables, to compare the 3 molecular groups of pLGGs (*BRAF* fusion, *BRAF* V600E, or wild-type). This procedure was followed by pair-wise comparison of the Dwass-Steel-Critchlow-Fligner method to compare 2 of the 3 molecular groups head-to-head, which provided the comparison of *BRAF* fusion and *BRAF* V600E.

RESULTS

Patients

Seventy patients (31 males and 39 females) were included in this study. The median age at diagnosis was 6.3 years (IQR, 2.3–11.7 years). Thirty patients (43%) had tumors with *BRAF* fusion, 19 (27%) with the *BRAF* V600E mutation, and 21 (30%) with wild-type (negative for *BRAF* V600E/*BRAF* fusion). A summary of patient demographic and clinical information is shown in Table 1. There was no statistically significant difference in the age of patients, sex, tumor location, or tumor mutation status when comparing the patients from the 2 different institutions (Online Supplemental Data).

Clinical and Histopathologic Characteristics

A summary of clinical and histopathologic characteristics of patients is shown in Table 2.

Patients with *BRAF* fusion were younger (median, 3.3 years) at diagnosis compared with the 2 other groups (*BRAF* V600E [9.7 years] and wild-type [10.5 years], $P = .0012$). Compared with the *BRAF* fusion and wild-type, there was a trend for *BRAF* V600E to show an increased frequency of WHO grade II histology ($P = .07$ and $P = .09$ for 2-group and 3-group comparisons, respectively). There was no statistically significant difference among the 3 groups with respect to metastatic status at diagnosis or tumor progression.

Interreader Agreement

Overall κ agreement among the readers for radiologic variables was substantial ($\kappa = 0.75$; 95% CI, 71.5–99.2).

MR Imaging Features

A summary of the imaging characteristics by molecular subtype can be found in the Online Supplemental Data.

Tumor location was strongly associated with molecular subtype because those with *BRAF* fusion tumors were more likely to be found in the posterior fossa (excluding the brainstem), while *BRAF* V600E tumors were more commonly found in a cerebral hemisphere ($P = < .0001$). *BRAF* fusion tumors compared with *BRAF* V600E and wild-type were larger ($P = .0022$) and demonstrated an increased frequency of moderate-to-massive mass effect ($P = .0053$) and hydrocephalus ($P = .0002$); these differences remained statistically significant when directly comparing *BRAF* fusion and *BRAF* V600E (all, $P = < .05$) (Fig 1). *BRAF* fusion tumors also showed an increased frequency of diffuse enhancement compared with *BRAF* V600E and wild-type tumors ($P = < .0001$) and when directly compared with *BRAF* V600E ($P = .0036$).

Tumors with *BRAF* V600E were more infiltrative compared with *BRAF* fusion and wild-type tumors ($P = .0002$) and when directly compared with *BRAF* fusion ($P = .0001$). *BRAF* V600E tumors were more likely to be isointense on T1WI compared with *BRAF* fusion and wild-type ($P = .0023$) and when directly compared with *BRAF* fusion ($P = .008$).

Diffusion restriction was uncommon in our cohort. However, when it occurred, only *BRAF* V600E tumors demonstrated diffusion

Table 2: Univariate analysis of demographics and clinical characteristics by molecular group

Variables	*KIAA1549:BRAF* Fusion No. (%)	*BRAF* V600E No. (%)	Wild-Type/Other No. (%)	P_1 (Fusion vs V600E vs WT)	P_2 (Fusion vs V600E)
Sex				.3583	.4436
Male	16 (53)	8 (42)	7 (33)		
Female	14 (47)	11 (58)	14 (67)		
Age at time of MR imaging (yr)				.0012	.0126
Median	3.3 (1.56–5.10)[a]	9.7 (5.08–14.25)[a]	10.5 (6.42–14.58)[a]		
Progression of disease				.5769	.3669
Yes	15 (50)	12 (63)	13 (62)		
No	15 (50)	7 (37)	8 (38)		
WHO grade				.0902	.0724
Grade I	27 (90)	13 (68)	18 (95)		
Grade II	3 (10)	6 (32)	1 (5)		
Tumor location				<.0001	<.0001
Brainstem	2 (7)	1 (5)	1 (5)		
Cerebral hemisphere	3 (10)	13 (68)	13 (62)		
OPHG	7 (23)	4 (21)	3 (14)		
Posterior fossa	17 (57)	0 (0)	4 (19)		
Spinal cord	1 (3)	1 (5)	0 (0)		
Metastatic status				.8107	1.0000
Yes	1 (3)	1 (5)	2 (10)		
No	29 (97)	18 (95)	19 (90)		

Note:—WT indicates wild-type; OPHG, optic pathway/hypothalamic glioma.
[a] Median and 95% confidence interval.

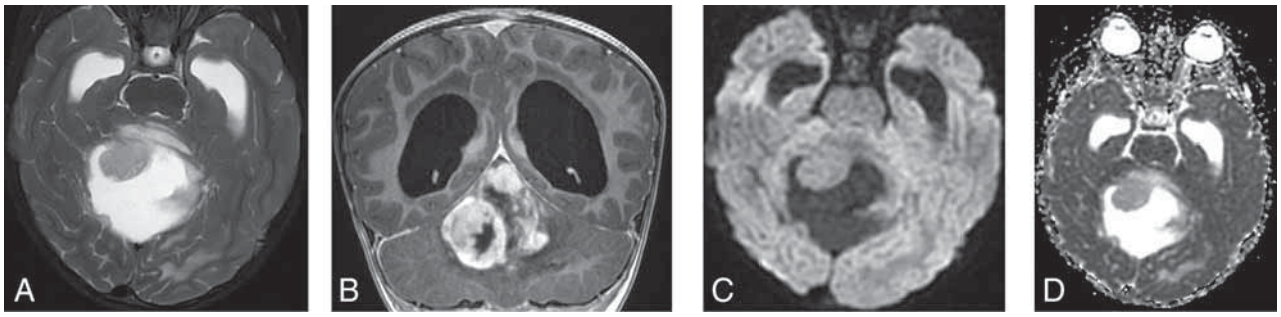

FIG 1. A 3-year-old girl who presented with symptoms related to increased intracranial pressure. The brain MR imaging shows a large complex cystic/solid mass lesion arising from the vermis and anteriorly compressing the fourth ventricle, therefore causing supratentorial massive hydrocephalus. The solid component of the tumor shows slight hyperintense signal on T2WI (*A*) and diffuse enhancement (*B*) but not with diffusion restriction (*C* and *D*). The tissue diagnosis was pilocytic astrocytoma with *KIAA1549:BRAF* fusion.

restriction. Qualitative assessment demonstrated diffusion restriction in 4 of 19 *BRAF* V600E tumors ($P = .0042$) (Fig 2). On quantitative assessment, *BRAF* V600E showed a lower ADC ratio compared with *BRAF* fusion and wild-type ($P = .003$), and this difference was more statistically significant when compared directly with *BRAF* fusion ($P = .0003$).

Only a subset of patients underwent MR imaging spectroscopy ($n = 21$; 30% [11 *BRAF* fusion, 7 *BRAF* V600E, and 3 wild-type]). While spectroscopy was not in any way discriminating across molecular subtypes ($P > .05$, all), most tumors had high Cho/Cr ($n = 19$; 90%), high Cho/NAA ($n = 19$; 90%), and elevated lactate ($n = 19$; 90%) (Online Supplemental Data).

DISCUSSION

In this bi-institutional study, we evaluated the relationship between MR imaging characteristics and pLGG molecular groups to distinguish among *BRAF* fusion, *BRAF* V600E, and wild-type tumors. Our results show features that enable some pretherapeutic prediction of pLGG molecular subtypes. In our series, *BRAF* V600E tumors were more infiltrative, were the only ones to show diffusion restriction with a low ADC ratio, and were likely to be located within the cerebral hemispheres, whereas *BRAF* fusion tumors were more well-defined, larger with significant mass effect including hydrocephalus, and more likely to demonstrate diffuse enhancement.

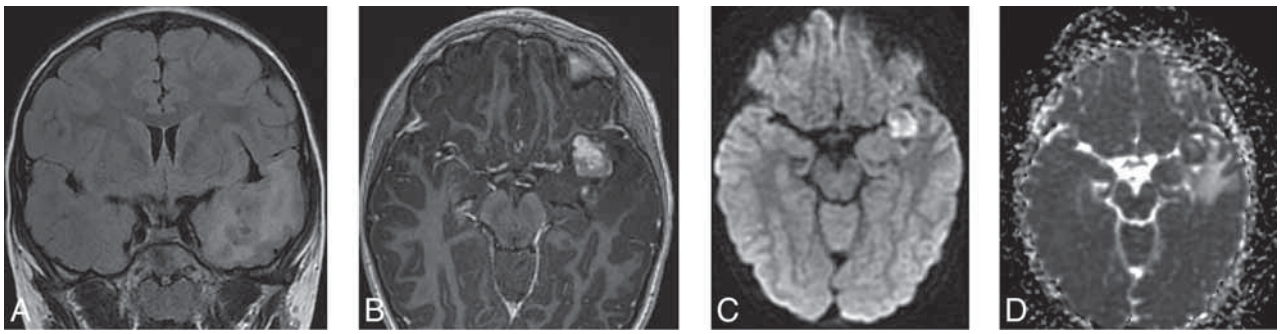

FIG 2. A 9-year-old boy with seizures. The brain MR imaging shows an ill-defined mass lesion with tiny internal cystic changes on T2 FLAIR (*A*) involving the mesial aspect of the left temporal lobe. The lesion shows moderate surrounding edema, mild mass effect against surrounding structures, as well as moderate enhancement (*B*). On DWI (*C*) and ADC (*D*), the mass shows diffusion restriction. The final tissue diagnosis was ganglioglioma with a *BRAF* V600E mutation.

Our study is the first to report the association of *BRAF* V600E and diffusion restriction, both qualitatively and quantitatively, findings suggestive of higher tumor cellularity and tumor aggressiveness.[20] *BRAF* V600E tumors were more infiltrative compared with *BRAF* fusion tumors. Ho et al,[21] in 2015, had comparable results, citing *BRAF* V600E tumors as having a low T2 signal and infiltrative margins, but in their study, diffusion restriction was not assessed. Ishi et al[17] found a lower T2WI signal and larger T2WI/contrast-enhanced FLAIR mismatch to be indicative of *BRAF* V600E mutation for optic pathway gliomas. However, signal mismatches were not assessed in our series. In contrast to previous studies that have found *BRAF* V600E tumors showing higher rates of tumor invasiveness and recurrence,[6,21-23] our study found a trend for *BRAF* V600E tumors to be classified as WHO grade II tumors but with no statistically significant difference in tumor progression compared with *BRAF* fusion tumors. This finding could be partially due to the retrospective nature of the study, in which tumors that progressed were more likely to have had molecular testing, leading to a potential over-representation of progression in these cohorts. This could also be due to the limited sample size in this study. Otherwise, our other key clinical results showing younger age and predilection of posterior fossa location for patients with *BRAF* fusion tumors corroborate the findings in the literature.[18,24]

BRAF fusion tumors, in our study, were associated with larger size and greater mass effect including hydrocephalus, yet were well-defined. The lack of diffusion restriction in *BRAF* fusion tumors supports a less aggressive biology. Our observation is supported by the findings of Hawkins et al,[25] in 2011, and Reitman et al,[26] in 2019, who postulated that *BRAF* fusion is associated with less aggressive tumor behavior, possibly because of the eventual predilection to undergo tumor senescence. Our observations suggest that one of the main reasons patients with *BRAF* fusion tumors come to medical attention is due to mass effect and the resultant hydrocephalus as opposed to the more infiltrative pattern noted in *BRAF* V600E tumors. The diffuse enhancement noted in *BRAF* fusion tumors may be related to angiogenesis, as opposed to higher cellularity.[27] In the current era, in which machine learning is increasing in the research setting, there has been a shift toward the use of genomics to assess the relationship between brain tumors and molecular subgroups, including pLGG.[6]

The main strength of our study is that we used a clinical model, simulating routine clinical practice, to assess both clinical and diagnostic imaging characteristics of pLGGs associated with molecular subtype using a relatively large number of patients and including all histologic types of pLGGs. Therefore, we believe that our findings may be used on a case-to-case basis during routine clinical practice, potentially impacting patient care. Recently, Wagner et al,[18] in 2021, used radiomic software for ROIs to determine the predictive factors of *BRAF* status in pLGGs of 115 pediatric patients via machine learning, followed by the development of a model to predict the mutational status of the tumor. However, they did not include wild-type tumors in their study, which constitute about one-third of patients with pLGGs,[9] and they solely used FLAIR sequences. To that end, our study seems more robust because it includes DWI/ADC, FLAIR, and gadolinium-based contrast agent–enhanced T1WI, which, altogether, constitute MR imaging sequences that allow evaluating the aggressiveness of brain tumors. Therefore, our results could be used in the routine clinical setting to support patient management.

Our study did not show the utility of MR spectroscopy in differentiating pLGG molecular subtypes from one another; however, only 30% of the cohort underwent spectroscopy, and larger studies are needed. In this study, no other advanced MR images were consistently used because some of our data were obtained before implementation of these techniques was more common in the clinical setting.

There are several limitations in this study. Given that it was retrospective and combined data from 2 centers, the imaging lacked homogeneity due to different scanners, MR field strengths, and techniques used. We cannot comment on the metastatic potential because of the low frequency of metastases. The sample size was also not large enough to be considered representative of the greater population. Further studies that incorporate clinical assessment of imaging features and MR machine learning approaches should be conducted.

CONCLUSIONS

This study simulates routine clinical practice in the assessment of clinical and diagnostic imaging characteristics of pLGG subtypes, *BRAF* fusion, *BRAF* V600E, and wild-type. We determined particular tumor features of *BRAF* fusion, such as younger age, posterior

fossa location, well-defined margins, larger size with a surrounding mass effect, and hydrocephalus. *BRAF* V600E tumors were found more commonly in the cerebral hemispheres, had a lower ADC ratio, and were more likely to be infiltrative. Our study offers a baseline for radiologic determination of pLGG molecular subtypes in the clinical setting, with high interreader agreement, which may aid future pLGG molecular subtype identification and therapeutic management strategies.

ACKNOWLEDGMENTS

The authors would like to thank John Bryden for his work in the diagnostic imaging department to de-identify subject imaging.

Disclosure forms provided by the authors are available with the full text and PDF of this article at www.ajnr.org.

REFERENCES

1. Ostrom QT, Gittleman H, Truitt G, et al. **CBTRUS statistical report: primary brain and other central nervous system tumors diagnosed in the United States in 2011-2015.** *Neuro Oncol* 2018;20:iv1–86 CrossRef Medline
2. Krishnatry R, Zhukova N, Guerreiro Stucklin AS, et al. **Clinical and treatment factors determining long-term outcomes for adult survivors of childhood low-grade glioma: a population-based study.** *Cancer* 2016;122:1261–69 CrossRef Medline
3. Armstrong GT, Conklin HM, Huang S, et al. **Survival and long-term health and cognitive outcomes after low-grade glioma.** *Neuro Oncol* 2011;13:223–34 CrossRef Medline
4. Stokland T, Liu J, Ironside JW, et al. **A multivariate analysis of factors determining tumor progression in childhood low-grade glioma: a population-based cohort study (CCLG CNS9702).** *Neuro Oncol* 2010;12:1257–68 CrossRef Medline
5. Bergthold G, Bandopadhayay P, Bi WL, et al. **Pediatric low-grade gliomas: how modern biology reshapes the clinical field.** *Biochim Biophys Acta* 2014;1845:294–307 CrossRef Medline
6. Ryall S, Zapotocky M, Fukuoka K, et al. **Integrated molecular and clinical analysis of 1,000 pediatric low-grade gliomas.** *Cancer Cell* 2020;37:569–83.e5 CrossRef Medline
7. Lassaletta A, Scheinemann K, Zelcer SM, et al. **Phase II weekly vinblastine for chemotherapy-naïve children with progressive low-grade glioma: a Canadian pediatric brain tumor consortium study.** *J Clin Oncol* 2016;34:3537–43 CrossRef Medline
8. Ater JL, Zhou T, Holmes E, et al. **Randomized study of two chemotherapy regimens for treatment of low-grade glioma in young children: a report from the children's oncology group.** *J Clin Oncol* 2012;30:2641–47 CrossRef Medline
9. Ryall S, Tabori U, Hawkins C. **Pediatric low-grade glioma in the era of molecular diagnostics.** *Acta Neuropathol Commun* 2020;8:30 CrossRef Medline
10. Fangusaro J, Onar-Thomas A, Poussaint TY, et al. **Selumetinib in paediatric patients with BRAF-aberrant or neurofibromatosis type 1-associated recurrent, refractory, or progressive low-grade glioma: a multicentre, phase 2 trial.** *Lancet Oncol* 2019;20:1011–22 CrossRef Medline
11. Hargrave DR, Bouffet E, Tabori U, et al. **Efficacy and safety of dabrafenib in pediatric patients with BRAF V600 mutation–positive relapsed or refractory low-grade glioma: results from a phase I/IIa study.** *Clin Cancer Res* 2019;25:7303–11 CrossRef Medline
12. Nobre L, Zapotocky M, Ramaswamy V, et al. **Outcomes of BRAF V600E pediatric gliomas treated with targeted *BRAF* inhibition.** *JCO Precis Oncol* 2020561–71 CrossRef Medline
13. Sievert AJ, Fisher MJ. **Pediatric low-grade gliomas.** *J Child Neurol* 2009;24:1397–1408 CrossRef Medline
14. Mata-Mbemba D, Zapotocky M, Laughlin S, et al. **MRI characteristics of primary tumors and metastatic lesions in molecular subgroups of pediatric medulloblastoma: asingle-center study.** *AJNR Am J Neuroradiol* 2018;39:949–55 CrossRef Medline
15. Patay Z, DeSain LA, Hwang SN, et al. **MR imaging characteristics of wingless-type-subgroup pediatric medulloblastoma.** *AJNR Am J Neuroradiol* 2015;36:2386–93 CrossRef Medline
16. Perreault S, Ramaswamy V, Achrol AS, et al. **MRI surrogates for molecular subgroups of medulloblastoma.** *AJNR Am J Neuroradiol* 2014;35:1263–69 CrossRef Medline
17. Ishi Y, Yamaguchi S, Yoshida M, et al. **Correlation between magnetic resonance imaging characteristics and BRAF alteration status in individuals with optic pathway/hypothalamic pilocytic astrocytomas.** *J Neuroradiol* 2021;48:266–70 CrossRef Medline
18. Wagner MW, Hainc N, Khalvati F, et al. **Radiomics of pediatric low-grade gliomas: Toward a pretherapeutic differentiation of *BRAF*-mutated and *BRAF* -fused tumors.***AJNR Am J Neuroradiol Neuroradiol* 2021;42:759–65 CrossRef Medline
19. Mistry M, Ryall S, Lassaletta A, et al. **Lg-19 immunohistochemistry is highly sensitive and specific for the detection of BRAF v600e status in pediatric low-grade glioma.** *Neuro Oncol* 2016;18:iii82.3–iii82 CrossRef
20. Kan P, Liu JK, Hedlund G, et al. **The role of diffusion-weighted magnetic resonance imaging in pediatric brain tumors.** *Childs Nerv Syst* 2006;22:1435–39 CrossRef Medline
21. Ho C, Mobley BC, Gordish-Dressman H, et al. **A clinicopathologic study of diencephalic pediatric low-grade gliomas with BRAF V600 mutation.** *Acta Neuropathol* 2015;130:575–85 CrossRef Medline
22. Lassaletta A, Zapotocky M, Mistry M, et al. **Therapeutic and prognostic implications of BRAF V600E in pediatric low-grade gliomas.** *J Clin Oncol* 2017;35:2934–41 CrossRef Medline
23. Horbinski C, Nikiforova MN, Hagenkord JM, et al. **Interplay among BRAF, p16, p53, and MIB1 in pediatric low-grade gliomas.** *Neuro Oncol* 2012;14:777–89 CrossRef Medline
24. Behling F, Schittenhelm J. **Oncogenic BRAF alterations and their role in brain tumors.** *Cancers* 2019;11:794 CrossRef Medline
25. Hawkins C, Walker E, Mohamed N, et al. **BRAF-KIAA1549 fusion predicts better clinical outcome in pediatric low-grade astrocytoma.** *Clin Cancer Res* 2011;17:4790–98 CrossRef Medline
26. Reitman ZJ, Paolella BR, Bergthold G, et al. **Mitogenic and progenitor gene programmes in single pilocytic astrocytoma cells.** *Nat Commun* 2019;10:1–17 CrossRef Medline
27. Bartels U, Hawkins C, Jing M, et al. **Vascularity and angiogenesis as predictors of growth in optic pathway/hypothalamic gliomas.** *J Neurosurg* 2006;104:314–20 CrossRef Medline

MR Imaging Detection of CNS Lesions in Tuberous Sclerosis Complex: The Usefulness of T1WI with Chemical Shift Selective Images

H. Fujii, N. Sato, Y. Kimura, M. Mizutani, M. Kusama, N. Sumitomo, E. Chiba, Y. Shigemoto, M. Takao, Y. Takayama, M. Iwasaki, E. Nakagawa, and H. Mori

ABSTRACT

BACKGROUND AND PURPOSE: CNS lesions of tuberous sclerosis complex are diagnosed mainly by T2WI, FLAIR, and sometimes T1WI with magnetization transfer contrast. The usefulness of T1WI with chemical shift selective images was recently reported in focal cortical dysplasia type IIb, which has histopathologic and imaging features similar to those of tuberous sclerosis complex. We investigated the usefulness of the T1WI with chemical shift selective images in detecting CNS lesions of tuberous sclerosis complex.

MATERIALS AND METHODS: We retrospectively reviewed 25 consecutive patients with tuberous sclerosis complex (mean age, 11.9 [SD, 8.9] years; 14 males) who underwent MR imaging including T1WI, T1WI with magnetization transfer contrast, T1WI with chemical shift selective, T2WI, and FLAIR images. Two neuroradiologists assessed the number of CNS lesions in each sequence and compared them in 2 steps: among T1WI, T1WI with magnetization transfer contrast and T1WI with chemical shift selective images, and among T2WI, FLAIR, and T1WI with chemical shift selective images. We calculated the contrast ratio of the cortical tubers and of adjacent normal-appearing gray matter and the contrast ratio of radial migration lines and adjacent normal-appearing white matter in each sequence and compared them.

RESULTS: T1WI with chemical shift selective images was significantly superior to T1WI with magnetization transfer contrast for the detection of radial migration lines and contrast ratio of radial migration lines. There was no significant difference between T1WI with chemical shift selective images and T1WI with magnetization transfer contrast for the detection of cortical tubers and the contrast ratio of the cortical tubers. Both T2WI and FLAIR were statistically superior to T1WI with chemical shift selective images for the detection of cortical tubers. T1WI with chemical shift selective images was significantly superior to T2WI and FLAIR for the detection of radial migration lines.

CONCLUSIONS: The usefulness of T1WI with chemical shift selective images in detecting radial migration lines was demonstrated. Our findings suggest that the combination of T1WI with chemical shift selective images, T2WI, and FLAIR would be useful to evaluate the CNS lesions of patients with tuberous sclerosis complex in daily clinical practice.

ABBREVIATIONS: CR = contrast ratio; FCD = focal cortical dysplasia; ICC = intraclass correlation coefficient; NAGM = normal-appearing gray matter; NAWM = normal-appearing white matter; RML = radial migration line; SEN = subependymal nodule; T1WI-CHESS = T1WI with chemical shift selective; T1WI-MTC = T1WI with magnetization transfer contrast; TSC = tuberous sclerosis complex

Tuberous sclerosis complex (TSC) is an autosomal dominant multisystem disorder characterized by hamartomas in multiple organ systems, including the brain, skin, heart, kidneys, and lungs. TSC is caused by mutations in the tumor-suppressor gene *TSC1* or *TSC2*, encoding hamartin and tuberin, respectively.[1,2] The TSC1-TSC2 (hamartin-tuberin) complex is a critical regulator of the mammalian target of the rapamycin signaling cascade, which serves as a ubiquitous regulator of cell metabolism, growth, proliferation, and survival.[3-5] Brain manifestations of TSC are characterized by cortical tubers, WM abnormalities (radial

Received March 2, 2022; accepted after revision May 24.

From the Departments of Radiology (H.F., N.Sato, Y.K., M.K., E.C., Y.S.), Pathology and Laboratory Medicine (M.M., M.T.), Child Neurology (N.Sumitomo, E.N.), and Neurosurgery (Y.T., M.I.), National Center Hospital, National Center of Neurology and Psychiatry, Kodaira, Tokyo, Japan; and Department of Radiology (H.F., H.M.), Jichi Medical University, School of Medicine, Shimotsuke, Tochigi, Japan.

This work was supported by The Tokumori Yasumoto Memorial Trust for Research on TSC and Related Rare Neurological Diseases (H.F.) and by an intramural fund of the National Center of Neurology and Psychiatry (3-8) and the Japan Agency for Medical Research and Development (JP21wm0425019) (M.T.).

Please address correspondence to Noriko Sato, MD, PhD, Department of Radiology, National Center Hospital, National Center of Neurology and Psychiatry, 4-1-1 Ogawa-Higashi, Kodaira, Tokyo 187-0031, Japan; e-mail: snoriko@ncnp.go.jp

Indicates open access to non-subscribers at www.ajnr.org

Indicates article with online supplemental data.

http://dx.doi.org/10.3174/ajnr.A7573

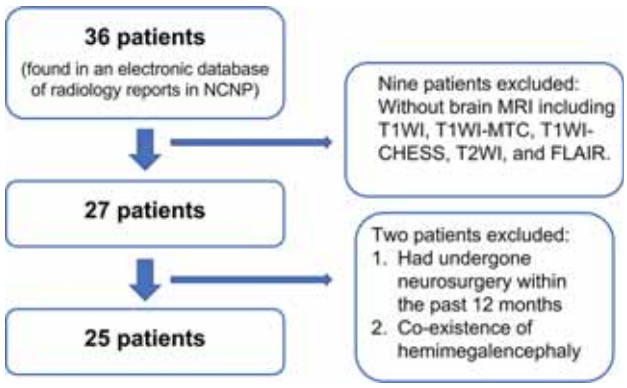

FIG 1. Study flow chart. NCNP indicates National Center of Neurology and Psychiatry.

migration lines [RMLs]), and periventricular subependymal nodules (SENs).[6-8] On MR imaging, cortical tubers and RMLs are diagnosed mainly by T2WI or FLAIR images.[9] The effectiveness of T1WI with magnetization transfer contrast (T1WI-MTC) imaging has been reported,[10-13] but the usefulness of other MR images has not been reported since then.

Today, somatic mutations in the mammalian target of rapamycin pathway genes are well-known as a common cause of focal cortical dysplasia (FCD).[14] Pathologically, balloon cells that have an enlarged cell body with eosinophilic cytoplasm are a pathognomonic cellular feature of FCD type IIb and TSC. On the basis of the morphologic and genetic similarities between FCD type IIb and cortical tubers in TSC, it has been hypothesized that FCD is a forme fruste of TSC.[15-17]

Earlier research demonstrated that a T1WI high-signal area of the WM lesions of FCD type IIb was correlated with the cellularity of balloon cells, independent of calcifications.[18] Another case report also observed that T1WI with chemical shift selective (T1WI-CHESS) imaging, which is the most frequently used technique for the fat-suppression pulse, could clearly visualize the T1WI high-signal area in FCD type IIb because of its background signal suppression due to the magnetization transfer effect and the fat suppression of normal WM, which contains fat-rich myelin.[19] Moreover, the superiority of T1WI-CHESS compared with T1WI-MTC was reported for neuromelanin imaging.[20]

With this background, we hypothesized that T1WI-CHESS can visualize RMLs more clearly than conventional MR images, including T1WI-MTC. We, thus, conducted the present study to investigate the usefulness of T1WI-CHESS in CNS lesions of patients with TSC.

MATERIALS AND METHODS

Patients

This retrospective study was approved by the institutional review board of Japan's National Center of Neurology and Psychiatry, and the need for patient informed consent was waived. We retrospectively analyzed the cases of 36 consecutive patients diagnosed with TSC who underwent brain MR imaging between July 2018 and June 2021 at the National Center of Neurology and Psychiatry. The diagnosis of TSC was made according to the updated diagnostic criteria issued by the 2012 International Tuberous Sclerosis Complex Consensus Conference.[21] Among the 36 patients, 27 underwent brain MR imaging including T1WI, T1WI-MTC, T1WI-CHESS, T2WI, and FLAIR, and these images were obtained for the imaging evaluation. The patient exclusion criteria were as follows: 1) the patient having undergone neurosurgery within the prior 12 months, 2) the coexistence of other intracranial diseases, and 3) the presence of severe motion or metal artifacts.[22] As a result, 2 patients were excluded from this study according to criteria 1 and 2, respectively (Fig 1). The cases of the remaining 25 patients were analyzed. In addition to the 25 patients with TSC, we examined the pathologic correlation with T1WI-CHESS in 1 patient whose preoperative MR imaging study did not have T1WI-MTC.

MR Imaging Procedures

All patients underwent MR imaging in a 3T MR imaging scanner (Magnetom Verio; Siemens) with a 32-channel head coil, including axial T1WI, T1WI-MTC, T1WI-CHESS, T2WI, and 3D-FLAIR imaging. The T1WI, T1WI-MTC, and T1WI-CHESS images were acquired with the following parameters: TR/TE/NEX = 620 ms/9.5 ms/3, matrix = 184 × 256, FOV = 210 × 167.3 mm, section thickness = 3 mm with 1.2-mm intersection gaps. Turbo spin-echo T2WI was performed with the following parameters: TR/TE/NEX = 5000 ms/81 ms/2, matrix = 348 × 512, FOV = 220 × 199.4 mm, section thickness = 3 mm. 3D-FLAIR images were acquired with the following parameters: TR/TE/NEX = 5000 ms/413 ms/1, matrix = 246 × 256, FOV = 250 × 250 mm, section thickness = 1 mm.

Definition of CNS Lesions

The definitions of cortical tubers, RMLs, and SENs were based on previous studies.[12,22] Cortical tubers were defined as gyral expansion or distortion and/or signal abnormalities in the subcortical WM. RMLs were defined as linear abnormalities oriented from the cortical surface to the ventricular wall or as the presence of focal nodular lesions in this pathway. SENs were defined as lesions that originated from the lateral ventricle walls and penetrated the ventricles. In this study, we did not differentiate the SENs from subependymal giant cell tumors because doing so was outside the scope of the study.

Visual Assessment

Two neuroradiologists (H.F. and Y.K., with 11 and 15 years of experience in neuroradiology, respectively) independently evaluated all images to assess the number of cortical tubers, RMLs, and SENs on T1WI, T1WI-MTC, T1WI-CHESS, T2WI, and FLAIR images. Differences in their evaluations were resolved by consensus. We compared the detectability of the cortical tubers, RMLs, and SENs in the following 2 steps: First, we compared it among the T1WI, T1WI-MTC, and T1WI-CHESS images to assess the detection ability of T1WI-CHESS (hereafter referred to as step 1). Next, we compared it among T2WI, FLAIR, and T1WI-CHESS images to assess the clinical usefulness of T1WI-CHESS as a routine sequence in daily clinical practice (hereafter referred to as step 2). We also calculated the interobserver reproducibility.

Semiquantitative Analysis

We determined the contrast ratio of the cortical tubers and adjacent normal-appearing gray matter (NAGM) on T1WI, T1WI-MTC, and T1WI-CHESS and compared the ratios among them. We measured the most evident cortical tuber in each patient as

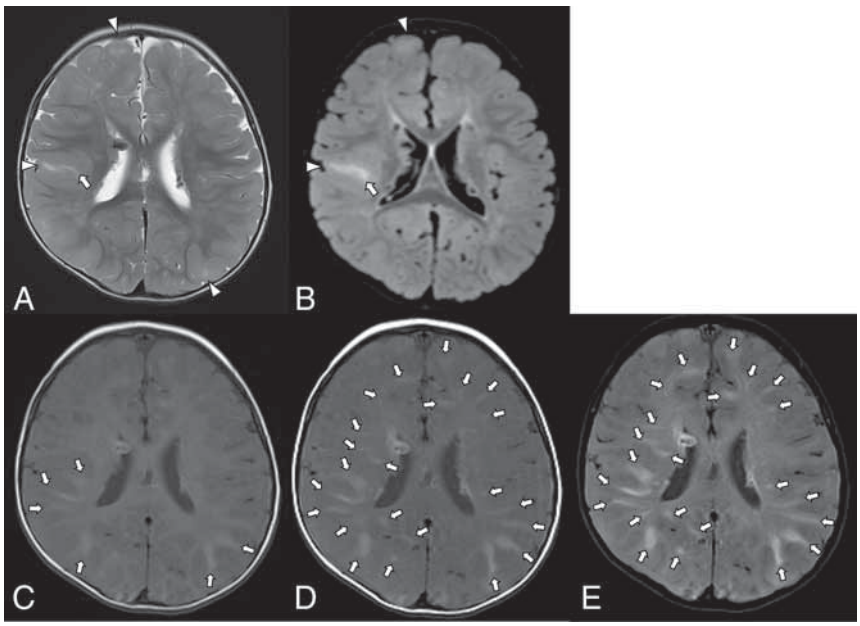

FIG 2. Patient 19. A 26-month-old boy. Axial T2WI (*A*), FLAIR (*B*), T1WI (*C*), T1WI-MTC (*D*), and T1WI-CHESS (*E*). T2WI and FLAIR images demonstrate swelling of the cortex and subcortical hyperintensity, plus a linear hyperintensity extending to the ventricle, representing cortical tubers and RMLs, respectively (*A* and *B*, *arrowheads* and *arrows*, respectively). On T1WI, several RMLs can be seen as hyperintensity (*C*, *arrows*). The RMLs are more apparent on T1WI-MTC and especially on T1WI-CHESS (*D* and *E*, *arrows*).

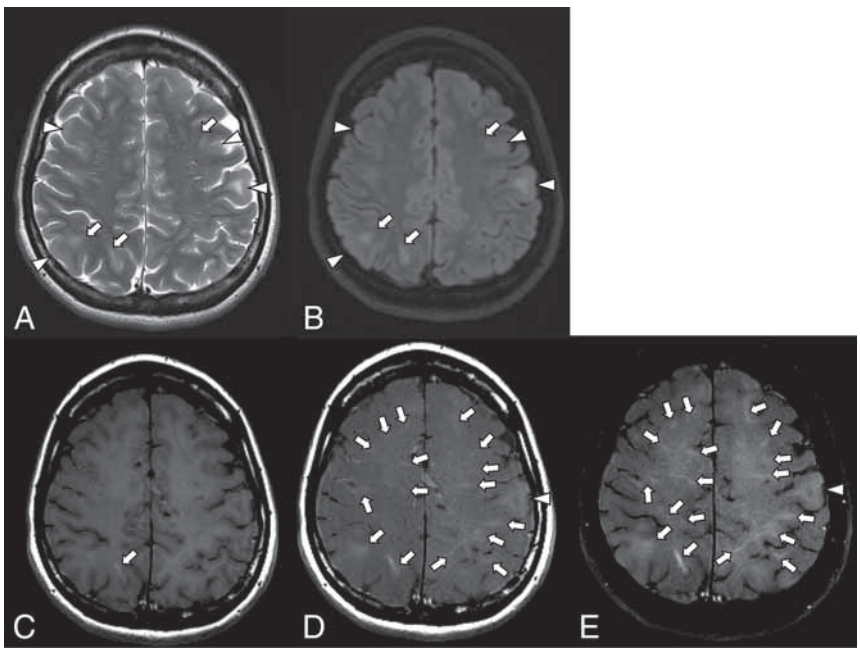

FIG 3. Patient 4. A 29-year-old woman. Axial T2WI (*A*), FLAIR (*B*), T1WI (*C*), T1WI-MTC (*D*), and T1WI-CHESS (*E*). T2WI and FLAIR images demonstrate swollen cortices, some of which are accompanied by subcortical hyperintensities, representing cortical tubers (*A* and *B*, *arrowheads*). Linear hyperintensities in the subcortical area extending to the ventricle are observed, representing the RMLs (*A* and *B*, *arrows*). On T1WI, an RML is found in the right parietal lobe (*C*, *arrow*). T1WI-TMC and T1WI-CHESS are able to detect more RMLs than T1WI, T2WI, and FLAIR (*D* and *E*, *arrows*). The RMLs are more apparent on T1WI-CHESS than on T1WI-MTC (*D* and *E*, *arrows*). Although no obvious cortical tuber is shown by T1WI, both T1WI-MTC and T1WI-CHESS detect a cortical tuber as a slight hyperintensity (*D* and *E*, *arrowheads*).

determined by the 2 evaluators. The signal intensities of the cortical tubers and adjacent NAGM were calculated using the ImageJ software program (National Institutes of Health). In each of the T1WI, T1WI-MTC, and T1WI-CHESS images, both evaluators measured the signal intensity of the cortical tuber using 7-mm^2 round cursors.[20] The signal intensity of the adjacent NAGM was measured in the same way, using 13-mm^2 round cursors.[20]

The contrast ratios (CRs) of the cortical tubers and the NAGM were calculated as $CR_{tuber} = (S_{tuber}/S_{NAGM})$, where S_{tuber} and S_{NAGM} denote the signal intensities of the cortical tubers and NAGM, respectively. In the same way, we evaluated the CRs of the RML and adjacent normal-appearing white matter (NAWM) on T1WI, T1WI-MTC, and T1WI-CHESS and compared the ratios among them. The CRs of the RML and the NAWM were calculated as $CR_{RML} = (S_{RML}/S_{NAWM})$, where S_{RML} and S_{NAWM} denote the signal intensities of the RML and NAWM, respectively. The 2 evaluators' values were averaged. We calculated the interobserver reproducibility of each evaluator's value.

Clinical Information

The patients' medical records were reviewed, and seizure frequency and intellectual disability were evaluated by a board-certified pediatric neurologist (N. Sumitomo). Seizure frequency was evaluated on a 5-point scale: 1 = seizure-free >1 year, 2 = yearly seizures, 3 = monthly seizures, 4 = weekly seizures, 5 = daily seizures.[23] Intellectual disability was categorized as 0–4 scores (0 = normal, 1 = mild disability, 2 = moderate disability, 3 = severe disability, 4 = profound disability).[24] We examined the correlation between seizure frequency and the number of CNS lesions and between the severity of intellectual disability and the number of CNS lesions.

Correlations between MR Imaging Findings and Pathologic Findings

The correlation between MR imaging findings and pathologic findings was examined, focusing on the cause of hyperintensity on T1WI-CHESS. Two patients had undergone an operation

Table 1: The number of CNS lesions in each sequence[a]

	T2WI	FLAIR	T1WI	T1WI-MTC	T1WI-CHESS
Cortical tuber	17.1 (SD, 10.8)	17.5 (SD, 10.8)	1.1 (SD, 2.3)	10.2 (SD, 6.7)	12.2 (SD, 7.7)
RML	3.56 (SD, 2.3)	10.5 (SD, 8.1)	1.4 (SD, 3.9)	20.4 (SD, 12.1)	24.8 (SD, 15.4)
Subependymal nodule	6.2 (SD, 4.3)	4.5 (SD, 3.0)	5.1 (SD, 3.2)	6.4 (SD, 3.7)	7.2 (SD, 3.9)

[a] Data are mean (SD).

Table 2: Interobserver reproducibility of the number of CNS lesions in each sequence

	T2WI	FLAIR	T1WI	T1WI-MTC	T1WI-CHESS
Cortical tuber	0.959	0.903	0.984	0.786	0.768
RML	0.648	0.866	0.887	0.883	0.799
Subependymal nodule	0.826	0.618	0.822	0.947	0.899

Table 3: Comparison of the detection of CNS lesions among T1WI, T1WI-MTC, and T1WI-CHESS

	Multiple Comparison (*P* Value)		
	T1WI vs. T1WI-MTC	T1WI vs. T1WI-CHESS	T1WI-MTC vs. T1WI-CHESS
Cortical tuber	<.001[a]	<.001[a]	.198
RML	.001[a]	<.001[a]	.022[a]
Subependymal nodule	.007[a]	<.001[a]	.35

[a] $P < .05$.

Table 4: Comparison of the detection of CNS lesions among T2WI, FLAIR, and T1WI-CHESS

	Multiple Comparison (*P* Value)		
	T2WI vs FLAIR	T2WI vs T1WI-CHESS	FLAIR v. T1WI-CHESS
Cortical tuber	1	.014[a]	.011[a]
RML	.007[a]	<.001[a]	.014[a]
Subependymal nodule	.027[a]	.085	<.001[a]

[a] $P < .05$.

and MR imaging including T1WI-CHESS; 1 patient was excluded from a detailed pathologic examination because of the presence of massive calcifications. The resected specimen was examined by a board-certified neuropathologist (M.M.).

Statistical Analyses

The interobserver reproducibility of the number of the CNS lesions, CR_{tuber}, and CR_{RML}, in each sequence was calculated using the intraclass correlation coefficient (ICC) and was deemed slight (ICC ≤ 0.2), fair (0.2 < ICC ≤ 0.4), moderate (0.4 < ICC ≤ 0.6), substantial (0.6 < ICC ≤ 0.8), or almost perfect (0.8 < ICC ≤ 1).

We used a nonparametric test, ie, the Friedman test, to perform the following: 1) compare the detection of the cortical tubers, RMLs, and SENs among T1WI, T1WI-MTC, and T1WI-CHESS in step one; 2) compare the detection among T2WI, FLAIR, and T1WI-CHESS in step 2; and 3) compare the CR_{tuber} and CR_{RML} values among T1WI, T1WI-MTC, and T1WI-CHESS. The significance level of the post hoc test was determined with a Bonferroni correction. The data are expressed as the mean (SD). A *P* value < .05 was considered significant.

We performed a Spearman rank correlation analysis to assess the association between seizure frequency and the number of cortical tubers, RMLs, and SENs in each sequence and to assess the association between intellectual disability and the number of cortical tubers, RMLs, and SENs in each sequence. The statistical analyses were performed using SPSS (Version 28.0; SPSS Tokyo).

RESULTS

Demographic Characteristics of the Patients with TSC

The 25 patients' characteristics are summarized in the Online Supplemental Data. Of the 25 patients, 14 were male, 11 were female, and the mean age was 11.9 [SD, 8.9] years. The mean seizure frequency and intellectual disability scores were 3.4 (SD, 1.6) and 2.1 (SD, 1.2), respectively. Representative images are shown in Figs 2 and 3.

Visual Assessment

The numbers of cortical tubers, RMLs, and SENs are listed in Table 1. The interobserver reproducibility of T1WI-MTC and T1WI-CHESS for cortical tubers, T2WI and T1WI-CHESS for RMLs, and FLAIR for SENs was substantial, and for the rest, it was almost perfect (Table 2).

The results of the comparison of the detection of the CNS lesions among T1WI, T1WI-MTC, and T1WI-CHESS in step 1 are provided in Table 3. Both T1WI-MTC and T1WI-CHESS were significantly superior to T1WI for the detection of cortical tubers, RMLs, and SENs. T1WI-CHESS was significantly superior to T1WI-MTC for detecting RMLs, whereas there was no significant difference between them in the ability to detect cortical tubers or SENs.

Table 4 presents the results of the comparison of the detection of CNS lesions among T2WI, FLAIR, and T1WI-CHESS in step 2. Both T2WI and FLAIR were significantly superior to T1WI-CHESS at detecting cortical tubers, and there was no significant difference between T2WI and FLAIR. In contrast, T1WI-CHESS was significantly superior to T2WI and FLAIR for the detection of RMLs, and FLAIR was significantly superior to T2WI. For the detection of SENs, FLAIR was significantly inferior to both T2WI and T1WI-CHESS, and there was no significant difference between T2WI and T1WI-CHESS.

Semiquantitative Analysis

The interobserver reproducibility of T1WI-MTC for CR_{tuber} and CR_{RML} was almost perfect, and for the rest, it was substantial (Table 5). Regarding CR_{tuber}, both T1WI-MTC and T1WI-CHESS were significantly superior to T1WI, but there was no significant difference between T1WI-MTC and T1WI-CHESS (Fig 4).

Regarding CR_{RML}, both T1WI-MTC and T1WI-CHESS were significantly superior to T1WI, and T1WI-CHESS was significantly superior to T1WI-MTC (Fig 5).

Correlations between the Number of CNS Lesions and the Clinical Information

There were no significant correlations between the patients' seizure frequency and the number of cortical tubers, RMLs, or SENs in each sequence or between the patients' intellectual disability scores and the number of cortical tubers, RMLs, or SENs in each sequence.

Correlations between MR Imaging Findings and Pathologic Findings

The surgical case was a 20-month-old boy with repeat epileptic seizures. On MR imaging, T2WI and FLAIR showed a swollen cortex and subcortical hyperintensity, indicating a cortical tuber (Fig 6*A*, -*B*). On T1WI-CHESS, these showed marked hyperintensity. Although T1WI, T2WI, and FLAIR could not detect other lesions, T1WI-CHESS could detect several RMLs, which led to the diagnosis of TSC (Fig 6*C*–*E*). The patient underwent resection of the cortical tuber. The resected specimen included a cortical tuber that demonstrated hyperintensity on T1WI-CHESS. Microscopically, there were many balloon cells in both the cortex and WM, without calcifications (Fig 7).

Table 5: Interobserver reproducibility of CR_{tuber} and CR_{RML} in each sequence

	T1WI	T1WI-MTC	T1WI-CHESS
CR_{tuber}	0.788	0.863	0.797
CR_{RML}	0.713	0.884	0.792

DISCUSSION

The results of our analyses demonstrated the superiority of T1WI-CHESS in detecting RMLs compared with conventional sequences, including T2WI, FLAIR, T1WI, and T1WI-MTC. Our findings also indicated that balloon cells may contribute to the hyperintensity on T1WI-CHESS. To the best of our knowledge, this study is the first attempt to evaluate the detection of CNS lesions of TSC using T1WI-CHESS. Our findings suggest that the combination of T1WI-CHESS, T2WI, and FLAIR would be useful to evaluate the CNS lesions of patients with TSC in daily clinical practice.

TSC and FCD type IIb often share several histopathologic features, including disruption of the cortical cytoarchitecture, dysmorphic neurons, and balloon cells. Particularly, balloon cells are a common pathognomonic cellular feature of these disorders. Reflecting the pathologic similarity, TSC and FCD type IIb also share radiographic characteristics: cortical thickening, blurring of gray-white matter junctions, and WM abnormal intensity areas oriented from the cortical surface to the ventricular wall. These are usually shown as hyperintensity on T2WI and FLAIR images and hypointensity on T1WI, but they sometimes show hyperintensity on T1WI.

Kimura et al[18] reported that T1 hyperintensity of the transmantle sign of FCD type IIb is associated with the high density of balloon cells, independent of the density of dysmorphic neurons, the severity of gliosis, and calcifications. In a study by Kusama et al,[19] T1WI-CHESS detected the transmantle sign of FCD type IIb as marked hyperintensity where numerous balloon cells were located in a resected specimen. In the present study, some cortical tubers and RMLs showed hyperintensity on T1WI, and T1WI-

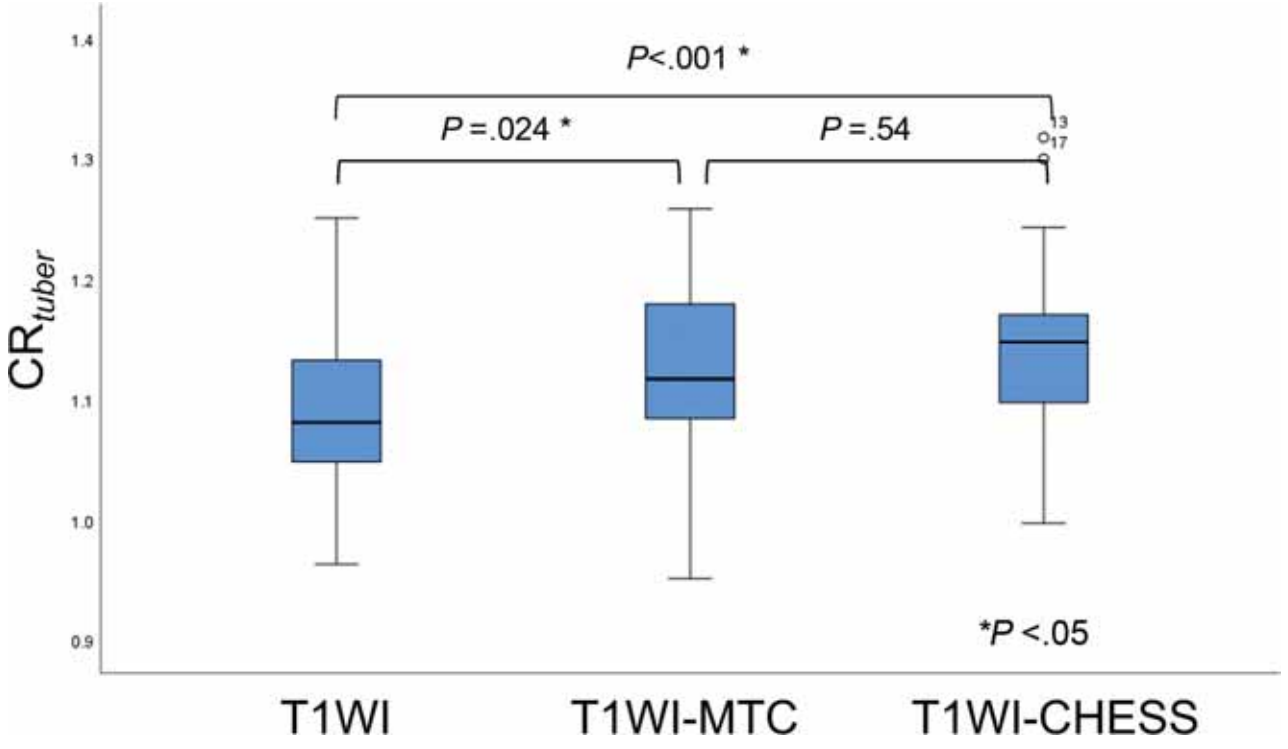

FIG 4. Comparison of the CR_{tuber} among T1WI, T1WI-MTC, and T1WI-CHESS.

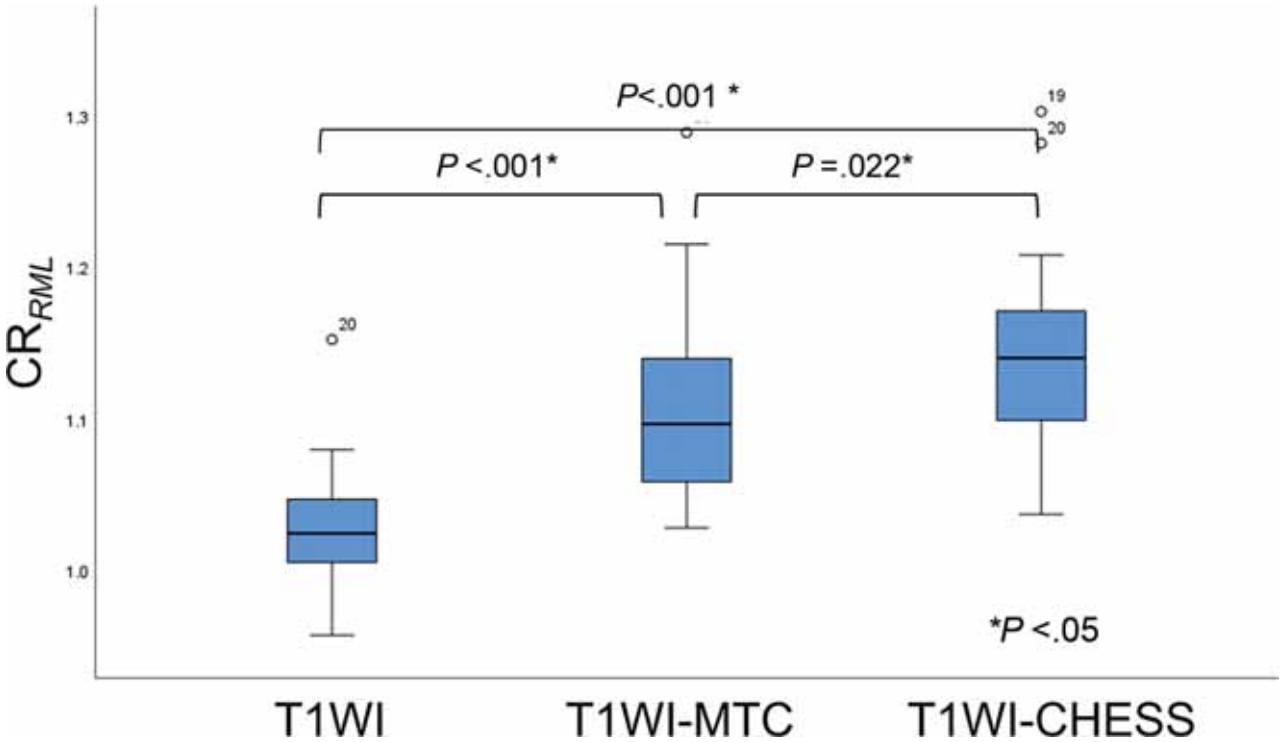

FIG 5. Comparison of the CR_{RML} among T1WI, T1WI-MTC, and T1WI-CHESS.

CHESS detected many more cortical tubers and RMLs, with higher contrast. In the surgical case of our present series mentioned above, the resected specimen included a cortical tuber that showed hyperintensity on T1WI-CHESS. The pathologic findings showed many balloon cells without calcification. This result suggests that balloon cells may contribute to the hyperintensity on T1WI, as shown in FCD type IIb.

Magnetization transfer is a technique for improving the image contrast in MR imaging based on the difference in magnetic field–induced frequencies of free water protons and macromolecule-bound water protons.[25] When an MTC pulse is applied, a radiofrequency pulse with frequency components distant from the resonant frequency of free water is excited, and the background signal intensity in the brain parenchyma decreases. In TSC, the alteration of tissue integrity leads to a disruption of the transfer of saturation effects between bound and free protons, causing a high signal on T1WI-MTC.[11,13] Several reports have demonstrated the usefulness of T1WI-MTC for detecting CNS lesions of the TSC, and some lesions were only detected on the T1WI-MTC.[11-13]

In the present study, we used T1WI-CHESS, which is the most common fat-suppression sequence in daily clinical practice. Like T1WI-MTC, T1WI-CHESS consists of a radiofrequency pulse and is reported to have the magnetization transfer effect.[26] Using the magnetization transfer effect of CHESS, Kusama et al[20] demonstrated that T1WI-CHESS images were significantly superior to T1WI-MTC images for neuromelanin imaging. The reason for that result was suspected to be that in addition to background suppression due to the magnetization transfer effect, the fat-suppression pulse decreased the background signal, which contains lipids in the myelin content of the brain. In the present study, T1WI-CHESS showed more RMLs with higher image contrast than T1WI-MTC, whereas they showed no significant differences in the detection of cortical tubers. We speculated that the difference in the amount of myelin in GM and WM and the difference in cell density between cortical tubers and RMLs affected this result. Although cortical tubers contain subcortical WM, a histopathologic study indicated that myelinated fibers are reduced in cortical tubers.[27]

While our present findings revealed the usefulness of T1WI-CHESS for detecting RMLs, cortical tubers were best detected by T2WI and FLAIR. As mentioned above, the density of myelinated fibers and the number of normal neurons are reduced in cortical tubers.[27] A diffusion-weighted MR imaging study also showed that cortical tubers had a higher free water content due to an increase in extracellular space and a decrease in the density of cellular elements, leading to hyperintensity on T2WI/FLAIR.[28] In addition, the effectiveness of signal suppression by magnetization transfer contrast is affected by cell density.[12] We suspect that T2WI/FLAIR was able to detect more cortical tubers than T1WI-CHESS in the present study for these reasons. Therefore, the combination of T1WI-CHESS, T2WI, and FLAIR would be useful to evaluate the CNS lesions of patients with TSC. The patient who underwent an operation had been transferred to our hospital with suspicion of FCD or a solitary cortical tuber. The use of T1WI-CHESS at our hospital detected several RMLs and led to the diagnosis of TSC (Fig 6). This case suggested the possibility of our misdiagnosing TSC as an FCD type IIb or a solitary cortical tuber.

The relationship between the number of cortical tubers observed by MR imaging and the severity of cerebral dysfunction of patients with TSC has been reported.[29,30] In addition to cortical tubers, several studies have focused on WM microstructural changes on DTI or neurite orientation dispersion and density imaging.[22,31-33] A study using DTI reported that RMLs were

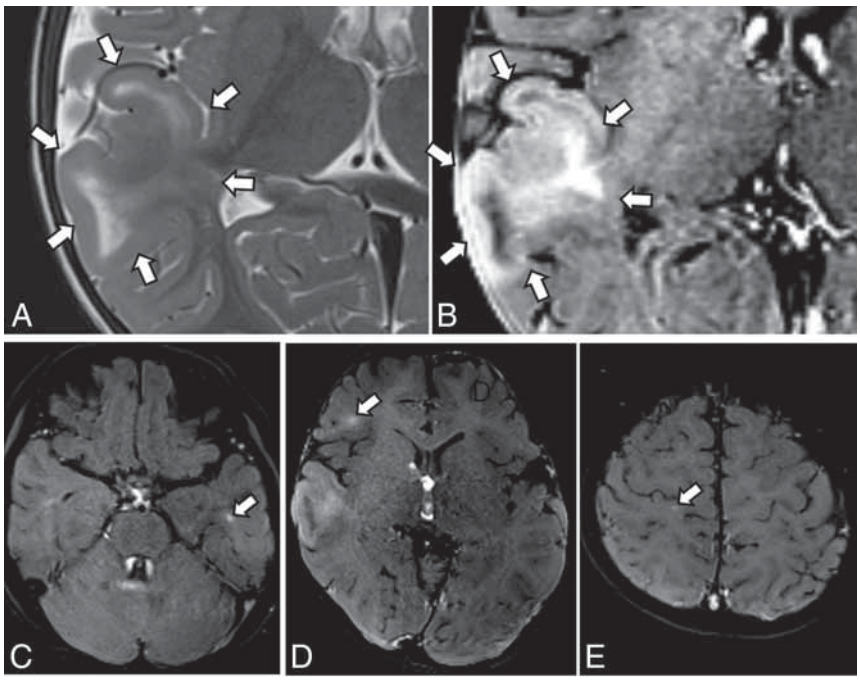

FIG 6. MR imaging findings of the surgical case, a 20-month-old boy with repeat epileptic seizures. *A*, Axial T2WI shows swelling of the cortex and subcortical hyperintensity (*arrows*), consistent with a cortical tuber. No other lesions are noted on T1WI, T2WI, and FLAIR (not shown); suggesting focal cortical dysplasia or a solitary cortical tuber. *B*, Axial T1WI-CHESS shows marked hyperintensity in the swollen cortex and subcortical white matter (*arrows*). *C–E*, Axial T1WI-CHESS shows several RMLs as linear hyperintense areas (*arrows*). On the basis of these findings, the patient was diagnosed with TSC.

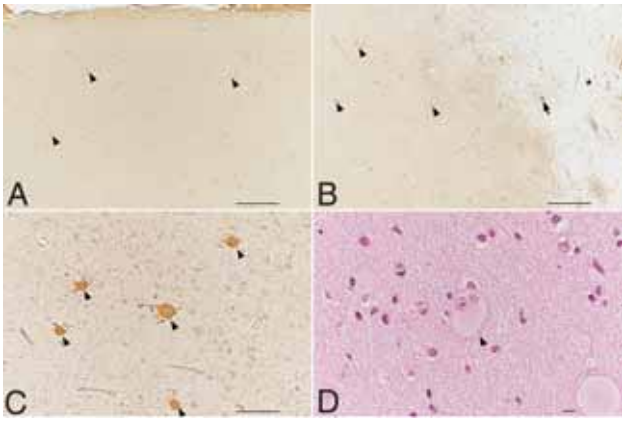

FIG 7. Pathologic findings of the surgical case, a 20-month-old boy with repeat epileptic seizures. *A*, Many balloon cells are seen in the thickened cortex (*arrowheads* as examples). *B*, In subcortical WM, many balloon cells (*arrowheads* as examples) are seen in the *left part of the white rectangle*. Rare balloon cells (*arrow*) are present in the *right* part of the rectangle (*star*). *C* and *D*, Many balloon cells are observed in the subcortical white matter (*arrowheads*) and are immunoreactive for a monoclonal antibody against vimentin (1:400, M7020; Dako). *A–C*, Monoclonal antivimentin antibody. *D*, Hematoxylin-eosin staining. Scale bars: *A* and *B*, 500 μm. *C*, 100 μm. *D*, 10 μm.

associated with abnormal DTI values (reflecting the disrupted myelination) and were strongly associated with neurocognitive morbidity.[22] That study also used quantitative neurocognitive outcomes such as full-scale intelligence quotients or developmental quotients and the Social Communication Questionnaire. Our present analyses showed no significant correlations between the number of CNS lesions and clinical information; however, we assessed only seizure frequency and intellectual disability with 5-point scale qualitative evaluations. The use of more detailed clinical information with a quantitative evaluation may have helped clarify the correlation between the number of CNS lesions and clinical outcomes in the present study.

There are several limitations in this study. The number of patients was not large ($n = 25$); however, this number is larger than that in most of the previous series.[10-12,32,33] This number of patients was also sufficient to statistically determine the usefulness of T1WI-CHESS for detecting RMLs. A second limitation was a weakness of pathologic proof ($n = 1$). However, our present findings were consistent with the radiology-pathology correlation in FCD type IIb.[18] Further radiology-pathology correlation studies are also needed for TSC. A third limitation is that the ages of the patients varied, including patients whose myelination is ongoing and those with completed myelination. Because there were 2 patients younger than 2 years of age whose myelination is ongoing and 1 of them had a SEN only, it was not possible to determine any difference in the detection ability of T1WI-CHESS between myelinated and unmyelinated brains. Future studies comparing the detectability of T1WI-CHESS between myelinated and unmyelinated brains are necessary.

CONCLUSIONS

We investigated the detection of cortical tubers, RMLs, and SENs by T1WI-CHESS. The results of our analysis demonstrated the usefulness of T1WI-CHESS for detecting RMLs, and they indicated that balloon cells may contribute to the hyperintensity on T1WI-CHESS, as shown in FCD type IIb. Our findings suggest that the combination of T1WI-CHESS, T2WI, and FLAIR would be useful to evaluate the CNS lesions of patients with TSC in daily clinical practice.

Disclosure forms provided by the authors are available with the full text and PDF of this article at www.ajnr.org.

REFERENCES

1. Fryer AE, Chalmers A, Connor JM, et al. **Evidence that the gene for tuberous sclerosis is on chromosome 9.** *Lancet* 1987;1:659–61 CrossRef Medline
2. Kandt RS, Haines JL, Smith M, et al. **Linkage of an important gene locus for tuberous sclerosis to a chromosome 16 marker for polycystic kidney disease.** *Nat Genet* 1992;2:37–41 CrossRef Medline

3. Tee AR, Fingar DC, Manning BD, et al. **Tuberous sclerosis complex-1 and -2 gene products function together to inhibit mammalian target of rapamycin (mTOR)-mediated downstream signaling.** *Proc Natl Acad Sci U S A* 2002;99:13571–76 CrossRef Medline
4. Gao X, Zhang Y, Arrazola P, et al. **TSC tumour suppressor proteins antagonize amino-acid-TOR signalling.** *Nat Cell Biol* 2002;4:699–704 CrossRef Medline
5. Inoki K, Li Y, Zhu T, et al. **TSC2 is phosphorylated and inhibited by Akt and suppresses mTOR signalling.** *Nat Cell Biol* 2002;4:648–57 CrossRef Medline
6. Roach ES, Sparagana SP. **Diagnosis of tuberous sclerosis complex.** *J Child Neurol* 2004;19:643–49 CrossRef Medline
7. Ridler K, Bullmore ET, De Vries PJ, et al. **Widespread anatomical abnormalities of grey and white matter structure in tuberous sclerosis.** *Psychol Med* 2001;31:1437–46 CrossRef Medline
8. DiMario FJ Jr. **Brain abnormalities in tuberous sclerosis complex.** *J Child Neurol* 2004;19:650–57 CrossRef Medline
9. Kalantari BN, Salamon N. **Neuroimaging of tuberous sclerosis: spectrum of pathologic findings and frontiers in imaging.** *AJR Am J Roentgenol* 2008;190:W304–09 CrossRef Medline
10. Jeong MG, Chung TS, Coe CJ, et al. **Application of magnetization transfer imaging for intracranial lesions of tuberous sclerosis.** *J Comput Assist Tomogr* 1997;21:8–14 CrossRef Medline
11. Girard N, Zimmerman RA, Schnur RE, et al. **Magnetization transfer in the investigation of patients with tuberous sclerosis.** *Neuroradiology* 1997;39:523–28 CrossRef Medline
12. Pinto Gama HP, da Rocha AJ, Braga FT, et al. **Comparative analysis of MR sequences to detect structural brain lesions in tuberous sclerosis.** *Pediatr Radiol* 2006;36:119–25 CrossRef Medline
13. Kadom N, Trofimova A, Vezina GL. **Utility of magnetization transfer T1 imaging in children with seizures.** *AJNR Am J Neuroradiol* 2013;34:895–98 CrossRef Medline
14. Baldassari S, Ribierre T, Marsan E, et al. **Dissecting the genetic basis of focal cortical dysplasia: a large cohort study.** *Acta Neuropathol* 2019;138:885–900 CrossRef Medline
15. Becker AJ, Urbach H, Scheffler B, et al. **Focal cortical dysplasia of Taylor's balloon cell type: mutational analysis of the TSC1 gene indicates a pathogenic relationship to tuberous sclerosis.** *Ann Neurol* 2002;52:29–37 CrossRef Medline
16. Barkovich AJ, Kuzniecky RI, Jackson GD, et al. **A developmental and genetic classification for malformations of cortical development.** *Neurology* 2005;65:1873–87 CrossRef Medline
17. Holmes GL, Stafstrom CE; Tuberous Sclerosis Study Group. **Tuberous sclerosis complex and epilepsy: recent developments and future challenges.** *Epilepsia* 2007;48:617–30 CrossRef Medline
18. Kimura Y, Shioya A, Saito Y, et al. **Radiologic and pathologic features of the transmantle sign in focal cortical dysplasia: the T1 signal is useful for differentiating subtypes.** *AJNR Am J Neuroradiol* 2019;40:1060–66 CrossRef Medline
19. Kusama M, Sato N, Tanei Z-I, et al. **Enhanced MR conspicuity of type IIb focal cortical dysplasia by T1WI with CHESS.** *Neurol Clin Pract* 2021;11:e750–52 CrossRef Medline
20. Kusama M, Sato N, Kimura Y, et al. **Quick MR neuromelanin imaging using a chemical shift selective pulse.** *Magn Reson Med Sci* 2021;20:106–11 CrossRef Medline
21. Northrup H, Krueger DA; International Tuberous Sclerosis Complex Consensus Group. **Tuberous sclerosis complex diagnostic criteria update: recommendations of the 2012 International Tuberous Sclerosis Complex Consensus Conference.** *Pediatr Neurol* 2013;49:243–54 CrossRef Medline
22. van Eeghen AM, Terán LO, Johnson J, et al. **The neuroanatomical phenotype of tuberous sclerosis complex: focus on radial migration lines.** *Neuroradiology* 2013;55:1007–14 CrossRef Medline
23. Gallagher A, Grant EP, Madan N, et al. **MRI findings reveal three different types of tubers in patients with tuberous sclerosis complex.** *J Neurol* 2010;257:1373–81 CrossRef Medline
24. Daily DK, Ardinger HH, Holmes GE. **Identification and evaluation of mental retardation.** *Am Fam Physician* 2000;61:1059–67 Medline
25. Wolff SD, Balaban RS. **Magnetization transfer imaging: practical aspects and clinical applications.** *Radiology* 1994;192:593–99 CrossRef Medline
26. Shin W, Gu H, Yang Y. **Incidental magnetization transfer contrast by fat saturation preparation pulses in multislice Look-Locker echo planar imaging.** *Magn Reson Med* 2009;62:520–26 CrossRef Medline
27. Richardson EP Jr. **Pathology of tuberous sclerosis: neuropathologic aspects.** *Ann N Y Acad Sci* 1991;615:128–39 Medline
28. Jansen FE, Braun KP, van Nieuwenhuizen O, et al. **Diffusion-weighted magnetic resonance imaging and identification of the epileptogenic tuber in patients with tuberous sclerosis.** *Arch Neurol* 2003;60:1580–84 CrossRef Medline
29. Goodman M, Lamm SH, Engel A, et al. **Cortical tuber count: a biomarker indicating neurologic severity of tuberous sclerosis complex.** *J Child Neurol* 1997;12:85–90 CrossRef Medline
30. Okanishi T, Fujimoto A, Kanai S, et al. **Association between diffuse cerebral MRI lesions and the occurrence and intractableness of West syndrome in tuberous sclerosis complex.** *Epilepsy Behav* 2020;103:106535 CrossRef Medline
31. Peters JM, Struyven RR, Prohl AK, et al. **White matter mean diffusivity correlates with myelination in tuberous sclerosis complex.** *Ann Clin Transl Neurol* 2019;6:1178–90 CrossRef Medline
32. Tsai JD, Ho MC, Lee HY, et al. **Disrupted white matter connectivity and organization of brain structural connectomes in tuberous sclerosis complex patients with neuropsychiatric disorders using diffusion tensor imaging.** *Magma* 2021;34:189–200 CrossRef Medline
33. Taoka T, Aida N, Fujii Y, et al. **White matter microstructural changes in tuberous sclerosis: evaluation by neurite orientation dispersion and density imaging (NODDI) and diffusion tensor images.** *Sci Rep* 2020;10:436 CrossRef Medline

Evaluation of the Prevalence of Punctate White Matter Lesions in a Healthy Volunteer Neonatal Population

S. Kular, H. Holmes, A. Hart, P. Griffiths, and D. Connolly

ABSTRACT

SUMMARY: Hypoxic-ischemic injury is the most common cause of neonatal encephalopathy. T1-weighted punctate white matter lesions have been described in hypoxic-ischemic injury. We have reviewed a healthy volunteer neonatal population to assess the prevalence of punctate white matter lesions in neonates with no clinical signs of hypoxic-ischemic injury. Fifty-two subjects were scanned on a neonatal-specific 3T MR imaging scanner. Twelve patients were excluded due to the lack of T1-weighted imaging, leaving a total of 40 patients (35 term, 5 preterm) assessed in the study. One had a solitary T1-punctate white matter lesion. We concluded that solitary punctate white matter lesions have a low prevalence in healthy neonates.

ABBREVIATIONS: HII = hypoxic-ischemic injury; PWML = punctate white matter lesion; SDH = subdural hematoma

Neonatal hypoxic-ischemic injury (HII) is the most common cause of neonatal encephalopathy, ahead of infection, metabolic disorder, and trauma.[1,2] HII can occur in preterm or term infants.[1] On MR imaging, HII with brain injury can manifest as signal abnormality within the posterior putamen, ventral-posterolateral thalamic injury, central sulcus cortical injury (acute profound asphyxia), or watershed injury (chronic partial asphyxia).[3] Punctate white matter lesions (PWMLs) are hyperintense on T1-weighted and iso- to hypointense on T2-weighted imaging. PWMLs have been described in association with hypoxic-ischemic injury.[4] PWMLs can be multifactorial, with a combination of gliotic scarring, hemorrhage, and mineralization contributing to their MR imaging appearance; however, it is often not possible to ascertain which of these is the causative factor in each case. A histologic study has, however, found that approximately 25% of PWMLs are secondary to hemorrhage.[5]

SWI may help differentiate hemorrhagic PWMLs from nonhemorrhagic PWMLs, with the latter attributed to early scarring or mineralization.[6] Hemorrhagic PWMLs are also associated with greater proportions of infantile intraventricular hemorrhage, with nonhemorrhagic PWMLs being associated more with ischemia-related injury.[7] In either etiology, the general consensus is that PWMLs are derived from pathologic processes occurring via hemorrhagic or ischemic pathways. Thus, these lesions, one would assume, should not be present in a healthy neonate who has not been subjected to any known pathologic insult.

In our study, we reviewed MR images of a healthy volunteer neonate population obtained on a specific neonatal MR imaging scanner to assess the prevalence of PWMLs in neonates without clinical signs of HII.

MATERIALS AND METHODS

A 3T neonatal MR imaging scanner (GE Healthcare) was installed in the neonatal unit of the local obstetric department.

Ethics approval was governed by the Medicines and Healthcare products Regulatory Agency of the UK. Conditions of use granted under the Medicines and Healthcare products Regulatory Agency were that the scanner was not to be used for primary diagnostic purpose and the manufacturer sponsored the study. Enrollment for up to 60 neonatal subjects was granted. Two groups were scanned. Group 1 consisted of healthy term neonates (≥37 weeks' gestational age) whose parents agreed to MR imaging before discharge. Group 2 involved premature neonates about to be discharged at term-corrected age, with no other clinical complications.

All subjects had 2 scheduled sonography examinations throughout pregnancy as per local guidelines, at approximately 12 and 19 weeks for the first and second scans, respectively. No subjects were found to have screening anomalies on fetal sonography.

All parents provided informed, written consent and completed an MR imaging safety form for the neonate and themselves because 1 parent could accompany their child during scanning.

Healthy volunteer subjects were imaged as part of the Firefly 3T MR imaging project evaluation.[8] The scans were performed

Received March 17, 2022; accepted after revision May 24.

From the Departments of Neuroradiology (S.K., H.H., P.G., D.C.) and Neurology (A.H.), Sheffield Children's Hospital, Sheffield, UK.

Please address correspondence to Saminderjit Kular, MD, Department of Neuroradiology, Royal Hallamshire Hospital, Glossop Rd, Sheffield, S10 2JF, United Kingdom; e-mail: skular2@doctors.org.uk

http://dx.doi.org/10.3174/ajnr.A7578

within 1 hour of feeding. The 3T magnet strength was deemed safe for neonatal scanning.[9] Subjects' vital observations encompassing body temperature, heart rate, and oxygen saturation were monitored throughout scanning. Scanning time was limited to 1 hour inclusive of the time for room acclimatization, monitoring, and subject positioning.

Initially, T2-weighted images were acquired in a trial format and optimized for contrast, resolution, and scan time before using them for both ultrafast single-shot FSE and T2-FSE imaging. The optimized T2-sequence parameters were subsequently used for all cases with long-TE single-voxel proton spectroscopy, T1-volume/spin-echo, DWI, and MR arteriography added as tolerated.

Inclusion criteria were patients with T2-weighted imaging and either or both standard T1-weighted spin-echo and T1-volumetric sequences. Excluded cases were those without T1-weighted imaging because they were unable to be adequately assessed for PWML.

Acquired images were reviewed by 2 consultant pediatric neuroradiologists. Further reviews were conducted by 2 post-board examination Royal College of Radiologists (FRCR, UK) neuroradiology fellows.

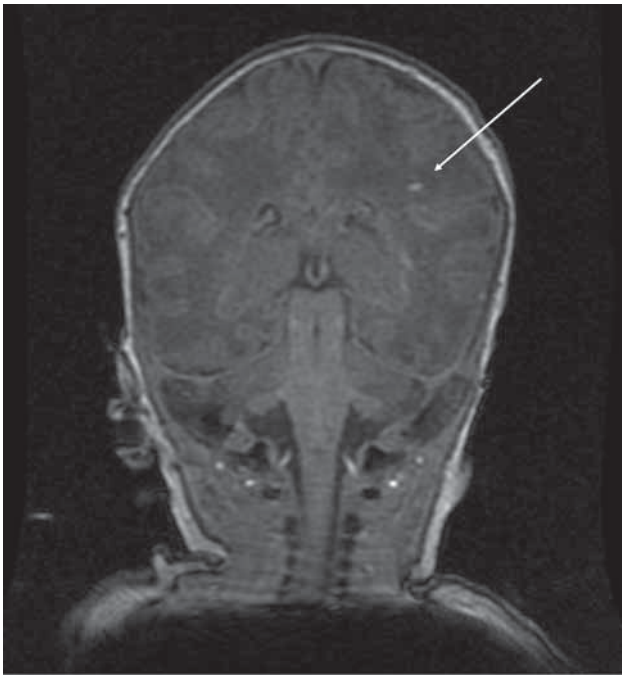

FIG 1. A solitary T1-weighted PWML was demonstrated in the left corona radiata of 1 study patient (*white arrow*).

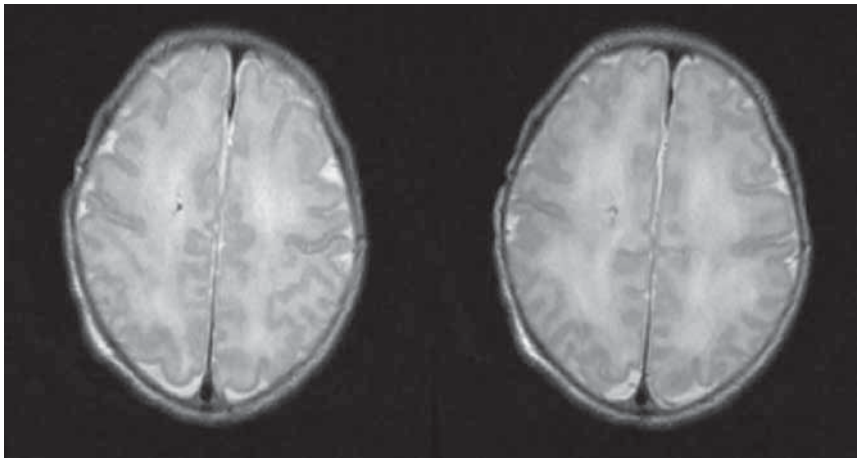

FIG 2. One subject demonstrated a right frontal developmental venous anomaly.

RESULTS

Fifty-two subjects were recruited into the study in total; however, 12 had no T1-weighted imaging; therefore, 40 cases were evaluated for evidence of PWML (35 in group 1, five in group 2).

One subject had a pre-existing bradycardia, and while having a normal sinus rhythm before scanning, the subject developed bradycardia during scanning. This was, however, not deemed to be attributed to MR imaging, and the neonate did not require further follow-up on discharge. No other subject demonstrated abnormal vital signs before, during, or immediately after MR imaging.

One hundred percent of imaging studies (40/40) were deemed evaluable, either completely or partially. Twenty-five percent (10/40) of studies were deemed partially evaluable, predominantly secondary to motion artifacts. The partially evaluable studies were, however, still thought to be accurate enough to identify notable abnormal findings on T1-weighted imaging.

Of the 40 subjects, 1 subject in group 1 (2.5%) had evidence of a 2-mm solitary PWML, which was hyperintense on T1-weighted imaging (Fig 1). It was not possible to further distinguish this PWML as hemorrhagic or nonhemorrhagic (scarring/mineralization) due to absence of SWI. In this case, no pre- or perinatal injury was known to have occurred, nor was there any evidence of neonatal encephalopathy. The finding was, therefore, of unknown etiology but highly unlikely to be from perinatal asphyxia. The long-term follow-up of this PWML is not known.

One group 2 subject (2.5%) had a finding of a right frontal developmental venous anomaly (Fig 2) with small-volume intraventricular hemorrhage; however, clinical review was unremarkable, and the subject was developing normally on 2-month assessment.

One group 1 subject (2.5%) had a cavum vergae, a normal anatomic variant with no clinical consequences (Fig 3). One group 1 subject (2.5%) also had a maturing left subdural hematoma (SDH) (Fig 4).

DISCUSSION

In our population, there was an overwhelmingly large proportion of subjects presenting with no evidence of PWMLs (97.5%). In the single patient presenting with a tiny, solitary PWML, no discernible signs of physiologic impairment were seen on early medical assessment of the infant. Recent studies performed at

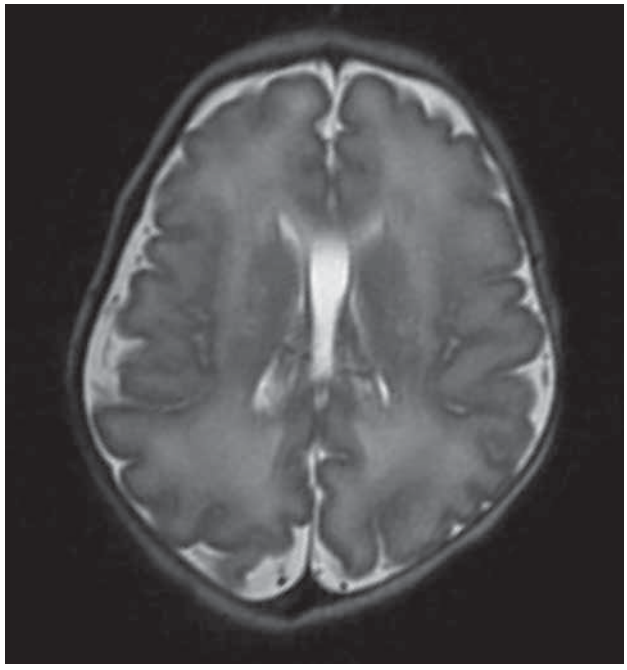

FIG 3. An incidental normal variant of a cavum vergae was seen in 1 study subject.

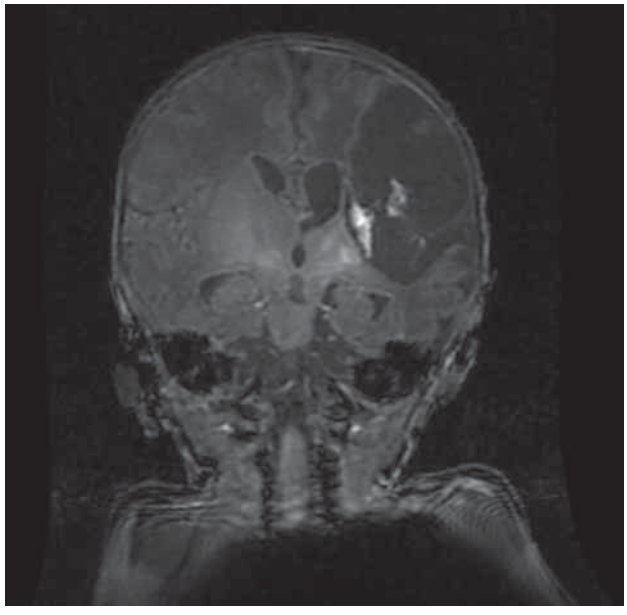

FIG 4. A moderate-sized left-convexity SDH was observed in 1 otherwise clinically well patient on T1-weighted imaging. This can be a common finding postbirth, seen in up to 38% of the population, spontaneously self-resolving in most cases.

approximately 18 months postpartum have demonstrated a similar, albeit slightly higher incidence of incidental PWMLs at approximately 12%; however, this is still consistent with a substantial minority within the population.[10] The slightly higher incidence in a delayed-scan cohort could potentially be secondary to a greater number of lesions being visible from gliosis or scarring, which may not necessarily have been immediately visible in our postpartum scan cohort; however, with time, these lesions may become more apparent.

The same proportion of subjects that presented with a PWML also presented with an incidental normal variant (cavum vergae) and a left-sided SDH. SDH is a common finding, seen in up to 38% of births.[11]

A limitation of our study was that some studies were affected by motion artifacts; therefore, not all studies were of an equivalent reading standard. Nevertheless, all studies were deemed by participating radiologists to be of sufficient quality to provide conclusive PWML identification/exclusion. Furthermore, there was a significant difference in subject numbers within the 2 groups (35 versus 5); and while the overall number of 40 subjects is low, given the limitations of the population, this is the largest cohort of healthy neonates in the literature to be scanned postpartum for PWMLs.

Our findings conclude that PWMLs have very low prevalence in healthy neonates, and the presence of 1 or 2 PWMLs in otherwise healthy patients is not likely to be of clinical relevance. Furthermore, PWMLs in these cases may not necessarily be secondary to hemorrhage or scarring, but from physiologic mineralization. In contrast, when several T1 PWMLs (approximating $\geq$6) are present, this is more likely related to perinatal asphyxia, and closer follow-up is recommended.[3]

CONCLUSIONS

We recommend that in the event of neonates demonstrating 1 or 2 PWMLs with no other clinical or radiologic abnormality, no routine follow-up imaging is indicated. Further long-term follow-up studies to investigate the chronic relevance of solitary PWMLs in otherwise healthy neonates are required.

Disclosure forms provided by the authors are available with the full text and PDF of this article at www.ajnr.org.

REFERENCES

1. Cowan F, Rutherford M, Groenendaal F, et al. **Origin and timing of brain lesions in term infants with neonatal encephalopathy.** *Lancet* 2003;361:736–42 CrossRef Medline
2. Wagenaar N, Chau V, Groenendaal F, et al. **Clinical risk factors for punctate white matter lesions on early magnetic resonance imaging in preterm newborns.** *J Pediatr* 2017;182:34–40.e1 CrossRef Medline
3. Hayman M, van Wezel-Meijler G, van Straaten H, et al. **Punctate white-matter lesions in the full-term newborn: underlying aetiology and outcome.** *Eur J Paediatr Neurol* 2019;23:280–87 CrossRef Medline
4. Martinez-Biarge M, Groenendaal F, Kersbergen KJ, et al. **MRI based preterm white matter injury classification: the importance of sequential imaging in determining severity of injury.** *PLoS One* 2016;11:e0156245 CrossRef Medline
5. Paneth N, Rudelli R, Monte W, et al. **White matter necrosis in very low birth weight infants: neuropathologic and ultrasonographic findings in infants surviving six days or longer.** *J Pediatr* 1990;116:975–84 CrossRef Medline
6. Childs AM, Cornette L, Ramenghi LA, et al. **Magnetic resonance and cranial ultrasound characteristics of periventricular white matter abnormalities in newborn infants.** *Clin Radiol* 2001;56:647–55 CrossRef Medline

7. Niwa T, de Vries LS, Benders MJ, et al. **Punctate white matter lesions in infants: new insights using susceptibility-weighted imaging.** *Neuroradiology* 2011;53:669–79 CrossRef Medline
8. Griffiths PD, Jarvis D, Armstrong L, et al. **Initial experience of an investigational 3T MR scanner designed for use on neonatal wards.** *Eur Radiol* 2018;28:4438–46 CrossRef Medline
9. International Electrotechnical Commission. Medical electrical equipment, Part 2-33: Particular requirements for the safety of MR equipment for medical diagnosis IEC 60601-2-33 ed 2.2 (Geneva, 2008) with amendments 1 and 2. https://standards.globalspec.com/std/1099061/iec-60601-2-33. Accessed October 9, 2021
10. Carney O, Hughes E, Tusor N, et al. **Incidental findings on brain MR imaging of asymptomatic term neonates in the Developing Human Connectome Project.** *EClinicalMedicine* 2021;38:100984 CrossRef Medline
11. Nikam RM, Kandula VV, Yue X, et al. **Birth-related subdural hemorrhage: prevalence and imaging morphology.** *Pediatr Radiol* 2021;51:939–46 CrossRef Medline

The Construction of a Predictive Composite Index for Decision-Making of CSF Diversion Surgery in Pediatric Patients following Prenatal Myelomeningocele Repair

F.T. Mangano, M. Altaye, C.B. Stevenson, and W. Yuan

ABSTRACT

BACKGROUND AND PURPOSE: There is a wide range of clinical and radiographic factors affecting individual surgeons' ultimate decision for CSF diversion for pediatric patients following prenatal myelomeningocele repair. Our aim was to construct a composite index (CSF diversion surgery index) that integrates conventional clinical measures and neuroimaging biomarkers to predict CSF diversion surgery in these pediatric patients.

MATERIALS AND METHODS: This was a secondary retrospective analysis of data from 33 patients with prenatal myelomeningocele repair (including 14 who ultimately required CSF diversion surgery). Potential independent variables, including the Management of Myelomeningocele Study Index (a dichotomized variable based on the shunt-placement criteria from the Management of Myelomeningocele Study), postnatal DTI measures (fractional anisotropy and mean diffusivity in the genu of the corpus callosum and the posterior limb of internal capsule), fronto-occipital horn ratio at the time of DTI, gestational ages, and sex, were evaluated using stepwise logistic regression analysis to identify the most important predictors.

RESULTS: The CSF diversion surgery index model showed that the Management of Myelomeningocele Study Index and fractional anisotropy in the genu of the corpus callosum were significant predictors ($P < .05$) of CSF diversion surgery. The predictive value of the CSF diversion surgery index was also affected by fractional anisotropy in the posterior limb of the internal capsule and sex with marginal effect ($.05 < P < .10$), but not by the fronto-occipital horn ratio ($P > .10$). The overall CSF diversion surgery index model fit the data well with statistical significance (eg, likelihood ratio: $P < .001$), with the performance (sensitivity = 78.6%; specificity = 86.5%, overall accuracy = 84.8%) superior to all individual indices in sensitivity and overall accuracy, and most of the individual indices in specificity.

CONCLUSIONS: The CSF diversion surgery index model outperformed all single predictor models and, with additional validation, may potentially be developed and incorporated into a sensitive and robust clinical tool to assist clinicians in hydrocephalus management.

ABBREVIATIONS: CDSI = CSF diversion surgery index; FA = fractional anisotropy; FOHR = fronto-occipital horn ratio; gCC = genu of the corpus callosum; MD = mean diffusivity; MMC = myelomeningocele; MOMS = Management of Myelomeningocele Study; PLIC = posterior limb of the internal capsule

Hydrocephalus is the most common surgical condition encountered in pediatric neurosurgical care. It is a complex, typically life-long disease for which no cure currently exists. Given its incidence of approximately 1 in 500 children, many resources have been dedicated to studying diverse etiologies, management strategies, and, ultimately, outcomes related to this disease. Further complicating the management of this patient population, the diagnosis of progressive hydrocephalus in a child with large ventricles can be difficult to establish and standardized diagnostic criteria are lacking.[1,2] Surgical intervention or the lack of a timely intervention can lead to complications, highlighting the need for improved patient selection for better long-term outcomes.

The scope of the current work is to study hydrocephalus in the context of patients who are born with open neural tube defects, specifically, those with myelomeningocele (MMC) who underwent prenatal repairs. MMC is the most common form of spina bifida. In addition to hydrocephalus, the condition is associated with other anomalies of the CNS such as Chiari II malformation, brainstem deformities, low-lying venous sinuses, and a small posterior fossa. To address the question of whether better functional results could be obtained with earlier MMC repair, the Management of

Received January 20, 2022; accepted after revision June 6.

From the Division of Pediatric Neurosurgery (F.T.M., C.B.S.), Division of Biostatistics and Epidemiology (M.A.), and Pediatric Neuroimaging Research Consortium (W.Y.), Division of Radiology, Cincinnati Children's Hospital Medical Center, Cincinnati, Ohio; and University of Cincinnati College of Medicine (F.T.M., M.A., C.B.S., W.Y.), Cincinnati, Ohio.

This study was supported, in part. by the Robert L. McLaurin, MD, Scholar Endowment in Neurosurgery at Cincinnati Children's Hospital Medical Center.

Please address correspondence to Weihong Yuan, PhD, Pediatric Neuroimaging Research Consortium, Division of Radiology, Cincinnati Children's Hospital Medical Center, 3333 Burnet Ave, MLC 5033, Cincinnati, OH 45229; e-mail: Weihong.Yuan@cchmc.org

Indicates article with online supplemental data.

http://dx.doi.org/10.3174/ajnr.A7585

Myelomeningocele Study (MOMS) prospectively compared patients undergoing prenatal repair with those who had standard postnatal repair.[3] The initial results were published in 2011, and the primary outcome related to the need for shunt placement demonstrated a statistically significant difference between the 2 groups (40% versus 82%, $P < .001$) in favor of the prenatal repair group.[3] Given the wide variety of clinical and radiographic factors affecting individual surgeons' ultimate decision for CSF diversion, the known propensity for children undergoing prenatal MMC repair to have large ventricles at baseline, and the overall lack of consensus in diagnosing hydrocephalus in the pediatric population at large, the decision to insert a ventriculoperitoneal shunt was based on an independent committee of neurosurgeons who reviewed the clinical and radiographic data for each child to ascertain the need for CSF diversion.

That these criteria are not universally accepted or applied is evidenced by the fact that while 64 of 91 children (70%) in the prenatal cohort of the MOMS trial met the criteria for shunting as recommended by the independent study committee, only 40 of the 91 children (44%) actually received a shunt, with the remainder believed not to truly have progressive hydrocephalus or require CSF diversion by their primary neurosurgical provider.

In the present study, we constructed a composite index (the CSF diversion surgery index [CDSI]) that integrates the information from conventional clinical measures and multiple objective noninvasive neuroimaging biomarkers on the basis of DTI parameters that have been applied frequently in previous hydrocephalus-related analysis.[4-16] We will identify the set of the most important predictors for the CDSI model based on stepwise logistic regression, and we hypothesized that the model will minimize the potential for clinical bias and help improve the diagnosis of progressive hydrocephalus, thereby providing guidance to clinicians in determining the need for CSF diversion in patients undergoing prenatal myelomeningocele repair.

MATERIALS AND METHODS

Participants

All participants were selected from a retrospective study approved and conducted under the guidelines of the Cincinnati Children's Hospital institutional review board. In a previous study, we reported the predictive value of DTI measures in a cohort of 35 pediatric patients with prenatal repair for their need for CSF diversion surgery and for the timing of surgery in those who did require surgical treatment. All these patients underwent DTI with a similar MR imaging protocol. Fifteen of the 35 patients later underwent CSF diversion surgery for hydrocephalus. All the prenatal MMC repairs, postnatal imaging, and CSF diversions surgeries (all treated with shunt placement) were performed in the same institution at the Cincinnati Children's Hospital. The details of the demographic and clinical information for these 35 participants can be found elsewhere.[4]

The participants in the present study included 33 of the 35 participants from the previous study. These 33 participants included 14 patients with prenatal MMC repair who underwent DTI and required CSF diversion surgery and 19 patients with prenatal repair who underwent DTI but did not require surgical treatment.

The decisions for shunt placement for all the participants in the present study were made by a single neurosurgeon on the basis of the criteria set forth by the MOMS trial, first using the original protocol[3] and then adopting the revised criteria by Tulipan et al.[17] According to the initial MOMS protocol, a patient with a prenatal MMC repair requires shunt insertion if the patient meets any of the 4 criteria.[3] The first criterion (criterion 1) is that the patient meets at least 2 of the 4 following components: a) increasing occipital frontal cranial circumference, crossing percentiles; b) bulging fontanelle or split sutures; c) increasing ventriculomegaly based on consecutive imaging; and d) head circumference greater that the 95th percentile at gestational age. Criteria 2, 3, and 4 from the MOMS trial for shunt placement are the presence of marked syringomyelia with ventriculomegaly, ventriculomegaly with symptomatic Chiari malformation, and CSF leakage, respectively.[3] In 2015, on the basis of the outcome of the MOMS trial, Tulipan et al suggested revising the original MOMS criterion 1 to require 1b and at least 1 of the other 3 components of criterion 1 (1a, 1c, and 1d), a change reflecting neurosurgeons' inclination to use overt clinical signs of increased intracranial pressure to justify shunt placement.[17]

The description of the clinical variable related to the MOMS criteria for shunt placement was extracted from the notes from patients' visits to the neurosurgery clinic. All these patients had close clinical follow-up after initial visits to the neurosurgery office. The assessment based on the MOMS criteria for shunt insertion was performed multiple times during these visits. For those patients who needed shunt placement, we used the information during the last visit when the patient met the criteria of MOMS protocol before the operation. For those patients in the no-shunt group, we reviewed the notes for all the visits to the neurosurgery office within 1 year after the DTI scan. This timeframe of 12 months as the follow-up time was decided to make sure these nonshunted children included in the present study were not shunted soon after the DTI scan. Two participants from the original study were excluded from the analysis in the present study because we were not able to identify the Neurosurgery Clinic Visit record for the MOMS criteria related to clinical variables for shunt placement. All 33 remaining patients had Chiari II malformation based on prenatal imaging. Three patients in the no-shunt group had grade II or grade II-III Chiari II malformation. The other 30 patients had grade III Chiari II malformation (Online Supplemental Data). Six of the 33 patients underwent both pre- and postrepair MR imaging: Five demonstrated reversal of hind brain herniation (from grade III to grade I), and one remained unchanged (grade II).[4] The detailed demographic and clinical information for these 33 participants are included in the Online Supplemental Data.

Potential Predictive Model for the CSF Diversion Surgery

In the present study, we aimed to construct a predictive model, the CDSI, for the need for CSF diversion surgery. This composite index model would include both clinically related variables and neuroimaging (DTI) based variables. In this study, a clinical measure related to the MOMS criteria for shunt placement, the "MOMS Index," was defined as a dichotomous variable in which 1 represents a patient who met ≥ 2 of the 4 components in criterion 1 of the MOMS protocol for shunt placement and zero means that

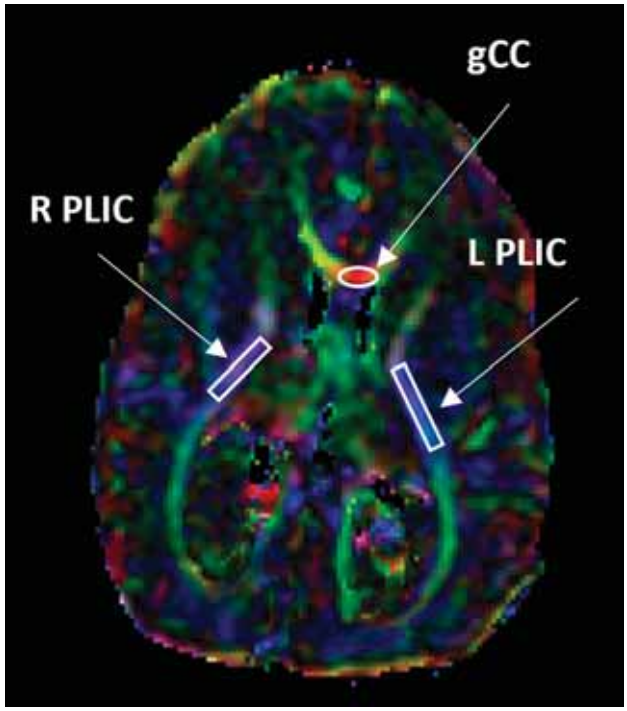

FIG 1. Illustration of ROI delineation in WM in children with prenatal MMC repair on a color-coded FA map. *Arrows* denote areas of the gCC, L PLIC, and R PLIC. L PLIC indicates left posterior limb of the internal capsule; R PLIC, right posterior limb of the internal capsule.

a patient met ≤1 of the 4 components. Patients meeting criterion 2, 3, or 4 from the MOMS protocol was rare in our study cohort: Six of 33 patients had syringomyelia (all small, between 2.5 and 4 mm); no patient had symptomatic Chiari malformation; and 1/33 had CSF leakage. Therefore, these 3 criteria were not included in the model.

DTI data were acquired with a 15-direction spin-echo EPI sequence on a 1.5T Optima MR430s scanner (GE Healthcare) customized for infant scanning.[18-20] Additional sequence specifications included the following: TR/TE = 10,000/93–98.1 ms; FOV = 200 × 200 mm; acquisition matrix = 128 × 28; in-plane resolution (resampled) = 0.78 × 0.78 mm; section thickness = 3 mm; 30 or 32 slices; b-value = all 800 with 1 exception of 1000 s/mm^2; 1 B_0; 1 average. All DTI data underwent preprocessing and analysis using the DTIStudio software (Johns Hopkins University). Additional details of the infant MR imaging scanner and the imaging sequence specifications have been reported elsewhere.[4,18-20] The neuroimaging variables derived from DTI measures included fractional anisotropy (FA) and mean diffusivity (MD) in 2 WM regions (Fig 1): the genu of the corpus callosum (gCC) and the posterior limb of the internal capsule (PLIC). On the basis of our previous data as well as reports in the literature, DTI values in these 2 ROIs were often found to be abnormal in pediatric patients with hydrocephalus or myelomeningocele.[5,13,21-25] The fronto-occipital horn ratio (FOHR),[26] based on MR imaging acquired at the time of DTI scan, was also included in the model to account for the potential effect of the severity of ventriculomegaly. Sex was tested for its significance in affecting the predictive value of the composite index. Two timing variables, including the gestational age at which the postnatal DTI data were acquired and the gestational age at which the MOMS criteria for shunt placement were assessed, were included as potential confounders in the model.

ROI placement was performed manually by a single operator. The FOHR measurement was performed by 2 operators. To evaluate the consistency of the manual performance, we assessed intrarater repeatability on the basis of the intraclass correlation coefficient,[27] using DTI values from 2 repeat trials of the same data sets. Interrater compatibility (interrater reliability) for the FOHR was assessed on the basis of the intraclass correlation coefficient using the results from the same data sets generated by the 2 operators. By means of the standard of Koo and Li[28] (poor: <0.5; moderate: 0.5–0.75; good: 0.75–0.9; excellent: >0.9), our evaluation showed that the study presented good-to-excellent repeatability and reliability with all intraclass correlation coefficient values between 0.85 and 0.95.

Statistical Analysis

All statistical analyses were performed using the Statistical Package for Social Sciences (SPSS; IBM). A logistic regression analysis was performed to assess the effects of the MOMS Index, DTI measures, the FOHR, and sex in predicting the likelihood that patients with prenatal MMC repair required shunting surgery. These independent variables, which included the MOMS Index, gCC_FA, gCC_MD, PLIC_FA, PLIC_MD, gestational age at postnatal DTI, gestational age at MOMS criteria assessment for shunt placement, sex, and the FOHR, were first assessed individually for their association with CSF diversion surgery. The continuous variables, including the 4 DTI measures, 2 age variables, and the FOHR, were *z* score–normalized before being used in the analysis, and subsequently, all these variables were evaluated in a stepwise logistic regression analysis to identify the set of most important predictors.

In the present study, the entry and remove probability was set at 0.2 and 0.25, respectively, in the stepwise logistic regression analysis. These liberal thresholds were selected to be more inclusive and allow quantitative evaluation of variables that were at a marginal level of statistical significance in the log(*P*) model. The variable selection was performed through the backward stepwise logistic regression implemented in SPSS. The selection process started with the full model, which included all the p predictors, and at each step, the potential covariate that contributed the least was excluded until all of the covariates satisfied the entry and exit criteria. No additional regularization was used in the process. To assess the risk of overfitting of the logistic regression model, we also performed leave-one-out cross-validation: The stepwise logistic regression model was derived from 32 patients and tested against the single hold-out patient and was subsequently repeated until the entire data set had been tested. The top-performing covariates from these 33 repetitions were identified to ensure model stability and generalizability.

RESULTS

Single-Predictor Logistic Regression Analysis

The results of the single-predictor logistic regression analysis with potential predictors tested individually (all with the intercept included) are summarized in Table 1. Among the 7 potential predictors tested, a significant relation between predictor and the

Table 1: Single-predictor logistic regression analysis for predicting patients who required CSF diversion surgery[a]

Predictor	β	SE	Wald χ^2	*df*	*P*	Exp(β) OR	Sensitivity	Specificity	Overall Accuracy
MOMS Index	2.262	0.841	7.236	1	.007	9.600	0.643	0.842	0.757
gCC_FA	–1.358	0.506	7.193	1	.007	0.257	0.572	0.842	0.727
gCC_MD	0.970	0.444	4.773	1	.029	2.638	0.571	0.737	0.667
PLIC_FA	–0.953	0.482	3.905	1	.048	0.386	0.500	0.842	0.697
PLIC_MD	0.794	0.506	2.464	1	.117	2.212	0.214	0.947	0.636
Sex	–0.773	0.728	1.129	1	.288	0.462	0.500	0.684	0.606
FOHR	0.173	0.362	0.230	1	.631	1.189	0.070	1.000	0.606

Note:—Sensitivity indicates the percentage of patients who were correctly predicted among patients who required surgery; Specificity, the percentage of patients who were correctly predicted among patients who did not require surgery; SE, standard error.
[a] All the predictors were tested individually with the intercept term included (not shown).

Table 2: Stepwise logistic regression analysis for predicting patients who required CSF diversion surgery

							95% CI for Exp (β)	
Predictor	β	SE	Wald χ^2	*df*	*P*	Exp (β)	Lower	Upper
MOMS Index	4.331	2.125	4.154	1	.042	76.026	1.181	4.895E + 3
gCC_FA	–1.976	0.943	4.390	1	.036	0.139	0.022	0.880
PLIC_FA	–1.283	0.747	2.953	1	.086	0.277	0.064	1.198
Sex	3.216	1.727	3.467	1	.063	0.040	0.001	1.184
FOHR	–1.335	1.078	1.508	1	.219	0.263	0.031	2.216
Constant	–0.308	0.816	3.855	1	.706	0.735	NA	NA

Note:—NA indicates not applicable.

need for surgery was found for the MOMS Index (Wald $\chi^2 = 7.236$, $P = .007$), the gCC_FA (Wald $\chi^2 = 7.193$, $P = .007$), the gCC_MD (Wald $\chi^2 = 4.773$, $P = .029$), and the PLIC_FA (Wald $\chi^2 = 3.905$, $P = .048$) based on the Wald χ^2 test. No significant association was found for the PLIC_MD, sex, and the FOHR (Table 1). The assessment of the predicted probability based on single-predictor logistic regression, including sensitivity, specificity, and overall accuracy, is also reported in Table 1.

CDSI Based on Stepwise Logistic Regression Analysis

The results from the stepwise logistic regression analysis showed the following model:

$$\begin{aligned}\text{CDSI} &= \text{logit}\,(\text{probability of CSF diversion surgery})\\ &= 4.33 \times \text{MOMS_Index} + (-1.98) \times \text{gCC_FA}\\ &\quad + (-1.28) \times \text{PLIC_FA} + (3.22) \times \text{Sex} + (-1.34)\\ &\quad \times \text{FOHR} - 0.31\end{aligned}$$

According to the model, the CDSI, which is the log of the odds of a patient with prenatal MMC repair undergoing CSF diversion surgery later, was positively associated with the MOMS Index with statistical significance based on the Wald χ^2 test (Table 2, $P = .042$). As expected, the model shows that given the values in other predictors holding constant, children who met the MOMS criteria for shunt placement were more likely (>76 times) to require CSF diversion surgery than those who did not meet these MOMS criteria (Table 2).

Among the 4 DTI measures that were entered in the stepwise logistic regression analysis, the CDSI was found to be negatively impacted by gCC_FA with statistical significance (Table 2, $P = .036$) and by the PLIC_FA with marginal significance in the association (Table 2, $P = .086$). This finding suggests that as the FA in the gCC becomes lower in value, the more likely it is that a child would require CSF diversion surgery. The gCC_MD and PLIC_MD were not significantly related to the CDSI and were excluded during the stepwise procedure in the construction of CDSI (see the Online Supplemental Data for variables not included in the equation).

The model also showed that CDSI was negatively related to the patient's sex. While the significance of the impact was marginal ($P = .063$), the data showed that the odds of a female patient who later underwent CSF diversion surgery were 24 time greater than that of a male patient (Table 2, $\text{Exp}(\beta_{\text{sex}}) = 0.04$).

Evaluation of the CDSI as Determined by the Stepwise Logistic Regression Analysis

On the basis of the likelihood ratio test, the overall model provided a better fit to the data as it improved significantly over the null model (Table 3, $P < .001$). As presented in the previous section, the statistical test of predictors included in the regression analysis showed that the regression coefficients were statistically significant for the MOMS Index and the gCC_FA and were marginally significant in the PLIC_FA and in sex based on Wald χ^2 test (Table 2). The Hosmer-Lemeshow test yielded a $\chi^2(8)$ of 7.412 and was insignificant ($P = .493$, Table 3), suggesting that the CDSI fit the data well when the null hypothesis defines a good fit between the model and the data. The variance based on the Cox-Snell test and Nagelkelke test was 54.3% and 73.0%, respectively (Table 3).

The assessment of the predicted probability based on the CDSI is summarized in Table 4. In the 33 patients assessed, the CDSI correctly predicted 11 of 14 for the CSF diversion surgery (78.6%) and 17 of 19 who did not require surgery (89.5%). The sensitivity, specificity, and false-positive and false-negative values of the CDSI are all included in Table 4.

Table 3: Overall model evaluation and goodness-of-fit for the stepwise logistic regression model

	χ^2	*df*	*P*
Overall model evaluation (likelihood ratio)	25.834	5	< .001
Goodness-of-fit test (Hosmer-Lemeshow)	7.412	8	.493
Cox-Snell test (R^2)		0.543	
Nagelkelke test (R^2)		0.730	

The leave-one-out cross-validation analysis correctly predicted the CSF diversion surgery for 28 of 33 patients. The 5 variables in the model derived from all 33 patients remained consistent in the model from the 33 repetitions of the leave-one-out cross-validation (32/33 for the MOMS Index, gCC_FA, and sex; 31/33 for the PLIC_FA and FOHR). Among these 5 variables, the MOMS Index and gCC_FA remained the top performing covariates for all the repetitions.

The Composite Index CDSI Benchmarked with Individual Indices

When we compared the CDSI on the basis of stepwise logistic regression and individual indices based on single-predictor logistic regression, the performance of the CDSI (Table 4: sensitivity = 78.6%; specificity = 89.5%, overall accuracy = 84.8%) was better than the performance of all of the individual indices in sensitivity and overall accuracy and better than most of the individual indices in specificity (Table 1). The only exceptions were the PLIC_MD and FOHR, which yielded higher specificity (94.7%, 100%, respectively) compared with CDSI. However, these 2 indices both had poorer sensitivity (21.4%, 7%, respectively) and lower overall accuracy (63.6%, 60.6%, respectively) compared with the performance of the composite index (Tables 1 and 4).

As shown in Fig 2*A*, the CDSI based on stepwise logistic regression is plotted in the order of the level of predicted probability for individual patients (solid circle). Among these, 3 patients who needed shunting and 2 patients who did not need shunting were misclassified (in the red solid circle and the blue solid circles, respectively) on the basis of the predictive model (cutoff = 0.5). By contrast, the predictive probability based on single-predictor logistic regression using the MOMS criteria for shunt placement (empty circle) yielded more cases of misclassification: 5 false-negatives and 3 false-positives (in red and blue empty circle, respectively). Figure 2*B* shows the receiver operating characteristic curve for the CDSI model performance with an area under the curve of 0.96.

DISCUSSION

In the present study, our objective was to create a composite index that could be used as a predictive model to objectively improve the capability to manage patients with ventriculomegaly and progressive hydrocephalus. Specifically, we chose a population of patients who had undergone prenatal myelomeningocele repair because these children very frequently have large ventricles at baseline, often in the absence of any detectable symptoms of increased intracranial pressure. This population is suitable for such a study in that it is homogeneous in its etiology of hydrocephalus. Additionally, surgical decision-making is not typically urgent because these patients seldom require CSF diversion

Table 4: The frequency of CSF diversion surgery and the predicted frequency by stepwise logistic regression[a]

	Predicted		
Observed	Yes	No	% Correct
Yes	11	3	78.6
No	2	17	89.5
Overall % correct			84.8

[a] Cutoff = 0.5; sensitivity = 11/(11 + 3) = 78.6%; specificity = 17/(2 + 17) = 89.5%; false-positive = 2/(2 + 17) = 10.5%; false-negative = 3/(11 + 3) = 21.4%.

shortly after birth, in contradistinction to infants undergoing standard postnatal MMC repair. Thus, the study of the fetal surgery group allows longer clinical and imaging observation for potential signs and symptoms of progressive hydrocephalus as well as radiographic markers of the condition.[29-31]

The present study was a secondary retrospective analysis using data from 33 patients with a history of prenatal MMC repair. In our previous work that used a 35-patient cohort (including the 33 patients in the present study), DTI measures were found to help differentiate patients who required shunt placement from those who did not require the surgery. More important, it was found that using DTI measures yielded higher performance in predicting future shunt placement compared with using ventricle size (FOHR), a common variable in the hydrocephalus diagnosis. In the present study, while still aiming to generate a predictive tool for shunt placement instead of testing a certain predetermined combination of 1 or 2 potential variables, we used stepwise logistic regression, a data-driven approach, to select the optimal combination of variables from 9 potential variables. In its current form, the CDSI comprises the initial MOMS trial and the subsequent MOMS Tulipan revised criteria for shunt surgery, with additional conventional clinical measures and objectives, noninvasive neuroimaging biomarkers based on well-established DTI parameters.[3,4,17] Specifically, we evaluated increasing occipital-frontal cranial circumference, bulging fontanelle or split sutures, progressively increasing ventriculomegaly based on consecutive imaging studies, head circumference greater than the 95th percentile at gestational age, and postnatal DTI measures of the FA and MD of the WM regions of the gCC and PLIC. Finally, we also included the FOHR and tested sex and age for significance.

The stepwise logistic regression analysis demonstrated the significance of the MOMS trial–related index and the DTI values in the gCC (and the marginal significance in FA in the PLIC) in the assessment of the need for hydrocephalus surgery. These findings corroborate our hypothesis and expectations on the basis of findings from other reports in the literature.[4,5,8,10,13,32,33] The potential influence of sex on the predicted probability (P = .06, Table 2) remains to be further examined for its generalizability. Currently, there is no support in the literature for the sex difference in the need for shunt placement in this patient population. It is unclear why the ventricle size variable (FOHR) was not a significant covariate in the final model from the stepwise logistic regression analysis. It may be attributed to the FOHR being an index of static measurement of ventricle size, while by contrast, the MOMS Index derived from the 4 components of the first criterion of the MOMS criteria for shunt insertion focused mainly on the trend of

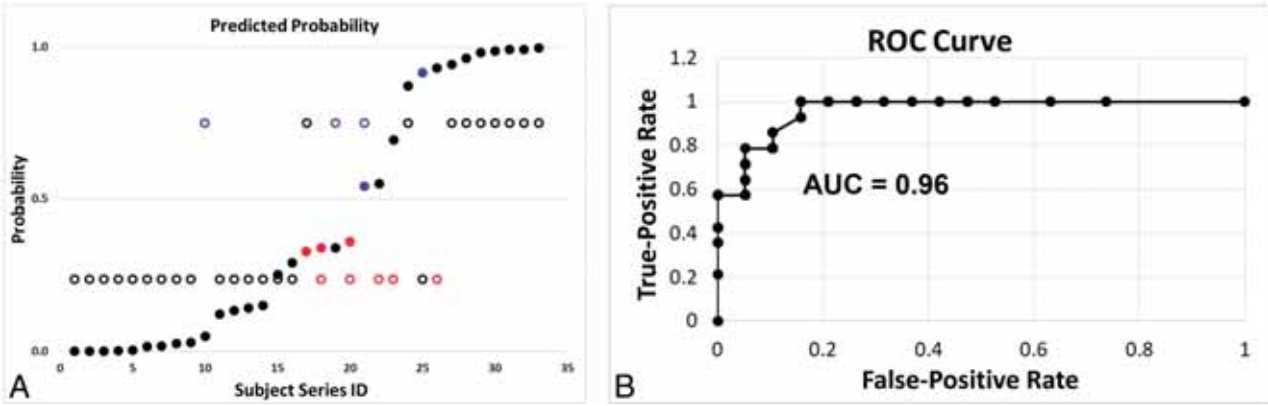

FIG 2. *A*, Comparison of the predicted probability using the CDSI model based on stepwise logistic regression (*solid circles*) and using a logistic regression model with a single predictor (the MOMS Index, in *empty circles*). The data are plotted in ascending order of the predicted probability using the CDSI model, which had 3 false-negative (*red solid circles*) and 2 false-positive cases (*blue solid circles*). The single-predictor logistic regression model using the MOMS Index yielded 5 false-negative (*red empty circles*) and 3 false-positive cases (*blue empty circles*). *B*, The receiver operating characteristic (ROC) curve demonstrating sensitivity and specificity based on the CDSI approach for predicting the need for CSF diversion surgery. AUC indicates area under the curve; ID, identification.

change of the ventricle size, which can be a more accurate reflection of the progression of the underlying disease. Potential confounding factors for the analyses in our study may involve the wide range of timing for different events, including MMC repair, imaging, and MOMS assessment (eg, the FOHR used in the model was assessed using data acquired at the time of postnatal DTI, before the assessment of the MOMS criteria for shunt placement) as well as a series of other factors such as gestational age at birth and socioeconomic status. However, these potential variables would be difficult to test in the scope of the present study due to the insufficient sample size.

As shown in Fig 2, in the 33 cases (14 needing shunt placement, 19 not needing shunt placement), there were 3 false-negative and 2 false-positive cases based on the CDSI model approach. While there is no conclusive evidence with statistical significance, there are some commonalities in the 3 false-negative cases that could help to explain the misclassification. Due to the retrospective nature, the DTI scans were all acquired before patient assessment using the MOMS criteria (and shunt placement for those who needed it). In all of these 3 false-negative cases, there were large increases in ventricle size from the time when DTI was acquired (and the FOHR calculated) to the time when these patients were assessed for their need for shunt insertion. Of note, one patient's ventricle size increased very rapidly and almost doubled in volume within 3 months after DTI scan. One patient, in whom the ventricle size increase was not as severe as in the other 2, presented with a pseudomeningocele (but no true CSF leakage), which would not resolve at the lumbar repair site. These 2 factors together were evidence of progressive hydrocephalus. In the 2 false-positive cases, 1 patient had colpocephaly with small frontal horns. Both patients presented with ventricular size increases and required continued close imaging and clinical follow-up, but the progressions were mild and did not warrant surgical intervention.

Overall, on the basis of our data analysis, the CDSI demonstrated a sensitivity of 78.6% and a specificity of 89.5%, with an overall accuracy of 84.8%, in predicting the need for CSF diversion. This result is better than the performance of all the individual indices based on sensitivity and overall accuracy and also better than most of the individual indices based on the specificity alone (Tables 1 and 4). The objective integration of noninvasive DTI measures with conventional clinical indices provides an evidence-based index that can generate highly accurate data for stratifying patients prospectively into surgical and nonsurgical treatment groups. The overall findings from this study may allow the group-based statistical analysis to be transitioned to individualized decision-making for treatment of this patient population presenting with ventriculomegaly and/or clinical hydrocephalus. As illustrated in Fig 2, the composite index of CDSI helps to integrate information from various aspects, demographic, clinical, and neuroimaging, and provides a quantitative measure of the overall evaluation, which becomes a highly convenient and clinically relevant tool for clinicians to test and apply in decision-making related to treatment in this group following prenatal myelomeningocele repair.

In a similar fashion, the model could be used to study long-term neuropsychological and functional outcomes for infants who have undergone prenatal myelomeningocele repair in comparison with those with postnatal myelomeningocele repair. Outcome studies from the MOMS trial and other post-MOMS trial investigations have reported many data with largely corroborative findings in ambulation, motor functions, and urologic functions at school age or older in these 2 patient populations.[34-39] Identifying significant predictors with the modeling approach for these patients in different subcategories would be highly relevant for the planning of therapeutic intervention and other aspects of the clinical management. In addition, the comprehensive modeling tool could also transform current subjective clinical guidelines for hydrocephalus treatment in other etiologies (eg, congenital hydrocephalus) as well as in patients presenting with hydrocephalus at older ages.

Given the retrospective nature of the current work, certain limitations of the study must be discussed. First, the study should be regarded as exploratory, given its sample-size limitation. We used liberal entry and removed probability thresholds in the stepwise

logistic regression analysis to allow assessing the potential contribution of the factors included in the model. However, the data in the present study need to be replicated with more stringent thresholds with larger-scale data to improve the generalizability of the findings. Second, multicollinearity among the predictors (eg, potential significant correlation between DTI values in the gCC and PLIC or between the MOMS Index and FOHR) may affect the precision of the estimated coefficients and could have led to biased estimates and inflated standard errors. Third, as stated in prior discussion, the timing difference between DTI and clinical evaluation may have contributed to misclassification. Including DTI as part of routine clinical MR imaging protocol and synchronizing it with clinical assessment may help to improve the predictive value of the composite index in future model development and validation studies. Fourth, we selected 2 ROIs, including the gCC and PLIC in the present study. These 2 ROIs are the WM structures that have often been reported to have DTI abnormalities. We also explored other WM regions, eg, the body and splenium of the corpus callosum, the anterior limb of internal capsule, the external capsule, and additional periventricular WM regions. However, due to the presence of ventriculomegaly, small brain size, and other factors, it is not feasible to delineate ROIs for these additional structures in a consistent manner and generate reliable data for all (or at least most) subjects.

In future prospective studies with larger group sizes, additional ROIs as well as biometric measures such as the size of the subarachnoid spaces may be included in the model in which the missing data points may be addressed analytically using imputation or other statistical approaches. Finally, also due to the insufficient power in the present study, not all clinical or radiographic variables were included in the statistical analysis, such as the presence of headache, vomiting, syringomyelia, symptomatic Chiari II malformation, or evidence of CSF leak from the myelomeningocele repair site, to name a few. Some of these factors were not included due to the low frequency of occurrence in our cohort. However, we believe that the data generated in this retrospective review have helped to close a critical knowledge gap and generated important data to support the design of a future clinical trial based on the CDSI with the long-term goal of improving the current standard of care for this patient population.

CONCLUSIONS

In the present study, we constructed a novel composite index that includes clinical, demographic, and neuroimaging measures, with the aim of assisting in the identification of hydrocephalus in patients following prenatal MMC repair. The performance of the CDSI model based on stepwise logistic regression outperformed all single-predictor models, including the models using indices derived from the MOMS trial criteria as well as a series of other variables that were tested separately. By integrating analysis of microstructural WM alterations into a comprehensive model predicting the need for surgical treatment, the CDSI may eventually serve as a robust tool to aid clinicians in their decision-making in hydrocephalus management.

Disclosure forms provided by the authors are available with the full text and PDF of this article at www.ajnr.org.

REFERENCES

1. Williams MA, McAllister JP, Walker ML, et al. **Priorities for hydrocephalus research: report from a National Institutes of Health-sponsored workshop.** *J Neurosurg* 2007;107:345–57 CrossRef Medline
2. Patel SK, Tari R, Mangano FT. **Pediatric hydrocephalus and the primary care provider.** *Pediatr Clin North Am* 2021;68:793–809 CrossRef Medline
3. Adzick NS, Thom EA, Spong CY, et al. **A randomized trial of prenatal versus postnatal repair of myelomeningocele.** *N Engl J Med* 2011;364:993–1004 CrossRef Medline
4. Yuan W, Stevenson CB, Altaye M, et al. **Diffusion tensor imaging in children following prenatal myelomeningocele repair and its predictive value for the need and timing of subsequent CSF diversion surgery for hydrocephalus.** *J Neurosurg Pediatr* 2019 Dec 20. [Epub ahead of print] CrossRef Medline
5. Hasan KM, Eluvathingal TJ, Kramer LA, et al. **White matter microstructural abnormalities in children with spina bifida myelomeningocele and hydrocephalus: a diffusion tensor tractography study of the association pathways.** *J Magn Reson Imaging* 2008;27:700–09 CrossRef Medline
6. Yuan W, Mangano FT, Air EL, et al. **Anisotropic diffusion properties in infants with hydrocephalus: a diffusion tensor imaging study.** *AJNR Am J Neuroradiol* 2009;30:1792–98 CrossRef Medline
7. Yuan W, Deren KE, McAllister JP 2nd, et al. **Diffusion tensor imaging correlates with cytopathology in a rat model of neonatal hydrocephalus.** *Cerebrospinal Fluid Res* 2010;7:19 CrossRef Medline
8. Jang SH, Kim SH. **Diffusion tensor imaging following shunt in a patient with hydrocephalus.** *J Neuroimaging* 2011;21:69–72 CrossRef Medline
9. Yuan W, McAllister JP 2nd, Lindquist DM, et al. **Diffusion tensor imaging of white matter injury in a rat model of infantile hydrocephalus.** *Childs Nerv Syst* 2012;28:47–54 CrossRef Medline
10. Scheel M, Diekhoff T, Sprung C, et al. **Diffusion tensor imaging in hydrocephalus: findings before and after shunt surgery.** *Acta Neurochir (Wien)* 2012;154:1699–1706 CrossRef Medline
11. Yuan W, McKinstry RC, Shimony JS, et al. **Diffusion tensor imaging properties and neurobehavioral outcomes in children with hydrocephalus.** *AJNR Am J Neuroradiol* 2013;34:439–45 CrossRef Medline
12. Rajagopal A, Shimony JS, McKinstry RC, et al. **White matter microstructural abnormality in children with hydrocephalus detected by probabilistic diffusion tractography.** *AJNR Am J Neuroradiol* 2013;34:2379–85 CrossRef Medline
13. Mangano FT, Altaye M, McKinstry RC, et al. **Diffusion tensor imaging study of pediatric patients with congenital hydrocephalus: 1-year postsurgical outcomes.** *J Neurosurg Pediatr* 2016;18:306–19 CrossRef Medline
14. Yuan W, Meller A, Shimony JS, et al. **Left hemisphere structural connectivity abnormality in pediatric hydrocephalus patients following surgery.** *Neuroimage Clin* 2016;12:631–39 CrossRef Medline
15. Herweh C, Akbar M, Wengenroth M, et al. **DTI of commissural fibers in patients with Chiari II-malformation.** *Neuroimage* 2009;44:306–11 CrossRef Medline
16. Assaf Y, Ben-Sira L, Constantini S, et al. **Diffusion tensor imaging in hydrocephalus: initial experience.** *AJNR Am J Neuroradiol* 2006;27:1717–24 Medline
17. Tulipan N, Wellons JC 3rd, Thom EA, et al. **Prenatal surgery for myelomeningocele and the need for cerebrospinal fluid shunt placement.** *J Neurosurg Pediatr* 2015;16:613–20 CrossRef Medline
18. Tkach JA, Hillman NH, Jobe AH, et al. **An MRI system for imaging neonates in the NICU: initial feasibility study.** *Pediatr Radiol* 2012;42:1347–56 CrossRef Medline
19. Tkach JA, Merhar SL, Kline-Fath BM, et al. **MRI in the neonatal ICU: initial experience using a small-footprint 1.5-T system.** *AJR Am J Roentgenol* 2014;202:W95–105 CrossRef Medline
20. Merhar SL, Tkach JA, Woods JC, et al. **Neonatal imaging using an on-site small footprint MR scanner.** *Pediatr Radiol* 2017;47:1001–11 CrossRef Medline

21. Ware AL, Juranek J, Williams VJ, et al. **Anatomical and diffusion MRI of deep gray matter in pediatric spina bifida.** *Neuroimage Clin* 2014;5:120–27 CrossRef Medline
22. Kulkarni AV, Donnelly R, Mabbott DJ, et al. **Relationship between ventricular size, white matter injury, and neurocognition in children with stable, treated hydrocephalus.** *J Neurosurg Pediatr* 2015;16:267–74 CrossRef Medline
23. Jang SH, Choi BY, Chang CH, et al. **The effects of hydrocephalus on the periventricular white matter in intracerebral hemorrhage: a diffuser tensor imaging study.** *Int J Neurosci* 2013;123:420–24 CrossRef Medline
24. Eskandari R, Abdullah O, Mason C, et al. **Differential vulnerability of white matter structures to experimental infantile hydrocephalus detected by diffusion tensor imaging.** *Childs Nerv Syst* 2014;30:1651–61 CrossRef Medline
25. Yuan W, Holland SK, Shimony JS, et al. **Abnormal structural connectivity in the brain networks of children with hydrocephalus.** *Neuroimage Clin* 2015;8:483–92 CrossRef Medline
26. O'Hayon BB, Drake JM, Ossip MG, et al. **Frontal and occipital horn ratio: a linear estimate of ventricular size for multiple imaging modalities in pediatric hydrocephalus.** *Pediatr Neurosurg* 1998;29:245–49 CrossRef Medline
27. McGraw KO, Wong SP. **Forming inferences about some intraclass correlation coefficients.** *Psychological Methods* 1996;1:30–46 CrossRef
28. Koo TK, Li MY. **A guideline of selecting and reporting intraclass correlation coefficients for reliability research.** *J Chiropr Med* 2016;15:155–63 CrossRef Medline
29. Heuer GG, Moldenhauer JS, Scott Adzick N. **Prenatal surgery for myelomeningocele: review of the literature and future directions.** *Childs Nerv Syst* 2017;33:1149–55 CrossRef Medline
30. Moldenhauer JS, Soni S, Rintoul NE, et al. **Fetal myelomeningocele repair: the post-MOMS experience at the Children's Hospital of Philadelphia.** *Fetal Diagn Ther* 2015;37:235–40 CrossRef Medline
31. Riva-Cambrin J, Kestle JR, Holubkov R, et al; Hydrocephalus Clinical Research Network. **Risk factors for shunt malfunction in pediatric hydrocephalus: a multicenter prospective cohort study.** *J Neurosurg Pediatr* 2016;17:382–90 CrossRef Medline
32. Mangano FT, Stevenson CB, Nagaraj U, et al. **Abnormal anisotropic diffusion properties in pediatric myelomeningocele patients treated with fetal surgery: an initial DTI study.** *Childs Nerv Syst* 2020;36:827–33 CrossRef Medline
33. Yuan W, Harpster K, Jones BV, et al. **Changes of white matter diffusion anisotropy in response to a 6-week ipad application-based occupational therapy intervention in children with surgically treated hydrocephalus: a pilot study.** *Neuropediatrics* 2016;47:336–40 CrossRef Medline
34. Brock JW 3rd, Carr MC, Adzick NS, et al; MOMS Investigators. **Bladder function after fetal surgery for myelomeningocele.** *Pediatrics* 2015;136:e906–13 CrossRef Medline
35. Danzer E, Thomas NH, Thomas A, et al. **Long-term neurofunctional outcome, executive functioning, and behavioral adaptive skills following fetal myelomeningocele surgery.** *Am J Obstet Gynecol* 2016;214:269 e261–69 CrossRef Medline
36. Farmer DL, Thom EA, Brock JW 3rd, et al. **The Management of Myelomeningocele Study: full cohort 30-month pediatric outcomes.** *Am J Obstet Gynecol* 2018;218:256 e1–13 CrossRef Medline
37. Brock JW 3rd, Thomas JC, Baskin LS, et al. **Effect of prenatal repair of myelomeningocele on urological outcomes at school age.** *J Urol* 2019;202:812–18 CrossRef Medline
38. Houtrow AJ, Thom EA, Fletcher JM, et al. **Prenatal repair of myelomeningocele and school-age functional outcomes.** *Pediatrics* 2020;145:e20191544 CrossRef Medline
39. Mohrlen U, Ochsenbein-Kolble N, Mazzone L, et al. **Benchmarking against the MOMS trial: Zurich results of open fetal surgery for spina bifida.** *Fetal Diagn Ther* 2020;47:91–97 CrossRef Medline

Percutaneous Sacroplasty with or without Radiofrequency Ablation for Treatment of Painful Sacral Metastases

Q.-H. Tian, K.-Han, T. Wang, D.-L. Min, and C.-G. Wu

ABSTRACT

BACKGROUND AND PURPOSE: Percutaneous sacroplasty is a variation of percutaneous vertebroplasty that has gained attention as a therapeutic option for patients with painful sacral insufficiency fractures due to osteoporosis or metastases. Additionally, percutaneous sacroplasty can also be used to treat painful sacral metastases without a pathologic fracture. The purpose of this retrospective study was to compare the efficacy and safety of fluoroscopy-guided percutaneous sacroplasty alone versus percutaneous sacroplasty plus radiofrequency ablation for the treatment of painful sacral metastases.

MATERIALS AND METHODS: For this retrospective study, 126 patients (with a total of 162 painful sacral metastases) were enrolled from October 2012 to February 2021 and assigned to receive either percutaneous sacroplasty plus radiofrequency ablation ($n = 51$, group A) or percutaneous sacroplasty alone ($n = 75$, group B). Four different approaches were used for percutaneous sacroplasty: transiliac, interpedicular, anterior-oblique, and posterior. The Visual Analog Scale, Oswestry Disability Index, and Karnofsky Performance Scale were used to evaluate outcomes.

RESULTS: The Visual Analog Scale, Oswestry Disability Index, and Karnofsky Performance Scale scores showed significant improvement in both groups after treatment ($P < .05$). The overall pain relief rate was significantly better in group A than in group B (90% versus 76%, $P = .032$). There were no significant differences in the incidence of polymethylmethacrylate leakage between the 2 groups or among the 4 different approaches ($P > .05$).

CONCLUSIONS: Both percutaneous sacroplasty alone and the combination of percutaneous sacroplasty and radiofrequency ablation are safe and effective for treatment of painful sacral metastases. The combination of percutaneous sacroplasty and radiofrequency ablation appears to be more effective than percutaneous sacroplasty alone.

ABBREVIATIONS: KPS = Karnofsky Performance Scale; ODI = Oswestry Disability Index; PMMA = polymethylmethacrylate; PSP = percutaneous sacroplasty; RFA = radiofrequency ablation; VAS = Visual Analog Scale

Bone metastasis is common in advanced cancers and is often the cause of severe pain. It is estimated that ~45% of patients with bone metastases do not receive adequate and appropriate treatment and therefore have avoidable pain.[1] Metastasis in the sacrum can cause intractable pain and dysfunction, confine the patient to bed, and seriously impair his or her quality of life. The current standard of treatment for sacral metastases includes systemic and local therapies. Conservative treatment with bed rest, analgesics, chemotherapy, and bisphosphonates[2] and radiation therapy—which are often used as first-line treatments—do not provide mechanical support or complete pain relief.[3] Meanwhile, surgical treatment is limited by the prolonged recovery time and the high risk of complications and mortality.[4]

Percutaneous sacroplasty (PSP), developed from percutaneous vertebroplasty, is a promising option for the treatment of osteoporotic sacral insufficiency fractures and sacral metastases.[5-8] However, the few studies to date on the use of PSP for the treatment of painful sacral metastases have had small sample sizes and/or did not examine the use of PSP in combination with other therapies.[9-12]

Received April 1, 2022; accepted after revision June 7.

From the Departments of Diagnostic and Interventional Radiology (Q.-H.T., T.W., C.-G.W.) and Oncology (K.-H., D.-L.M.), Shanghai Jiao Tong University Affiliated Sixth People's Hospital, Shanghai, China.

This work was sponsored by grants from the National Natural Scientific Fund of China (grant No. 81701798, 81703751), the Natural Fund from Shanghai Science and Technology Commission (grant No. 19411971800), and the Natural Fund from Shanghai Municipal Health Commission (grant No. 202040340).

All the funding played important roles in design of the study and collection, analysis, and interpretation of data and in writing the manuscript.

Please address correspondence to Chun-Gen Wu, MD, PhD, Shanghai Jiao Tong University Affiliated Sixth People's Hospital, No. 600 Yishan Road, Shanghai 200233, China; e-mail: 649514608@qq.com

Indicates open access to non-subscribers at www.ajnr.org

Indicates article with online supplemental data.

http://dx.doi.org/10.3174/ajnr.A7587

Baseline characteristics and clinical outcomes in patients with sacral metastatic tumors between the 2 groups

Characteristic	PSP + RFA (Group A; *n* = 51)	PSP (Group B; *n* = 75)	*P*
Age (mean) (yr)	57.22 (SD, 11.41)	62.11 (SD, 13.37)	.132
Male/female	27:24	42:33	.085
Lung cancer/other cancer (No./No)	17/34	27/48	.758
Postoperative radiation/no radiation (No./No.)	17/34	29/46	.542
Zone I/other zones (No./No.)	32/26	63/41	.503
Lesion volume (mean) (mL)	7.22 (SD, 1.74)	6.69 (SD, 1.96)	.124
Posterior approach/other approaches (No./No.)	19/37	41/50	.183
Technical success (No.) (%)	51 (100)	75 (100)	.999
Operation time (mean) (min)	47.56 (SD, 5.31)	38.67 (SD, 5.19)	.002
Cement leakage (No.) (%)	10 (17.24)	20 (19.23)	.361
Cement filling volume (mean) (range) (mL)	6.42 (SD, 1.73) (3–8)	5.31 (SD, 1.52) (2–8)	.001
Degree of cement filling (%)	84.82% (SD, 0.37%)	76.16% (SD, 0.77%)	.001
Clinical follow-up (mean) (mo)	10.08 (SD, 6.28)	10.18 (SD, 5.59)	.823

The aim of this retrospective study was to assess the safety and efficacy of PSP under fluoroscopy for the treatment of painful sacral metastases unresponsive to conservative treatments and to compare long-term outcomes after treatment with PSP alone versus PSP plus radiofrequency ablation (RFA).

MATERIALS AND METHODS

All procedures performed in studies involving human participants were in accordance with the ethical standards of the institutional and/or national research committee and with the 1964 Helsinki declaration and its later amendments or comparable ethical standards.

Patients

The institutional ethics committee of our hospital approved this study. Informed consent was obtained from all individual participants included in the study. Consecutive patients presenting with sacral metastases and severe pain at our clinic between October 2012 and February 2021 were approached for enrollment in this study. Those who expressed a willingness to participate were assigned to receive either PSP plus RFA or PSP alone. The inclusion criteria were the following: 1) older than 18 years of age; 2) sacral metastases with severe pain and an inability to walk or sit; 3) metastasis of ≤3 cm in diameter; 4) no relief with conventional treatments (opioids, radiation therapy, and chemotherapy); 5) unwilling to undergo or unfit for surgical treatment due to poor performance status; 6) life expectancy ≥3 months; and 7) willingness to provide a signed consent. The exclusion criteria were the following: 1) erosion of the neuroforamina or epidural tumor; 2) systemic infection; 3) uncorrectable coagulation disorder (international normalized ratio > 1.50, platelet count < 90×10^9/L); 4) allergy to polymethylmethacrylate (PMMA); or 5) concurrent severe cardiopulmonary disease. Before 2017, only PSP was performed in these patients. Since 2018, with the introduction of radiofrequency equipment, we have adopted a combination of PSP and RFA to treat these patients. Of the 126 patients who met the eligibility criteria, 51 were assigned to receive PSP plus RFA (group A), and 75, to receive PSP alone (group B). The ethics committee of our hospital approved this study. Informed consent was obtained from all participants.

Lesions

Although sacral metastases in the present study were not associated with pathologic fractures, these lesion zones were classified according to the Denis fractured zones.[13] Among the 126 patients, there were 95 zone 1 metastases (ie, metastasis of the sacral ala lateral to the neural foramina); 30 zone 2 metastases (ie, metastasis in foramina area); and 37 zone 3 metastases (ie, metastasis involving the sacral body and spinal canal). The primary cancers included lung ($n = 44$), liver ($n = 22$), thyroid ($n = 21$), breast ($n = 16$), prostate ($n = 10$), kidney ($n = 8$), epithelioid hemangiosarcoma ($n = 2$), gallbladder ($n = 1$), colon ($n = 1$), and parotid ($n = 1$). Among the 126 patients with sacral metastases, 76 also received treatment for lesions at other locations, ie, the spine (56 patients) and the pelvis (20 patients). The PSP/RFA procedures were performed after radiation therapy in 17 group A patients and 29 group B patients. Radiation therapy was not indicated in 34 group A patients and 46 group B patients before the PSP/RFA procedures. All patients routinely received systemic medical therapy (including bisphosphonate). The Table shows the patients' baseline characteristics and a summary of the results.

Procedure

Three doctors, all with >15 years of extensive experience in musculoskeletal intervention, performed PSP/RFA. The patient was placed on the operating table in the prone position. All procedures were performed with the patient under local anesthesia (2% lidocaine) and conscious sedation. Strict aseptic techniques were followed. The approach chosen (posterior, anterior-oblique, interpedicular, and transiliac) depended on the location of the lesion, with the aim being to reach the targeted lesion via the shortest distance without causing vessel or nerve damage (Figs 1 and 2). Generally, the anterior-oblique, transiliac, or posterior approaches were selected for lesions in the sacral ala, while the posterior approach was selected for lesions in other parts of the sacrum; the interpedicular approach was used for metastases in the sacral bodies.

The bone puncture needle—either a 13.8-cm 15-ga C1616A Bard TruGuide Disposable Coaxial Biopsy Needle (Bard Peripheral Vascular) or a 10-cm 13-ga beveled Murphy I bone puncture needle (Cook)—was inserted into the lesion under fluoroscopic guidance. Lateral and anterior-posterior fluoroscopic guidance was used to ensure a safe distance between the needle tip and critical structures such as sacral foramina and anterior surface of the sacrum. When necessary, the needle tip was rotated so that the beveled side faced the structure to be protected. In some cases, >1 needle was used. After the needle tip had entered the target lesion, PMMA (Palacos

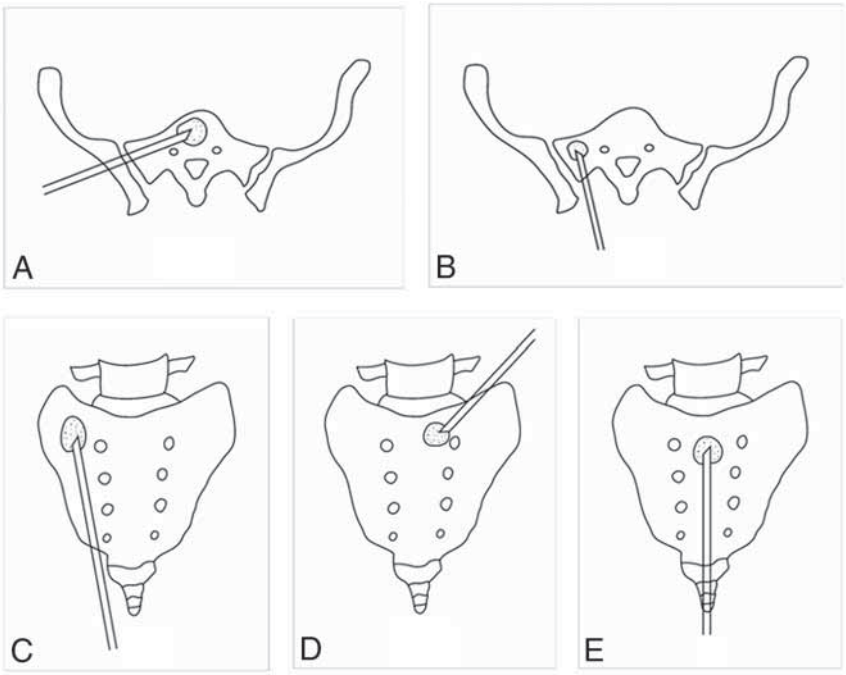

FIG 1. Drawings show the puncture needles in place for the 4 different approaches: the transiliac approach (*A*), short-axis technique of posterior approach (*B*), long-axis technique of posterior approach (*C*), anterior-oblique approach (*D*), and interpedicular approach (*E*).

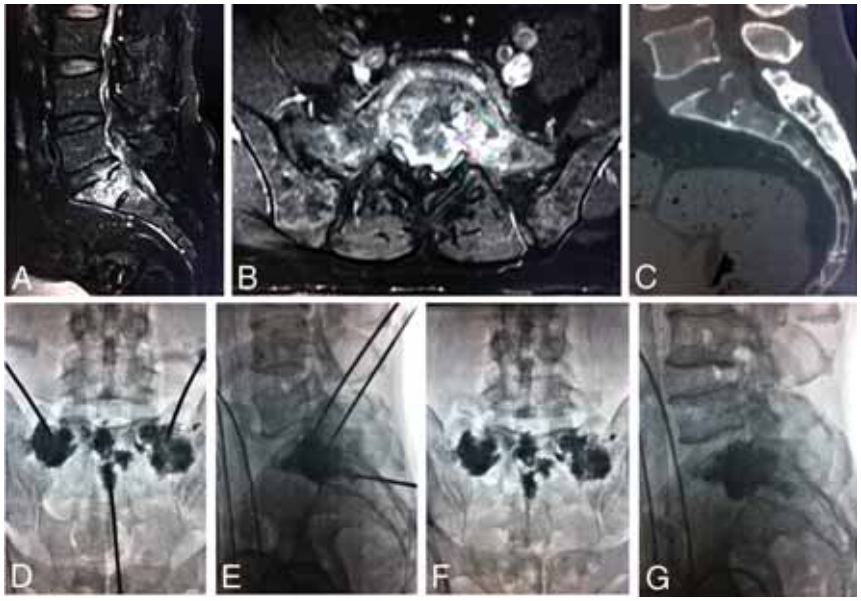

FIG 2. PSP procedure. *A–C*, Metastatic lesions in the sacral ala and bodies can be seen on enhanced sagittal and axial T1-weighted MR imaging and sagittal reconstruction CT images. *D* and *E*, Radiographs obtained during percutaneous cement injection with the patient in the supine position. *F* and *G*, After PSP, there is homogeneous and sufficient distribution of bone cement in the lesions.

V; Heraeus Medical) was injected under continuous bilateral fluoroscopic monitoring. The injection was stopped when the bone cement reached the posterior wall of the sacrum, the edge of a sacral foramina, or the margin of the sacroiliac joint.

For patients receiving PSP plus RFA, the RFA was performed first. After installation of the bone needle, an RFA electrode with a 1- to 3-cm active tip (UniBlate 17-ga; AngioDynamics) was inserted coaxially into the needle, and ablation was applied with a power setting of 30 W. The ablation range was determined by lesion size, which was assessed by enhancement MR imaging and CT beforehand. The temperature at the tip of the needle ranged from 70°C to 90°C. Complete ablation was defined either by reaching a mean target temperature of 85°C maintained for at least 10 minutes or by reaching an obvious increase of impedance (so-called "roll-off") twice, corresponding to a complete coagulation necrosis. In addition, neural reflex including acute severe sacral pain and paresthesia and/or dyspraxia in the levator ani or urethral sphincter of any patient was closely observed, and RFA was immediately stopped if the patient developed neurologic symptoms. After RFA, PMMA cement was carefully injected into the lesion. CT was performed immediately after the procedure to evaluate the cement distribution and identify leakage.

Outcome Evaluation

Two of the authors performed thorough clinical examinations of all patients before treatment, at 1 day after treatment, and then at 1, 3, 6, and 12 months after treatment. Outcome measures were technical success, complications, and improvement of pain and mobility. Technical success was defined as successful performance of puncture, RFA, and cement injection without major complications. The volume of each lesion was measured on the CT scans.[14] The degree of cement filling was calculated by the maximum diameter of the cement deposit compared with the maximum diameter of the lesion.[11] Clinical efficacy was assessed by measuring improvement in pain and function. Pain relief was measured by the changes in analgesic use, analgesic scale, Visual Analog Scale (VAS) score, and the overall rate of pain relief.[5,15,16] Functional outcome was assessed using the Oswestry Disability Index (ODI) and Karnofsky Performance Scale (KPS).[17,18] Major and minor complications were defined according to the reporting standards of the Society of Interventional Radiology.[19]

Major complications were those resulting in persistent morbidity or requiring an operative intervention, and minor complications were those that were transient, requiring only a temporary medical intervention.

Statistical Analysis

SPSS Statistics 22 (IBM) was used for statistical analysis. Normally distributed continuous variables were summarized as mean (SD) and compared between groups using the independent samples *t* test. Categoric variables were summarized as percentages and compared using the χ^2 test. Statistical significance was at $P < .05$.

RESULTS

The 126 patients (69 men and 57 women) in this study had a mean age of 58.35 (SD, 13.62) years (age range, 18–89 years). A total of 162 lesions were treated in these 126 patients: 58 lesions in the 51 group A patients and 104 lesions in the 75 group B patients. The mean volumes of lesions were 7.22 (SD, 1.74) mL and 6.69 (SD, 1.96) mL in groups A and B, respectively ($P > .05$). Some adjacent lesions were treated through a single bone puncture needle. The procedures were well-tolerated by all patients, and the technical success rate was 100%. In the present study, 147 approaches were used for 162 lesions in total. The posterior approach was used in 60 patients; the transiliac approach, in 16 patients; the anterior-oblique approach, in 32 patients; and the interpedicular approach, in 39 patients. The mean procedural time was 45.5 (SD, 4.3) minutes (range, 37–49 minutes). The number of needles used per lesion ranged from 1 to 3 (mean, 1.38 [SD, 0.78]). The mean amount of cement injected per lesion was 6.42 (SD, 1.73) mL; range, 3–8 mL in group A versus 5.31 (SD, 1.52) mL; range, 3–8 mL in group B ($P < .001$). The mean degree of cement filling was 84.82% (SD, 0.37%) in group A, while it was 76.16% (SD, 0.77%) in group B ($P < .05$). In group A, the mean number of overlapping RFAs and complete ablation cycles was 1.89 (SD, 0.75) and 2.03 (SD, 1.54), respectively. The mean time taken for RFA was 7.54 (SD, 2.62) minutes.

No major complications occurred in group A; and only 1 major complication of extravasated cement requiring surgical intervention, in group B. Cement leakage occurred in 10/58 (17%) of the treated lesions in group A and 20/104 (19%) of treated lesions in group B. No group A patient had symptoms. However, 3 group B patients had symptoms: One had radicular pain, and 2 had of focal stabbing pain, which was due to soft-tissue cement extravasation; one of these patients needed surgical resection of the extravasated cement for relief of pain.

The mean hospital stay was 4.51 (SD, 1.69) days (range, 2–7 days), and mean postprocedural follow-up was 10.13 (SD, 6.78) months (range, 3–12 months). In group A, the mean VAS score decreased from 7.43 (SD, 1.56) before the procedure to 2.25 (SD, 1.35) on day 1 after the procedure ($P < .001$). On day 1 after the procedure, 46 patients reported pain relief, but 5 patients had no improvement. In group B, the mean VAS score decreased from 7.45 (SD, 1.61) before the procedure to 3.02 (SD, 1.55) on day 1 after the procedure ($P < .001$) (Online Supplemental Data). While 57 had pain relief, 19 had no improvement. The overall pain relief rate was significantly better in group A than in group B (90% versus 76%, $P = .032$).

On day 1 after the procedure, 46/51 (90.19%) patients in group A discontinued or reduced the dosage of narcotic analgesics. Postprocedural pain was controlled with weak opioid analgesics (4 patients) or nonsteroidal anti-inflammatory drugs (7 patients); the remaining 35 patients did not require any analgesic therapy after the procedure. The mean analgesic scale decreased from 3.28 (SD, 1.42) before the procedure to 0.93 (SD, 1.38) postprocedure ($P < .001$). In group B, 57/75 (76%) patients discontinued or reduced analgesic drug dosages on day 1 after the procedure. Postprocedural pain was controlled with weak opioid analgesics (9 patients) or nonsteroidal anti-inflammatory drugs (18 patients); no analgesic therapy was necessary for the remaining 30 patients. The mean analgesic scale decreased from 3.47 (SD, 1.31) before the procedure to 1.83 (SD, 2.04) postprocedure ($P < .001$). Furthermore, in both groups, the mean VAS, ODI, and KPS scores at each follow-up were significantly different from baseline scores ($P < .05$; Online Supplemental Data). Meanwhile, the changes in KPS, VAS, and ODI scores were not significantly different between patients with lesions in the 3 different zones and those treated via the 4 different approaches ($P > .05$).

DISCUSSION

The spine is the most common site of skeletal metastases, with 1%–7% of all skeletal metastases being in the sacrum.[20] Sacral metastases reduce mechanical support and result in intractable radiating pain, often associated with immobility and a severely impaired quality of life. Currently, there is no consensus on the best treatment for sacral metastases. Traditional treatments, which include chemotherapy, surgery, targeted drugs, and radiation therapy, can kill tumor cells and reduce pain severity, but they act slowly and do not compensate for bone loss.[21-24] Moreover, >80% of patients with sacral metastases have an advanced tumor stage and poor physical condition, making them ineligible for surgical treatment.[25]

PSP is a minimally invasive procedure that has been proved to effectively repair bone defects, inactivate metastatic cells, and relieve pain in patients with osteoporotic insufficiency or pathologic fractures in the sacrum.[1,5-7] The present study—comprising 126 patients with 162 metastatic lesions—is one of the largest studies to date on the use of PSP to treat sacral metastases; the previously published largest study was on a cohort of 42 patients.[2] Consistent with previous reports, we found that PSP with or without RFA could provide immediate and lasting pain relief and allow functional recovery in patients with lesions in any part of the sacrum; significant improvement was noted in the VAS, ODI, and KPS scores after treatment with both PSP alone and PSP plus RFA.

With advances in technology, PSP continues to evolve. Modified PSP can be applied with balloon dilation, ablation, screw fixation, and high-viscosity cement augmentation.[26-30] Balloon dilation immediately after needle placement creates an easily accessible cavity that will allow more cement filling.[26] Radiofrequency sacroplasty brings a low rate of leakage with highly viscous cement insertion and good results with regard to pain reduction.[27] Lee et al[28] reported that PSP combined with cryoablation could effectively treat sacral tumoral pain refractory to medical therapy. Andresen et al[29] compared balloon sacroplasty with radiofrequency sacroplasty and concluded that both can enable reliable cement

augmentation and achieve equally good clinical outcomes in the medium term. Contrary to the results of the present study, a previous meta-analysis indicated that these technical modifications were not associated with increased or decreased VAS study effect size compared with standard PSP.[30]

In theory, RFA before PSP can decrease tumor cell spread and the risk of cement extravasation by destroying viable tumor cells and embolizing venous channels; this result can be especially important in patients with a long life expectancy. Therefore, the combination of ablation and PSP is often recommended. In the present study, we found significantly better improvement in overall pain and mobility in patients treated with PSP plus RFA than in patients treated with PSP alone, indicating that PSP and RFA may act synergistically to provide pain relief. RFA can efficiently destroy tumor cells, decrease needle tract implantation metastases, and help avoid bone cement extravasation.[11] The analgesic effect of RFA is due to destruction of pain-carrying nerves and tumor cells that produce pain-intensifying cytokines and growth factors. Meanwhile, PSP can provide immediate bone consolidation and anesthesia. This synergistic action is especially important for patients with a relatively long life expectancy. We believe that PSP plus RFA should be the preferred treatment for painful sacral metastases, regardless of the medical expense.

Because of the complex anatomy of the sacrum, the technique of PSP continues to evolve. Currently, the safest guidance system for interventional treatment is angiography with integrated CT, which enables precise puncture and real-time monitoring of the cement injection. In this study, we chose fluoroscopic guidance mainly because it allows real-time imaging during both PSP and RFA; it is especially useful during the cement-filling process. Except for 1 case of cement leakage that required surgery, none of the remaining patients experienced major complications, confirming the safety and reliability of fluoroscopic guidance.

Currently, there are 4 different approaches for PSP: transiliac, interpedicular, anterior-oblique, and posterior (which include the long-axis technique and the short-axis technique).[31-34] In the present study, the efficacy and safety of the different approaches were similar. Because it is the practice in our institution for examinations and interventional procedures to be scheduled during 1 hospitalization, a prolonged hospital stay was observed, and the mean hospital stay was 4.51 (SD, 1.69) days in this study.

The main limitations of the present study are its single-center nature, lack of comparison with conservative or surgical treatments, and the heterogeneity of the metastatic tumor site and size. In addition, providers who clinically assessed patients were not blinded to PSP with or without RFA. This feature may also be a confounding factor in drawing more objective conclusions.

CONCLUSIONS

PSP, used alone or in combination with RFA, is safe and effective for the treatment of sacral metastases not responding to conservative treatments. The combination of PSP and RFA may provide better pain relief and mobility improvement. Large multicenter prospective studies are required to confirm these results.

Disclosure forms provided by the authors are available with the full text and PDF of this article at www.ajnr.org.

REFERENCES

1. Meuser T, Pietruck C, Radbruch L, et al. **Symptoms during cancer pain treatment following WHO-guidelines: a longitudinal follow-up study of symptom prevalence, severity and etiology.** *Pain* 2001;93:247–57 CrossRef Medline
2. Pereira LP, Clarençon F, Cormier E, et al. **Safety and effectiveness of percutaneous sacroplasty: a single-centre experience in 58 consecutive patients with tumors or osteoporotic insufficient fractures treated under fluoroscopic guidance.** *Eur Radiol* 2013;23:2764–72 CrossRef Medline
3. Agarawal J, Swangsilpa T, Van der Linden Y, et al. **The role of external beam radiotherapy in the management of bone metastases.** *Clin Oncol (R Coll Radiol)* 2006;18:747–60 CrossRef Medline
4. Sun M, Zuo D, Wang H, et al. **Surgical treatment of sacral metastatic tumors.** *Front Oncol* 2021;11:640933 CrossRef Medline
5. Kortman K, Ortiz O, Miller T, et al. **Multicenter study to assess the efficacy and safety of sacroplasty in patients with osteoporotic sacral insufficiency fractures or pathologic sacral lesions.** *J Neurointerv Surg* 2013;5:461–66 CrossRef Medline
6. Gupta AC, Chandra RV, Yoo AJ, et al. **Safety and effectiveness of sacroplasty: a large single-center experience.** *AJNR Am J Neuroradiol* 2014;35:2202–06 CrossRef Medline
7. Frey ME, Warner C, Thomas SM, et al. **Sacroplasty: a ten-year analysis of retrospective patients treated with percutaneous sacroplasty.** *Pain Phys* 2017;7:E1063–72 CrossRef Medline
8. Yang SC, Tsai TT, Chen HS, et al. **Comparison of sacroplasty with or without balloon assistance for the treatment of sacral insufficiency fractures.** *J Orthop Surg (Hong Kong)* 2018;26:2309499018782575 CrossRef Medline
9. Andresen R, Radmer S, Lüdtke CW, et al. **Balloon sacroplasty as a palliative pain treatment in patients with metastasis-induced bone destruction and pathological fractures.** *Rofo* 2014;186:881–86 CrossRef Medline
10. Moussazadeh N, Laufer I, Werner T, et al. **Sacroplasty for cancer-associated insufficiency fractures.** *Neurosurgery* 2015;76:446–50 CrossRef Medline
11. Burgard CA, Dinkel J, Strobl F, et al. **CT fluoroscopy-guided percutaneous osteoplasty with or without radiofrequency ablation in the treatment of painful extraspinal and spinal bone metastases: technical outcome and complications in 29 patients.** *Diagn Interv Radiol* 2018;24:158–65 CrossRef Medline
12. Madaelil TP, Wallace AN, Jennings JW. **Radiofrequency ablation alone or in combination with cementoplasty for local control and pain palliation of sacral metastases: preliminary results in 11 patients.** *Skeletal Radiol* 2016;45:1213–19 CrossRef Medline
13. Denis F. **The three column spine and its significance in the classification of acute thoracolumbar spinal injuries.** *Spine (Phila Pa 1976)* 1983;8:817–31 CrossRef Medline
14. Kothari RU, Brott T, Broderick JP, et al. **The ABCs of measuring intracerebral hemorrhage volumes.** *Stroke* 1996;27:1304–05 CrossRef Medline
15. Zanoli G, Stromqvist B, Jonsson B. **Visual analog scales for interpretation of back and leg pain intensity in patients operated for degenerative lumbar spine disorders.** *Spine (Phila Pa 1976)* 2001;26:2375–80 CrossRef Medline
16. Farrar JT, Young JP Jr, LaMoreaux L, et al. **Clinical importance of changes in chronic pain intensity measured on an 11-point numerical pain rating scale.** *Pain* 2001;94:149–58 CrossRef Medline
17. Fairbank J, Pynsent P. **The Oswestry Disability Index.** *Spine (Phila Pa 1976)* 2000;25:2940–53 CrossRef Medline
18. Yıldız Çeltek N, Süren M, Demir O, et al. **Karnofsky Performance Scale validity and reliability of Turkish palliative cancer patients.** *Turk J Med Sci* 2019;49:894–98 CrossRef Medline
19. Cardella JF, Kundu S, Miller DL, et al; Society of Interventional Radiology. **Society of Interventional Radiology clinical practice guidelines.** *J Vasc Interv Radiol* 2009;20:S189–91 CrossRef Medline

20. Perrin RG, Laxton AW. **Metastatic spine disease: epidemiology, pathophysiology, and evaluation of patients.** *Neurosurg Clin N Am* 2004;15:365–73 CrossRef Medline
21. Zhang J, Wu CG, Gu YF, et al. **Percutaneous sacroplasty for sacral metastatic tumours under fluoroscopic guidance only.** *Korean J Radiol* 2008;9:572–76 CrossRef Medline
22. Quraishi NA, Giannoulis KE, Edwards KL, et al. **Management of metastatic sacral tumors.** *Eur Spine J* 2012;21:1984–93 CrossRef Medline
23. Matcuk GR Jr, Mahanty SR, Skalski MR, et al. **Stress fractures: pathophysiology, clinical presentation, imaging features, and treatment options.** *Emerg Radiol* 2016;23:365–75 CrossRef Medline
24. Chow R, Hoskin P, Hollenberg D, et al. **Efficacy of single fraction conventional radiation therapy for painful uncomplicated bone metastases: a systematic review and meta-analysis.** *Ann Palliat Med* 2017;6:125–42 CrossRef Medline
25. Laitinen MK, Parry MC, Albergo JI, et al. **Is computer navigation when used in the surgery of iliosacral pelvic bone tumours safer for the patient?** *Bone Joint J* 2017;99:261–66 CrossRef Medline
26. Andresen R, Radmer S, Kamusella P, et al. **Individual approaches adapted to the course of the fracture in CT-assisted balloon sacroplasty for the treatment of insufficiency fractures of the sacrum.** *Bone* 2012;50:S162 CrossRef
27. Andresen R, Lüdtke CW, Radmer S, et al. **Radiofrequency sacroplasty (RFS) for the treatment of osteoporotic insufficiency fractures.** *Eur Spine J* 2015;24:759–63 CrossRef Medline
28. Lee JH, Stein M, Roychowdhury S. **Percutaneous treatment of a sacral metastasis with combined embolization, cryoablation, alcohol ablation and sacroplasty for local tumor and pain control.** *Interv Neuroradiol* 2013;19:250–53 CrossRef Medline
29. Andresen R, Radmer S, Andresen JR, et al. **Comparison of the 18-month outcome after the treatment of osteoporotic insufficiency fractures by means of balloon sacroplasty (BSP) and radiofrequency sacroplasty (RFS) in comparison: a prospective randomised study.** *Eur Spine J* 2017;26:3235–40 CrossRef Medline
30. Chandra V, Wajswol E, Shukla P, et al. **Safety and efficacy of sacroplasty for sacral fractures: a systematic review and meta-analysis.** *J Vasc Interv Radiology* 2019;30:1845–54 CrossRef Medline
31. Fırat AK, Gümüş B, Kaya E, et al. **Interpedicular approach in percutaneous sacroplasty for treatment of sacral vertebral body pathologic fractures.** *Cardiovasc Intervent Radiol* 2011;34:282–87 CrossRef Medline
32. Dmytriw AA, Talla K, Smith R. **Percutaneous sacroplasty for the management of painful pathologic fracture in a multiple myeloma patient: case report and review of the literature.** *Neuroradiol J* 2017;30:80–83 CrossRef Medline
33. Tian QH, Liu HF, Wang T, et al. **Percutaneous sacroplasty for painful sacral metastases involving multiple sacral vertebral bodies: initial experience with an interpedicular approach.** *Korean J Radiol* 2019;20:939–46 CrossRef Medline
34. Tian QH, Liu HF, Wang T, et al. **Fluoroscopy-guided percutaneous sacroplasty for painful metastases at the sacral ala.** *J Pain Res* 2020;13:151–56 CrossRef Medline

2018–2022 Radiology Residency and Neuroradiology Fellowship Match Data: Preferences and Success Rates of Applicants

The demand for radiology residency positions varies from year to year. Such demand may be affected by several factors such as job market forces, advancements in technology (artificial intelligence, new modalities, and noninvasive treatments),[1] and the growing use of remote telemedicine solutions. The coronavirus disease 2019 (COVID) pandemic has disproportionately affected those specialties with direct face-to-face patient care (eg, internal medicine, emergency medicine, family medicine, pediatrics) over such specialties as radiology, whose practitioners may be able to conduct nearly all of their work via remote practice. We analyzed the data of the 2021 and 2022 National Resident Matching Program (NRMP) (COVID years), comparing diagnostic radiology versus other specialties, and those years from 2018 to 2020. We also studied the Neuroradiology Fellowship match statistics from 2018 to 2022. We hypothesized the following: 1) Radiology remains a highly sought-after specialty, 2) its competitiveness for positions is in the top tier of residency specialty programs, and 3) the changes in match results during the pandemic years of 2021 and 2022 would be minimal.

We used the online "Advanced-Data Tables for 2022 Match" and the "Results and Data of the 1998–2021 Main Residency Match" from the NRMP archives of the 2018–2022 residency match[2] to compare radiology applicant numbers and match rates with other specialties. We included all fields of medicine that had >1000 applicants to the specialty. The definition of the match success in this study was a match to the preferred specialty that was the applicant's first-ranked program. Matching to another specialty or failure to match at any slots was considered a lack of success in the match according to the analysis algorithm of the NRMP. Success rates were determined by dividing the number that matched according to their specialty preferences by the number of applicants applying.[2,3]

For all applicants in 2022, radiology was the ninth most popular specialty after internal medicine, family medicine, pediatrics, emergency medicine, general surgery, psychiatry, anesthesiology, and obstetrics-gynecology (Table).[2] This finding remained true each year from 2018 to 2022, for both US Medical Doctor seniors (USMDs) and US Doctor of Osteopathy seniors (USDOs). Radiology had the highest rate of increased applications (20%) of all specialties between 2020 and 2022.[2,3] For USMD and USDO students, radiology was the most competitive specialty in 2022 with the lowest successful match rates (64.5% and 45.1%, respectively).

Popularity ranking (by number of applicants) of specialties with >1000 applicants[a]

Specialty	2022 (Total Applicants)	2021	2020	2019	2018	Percentage Change 2020–2022
Internal medicine	1 (13,844)	1 (13,787)	1 (13,118)	1 (12,527)	1 (11,917)	+5.2%
Family medicine	2 (7425)	2 (7496)	2 (7175)	2 (6652)	2 (6421)	+3.4%
Pediatrics	3 (3824)	3 (3976)	3 (3728)	3 (3638)	3 (3647)	+2.5%
Emergency medicine	4 (3081)	4 (3734)	4 (3323)	4 (3048)	4 (2901)	−7.9%
General surgery	5 (3071)	6 (2908)	6 (2713)	6 (2563)	6 (2391)	+11.7%
Psychiatry	6 (2908)	5 (2948)	5 (2798)	5 (2767)	5 (2739)	+3.8%
Anesthesiology	7 (2691)	7 (2706)	7 (2418)	7 (2226)	7 (2011)	+10.1%
OBGYN	8 (2161)	8 (2030)	8 (2014)	8 (2026)	8 (1879)	+6.8%
Diagnostic radiology	9 (1850)	9 (1657)	9 (1480)	9 (1520)	9 (1603)	+20%
Orthopedic surgery	10 (1470)	11 (1289)	11 (1192)	11 (1037)	11 (1017)	+19.9%
Neurology	11 (1463)	10 (1441)	10 (1226)	10 (1152)	10 (1143)	+16.2%

Note:—OBGYN indicates Obstetrics-Gynecology.

[a] Radiology has remained the ninth most popular specialty throughout the 5-year period as far as the number of applicants with internal medicine, family medicine, pediatrics, and emergency medicine having the most applicants year after year.

http://dx.doi.org/10.3174/ajnr.A7565

From 2018 to 2021, radiology ranked between the second and fourth most competitive specialty.[2] International medical graduates (IMGs) accounted for 9.1% (91/996) of successful matches in radiology in 2022, down from 13.0% in 2021.

From 2018 to 2021, the number of positions offered in neuroradiology increased from 241 to 285, with successful matches increasing from 163 (67.6%) to 226 (79.3%), respectively.[4] While the percentage of USMDs filling neuroradiology slots decreased from 78.5% to 61.9% during that time, the percentage rebounded in 2022 to 69.7% (168/241 filled).[4] The percentage of 2022 neuroradiology-matched positions filled by IMGs was 20.3% (49/241). These IMG rates are much higher than those seen in diagnostic radiology year to year. Neuroradiology remained the most sought-after specialty in the radiology fellowship match from 2018 to 2022. We conclude that radiology remains in the upper echelon of preferred fields of medicine and was the most competitive field to enter in 2022. During the COVID years, applications to radiology have surged. This has resulted in more USMD acceptances in radiology residencies. Overall, neuroradiology remains the most popular radiology subspecialty and has seen a higher rate of IMGs entering the field across time, peaking in 2021.

Disclosure forms provided by the authors are available with the full text and PDF of this article at www.ajnr.org.

REFERENCES

1. Burgess L. **Why I decided to become a radiologist.** *The MDU Student Journal* 2018
2. Lamb DL. **National Resident Matching Program, Results and Data: 2022 Main Residency Match and Research Reports, Charting Outcomes in the Match 2018, 2019, 2020, 2021.** National Resident Matching Program. https://www.nrmp.org/match-data-analytics/residency-data-reports/. Accessed March 22, 2022
3. Lamb DL. **Results and Data: 2021 Main Residency Match Results.** National Resident Matching Program. 2022. https://www.nrmp.org/wp-content/uploads/2021/08/MRM-Results_and-Data_2021.pdf. Accessed March 22, 2022
4. Lamb DL. **Fellowship Match Data & Reports.** 2022. https://www.nrmp.org/match-data-analytics/fellowship-data-reports/. Accessed May 2, 2022

F. Rafiee
Massachusetts General Hospital
Boston, Massachusetts

M. Hosseiny
Department of Radiology
University of California, San Diego
San Diego, California

F.D. Firouzabadi
Department of Radiology and Imaging Science
National Institutes of Health Clinical Center
Bethesda, Maryland

D.M. Yousem
Russell H. Morgan Department of Radiology and Radiological Science
Johns Hopkins Medical Institution
Baltimore, Maryland

The Nosologic Term "Conversive" Disorder Should Be Abandoned

We found the article by Prodi et al[1] on the usefulness of a multimodal CT protocol in the diagnosis of stroke mimics very interesting. Among the pathologies evaluated is the so-called "conversive disorder," a disorder in which diagnostic imaging was not useful.

The nosologic term "conversive disorder" should be abandoned, and instead the term "functional neurologic disorder" (FND) should be used. Recent research has made it clear that FND is not a rule-out diagnosis but a rule-in diagnosis based on positive physical examination findings.[2] The term conversive disorder implies a psychiatric disease and leads the treating physician to think that there is no structural brain alteration; therefore, there should be no alteration in the diagnostic images. In recent years, it has been established that these patients do have subtle alterations on MR imaging,[3-5] such as smaller volume of the thalamus,[5] an increased cortical thickening in the premotor cortex,[3] and an inverse association between somatoform dissociation and left caudal anterior cingulate cortical thickness.[4]

The emergence of FND as a brain disease with an organic substrate and probable structural alterations should lead us to change the paradigm of the mental-versus-organic dichotomy.

http://dx.doi.org/10.3174/ajnr.A7504

Disclosure forms provided by the authors are available with the full text and PDF of this article at www.ajnr.org.

REFERENCES

1. Prodi E, Danieli L, Manno C, et al. **Stroke mimics in the acute setting: role of multimodal CT protocol.** *AJNR Am J Neuroradiol* 2022;43:216–22 CrossRef Medline
2. Aybek S, Perez DL. **Diagnosis and management of functional neurological disorder.** *BMJ* 2022;376:064 CrossRef Medline
3. Aybek S, Nicholson TR, Draganski B, et al. **Grey matter changes in motor conversion disorder.** *J Neurol Neurosurg Psychiatry* 2014;85:236–38 CrossRef Medline
4. Perez DL, Matin N, Williams B, et al. **Cortical thickness alterations linked to somatoform and psychological dissociation in functional neurological disorders.** *Hum Brain Mapp* 2018;39:428–39 CrossRef Medline
5. Nicholson TR, Aybek S, Kempton MJ, et al. **A structural MRI study of motor conversion disorder: evidence of reduction in thalamic volume.** *J Neurol Neurosurg Psychiatry* 2014;85:227–29 CrossRef Medline

D. A. Lizarazo
A. Guarnizo
Fundación Santa Fe de Bogotá
Universidad El Bosque
Bogotá, Colombia

REPLY:

We thank Drs Lizarazo and Guarnizo for their comment on our article "Stroke Mimics in the Acute Setting: Role of Multimodal CT Protocol."[1]

We acknowledge the comment about the denomination of "functional neurological disorder" (FND) instead of "conversion disorder." Indeed, in *Diagnostic and Statistical Manual of Mental Disorders*, 5th ed, 2022 text revision, terminology has been updated.[2]

FND, previously regarded as a diagnosis of exclusion, is now a rule-in diagnosis that relies on tests with positive findings such as the Hoover test for functional leg weakness and others. Nevertheless, the differential diagnosis versus an acute stroke may be uncertain in the acute setting, leading the clinician to perform an imaging evaluation to rule out stroke.[3]

FND is now considered a multinetwork brain disorder with impairment within and across the limbic system/salience network, self agency, multimodal integration, attention and sensorimotor circuits. Although FND is a clinical diagnosis, neuroimaging has provided evidence of functional and subtle structural brain changes in patients with this disorder, arguing against a strict functional-structural dichotomy in this condition.[4] Nevertheless, these subtle abnormalities (ie, smaller volume of the thalamus, increased cortical thickening in the premotor cortex) cannot be evaluated with a multimodal CT protocol such as in our study.

REFERENCES

1. Prodi E, Danieli L, Manno C, et al. **Stroke mimics in the acute setting: role of multimodal CT protocol.** *AJNR Am J Neuroradiol* 2022;43:216–22 CrossRef Medline
2. American Psychiatric Association. *Diagnostic and Statistical Manual of Mental Disorders*. 5th ed, text revision. American Psychiatric Association, 2022
3. Jones A, O'Connell N, David AS, et al. **Functional stroke symptoms: a narrative review and conceptual model.** *J Neuropsychiatry Clin Neurosci* 2020; 32:14–23 CrossRef Medline
4. Roelofs JJ, Teodoro T, Edwards MJ. **Neuroimaging in functional movement disorders.** *Curr Neurol Neurosci Rep* 2019;19:12 CrossRef Medline

http://dx.doi.org/10.3174/ajnr.A7584

E. Prodi
L. Danieli
Department of Neuroradiology
Neurocenter of Southern Switzerland
Ente Ospedaliero Cantonale
Lugano, Switzerland

C. Manno
Department of Neurology
Neurocenter of Southern Switzerland
Ente Ospedaliero Cantonale
Lugano, Switzerland

A. Pagnamenta
Unit of Clinical Epidemiology
Ente Ospedaliero Cantonale
Bellinzona, Switzerland
Department of Intensive Care Medicine
Ente Ospedaliero Cantonale
Mendrisio, Switzerland
Division of Pneumology
University Hospital of Geneva
Geneva, Switzerland

E. Pravatà
Department of Neuroradiology
Neurocenter of Southern Switzerland
Ente Ospedaliero Cantonale
Lugano, Switzerland
Faculty of Biomedical Sciences
Università della Svizzera Italiana
Lugano, Switzerland

L. Roccatagliata
Department of Health Science
University of Genova
Genova, Italy

C. Städler
C.W. Cereda
Department of Neurology
Neurocenter of Southern Switzerland
Ente Ospedaliero Cantonale
Lugano, Switzerland

A. Cianfoni
Department of Neuroradiology
Inselspital Bern, University of Bern
Bern, Switzerland
Department of Neuroradiology
Neurocenter of Southern Switzerland
Ente Ospedaliero Cantonale
Lugano, Switzerland